8-2019

Effects of Irradiation and Thermal Annealing on the Mechanical and Microstructural Properties of Bulk Metallic Glasses

Jamieson Brechtl
University of Tennessee

To the Graduate Council:

I am submitting herewith a dissertation written by Jamieson Brechtl entitled "Effects of Irradiation and Thermal Annealing on the Mechanical and Microstructural Properties of Bulk Metallic Glasses." I have examined the final electronic copy of this dissertation for form and content and recommend that it be accepted in partial fulfillment of the requirements for the degree of Doctor of Philosophy, with a major in Energy Science and Engineering.

Steven Zinkle, Major Professor

We have read this dissertation and recommend its acceptance:

Peter Liaw, Maik Lang, Kurt Sickafus

Accepted for the Council:

Dixie L. Thompson

Vice Provost and Dean of the Graduate School

(Original signatures are on file with official student records.)

Effects of Irradiation and Thermal Annealing on the Mechanical and Microstructural Properties of Bulk Metallic Glasses

A Dissertation Presented for the

Doctor of Philosophy

Degree

The University of Tennessee, Knoxville

Jamieson Michael Brechtl

August 2019

ACKNOWLEDGEMENTS

First and foremost, I would first like to thank my advisor, Dr. Steven Zinkle, for all his advice, support, and inspiration throughout my doctoral studies. This experience has definitely made me a better researcher and experimentalist. I would also like to personally thank the rest of my doctoral committee, Dr. Peter Liaw, Dr. Kurt Sickafus, and Dr. Maik Lang, for their thought-provoking discussions in addition to their excellent guidance and support. I would also like to especially thank my group's research members that helped me throughout my graduate career, including Dr. Shradha Agarwal, Dr. Tengfei Yang, Dr. Congyi Li, Dr. Kelsa Benensky, Dr. Caleb Massey, Peter Doyle, Ling Wang, Yan-Ru Lin, Tyler Smith, Adrien Terricabras, Yajie Zhou, and Pengcheng Zhu. I also enjoyed collaborating with all the rest of Zinkle's research group members as it was a pleasure to exchange ideas.

I would also like to extend a very special thank you to Dr. Liaw's research group with regards to my journey into the analysis of serrated flow and other fluctuating phenomena. These members include Dr. Xie Xie, Dr. Shuying Chen, Dr. Bilin Chen, Dr. Haoyan Diao, Chanho Lee, Peiyong Chen, Xuesong Fan, Rui Feng, Yunzhu Shi, and Zhong Wang. A special thanks to Dr. Rawn's group at the Joint Institute for Advanced Materials for helping me perform my X-ray diffraction experiments. These people include Dr. Michael Koehler and Dr. John Salasin. I am also indebted to Dr. Bill Weber and Dr. Miguel Crespillo for access to the Ion Beam Materials Laboratory. A very special thanks to Dr. Crespillo for tirelessly operating the ion beam accelerator, since without him I would not have been able to conduct my ion irradiation experiments.

I would also like to personally thank the staff at Oak Ridge National Laboratory for their help with my experimental work. A special thanks to Dr. Maxim Gussev for his help with nanoindentation and bend test experiments. Also, much thanks to Dr. Hongbin Bei for sample

fabrication. I am also eternally grateful to the technical staff at Oak Ridge for their hard work and dedication with regards to sample preparation for my neutron irradiation experiments. These people include Josh Schmidlin, Michael McAlister, Luis Mora, Bill Comings, Patricia Tedder, Stephanie Curlin, James Dixon, Brian Eckhart, and Jesse Werden. Furthermore, I am very thankful for Dr. Egami, Dr. Wojiech Dmowski, Dr. Joerg Neuefeind, and Dr. Michelle Everett for their guidance and help with regards to the neutron diffraction experiments. I would also like to sincerely thank Hui Wang for performing the in situ X-ray diffraction experiments at Argonne National Laboratory. It was also a pleasure receiving guidance from Dr. Alex Perez-Bergquist and Dr. N.A.P. Kiran Kumar during their tenure at the laboratory. Finally, I would like to thank Dr. Chad Parish for giving me excellent advice regarding transmission electron microscopy characterization techniques.

As for the helium diffusion experiments, I am very indebted to the staff at the Center for Integrated Nanotechnologies at Los Alamos National Laboratory. In particular, I am deeply thankful to Dr. Yongqiang Wang and Dr. Shradha Agarwal for the planning and preparation of the experimental work and assistance in performing the experiments. Further thanks to Matthew Chancey for his outstanding efforts in operating the nuclear reaction analysis beamline and Dr. Di Chen for performing the transmission electron microscopy characterization on the implanted samples. Finally, much thanks to Dr. Xunxiang Hu for performing the thermal desorption spectroscopy experiments and aiding in the data analysis.

To all, I will be forever grateful that you took the time out of your schedules to help me succeed.

ABSTRACT

A series of ion irradiation and annealing experiments have been performed on $Zr_{52.5}Cu_{17.9}Ni_{14.6}Al_{10}Ti_5$ "BAM-11" and $Cu_{60}Zr_{20}Hf_{10}Ti_{10}$ bulk metallic glass (BMG) specimens to evaluate their irradiation- and temperature-induced microstructural and mechanical property evolution. These experiments covered four main themes, namely, ion irradiation, neutron irradiation, thermal annealing, and helium implantation. For the ion irradiations, samples were exposed to 9 MeV Ni and 5.5 MeV C ions at temperatures ranging from room temperature to 360 ^{o}C. For the Ni ion irradiations the samples were exposed to midrange (~1.5 μm depth) doses of 0.5 and 10 displacements per atom (dpa), while the C ion irradiations samples were irradiated to a midrange dose of 0.5 dpa. For the neutron irradiations, samples were irradiated by neutrons (E > 0.1 MeV) at ~70 ^{o}C to fluences of 1.4×10^{20} n/cm^2 and 1.4×10^{21} n/cm^2 (doses of 0.1 and 1 dpa). Thermal annealing experiments involved heating the samples to various temperatures ranging from 25 - 770 ^{o}C. For the helium implantation experiments, amorphous and partially crystallized BMGs were exposed to helium fluences of 2×10^{15} and 5×10^{15} cm^{-2}. The mechanical property and microstructural characterization included nanoindentation, compression testing, bend testing, X-ray diffraction (XRD), neutron diffraction, thermal desorption analysis (TDS), and nuclear reaction analysis. From the experiments, several important conclusions were obtained. The results of the XRD and nanoindentation characterizations of the ion irradiated and thermal annealed specimens indicate good stability during irradiation at 25 to 290 ^{o}C up to at least 10 dpa but suggest that the BAM-11 BMG is not suitable for irradiation environments where temperatures exceed 300 ^{o}C for prolonged periods of time. As for the neutron irradiation and thermal annealing experiments, significant softening was observed in the sample irradiated by neutrons, while post-irradiation annealing led to a marked increase in hardening. Neutron diffraction results indicated

that primary knock-on events caused rejuvenation (disordering) while annealing resulted in structural relaxation. The results of the TDS experiments found that for the lower He implantation fluence, He desorbed more quickly in the partially crystallized alloy, indicating a structural effect on the mobility of He.

TABLE OF CONTENTS

LIST OF TABLES

LIST OF FIGURES

CHAPTER 1 INTRODUCTION

1.1 Nuclear Fusion Energy

The future of the world will depend on the generation of energy that is both environmentally sustainable and economically viable [1]. One source of energy that can meet both requirements is nuclear fusion, which relies on the fusing of smaller atoms to generate power [2]. Decades after the discovery of Einstein's famous mass-energy equivalence principle [3-6], scientists began pondering whether energy could be harnessed not only from the breaking apart of atoms [7], but also by fusing them together [8]. The fusion process typically involves light particles such as deuterium and tritium, and can be succinctly described by the following equation [9]:

$$ {}_{1}^{2}D + {}_{1}^{3}T \rightarrow {}_{2}^{4}He + {}_{0}^{1}n \quad ; \quad Q = 17.59\ MeV \tag{1-1} $$

where D is the deuteron, T is the tritium, He is the helium, n is the neutron, and Q is the energy released (in the form of heat) as a byproduct of the reaction. To overcome the coulombic repulsive forces of the fusing nuclei requires kinetic energies on the order of ~20 keV to achieve the fusion reaction rates appropriate for commercial energy production [1]. The above energy corresponds to fuel temperatures exceeding ~2×10^8 ^{o}C. Interestingly, this type of reaction is exactly what happens in the sun on a regular basis. Thus, scientists are trying to obtain the equivalent of the philosopher's stone in the modern age, that is, to harness the power of a star inside a facility that is no larger than a typical sports arena.

The resultant heat of the reaction then transforms a working fluid circulating past the reactor core into steam which drives a turbine. The motion of the turbine produces electrical energy which is used to power nearby residential areas or other infrastructure. It is estimated that

the fusion of one gram of hydrogen equals the thermal energy released from burning ~ 5,000 gallons of gasoline or 20 tons of coal [10]. From the above statement, one can clearly see how important this vital source of energy will be as the amount of available fossil fuel dwindles in the coming years.

One of the earliest fusion reactor concepts was the Tokamak, as proposed by Sakharov in 1952 [11]. A schematic of the tokamak is displayed in figure 1-1 [12]. As can be seen, the tokamak consists of various components, which include transformer coils that induce the toroidal current, and outer poloidal field coils that position and shape the plasma. Furthermore, the toroidal plasma current, which is induced by the behavior of the transformer, produces the poloidal magnetic field current which flows in the plasma. For more details on the basics of Tokamak reactors, please see [13-16].

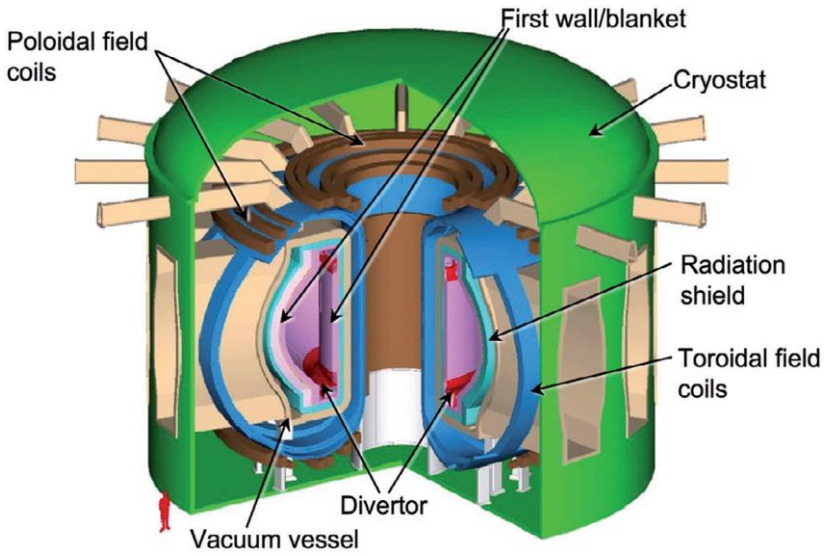

Figure 1-1 Schematic of a tokamak. The toroidal current is induced by a transformer and the outer poloidal field coils are used to manipulate and shape the plasma (from Ref. [12]).

More recently, ITER [17] was created as an ambitious energy project with the intent of building the world's largest tokamak. One goal of the project will be to produce 500 MW of power from only 50 MW of input heating power (Q = 10). As a comparison, the TFTR device in the USA achieved a Q value of 0.27 in the mid 1990's [18]. Figure 1-2 presents a cross-section of the ITER tokamak, which includes the position dependent total neutron fluxes and a comparison of the calculated fast neutron fluences for several key components in ITER and in a demonstration fusion reactor [18]. It should also be stated that the results of the position-dependent total neutron fluxes were based on the work of R. Feder & M. Youssef, while the neutron fluences for several key components in ITER were based on input from M. Sawan.

a

ITER: lifetime fast neutron fluence (n/m^2; $E > 0.1$ MeV)	DEMO fusion power reactor: annual fast neutron fluence (n/m^2; $E > 0.1$ MeV)	Component
3.7×10^{21}	5×10^{22}	Blanket
5.1×10^{14}	7×10^{15}	Magnet
1.9×10^{21}	2.6×10^{22}	Divertor
1.1×10^{19}	1.5×10^{20}	Vacuum vessel
3.4×10^{11}	4.5×10^{12}	Cryostat

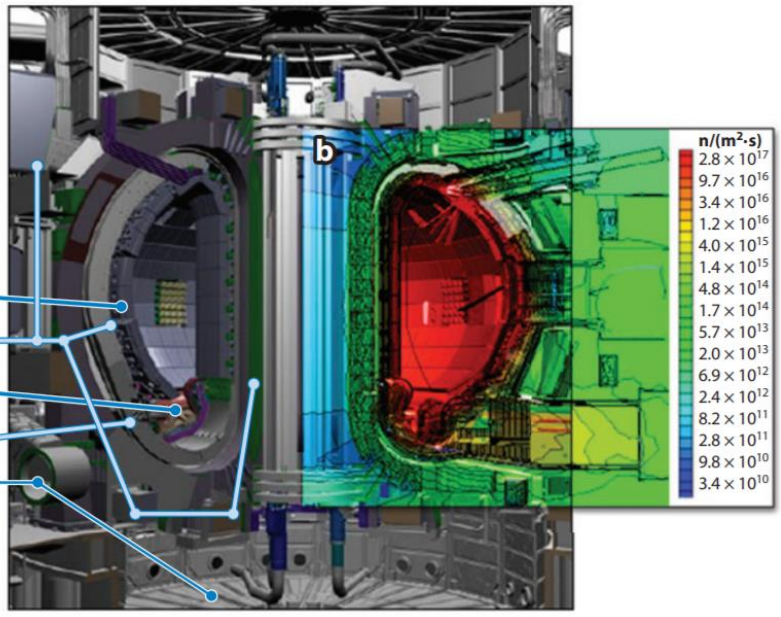

Figure 1-2 View of the neutronics of the ITER tokamak with (a) a comparison of the calculated fast neutron fluences for several key components in ITER and in a demonstration fusion reactor and (b) the position-dependent total neutron fluxes (from Ref. [18]).

1.2 Material Challenges in Fusion Energy Systems

Similar to nuclear fission energy systems, which are subject to a host of material degradation issues such as swelling, stress corrosion cracking, and fuel-cladding chemical interactions [19-26], numerous factors must be considered in the selection of structural materials for fusion energy systems. These factors include material cost and fabricability, mechanical and thermophysical properties, radiation effects (degradation of properties), chemical compatibility and corrosion issues, and nuclear properties [27]. Inside the region where the plasma flows, the facing material must be able to perform various functions [11]. These roles include sustaining the impact of the energetic particles associated with the plasma, transfer a heat load ranging from 0.5 to 1 MW/m^2 emanating from the plasma to a cooling medium, and be able to withstand high heat loads associated with anomalous behavior such as disruptions, and to minimize the tritium retention.

In addition, structural materials must operate at elevated temperatures for extended lifetimes under severe conditions, including high fluxes of high energy (14 MeV) neutrons [28]. These materials will be submitted to a high heat flux of energetic particles (0.1-20 MW/m^2), high temperatures (775-3475 K), electromagnetic radiation, sputtering erosion, blistering and exfoliation, and high levels of neutron-irradiation (3-30 dpa/year) [29]. A summary of the possible types of interactions between energetic particles comprising the fusion plasma and exposed material is displayed in figure 1-3 [18, 30]. As can be seen, the above process is of a very complex nature and can be extremely deleterious to the plasma facing components (PFCs). The underlying interactions of this process include ion implantation, sputtering, surface atom recombination, and chemical removal arising from electron exchange between the material and the ion. Importantly,

this type of exposure, over time, can lead to localized erosion and surface buildup in different regions on PFC surfaces [18, 30-32].

Furthermore, the materials must be able to withstand exposure to a combination of intense neutron irradiation and high heat and particle fluxes [30, 32, 33]. Additionally, neutrons that are produced as a byproduct of the fusion reaction (see Eq. 1.1) inevitably encounter the surrounding materials. As they travel through the matrix, energy is transferred through inelastic collisions with the surrounding atoms [34]. These interactions introduce a wide range of temperature-dependent microstructural alterations and changes in material properties, as summarized in figure 1-4, including dislocation loops and phase formation (hardening/embrittlement), and void swelling.

Over time, these events can lead to the buildup of deleterious effects in the alloy and perhaps even failure. For instance, neutron irradiation in the BOR-60 fission reactor up to doses of 5 and 7 dpa at irradiation temperatures of 335 ^{o}C and 345 ^{o}C, respectively, resulted in disastrous embrittlement of pure copper when mechanically tested at $\geq$ 300 ^{o}C [35, 36]. It was found that the drop in plasticity was accompanied by the transition to a brittle intergranular fracture [35].

In addition to the facing components, nonstructural materials will must be able to function while exposed to irradiation at a wide range of temperatures [1]. Applications for these materials include insulators (electrical and thermal), windows, diagnostic sensors, plasma heating feedthroughs and cabling, and the constituents of superconducting magnets [37-39]. Importantly, materials in these situations are operating at temperatures that are much lower than their melting point, which limits their ability to thermally recover from radiation damage due to reduced defect mobility [1].

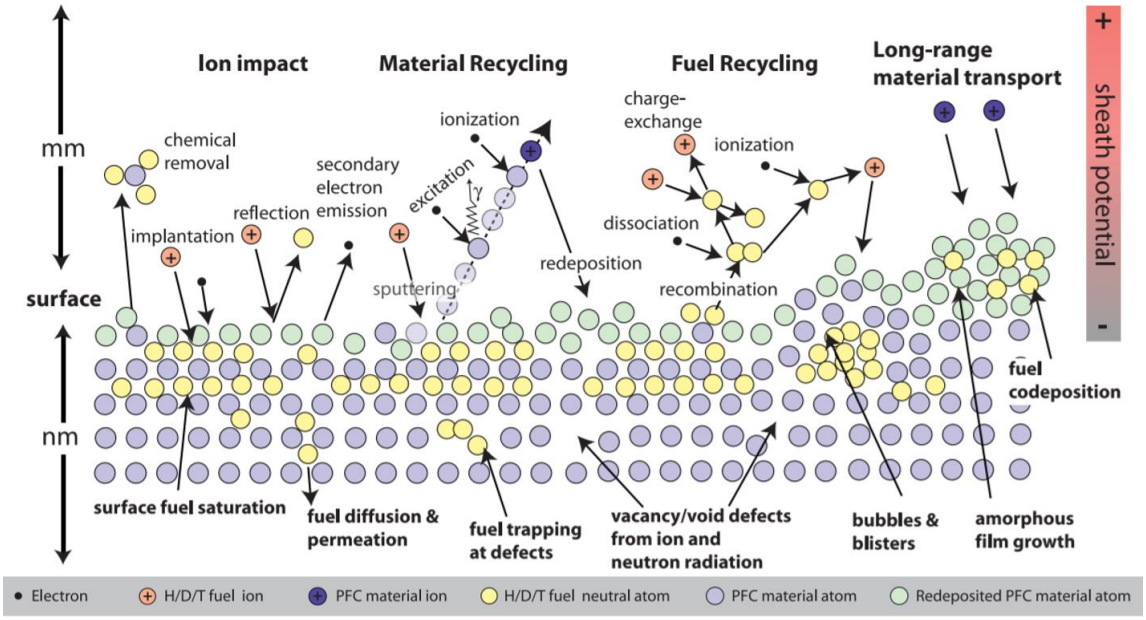

Figure 1-3 Schematic illustration of the complex plasma-surface interactions which involve the contact of gamma ray, hydrogen, deuterium, and tritium (each denoted γ, H, D, and T, respectively) with near-surface lattice (from Ref. [18, 30]).

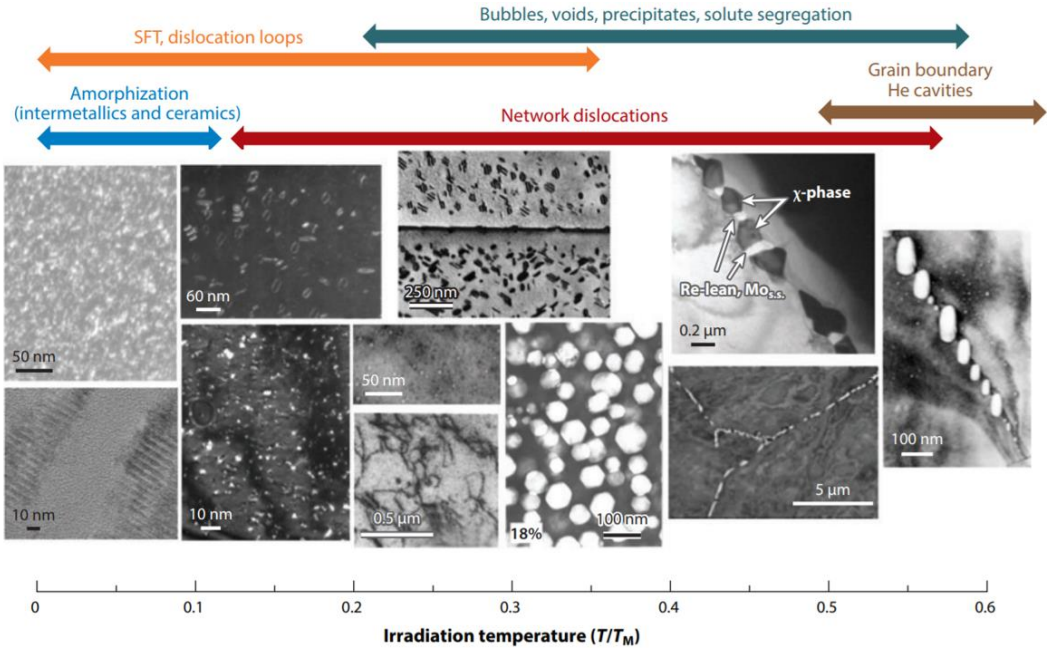

Figure 1-4 A showcase of potential microstructures in materials exposed to irradiation displacement damage in various temperature regimes. Here, SFT denotes stacking fault tetrahedra (from Ref. [1]).

1.3 Helium Embrittlement in Fusion Reactor Materials

Currently, one of the major impediments for materials in fusion environments involves helium retention. Helium, when trapped in a material over time, can lead to deleterious effects such as embrittlement and swelling. During neutron irradiation, virtually all elements in reactor materials (such as stainless steel) produce helium to some degree via (n, α) reactions [40]. In reactor cladding, for example, He is formed through a two-step reaction involving thermal neutrons and Ni [23]:

$$Ni^{58} + n^{1} \rightarrow Ni^{59} \tag{1-2}$$

$$Ni^{59} + n^{1} \rightarrow Fe^{56} + He^{4} \tag{1-3}$$

After production, He remains insoluble in the matrix, where it can form bubbles with vacancies and other He atoms. It has also been shown that helium bubbles are precursors to void formation in an alloy [41]. Furthermore, He is a huge issue for reactor materials due to its interactions with crystalline defects such as grain boundaries and dislocations. For example, He atoms diffuse to grain boundaries once the temperature of the material reaches ~ 0.5 T_m, where they become trapped [42]. Once the He is trapped, applied stresses can lead to bubble growth and subsequent swelling. Figures 1-5 (a)-(c) and 1-6 (a)-(c) compares the growth of helium bubbles in Fe-12Cr-17Ni (weight %), as observed in transmission electron microscopy (TEM), of austenitic stainless steel foil specimens (0.12 mm thick) after annealing at 750 ^{o}C with and without an applied stress. The compressive stress was 19.6 MPa and while the annealing times ranged from 2.88 × 10^4 s to 2.16

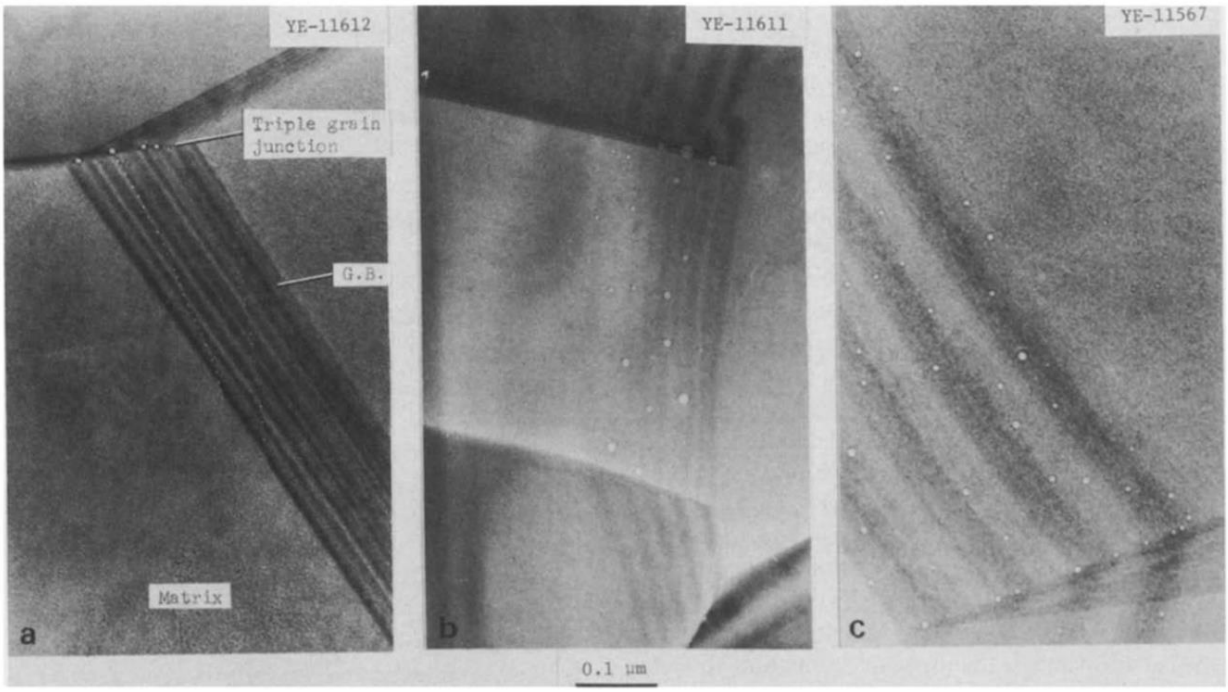

Figure 1-5 Growth of helium bubbles in unstressed Fe-17Cr-17Ni (wt. %) specimens after annealing at 750 ^{o}C for (a) 2.88×10^4 s, (b) 6.48×10^4 s and (c) 2.16×10^4 s (from Ref. [43]).

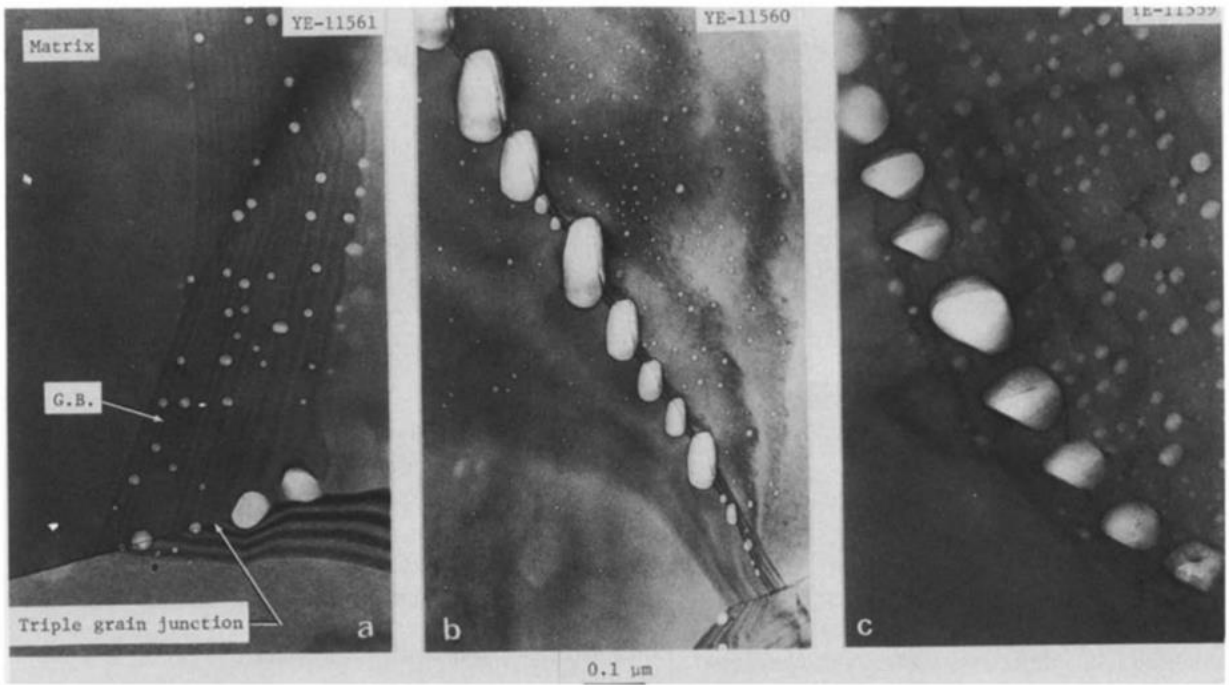

Figure 1-6 Growth of helium bubbles in Fe-17Cr-17Ni (wt. %) after annealing at 750 ^{o}C with a stress of 19.6 MPa for (a) 2.88×10^4 s, (b) 6.48×10^4 s, and (c) 2.16×10^5 s (from Ref. [43]).

$\times 10^5$ s [43]. The He content of the implanted foils ranged from 73 to 180 atomic parts per million (appm). As can be seen in the figures, the bubbles were orders of magnitude larger for the tensile loaded specimens as compared to the non-stressed samples.

Helium can become a problem over time as it can lead to embrittlement and enhanced cavity swelling. Woodford et al. suggested that He induces embrittlement by hampering dislocation motion [44]. Here the impedance of dislocation lines leads to an increased strength in the material which prevents relaxation of stress concentrations at the grain-boundary triple points. Unfortunately, a lack of stress relaxation at these points leads to enhanced failure via the propagation of wedge cracks [43]. An example of helium induced embrittlement can be seen in figure 1-7 [45]. The embrittled material was gas tungsten arc welded neutron irradiated 304 stainless steel (fast neutron fluence 1.0×10^{16} - 7.6×20^{20} n/cm^2) that produced measured helium concentrations from 0.85 to 12.0 appm helium. It was found that the retained helium, when combined with the increased weld heat input, resulted in a greater amount of cracking in the weld.

There is significant research being performed to gain further knowledge on the behavior of materials when exposed to transmutant helium levels that are typical of fusion reactor first-wall and blanket structures [46, 47]. Figure 1-8 summarizes the capabilities of several prior, current and proposed irradiation facilities for production of transmutant helium in 9-14%Cr reduced-activation ferritic/martensitic (RAFM) steels as a function of the displacement damage level [1]. As indicated in this figure, these materials in fusion systems will be exposed to 50-100 times the amount of He/dpa in demonstration (DEMO) fusion reactors as compared to in conventional fission reactors.

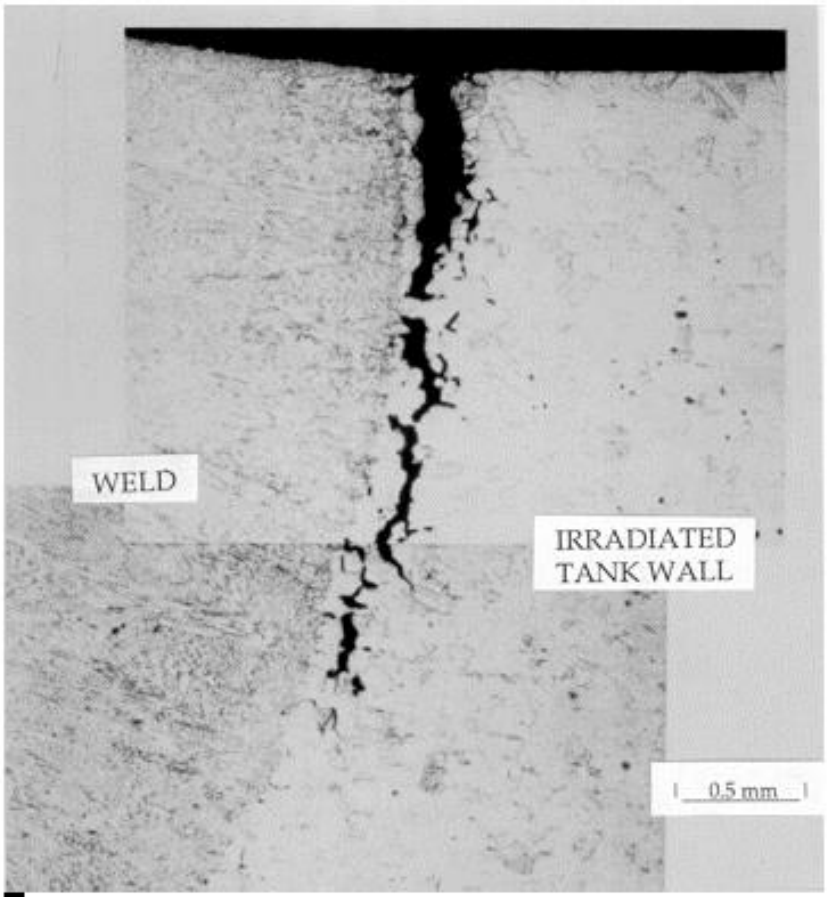

Figure 1-7 Conventional gas tungsten arc weld on irradiated 304 stainless steel containing 1.5 appm helium (from Ref. [45]).

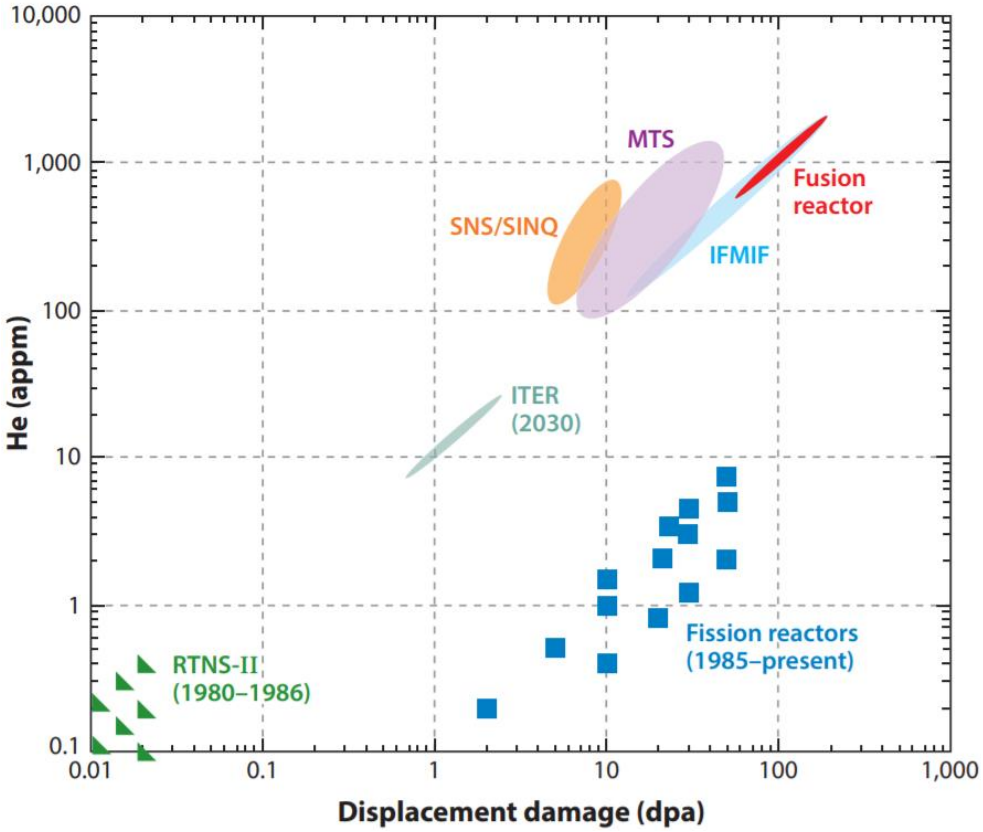

Figure 1-8 Summary of the RAFM steel experimental database in terms of transmutant He versus displacement damage in various nuclear reactor technologies (from Ref. [1]).

1.4 Recently Proposed Material Systems for Fusion Reactor Technology

Based on the discussion above, it can be said that the viability of fusion power technology will be largely dependent on the development of high-performance, reduced activation materials [48-52]. A major step that will help accomplish this goal will be to develop structural materials with simultaneous improvements in strength and radiation resistance without any degradation in ductility or fracture toughness [18]. Recently, more advanced materials such as oxide-dispersion strengthened (ODS) steels [53-58], high entropy alloys (HEAs) [59-69], and bulk metallic glasses

(BMGs) [70] have been proposed as viable candidate in fusion systems. The purpose of the next section will be to introduce the reader to BMGs.

1.5 Bulk Metallic Glasses

The first bulk metallic glass (BMG), which was developed by Chen in 1974, was composed of palladium, copper and silicon and required a cooling rate of 10^3 K/s [71]. Results of the study indicated that glasses containing atoms of different sizes increased the glass forming ability of the alloy. It was theorized that the increased glass forming ability arose from the strong interactions between unlike atoms, which lowered the melting temperature and raised the glass transition temperature. Furthermore, the addition of metalloids such as silicon appeared to distort the short-range order of the metallic glass, leading to the high stability of its bulk form.

More recently, BMGs with diameters that exceed the micrometer-thicknesses in the 1960s have been produced [72]. For example, $Pd_{40}Cu_{30}Ni_{10}P_{20}$ BMG was fabricated using a cooling rate of only 0.1 K/s [73], with a corresponding diameter of 7.2 cm. It is important to note that the required cooling rate is 4 orders of magnitude lower as compared to the BMG that was produced by Chen. In the past few years, additive manufacturing methods have been used to successfully produce BMGs [74-76]. For instance, a direct metal laser sintering process was used to fabricate fully amorphous FeCrMoCB BMG whose thickness was more than 15 times the critical casting thickness (3 mm) in all dimensions [74].

Figure 1-9 shows schematically the structure formation during quenching from the melt by the time–temperature phase transition diagram [71]. The parabolic curves in the middle of the graph arise from the competition between the increasing driving force for crystallization and the slowing down of atomic kinetics [77]. To prevent the transition from a liquid to a crystalline phase

the melt must be cooled at rates such as those mentioned above. If a sufficiently fast cooling rate is achieved, the liquid melt can reach its glass transition temperature T_g, where it will transition into a glassy structure.

Inoue determined that there are three empirical rules which lead to high glass-forming ability (GFA) in supercooled liquids [78]. The first rule is that a multicomponent system must have more than three elements. For instance, the quaternary BMG alloy $Pd_{40}Cu_{30}Ni_{10}P_{20}$ can be formed with a cooling rate of 0.10 K/s. This rate is 4 orders of magnitude lower than the rate required to form the alloy procured by Chen [77]. The second rule is that the size difference between the three main constituent atoms must be at least 12 %. The first and second rule leads to what is known as the "confusion principle", where the number of atoms and mismatch in sizes lead to poor bonding. The poor bonding between atoms inhibits the formation of crystal structure and consequently lowers the cooling rate required for amorphization [79]. The third rule for GFA is negative heats of mixing among the three main constituent elements.

In terms of material properties, BMGs possess excellent properties such as high hardness [80, 81], high strength [82, 83], exceptional corrosion resistance [84-86], good fatigue resistance [87-90], high fracture strength [78, 91], and excellent magnetic properties [92, 93]. BMGS do not work harden like crystalline alloys, and exhibit deformation in the form of shear bands [94]. It is interesting to note that although the percent strain within a shear band is quite large, it does little to contribute to the overall plastic strain [95]. Furthermore, shear bands correspond to server localization of plastic deformation. When combined with the lack of dislocations and slip systems in BMGs, these factors result in undesirable effects on their post-yield plastic deformation [96].

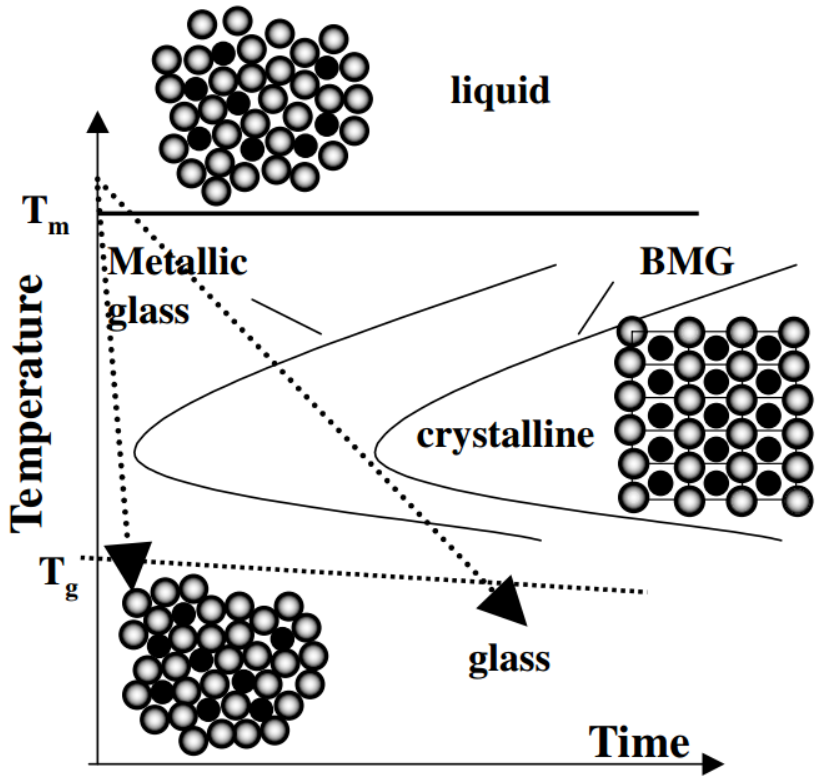

Figure 1-9 Schematic time–temperature-transition diagram of structure formation during quenching from the melt (from Ref. [71]).

Consequently, these materials exhibit virtually no tensile ductility and catastrophic failure after yielding, which are undesirable features for structural materials.

A lack of crystalline structure in metallic glass leads to an absence of crystal defects such as twin boundaries, grain boundaries, or dislocations [79]. Furthermore, this lack of crystalline structure in amorphous alloys may provide substantial advantages in terms of radiation resistance,since the concept of vacancies and interstitials does not apply to amorphous materials. Although irradiation has been found to produce point defects and macroscopic changes in amorphous materials in a manner similar to what happens in crystalline alloys [97, 98], there is

some evidence that the amount of retained displacement damage can be significantly less in amorphous materials [70].

Another factor which may make amorphous metals desirable is their potentially high helium permeability due to their large free atomic volume and lack of grain boundaries which can act as helium traps [99]. In contrast to crystalline alloys, metallic glasses do not possess defects such as dislocations and grain boundaries due to their amorphous structure [49]. This lack of conventional defects should in theory prohibit the formation of large He bubbles in the material. Furthermore, the free volume content of amorphous alloys should lead to a higher diffusivity of He in the material. The higher diffusivity should lead to a faster escape of He from the material, which will lead to reduced swelling in the material. This superior resistance to He-induced cavity formation and high diffusivity has been verified in at least one amorphous material [100].

This higher diffusivity would potentially give metallic glasses an advantage over crystalline materials since He is a huge issue in nuclear reactors due to its ability to embrittle and swell reactor materials. This lack of entrapped He in BMGs could lead to good resistance to cavity swelling at elevated temperatures. If a high density of cavities is not present, the amount of tritium trapped in the bulk metallic glass under prototypic fusion reactor conditions might also be very low [1] . Therefore, it can be surmised that bulk metallic glasses could be a viable material for use in different components of a fusion reactor such as piping, breeding blanket structure or the reactor pressure vessel, given that the surrounding temperature remains below the glass transition.

A key aspect for achieving BMGs with sufficient radiation resistance will be to identify amorphous atomic configurations that can withstand irradiation induced bond rearrangements. Therefore, an important stability criterion for amorphous materials is the potential, or lack thereof,

for radiation-induced recrystallization [101]. Interestingly, it has been found that different BMG alloys may not experience the same volumetric change under the same irradiation condition [99]. Specifically, two different alloys may undergo volumetric expansion, minimal change, or contraction during irradiation.

1.6 Research Goals

The purpose of this thesis research is fourfold. First, the project will perform fundamental science to understand whether the BMG short range atomic configuration is changed by energetic atomic mixing (i.e., is the BMG in its lowest energy configuration, or does particle irradiation mixing introduce metastable configurations). Second, it will explore the radiation effects in a material where the conventional radiation defects such as vacancies and self-interstitial atoms are not produced. Third, the project will examine the effects of increased free volume and lack of grain boundaries on helium diffusion in BMGs. Fourth, this investigation will examine the microstructural and mechanical response of BMGs when exposed to different thermal and irradiation spectrum environments.

1.7 Thesis Outline

This thesis consists of six chapters, including a literature review of prior radiation effects studies on BMGs that will be discussed in chapter 2. Chapter 3 discusses the experimental techniques utilized for the investigations on the irradiation and thermal response completed for this thesis. Chapter 4 provides the detailed results and the corresponding analysis of the experimental data while chapter 5 provides a discussion of the results. Finally, chapter 6 details

the conclusions arising from the outcome of the experiments and outlines some recommendations for future research projects.

CHAPTER 2 LITERATURE REVIEW

2.1 Atomic Structure of Metallic Glasses

The atomic arrangements of an amorphous solid resemble that of a liquid more than a crystalline solid. Figure 2-1 compares the radial distribution function (RDF) between the liquid, solid and amorphous solid phases [102]. As can be seen, the amorphous structure has a similar radial distribution function to that of the liquid phase. Furthermore, the left figure shows how the radial distribution function relates to the geometric spacing of the atoms in the metal. The area under each curve represents a shell consisting of a number of atoms within a distance of r and r + dr. Zhang et al. calculated the average atomic radii of different amorphous alloys [103], which are listed in Table 2-1. As can be seen, the average atomic radius ranges from 1.4 – 2.0 Å.

In addition, an amorphous metal is composed of a random distribution of different sized polyhedra. The theory of polyhedral clustering dates back to the work of Bernal, who investigated the atomic structure of liquids [104-106]. Bernal determined that when atoms are arranged in one of five specific types of polyhedra, long range order can be prevented. The five types of polyhedra which inhibit the long-range ordering can be seen in figures 2-2(a)-(e), and are the tetrahedron, the octahedron, the trigonal prism, the Archimedean antiprism, and the tetragonal dodecahedron [104]. Bernal also found that the irregularity of the neighborhood polyhedra is the essential condition for liquid as against crystalline structures [105].

Although Bernal's model is satisfactory for monoatomic metals and alloys which have atoms of comparable size, it does not account for the observed short range or medium range order (SRO and MRO, respectively) in metallic glasses [107]. Here short range is defined as 1-2 nearest neighbors of an atom while medium range order is approximately 1-1.5 nm [108]. In contrast to Bernal's model however, atom sizes must differ by at least 12 % to produce stable multicomponent bulk metallic glasses [78].

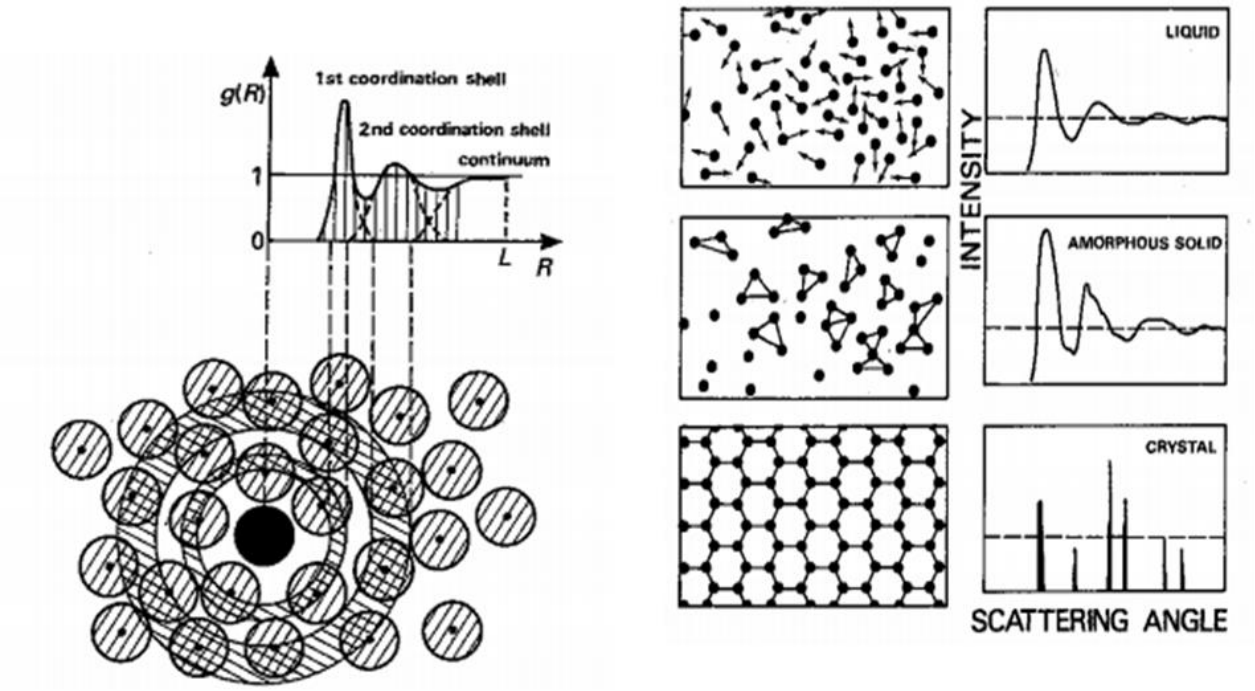

Figure 2-1 Left: Relationship between radial distribution function and atomic spacing in an amorphous solid. Right: Pictorial representation of atom distribution in matter with their expected typical diffraction patterns (from Ref. [102]).

Table 2-1 Average atomic radii of select amorphous alloys (from Ref. [103]).

Composition (at. %)	Average atomic radii (Å)	Composition (at.%)	Average atomic radii (Å)
$Zr_{62}Cu_{15.4}Ni_{12.6}Al_{10}$	1.67	$Fe_{70}Mo_5Ni_5P_{12.5}C_5B_{2.5}$	1.40
$Zr_{59}Ta_5Cu_{18}Ni_8\ Al_{10}$	1.67	$Fe_{61}Mn_{10}Cr_4Mo_6Er_1C_{15}B_6$	1.40
$Zr_{41.2}Ti_{13.8}Cu_{12.5}Ni_{10}Be_{22.5}$	1.58	$Pd_{64}Ni_{16}P_{20}$	1.44
$Cu_{47.5}Zr_{47.5}Al_5$	1.61	$Pt_{57.5}Ni_5Cu_{14.7}P_{22.8}$	1.49
$Cu_{60}Zr_{20}Hf_{10}Ti_{10}$	1.56	$Pt_{60}Ni_{15}P_{25}$	1.50
$(Ti_{0.5}Cu_{0.5})_{84}Ni_7Hf_5Zr_3Si_1$	1.54	$Ni_{60}Nb_{35}Sn_5$	1.50
$Ni_{62.5}Zr_{20}Nb_{15}Pd_{2.5}$	1.52	$Ni_{60}(Nb_{0.8}Ta_{0.2})_{34}Sn_6$	1.50
$Ni_{60}Zr_{20}Nb_{15}Pd_5$	1.52	$Zr_{50}Cu_{50}$	1.51
$Ni_{57.5}Zr_{20}Nb_{15}Pd_{7.5}$	1.52	$Zr_{48}Cu_{48}Al_4$	1.60
$Ni_{55}Zr_{20}Nb_{15}Pd_{10}$	1.53	$Ca_{65}Mg_{8.54}Li_{9.96}Sn_{16.5}$	1.61
$Ni_{52.5}Zr_{20}Nb_{15}Pd_{12.5}$	1.53	$Ca_{65}Mg_{8.31}Li_{9.69}Sn_{17}$	2.00
$[(Fe_{0.8}Co_{0.1}Ni_{0.1})_{0.75}B_{0.2}Si_{0.05}]_{96}Nb_4$	1.40	$Yb_{62.5}Mg_{17.5}Cu_5Zn_{15}$	2.00
$[(Fe_{0.6}Ni_{0.4})_{0.75}B_{0.2}Si_{0.05}]_{96}Nb_4$	1.40	$Ce_{70}Al_{10}Ni_{10}Cu_{10}$	1.97
$Fe_{76}Si_{9.6}B_{8.4}P_6$	1.47	$(Ce_{20}La_{80})_{68}Al_{10}Cu_{20}Co_2$	1.89
$(Fe_{0.76}Si_{0.096}B_{0.084}P_{0.06})_{99.9}Cu_{0.1}$	1.47	$Ce_{68}Al_{10}Nb_2Cu_{20}$	1.88
$Zr_{65}Cu_{10}Ni_{10}Al_{10}$	1.67	$(Ce_{80}La_{20})_{68}Al_{10}Cu_{20}Co_2$	1.88
$Zr_{64.13}Cu_{15.75}Ni_{10.12}Al_{10}$	1.67	$Ce_{68}Al_{10}Co_2Cu_{20}$	1.88
$Zr_{61.88}Cu_{18}Ni_{10.12}Al_{10}$	1.66	$Ce_{68}Al_{10}Ni_2Cu_{20}$	1.87
$Zr_{55}Cu_7Co_{19}Al_{19}$	1.66	$La_{60}Al_{20}Co_{20}$	1.87
$Zr_{57}Cu_{15.4}Nb_5Al_{10}Ni_{12.6}$	1.66	$Dy_{55}Al_{25}Co_{20}$	1.85
$Zr_{57}Cu_{20}Ti_5Al_{10}Ni_8$	1.66	$Pr_{55}Al_{25}Co_{20}$	1.78
$Au_{49}Ag_{5.5}Pd_{2.3}Cu_{26.9}Si_{16.3}$	1.63	$Tb_{55}Al_{25}Co_{20}$	1.82
$(Zr_{0.59}Cu_{0.22}Ti_{0.06}Ni_{0.13})_{85.7}Al_{14.3}$	1.62	$Ho_{55}Al_{25}Co_{20}$	1.78
$Zr_{45}Cu_{45}Gd_3Al_7$	1.62	$Er_{55}Al_{25}Co_{20}$	1.76
$Au_{55}Cu_{25}Si_{20}$	1.62	$Tm_{55}Al_{25}Co_{20}$	1.75
$Zr_{54}Cu_{46}$	1.60	$Tm_{39}Y_{16}Al_{25}Co_{20}$	1.75
$Zr_{46.75}Ti_{8.25}Cu_{10.15}Ni_{10}Be_{27.25}$	1.59	$Lu_{39}Y_{16}Al_{25}Co_{20}$	1.75
$Zr_{41}Ti_{14}Cu_{12.5}Ni_{10}Be_{22.5}$	1.57	$Lu_{45}Y_{10}Al_{25}Co_{20}$	1.74
$Zr_{48}Fe_8Cu_{12}Nb_8Be_{24}$	1.59	$Lu_{55}Al_{25}Co_{20}$	1.74
$Ni_{45}Zr_{25}Ti_{20}Al_{10}$	1.56	$Mg_{65}Cu_{25}Gd_{10}$	1.74
$Pd_{77.5}Cu_6Si_{16.5}$	1.56	$Mg_{65}Cu_{25}Y_9Gd_1$	1.71
$Pd_{60}Cu_{20}P_{20}$	1.51	$Mg_{65}Cu_{25}Y_{10}$	1.70
$Pd_{40}Cu_{40}P_{20}$	1.50	$Mg_{65}Cu_{25}Y_8Gd_2$	1.70
$Pd_{39}Ni_{10}Cu_{30}P_{21}$	1.47	$Mg_{65}Cu_{25}Y_5Gd_5$	1.69
$Fe_{53}Cr_{15}Mo_{14}Er_1C_{15}B_6$	1.47	$Mg_{65}Cu_{25}Tb_{10}$	1.68
$Fe_{74.5}Mo_{5.5}P_{12.5}C_5B_{2.5}$	1.47		

Inoue classified bulk metallic glasses into three types, namely, metal-metal-type alloys, metal-metalloid-type alloys, and the Pd-metalloid-type alloys [78]. The atomic configurations for the three structures are shown in figure 2-3 [109]. As can be seen, the three different types of metallic glasses have distinct structures containing different morphologies. In the metal-metal alloy, high-resolution transmission electron microscopy (TEM), X-Ray diffraction (XRD) and neutron diffraction studies reveal that the glass consists of icosahedral clusters [110-113].

For the metal-metalloid-type glassy alloys, a network of atomic configurations consisting of trigonal prisms which are connected with each other through glue atoms comprising Zr, Nb, Ta or lanthanide metal are commonly found [113]. It has been found that the chemical short range ordering in these types of alloys are pronounced [107, 114]. Furthermore, the Pd-based BMGs consist of two large clustered units of trigonal prism caped with three half-octahedra for the Pd-Ni-P and a tetragonal dodecahedron for the Pd-Cu-P region, as shown in figures 2-4(a)-(b).

Frank was the first to suggest that icosahedral structure might be the reason for the stability of supercooled metals [115]. He theorized that the stability of local icosahedral order is due to its highly close packed structure, lack of long-range order and difficulty of growth [113]. Frank's assertion was later confirmed through experiments involving synchrotron X-ray structural studies on deeply supercooled liquids [116, 117]. Later studies showed that metallic glasses with excellent GFA are composed predominantly of full icosahedron with Voronoi index <0,0,12,0> [118, 119].

Although SRO plays a dominant role in the structure of metallic glasses, as was discussed above, it has also been found that MRO plays a significant role as well. Diffraction studies have shown that there is a significant degree of MRO in these disordered materials [120, 121]. In particular, Sietsma et al. found that for three different amorphous alloys, the medium range

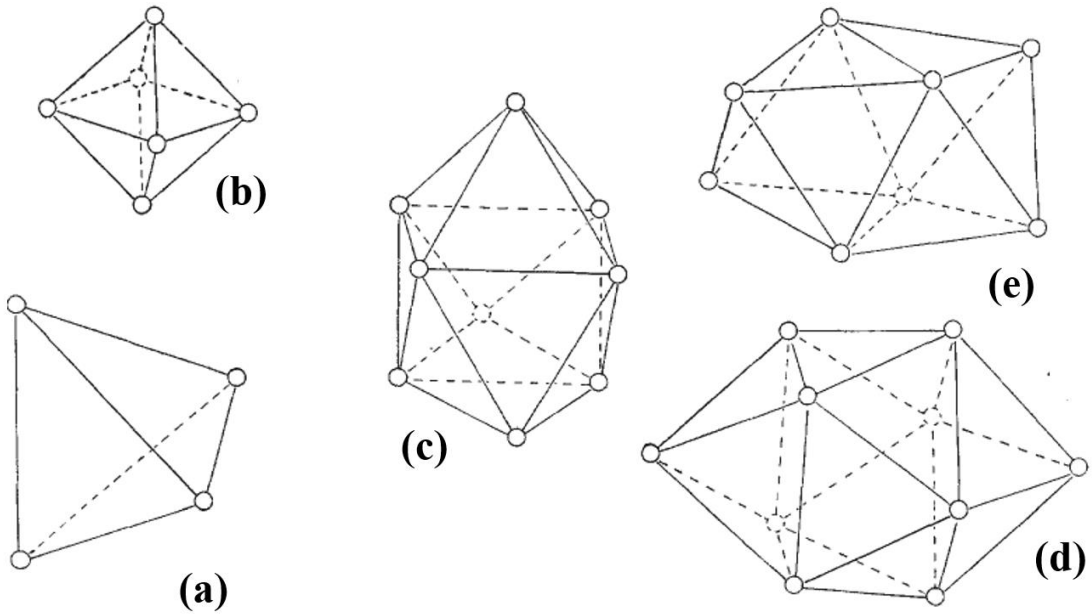

Figure 2-2 The five types of polyhedra which prevent the occurrence of long range ordering in liquids: (a) Tetrahedron; (b) octahedron; (c): trigonal prims; (d): Archimedean antiprism; (e): tetragonal dodecahedron (from Ref. [104]).

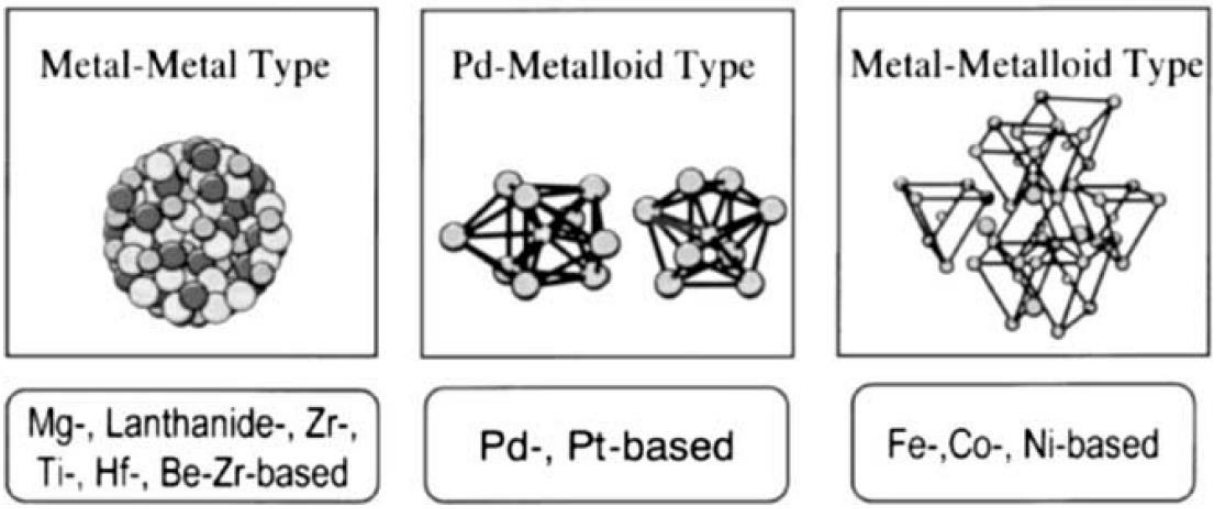

Figure 2-3 The different atomic configurations of three types of BMGs (from Ref. [109], Copyright (2002) by The Japan Institute of Metals.)

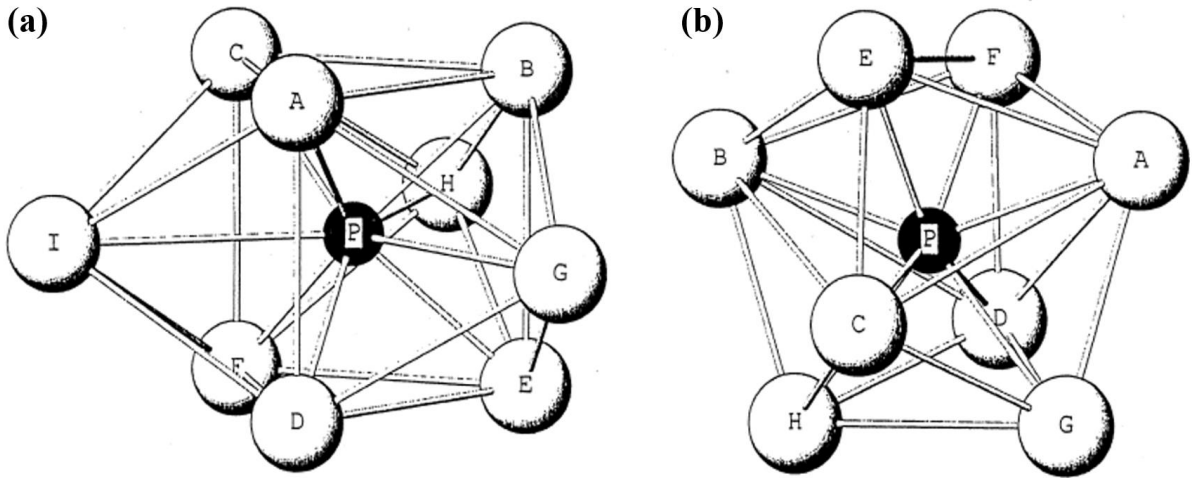

Figure 2-4 (a) Schematic illustration of a trigonal prism capped with three half-octahedra consisting of Pd, Ni and P atoms and (b) a tetragonal dodecahedron consisting of Pd, Cu and P atoms (from Ref. [78]).

distance statistics of the RDF closely resembled that for Fe-Fe correlations in crystalline Fe_3B [122].Miracle et al. proposed a way to model the MRO in metallic glasses using the concept of efficiently packed solute centered atom clusters [a 2-dimensional (2D) representation can be seen in figures 2-5(a)-(b)] [123, 124]. For the model, the local structural units are thought to be composed of efficiently packed solute-centered atomic clusters which are arranged in face centered cubic (fcc) and hexagonal closed packed configurations [123]. The solvent atoms are designated Ω, while solute atoms are labelled α and β.

Wu et al. investigated the connection between MRO and GFA in Al-based metallic glass [118]. Here the medium range order of $Al_{86}Ni_{14-x}Y_x$ (x = 2 - 9 %) metallic glasses was examined via conventional and synchrotron high-energy X-ray diffraction. With respect to the XRD curves, the ratio of the area under the pre-peak curve to the area under the total main peak, indicated that

the GFA of the alloy increased with respect to the MRO content. The above result therefore provides evidence that the MRO of an amorphous alloy aids in the "confusion effect" [125], thus inhibiting crystal phase formation in the material. The experimental results suggest that the icosahedral cluster structure, as shown in figure 2-6, is a viable MRO motif for metallic glasses.

2.2. Microscopic Theory on the Mechanical Behavior of Metallic Glasses

2.2.1 Free-Volume Model

As described by Spaepen, the free volume is that part of an atoms nearest neighbor cage in which the atom can move around without an energy change [126]. Furthermore, Turnbull et al. derived a free volume diffusion coefficient based on the theory for molecular transport in liquids and glasses [127]. Here they found that the diffusion coefficient predicted that liquids of even the simplest structure would go through the glass transition if sufficiently undercooled and crystallization did not occur.

To create free volume, an atom with volume υ must have sufficient energy ΔG^m in order to squeeze into a smaller hole of size υ*. The required energy may be provided through an externally applied force such as compression, which causes a localized shearing event. The driving energy for the creation of free volume is written as [126]:

$$\Delta G = \tau\Omega - S\frac{(v^* - v)^2}{v} = \tau\Omega - \frac{2}{3}\mu\frac{1+v}{1-v}\frac{(v^* - v)^2}{v} \qquad (2\text{-}1)$$

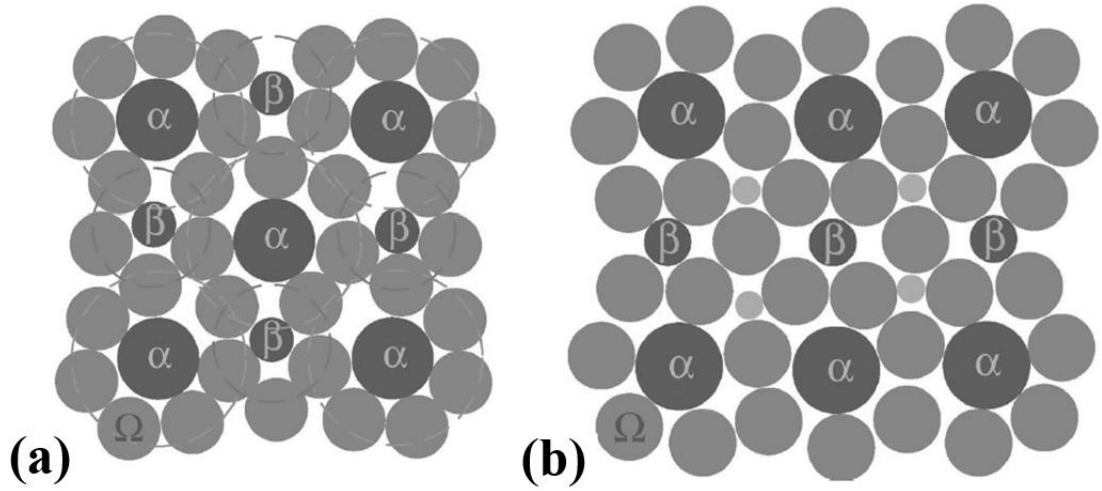

Figure 2-5 2D representations of an efficient cluster packing structure in (a) plane of a single fcc n (a) the {1 0 0} plane and (b) the {1 1 0} plane of a single fcc cluster unit cell. The dashed circles in (a) represent an overlap between the α and β clusters (from Ref. [123]).

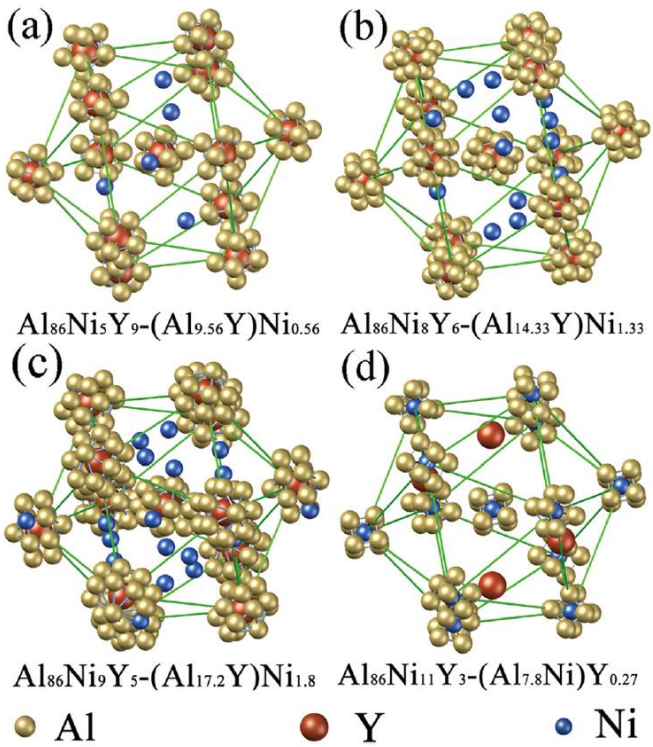

Figure 2-6 MRO structural configurations of (a) $Al_{86}Ni_5Y_9$ [$(Al_{9.56}Y)Ni_{0.56}$], (b) $Al_{86}Ni_8Y_6$ [$(Al_{14.33}Y)Ni_{1.33}$], (c) $Al_{86}Ni_9Y_5$ [$(Al_{17.2}Y)Ni_{1.8}$], (d) $Al_{86}Ni_{11}Y_3$ [$(Al_{7.8}Ni)Y_{0.27}$] MGs from Ref. [118]).

here τ is the atomic level shear stress, Ω is the atomic volume, μ is the shear modulus, υ is Poisson's ratio, and S is the elastic distortion energy required to squeeze the atom into the smaller hole. After a hopping event, the atom experiences a change in its free energy equal to the difference between the driving term τΩ and the elastic distortion energy. Figure 2-7 illustrates the creation of free volume due to an applied shear stress on an atom and its nearest neighbors.

Once the free volume is created, there is a chance for it to be annihilated due to diffusive motion. The number of diffusive jumps required for annihilation can vary anywhere from 1 to 10 [126]. The hypothesis of diffusive annihilation has been supported by a two-dimensional amorphous dynamic hard sphere model [39]. In this model it was found that an artificially created quasi-vacancy in an amorphous material is annihilated in just a few atomic hops, which is in contrast to crystalline alloys, where vacancies require a large number of diffusive jumps in order to be annihilated.

From the above concepts, Spaepen derived an equation which determines the total change in free volume due to applied stress and diffusive events:

$$\Delta v_f = \Delta v_f^+ + \Delta v_f^- = \frac{\gamma v^*}{v_f}\frac{2kT}{S}\left[\cosh\left(\frac{\tau\Omega}{2kT}\right) - 1\right] N\nu e^{-\frac{\Delta G^m}{kT}} e^{-\frac{\gamma\nu^*}{v_f}} + \frac{\nu^*}{n_D} N\nu e^{-\frac{\gamma\nu^*}{v_f}} e^{\frac{\Delta G^m}{kT}} \quad (2\text{-}1)$$

where Δv_f^+ and Δv_f^- are respectively the increase and decrease in free volume, γ is the macroscopic shear strain, k is Boltzmann's constant, T is the temperature, N is the total number of atoms, n_D is the number of diffusive jumps required to annihilate a free volume ν^*, ΔG^m is shown in figure 2-7 above, v_f is the free volume, in the matrix. Furthermore, Ω and S are as defined in Eq. 2-1. Spaepen

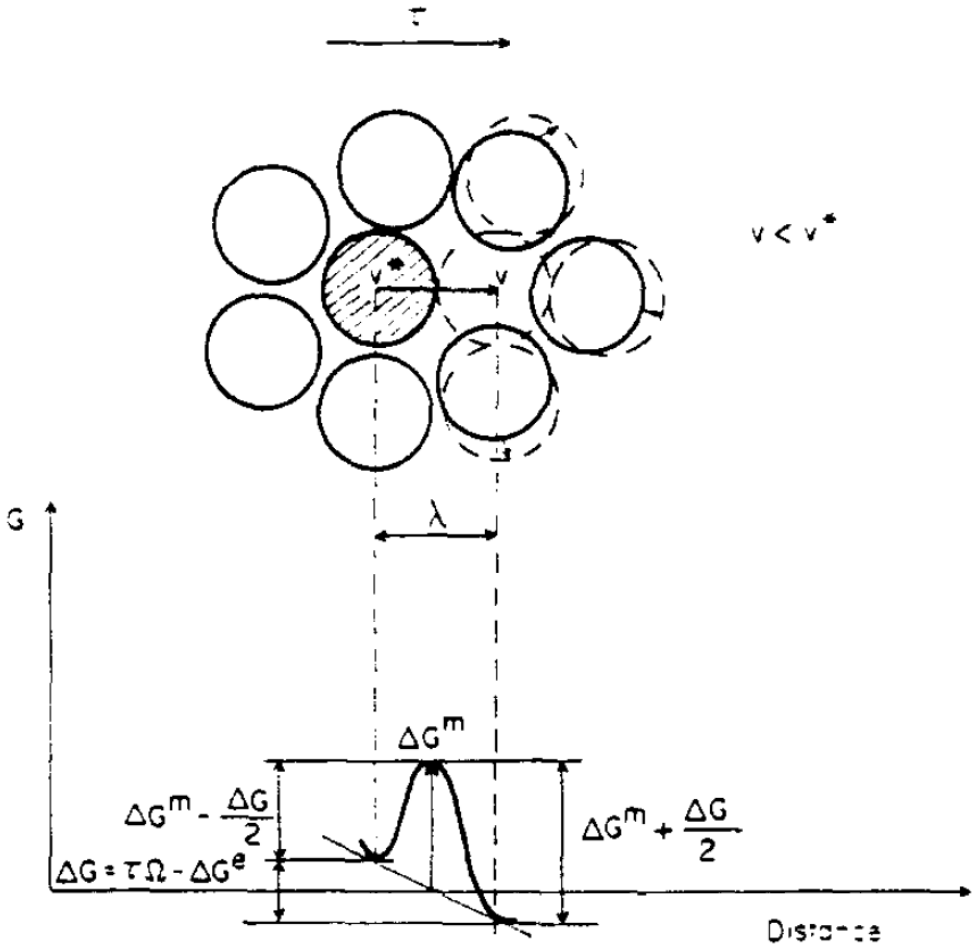

Figure 2-7 Illustration of the creation of free volume by squeezing an atom of volume v* into a neighboring hole of smaller volume v (from Ref. [126]).

determined that at small loads can decrease the average free volume in the steady-state condition [126].

A number of studies have theorized that the increase in ductility in amorphous alloys following irradiation is due to an increase in the free volume of the material [128-131]. This increase in the free volume was observed as a decrease in the relative density of the alloy. It is believed that an amorphous alloy with a higher free volume content can better accommodate local shear strains. This accommodation leads to the deterrence of shear band propagation and subsequently increased ductility in the metallic glass [130]. However, it is still unclear why certain amorphous alloys exhibit an increase in free volume content during irradiation while other alloys do not.

2.2.2 Shear Transformation Zone

A shear transformation zone model was first proposed by Argon, which arises from multi-atomic sized flow units which exhibit nonlinear resistance to deformation in the solid [132]. During the shear transformation event, deformation occurs between two short rows of 4-6 atoms around a free volume site, in which its shear resistance behavior can be modeled according to a skewed sinusoid [132, 133]. Specifically, this type of process resembles the nucleation of a dislocation loop that does not expand. Furthermore, the energetically favored transformation configuration is in the shape of a thin disk containing the shear transformation direction in its plane.

Argon also mathematically described the change in the excess free volume fraction f_v of metallic glass during shear transformation [132]:

$$\frac{df_v}{dt} = \varepsilon_v(1-f_v)v_G e^{-\left[\frac{\Delta G^*\left(\frac{\sigma}{\tau'}\right)}{kT}\right]} - \varepsilon_v f_v(1-f_v)v_D e^{-\left[\frac{\Delta G_D(1-f_v)}{kT}\right]} \quad (2\text{-}3)$$

here k is Boltzmann's constant, T is the temperature, ε_v is the local transformation dilatation in the transformation region, $\varepsilon_v(1\text{-}f_v)$ is a first order correction for the decrease in local dilatation in a structure that has already accumulated an average excess free volume fraction f_v. In addition, v_G and v_D are respectively frequency factors for the shear transformation and diffusive rearrangements while ΔG^* and ΔG_D are respectively the activation free enthalpy of a transformation and activation free energy for a net diffusive rearrangement in the inactivated structure. The variables σ and τ' are the applied stress and the elevated shear stress due to STZ activation respectively.

The first term on the right-hand side of Eq. (2-3) represents the rate of production of excess free volume during a shear transformation event and the second term represents the elimination of free volume due to diffusive rearrangements in the post-transformation structure. Later on it will

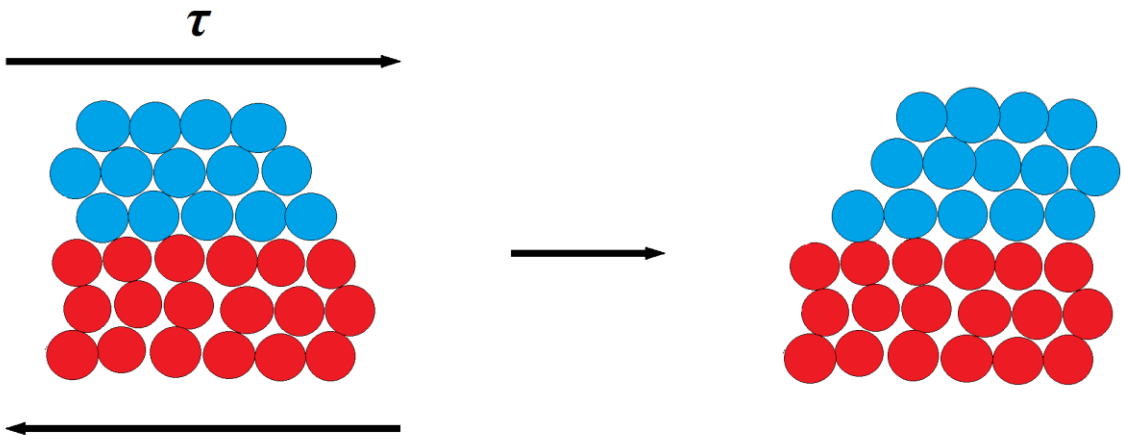

Figure 2-8 A two-dimensional schematic of a shear transformation zone in an amorphous metal. A shear displacement occurs to accommodate an applied shear stress τ, with the darker upper atoms moving with respect to the lower atoms (from Ref. [72]).

be argued that the frequency factors and free energy variables may depend on irradiation dose since knock on events cause atomic rearrangements in the metallic glass.

Langer extended the STZ theory to include two state dynamics of the zones and an effective disorder temperature, which provides an accurate account of large-scale deformation in metallic glasses [134]. The first state involves system jamming when all available STZs have been transformed due to an applied stress, preventing plastic deformation in the direction of stress. The second state occurs at higher stresses, where the system becomes unjammed due to the rapid creation and annihilation of STZs.

2.2.3 Shear Banding

Despite having relatively high strengths and elastic limits, metallic glasses exhibit poor ductility that is caused primarily by the formation of shear bands which subsequently leads to cracking [72, 135]. This lack of plasticity in amorphous alloys can be seen during tensile testing, where the material will fracture without appreciable elongation. However, amorphous specimens undergoing compression testing may display some ductility before failure.

Shear bands are primarily initiated by structural inhomogeneity and defects that introduce stress concentrations into the material [95]. This non-uniformity in structure can arise from the local production of free volume or the evolution of structural order. Once initiated, the shear band will propagate until the applied strain is fully accommodated by the shear accumulated within the band [95]. In terms of the macroscopic structure of shear bands, there are two types, primary and secondary. Figures 2-9(a)-(b) shows both types of shear bands on the fractured surface of a $Zr_{64.13}Cu_{15.75}Ni_{10.12}Al_{10}$ BMG after compression at a strain rate of $5 \times 10^{-5}\ s^{-1}$ [136]. As displayed

in the figure 2-9(a), the primary shear bands propagate through the material at ~45^{o} and can initiate failure. While the secondary bands are displayed in figure 9(b), where they appear to be significantly smaller and branch off of the primary type.

A number of studies have examined the microstructure of shear bands using transmission electron microscopy [137-142]. In [138, 139], TEM imaging revealed that nanocrystalline phases had formed in the shear bands, which was hypothesized to be caused by deformation-assisted atomic transport. Hirotsu et al. used a spherical-abberration-corrected (C_s corrected) HRTEM to examine the local structure of shear bands in $Pd_{40}Ni_{40}P_{20}$ BMG [95, 141]. Here phosphide compound-like nanoclusters with sizes 1-2 nm and composed of FCC Pd-Ni type were observed (see figure 2-10).

During tensile and compression testing, shear band propagation is characterized by fluctuations in the stress-displacement behavior of the glass, which are called serrations [136]. An

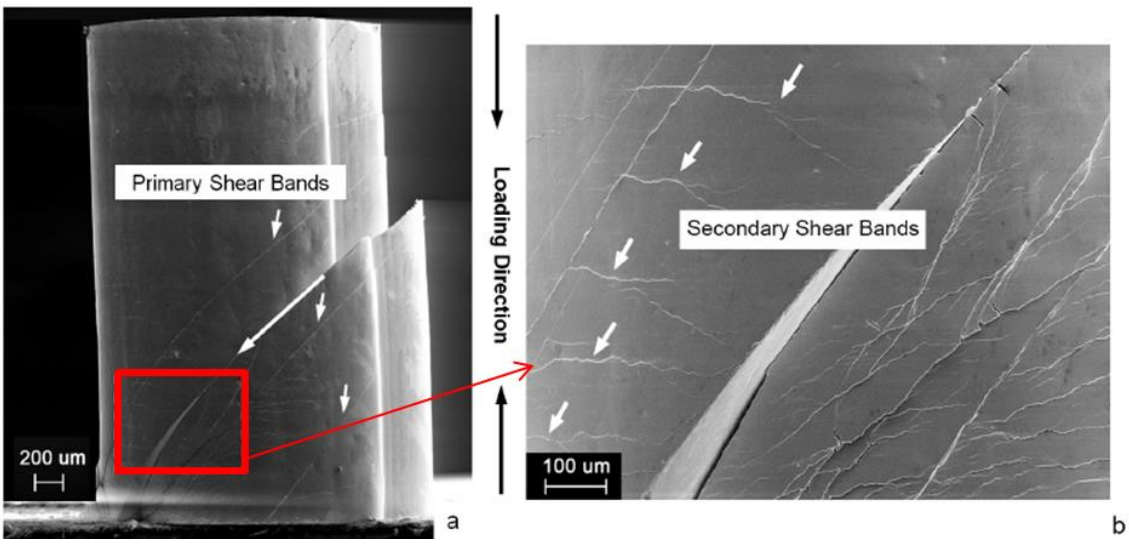

Figure 2-9 (a) lateral surface of a fractured BMG sample, $Zr_{64.13}Cu_{15.75}Ni_{10.12}Al_{10}$, after compression at a strain rate of 5×10^{-5} s^{-1}, and (b) magnified region indicated by a rectangle in (a) showing the interaction of multiple shear bands (from Ref. [136]).

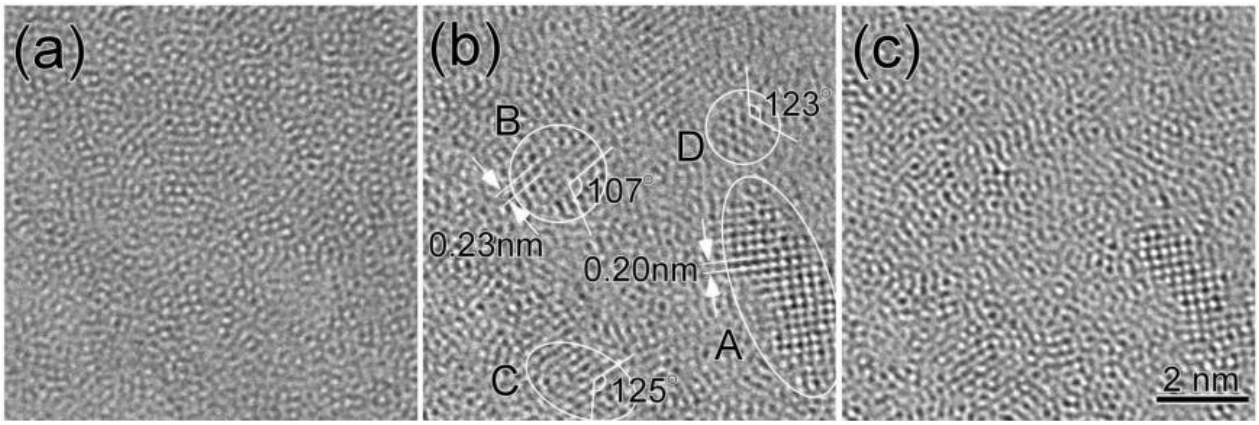

Figure 2-10 HRTEM images of shear bands taken by a C_S corrected HRTEM at C_S = 2 μm and Δf = 1 nm (a) 5 nm (b) and 9 nm (c) (from Ref. [141]).

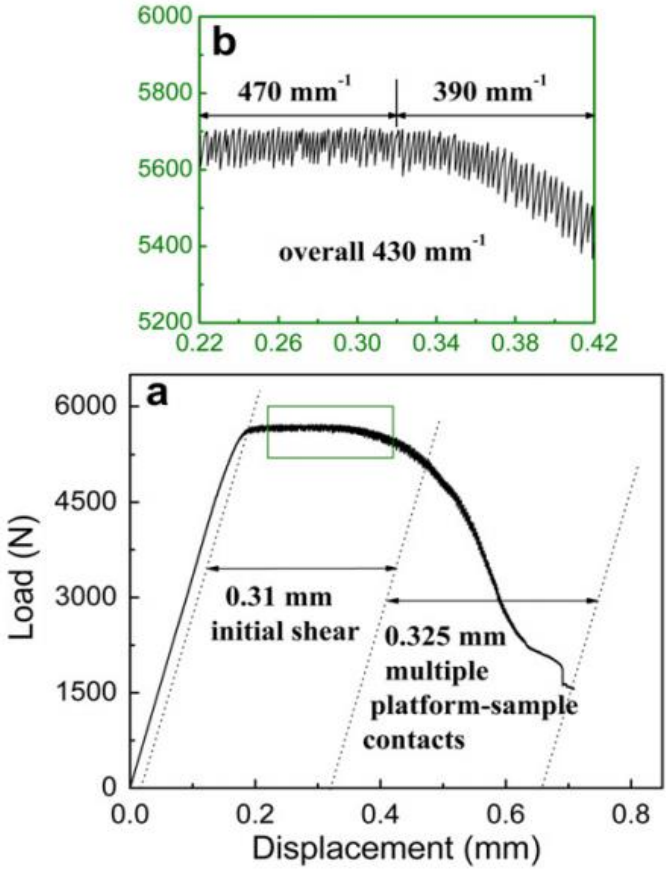

Figure 2-11 (a) Compressive load-displacement curve of $Zr_{64.13}Cu_{15.75}Ni_{10.12}Al_{10}$ BMG at a nominal strain rate of 2×10^{-4} s^{-1}. (b) Enlarged view of the serrated region (from Ref. [135]).

example of serration behavior can be seen in figure 2-11 for $Zr_{64.13}Cu_{15.75}Ni_{10.12}Al_{10}$ BMG undergoing compression at a strain rate of 2×10^{-4} s^{-1}. In addition, Rodriguez determined that there are primarily 5 types of serrations which occur during serrated flow in a material [143]. For metallic glasses, serrations usually disappear at high strain rates (≥ 0.1 s^{-1}) and cryogenic temperatures [135].

The size of shear bands has also been analyzed using TEM. It has been found that shear band geometries consist of widths ranging from 120-200 nm and thicknesses between 10-20 nm [142, 144]. However, other studies have found shear bands with thicknesses with ranges of 10-100 nm [95]. It has suggested that local heating, as a result of plastic energy dissipated within a shear band, increases the temperature within a shear band to approximately T_g [61]. This temperature rise is accompanied by a dramatic drop in the viscosity inside the shear band, which leads to significant softening that can cause rapid shear band propagation and catastrophic failure in BMGs [72]. To better understand thermal behavior of shear banding, Yang et al. performed tensile testing on $Zr_{52.5}Cu_{17.9}Ni_{14.6}Al_{10}Ni_5$ BMG and recorded heat measurements using a high-speed thermographic camera on a [72, 145]. Using the STZ model, Yang calculated the change in the temperature of the shear band with the following equation:

$$\Delta T_s = \frac{\alpha \sigma_f}{2\rho C_p} \tag{2-4}$$

where ρ is the density, σ_f is the nominal fracture strength, C_p is the heat capacity, and α is the ratio of plastic work converted to heat and approximately equal to 0.9. From the heat measurements,

they determined ΔT_s for the Zr BMG and the corresponding shear-band temperature T_s at fracture. Using Eq. (2-4) and mechanical property data from literature, they were able to calculate T_s for 8 other amorphous alloy.

Figure 2-12 shows the plot of T_s vs. T_g for 9 BMG alloys, and as can be seen, the calculated T_s is in relatively good agreement with known T_g values. The results of the investigation provide evidence that a temperature rise does occur in the shear bands which leads to subsequent catastrophic failure in the BMG.

However, some have suggested that other factors may account for the reduced viscosity in shear bands, such as free volume accumulation due to the dynamic strain rate [135]. Specifically, Nieh et al. used Spaepen's free volume model [126] to derive an equation which calculates the viscosity change in a propagating shear band:

$$\frac{\eta_2}{\eta_1} = e^{\alpha \upsilon^* \left[\frac{1}{\upsilon_{f_2}(\dot{\varepsilon})} - \frac{1}{\upsilon_{f_1}}\right]} \tag{2-5}$$

where $\alpha = 1$, υ^* is the atomic volume of the glass, and υ_{f1}, η_1 and $\upsilon_{f2,}$ η_2 are respectively the free volume and viscosity of the glass before and after a shear band event. Based on Eq. (2-5), a 1 % increase in the free volume would lead to a factor of 10 decrease in the viscosity of a shear band in Zr based BMG at room temperature [146]. Here υ_{f2} is a function of $\dot{\varepsilon}$ since it was shown that the free volume decreases with respect to the applied strain rate [135]. An example of this decreasing trend ($Zr_{41.2}Ti_{13.8}Cu_{12.5}Ni_{10}Be_{22.5}$ BMG) can be seen in figure 2-13 [147].

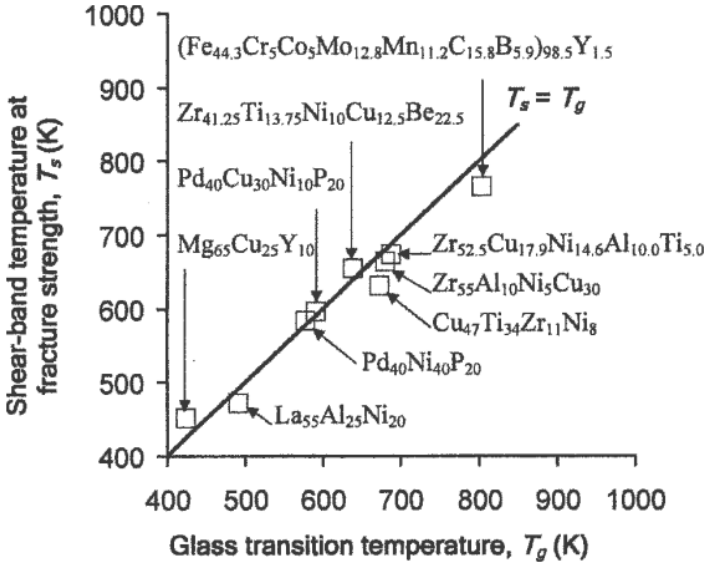

Figure 2-12 Comparison between glass-transition temperature and calculated shear-band temperature at fracture strength for different BMGs (from Ref. [145]).

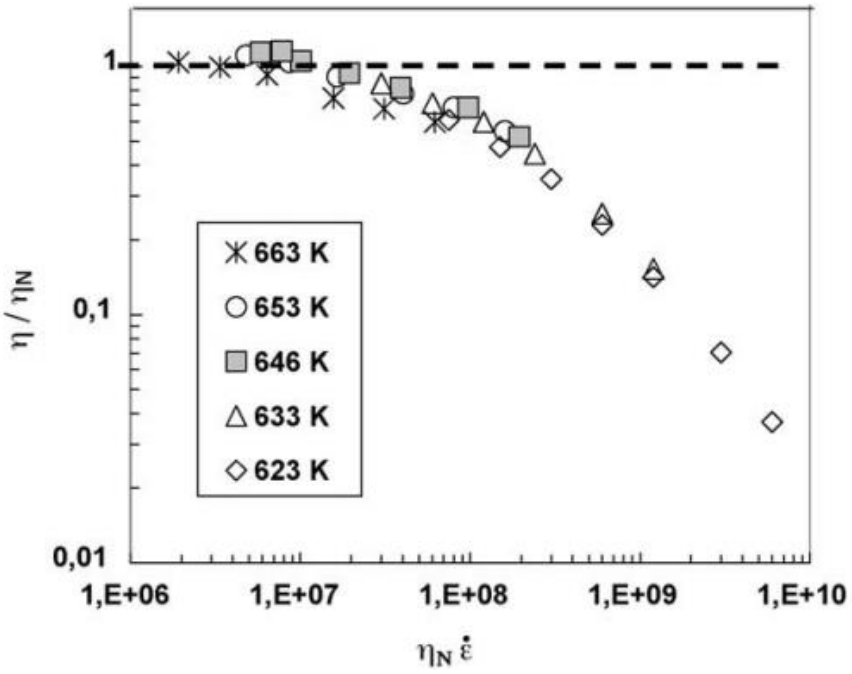

Figure 2-13 Normalized viscosity (viscosity/Newtonian viscosity) as a function of normalized strain rate for $Zr_{41.2}Ti_{13.8}Cu_{12.5}Ni_{10}Be_{22.5}$ (Vitreloy 1) BMG (from Ref. [147]).

2.3 Material and Mechanical Properties of Amorphous Alloys

BMGs have elastic moduli which are slightly lower than crystalline materials. Figures 2-14(a)-(b) show the fracture toughness and fracture energy, as a function of the Poisson's ratio, υ, for a wide range of different amorphous alloys [148]. As can be seen, the fracture toughness and energy exhibit an increasing trend with respect to the Poisson's ratio. Furthermore, the range of toughness values as seen in figure 2-14(a) range from ~2 $MPa \cdot m^{1/2}$ for the Mg based metallic glasses to 100 $MPa \cdot m^{1/2}$ for the Pd and Pt based amorphous alloys. However, Pt- and Pd- BMGs are not practical due to their high manufacturing costs. Zr based alloys, on the other hand, had fracture toughness values comparable to certain steel and titanium alloys, which makes these alloys very attractive due to their relatively lower manufacturing costs as compared to Pt- BMGs. Figure 14(c) compares the tensile strength and Young's modulus for several BMGs and conventional alloys [149]. The metallic glasses shown here have significantly higher tensile strength and lower Young's modulus as compared to conventional steels. The difference in these values between the BMG and crystalline alloys is as large as 60 % [113]. This combination of high tensile strength and low Young's modulus make them a very interesting material with many possible applications.

A number of studies have investigated the fracture toughness of BMGs using fatigue pre-cracked BMG specimens. For instance, investigations that examined the fracture toughness (K_c) of vitreloy 1 found that K_C ranged from 30-68 $MPa \cdot m^{1/2}$ [150, 151], while another study recorded a measured value of ~17.9 $MPa \cdot m^{1/2}$ [152]. Another BMG alloy with the composition of $Zr_{52.5}Cu_{17.9}Ni_{14.6}Al_{10}Ti_5$ (BAM-11) exhibited toughness values ranging from 28 to 69 $MPa \cdot m^{1/2}$ [153].

Figure 2-15 summarizes the relationship between Young's modulus (E) and tensile fracture strength ($\sigma_{t,f}$) or Vickers hardness (H_v) for various BMGs [113]. There is an observable linear

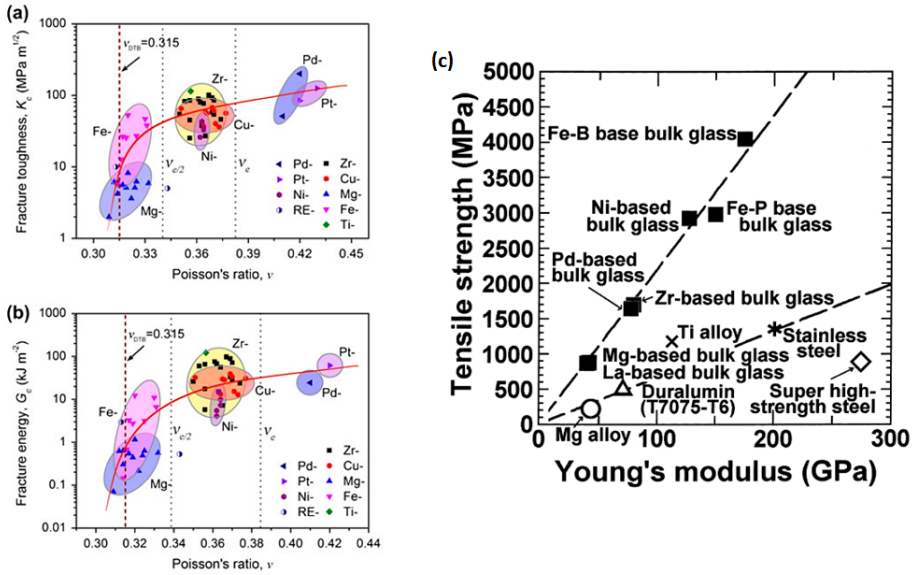

Figure 2-14 (a) Fracture toughness and (b) fracture energy vs. ν for different metallic glasses (MGs). The MGs are categorized into four groups separated by dashed lines (from Ref. [148]). (c) Tensile strength vs. Young's modulus for various alloys (from Ref. [149]).

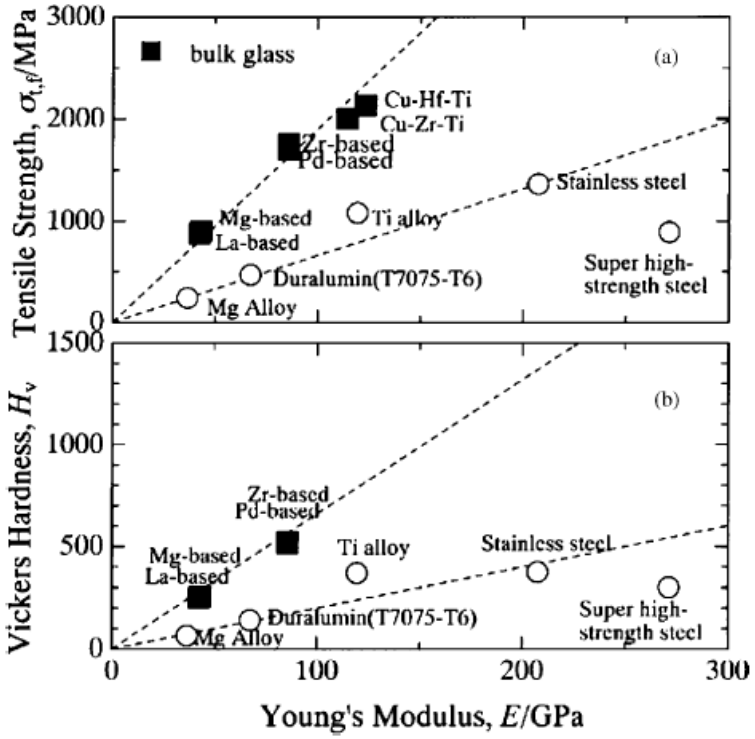

Figure 2-15 The relations between the mechanical properties of typical BMGs: (a) tensile fracture strength and (b) Vicker's hardness as a plot of Young's modulus (from Ref. [113]).

Table 2-2 Summary of the properties of metallic glasses listed in Ref. [154].

Alloy	ρ (g/cm^3)	E (GPa)	G (GPa)	B (GPa)	υ	σ_y (GPa)	T_g (K)
$Zr_{41.2}Ti_{13.8}Ni_{10}Cu_{12.5}Be_{22.5}$	5.9	95	34.1	114.1	0.352	1.86	618
$Zr_{48}Nb_8Ni_{12}Cu_{14}Be_{18}$	6.7	93.9	34.3	118	0.367	1.95	620
$Zr_{55}Ti_5Cu_{20}Ni_{10}Al_{10}$	6.62	85	31	118	0.375	1.63	625
$Zr_{57.5}Nb_5Cu_{15.4}Ni_{12}Al_{10}$	6.5	84.7	30.8	117.6	0.379	1.58	663
$Zr_{55}Al_{19}Co_{19}Cu_7$	6.2	101.7	37.6	114.9	0.352	2.2	733
$Pd_{40}Cu_{30}Ni_{10}P_{20}$	9.28	92	34.5	151.8	0.399	1.72	593
$Pd_{60}Cu_{20}P_{20}$	9.78	91	32.3	167	0.409	1.70	604
$Pd_{40}Cu_{40}P_{20}$	9.30	93	33.2	158	0.402	1.75	548
$Ni_{45}Ti_{20}Zr_{25}Al_{10}$	6.4	109.3	40.2	129.6	0.359	2.37	791
$Ni_{40}Ti_{17}Zr_{28}Al_{10}Cu_5$	6.48	127.6	47.3	140.7	0.349	2.59	862
$Ni_{60}Nb_{35}Sn_5$	8.64	183.7	66.32	267	0.385	3.85	885
$Ni_{60}Sn_6(Nb_{0.8}Ta_{0.2})_{34}$	9.24	161.3	59.41	189	0.357	3.50	875
$Ni_{60}Sn_6(Nb_{0.6}Ta_{0.4})_{34}$	9.80	163.7	60.1	197.6	0.361	3.58	882
$Cu_{64}Zr_{36}$	8.07	92	34	104.3	0.352	2.0	787
$Cu_{46}Zr_{54}$	7.62	83.5	30.0	128.5	0.391	1.40	696
$Cu_{46}Zr_{42}Al_7Y$	7.23	84.6	31	104.1	0.364	1.60	713
$Pd_{77.5}Cu_6Si_{16.5}$	10.4	89.7	31.8	166	0.409	1.5	550
$Pt_{60}Ni_{15}P_{25}$	15.7	96.1	33.8	202	0.420	1.4	488
$Pt_{57.5}Cu_{14.7}Ni_5P_{22.8}$	15.2	95.7	33.4	243.2	0.434	1.45	490
$Pd_{64}Ni_{16}P_{20}$	10.1	91.9	32.7	166	0.405	1.55	452
$MgGd_{10}Cu_{25}$	4.04	49.1	18.6	46.3	0.32	0.98	428
$La_{55}Al_{25}Cu_{10}Ni_5Co_5$	6.0	41.9	15.6	44.2	0.342	0.85	430
$Ce_{70}Al_{10}Ni_{10}Cu_{10}$	6.67	30.3	11.5	27	0.313	0.65	359
$Cu_{50}Hf_{43}Al_7$	11.0	113	42	132.8	0.358	2.2	774
$Cu_{57.5}Hf_{27.5}Ti_{15}$	9.91	103	37.3	117.5	0.356	1.94	729
$Fe_{61}Mn_{10}Cr_4Mo_6Er_1C_{15}B_6$	6.89	193	75	146	0.280	4.16	870
$Fe_{53}Cr_{15}Mo_{14}Er_1C_{15}B_6$	6.92	195	75	180	0.32	4.2	860
$Au_{49.5}Ag_{5.5}Pd_{2.3}Cu_{26.9}Si_{16.3}$	11.6	74.4	26.5	132.3	0.406	1.20	405
$Au_{55}Cu_{25}Si_{20}$	12.2	69.8	24.6	139.8	0.417	1.00	348

relationship between both the tensile strength and Vickers hardness with respect to Young's modulus. In addition, crystalline alloys such as stainless steel also exhibit the same linear trend, albeit with a lower slope. This higher slope indicates a larger elastic limit of the BMGs as compared to the crystalline alloys. Furthermore, the BMGs in the graph show a more linear trend in the data, which can be attributed to the formation of an ideally homogenized solid solution over the whole composition range [113].

2.4 Mechanical Testing of Amorphous Alloys

2.4.1 Compression Testing and Serrated Flow

As discussed in the previous section, a BMG may experience jerky motion during compression testing that is characterized by fluctuations in the corresponding stress-strain graph. This type of mechanical behavior is known as the serrated flow and is characterized by either rapid drops in the applied stress or a mix of decreasing and increasing stress values. Serration behavior is significant because it is typically associated with plastic instabilities and significant changes in the microstructure [155, 156]. This type of mechanical behavior has been observed in BMGs (see figure 2-16) [136, 157-162], steels [163-169], HEAs [164, 170-177] and Al-Mg alloys [178-183]. In bulk metallic glasses, serrated plastic flow is observed, and attributed to shear banding dynamics [136, 158, 164]. This behavior contrasts with that exhibited by crystalline materials, where a major cause of serrations is the locking of dislocations by solute atoms [163, 170, 184].

Serrations may display different behavior which typically depends on the teste temperature or the applied strain rate [136, 164, 171]. During dynamic strain aging that occurs during compression, serrations typically exhibit three distinct types of behavior. These types have been

labelled as A, B, and C, and can be seen in figure 2-17 [155, 164, 171]. As can be seen in the figure, Type-A serrations rise above the general level of stress values before experiencing a drop in the stress. Furthermore, their behavior is periodic in nature and is associated with high strain rates. Type-B serrations, on the other hand, fluctuate rapidly about the general level of stress and occur with less spatial correlations as compared to Type-A serrations. Finally, Type-C serrations occur during compression at lower applied strain rates and consist of stress drops that ensue below the stress-strain curve.

2.4.2 Modeling and Analysis of Serrated Flow

Several techniques have been used to evaluate the complexity of time series data that is generated from nonlinear dynamical systems [185]. One such technique that can analyze this type of behavior is known as the refined composite multiscale entropy (RCMSE) algorithm, which was proposed as a technique to overcome the limitations of previous multiscale entropy methods [186]. The magnitude of the complexity, as determined by the algorithm, is typically denoted as the sample entropy in which a higher value is typically characteristic of a less predictable time series. In contrast, a time series that is more predictable is usually characterized by lower values.

Furthermore, this algorithm estimates the probability that two sequences of m consecutive data points, which are similar, will remain similar when an additional consecutive point is included [187]. The RCMSE algorithm consists of a two-step process where the first step involves a coarse-graining procedure that is used to derive the representations of a system's dynamics on different time scales [188]. To begin the analysis, one first eliminates the trend that arises in the strain hardening regime [163], where the stress vs. time data is fitted using a third order polynomial. After the fit is made it is subtracted from the original data [189]. Figures 2-18 (a)-(b) show the

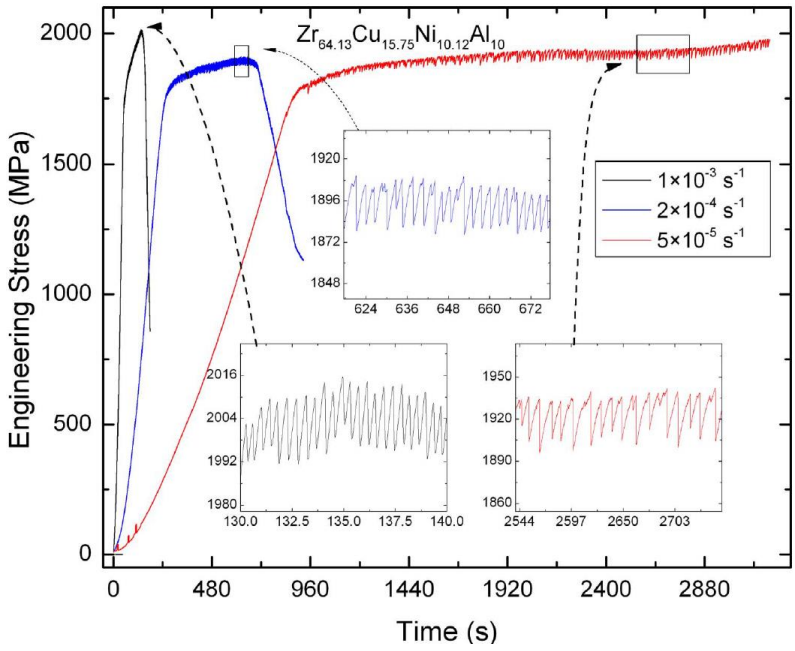

Figure 2-16 Compression stress-time profiles of $Zr_{64.13}Cu_{15.75}Ni_{10.12}Al_{10}$ BMG cylindrical samples. Samples were compressed at strain rates of 1×10^{-3} s^{-1}, 2×10^{-4} s^{-1}, and 5×10^{-5} s^{-1} at room temperature (from Ref. [136]).

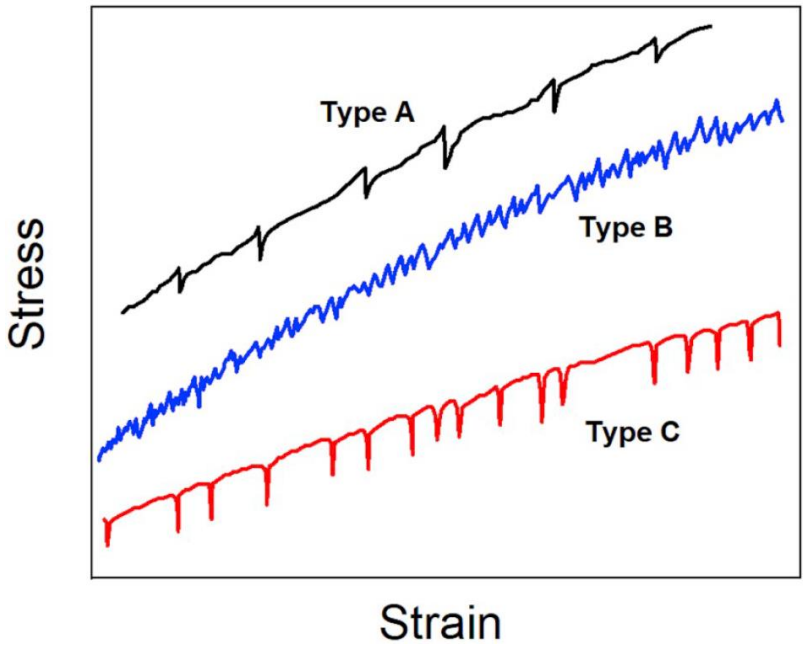

Figure 2-17 Type-A, Type-B, and Type-C serrations (from Ref. [177]).

true stress-strain serration data for an as-extruded Al-Mg sample compressed at 10^{-4} s^{-1} and its detrended counterpart [189]. From the detrended data one creates the coarse-grained time series [186]:

$$y_{k,j}^{\tau} = \frac{1}{\tau} \sum_{i=(j-1)\tau+k}^{j\tau+k-1} x_i \quad ; \; 1 \leq j \leq \frac{N}{\tau} \qquad 1 \leq k \leq \tau \tag{2-6}$$

where x_i is the ith point from the original time-series data, X, N is the total number of data points from the original time series, k is an indexing factor, which tells us at which data point in the series to begin the modeling and analysis, and τ is the scale factor. One should notice that for k, τ = 1 indicates that one recovers the original time series. Figure 2-19 present the schematic for the coarse-grained series with k = 1 – 2 and τ = 2 – 3 [186]. Once $y_{k,j}^{\tau}$ is constructed, one writes the time series of y_k^{τ} as a vector for each τ [186]:

$$\boldsymbol{y_k^{\tau}} = \left\{ y_{k,1}^{\tau} \;\; y_{k,2}^{\tau} \;\; .... \;\; y_{k,M}^{\tau} \right\} \tag{2-7}$$

where M = N/τ, and each $y_{k,j}^{\tau}$ is determined using Eq. (2-6). From here, creates the template vectors of dimension m (typically m = 2):

$$\boldsymbol{y_{k,i}^{\tau,m}} = \left\{ y_{k,i}^{\tau} \;\; y_{k,i+1}^{\tau} \;\; .... \;\; y_{k,i+m-1}^{\tau} \right\} \;\; ; \quad 1 \leq i \leq N - m \, ; 1 \leq k \leq \tau \tag{2-8}$$

The next step in the process is to find n-matching sets of distinct template vectors for a given value of k. The total number of matching vector sets for a given k, τ, and m are designated as $n_{k,\tau}^{m}$. The infinity norm, $d_{jl}^{\tau,m}$, which defines the distance between two template vectors, is used as a criterion to determine if two vectors are matching pairs. This quantity is defined as [190]:

$$d_{jl}^{\tau,m} = \left\| \boldsymbol{y_j^{\tau,m}} - \boldsymbol{y_l^{\tau,m}} \right\|_{\infty} = \max\left\{ \left| y_{1,j}^{\tau} - y_{1,l}^{\tau} \right| \ldots \left| y_{i+m-1,j}^{\tau} - y_{i+m-1,l}^{\tau} \right| \right\} < r \qquad (2\text{-}9)$$

here r is a predefined tolerance value. Two vectors will match if $d_{jl}^{\tau,m}$ is less than r. In [191-193], r is chosen as 0.15 times of the standard deviation of the data since it imposes a normalization effect on the data such that the sample entropy will not depend on its variance. One repeats this process for m + 1, thus finding the number of matching vectors, $n_{k,\tau}^{m}$ for both m and m + 1. Then one sums $n_{k,\tau}^{m}$ from k = 1 to τ (for both m and m + 1). To find the refined composite multiscale entropy (RCMSE) value for the original data, the natural log of the ratio of these two sums is calculated using [186]:

$$RCMSE(\boldsymbol{X}, \tau, m, r) = Ln\left(\frac{\sum_{k=1}^{\tau} n_{k,\tau}^{m}}{\sum_{k=1}^{\tau} n_{k,\tau}^{m+1}} \right) \qquad (2\text{-}10)$$

The RCMSE technique has been used to evaluate various phenomena, including the serrated flow in an Al-containing HEA, colored noise, chaos, and physiological signals [190, 194-199]. In [190], the logistic map [200] was analyzed using the RCMSE method. Here the data analyzed the data in which the bifurcation parameter, R, was varied from 2.8 to 4. The results are displayed in figure 2-20, where the complexity results were compared with the map's bifurcation diagram. The bifurcation diagram was divided into subsections where a black box denotes each subsection in the figure. Here, arrows link the sample-entropy curves with the respective subsections of the bifurcation diagram. As can be observed in the figures, the increase in the sample entropy curves with respect to R corresponded to an increase in the to the number of asymptotic values visited there.

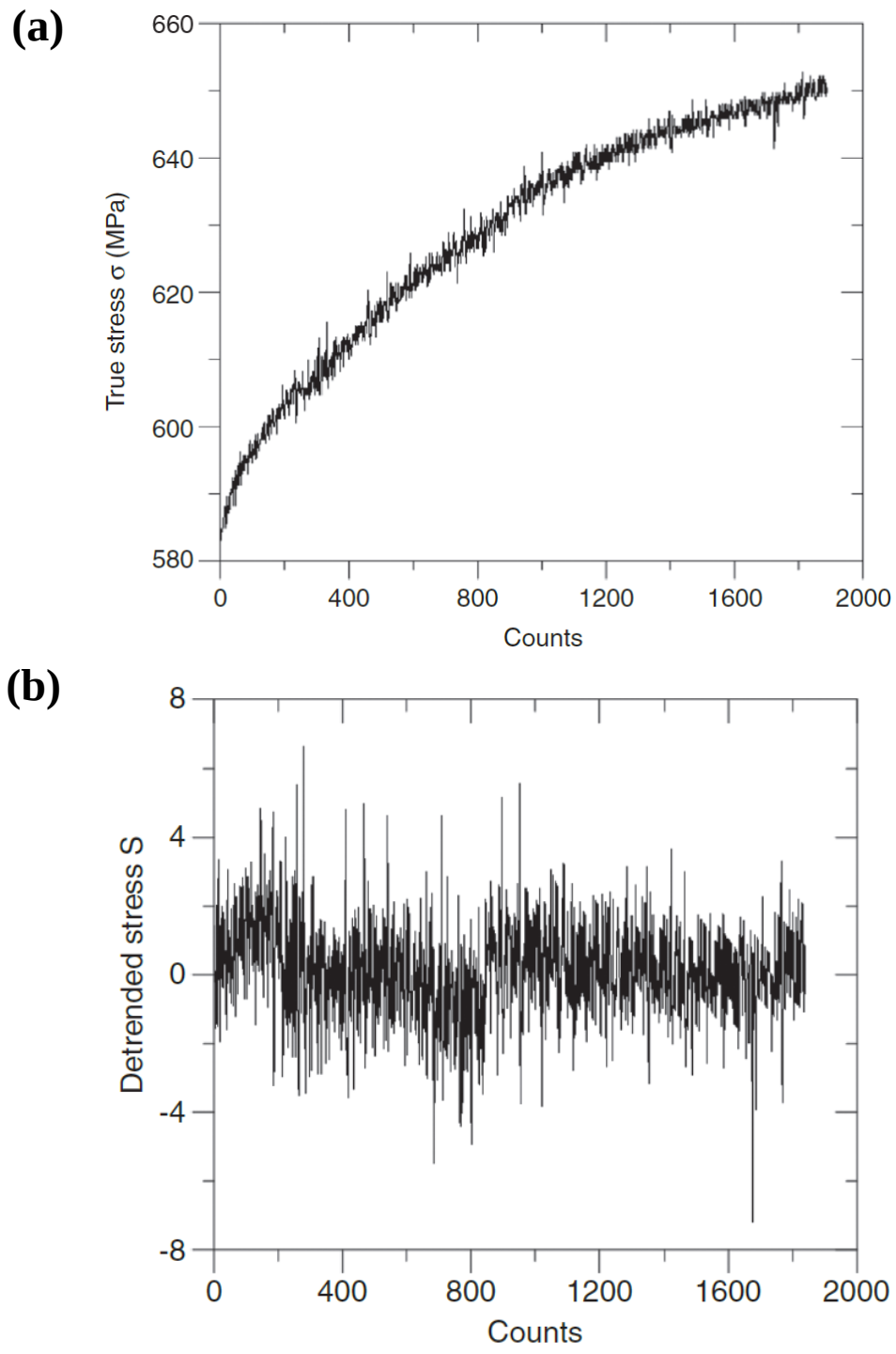

Figure 2-18 Graphs for (a) the serrations of the true stress curve for as-extruded Al-Mg alloy compressed at a strain rate of 10^{-4} s^{-1} at room temperature and (b) the corresponding detrended time series (from Ref. [189]).

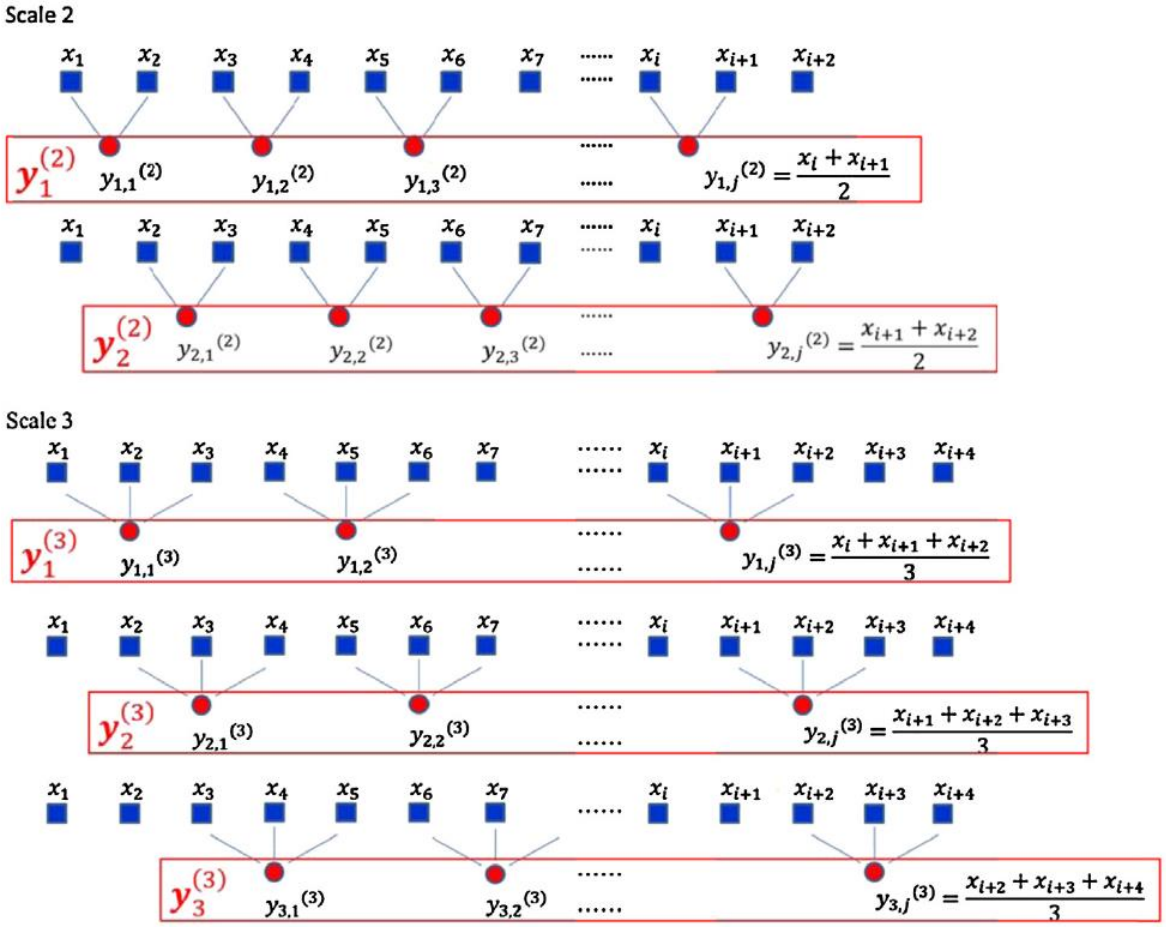

Figure 2-19 Schematic illustration of the coarse-graining procedure (from Ref. [186]).

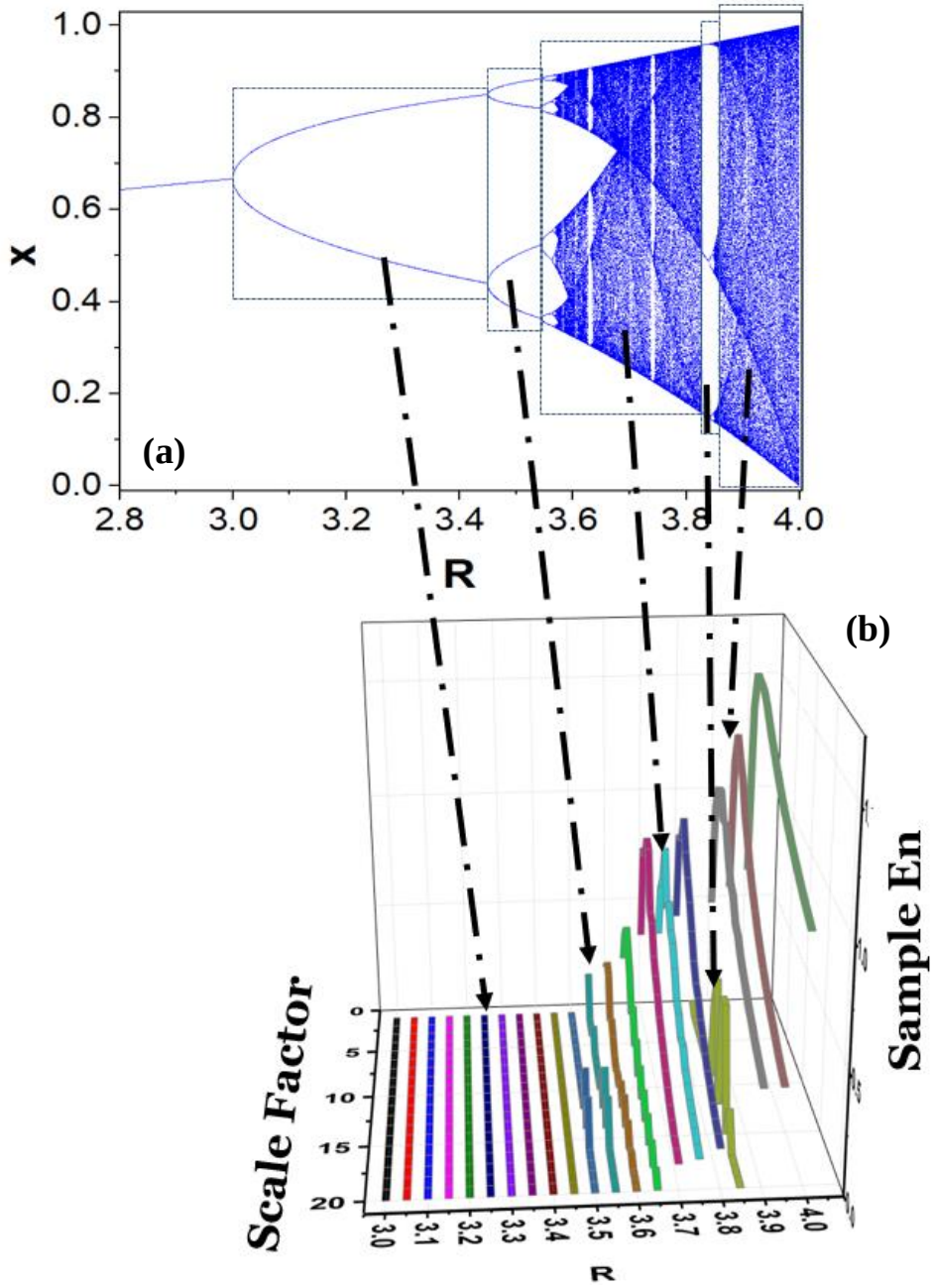

Figure 2-20 (a)-(b) The bifurcation diagram (plotted for $2.8 \leq R \leq 4.0$) for the logistic map with arrows that link the various regions of the map to its corresponding sample-entropy curves from (Ref. [190]).

2.4.3 Nanoindentation

Recently, there has been considerable interest in the mechanical characterization of thin film systems and small volumes of material using depth-sensing indentation tests with either spherical or pyramidal indenters [201]. Nanoindentation has been able to meet this need by being able to examine materials at the sub-micron scale. In this type of test, the applied load and the depth of penetration of an indenter into the specimen are recorded and used to indirectly determine the area of contact and hence the hardness of the test specimen [202]. Properties which are usually measured using this technique are nanoindentation hardness and Young's modulus. Nanoindentation hardness is defined as the mean pressure the material will support under a given load [203].

Many indentation tests use what is called a "Berkovich indenter" for which the typical load- displacement data is shown in figure 2-21(a)-(b) [203, 204]. The graph from figure 2-21(a) also features the geometry of the Berkovich tip geometry. The quantities shown in figure 2-21(b) include the peak indentation load P_{max}, the indenter displacement at peak load h_{max}, the final depth of the contact impression after unloading h_f, and the initial unloading stiffness, S. As with the observed graphs, the loading curves typically have a parabolic like shape. Figure 2-22(a) shows the cross section of an indentation and identifies other parameters used in the analysis such as the contact depth h_c, h_s which is the displacement of the surface at the perimeter of the contact, and the radius of contact at peak load (labelled a in the figure) [203]. The value h_f represents the final depth of the residual hardness impression once the load is fully removed.

The loading and unloading curves exhibit a power law behavior which are typically written as [203, 205]:

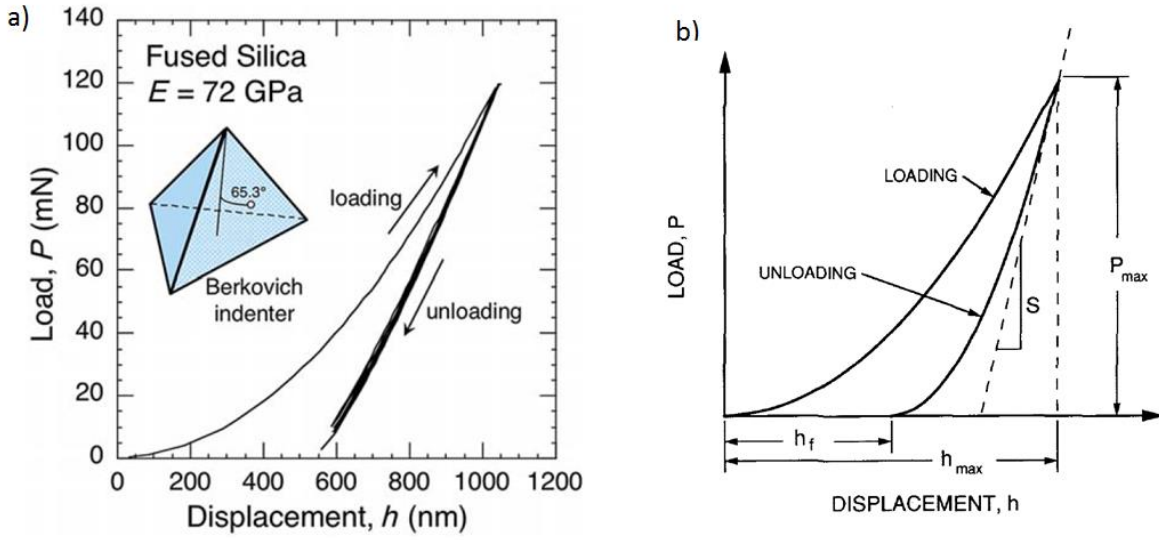

Figure 2-21 (a) Typical load-displacement data obtained in the calibration material fused silica using a Berkovich indenter, a three-sided pyramid. (b) Load versus indenter displacement data for an indentation experiment (From Ref. [203]).

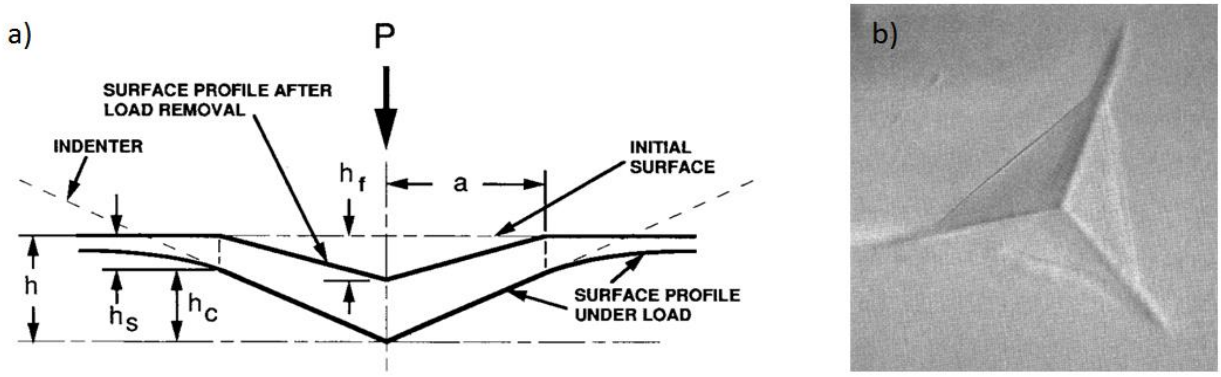

Figure 2-22 (a) Schematic illustration of the unloading process showing parameters characterizing the contact geometry (from ref. [205]) (b) A scanning electron micrograph of a 40 mN indentation in fused silica (from Ref. [203]).

$$P_{load} = \beta h^n \tag{2-11}$$

$$P_{unload} = \alpha\left(h - h_f\right)^m \tag{2-12}$$

For the Berkovich indenter, unloading curves typically have exponent values between 1.2-1.5 (see Table 2-3 [203]). The three important factors for nanoindentation data analysis are the maximum load P_{max}, the stiffness S, and the indenter depth at maximum load (h_{max}). The contact stiffness, S, is defined as the derivative dP/dh at the maximum load and is written as [202, 205]:

$$S = \beta \frac{2}{\sqrt{\pi}} E_r \sqrt{A} \tag{2-13}$$

Oliver and Pharr added the β value to account for any physical process which may affect the constant in Eq. (2-13). The reduced (or effective) modulus, E_r, is defined as [206]:

$$\frac{1}{E_r} = \frac{1 - \upsilon^2}{E_s} + \frac{1 - \upsilon_i^2}{E_i} \tag{2-14}$$

here, E_s and υ_s are Young's modulus and Poisson's ratio for the specimen and E_i and υ_i are the same parameters for the indenter tip material. For a diamond tip, E_i and υ_i are 1,141 GPa and 0.07, respectively [207].

Table 2-3 Values of parameters characterizing unloading curves as observed in nanoindentation experiments with a Berkovich indenter (from Ref. [203]).

Material	α (mN/nm^m)	m	Correlation coefficient, R
Aluminum	0.265	1.38	0.999938
Soda-lime glass	0.0279	1.37	0.999997
Sapphire	0.0435	1.47	0.999998
Fused silica	0.0500	1.25	0.999997
Tungsten	0.141	1.51	0.999986
Silica	0.0215	1.43	0.999985

The contact area at peak load, A, is a function determined by the geometry of the indenter and the depth of contact h_c. The area function, A, is a truncated power series with the following form [201]:

$$A(h_c) = \sum_{k=1}^{8} A_k h_c^{2^{2-k}} \tag{2-15}$$

For the ideal Berkovich indenter, $A_1 = 24.5$. The importance of the area function cannot be overstated since it must be known prior to analyzing nanoindentation data. To determine the area function, we must first determine h_c. The contact depth can be determined from the maximum displacement using the following equation:

$$h_c = h_{max} - \varepsilon \frac{P}{S} \tag{2-16}$$

Equation (2-16) is known as the Oliver and Pharr method [203-205]. Here ε depends on the indenter geometry, but is typically 0.75 for the Berkovich indenter. The aforementioned method was introduced as a necessary modification of the flat punch approximation since it did

not adequately describe the behavior of materials indented by a Berkovich tip. From the area function, A, the nanoindentation hardness, H, can be determined at h_c:

$$H = \frac{P_{max}}{A(h_c)} \tag{2-17}$$

2.4.3.1 Indentation Size Effect

The indentation size effect (ISE) is observed during indentation experiments and is characterized by a decrease in hardness with increasing indentation load [208]. This phenomenon has been observed in metallic glasses [209, 210], polymers [211], and crystalline alloys [212, 213]. One such model that has examined the ISE in crystalline materials is known as the Nix Gao model [212]. This method has its origins in the Taylor dislocation model and is based on the theory of geometrically necessary dislocations. Based on this model, Nix and Gao were able to derive an equation that can extrapolate nanoindentation hardness data in order to estimate the bulk hardness of a given material. The extrapolation is performed through the following equation:

$$\frac{H}{H_0} = \sqrt{1 + \frac{h^*}{h}} \tag{2-18}$$

where H is the hardness at an indentation depth h, H_o is the hardness in the limit of infinite depth and h^* is a characteristic length that depends on the shape of the indenter [72]. It should also be mentioned that H_o is the hardness which arises from the statistically stored dislocations and is written as:

$$H_0 = 3\sqrt{3}\alpha\mu b\sqrt{\rho_s} \tag{2-19}$$

here μ is the shear modulus, ρ_s is the density of statistically stored dislocations, b is the Burger's vector, and α is a constant (taken as 0.5 in [212]). Using Eq. (2-19) and the half angle θ of the indenter tip we can solve for h^* with the following equation:

$$h^* = \frac{81}{2} b\alpha^2 \tan^2\theta \left(\frac{\mu}{H_0}\right)^2 \tag{2-20}$$

To account for a non-uniform dislocation spacing, Eq. (2-20) is usually modified into the following form:

$$h^* = \frac{27}{2} b\alpha^2 \tan^2\theta \left(\frac{\mu}{H_0}\right)^2 \tag{2-21}$$

To determine the theoretical bulk hardness of a material, one simply plots H^2 vs. 1/h and extrapolates a straight line to the limit $1/h \rightarrow 0$, which correlates to an infinite indentation depth. The y intercept determines the bulk hardness H_o and the slope determines h^*. Once H_o and h^* are found, one plots the data on a $(H/H_o)^2$ vs. 1/h graph. An illustration of the extrapolation technique for (111) single crystal and cold worked polycrystalline Cu can be seen in figures 23 (a)-(c) below [72, 75].

More recently, other models have been used to analyze the ISE [211, 213-215]. For example, Lam and Chong proposed a model which they applied to glassy polymers [211]. This

model was based off the work done by Argon [216], which replaced statistically stored and geometrically necessary dislocations with analogous kink pairs. Here, the formation of kinks canbe thought of as changes of entropy associated with the straightening of polymer chains and strain hardening effect [211]. In terms of the hardness, the extrapolated hardness is written as:

$$H = H_0\left(1 + \sqrt{\frac{h^*}{h}}\right) \tag{2-22}$$

Here, the extrapolated hardness is defined as:

$$H_0 = \frac{3\sqrt{3}}{8}G(1 + \psi L n n_{ks})^{6/5} \tag{2-23}$$

where G is the shear modulus, ψ is a dimensionless constant that depends on G and the temperature, and n_{ks} proportional to the density of statistically stored kinks. The characteristic depth is defined as:

$$h^* = \frac{81 z^* \alpha^2 G^2 \psi^2 \tan^2\theta}{128 H_0^2 \exp\left(\frac{16\sqrt{3}\sigma_0 - 3G}{3\psi G}\right)} \tag{2-24}$$

here, z^* is the activate kink length of a kink pair, σ_0 is a reference stress.

Lam and Chong derived a model to examine the ISE in metallic glasses [209], in which the depth dependent terms depend on material parameters such as the extrapolated hardness and the number of atomic cluster defects in the amorphous matrix. This model consists of an equation that

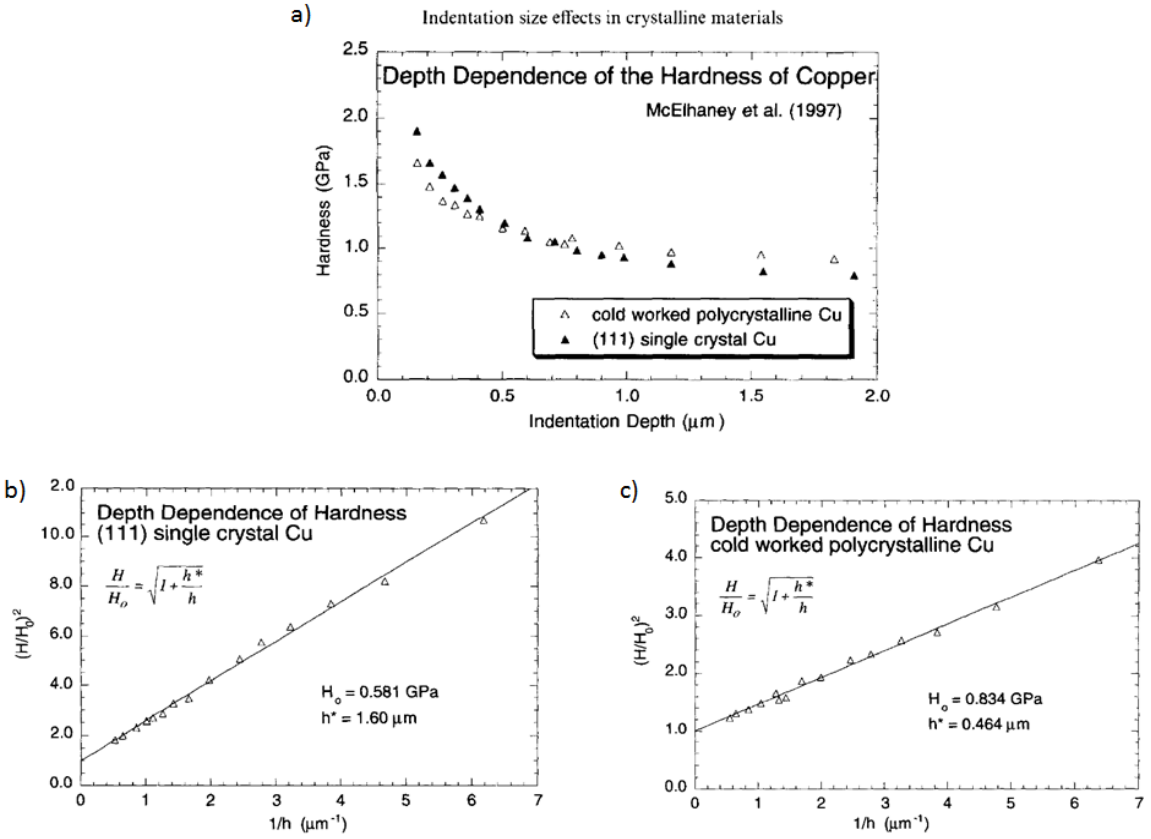

Figure 2-23 (a) Hardness of (111) single crystal and cold worked polycrystalline copper, (from Ref. [212]). (b) Nix-Gao extrapolation of the hardness data of (111) single copper, and (c) Nix-Gao extrapolation of the hardness data of polycrystalline copper.

is similar to the one as proposed by Nix and Gao:

$$H = H_0\left(1 + \frac{h^*}{\sqrt{h}}\right) \tag{2-25}$$

where H is the nanoindentation hardness, H_0 is the extrapolated (bulk) hardness value, H_0 is the hardness arising from the statistically stored clusters in the absence of the geometrically-necessary clusters that are associated with strain gradients [209, 217], h is the indentation depth, and h^* is a term which characterize the depth dependence of the hardness. For this model, h^* depends on other parameters such as the temperature, the angle between the tip and surface of the specimen, the Helmholtz free energy associated with the shear transformation of clusters, the local shear strain required to modify a single cluster, and the number of clusters associated with the strain.

2.5. Microstructural Characterization Techniques

2.5.1 X-ray Diffraction

X-rays were accidentally discovered by Wilhelm Röntgen during vacuum tube experiments in 1895 [218]. He named this mysterious type of radiation "X-ray" since in mathematics the "X" represents an unknown quantity [219]. Subsequently, Bragg et al. used X-rays to probe the structure of matter [220, 221]. From their work, they formulated what is known today as Bragg's Law, which is used to characterize the lattice structure in crystalline materials [222]:

$$n\lambda = 2dsin\theta \tag{2-26}$$

where n is a positive integer, λ is the wavelength of the incident X-ray, d is the spacing between atomic planes, and θ is the scattering angle of the X-ray. Figure 2-24 presents a schematic

illustration of incident radiation diffraction by a crystal lattice [223]. In the figure, two separate X-rays (with same wavelength), labeled 1 and 2, strike a crystal structure. From the figure it can be observed that as compared to Ray 1, Ray 2 must travel a longer distance before being reflected. If this distance ($2d\sin\theta$), is equal to an integer multiple of the wavelength, then the two X-rays will be in phase and constructively interfere upon exiting the crystal. This interference will be observed as intensity peaks as a function of scattering angle (see figure 2-25 [224]). Importantly, the scattering angle associated with the intensity peaks can be used to determine the lattice spacing for a given crystalline material.

Due to their amorphous structure, BMGs do not contain lattice planes. This lack of lattice planes leads to a broad peak in the diffraction pattern (DP). To put it into perspective, figure 2-26 displays a normalized intensity vs. scattering angle for a fully amorphous and partially crystallized $Cu_{60}Zr_{20}Hf_{10}Zr_{10}$ BMG. As can be seen, the patterns are noticeably different.

As to date, there have been numerous studies that have used X-ray diffraction (XRD) to examine the temperature dependent crystallization behavior of different metallic glasses [225-237]. In a couple of investigations [228, 229], a link was established between the corrosion behavior and the degree of crystallinity of the glass [227]. Another investigation found that the activation energies of crystallization in metallic glass ribbons gradually increased, respectively, with a decreasing Zr:Ni ratio [233]. Xu et al. surmised that oxidation in amorphous alloys occurs at a faster rate as compared to their crystalline counterparts due to its free volume content [238], which is believed to enhance the diffusion of oxygen [234].

For the above investigations, diffraction patterns were taken ex-situ, which means that the kinetics of the crystallization behavior could not be ascertained. However, more recent techniques

have employed characterization methods that have examined the in-situ kinetics of phase transformations in real time. Typically, this method is performed via the rapid collection of diffraction patterns during heating. Importantly, this technique has evolved in such a manner that the experimentalist can now perform the work in a typical laboratory setting, without the need for a synchrotron X-ray source [239].

With regards to evaluating the crystallization kinetics, it can be performed by analyzing the integrated area under the diffraction peaks [240, 241]. Furthermore, the fraction of the different crystalline phases that form in the matrix during heating can be determined via Rietveld Refinement [242]. The experimental kinetic data, with regards to the isothermal data, can be transformed to what is referred to as the experimental master plots that are used to determine the appropriate kinetic model [243]. This plot involves plotting This model depends on the parameter α, which is defined as the fraction of total reaction product formed at time t [244]. Next f(α) is

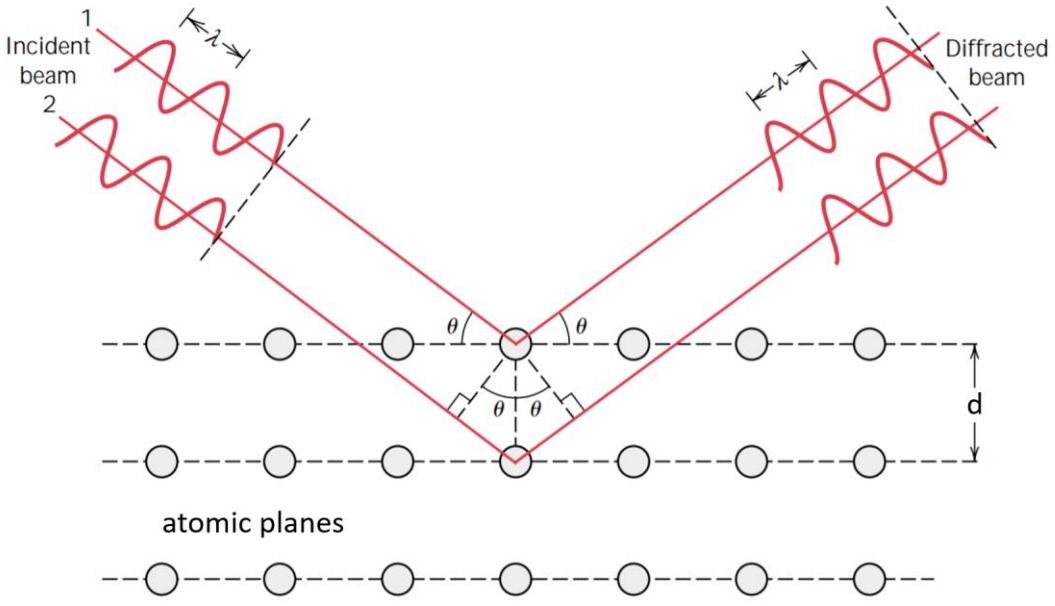

Figure 2-24 Schematic illustration of incident radiation diffraction by a crystal lattice (from Ref. [223]).

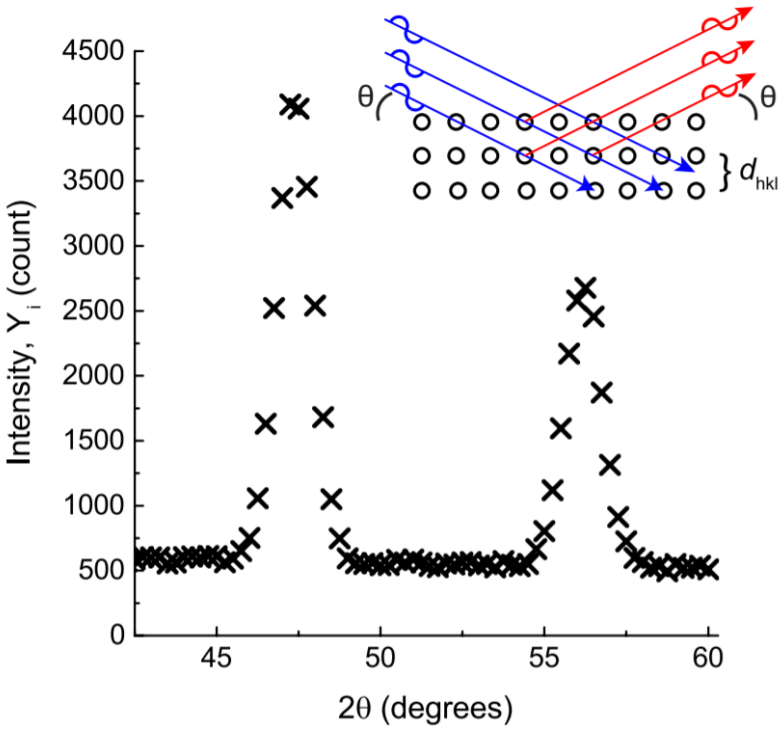

Figure 2-25 Constructive interference of X-rays scattered from planes of atoms which results in the observed peaks at various scattering angles (2θ) (from Ref. [224]).

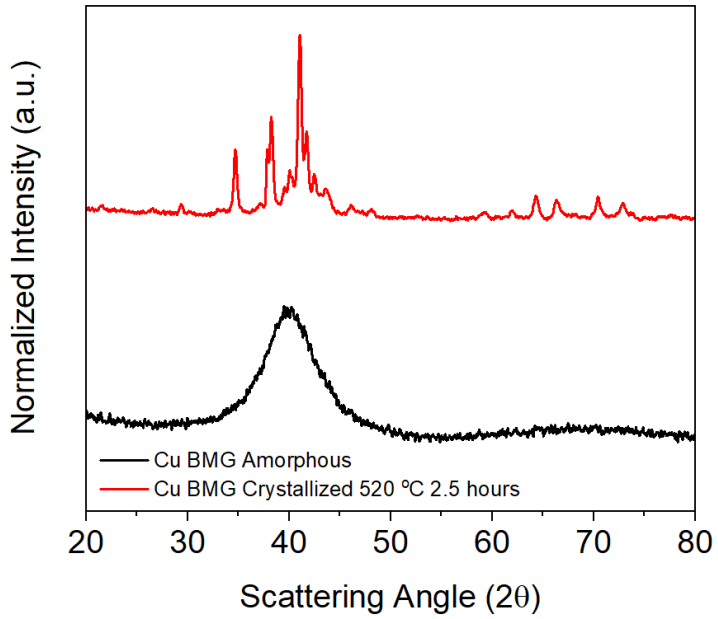

Figure 2-26 X-ray diffraction pattern of as cast and partially crystallized $Cu_{60}Zr_{20}Hf_{10}Ti_{10}$ BMG.

defined, which is a function that is representative of the kinetic model guiding the crystallization mechanism, and corresponds to the reaction rate dependence on α [245]. Another important mechanism of crystal growth is the Johnson-Mehl-Avrami-Kolmogorov (JMAK) model [246-250]. This model is tied to the random nucleation and growth of crystal nuclei in a matrix, and the guiding equations is written as [239]:

$$\alpha = 1 - \exp[-k(t - t_0)^n] \tag{2-27}$$

where the temperature-dependent rate constant, k, and JMAK exponent, n, equate to:

$$k = \sqrt[n]{\frac{f_d v e^{\frac{\Delta S}{k_b}} U^{n-1}}{n}} \tag{2-28}$$

$$n = \frac{d}{m} + 1 \tag{2-29}$$

here, f_d is the dimensionality of growth, v is the effective attempt frequency, ΔS is the system entropy, k_b is Boltzmann's constant, U is the particle growth rate, d is the dimensionality of the growth mechanism, and m is the growth mode factor. To determine the growth mode, one first graphs the master plot f(α)/f(0.5) vs. α and then fits the data for $\frac{d\alpha}{dt} / \frac{d\alpha}{dt}_{\alpha=0.5}$ vs. α to the various plots. To evaluate the rate constant, k, and the JMAK exponent, n, one applies linear regression analysis to the plot of $\mathrm{Ln}\left[\mathrm{Ln}\left(\frac{1}{1-\alpha}\right)\right]$ vs. $\mathrm{Ln}(t - t_0)$.

Table 2-4 lists the kinetic mechanism, the corresponding symbol, and the representative function f(α) for the different solid-state kinetic transformations [239]. These transformations can range from two dimensional phase boundary controlled to three dimensional diffusion (Ginstein-Brounshtein equation) [243].

With respect to diffusion-controlled transformations, diffusion typically affects the rates of reaction between two reacting solids when they coexist as distinct crystal lattices [251]. In other words, the atomic mobility essentially controls the transformation rate. Furthermore, the rate of product formation decreases proportionally with the thickness of the product barrier layer [252]. For heterogenous transformations, the solid-state reactions often occur between crystal lattices that eventually permeate into lattices where the motion is restricted and may depend on lattice defects [253].

Figures 2-27(a)-(b) show a basic schematic of the JMAK and heterogenous processes that would occur in the matrix over time. As apparent in the figures, both mechanisms have slightly

Table 2-4 The kinetic mechanisms, the corresponding symbol, and the representative function f(α) for the solid-state kinetic transformation. Reproduced from [239].

Kinetic Mechanism	Symbol	f(α)
Unimolecular decay law	F1	$1-\alpha$
Phase boundary controlled (Two-dimensional)	R2	$(1-\alpha)^{1/2}$
Phase boundary-controlled reaction (Three-dimensional)	R3	$(1-\alpha)^{1/3}$
Two-dimensional diffusion	D2	$-\frac{1}{\ln(1-\alpha)}$
Three-dimensional diffusion (Jander equation)	D3	$\frac{3(1-\alpha)^{2/3}}{2(1-\alpha)^{1/3}}$
Three-dimensional diffusion (Ginstein-Brounshtein equation)	D4	$\frac{3}{2[(1-\alpha)^{-1/3}-1]}$
Random nucleation and growth (JMAK)	Am	$n(1-\alpha)[-\ln(1-\alpha)]^{1-1/n}$

different characteristics. With regards to the JMAK model, as shown in figure 2-27(a), the particlesnucleate randomly throughout the matrix in which they expand uniformly in all directions. Whereas for the diffusion-controlled process [see figure 2-27(b)] two separate phases interact with each other, thereby producing a third phase which increases in size over time.

2.5.1.1 High Energy In Situ X-ray Diffraction

High energy X-ray diffraction has been used to probe the microstructure of crystalline materials in various ways [254]. This technique is especially useful when examining samples that are poor diffractors or are extremely small. Due to the amorphous structure of BMGs, an imposed compressive field during XRD reveals the nature of the structure due to a broken symmetry that would otherwise not be observed without the field [255]. Because of the elastic deformation induced anisotropy [256], the PDF analysis of the anisotropic and the isotropic data for the BMG

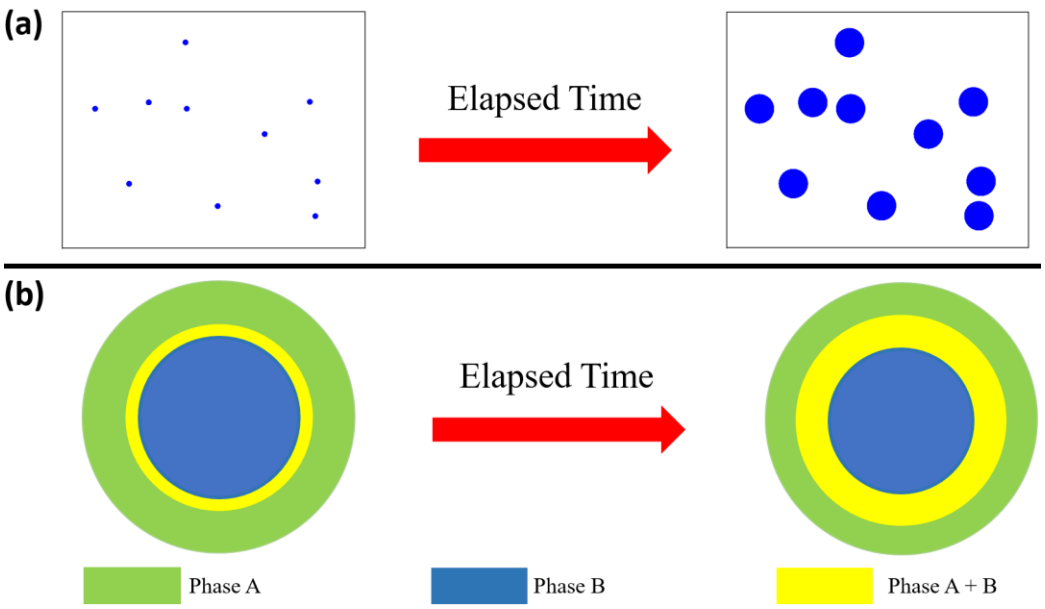

Figure 2-27 Schematic of the (a) JMAK, and the (b) heterogeneous diffusion transformation processes (from Ref. [239]).

can be applied [257]. The isotropic PDF is related to the structure function in the following manner:

$$\rho_0 g(r) = \frac{1}{2\pi^2 r}\int_0^\infty [S(Q) - 1]\sin(Qr)\, Q dQ \tag{2-30}$$

where g(r) is the radial distribution, S(Q) is the structure function, Q is the diffraction vector that is equal to $4\pi\sin\theta/\lambda$ where θ is the diffraction angle, λ is the wavelength of the probe, and ρ_0 is the number density of the atoms in the BMG [256]. To examine the changes to the anisotropic behavior of a BMG under an applied stress, the anisotropic pair density function (PDF) method can be applied to the in situ compression data [258], which is based on spherical harmonics, is applied.

The anisotropic PDF is related to the structure function via a Bessel transformation:

$$\rho_0 g_l^m(r) = \frac{i^l}{2\pi^2}\int_0^\infty S_l^m(Q) J_l(Qr) Q^2 dQ \tag{2-31}$$

here $J_l(Qr)$ is the spherical Bessel function [259], and the functions $g_l^m(r)$ and $S_l^m(Q)$ are related to the functions g(r) and S(Q) via the spherical harmonic relations:

$$g(\boldsymbol{r}) = \sum_{l,m} g_l^m(r) Y_l^m\left(\frac{\boldsymbol{r}}{r}\right) \tag{2-32}$$

$$S(\boldsymbol{Q}) = \sum S_l^m(Q) Y_l^m\left(\frac{\boldsymbol{Q}}{Q}\right) \tag{2-33}$$

where Y_l^m are the spherical harmonics. Another important quantity is the affine anisotropic PDF, $g_{2,aff}^0(r)$ [255, 260]:

$$g^0_{2,aff}(r) = -\varepsilon_{zz,aff}\frac{2(1+\upsilon)}{3\sqrt{5}} r \frac{d}{dr} g^0_0(r) \quad (2\text{-}34)$$

where $-\varepsilon_{zz,aff}\frac{2(1+\nu)}{3\sqrt{5}}$ is a fitting parameter, $-\varepsilon_{zz,aff}$ is the affine strain, and υ is Poisson's ratio. Figure 2-28 compares the anisotropic PDF $g^0_2(r)$ and the affine PDF (red curve) for the $Zr_{55}Cu_{30}Ni_5Al_{10}$ BMG when compressed by 1,000 MPa for 1 hr. at 623 K [255].

2.5.2 Transmission Electron Microscopy

Historically, transmission electron microscopes (TEM) were developed because of the limited age resolution in light microscopes, which is imposed by the wavelength of visible light [261]. The resolution of modern TEMs is 2 Å while the theoretical resolution for optical microscopes is 200 nm. Although the superior magnification is a distinct advantage, TEMs do have some disadvantages such as the requirement of very thin samples (< 100 nm [262]) and high operational expenses.

A basic schematic of a TEM can be seen in figure 2-29. At the top of the TEM is either a thermionic or field emission gun (FEG) (see Table 13 from Ref. [157] for different electron sources). It should be noted that the design of the thermionic gun is different than that of a field emission gun. For example, in a thermionic gun, the electrons are boiled off through resistively heating the gun, while in a FEG the electrons are removed through an electrostatic potential. For TEM, bright-field (BF) and dark-field (DF) are the main types of images used, and are formed by a combined use of the objective lens and objective aperture. Specifically, a BF image is formed by the direct-beam electrons while a DF image is formed by the diffracted beam (high angle electrons) [263]. If instead a diffraction pattern (DP) is desired, a SAD aperture is inserted in

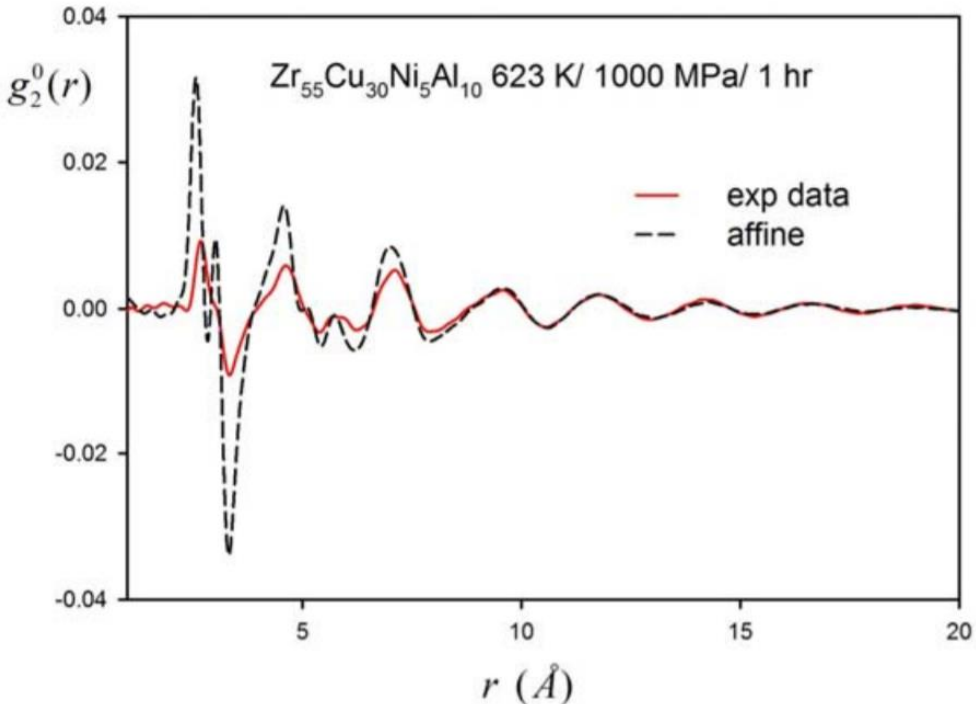

Figure 2-28 Comparison of the anisotropic PDF $g_2^0(r)$ and the affine PDF (red curve) for the $Zr_{55}Cu_{30}Ni_5Al_{10}$ BMG when compressed by 1,000 MPa for 1 hr. at 623 K (from Ref. [255]).

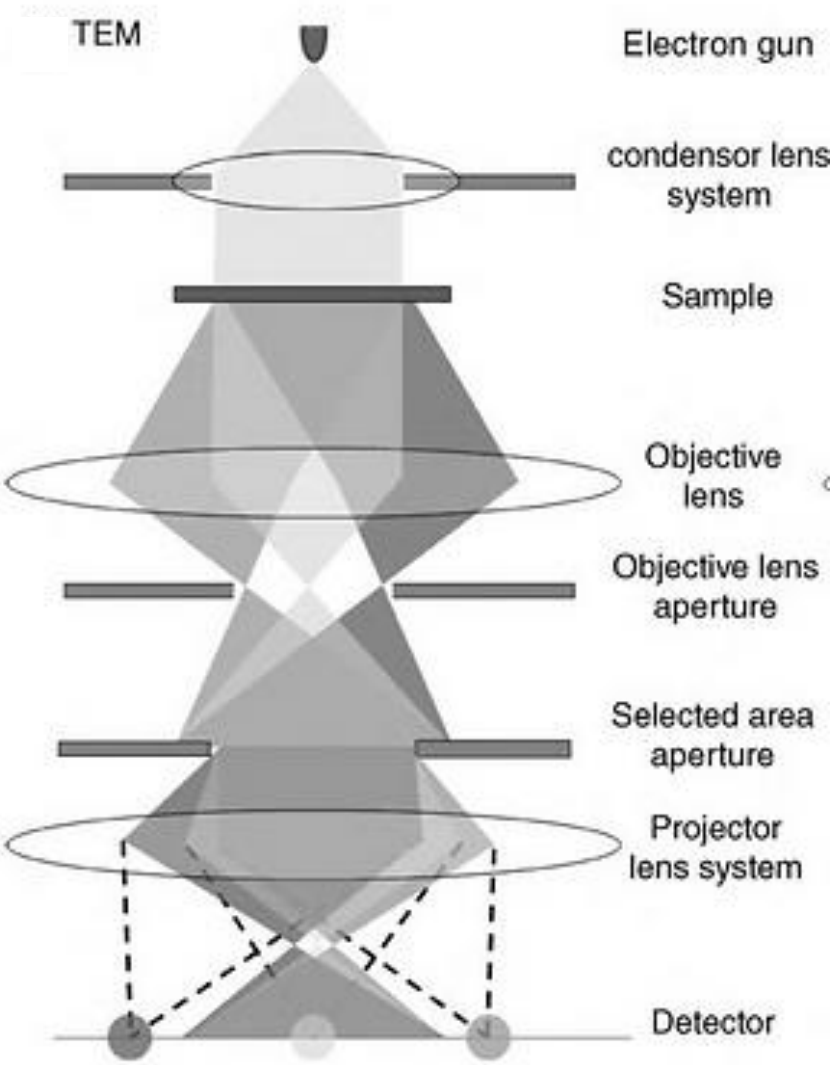

Figure 2-29 Simplified Schematic diagram of the principles of TEM imaging and diffraction (from Ref. [265]).

place of the objective aperture. Here, the SAD is inserted into the image plane of the objective lens. While in the image plane the SAD aperture will permit only those electrons inside the area defined by the virtual aperture. A DP for nanocrystalline Al can be seen in figure 2-30, which includes the corresponding BF and DF images [262]. Notice the complimentary nature of the BF and DF images.

Inelastic scattering of electrons can lead to beam damage of the material, which can be in the form of knock on damage or heating [261]. Knock on damage occurs when, just as the name suggests, an electron collides with an atom in such a way that the atom is displaced from its original lattice site. The resultant interstitial vacancy combination is known as a Frenkel pair [34].

However, due to their amorphous structure, Frenkel pairs cannot be created in an amorphous alloy during irradiation. Although for these materials, both knock-on collisions and beam heating can increase the temperature of the material, which can fundamentally alter the short-range ordering of the glass and even cause crystallization. This is because both phenomena can heat the alloy, causing the temperature to rise above its glass transition. Although it was not discussed earlier, knock on collisions can lead to displacement cascades, which exhibit a sharp increase in temperature in the region where the knock on occurs. Therefore, beam heating should always be minimized when examining metallic glass specimens in TEM.

Liu et al. examined the crystallization behavior of $(Fe_{0.99}Cu_{0.01})_{78}Si_9B_{13}$ amorphous alloy ribbons by in situ transmission electron microscopy [264]. The specimen was heated to temperatures ranging from 583-813 K using an electron microscope specimen holder. During

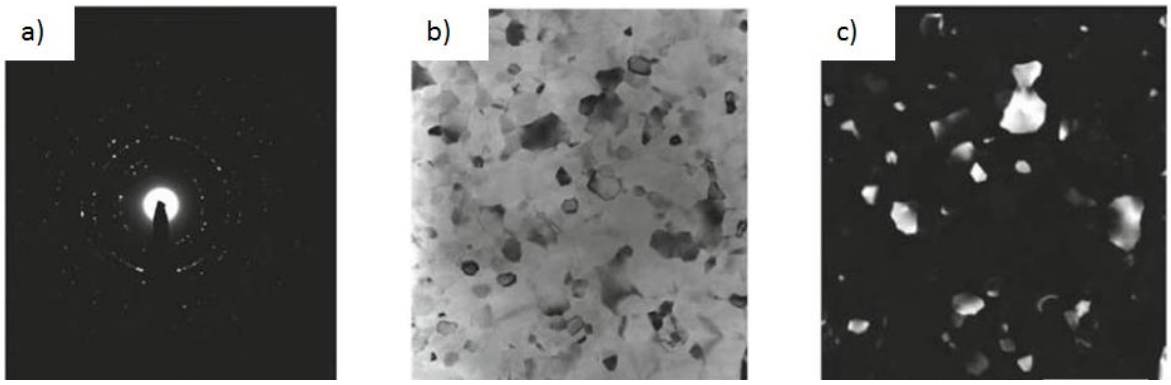

Figure 2-30 (a) Diffraction pattern of a nanocrystalline Al film. (b) Corresponding BF image. (c) Corresponding DF image (from Ref. [262]).

annealing, crystal nuclei were observed forming around the edge of the thin area of the sample. The crystalline region grew to a thickness of 150 nm after exposure to 583 K for 10 minutes.

Moreover, it was found that after 15 minutes of annealing that the average grain size of the crystallites were about 15 nm. After heating to 723 K, the sample was observed to fully crystallize. Figure 2-31 shows the bright field (BF) TEM and selected area electron diffraction pattern corresponding for the as-quenched and annealed samples. When heated to 583 K for 15 minutes, a crystalline phase composed of α-Fe(Si) (bcc structure) with a random orientation formed in the sample. After annealing for 723 K for 10 minutes, the sample underwent full crystallization accompanied by the formation of a Fe_2B crystalline phase. In contrast to the above conditions, no new crystalline phases were observed when the sample was exposed to 813 K. It was also observed that there was increased grain growth around the edge of the thinned area.

Pekarskaya et al. performed room temperature in situ straining TEM experiments to study shear band propagation in $Zr_{56.3}Ti_{13.8}Cu_{6.9}Ni_{5.6}Nb_{5.0}Be_{12.5}$ BMG based composite [144]. For this study a JEOL 4000 EX operating at 300 kV was used and images were taken using both bright-

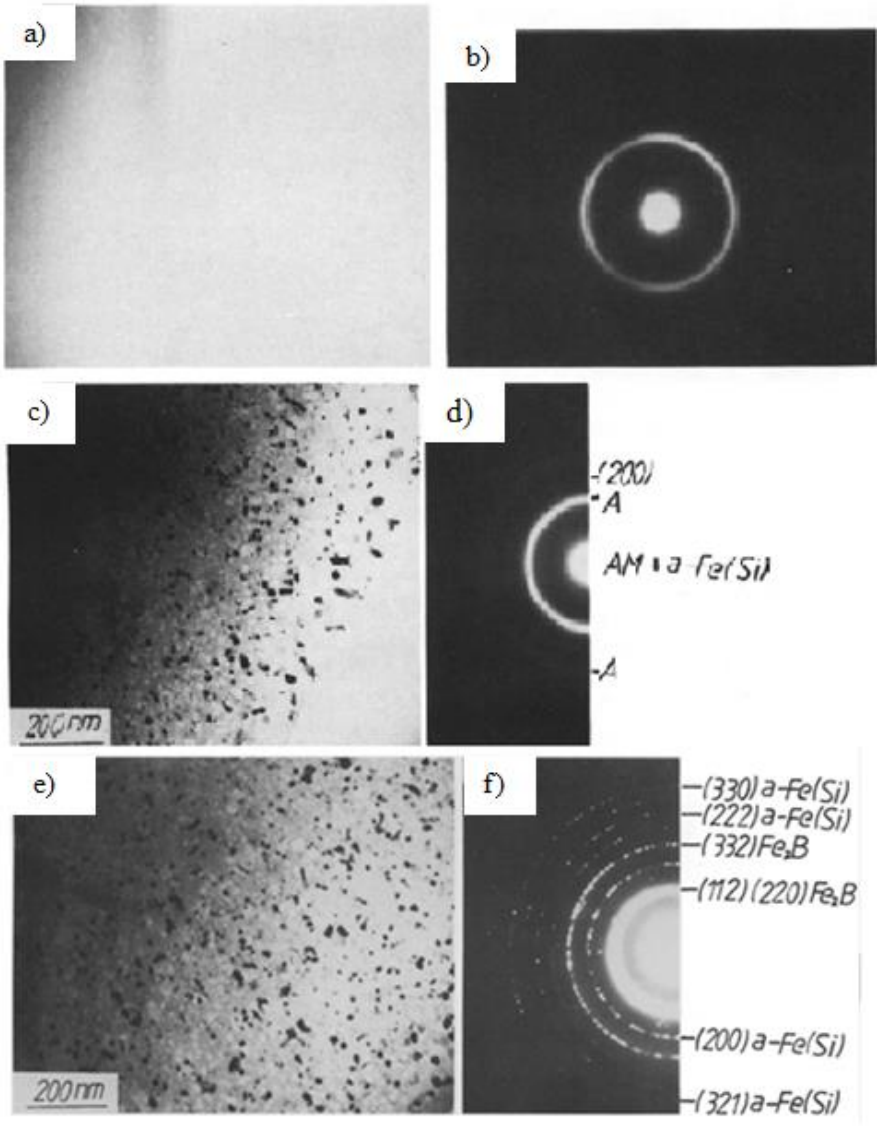

Figure 2-31 BF TEM images and DPs for $(Fe_{0.99}Cu_{0.01})_{78}Si_9B_{13}$ (a) as-quenched (c) annealed (583 K, 15 min) (e) fully crystallized. Here, (b), (d), and (f) are the corresponding diffraction patterns for (a), (c), and (e) respectively (from Ref. [264]).

field and dark-field techniques. However, contrast issues with dark-field techniques led to using bright–field as the primary technique for imaging shear bands. In terms of sample preparation, specimens were prepared by ion milling. Figure 2-32 shows the microstructure and corresponding diffraction pattern of the composite material. In terms of composition, the material consisted of an amorphous matrix which contained crystalline β-phase dendrites with bcc structure which had a lattice parameter of 3.5 Å. However, the presence of twins in the body centered cubic (bcc) structure indicated there was instability in the dendritic configuration.

Figure 2-33 shows a crack which had propagated through the amorphous matrix. Shear bands were observed to form at the crack tips and were characterized by a lighter contrast as compared to the rest of the material. The lighter contrast indicates that the shear band regions were less dense than the undeformed material. Furthermore, shear bands were observed to have a width ranging from 120-200 nm, which were similar to results obtained from scanning electron microscopy imaging, and varied between 200-300 nm.

Figure 2-34 shows a typical interaction between the shear band and the β-phase dendrite. It was found that the localization of deformation in the crystalline phase only occurred when a shear band interaction was accompanied by a large amount of shear in the amorphous phase. Here an adequately strong shearing event will lead to the formation of dislocations in the β-phase that corresponds to deformation in the crystallites.

Koziel et al. investigated the crystallization of $Fe_{72}Si_{9.1}B_{14.8}Cr_{2.2}C_{1.9}$ amorphous ribbons with a 3 mm width and thickness of 20 μm [266]. To achieve crystallization, the material was heated to 923 K using a heating rate of 5 K/min. To examine the structure of the crystallized alloy, a JEM 200 CX TEM (JEOL, Tokyo, Japan) operated at 200 kV was used. Differential scanning

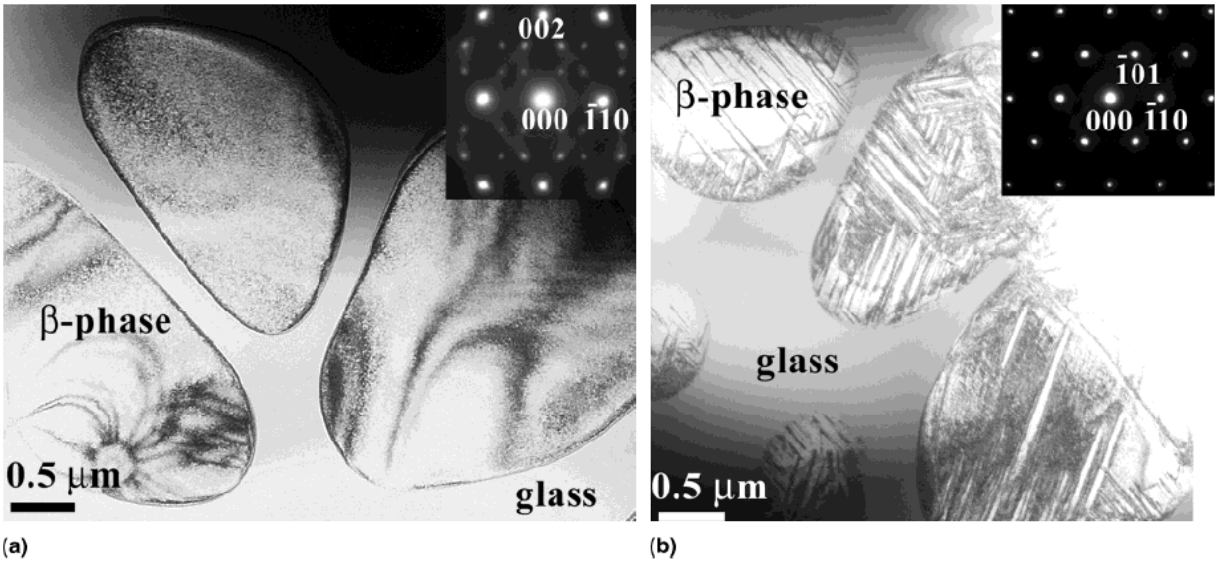

Figure 2-32 (a) TEM micrograph of the microstructure of the composite material and corresponding diffraction pattern. (b) TEM image of the twins in the β-phase with diffraction pattern for the [111] zone axis (from Ref. [144]).

calorimetric (DSC) analysis was utilized to examine the crystallization process. Here the TEM specimens were standard 3 mm discs cut out from the as-spun and crystallized ribbon and thinned by ion milling at 2.5 kV and 0.5 mA. TEM studies revealed the presence of α-Fe_3(Si) solution, $Fe_{23}(C,B)_6$, Fe_3B and Fe_2B crystalline phases [266].

Figures 2-35(a)-(b) shows TEM bright-field selected area electron diffraction of the as-spun and annealed ribbon. The diffraction pattern in figure 2-35(b) exemplify the crystalline phases α-Fe_3(Si) and $Fe_{23}(C,B)_6$. From the results of the DSC analysis, it was concluded that during crystallization, metastable borides initially formed in the $Fe_{72}Si_{9.1}B_{14.8}Cr_{2.2}C_{1.9}$ amorphous alloy, followed by the formation of a stable Fe_2B phase.

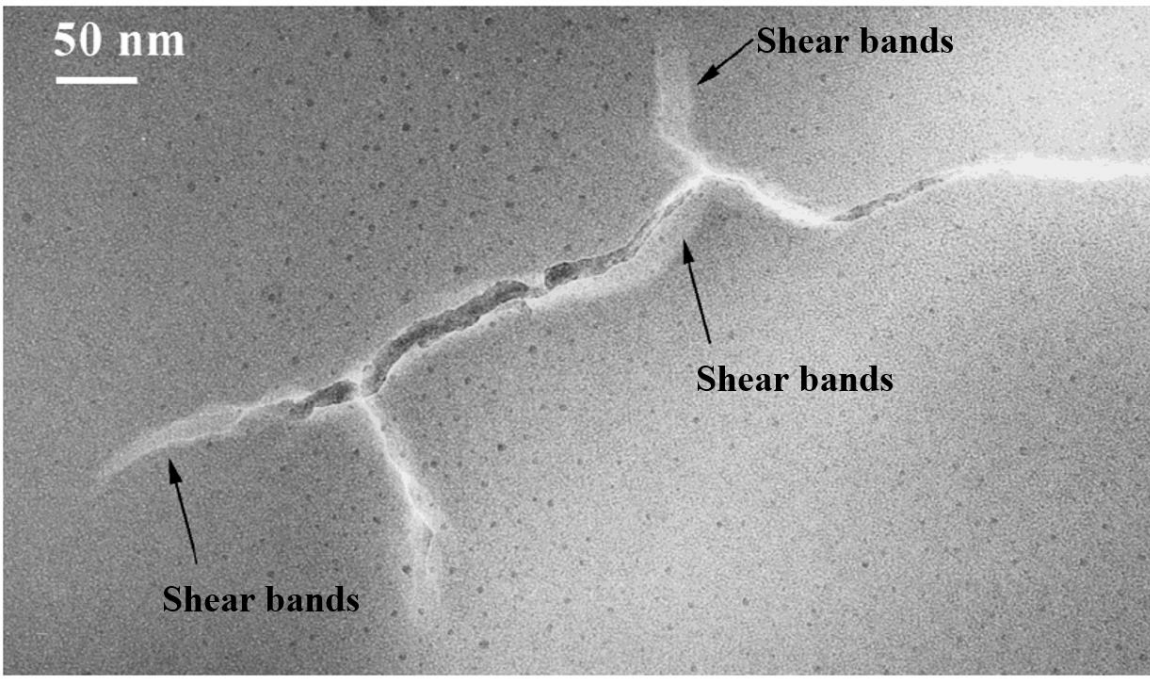

Figure 2-33 Crack propagation with shear banding in the glassy phase (from Ref. [144]).

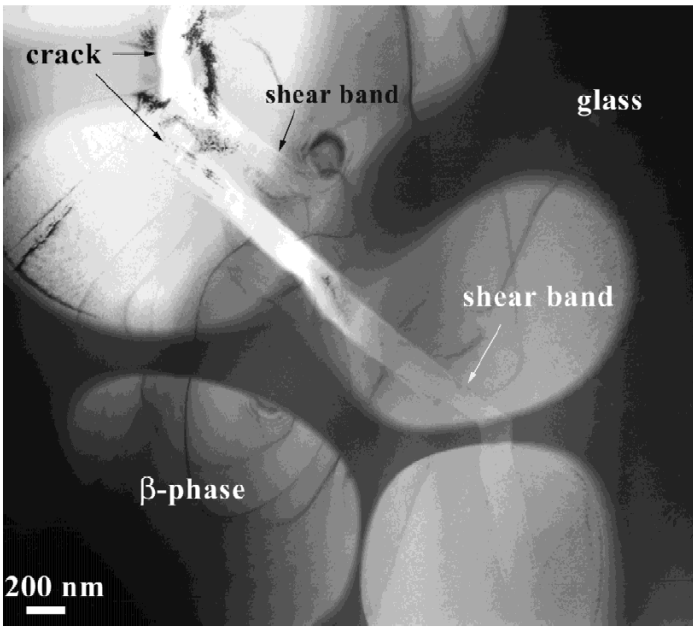

Figure 2-34 TEM image of the shear band propagation through the amorphous and crystalline regions $Zr_{56.3}Ti_{13.8}Cu_{6.9}Ni_{5.6}Nb_{5.0}Be_{12.5}$ BMG based composite. Localization of deformation is observed in the β-phase (from Ref. [144]).

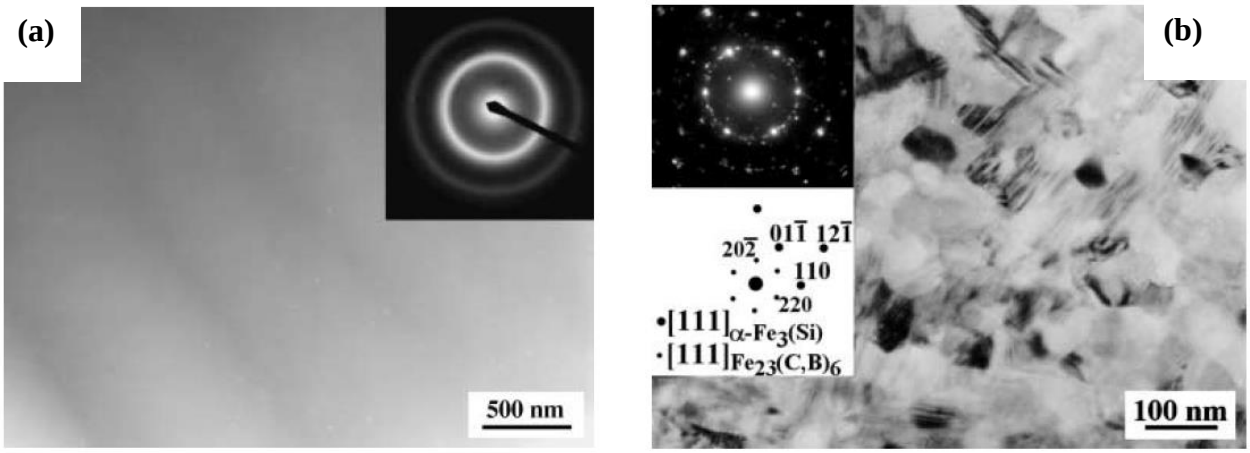

Figure 2-35 TEM bright-field SAED Patterns for $Fe_{72}Si_{9.1}B_{14.8}Cr_{2.2}C_{1.9}$ amorphous alloy (a) The as-spun ribbon, (b) Ribbon heated up to 923 K (from Ref. [266]).

Jang et al. studied the crystallization kinetics of $Zr_{60}Al_{7.5}Cu_{17.5}Ni_{10}Si_4B_1$ metallic glass ribbons under isothermal annealing [267]. Here annealing temperatures were 709 K, 714 K, 719 K and 724 K with respective heating times of 2600 s, 1381 s, 1270 s and 562 s. A Philips Tecnai G2 TEM with an operating voltage of 200 kV was used in conjunction with a DSC 2920 differential scanning calorimeter to determine crystallization kinetics. SAD patterns for the sample annealed at 714 K consisted of diffraction spots with Miller indices of (213), (006), (103) and (110) which indicated the formation of Zr_2Cu-type crystalline phase in the matrix. Isothermal differential calorimetry analysis revealed that the radius of the crystal (also labelled grain) was found to be 5 nm after an annealing time of 119 s, but grew to asize of 17 nm after 619 s. The calorimetric analysis was then extended to all heat treatment conditions for which the results can be seen in figure 2-36.

The activation energy for crystal growth in the $Zr_{60}Al_{7.5}Cu_{17.5}Ni_{10}Si_4B_1$ metallic glass was found to be 210 ± 25 kJ/mol. For reference, the activation energies for $Zr_{65}Cu_{27.5}Al_{7.5}$ and $Zr_{65}Cu_{35}$ amorphous alloys are 165 kJ/mol and 440 kJ/mol respectively [268, 269]. From the results it was

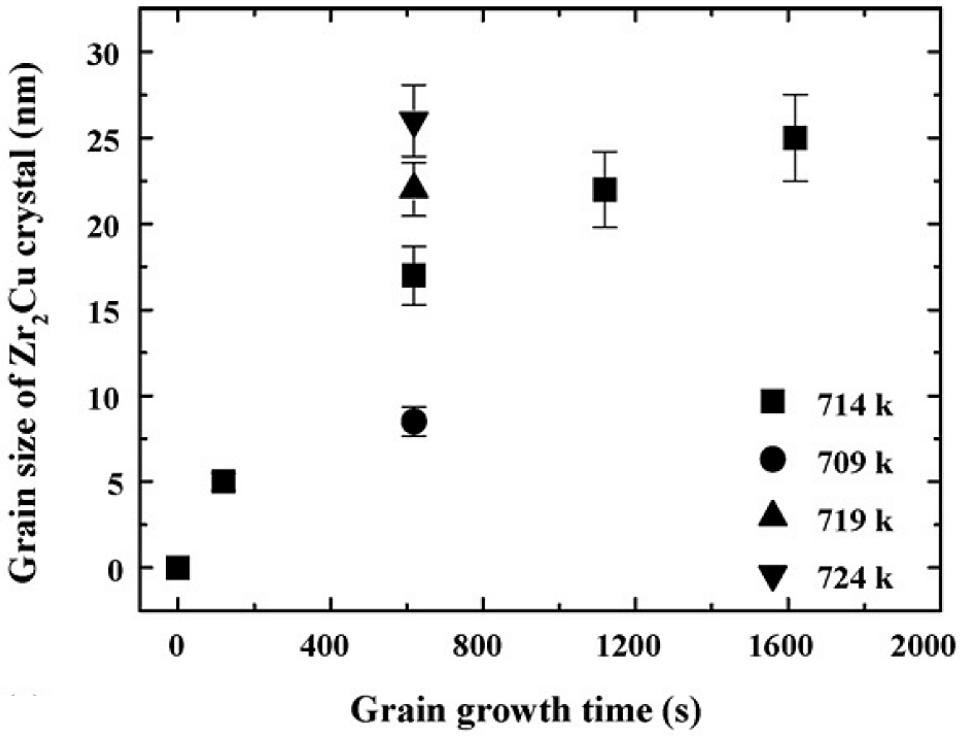

Figure 2-36 Relationship between the particle size of Zr_2Cu and annealing time at different temperatures (From Ref. [267]).

suggested that lower activation energies for crystallization growth corresponds to rearrangement of smaller atoms such as Al or Si [267]. In contrast, higher activation energies for growth may be due to the diffusion of larger atoms, such as Zr, in the metallic glass [270]. For more studies on TEM experiments involving metallic glasses, see [271-279].

2.6 Irradiation Theory

The effects of irradiation on the mechanical and microstructural behavior of different material systems is a broad field which has been intensively studied for over a century. With the advent of nuclear reactor technology, the field has only accelerated because of a need to understand the deleterious effects of irradiation on the properties of reactor materials. Specifically, neutron bombardment of a material over time can fundamentally alter its microstructure, eventually leading to embrittlement and fracture. Therefore, gaining a thorough understanding of the underlying mechanisms which contribute to irradiation induced degradation of structural materials can improve predictive capabilities that is expected to improved reactor performance and lifetime.

In the field of radiation material science, neutron bombardment is not the only means to study the irradiation effects in materials. Charged particles such as ions and electrons have also been used to gain a better understanding of how materials respond to irradiation damage. However, unlike neutrons, which interact with the nucleus of an atom, charged particles interact with both the nucleus and the electron cloud [34]. The reason ions and electrons are used is because of their significantly higher defect production rates as compared to neutrons [280].

2.6.1 Defect Production

2.6.1.1 Knock-On Collisions

When a material is irradiated by neutrons or charged particles, collisions occur between the incoming particle and the constituent atoms. For crystalline materials, collisions lead to atoms being knocked off their lattice site, forming interstitial-vacancy pairs called Frenkel defects. To calculate the amount of defects produced in a material the damage rate equation is used [34, 281]:

$$R_d = N \int_{E_{min}}^{E_{max}} \phi(E_i) \left[\int_{T_{min}}^{T_{max}} \sigma(E_i, T) \upsilon(T) dT \right] dE_i \tag{2-35}$$

here N is the lattice atom density, $\phi(E_i)$ is the energy-dependent particle flux, $\sigma(E_i,T)$ is the probability that a particle of energy E_i will impart a recoil energy T to a struck lattice atom, and $\upsilon(T)$ is known as the damage function which describes the number of displaced atoms resulting from such a collision. According to the modified Kinchin-Pease model (often referred to as the Norgett-Robinson-Torrens (NRT) model [282]), the function $\upsilon(T)$ can be written as [283, 284]:

$$\upsilon(T) = \begin{cases} 0 & for\ T < T_d \quad (2\text{-}36) \\ 1 & for\ T_d < T < 2.5T_d \quad (2\text{-}37) \\ 0.8\dfrac{E_D(T)}{2T_d} & for\ T > 2.5\ T_d \quad (2\text{-}38) \end{cases}$$

where T_d is the average threshold energy for displacements, and $E_D(T)$ is the portion of the recoil energy T available for producing displacements [285]. It is now known, however, that the

modified Kinchin-Pease model overestimates the defect production by a factor of 3-5 in most metals and also underestimates atomic mixing effects [286, 287].

2.6.1.2 Collision Cascades

When a primary knock-on event occurs, a collision cascade typically follows. If the energy is large enough, multiple sub-cascades are produced instead of one large cascade. For example, well-defined subcascades begin to form in copper for PKA energies above roughly 20 keV [287]. The large number of ions set into motion in a displacement cascade gives rise to a "mixing" of atoms in the solid (see figure 2-37) [288].

Cascade mixing is a process which involves multiple collisions that cause the recoiled atoms to be randomly implanted. A parameter which can estimate the magnitude of cascade mixing is known as the mixing parameter Q, and is defined as [288]:

$$Q = \frac{0.4\beta\lambda^2}{N_0 E_d} \tag{2-39}$$

here λ is the jump distance, β is the number of "replacements" per atomic displacement, N_o is the atomic volume and E_d is the threshold displacement energy. Table 2-5 lists the mixing parameters of several metals [288, 289]. The mixing parameter is an accurate measure for metals that have average to low atomic numbers and high melting temperature (T_m), but inaccurate for metals with high Z and T_m.

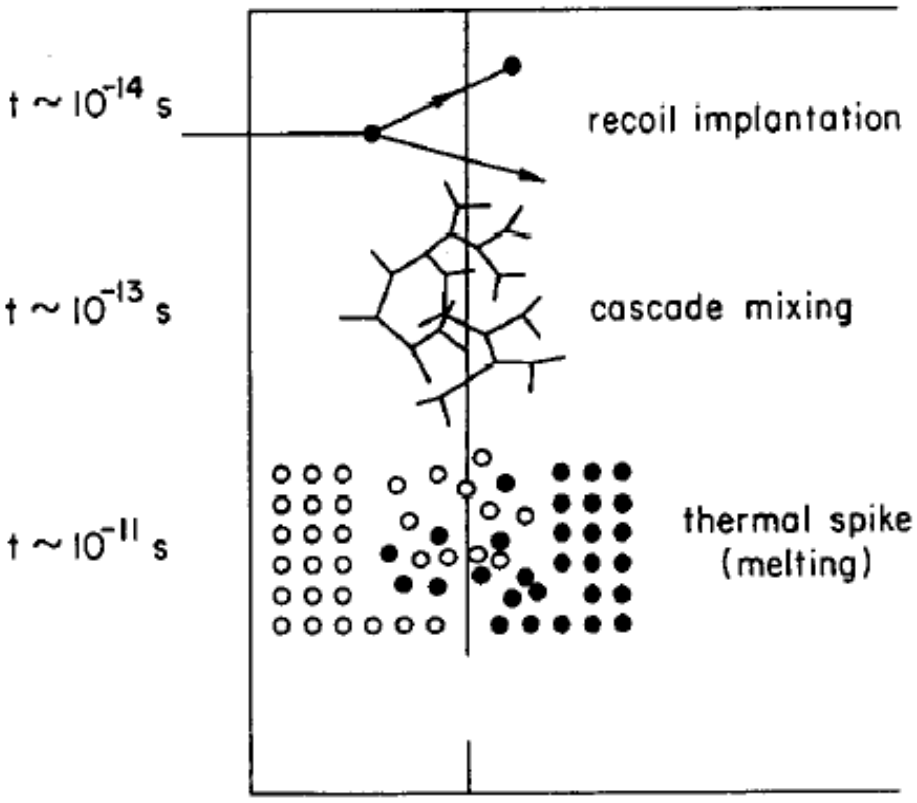

Figure 2-37 Schematic depiction of the three mechanisms of ion beam mixing (from Ref. [288]).

Table 2-5 Mixing parameter in several metals [288, 289]**.**

	Al	**Ti**	**Fe**	**Ni**	**Cu**	**Ag**	**Pd**	**Au**	**Pt**
Z	13	22	26	28	29	47	46	79	78
T_m (K)	933	1933	1,807	1,726	1,357	1,235	1,825	1,337	2,045
Q ($Å^5$/eV)	120	24	36	42	135	450	72	720	114

Another process which occurs during collision cascades is thermal mixing, and is believed to be a factor in the amorphization of crystalline materials during irradiation. Mixing during this process is larger for metals with low melting temperatures and high energy densities [288]. A solution for the temperature distribution within the spike was derived by Vineyard and is written as [290]:

$$T(r,t) = \frac{\varepsilon}{4\pi\kappa_0 t} e^{-\frac{c_o r^2}{4\kappa_o t}} \tag{2-40}$$

here C_o, κ_o and ε are respectively the thermal conductivity, heat capacity and the energy density of the target material.

2.6.1.3 Primary and Weighted Recoil Spectra

An important concept in defect production is the primary recoil and weighted average recoil spectra [34, 288]. Here the primary recoil spectrum is defined as the relative number of collisions in which an energy between T and T + dT is transferred from the primary recoil atom to other target atoms. It is also represented by the following normalized equation:

$$P(E,T) = \frac{1}{N}\int_{E_d}^{T} \frac{d\sigma(E_i,T)}{dT}\, dT \tag{2-41}$$

here N is the total number of primary recoils and dσ is the differential cross section for a particle of energy E_i to produce a recoil of energy T. The left side of figure 2-38 gives a qualitative representation of the primary recoil spectra for 1 MeV particles in Cu [288]. An important quantity

is $T_{1/2}$, which is the median cascade energy. The circles represent the relative location and recoil energy of knock on collisions. On the right side of figure 2-38 is displayed a plot of the fraction of recoils with energy above E_d and below T. Here each point on the curve represents the fraction of total recoils with energy between E_d and recoil energy T. As can be seen in both figures, heavier ions undergo a larger number of higher energy collisions as compared to their lighter counterparts. Furthermore, as indicated on the left side of figure 2-38, neutrons produce recoils with typically higher energies than charged particles although they occur less frequently.

Another important quantity in analyzing defect production is the weighted recoil spectra (WRS), which is the fraction of defects and damage energy that are produced in recoils of a particular energy [34]. This quantity has an integral form similar to that used by the primary recoil spectra and is written as:

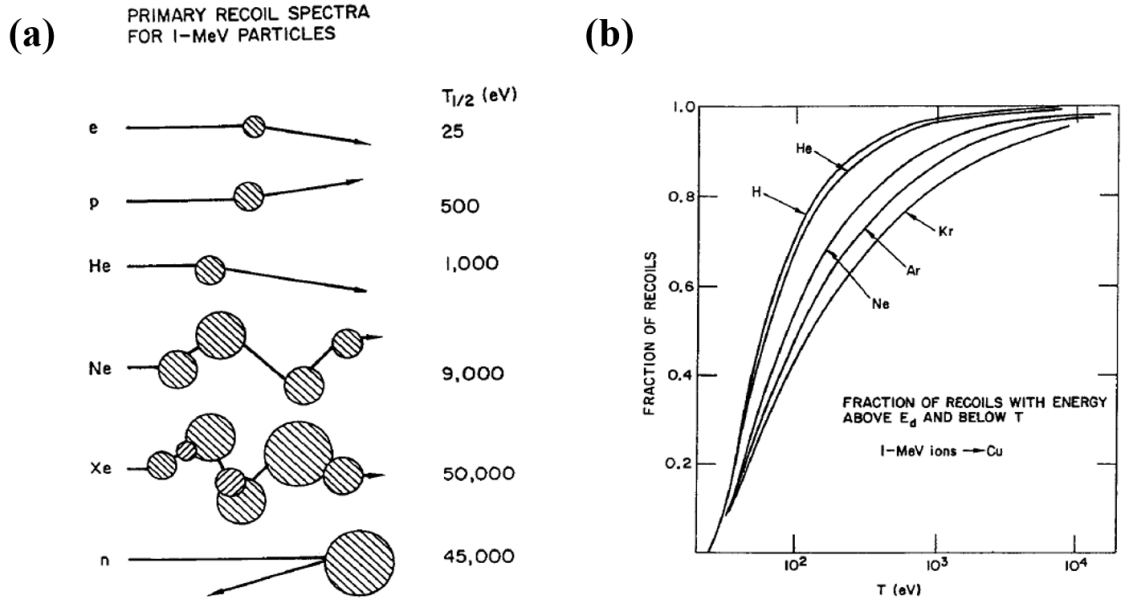

Figure 2-38 (a) Visualization of primary recoil spectra (RS) for 1 MeV particles in Cu. Circles' location and size represent the recoil location and magnitude, respectively. (b) Integral primary RS based on the equation for 1 MeV particles in Cu (from Ref. [288]).

$$W(E,T) = \frac{1}{E_D(E_i)} \int_{E_d}^{T} \frac{d\sigma(E_i,T)}{dT} E_D(T) dT \tag{2-42}$$

Where $E_D(T)$ is the damage energy created by a recoil of energy T and $E_D(E_i)$ is defined as:

$$E_D(E_i) = \frac{1}{E_D(E_i)} \int_{E_d}^{T_{max}} \frac{d\sigma(E_i,T)}{dT} E_D(T) dT \tag{2-43}$$

If electron excitations are ignored, the damage energy $E_D(T) = T$ and inserting the differential cross sections from [34] (here they use σ instead of a differential form) into Eq. (2-43) yields:

$$W_c = \frac{Ln(T) - Ln(T_{min})}{Ln(T_{\max}) - Ln(T_{\min})} \tag{2-44}$$

$$W_{HS} = \frac{T^2 - T_{min}^2}{T_{max}^2} \tag{2-45}$$

here W_C and W_{HS} denote the Coulomb and hard sphere WRS respectively. The value W_C is a good approximation for proton irradiations while W_{HS} is used for particles such fast neutrons [34]. The WRS for heavier ions such as Ne and Kr is derived using Lindhard cross sections which are based on screened Coulomb fields [291].

2.6.1.4 Stopping Power

So far collisions have been treated primarily as single processes when in reality multiple collisions are occurring during irradiation. In the latter scenario, the irradiating specie is undergoing multiple knock on events as it travels through the solid, losing energy with each successive collision. For ions, the energy loss occurs through processes such as ionization or electronic excitation. Because successive knock-ons occur over extremely small distances, the discrete nature of collisions may be approximated as a continuous event. This approximation allows one to denote the collisional loss in energy per unit length as a differential quantity, and is defined as [292]:

$$\frac{dE}{dx} = \frac{dE}{dx}\Big|_e + \frac{dE}{dx}\Big|_n \tag{2-46}$$

here $\frac{dE}{dx}\Big|_e$ and $\frac{dE}{dx}\Big|_n$ are respectively the electronic and nuclear stopping powers. The stopping power is written as $S_i = 1/N \times \frac{dE}{dx}|_i$ and has units of MeV nm^2. Figures 2-39(a)-(b) shows in what recoil energy regimes that each stopping power dominates [34]. At higher energies, electronic excitations are the primary means of energy loss and therefore electronic stopping dominates. At lower energies where elastic collisions with the atomic nuclei occur, the nuclear stopping power is the primary energy loss mechanism. Since ions have higher energies when they first penetrate the material, electronic stopping will dominate at shallower depths. At a critical depth, however, the ion will have lost enough energy such that only elastic collisions will occur and therefore nuclear stopping dominates.

2.6.2 Ion Range & SRIM Calculations

The range of an ion in matter is simply defined as the total distance R that a projectile of initial energy E_i will travel before coming to rest. Since ion implantation is a stochastic process, a more rigorous definition of the range is the most probable location for an ion to come to rest [292]. The mathematical definition for range involves integrating the nuclear and electronic stopping powers:

$$R = \frac{1}{N}\int_0^{E_i} \frac{1}{[S_n(E) + S_e(E)]}\, dE \tag{2-47}$$

where E_i is the initial ion energy before impinging on the material surface and the rest of the terms are defined as above. Due to the stochastic nature of ion trajectories, the range should typically be calculated using computer software programs. The Stopping and Range of Ions in Matter (SRIM) is a Monte Carlo based computer program which can estimate the ion range [293]. For explanations on the theory behind the code, please see [294-296]. In particular, SRIM is used tocalculate the interactions of energetic ions with amorphous targets. The statistical accuracy of SRIM in calculating the stopping power for a range of atoms has been steadily improving since the software was created in 1985 [297].

Although the developers of this software recommend using the full cascade mode [293], Parish et al. recommend using the "quick" Kinchen and Pease option as suggested by Stoller et al. [298, 299]. In addition to using the "quick" option, one should also use the recommended displacement threshold energies as listed in [300], and set the lattice binding energy to zero. Although a value of zero is recommended in [299], it tends to crash the program, and so a reasonably small value such as 10^{-6} is instead suggested.

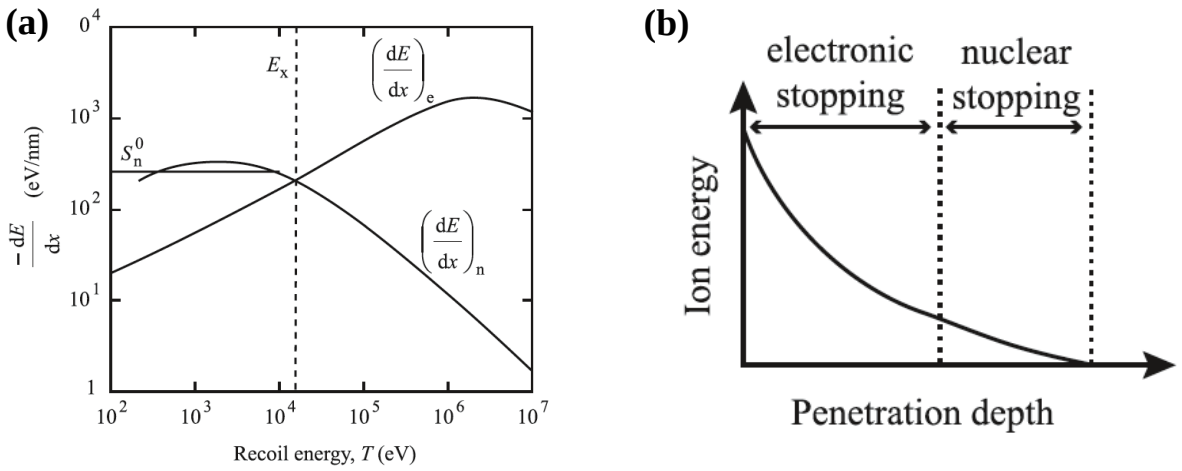

Figure 2-39 (a) Energy loss from electron and nuclear stopping as a function of energy and depth. (b) Ion energy as a function of depth in both the electronic and nuclear stopping regimes from Ref. [34]).

After the ion range is calculated using SRIM, the displacements per atom rate (dpa/s) can be calculated from the following equation [281]:

$$\frac{dpa}{s} = \frac{0.4\phi E_D}{NRE_d} \tag{2-48}$$

here 0.4 is a constant based on the displacement efficiency from the NRT model, ϕ is the incident particle flux, N is the atomic density of the target, E_D is the damage energy, R is the ion range and E_d is the spatial-average displacement threshold energy. Although dpa is very useful in estimating irradiation damage, it does not account for the number of atomic replacements in which an atom that is displaced during a collision event is replaced by another atom on the same lattice site [299].

Figure 2-40 compares the displacement rates as a function of penetration depth for energetic particles of various mass and energy [301]. As observed in the graph, ions with higher

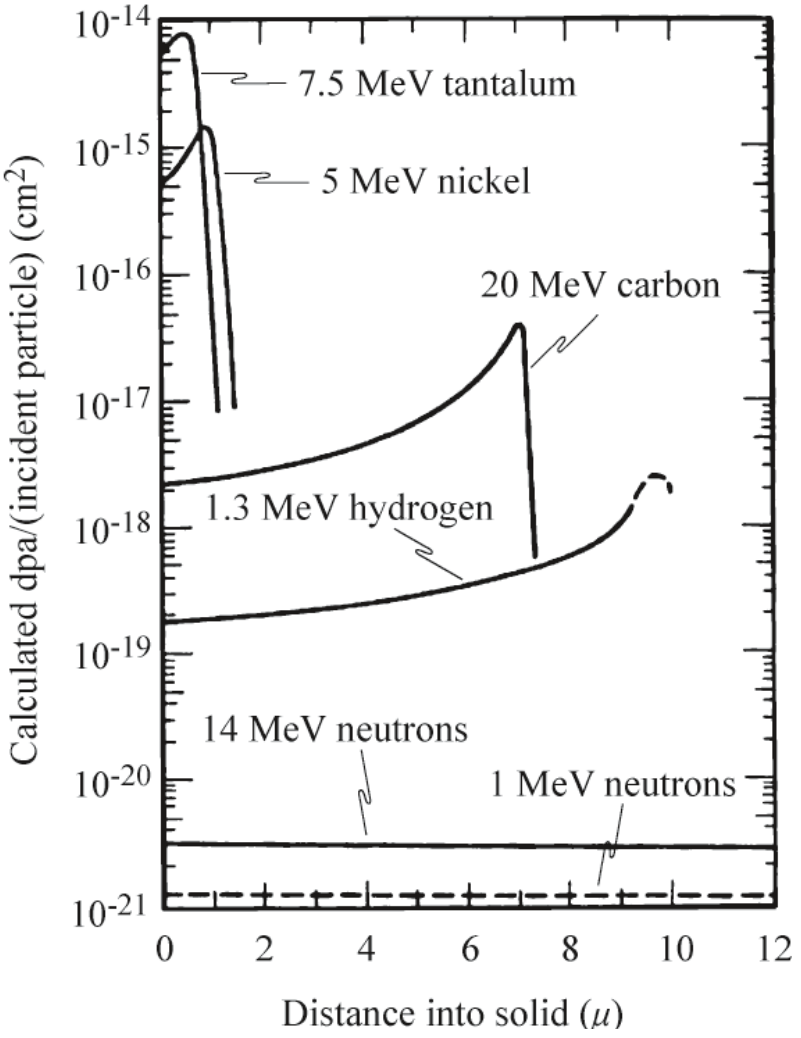

Figure 2-40 Displacement rate as a function of penetration depth for energetic particles with various masses and energies (from Ref. [301]).

masses tend to have a shorter range as compared to lighter ions of comparable energy. Furthermore, neutrons have a significantly higher range as compared to ions since they tend to collide less often and do not lose energy through electronic stopping.

2.7 Irradiation Effects in Amorphous Alloys

Irradiation with high-energy particles can prompt the crystallization of amorphous phases in a metallic glass due to temperature and irradiation induced increases in short-range ordering and the atomic diffusivity [302]. The resulting change in microstructure can fundamentally alter the macroscopic properties such as ductility, hardness and Young's modulus. In some cases, however, irradiation of an amorphous alloy has led to the recovery of the plasticity lost due to heat treatment [303].

2.7.1 Ion Irradiation Effects

Table 2-6 summarizes the results of different studies on the irradiation response of metallic glass alloys. The table features the alloy, the specimen type, ion species, ion energy, ion fluence, irradiation temperature, and whether the specimen crystallized during irradiation. Interestingly, there were mixed results as to whether a give amorphous alloy would crystallize during irradiation or not.

Carter et al. performed a couple studies involving the ion irradiation of $Cu_{50}Zr_{45}Ti_5$ [304-306]. In [305, 306], the copper alloy was irradiated with 140 keV He ions to a fluence of 1.7×10^{17} ion/cm^2. Vicker's hardness tests found that there was increase in hardness in the irradiated samples. Specifically, they found that the Vicker's hardness increased by 20 % in the irradiated

samples. Iqbal et al. found similar results in Ar irradiated $[Zr_{65}Cu_{18}Ni_9Al_{0.08}]_{98}Gd_2$ and $[Zr_{65}Cu_{18}Ni_9Al_{0.08}]_{98}Er_2$ bulk amorphous alloy [307]. TEM characterization showed that nanocrystals had formed in the regions most associated with the increase in hardness [305]. Furthermore, HRTEM, nano-beam electron diffraction (NBD) and X-ray energy dispersive spectrometry (EDS) results showed that the formed crystalline phases were a mixture consisting of orthorhombic $Cu_{10}Zr_7$ phase, a tetragonal $CuZr_2$ phase, and a monoclinic CuZr phase.

In [304], Carter et al. involved the 1 MeV Cu irradiation of the same copper-based alloy [223]. Results from the XRD and TEM analysis indicated that nanocrystalline phases formed and were composed of $Cu_{10}Zr_7$ and $CuZr_2$. The diameters of the nanocrystals ranged from 2 to 14 nm, with a typical size of 6 nm. Table 2-7 shows the interplanar distances as calculated from the selected area diffraction SAD pattern (see figure 2-41). As can be seen in the table, the d spacing is similar to values found in the literature, and indicates the presence of the phases listed in the table.

A few studies have examined the radiation stability of $Zr_{55}Ni_5Al_{10}Cu_{30}$ metallic glass [308-311]. The studies from [309, 310] found that the alloy crystallized when irradiated, while the other investigations did not [308, 311]. The study by Carter et al. used XRD in addition to transmission electron micrography (TEM) to examine the microstructure of the Zr based alloy post irradiation [310]. Using selected area diffraction, they found that the intermetallic phases $Cu_{10}Zr_7$ and $(Ni_x, Cu_{1-x})Zr_2$ formed during irradiation by 1 MeV Cu ions at room temperature to a fluence of 1×10^{16} ions/cm^2 (see figure 2-42).

Nagata et al. conducted two conflicting studies on the effects of ion irradiation on $Zr_{55}Al_{10}Ni_5Cu_{30}$ amorphous alloy [308, 309]. In [312], they irradiated 50-100 micron foils with

Table 2-6 Summary of ion irradiation studies in amorphous alloys R.T.: Room temperature.

Alloy	Specimen Type	Ion Species	Ion Energy (keV)	Ion fluence (cm^{-2})	Irr. Temp (^0C)	Crystallized? (Y/N)	Ref.
$Cu_{50}Zr_{45}Ti_5$	Ribbon	He	140	1.7×10^{17}	R.T.	Y	[305, 306, 313]
$Cu_{50}Zr_{45}Ti_5$	Ribbon	Cu	1,000	1×10^{16}	R.T.	Y	[304]
$(Cu_{47}Zr_{45}Al_8)_{98.5}Y_{1.5}$	Bulk	He	500	$2 \times 10^{17} – 2 \times 10^{18}$	-	N	[314, 315]
$[Zr_{0.65}Cu_{0.18}Ni_{0.09}Al_{0.08}]_{98}M_2$	Bulk	Ar	10	1.44, 2.17×10^{17}	-	Y	[307]
$Ti_{45}Cu_{40}Zr_5Ni_5Sn_5$	Ribbon	N	170	5×10^{15}-2×10^{16}	-	N	[316]
$Zr_{50.7}Al_{12.3}Cu_{28}Ni_9$	Thin Foil	Ar	70	1.43×10^{16}	-	Y	[317]
$Zr_{50.7}Al_{12.3}Cu_{28}Ni_9$	Thin Foil	Xe	7,000	6×10^{15}	R.T.	Y	[318]
$Zr_{64}Cu_{17.8}Ni_{10.7}Al_{7.5}$	Bulk	He	500	$2 \times 10^{17} – 2 \times 10^{18}$	R.T.	N	[315]
$Fe_{80}Si_{7.43}B_{12.57}$	Thin Foil	H	250	1×10^{17}- 1×10^{18}	R.T.	N	[319]
$Fe_{40}Ni_{38}Mo_4B_{18}$	Ribbon	He	2,800	1×10^{16}-1×10^{17}	R.T.	Y	[320]
$Fe_{78}B_{13}Si_9$	Ribbon	He	2,800	1×10^{16}-1×10^{17}	R.T.	Y	[320]
$Fe_{66}Co_{18}B_{15}Si_1$	Ribbon	He	2,800	1×10^{16}-1×10^{17}	R.T.	Y	[320]
$Fe_{79}B_{16}Si_5$	Ribbon	He	5	1×10^{20}	-	N	[302]
$Fe_{40}Ni_{40}P_{14}B_6$	Ribbon	He	40	1×10^{18}	400	Y	[321]
$Fe_{80}Si_{7.43}B_{12.57}$	Strip	He	500	1×10^{17}-1×10^{18}	R.T.	N	[322]
$Zr_{55}Ni_5Al_{10}Cu_{30}$	Bulk	Au	500	8×10^{16}	R.T.	Y	[309]
$Zr_{55}Ni_5Al_{10}Cu_{30}$	Thin Foil	H, Cu, Ag, Au	150-500	8×10^{16}	R.T.	N	[308]
$Zr_{55}Ni_5Al_{10}Cu_{30}$	Ribbon	Cu	1,000	1.0×10^{16}	R.T.	Y	[310]
$Zr_{55}Ni_5Al_{10}Cu_{30}$	Bulk	Ar	10	2.7×10^{17}	-	N	[311]
$Zr_{50}Cu_{35}Al_7Pd_5Nb_3$	Ribbon	Kr	1,000	4.3×10^{13}	420	Y	[323]

Table 2-6 continued.

Alloy	Specimen Type	Ion Species	Ion Energy (keV)	Ion fluence (cm^{-2})	Irr. Temp (^0C)	Crystallized? (Y/N)	Ref.
$Ni_{52.5}Nb_{10}Zr_{15}Ti_{15}Pt_{7.5}$	Ribbon	Xe	18,000	5×10^{10}	-	N	[324]
$Zr_{55}Cu_{28}Al_{10}Ni_7$	Bulk	Ar	200, 75	1×10^{16}, 5×10^{15}	347	N	[325]
$Ti_{40}Zr_{10}Cu_{38}Pd_{12}$	Bulk	Ar	200, 75	1×10^{16}, 5×10^{15}	347	Y	[325]
$Zr_{52.5}Cu_{17.9}Ni_{14.6}Al_{10}Ti_5$	Bulk	Ni	3,000	4.2×10^{13}, 4.2×10^{16}	200	N	[98]
$Co_{61.2}B_{26.2}Si_{7.8}Ta_{4.8}$	Bulk	He	500	$2 \times 10^{17} - 2 \times 10^{18}$	-	N	[315]
$Ni_{52.5}Nb_{10}Zr_{15}Ti_{15}Pt_{7.5}$	Ribbon	Ni	1,000	1×10^{16}	R.T.	Y	[326]
$Zr_{50}Cu_{40}Al_{10}$	Bulk	Al	5,000	3×10^{14}	R.T.	N	[327]
$Fe_{81}B_{13.5}Si_{3.5}C_2$	Ribbon	He	2,800	1×10^{16}	R.T.	Y	[328]
$Ti_{40}Zr_{25}Be_{30}Cr_5$	Bulk	C, Cl	25,000	9.6×10^{14} (C) 7.63×10^{15} (Cl)	R.T.	N	[329]

Table 2-7 Interplanar distances of crystalline phases produced in $Cu_{50}Zr_{45}Ti_5$ during irradiation by 1 MeV Cu^+ ions (from Ref. [304]).

Experimental data from the present study	$Cu_{10}Zr_7$ standard d-spacing/orientation	$CuZr_2$ standard d-spacing/orientation
3.178	3.174/(004)	
2.889	2.880/(311)	
2.755		2.782/(004)
2.642	2.621/(204)	
2.463		2.429/(103)
2.416	2.420/(313)	
2.252	2.287/(224)	2.269/(110)
1.933	1.923/(315)	
1.759	1.746/(117)	1.761/(114)
1.603	1.598/(442)	1.607/(200)
1.433	1.437/(662)	1.429/(211)
1.372	1.378/(119)	
1.260	1.262/(248),(713)	
1.116		1.117/(010)
1.035		1.030/(303)

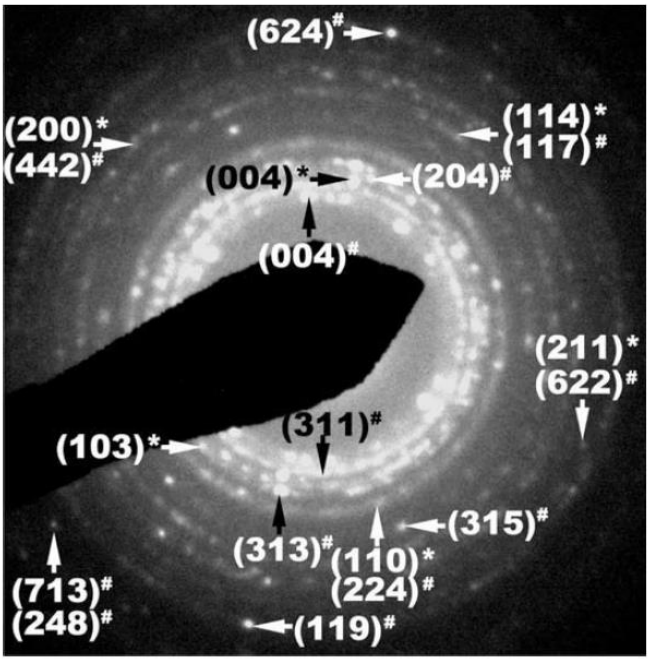

Figure 2-41 The SAD pattern of Cu ion irradiated $Cu_{50}Zr_{45}Ti_5$ glass. The miller indices correspond to crystalline $Cu_{10}Zr_7$ (#) and $CuZr_2$ (*) phases. (from Ref. [304]).

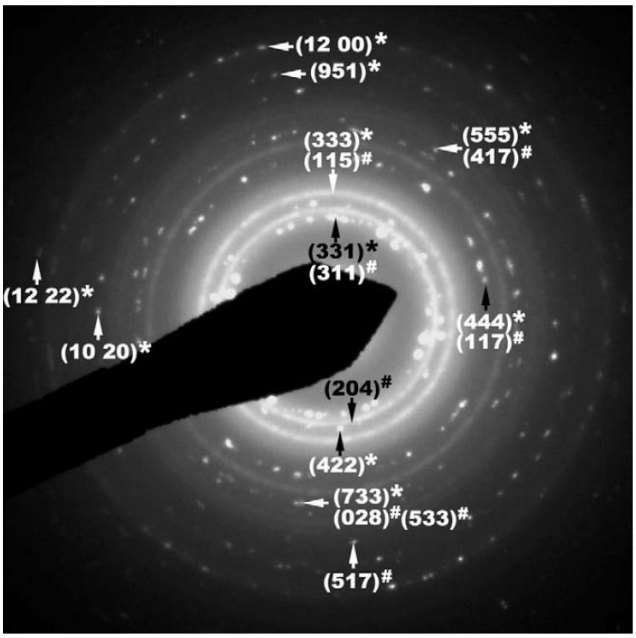

Figure 2-42 The (SAD) pattern of Cu-ion-irradiated $Zr_{55}Cu_{30}Al_{10}Ni_5$ glass. The indexing indicates the co-existence of $Cu_{10}Zr_7$ (#) and $NiZr_2$ (*) phases (from Ref. [310]).

H, Cu, Ag and Au ions possessing energies of 150 to 500 keV to fluences of 8×10^{16} ions/cm^2. X-ray diffraction results indicated that the amorphous alloys did not crystallize under any irradiation condition. However, Carter et al. points out that the lack of detection of nanocrystalline phases in Nagata's study was puzzling since it involved similar ion fluences as the study in [310]. It was surmised in [310] that the high detection limits of XRD may have prevented the observance of crystalline phases and therefore should have been used in combination with TEM and SAD techniques.

Unlike in [308], the other study conducted by Nagata et al. did involve the use of TEM in combination with XRD [309]. Specifically, their research involved 500 keV Au ion irradiation in bulk $Zr_{55}Al_{10}Ni_5Cu_{30}$ amorphous alloy (at a fluence the same as [308]). Although x-ray diffraction results initially suggested that the alloy did not crystallize, bright field TEM showed the formation of nano-crystalline precipitates with sizes of roughly 50 nm. From the results it was theorized that the nano-crystals which formed during irradiation were probably composed of fcc-Zr_2Ni and fcc-Zr_2Cu.

A study conducted by Huang et al. found that irradiated $Ti_{45}Cu_{40}Zr_5Ni_5Sn_5$ amorphous ribbons exhibited an increase in hardness while remaining amorphous [316]. For this study, the metallic glass was irradiated with 170 keV nitrogen ions to fluences ranging from 5×10^{15}-2×10^{16} ions/cm^2. X-ray diffraction results showed a shift in the intensity peaks I(Q) to higher values which implies a decrease in the atomic spacing. There was also an increase in the Young's modulus with respect to irradiation fluence, which is further proof for the decrease in atomic spacing.

Kraposhin et al. examined the effects of Ar irradiation on three different Co based amorphous alloys [330]. For their study, they irradiated $Co_{83.7}Fe_{5.6}Si_{8.6}B_{2.2}$, $Co_{82}Fe_{4.3}Si_{7.2}Cr_4B_{2.5}$ and $Co_{86.7}Fe_{3.6}Si_{2.7}Mn_{3.5}B_{3.5}$ alloys with 30 keV Ar ions to a fluence of 1.5×10^{18} ions/cm^2 to temperatures ranging from 100-600 ^{o}C. XRD results showed that all three alloys crystallized at temperatures $\leq 300\ ^0$C. For the $Co_{83.7}Fe_{5.6}Si_{8.6}B_{2.2}$ glass, crystallites began to form at 100 ^{o}C and were composed of CoB, Co-based solid solution (a mixture of hexagonal closed packed and face centered cubic modifications) and Co_2Si. Like the first alloy, the $Co_{82}Fe_{4.3}Si_{7.2}Cr_4B_{2.5}$ alloy produced crystalline phases consisting of Co solid solution and CoB, which occurred after irradiation at 300 ^{o}C. The third alloy also produced the same crystalline phases as the alloy with the Cr additions under irradiation at 200 ^{o}C. However, unlike the first two alloys, the most intensive peaks of the XRD belonged to the Co-based solution, and not the CoB phase. Furthermore, diffraction peaks of an unknown cubic aperiodical phase were observed and were determined to be based on the α-Mn structure. The study also found that the third alloy recovered its amorphous structure after annealing to 250 ^{o}C.

Miglierini et al. used ^{73}Fe conversion electron Mössbauer spectroscopy (CEMS) to study the effects of proton and nitrogen irradiation on the short range order in $Fe_{76}Mo_8Cu_1B_{15}$ and $Fe_{74}Nb_3Cu_1Si_{16}B_6$ amorphous ribbons [331]. CEMS was chosen due to its sensitivity to structural modifications. In addition, a similar experiment was performed on the second alloy where they examined the irradiation effects of nitrogen and gold [332]. For the experiment involving proton and nitrogen irradiation, the researchers found that $Fe_{76}Mo_8Cu_1B_{15}$ was sensitive to radiation damage while $Fe_{74}Nb_3Cu_1Si_{16}B_6$ was not.

Chen et al. found that nanocrystals formed in $Zr_{50.7}Al_{12.3}Cu_{28}Ni_9$ amorphous thin films when exposed to 70 keV Ar irradiation (fluences up to 1.43×10^{16} ions/cm^2) [317]. Here

nanocrystals (diameter of 10-30 nm) containing either an fcc Cu phase or an fcc $AlNi_3$ phase or both were observed. In addition to the nanocrystals, they found Cu- enriched and Ni- depleted nanostructures, which were attributed to the migration of Cu and Ni atoms. Furthermore, they believed that the nanocrystals acted as nuclei for the formation of these Cu- and Ni- enriched nanostructures.

Another study conducted by Chen et al. examined the irradiation effects of 7 MeV Xe ions on the same alloy [318]. Selected area diffraction and scanning tunneling electron microscope (STEM)-energy dispersive x-ray spectroscopy analysis suggested that the needle-like nanocrystals were composed primarily of $Cu_{10}Zr_7$. Furthermore, the crystals were observed to form along the (311) plane, which was caused by irradiation induced diffusion of atoms along that direction. In addition to the formation of the crystalline phase, evidence showed that the substitutional intermetallic $(Ni_xCu_{1-x})_{10}Zr_7$ phase may have formed as well.

There have also been studies regarding radiation enhanced diffusion (RED) in amorphous alloys. R. Averback et al. found that in Ni-Zr amorphous alloys, radiation enhanced diffusion occurred but did not necessarily lead to crystallization [333]. It was concluded that the reason why the binary alloy did not crystallize was because of the fact that although nickel diffused, zirconium remained immobile. Another study by Averback et al. involving an amorphous Ni-Zr diffusion couple found that Ni is far more mobile than Zr, which supports the results of the study above [334].

Another study of RED in amorphous alloys involved the irradiation of $Fe_{40}Ni_{40}B_{20}$ by 300 keV ^{58}Ni ions [335]. Results indicated that diffusion under irradiation was strongly enhanced in comparison to thermal diffusion. Together with other results [336, 337], they concluded that the

diffusion behavior was best described by atomic transport via irradiation-induced, point defect like entities which perform long-range diffusion and can undergo a recombination reaction.

Jung examined the effects of proton irradiation on the creep of $Ni_{78}B_{14}Si_8$ amorphous ribbons [338]. For this experiment they irradiated the metallic glass with 6.3 MeV protons with fluxes up to 1.1×10^{14} p/cm^{2}s and temperatures of 420 ± 15 K. Uniaxial tests revealed that the irradiation creep rate in this metallic glass alloy was approximately 25 times higher than compared to its crystalline counterpart. From the results they theorized that the high irradiation creep rates may be beneficial in reducing irradiation-induced internal stresses but would be disadvantageous in terms of dimensional stability for application in irradiation environments.

The effects of He ion irradiation on $Fe_{40}Ni_{40}P_{14}B_6$ were examined by Hayashi et al. [321]. Here they irradiated 80 μm thick ribbons with 40 keV He ion irradiation to a fluence of 1×10^{18} ions/cm^2 at 400 ^{o}C. Mössbauer spectroscopy indicated that crystallization occurred in the alloy when exposed to the above conditions. However, thermally induced crystalline ferromagnetic phases such as α-iron, Fe_2B or Fe_3P were not detected (which were expected to form [339, 340]), but instead paramagnetic phases such Fe_2P and $(Fe_{1-x}Ni_x)P_2$ may have formed instead. Auger electron spectroscopy results indicated that nickel enriched portions were separated from iron enriched portions in this region. This separation indicates that ion irradiation may induce long range diffusion of the metal and metalloid atoms in addition to the creation of vacancy like defects in the affected region.

Hou et al. compared the radiation resistance of $Fe_{80}Si_{7.43}B_{12.57}$ amorphous alloy, polycrystalline W and crystalline $V_{90.62}Cr_{4.69}Ti_{4.69}$ [322]. For this experiment the three alloys were exposed to 500 keV He^{2+} irradiation to fluences ranging from 1×10^{17} - 1×10^{18} ions/cm^2. XRD

and TEM revealed that the Fe based amorphous alloy did not crystallize under any fluence. Furthermore, helium bubble layers were observed at approximately 1.1 μm beneath the surface. Atomic force microscopy measurements revealed that the surface roughness of the Fe-based metallic glass did not increase significantly while the surface roughness of the polycrystalline W increased significantly at the maximum fluence. In addition, $V_{90.62}Cr_{4.69}Ti_{4.69}$ blistered and flaked at the fluence of 5×10^{17} ions/cm^2 and exhibited multi-layer scaling and peeling at the fluence of 1×10^{18} ions/cm^2. The results above indicate that the iron based amorphous alloy had higher He^{2+} ion radiation resistance as compared to the other two alloys.

Similar to the study conducted by Hou et al., Wang et al. compared the effects of He^{2+} ion irradiation resistance of $Zr_{64}Cu_{17.8}Ni_{10.7}Al_{7.5}$ and metallic W [341]. Here the two alloys were irradiated with 500 keV He^{2+} to ion fluences ranging from 2×10^{17} - 2×10^{18} ions/cm^2 at ambient temperature. Like the previous investigation, He^{2+} irradiation resistance in the amorphous alloy was found to be superior to that of the metallic W alloy. AFM revealed that the initially, the surface roughness of the amorphous alloy increased, but then became smooth at higher doses. This was in contrast to the metallic W, which began to exhibit lamination and peeling on the surface at a fluence of 1×10^{18} ions/cm^2. In addition, the Zr alloy did exhibit irradiation induced crystallization at any ion fluence.

In the $Zr_{64}Cu_{17.8}Ni_{10.7}Al_{7.5}$ alloy, a helium bubble layer appeared within the range of 1.2-1.4 microns away from the surface corresponding to the mean implanted He region, as can be seen in figure 2-43(a). Bubble morphology was divided into three zones which were labeled A, B and C in the figure. In zone A (near the irradiated surface), the helium bubbles were mostly round, with sizes ranging from nanometers to several tens of nanometers. In zone B (0.3-1.3 μm away from the surface), the bubble size was much smaller. In zone C, however, there was a helium

bubble layer which formed and consisted of bubbles which were irregularly polygonal in shape and several tens of nanometers in diameter. Furthermore, bubbles coalesced in this zone which can be seen in figure 2-43(b). For a similar study comparing the He^{2+} ion irradiation effects in $(Cu_{47}Zr_{45}Al_8)_{98.5}Y_{1.5}$ amorphous alloy and polycrystalline W, see [314].

Wang et al. investigated the He^{2+} resistance of 4 different alloys [315]. Here, they irradiated three different amorphous alloys and compared the radiation response with polycrystalline W. Specifically, the amorphous alloys which were irradiated were $(Cu_{47}Zr_{45}Zl_8)_{98.5}Y_{1.5}$, $Zr_{64}Cu_{17.8}Ni_{10.7}Al_{7.5}$ and $Co_{61.2}B_{26.2}Si_{7.8}Ta_{4.8}$ at room temperature. The ion energy and fluence were 500 keV and 2×10^{17}-2×10^{18} ions/cm^2, respectively. Figures 2-44 and 2-45 show the SEM surface morphology before and after irradiation. After an irradiation fluence of 1×10^{18} ions/cm^2 it was observed that the tungsten alloy began to roughen, peel and flake, while no such changes were seen in the three metallic glasses. At an irradiation dose of 2×10^{18} ions/cm^2 the Co based metallic glass began to experience surface roughening, while the Zr and Cu based amorphous alloys did not. Furthermore, helium bubbles were found to congregate at the grain boundaries in the polycrystalline W, which can lead to embrittlement.

2.7.1.1 Ion Irradiation Effects on Nanoindentation Behavior

Menendez et al. irradiated $Zr_{55}Cu_{28}Al_{10}Ni_7$ and $Ti_{40}Zr_{10}Cu_{38}Pd_{12}$ with Ar ions in a consecutive two-step process [325]. The first step consisted of irradiating the alloys with ion energies of 200 keV to a fluence of 1×10^{16} ions/cm^2 while the second step consisted of an ion energy and fluence of 75 keV and 5×10^{15} ions/cm^2 respectively. Both irradiations were conducted at room temperature and 347 ^{o}C. It was found that the ion irradiations at room temperature cause an increase in nanoindentation depth with respect to the as-cast state for both alloys. However,

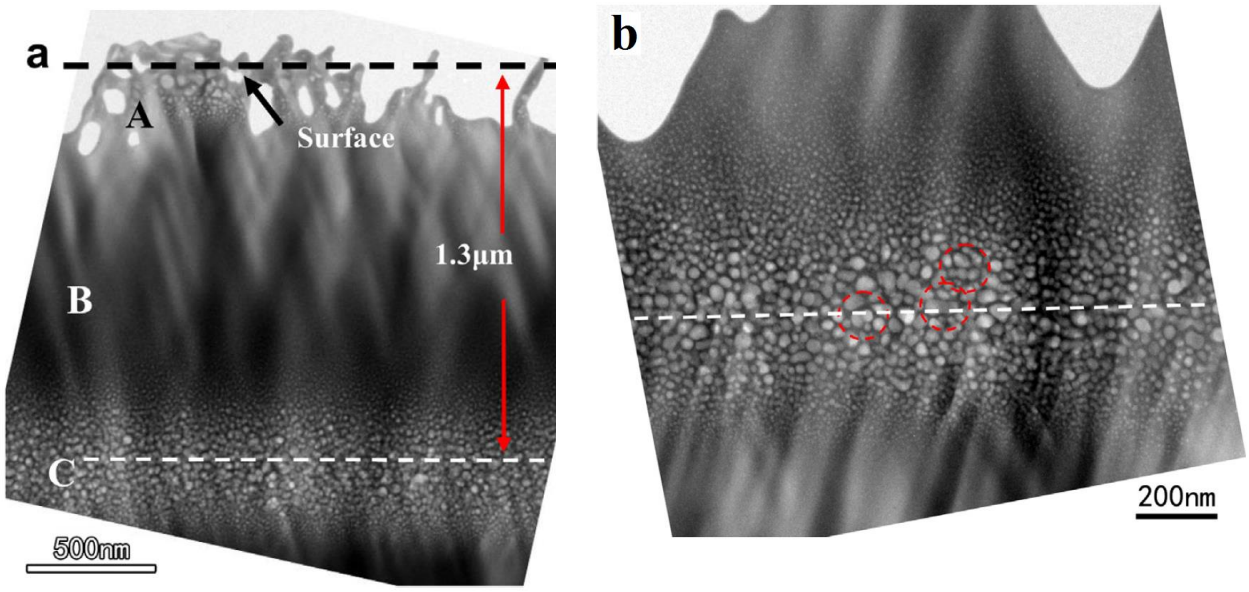

Figure 2-43 (a) TEM image of sample of 500 keV He^{2+} irradiated $Zr_{64}Cu_{17.8}Ni_{10.7}Al_{7.5}$ metallic glass with fluences of $2 \times 10^{18}/cm^2$ and (b) TEM image of the He-ion range of sample. Red circles indicate coalescence growth of two or more bubbles (from Ref. [341]).

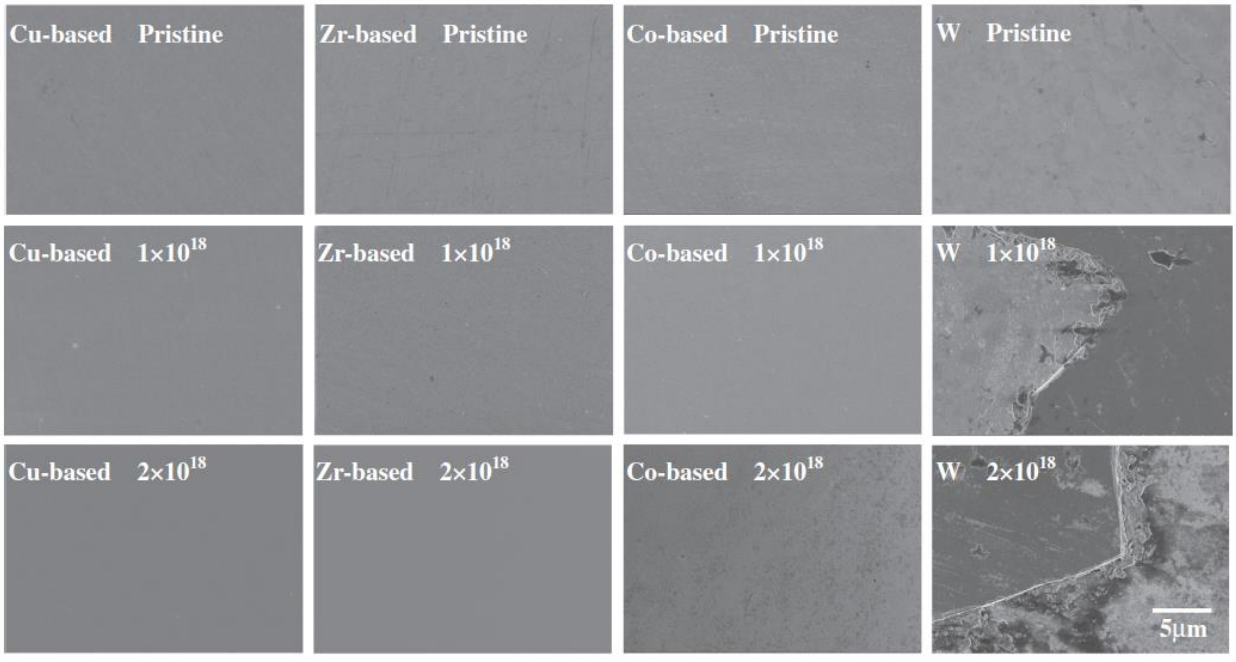

Figure 2-44 SEM images for pristine and 500 keV He^{2+} ion irradiated ($(Cu_{47}Zr_{45}Al_8)_{98.5}Y_{1.5}$, $Zr_{64}Cu_{17.8}Ni_{10.7}Al_{7.5}$, $Co_{61.2}B_{26.2}Si_{7.8}Ta_{4.8}$ and metallic W at different fluences (from Ref. [315]).

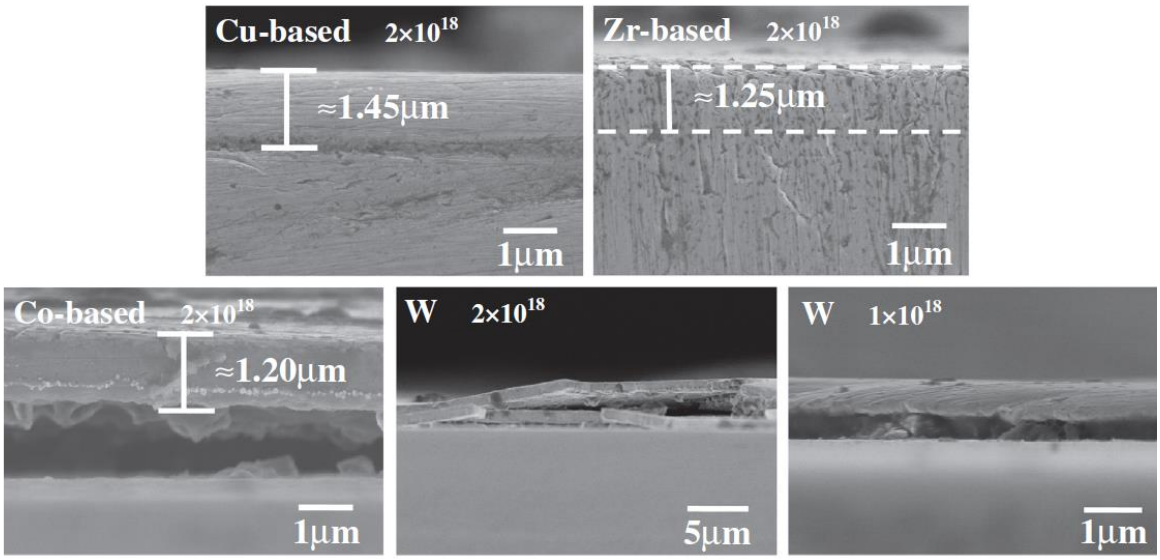

Figure 2-45 The cross-sectional SEM images of irradiated $((Cu_{47}Zr_{45}Al_8)_{98.5}Y_{1.5}$, $Zr_{64}Cu_{17.8}Ni_{10.7}Al_{7.5}$, $Co_{61.2}B_{26.2}Si_{7.8}Ta_{4.8}$ and metallic W at different fluences from (Ref. [315]).

the nanoindentation depth decreased in both alloys for ion irradiations at 347 ^oC. Moreover, nanoindentation hardness and Young's modulus decreased in both alloys irradiated at room temperature and increased in both alloys irradiated at 347 ^oC. The reduction in hardness and Young's modulus was attributed to a decrease in free volume concentration. It was also reported that the Zr based bulk metallic glass remained amorphous while the Ti alloy crystallized during irradiation at 347 ^oC.

In addition to the above study, changes in free volume have also been found in ion irradiated Zr-Ti-Cu-Ni-Be metallic glass [342, 343]. Raghavan et al. examined the effects of Ni ion irradiation on $Zr_{42.1}Ti_{13.8}Cu_{12.5}Ni_{10}Be_{22.5}$ (Vitreloy 1) metallic glass through micropillar compression and nanoindentation experiments [342, 343]. They found that ion irradiation led to an increased ductility which correlated with a decrease in stress drops during serrated flow. Specifically, stress drops decreased from 880 ± 224 MPa in the as cast alloy to 121 ± 40 MPa in

the sample irradiated to 100 dpa. It was theorized that the increased ductility was due in part to the irradiation induced creation of shear bands. Enhanced shear band initiation is thought to promote shear band intersections, which are necessary for increased plastic strains before failure [343, 344].

Perez-Bergquist et al. investigated the effects of Ni ion irradiation on the nanoindentation behavior and microstructure of $Zr_{52.5}Cu_{17.9}Ni_{14.6}Al_{10}Ni_5$ bulk metallic glass [98]. For this investigation, the Zr based alloy was irradiated with the above alloy with 3 MeV Ni ions to fluences of 4.2×10^{13} and 4.2×10^{14} ions/cm^2 (peak doses of 0.1 and 1 dpa) at room temperature and 200 ^{o}C. Hardness and elastic modulus both decreased for the specimens irradiated at room temperature. However, for irradiations at 200 ^{o}C, the hardness exhibited a slight decrease while the Young's modulus was found to increase. Furthermore, TEM characterization revealed that irradiation did not lead to any observable changes in the microstructure.

Lucca et al. examined the mechanical response of an irradiated Ni free Ti based metallic glass by nanoindentation [130]. For this study they irradiated $Ti_{40}Cu_{32}Pd_{32}Zr_{10}Sn_2Si_2$ metallic glass ribbons with 4 MeV Fe^{2+} ions at 25 ^{o}C over a range of fluences from 1×10^{12} to 1×10^{15} ions/cm^2. Nanoindentations were performed using both Berkovich and spherical diamond indenters. Results revealed that the ion irradiated samples exhibited a decrease in elastic modulus and hardness in addition to a shift in the deformation mechanism toward less shear localization and more homogenous plastic flow. This shift was attributed to an increase in free volume due to ion irradiation.

In addition, the study analyzed the irradiation effects on nanoindentation pop-ins, which occur at the onset of plastic deformation in the metallic glass. It was found that the force at first

displacement increased from ~1 mN in the as-cast sample to ~2.6 mN in the sample irradiated to a fluence of 1×10^{13} ion/cm^{2}s at room temperature. Since pop-ins are intimately related to shear banding, the increased force at the first displacement burst indicates that ion irradiation alters the way the shear bands form and propagate in the material [329]. In addition, the initial pop-in force decreased to ~1.8 mN when the sample was irradiated to the same fluence at 300 ^{o}C. It is known that amorphous alloys with a higher free volume content can accommodate local shear strain, and hence deter the propagation of shear bands [130]. Therefore, thermal treatment annihilates the free volume that is created under ion irradiation, which is exhibited in a drop in the required force to initiate displacement bursts.

Hu et al. compared the effects of heavy and light ion irradiations in $Ti_{40}Zr_{25}Be_{30}Cr_5$ [329]. For this study, the team irradiated the Ti alloy with 25 MeV C^{4+} and Cl^{4+} ions at room temperature. The ion fluences for the carbon chlorine irradiations were 9.60×10^{14} ions/cm^2 and 7.63×10^{15} ions/cm^2 respectively. XRD results indicated that the amorphous alloy did not crystallize under either irradiation condition. Nanoindentation hardness decreased from 7.18 GPa in the as cast sample to 7.16 and 6.74 GPa in the C^{4+} and Cl^{4+} irradiated samples respectively. The above results indicate that heavier ions cause significantly more softening in the material than do light ions. In contrast to the hardness, the average Young's modulus was not affected by either type of ion irradiation.

Luo et al. examined the effects of 300 keV Ar ion irradiation on $Zr_{61.5}Cu_{21.5}Fe_5Al_{12}$ bulk amorphous alloy [345]. Here they irradiated the material to doses ranging from 3×10^{15} - 3×10^{16} ions/cm^2 at room temperature. Using HRTEM and SAD techniques it was discovered that nanocrystal precipitates formed at doses of 1×10^{16} ions/cm^2 and had an average size of 5 nm.

Furthermore, nanoindentation experiments revealed that both the average hardness and modulus increased with respect to irradiation fluence.

2.7.2 Neutron Irradiation Effects

Table 2-8 presents a summary of neutron irradiation studies that include the alloy, its material type, the neutron energy, the neutron fluence, the irradiation temperature, and whether the sample crystallized or not. As can be seen, none of the alloys crystallized during irradiation. Gupta et al. found that $Fe_{40}Ni_{40}B_{20}$ and $Fe_{78}Si_9B_{13}$ metallic glass ribbons became brittle after neutron irradiation [346]. For their study the above iron based amorphous alloys were exposed to thermal neutrons with a flux of 10^{13} n/cm^{2}s. They found that after an irradiation dose of 10^{19} n/cm^2 that all the specimens became highly brittle. Using Mössbauer spectroscopy, they found that helium formation was the possible cause of embrittlement, and not phase separation or cluster formation. This was in contrast to earlier studies which indicated that the cause of embrittlement was attributed to phase separation or cluster formation in the amorphous alloy [131].

Another study conducted on the neutron irradiation response of $Fe_{40}Ni_{40}B_{20}$ was conducted by Gerling et al. [347]. For their study they irradiated the above alloy with both thermal ($E < 0.1$ eV) and fast ($E > 0.1$ MeV) neutrons to a fluence of 6×10^{13} n/cm^2 and 4.3×10^{19} n/cm^2, respectively. Transmission electron microscopy (TEM) results indicated that specimens remained amorphous even after irradiation to 26 dpa. Furthermore, no irradiation induced defects or He-bubble formation were observed under TEM.

In terms of density, Gerling et al. found that the density of amorphous $Fe_{40}Ni_{40}B_{20}$ ribbons decreased with respect to thermal neutron dose [348]. As can be seen in figure 2-46, the relative

swelling density decreased by ~0.8 % after a neutron fluence of 1×10^{19} n/cm^2. Furthermore, swelling approached a constant value around a fluence of 3×10^{19} n/cm^2, which is roughly equivalent to 12 displacements per atom. It is interesting to note that at the time the article was published, such a pronounced saturation behavior of the swelling rate had never been observed in crystalline materials [348]. It was theorized that the observed swelling was caused by radiation defects and not by any changes in composition during irradiation. A study regarding the structural restoration of neutron irradiation on $Fe_{40}Ni_{40}B_{20}$ may be found in [129].

Kramer et al. explored the effects of neutron irradiation on a superconducting metallic glass [128]. Here they irradiated $(Mo_{0.6}Ru_{0.4})_{82}B_{18}$ metallic glass ribbons with 1 MeV neutrons at room temperature. XRD revealed that the alloy did not crystallize when exposed to fluences of 1×10^{19} n/cm^2. Furthermore, the alloy exhibited a decrease in density from 10.37 to 10.22 g/cm^3, (~1.5 %) which corresponded to an increase in the free volume content and corresponding increase in ductility. Johnson and Williams have reported that there is positive correlation between excess structural volume and ductility of $(Mo_{0.6}Ru_{0.4})_{1-x}B_x$ alloys [349].

A study conducted by I. Skorvanek et al. found that ductility of thermally embrittled $Fe_{73.5}Cu_1Nb_3Si_{13.5}B_9$ amorphous ribbons could be restored by neutron irradiation [350]. For their research, they compared the fracture strain of thermally treated, and neutron irradiated iron based metallic glass after exposure to thermal neutrons to fluences ranging from 3×10^{17} to 10^{19}. As can be seen in figure 2-47, all the thermally-embrittled amorphous samples regained ductility after neutron irradiation. Furthermore, the metallic glass ribbons did not undergo crystallization from neutron irradiation. Based on previous results in addition to this study, embrittlement was caused by thermal annealing (decrease in excess free volume), while a restoration of ductility occurred via neutron irradiation by a generation of excess free volume or swelling [129, 348].

Table 2-8 Summary of neutron irradiation studies in amorphous alloys. R.T. : Room temperature.

Alloy	Material Type	Neutron Energy	Neutron Fluence (cm^{-2})	Irr. Temp (^0C)	Crystallized? (Y/N)	Source
$Fe_{40}Ni_{40}B_{20}$	Ribbon	Thermal	10^{18}- 10^{19}	~R.T.	N	[346]
$Fe_{78}Si_9B_{13}$	Ribbon	Thermal	10^{18}- 10^{19}	~R.T.	N	[346]
$Fe_{40}Ni_{40}B_{20}$	Ribbon	Thermal, fast	8×10^{19}	< 70	N	[131]
$Fe_{40}Ni_{40}B_{20}$	Ribbon	Thermal, fast	6.5×10^{19} (thermal) 4.3×10^{19} (fast)	< 120	N	[347]
$(Mo_{0.6}Ru_{0.4})_{82}B_{18}$	Foil	1 MeV	1×10^{19}	R.T.	N	[128]
$Fe_{73.5}Cu_1Nb_3Si_{13.5}B_9$	Ribbon	Thermal	3×10^{17}- 10^{19}	< 70	N	[350]

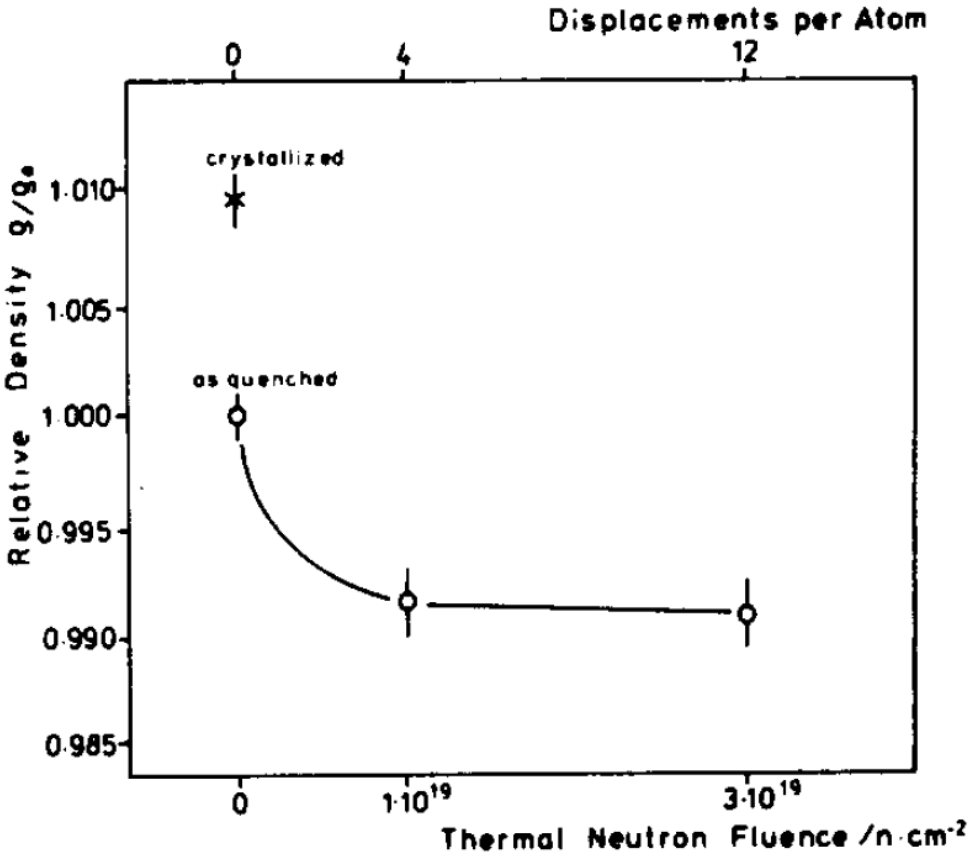

Figure 2-46 The relative density for $Fe_{40}Ni_{40}B_{20}$ in the as-quenched state, crystallized, and neutron irradiated to 12 dpa (from Ref. [348]).

The effects of neutron irradiation on the short-range order in amorphous alloys have also been the subject of previous research. One study involved the irradiation of $Fe_{78-x}NI_xSi_8B_{14}$ (with x = 0, 15, 25, 38, 53, 58) amorphous ribbons with thermal neutrons to a fluence of 10^{19} n/cm^2 [351]. Mössbauer spectroscopy revealed that before irradiation, increasing the Ni concentration in (Fe, Ni)-metalloid glass drove Fe atoms to sites with higher metalloid near neighbors. However, it was found that neutron irradiation tended to randomize the system, partially destroying the occupancy of metalloid depleted sites by Ni. Furthermore, the increase in randomization by neutron irradiation was thought to cause an increase in the average magnetic moment of Fe atoms which in turn increased the Curie temperature of the alloy.

2.7.3 Summary of Irradiation Studies

Based on Table 2-6, there is not conclusive evidence whether metallic glasses will crystallize during ion irradiation or not. Crystalline phases which formed in the amorphous alloys during irradiation were observed as either spikes in the XRD patterns or spots in the TEM (SAD) diffraction patterns. In alloys which crystallized, diffraction patterns indicated that the primary phase which formed was binary in nature and consisted of bcc, fcc, or hcp structures [305, 309, 330].

In addition, a few studies on the crystallization behavior of Cu^+ irradiated $Zr_{55}Ni_5Al_{10}Cu_{30}$ reported contradictory results [305, 308, 309, 311]. For instance, Carter et al. [305] suggested that the high detection limits of XRD may have prevented the observance of crystalline phases in [308]. They also stated that XRD should have been used in combination with TEM and SAD techniques.

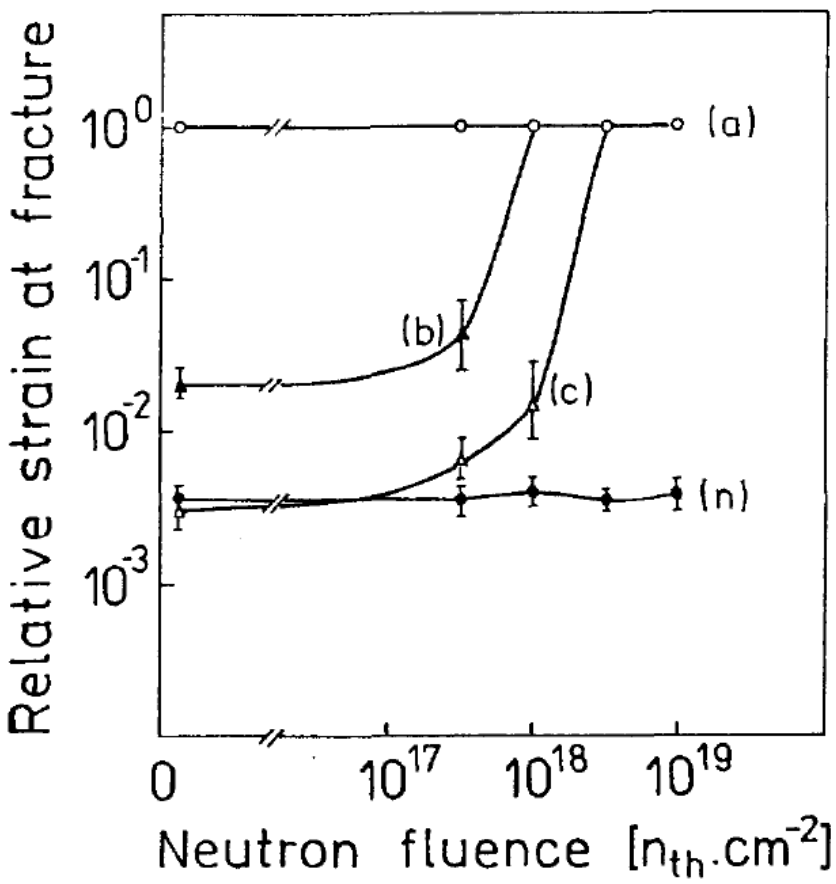

Figure 2-47 The relative fracture strain vs. the neutron fluence for $Fe_{73.5}Cu_1Nb_3Si_{13.5}B_9$ alloy (a) as-quenched, (b) annealed at 300 ^oC/1hr (amorphous), (c) annealed at 400 ^oC/1hr (amorphous), (n) annealed at 545 ^oC/1hr (nanocrystalline) (from Ref. [350]).

In terms of mechanical properties, a number of investigations reported that ion irradiation led to a decrease in nanoindentation hardness or Young's modulus which was thought to correspond to an increase in the free volume of the alloy [98, 130, 325, 329]. Additionally, Hu et al. found that significantly more softening occurred with heavier ion (Cl^{4+}) irradiation which was attributed to the excess creation of atomic-scale defects [329]. In contrast to the above results, a study by Huang et al. found that ion irradiation led to an increase in Hardness and Young's modulus in Ni^{+} irradiated $Ti_{45}Cu_{40}Zr_5Ni_5Sn_5$ [316]. Another study found that bulk metallic glass samples which had undergone ion irradiation induced crystallized exhibited higher nanoindentation hardness and Young's modulus as compared to the as-cast condition [345]. The nanoindentation results were echoed by studies involving Vickers hardness testing of metallic glasses which had also undergone irradiation induced crystallization [304-307].Investigations into the RED of amorphous alloys found that diffusion in $Fe_{40}Ni_{40}B_{20}$ was greatly enhanced under irradiation [335]. Along with a couple of other studies [336, 337] it was concluded that the RED behavior was best described by atomic transport via irradiation-induced, point defect like entities which perform long-range diffusion and can experience recombination reactions. Similar behavior was observed in study involving He irradiation of $Fe_{80}Si_{7.43}B_{12.57}$ amorphous alloy [321].

Some studies have also found that metallic glasses exhibit a higher resistance to He irradiation as compared to crystalline alloys [315, 322, 341]. In particular, He irradiation induced little changes in the surface morphology of the BMG alloys while there was observed blistering and peeling in their crystalline counterparts. However, the results of another study suggested that He formation in neutron irradiated $Fe_{40}Ni_{40}B_{20}$ and $Fe_{78}Si_9B_{13}$ metallic glass ribbons led to embrittlement of the alloy [346], although other studies found that it was most likely due to phase separation or cluster formation [131].

A few studies found that neutron irradiations increased the free volume in metallic glass alloys as evident in relative density measurements [128, 129, 348]. It was found that the increase in free volume correlated to an increase in the ductility of the amorphous alloy [129, 348]. In addition, it was observed that neutron irradiation could restore the ductility in an alloy which had been previously annealed (decrease in free volume). However, other studies have found that neutron irradiation led to an embrittlement, which was most likely caused by phase separation or cluster formation in the alloy [131, 346].

Based on the above discussion, there are some questions which still need to be answered. It is still unknown why some metallic glasses crystallize during irradiation while others remain amorphous. Although irradiation resistant BMGs are thought to contain SRO configurations which maintain stability during energetic atomic mixing; it is still not fully known. Furthermore, the absence of conventional defects such as Frenkel pairs in BMGs only adds to the complexity of its irradiation behavior. Moreover, He and ^{3}H behavior in amorphous alloys is still not fully understood. The absence of grain boundaries and higher volume content in BMGs should lead to an increased outgassing of He and correspondingly less embrittlement and cavitation (leading to decreased ^{3}H retention) as compared to their crystalline counterparts. However, the results of [346] indicate that He production in a given amorphous alloy can cause embrittlement, contradicting this assertion. Therefore, further investigation is required to fully resolve these issues.

CHAPTER 3 EXPERIMENTAL PROCEDURES

3.1 Experimental Specimens

For this research project, two BMG alloys were used which have the following compositions: $Zr_{52.5}Cu_{17.9}Ni_{14.6}Al_{10}Ti_5$ (BAM-11) and $Cu_{60}Zr_{20}Hf_{10}Ti_{10}$. Both alloys have relatively high compressive ductility and fracture toughness (see figures 3-1 to 3-3). For BAM-11, attributes such as high strength (~1,700 MPa [352, 353]), a relatively high reported fracture toughness of 49 MPa·$m^{1/2}$ [153, 354], a critical cooling rate as low as 10 K/s [355], and the fact that it does not contain beryllium, make BAM-11 BMG a particularly attractive candidate for use in mechanical components [356]. $Cu_{60}Zr_{20}Hf_{10}Ti_{10}$ was chosen as the second alloy for this study not only because of its different composition (and hence different atomic structure) as compared to BAM-11, but also because of its relatively high fracture toughness (67 MPa·$m^{1/2}$ [357]), high strength (~1,960 MPa [358]), comparable ductility to as-cast Zr-based metallic glass alloys [358], and low cost as compared to Zr-based and Pd-based BMGs [358, 359].

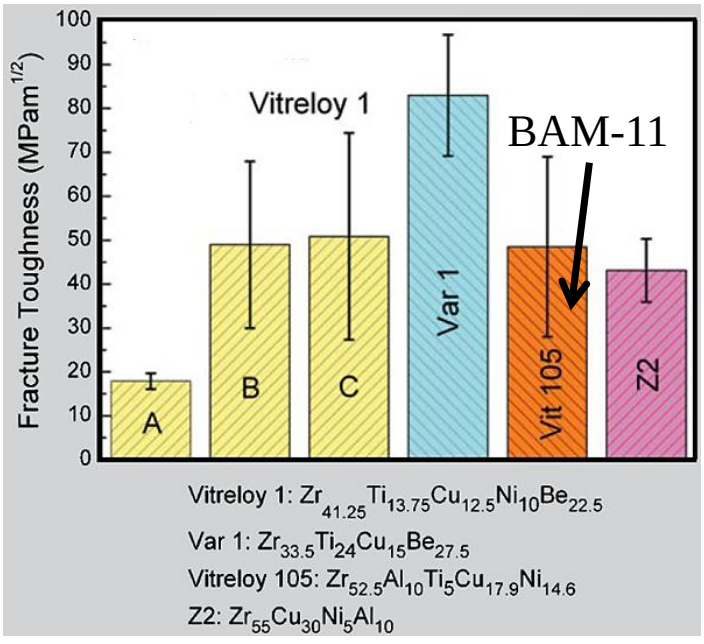

Figure 3-1 Fracture toughness of BAM-11 BMG as compared to other Zr based BMGs (from Ref. [354]).

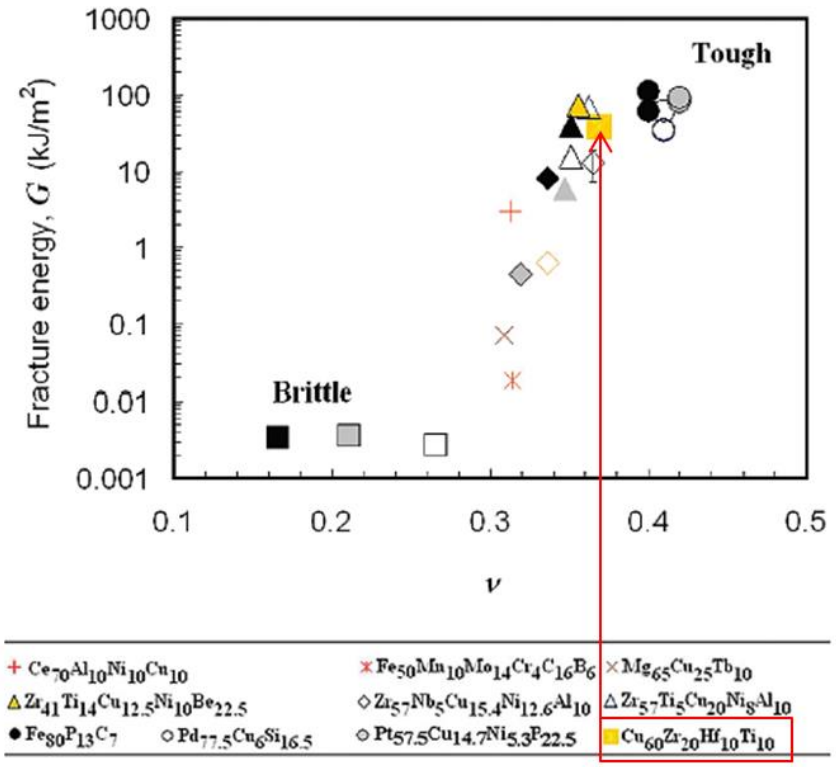

Figure 3-2 The correlation of fracture energy G with Poisson's ratio υ for all the as-cast metallic glasses (all compositions in atomic percent (at.%)). $Cu_{60}Zr_{20}Hf_{10}Ti_{10}$, one of the amorphous alloys chosen for this thesis, is highlighted in red (from Ref. [357]).

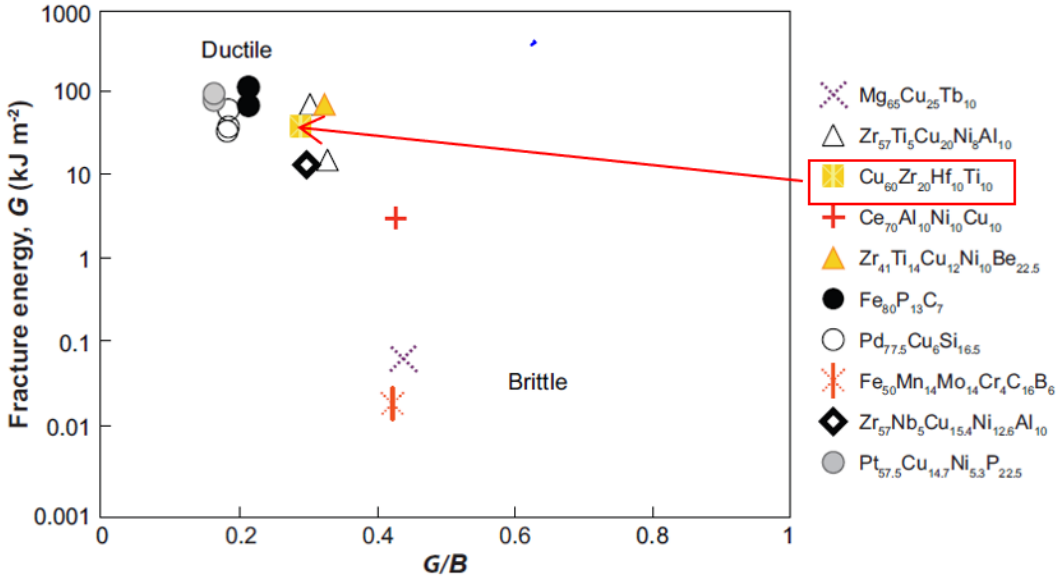

Figure 3-3 The correlation of fracture energy E with elastic modulus ratio G/B for different metallic glasses (from Ref. [107]).

Each of these materials have interesting characteristics of potential benefit to fusion and their study may provide critical insight into the development of next-generation fusion materials. This study uses a mixture of neutron and ion irradiation studies to explore the overall phase stability, short range atomic configurations and He/H retention in the proposed materials. Identification of promising radiation resistant attributes in either of these alloys may provide new opportunities for developing suitable reduced activation materials for the hostile environment in fusion reactor systems.

BAM-11 and $Cu_{60}Zr_{20}Hf_{10}Ti_{10}$ BMGs were fabricated by Dr. Hongbin Bei via arc melting in an argon atmosphere using a mixture of base metals with the following purities: 99.5% Zr, 99.99% Cu, 99.99% Ni, 99.99% Al, and 99.99% Ti. The preform alloys was then remelted and drop cast into a cylindrical copper mold with 3 mm diameters in a Zr-gettered helium atmosphere. Figure 3-4 presents the as-cast rod of both alloys. Five ingots of BAM-11 BMG and three ingots

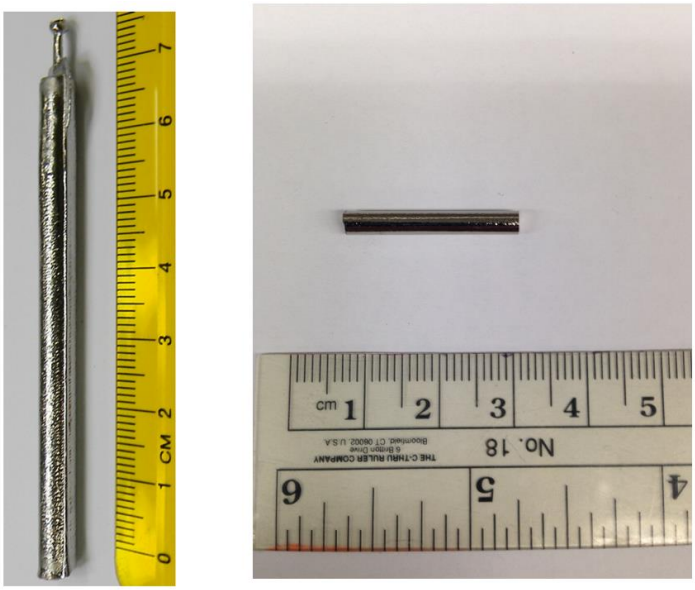

Figure 3-4 Left) 5 mm diameter rod of the as-cast $Zr_{52.5}Cu_{17.9}Ni_{14.6}Al_{10}Ti_5$ BMG and Right) 3 mm diameter rod of the as-cast $Cu_{60}Zr_{20}Hf_{10}Ti_{10}$ BMG.

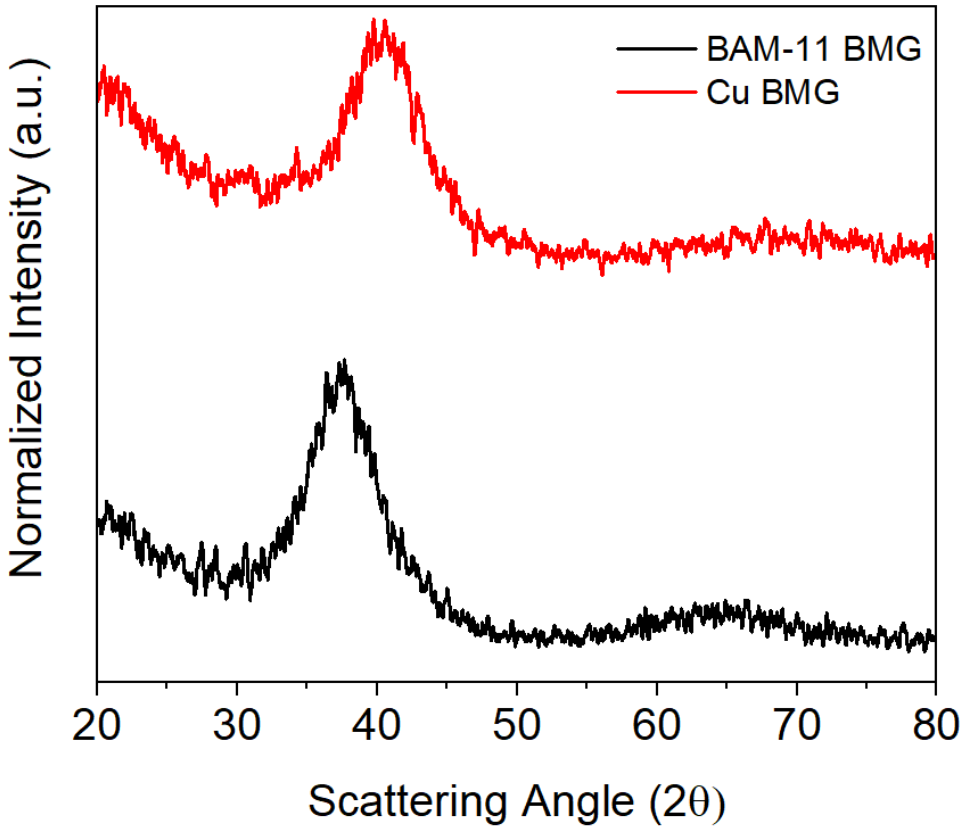

Figure 3-5 XRD patterns for the as-cast $Zr_{52.5}Cu_{17.9}Ni_{14.6}Al_{10}Ti_5$ (BAM-11) and $Cu_{60}Zr_{20}Hf_{10}Ti_{10}$ BMG alloys.

of Cu BMG were fabricated for the experimental work performed for this thesis. Subsequent X-ray diffraction (XRD) and differential scanning calorimetry both confirmed that the material was in the fully amorphous state. Figure 3-5 shows the XRD of the as-cast state for both specimens, where the single, broad peak indicate that they are fully amorphous.

3.2 Ion Irradiation Experiments

3.2.1 Ion Irradiation Facility

The BMG samples were irradiated at the ion accelerator at the Ion Beam Materials Laboratory (IBML) located at the University of Tennessee-Knoxville (UTK) [360]. The Beamline is equipped with two ion sources, a 3 MV tandem accelerator, three beamlines, and four end-stations [360]. In addition, the implantation capabilities of the facility include ions of most elements, energies from a few hundreds of keV up to tens of MeV (depending on ion and currentneeded), and controlled irradiation temperatures from -150 to 800 °C (depending on the beamline). The beam is generated by an ion sputtering source and a source of He^- ions. Figures 3-6 and 3-7 show an overview of the accelerator facility at the University of Tennessee and a schematic of the laboratory. Table 3-1 gives the technical specifications for the 3-MV tandem electrostatic accelerator [361].

The creation of the ion beam is a complex process which involves many components. Initially, heavy anions are created through a Source of Negative Ions by Cesium Sputtering (SNICS) system [362]. Helium ions may also be created through the Alphatross system which is adjacent to the SNICS source. With respect to the sputtering process, a reservoir of Cs and a tube

leading into the ion source are heated, creating a vapor of Cs which is sprayed onto the negative ion source [363]. Once the beam leaves the SNICS, an injection magnet bends the beam 30^{o} such that it enters the beamline. An extraction electrode provides a potential which accelerates the negative ions into the injection beamline. To avoid contamination of the outgoing beam, a 90^{o} double focusing magnet is used to analyze the beam and remove impurities.

After passing through the injection magnet, the beam travels into a 3.0 MV Pelletron (model 9SDH-2) tandem electrostatic accelerator (manufactured by National Electrostatics Corporation) [360]. Here, the negative ions are accelerated in a first tube from a ground potential to a positively charged terminal at high-voltage in the middle of the tank [364]. In the terminal, the ions come into contact with a nitrogen gas that strip electrons from the ions, converting them into positive ions. After the conversion process a potential drop accelerates the positive ions towards the other end of the accelerator. Upon exiting the accelerator, the energetic ions are focused using a magnetic quadrupole and a Y-axis electrostatic steerer into the analyzing magnet [360]. Here the analyzing magnet, via the Lorentz force, directs the portion of the beam with the desired energy (charge state and mass) into the target chamber, where it irradiates the specimen.

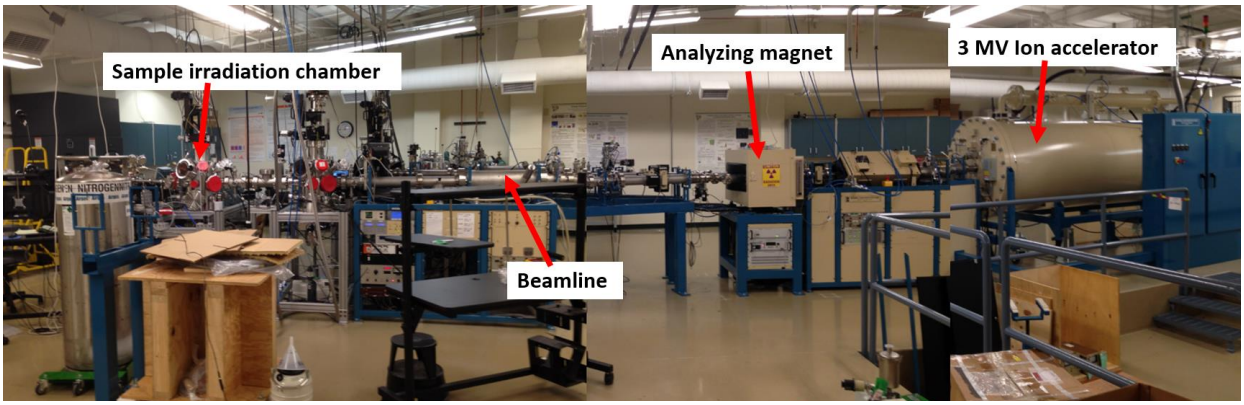

Figure 3-6 The research beamline which includes the 3 MV ion accelerator, the analyzing magnet, the L3 beamline, and the sample irradiation chamber.

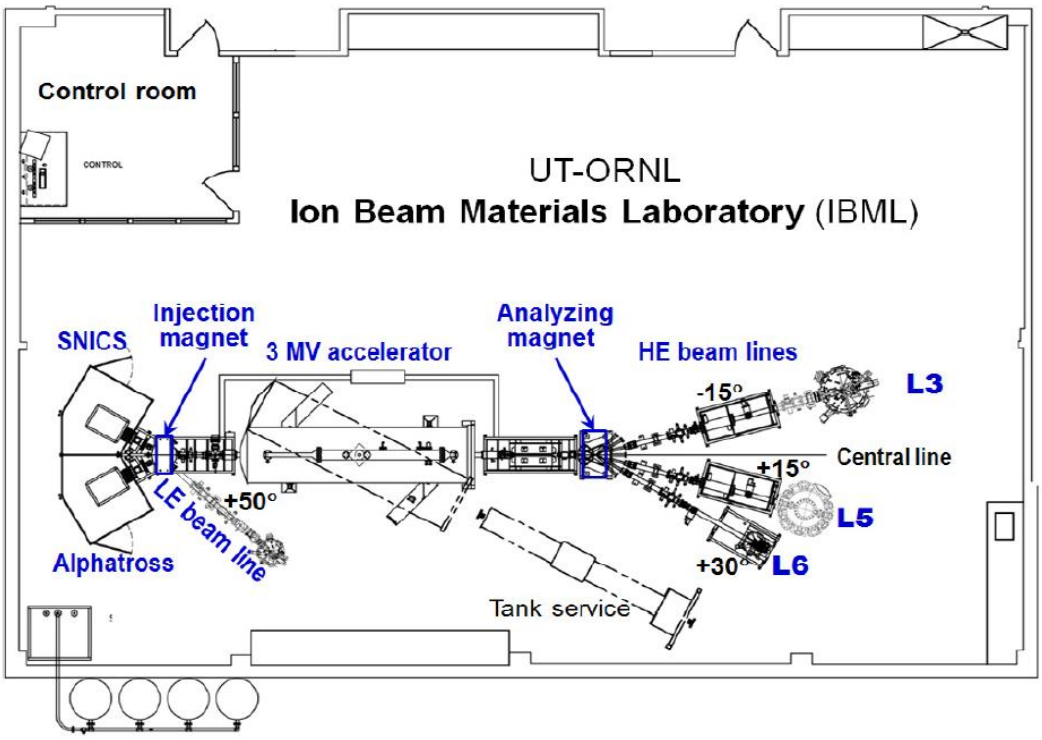

Figure 3-7 Schematic layout of the UT-ORNL IBML, including a separated control room, the two ion sources, a 3 MV tandem accelerator, beamlines and end-stations (from Ref. [360]).

Table 3-1 Technical specifications for a typical 3-MV tandem electrostatic accelerator (from Ref. [361]).

Parameter	Value
Terminal high voltage current	250 μA
Chamber pressure	1-5 $\times 10^{-8}$ torr
Insulating column voltage	3 MV
Voltage Stability	>1kV
Voltage ripple (peak-to-peak)	<=500V
Ion energy range	0.5-26 MeV

Figure 3-8 illustrates the typical schematic of a heavy ion irradiation target chamber and its associated vacuum system [281]. The system consists of many different components such as a Faraday cup and multiple vacuum pump systems. In the chamber a Faraday cup is used to monitor the beam current and the vacuum pumps ensure a satisfactory pressure during irradiation.

3.2.2 Sample Preparation

After fabrication, samples were mechanically ground and polished to a mirror finish at ORNL. Here, the cylinder rods were cut with a diamond saw into discs that were 3 mm in diameter with a thickness of ~ 300 μm. A Buehler MiniMet 1000 semi-automatic grinder/polisher was used for grinding and polishing [316] (see figure 3-9). The device operates under a range of speeds and pressures (2 – 10 lbf) and contains a sample holder which allows for grinding to a precision of tens of microns.

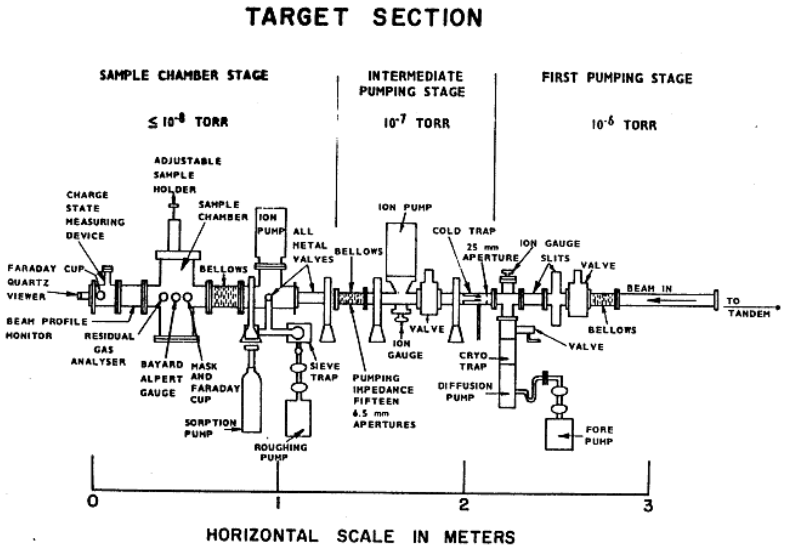

Figure 3-8 Schematic of a typical heavy ion irradiation target chamber and vacuum system (from Ref. [281]).

Figure 3-9 Left) Buehler MiniMet 1000 semi-automatic grinder/polisher. Right) Adjustable sample holder which allows for grinding of sample to a precision of tens of microns.

Figure 3-10 Cu based BMG 3 mm disc specimen secured in the top holder device.

For polishing, samples were first adhered to a glass disc with Crystalbond^{TM} low melting temperature mounting adhesive and then secured into the top holder device (see figure 3-10). For the thinning process, specimens were ground with progressively finer SiC paper (grits of 320, 600 and 1200) where water was used as the lubricant. Due to the roughness of the 320 and 600 grit papers, they can efficiently thin the sample down to a desired thickness in only a few steps. The applied force and duration during these steps respectively varied from 0 - 4 lbf and 2.5 - 4 minutes.

To start the grinding process, the zero point of the sample was set. This step of the process involves rotating the top holder piece (see figure 3-9 right) to adjust the height of the sample with respect to the grinding paper. The dial was rotated until the sample experienced minimum contact friction with the grinding paper, which corresponded to a slight resistance when trying to move the top holder piece. Once the zero point was set, the dial was rotated clockwise to set the amount of material to be ground away. The sample thickness was measured after the completion of a grinding step using digital calipers and then was repeated until the desired specimen thickness was achieved. Between steps, the sample and holder were rinsed with ethanol to reduce contamination by surface particles removed during grinding.

Once the desired thickness was achieved, 1200 grit was used to remove a majority of the remaining large scratches. After each step, the sample surface was examined using a Omano OM4424 Dual-Power 20X / 40X Stereo microscope. The surface was examined after each step until relatively larger scratches were no longer visible. To remove contaminant particles produced by grinding, sample and holder were cleaned with acetone and then allowed to air dry in between each step. Figure 3-11 shows a picture of the microscope.

After grinding, smaller scratches were eliminated by polishing the samples with diamond polishing (DP) cloths ranging from 6, 3 and 1 μm. The lubricant used for these steps consisted of DP-Purple diamond polish. Furthermore, an applied force of 0 - 1 lbf. was used for a duration of 2.5 minutes. Again, a microscope was used to observe changes in surface quality. The polishing steps were repeated until there remained only 1 - 2 noticeable scratches. After the 1 μm polishing step, samples were polished using OP-U colloidal silica polish combined with a DP Nap 200 mm cloth. Each polishing step involved using a compressive force of 0 - 1 lbf with a duration of 4 minutes. In addition, a minimum of ten polishing steps with colloidal silica were used in which the surface was examined between each step with the same optical microscope as mentioned previously.

Once the sample surface was of sufficient quality, it was cleaned with acetone, methanol and ethanol under a fume hood and then placed onto a Kimwipe to air dry. After the sample was cleaned and dried it was stored in a cool, dry place. For further details on the complete grinding and polishing process, please refer to Table 3-2.

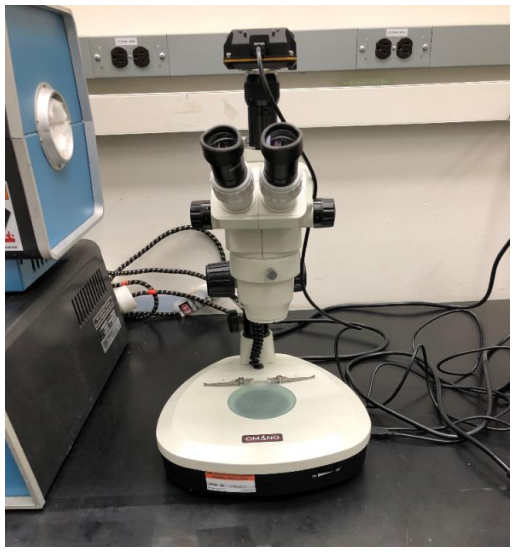

Figure 3-11 Omano OM4424 Dual-Power 20X / 40X Stereo microscope used to inspect samples as they were being polished.

Table 3-2 Summary of grinding/polishing steps for bulk metallic glass specimens.

Procedure	Pad	Machine Settings			Lubricant/Polishing Solution
		Force (lbf.)	Speed	Time (min.)	
Grinding	320 Grit SiC	4	35	4.0	Water
	600 Grit SiC	3	35	4.0	
	1200 Grit SiC	1	45	2.5	
Polishing	6 μm DP Cloth 3 μm DP Cloth 1 μm DP Cloth	1	45	2.5	DP-Purple Diamond Polish
	DP Nap 200 mm	0		4.0	OP-U Colloidal Silica Polish

3.2.3 Ion Irradiation Stage

For the ion irradiations, a specimen platen was obtained from the Thermionics Vacuum Products that is compatible for the IBML vacuum chamber and stage system. Because the sample holder was initially unable to hold multiple small samples such that there was adequate thermal contact between the specimens and the heated back plate, the system was modified accordingly [365]. Figure 3-12 displays a schematic of the platen system, and as can be seen, the middle plate contains three circular slots that have a diameter somewhat larger than the samples.

To ensure that the samples were properly contained in the device, the middle plate was machined to have a thickness greater than the samples, which corresponded to approximately 0.5 mm. To account for any potential thickness variations in the middle plate and to ensure that the samples had adequate thermal contact with the Mo base plate, crushable niobium wire rings (0.25 mm diameter) were positioned onto the sample surfaces. In terms of the top plate, it contains 2.1 mm diameter holes that are positioned directly over the sample surfaces. The peripheral surface on the inside surface of the top plate, when placed onto the middle plate, is intended to apply a uniform pressure on the Nb rings to keep the specimens secured in the holder. Moreover, this uniformly applied pressure will ensure that the samples will maintain a good thermal contact with the base plate during irradiation. Once the top plate is positioned correctly, it is fastened to the stage via six stainless steel screws that are threaded through the outer holes of all three plates. To distribute the pressure of the screws evenly over the surface of the top plate, the screws were placed through stainless steel washers with a ~100 μm tolerance before fastening them to the device.

To adequately monitor the temperature during irradiation, two K-type (aluminel-chromel) thermocouple wires were attached to the stage. The first thermocouple wire was welded to a ~3mm diameter iron-chromium-aluminium (FeCrAl) [366, 367] disc which was placed into one of the

three sample positions in the middle plate, and was secured in place with a molybdenum clip. Furthermore, the second thermocouple wire was secured firmly onto the base plate via a Mo screw. The two separate thermocouples were used to ensure a more accurate temperature reading during irradiation. In addition, ceramic insulating tubes were placed around the wires to minimize electrical contact between the wires and the environment to minimize errors that are associated with incorrect temperature measurements. An alumina piece was attached to the top place of the specimen stage to help align the ion beam appropriately before irradiation commenced. Figure 3-13 shows the fully assembled irradiation stage, while figures 3-14(a)-(b) displays the stage mounted properly in the irradiation chamber.

Previous work was performed by Daniel Clark and Dr. Congyi Li at UTK to calibrate the thermocouple system [365]. Here, they monitored the temperature distribution of the irradiation stage during exposure to temperatures ranging from ambient to 800 ^{o}C. An infrared camera was used to verify that there was uniform heating across the holder. It was found that the temperature remained relatively uniform across the surface of the top plate.

3.2.4 SRIM Calculations

To estimate the ion range, depth dependent dpa, and the corresponding ion concentrations for the experiment, SRIM 2013 [294, 297] was used. These values were calculated using the quick Kinchin-Peace option [297], as suggested by Stoller et al. [299], using threshold displacement energies of 40 eV. Moreover, the densities used for the Cu and BAM-11 BMG calculations were 8.6 g cm^{-3} and 6.7 g cm^{-3}, respectively. Figures 3-15 (a)-(d) shows the results of the SRIM calculations. For both alloys, the calculated Ni^{3+} damage and displacements per atom (dpa) for

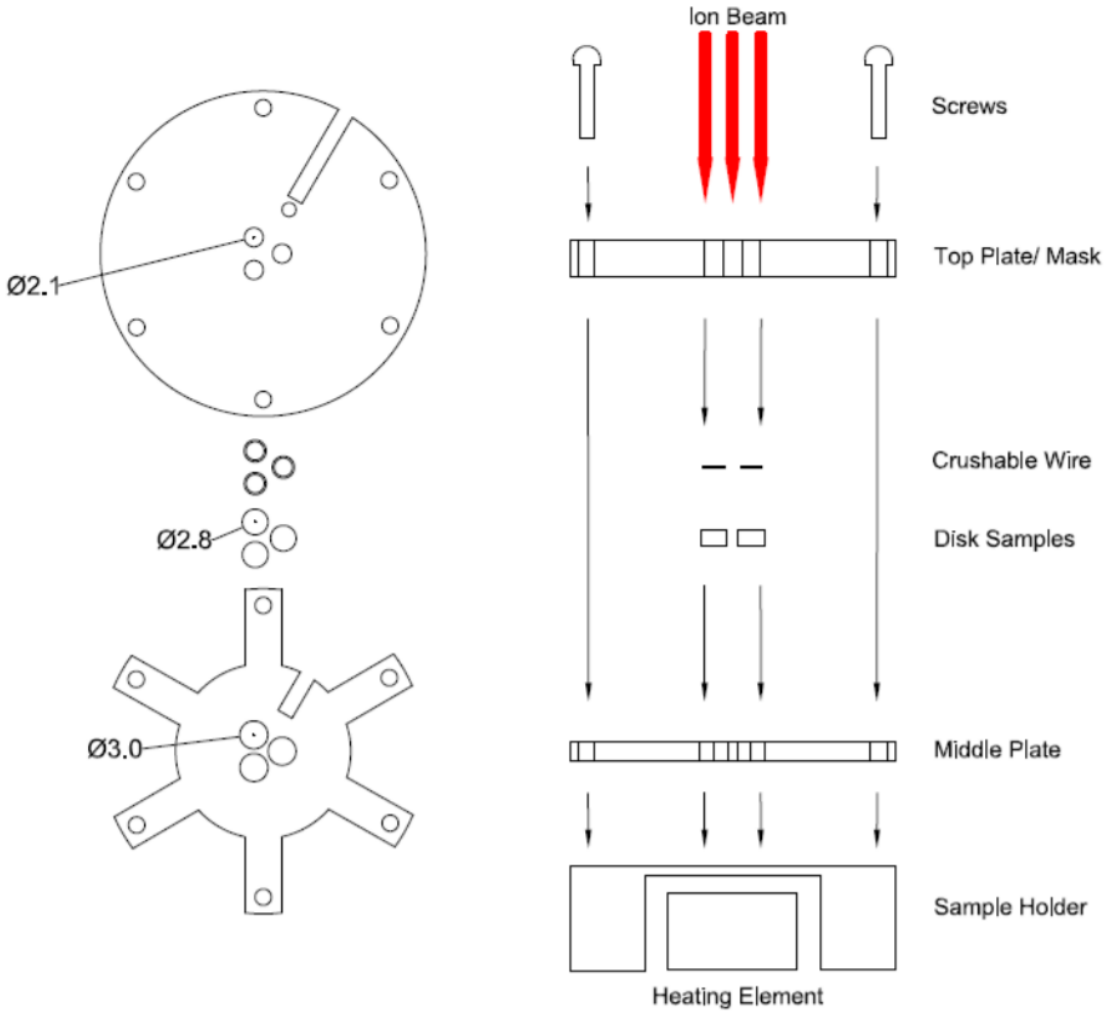

Figure 3-12 Modified sample holder schematic (from Ref. [365]).

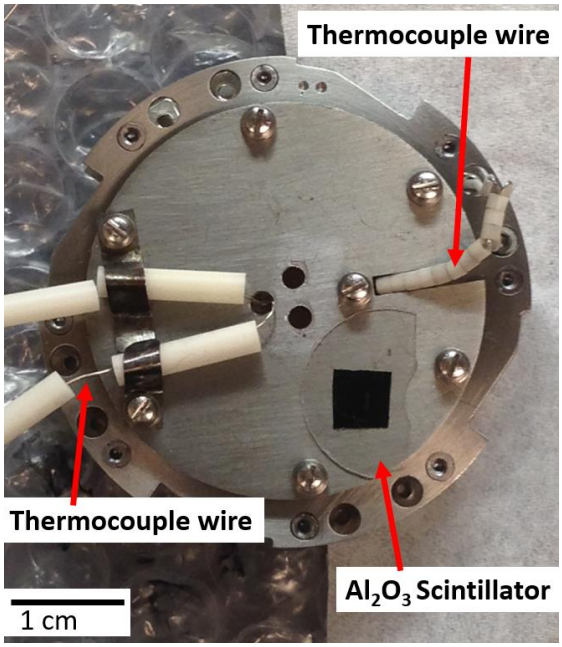

Figure 3-13 Top view of the fully assembled ion irradiation sample stage with the attached thermocouple wires (encased in ceramic beads) and Al_2O_3 scintillator piece.

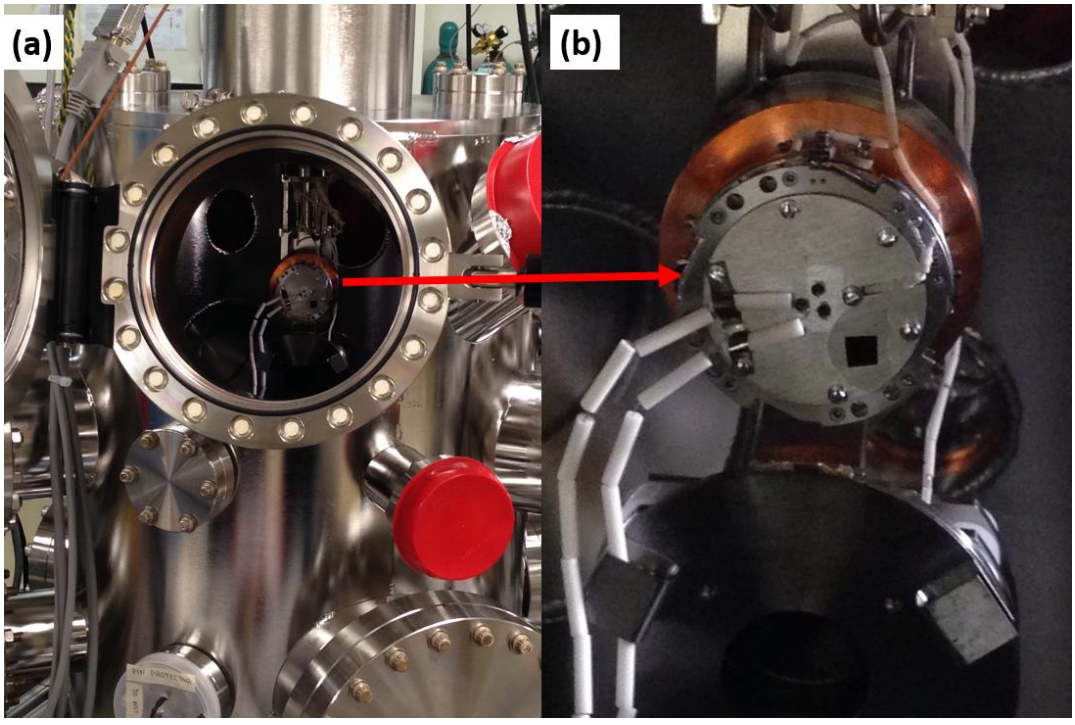

Figure 3-14 Images of the (a) Irradiation stage properly mounted into the beamline irradiation chamber and (b) a close-up of the stage.

the midrange and peak doses, respectively, were 10 and 25 dpa. The dotted line corresponds to the depth at which the midrange dose occurs. Furthermore, the projected ion range was calculated to be ~3.0 μm, which corresponded to implanted Ni concentrations of ~0.42 and ~0.36 atomic % (at. %) for the BAM-11 and Cu BMG, respectively. In terms of the C^+ irradiations, the calculated damage and displacements per atom (dpa) for the midrange and peak doses, respectively, were 0.5 and 5.5 dpa. Like with the Ni^{3+}, the projected ion range was ~3.0 μm, which corresponded to implanted C concentrations of ~2.0 and ~1.7 at. % for the BAM-11 and Cu BMG, respectively.

3.2.5 Ion Irradiations

The Cu and BAM-11 BMG specimens were irradiated by 9 MeV Ni^{3+} and 5.5 MeV C^+ ions at three different temperatures of 25, 290, and 360 ^oC. For these experiments, Dr. Miguel Crespillo operated the beamline during the irradiations. The maximum temperature of 360 ^oC was selected since it well below the reported crystallization temperatures of the alloys, which are 452 ^oC for the BAM-11 BMG [368] and 510 ^oC for the Cu BMG [358]. For the Ni^{3+} irradiations, samples were irradiated to midrange doses of 0.5 and 10 dpa, while for the C^+ irradiation they were irradiated to 0.5 dpa. The ion energy was selected to produce a reasonably deep irradiated region to mitigate issues associated with diffusional broadening [369, 370] and "swift heavy ion" effects that emerge at higher ion energies. To achieve the prescribed doses during irradiation, an ion flux of ~ 10^{12} $cm^{-2}s^{-1}$ was used. For the Ni^{3+} irradiation, the time required to reach the midrange doses of 0.5 and 10 dpa were respectively 20 minutes and 7 hours. Moreover, the irradiation time required for the C^+ irradiation to reach a midrange dose of 0.5 dpa in the specimens was 7 hours.

With respect to each irradiation condition, both types of BMG were irradiated simultaneously. Table 3-3 lists the ion specie, the midrange dose, the ion fluence, the irradiation

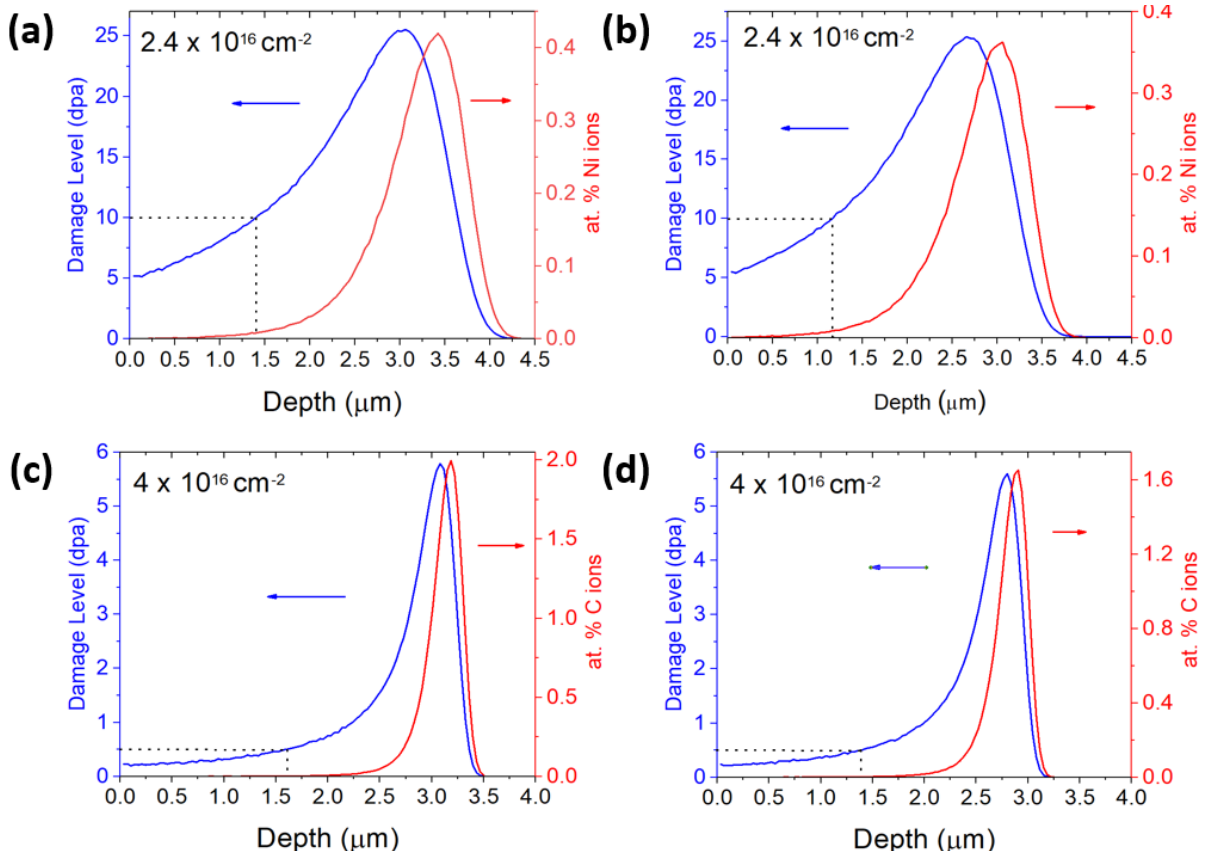

Figure 3-15 Irradiation damage (dpa) profile (blue curve) and at. % (red curve) versus depth for (a) BAM-11 BMG and (b) Cu BMG irradiated by 9 MeV Ni^{3+} (midrange dose of 10 dpa), (c) BAM-11 BMG and (d) Cu BMG irradiated by 5.5 MeV Cu^{+} (midrange dose of 0.5 dpa).

Table 3-3 Ion Irradiation Matrix.

Ion Species	Midrange damage (dpa)	Fluence (ions/cm^2)	Temp (°C)	Irr. Time (h)
9 MeV Ni^{3+}	0.5	1.2×10^{15}	25	0.3
	10	2.4×10^{16}		7
	0.5	1.2×10^{15}	290	0.3
	10	2.4×10^{16}		7
	0.5	1.2×10^{15}	360	0.3
	10	2.4×10^{16}		7
5.5 MeV C^{+}	0.5	2.4×10^{16}	25 290 360	7

temperature, and the irradiation time for each experiment. To minimize the inaccuracies associated with surface effects and diffusional broadening of the implanted ions [369-372] the microstructure and mechanical properties were examined at an intermediate depth of approximately 1.5 μm which corresponds to the prescribed midrange doses of 0.5 (for C^{+}) and 0.5 and 10 dpa (for Ni^{3+}) (dotted line in figures 3-15 (a)-(d)).

With respect to each irradiation condition, both types of BMG were irradiated simultaneously. Table 3-3 lists the ion specie, the midrange dose, the ion fluence, the irradiation temperature, and the irradiation time for each experiment. To minimize the inaccuracies associated with surface effects and diffusional broadening of the implanted ions [369-372] the microstructure and mechanical properties were examined at an intermediate depth of approximately 1.5 μm which corresponds to the prescribed midrange doses of 0.5 (for C^{+}) and 0.5 and 10 dpa (for Ni^{3+}) (dotted line in figures 3-15 (a)-(d)).

The accumulated ion fluence on the samples during the irradiation was calculated from the beam spot size that is normally regulated by the double slits on the beamline close to the target chamber. To mitigate issues associated with beam heating and charge accumulation on the samples, a low beam current density of ~ 4.8×10^2 nA/cm^2 was used to minimize beam heating and charge accumulation on the samples [373]**.** Before the irradiation began, the ion beam was located and calibrated using an alumina piece that was attached to the top plate of the specimen stage.

During the ion implantations, the ion beam was scanned both vertically and horizontally for lateral homogeneity of the beam and was found to be within 10 % throughout the irradiated area. Here an ion beam area of 4×9 mm^2 was directed onto the sample surface during irradiation using adjustable slits. Beam homogeneity was within 10% throughout the irradiated area, which

was validated by checking the ion beam induced luminescence (IL) on Al_2O_3 (used as a scintillator) monitored with a CCD camera (more details can be found elsewhere [360, 374]).

During the entire experiment, the temperature was continuously monitored using two K-type (chromel-alumel) thermocouples to ensure that the target holder did not exceed the desired temperature during irradiation. To avoid surface contamination during irradiation, the chamber was continuously monitored and was maintained at ~ 10^{-7} torr during operation. Table 3-4 shows the recorded thermocouple temperatures and chamber pressure, as a function of time, during the heat up process for a 360 ^{o}C ion irradiation experiment. As can be seen in the table, the temperature difference between the two thermocouples never exceeded 5 ^{o}C during a typical monitoring process. Once the chamber pressure and temperature reached the desired values, they were monitored for another 20 minutes to ensure minimal deviation (± 5 ^{o}C and ± 5 × 10^{-8} torr) before initiating the irradiation.

During irradiation, there is a chance that there will be a significant temperature variability between the individual specimens. These differences could arise from factors such as poor thermal contact between the sample and the thermocouple and/or a temperature gradient across the stage. This variability could result in specimen temperatures exceeding the glass transition, or even crystallization temperature of the BMG, although it is unlikely.

3.2.6 X-Ray Diffraction Characterization

Bulk and glancing X-ray diffraction (XRD) was carried out on the as-cast and irradiated specimens at the Joint Institute for Advanced Materials (JIAM) Diffraction Facility at the University of Tennessee. The XRD was performed using a PANalytical Empyrean diffractometer equipped with a Xe proportional detector. Figure 3-16 shows the basic setup of the instrument

Table 3-4 Typical recorded thermocouple temperature and irradiation chamber pressure as a function of time during the heating up period of the ion irradiation experiment. T. C.: Thermocouple.

Time	T. C. 1 Temperature (ºC)	T. C. 2 Temperature (ºC)	Chamber Pressure (torr)
11:30 A.M	20	20	6.1×10^{-8}
11:39 A.M	18	20	6.5×10^{-8}
11:46 A.M	19	20	1.1×10^{-7}
11:52 A.M	32	31	1.0×10^{-7}
11:57 A.M	50	48	3.1×10^{-7}
12:06 P.M	112	110	9.6×10^{-7}
12:11 P.M	176	172	6.2×10^{-7}
12:20 P.M	208	206	1.2×10^{-6}
12:26 P.M	265	262	7.5×10^{-7}
12:31 P.M	273	269	6.5×10^{-8}
12:38 P.M	318	312	6.5×10^{-8}
12:44 P.M	322	316	6.5×10^{-8}
12:49 P.M	357	353	6.5×10^{-8}
12:55 P.M	358	353	6.5×10^{-8}
1:00 P.M	354	350	6.5×10^{-8}
1:06 P.M	354	349	6.5×10^{-8}
1:12 P.M	356	353	6.5×10^{-8}
1:17 P.M	360	358	6.5×10^{-8}

which includes the X-ray source, the PreFix modulus/optics, the sample holder, and the Xe proportional detector. The left PreFix module consists of the incident X-ray beam before it impinges on the specimen. Figure 3-17 shows the associated optical components which include the soller slits, the programmable divergence slit, and the fixed incident beam mask.

Furthermore, the right PreFix module contains two beam paths, one of which is used for the glancing XRD, while the other that is used for the bulk XRD measurements. Figure 3-18(a) shows the optical components used for the glancing XRD, while figure 3-18(b) displays the optics involved with the bulk XRD measurements. As for figure 3-18(a), the diffracted beam optics include the parallel plate collimator, the large soller slits, and the previously mentioned Xe proportional detector. On the other hand, figure 3-18(b) shows the optics used for the bulk XRD experiment, which include the large soller slits, the beta nickel filter, and the PIXcel^{3D} detector. Finally, figure 3-19 displays the soller slits, the mask, the anti-scatter slit, the large soller slit and the Ni filter.

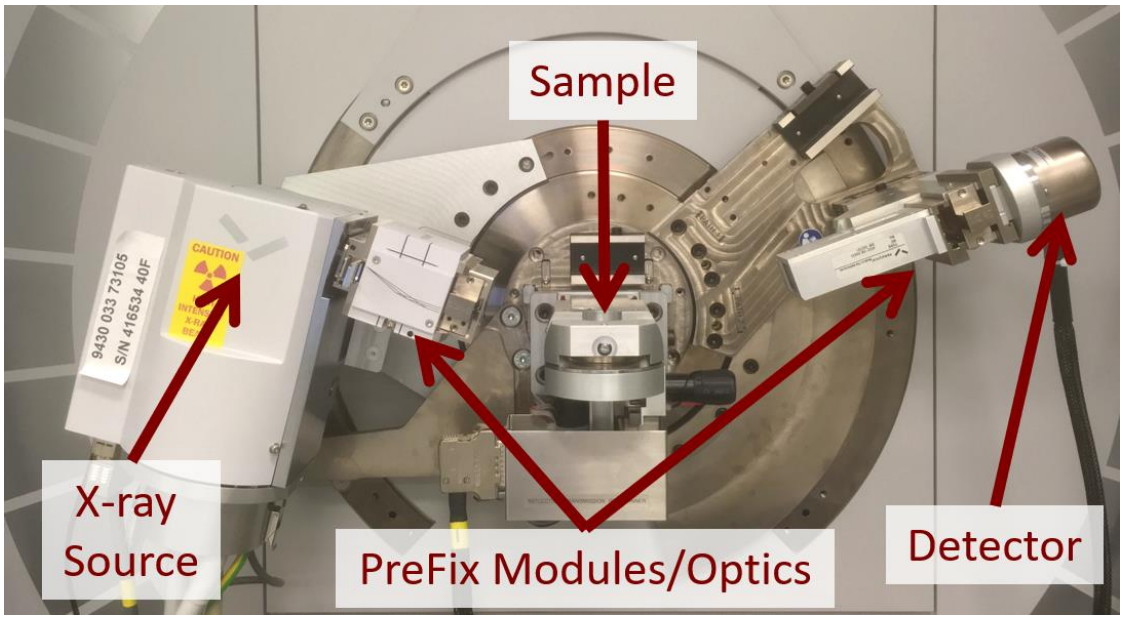

Figure 3-16 PANanalytical Empyrean X-ray diffraction instrument.

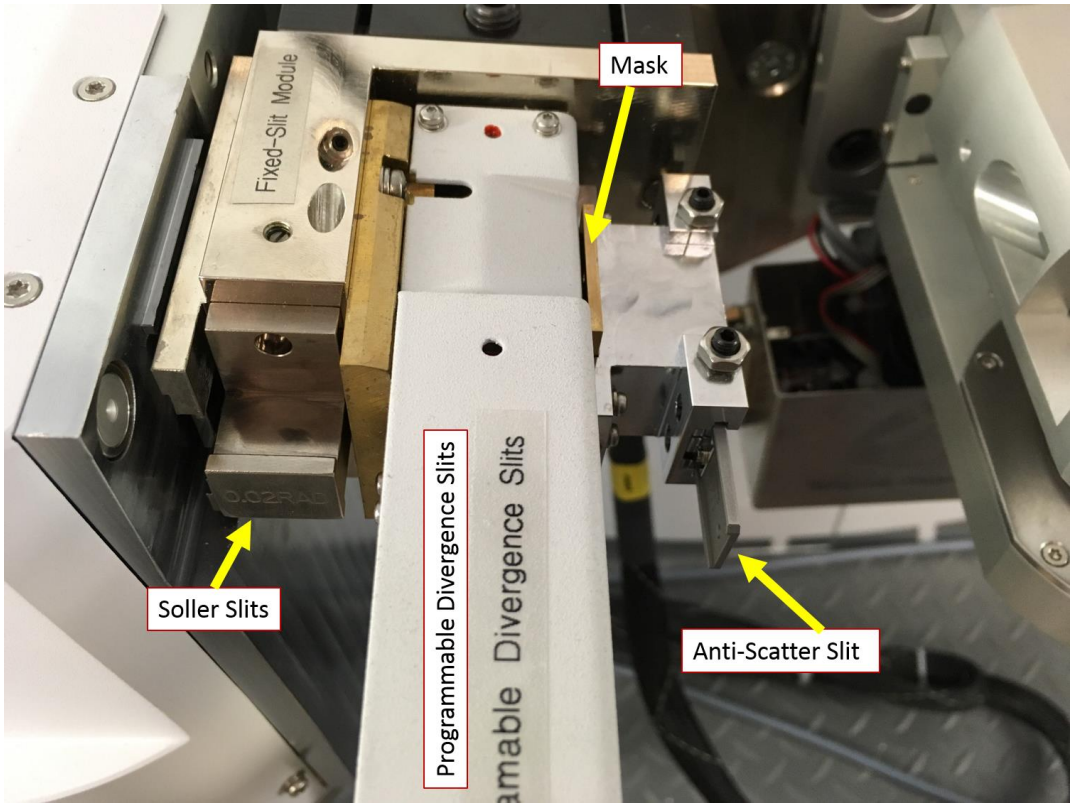

Figure 3-17 Schematic of optics used on the incident beam side of the instrument (from Ref. [375]).

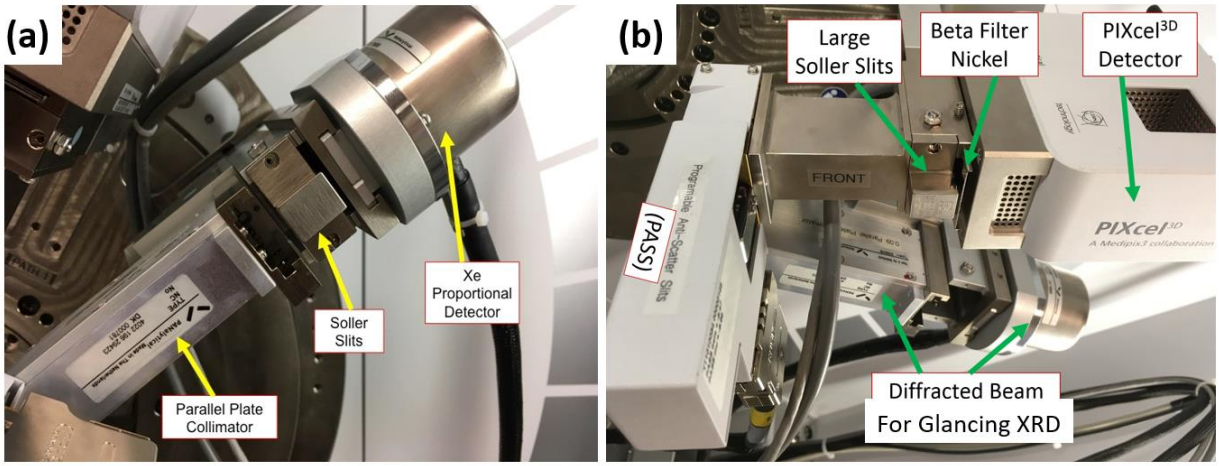

Figure 3-18 Schematic of optics used on the diffracted beam side of the instrument (from Ref. [375]).

To begin the XRD measurement, specimens were placed on a zero-background holder to shield out diffraction patterns that were not associated with the sample. Using an alignment camera, the sample was centered on the stage to maximize counting statistics. The X-ray consisted of a Cu beam with a K-alpha wavelength of 1.54 Å, in addition to an accelerating voltage and current of 45 kV and 40 mA. Furthermore, the diffraction angle 2θ ranged between 20 - 80^{o} where data was taken every 0.013 degrees. The Powder Bragg-Brentano method was used to examine the specimens. Table 3-5 summarizes the experimental parameters used for the both the glancing incidence and bulk XRD experiments.

Glancing angles ranging from 0.5-1 degree were used to examine whether any crystallization or phase decomposition occurred in the ion irradiation region. The glancing angles were calculated using the method described in [376]. The penetration depth, *D*, of an X-ray into a sample is based on the glancing angel, ϕ, through the following equation:

$$D(\phi) = \frac{\lambda}{2\sqrt{2}\pi\left[\sqrt{(\phi^2 - \phi_c^2)^2 + 4\delta_i^2} + \phi_c^2 - \phi^2\right]^{1/2}} \quad (3\text{-}1)$$

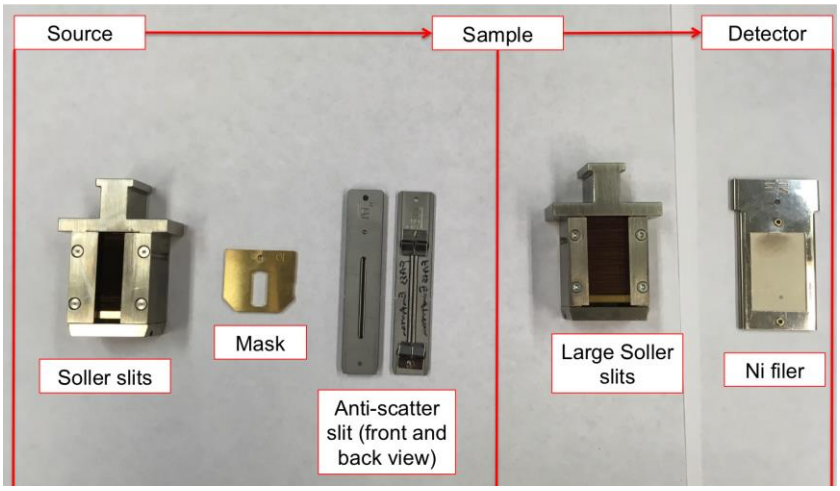

Figure 3-19 Some of the optics used in the PANalytical XRD instrument optics (from Ref. [375]).

Table 3-5 Optics used for bulk and glancing XRD.

Parameter/Optic	Glancing	Bulk
Fixed Incident Beam Mask	Fixed mask 4 mm	Fixed incident beam mask 10 mm
Divergence Slit	1/16º	1/16º
Anti-Scatter Slit	-	1/8º
Incident beam Soller Slit	0.04 rad	0.04 rad
Diffracted Beam Soller Slit	Large 0.04 rad	Large 0.04 rad

where ϕ_c is the critical angle below which total external reflection occurs, δ_i is a value related to the index of refraction, and λ is the X-ray wavelength. The critical angle, ϕ_c, and δ_i are both defined as:

$$\phi_c = \sqrt{\frac{N_o e^2 Z \rho}{\pi m c^2 A}} \lambda \tag{3-2}$$

$$\delta_i = \frac{\mu \lambda}{4\pi} \tag{3-3}$$

here N_o is Avogadro's number, e is the electron charge, Z is the average atomic number, ρ is the mass density, m is the electron mass, c is the velocity of light, A is the average atomic mass, and μ is the linear absorption coefficient.

3.2.7 TEM Characterization

To determine whether irradiation induced nanocrystalline formation had occurred in the alloy, transmission electron microscopy (TEM) characterization was performed in the Low Activation Materials Development and Analysis (LAMDA) laboratory at ORNL [377]. TEM foils were fabricated using an FEI Quanta Dual-beam focused ion beam (FIB)/SEM, which is displayed in figure 3-20. The foils were cut and lifted out of the sample using an omniprobe needle and then deposited onto a molybdenum FIB lift-out grid. After welding the lift-out specimen to the grid, 2 kV Ga^+ ions were used for the thinning steps where the energy was gradually reduced from 30 keV to 3 keV. Figure 3-21 shows an as-cast BAM-11 BMG welded sample before thinning was commenced. An ion current of 30 pA with a glancing angle of about 4° was used during the final thinning step to minimize ion beam milling damage. A Fischione Nanomill (model 1040)

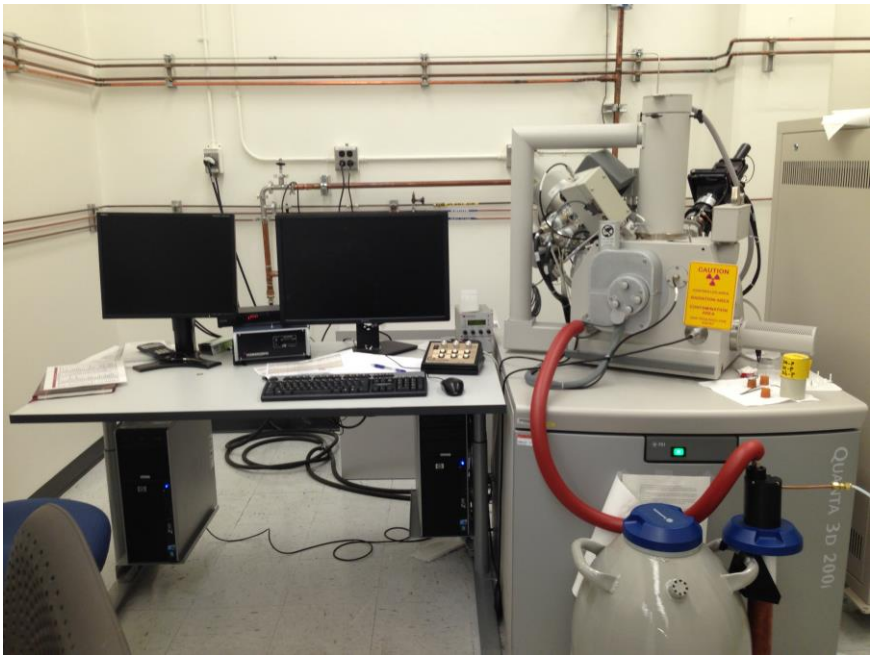

Figure 3-20 FEI Quanta Dual-beam FIB/SEM that is located in the LAMDA facility in ORNL.

.

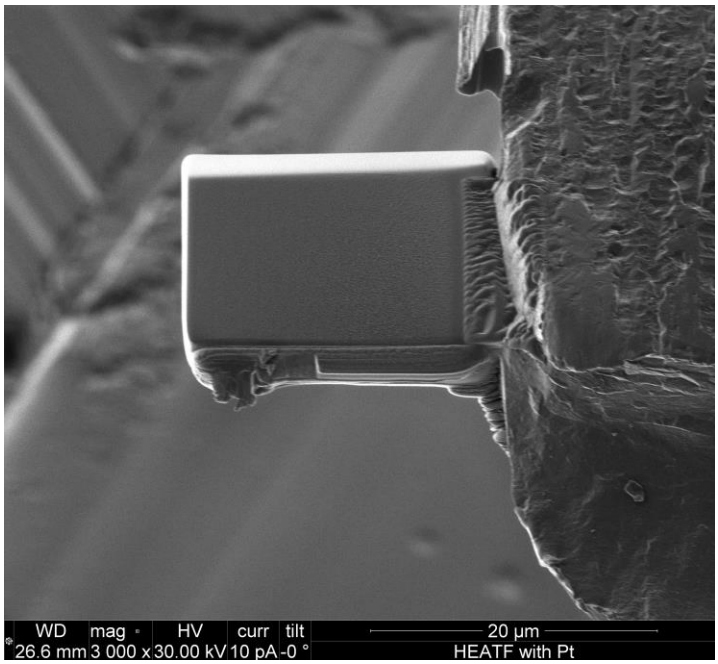

Figure 3-21 As-cast BAM-11 BMG lift-out sample that was welded to a Mo grid before thinning steps were commenced.

4 keV Ar^+ ion polisher (at low incident angles) was used to polish the specimens after the thinning of the specimen was completed. After polishing, the welded lift-out specimens were then examined and analyzed in a JEOL JEM-2100F TEM/STEM at 200 kV (see figure 3-22) using bright field (BF) imaging and selected area diffraction (SAD). The TEM characterizations of the ion irradiated specimens were performed by Dr. Tengfei Yang. The selected area diffraction was performed to determine whether there were any diffraction spots, which corresponds to the presence of crystalline phases in the matrix.

3.2.8 Nanoindentation Testing

Nano-indentation hardness tests were performed at room temperature using a KLA-Tencor G200 Nano-indenter with a Berkovich diamond (3-sided pyramidal tip) in continuous stiffness measurement mode. For the ion irradiated specimens, they were glued to a metal stage using

Figure 3-22 The JEOL JEM-2100F TEM/STEM system (from Ref. [377]) located in the LAMDA facility in ORNL.

epoxy. Prior to indenting, specimens were mounted on a JEOL JSM 840 Aluminum standard sample mount (from Electron Microscopy Sciences©) using Crystalbond adhesive. The nanoindenter was programmed to run using the Nanosuite software which is run on a Hewlett-Packard© personal computer equipped with a Windows 7 operating system. Figure 3-23(a) shows the setup of the device in LAMDA while figure 3-23(b) shows a close-up of the indenter, microscope and sample contained in the sample tray. In addition, figure 3-24 shows a top view of the mounting stage.

To begin nanoindentations, the nanosuite software was initialized and the desired indentation program was selected. The sample tray was then brought into the loading position and the hood of the indenter system was opened. To prevent the stage from swiveling that could lead to damage, two screws were inserted into mounting holes in the front of the nanoindenter instrument and then fastened. These screws prevent the instrument from experiencing any unnecessary movements during loading that may damage the instrument. With the screws in place, the sample was mounted into the tray and then moved into a position beneath the microscope. During the loading process, extreme care was taken to make sure that the stage was adequately beneath the microscope and indenter to avoid damage to the components.

After sample placement, the hood was closed and the specimen was placed under the microscope via the computer interface. Then the microscope was turned on via the computer interface and its height was adjusted until the sample surface came into focus. The area function of the tip, in addition to the machine stiffness for the nanoindenter, was calibrated by indenting on a standard fused silica sample [98]. After calibration, nanoindentation tests were conducted. The experiments were performed using a constant loading rate of 400 μN/s.

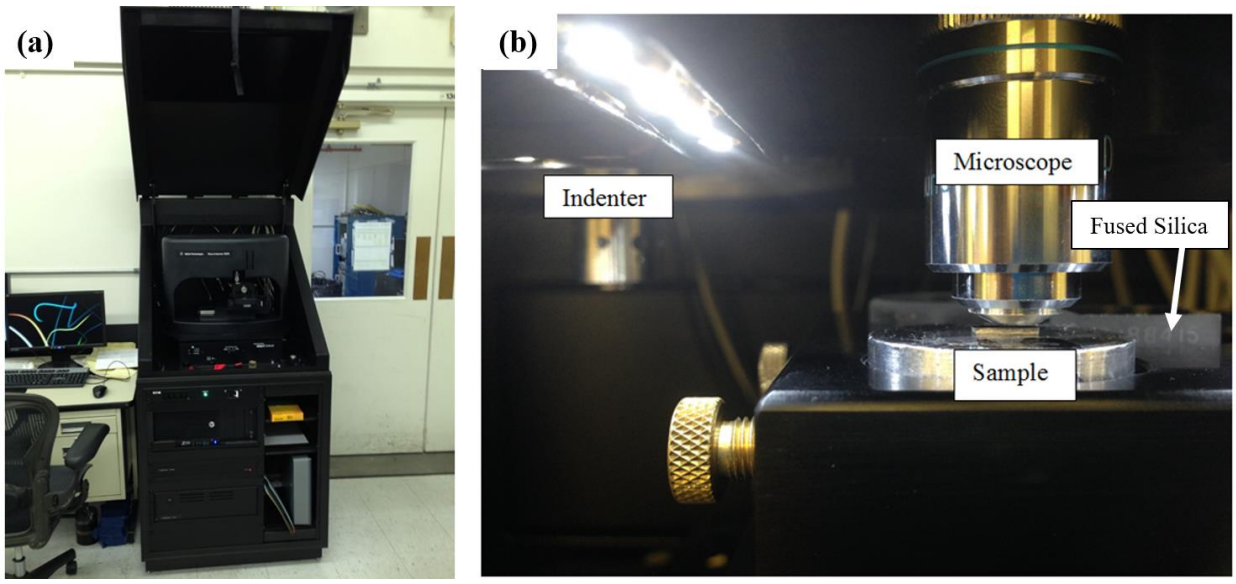

Figure 3-23 (a) KLA-Tencor G200 nanoindenter. (b) Close up view of microscope, sample in tray, indenter mechanism, and fused silica sample.

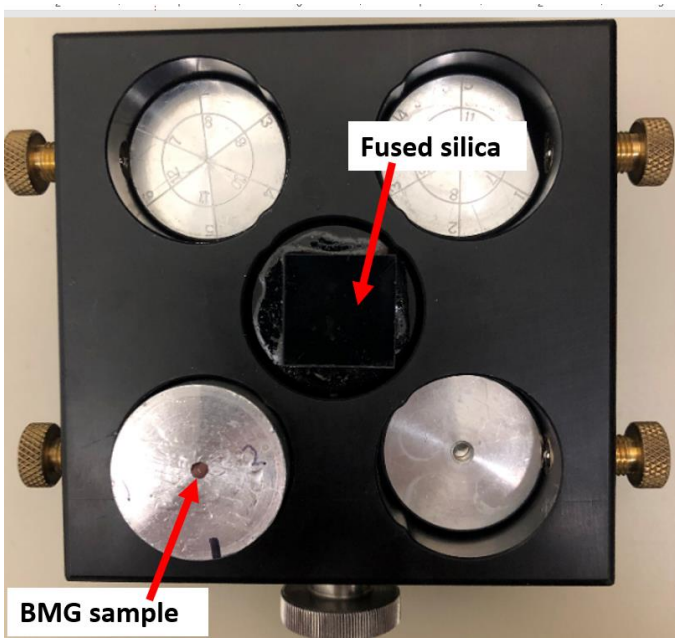

Figure 3-24 Top view of the sample stage with the fused silica piece that is used for calibrating the instrument and a mounted BMG specimen.

was used for the BAM-11 and Cu based BMGs [207, 378]. Table 3-6 lists the parameters typically used in a nanoindentation experiment. The other parameters that were not discussed here, such as the harmonic displacement target, were default values that were already set into the instrument and therefore were not altered for the experiment. After the input parameters were chosen, locations for the indents were selected. For this process, the locations were placed at least 50 μm apart to mitigate the overlap of indentation strain fields [379]. Once the indent locations were placed, the machine was programmed to run after the work-day was over to minimize indentation error due to external vibrations.

For statistical accuracy, ~25 indents were made where hardness and Young's modulus were measured as a function of depth from the point of contact of the nanoindenter with the surface to a depth of ~2,500 nm. The resulting nanoindentation hardness and Young's modulus data were analyzed using matlab software [380]. For the analysis, outliers were removed from the set of data. Furthermore, the hardness data below a depth of ~100 nm from the specimen surface was omitted due to large data scatter associated with surface roughness. Hardness was calculated using the Oliver and Pharr method [381, 382].

Table 3-6 Typical values programmed into the G200 nanoindentation system for a nanoindentation experiment.

Parameter	Value
Surface Approach Distance	1,000 nm
Surface Approach Velocity	10 nm/s
Loading Rate Input	400 μN/s
Thermal Drift Rate	0.05 nm/s
Harmonic Displacement Target	2 nm
Frequency Target	45 Hz
Depth Limit	2,500 nm
Poisson's Ratio	0.37

After the tests were finished, the data was filtered and then uploaded into an Excel file where it was later analyzed using indentation size effect (ISE) models [209, 211, 212] and other techniques. The ISE models were used to analyze the data to avoid discrepancies associated with surface defects and underlying substrate effects. Once the Excel file was uploaded, the sample was removed from the instrument.

3.2.8.1 Indentation size effect analysis

To examine the influence of irradiation and annealing on the indentation size effect (ISE) [209, 211, 212, 217] of the BMG, the hardness was plotted according to the following equations [209, 212]:

$$H = H_0\sqrt{1 + \frac{h_1^*}{h}} \tag{3-4}$$

$$H = H_0'\left(1 + \sqrt{\frac{h_2^*}{h}}\right) \tag{3-5}$$

where H is the nanoindentation hardness, H_0 is the extrapolated (bulk) hardness value, H_0 is the hardness arising from the statistically stored clusters in the absence of the geometrically-necessary clusters that are associated with strain gradients [209, 217], h is the indentation depth, and h_1^*, h_2^* are length scale terms which characterize the depth dependence of the hardness. It should be mentioned that Eq. (3-4) was first derived by Nix and Gao [212] to examine the ISE in crystalline alloys while the Eq. (3-5) was developed by Lam and Chong to examine the ISE behavior in metallic glasses [209]. With respect to the first model, the characteristic depth term is dependent

on factors such as the statistically stored dislocation density and the shear modulus. In contrast, h_2^* depends on parameters of the metallic glass such as the local shear strain required to transform a single atom cluster, or the Helmholtz free energy associated with the shear transformation of clusters occurring and the experimental temperature. In the present work, the concept of cluster defects will be extended to include other defect types such as liquid-like sites and soft-zones [206, 256].

3.3 Neutron Irradiation Experiments

3.3.1 Neutron Irradiation Facility

The high flux isotope reactor (HFIR) is a multipurpose isotope production and test reactor located in ORNL [383]. It was initially designed to produce gram quantities of transuranium isotopes such as californium-252 [384]. The reactor has a power output of 85 MW and is light water moderated and cooled [385]. Furthermore, HFIR also contains a reflector which is composed of beryllium (approximately 1 ft. thick) and burnable poison (boron-10) is included in the inner fuel element [384]. The core of the HFIR is a cylinder approximately 2 feet tall by 17 inches in diameter which contains approximately 9.4 kg of 93 % enriched ^{235}U in two concentric annular elements [385]. A fuel element has a lifetime at 100 MW of about 20 days [386]. The fast neutron flux of the HFIR is approximately 10^{15} n/cm^{2}s.

Figures 3-25 and 3-26 show different schematics of the cross section of the HFIR at the horizontal midplane [384, 385]. As can be observed in figure 3-25, HFIR consists of may components such as outer fuel elements, horizontal beam tubes, and a target bundle in flux trap. Moreover, the flux trap target region (FFT) of the HFIR has 37 experimental sites [385]. As can

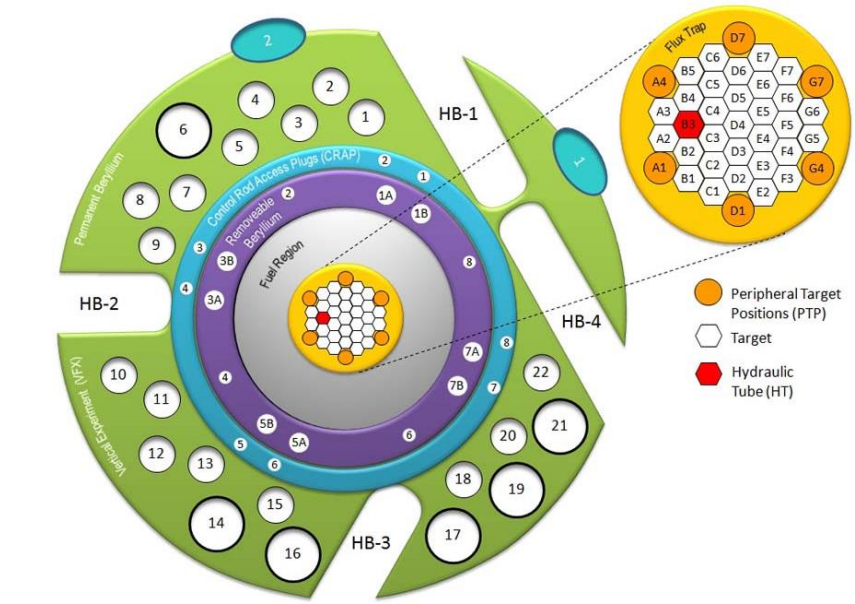

Figure 3-25 Reactor core assembly showing flux trap positions (from Ref. [385]).

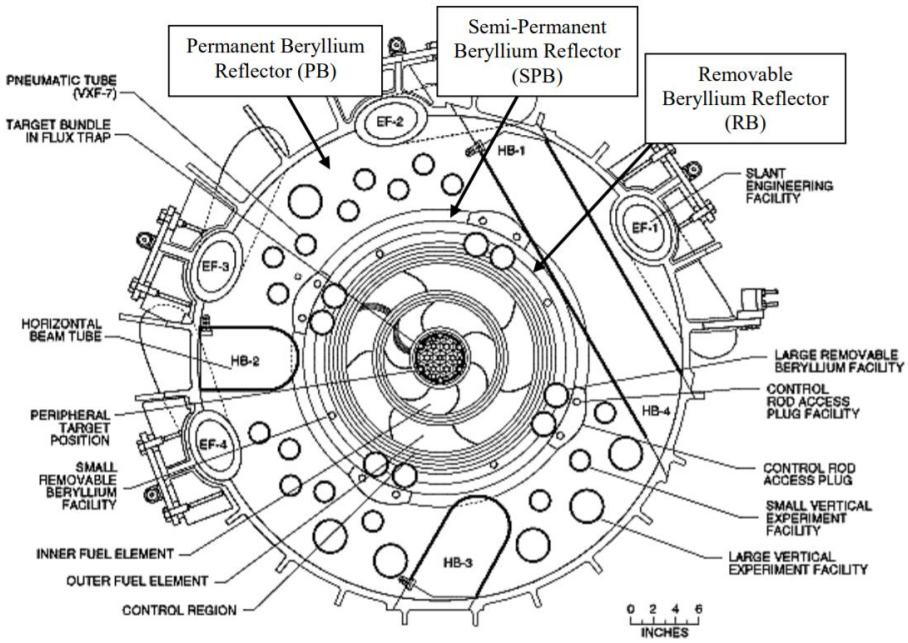

Figure 3-26 Cross-section of HFIR that shows the many functional components (from Ref. [384]).

be seen in figure 3-25, 31 of these positions (white hexagons) are located in the interior of the basket while 6 (yellow circles) sites are on the periphery. There is also a hydraulic tube which allows for the insertion and removal of samples while the reactor is operating. The normal operating schedule of HFIR consists of approximately 6 irradiation cycles per year, with an average of ~24 days per cycle.

For this project, BAM-11 BMG samples were irradiated in the PTP positions where the fast neutron flux is the highest. Samples with various dimensions were encased in a perforated rabbit capsule which allowed the coolant water (flow rate of 15.1 min^{-1}) to directly contact the samples at ~60 ^{o}C. Figure 3-27 shows a schematic of the rabbit capsule assembly [387]. The fins that are on the periphery of the tube are utilized to keep the rabbit separated from the tube wall, ensuring adequate cooling to the entire assembly.

The BAM-11 BMG samples were wrapped in aluminum foil to avoid potential aqueous corrosion during irradiation [388]. After encapsulation, the specimens were irradiated using

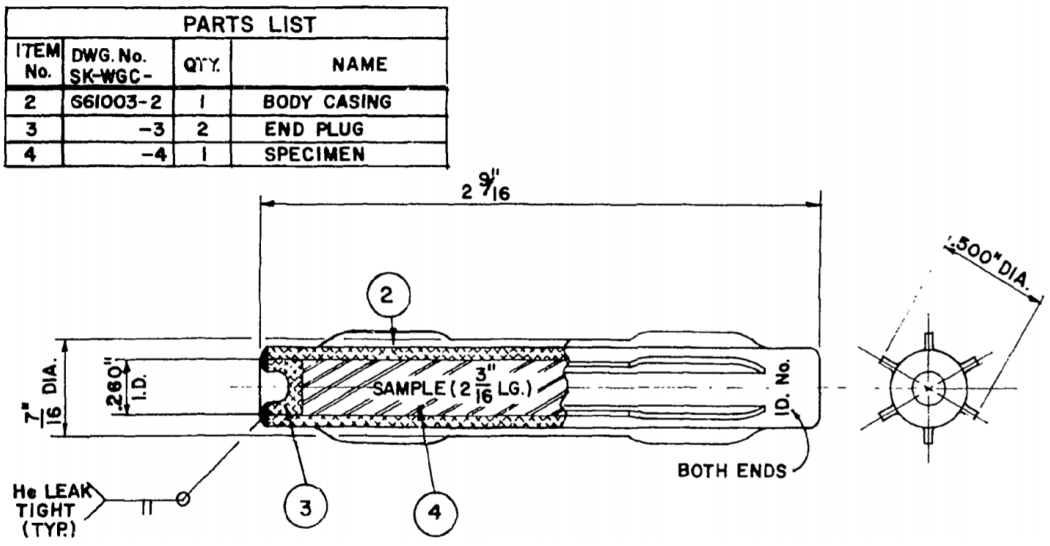

Figure 3-27 HFIR rabbit assembly (from Ref. [387]).

fission neutrons at the ORNL High Flux Isotope Reactor (HFIR) in hydraulic tube 2 (HT-2). Here the samples were exposed to a neutron fluences of 1.40×10^{20} n/cm^2 and 1.40×10^{21} n/cm^2 (E > 0.1 MeV), which corresponds to ~0.1 dpa and 1 dpa, respectively. After consideration of internal nuclear heating effects in the samples, the estimated average sample temperature is ~70 ^{o}C. For this irradiation, samples with various dimensions were irradiated. These specimens include 4 charpy bars with linear dimensions of $3 \times 2 \times 14$ mm^3, 4 bend test bars with geometries of $3 \times 2 \times 27$ mm^3, and TEM discs with dimensions of Ø 3 x 0.4 mm.

3.3.2 Post Irradiation Annealing

After the neutron irradiation, the BAM-11 BMG samples were annealed. These annealing conditions include 300 ^{o}C for two weeks and 325 ^{o}C for 72 hours. These temperatures were chosen since they are sufficiently below the glass transition temperature of the BAM-11 alloy (393 ^{o}C [98]). Here, the specimens were annealed under a pressure of ~10^{-6} torr in a materials research furnace MRF© (figure 3-28). The heating system consists of a front-loading multi-application furnace, which is located in the LAMDA facility at ORNL. The furnace has a maximum operating temperature and vacuum of 1800 ^{o}C and 10^{-8} torr. The vacuum is achieved through a turbo pumping system which consists of a mechanical dry diaphragm pump MD-60, a V-550 turbo pump with turbo controller and a 6" electro-pneumatic large port high vacuum valve. Table 3-7 displays the neutron irradiation and post-irradiation annealing conditions.

3.3.3 Neutron Diffraction Experiments

Microstructural characterizations of the irradiated and annealed BMG specimens were

performed via powder neutron diffraction at the Nanoscale Ordered Materials Diffractometer (NOMAD) [389], which is housed in the Spallation Neutron Source (SNS) at ORNL. Figure 3-29 shows a schematic diagram of NOMAD while figure 3-30 displays the control room that operates the instrument. The instrument is a high-flux, medium-resolution diffractometer that utilizes the time-of-flight (TOF) technique [390]. The TOF set-up allows for 3 Å neutrons to reach the detector at 22 m from the hydrogen moderator before fast neutrons from the next pulse arrive at the detector [391]. Importantly, this instrument can analyze the local order in amorphous materials via a large range of neutron energies and wide detector coverage. Table 3-8 displays instrument specifications.

For the neutron diffraction experiments, samples were carefully suspended in 6 mm diameter vanadium cups in which glass wool was centered on top of the canister. The specimen conditions for the experiment can be seen in Table 3-7. Samples were positioned such that their cross-sectional area was perpendicular to the neutron beam. Here samples with a mass of ~0.5 g (linear dimensions of 3 × 2 × 14 mm^3) were exposed to a neutron flux of ~10^8 n/cm^2s and environmental temperature of 25 ^oC for a duration of three hours.

Table 3-7 The sample conditions for the neutron irradiation experiments.

Sample Condition
As-cast
Annealed 300 ^oC for two weeks
Neutron irradiated to 0.1 dpa
Neutron irradiated to 0.1 dpa and then annealed 325 ^oC for 72 hours
Neutron irradiated to 0.1 dpa and then annealed 300 ^oC for two weeks

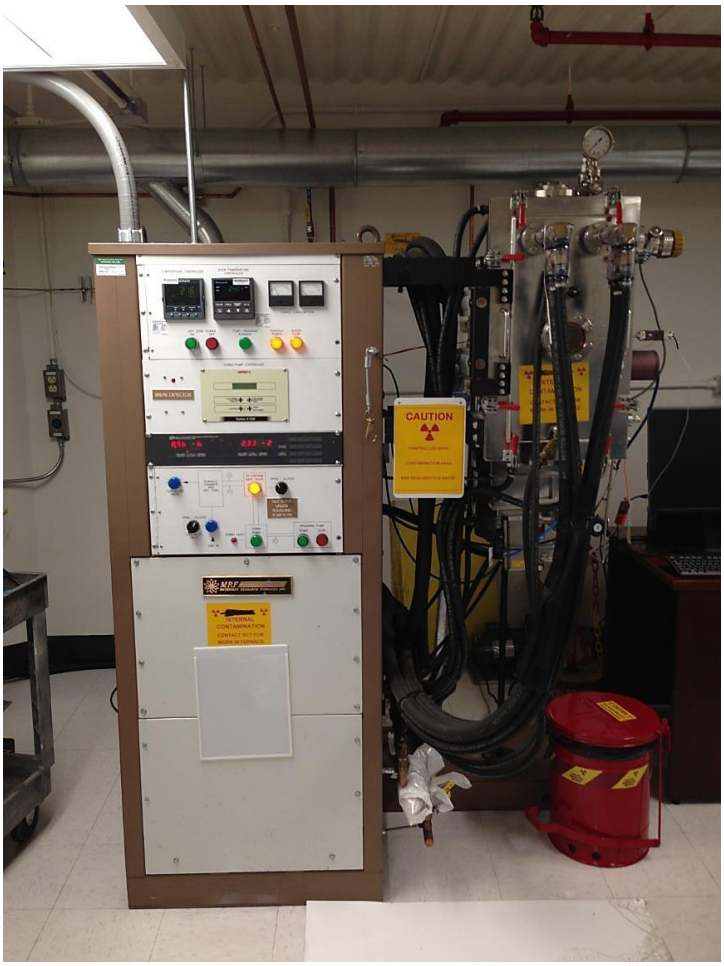

Figure 3-28 MRF© Materials Research Furnace located in LAMDA.

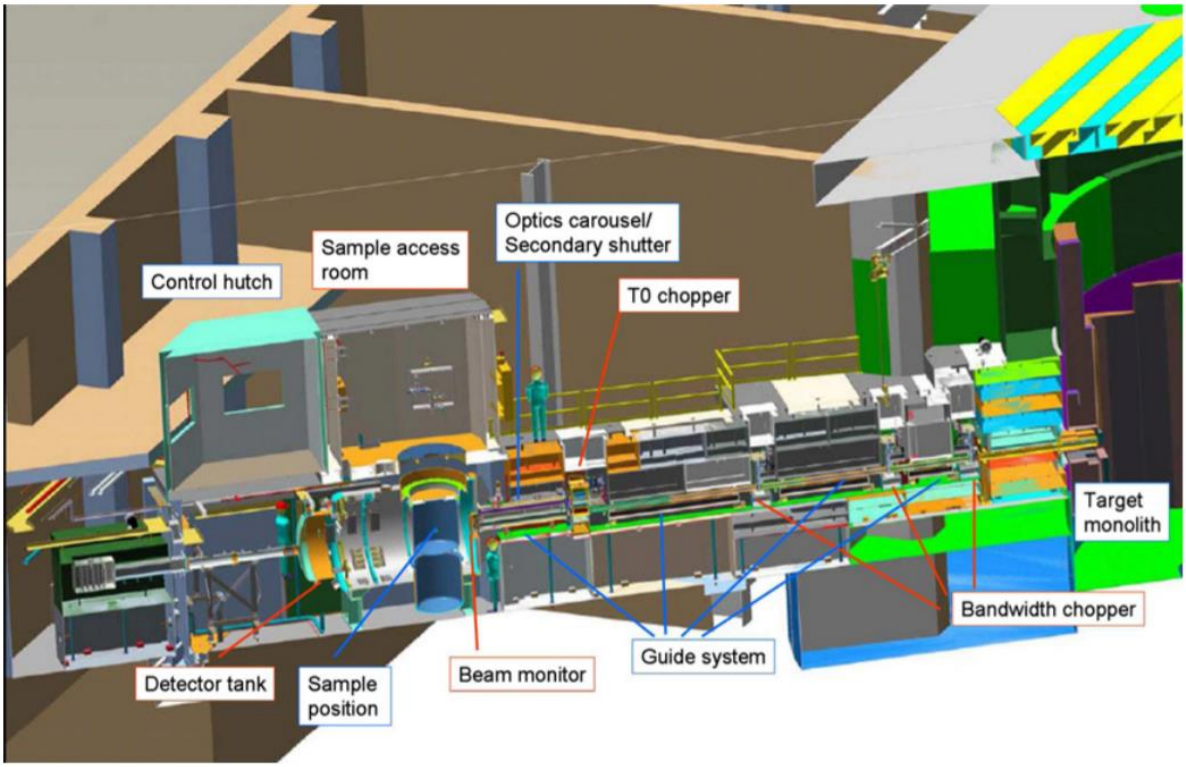

Figure 3-29 Schematic diagram of NOMAD (from Ref. [391]). (from Ref. [391]).

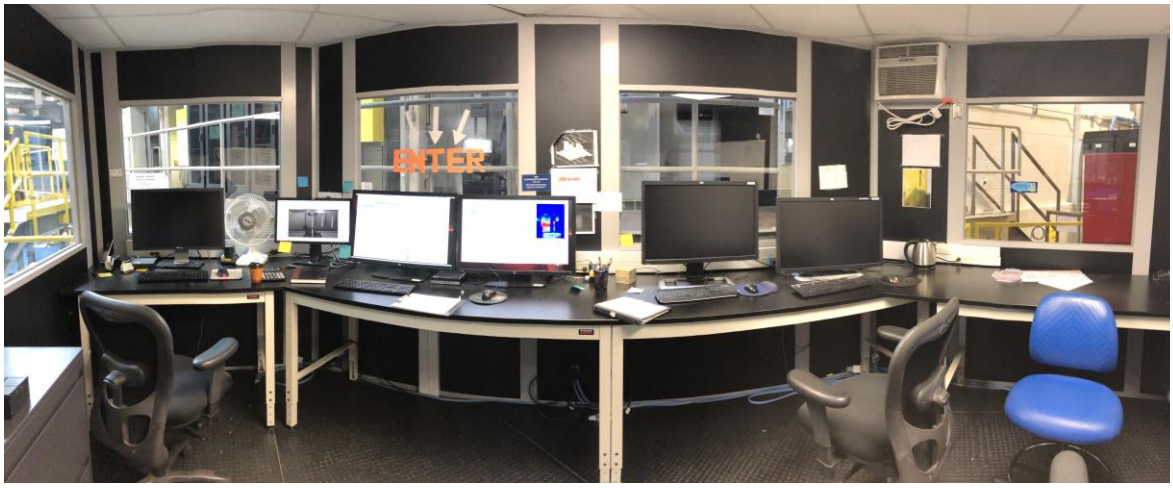

Figure 3-30 NOMAD instrument control room.

Table 3-8 Beamline-1B NOMAD instrument specifications (from Refs. [389, 392]).

Specification	Description/Value
Applications	– Total scattering (PDF) – High flux measurements – High throughput capabilities – Small samples
Neutron beam	TOF
Resolution (Δd/d)	5×10^{-3} - 5×10^{-2}
Q-range	0.2 - 50 Å
Beam size at sample	Variable. Typical is 0.6 × 0.6 cm
Measurement times	Sample dependent, typical range is 1-60 min
Moderator	Decoupled poisoned supercritical hydrogen
Moderator-to-sample distance	0.5 - 3 m
Wavelength range	0.1 - 3 Å
Momentum transfer range	0.04 – 100 $Å^{-1}$
Detector angular range	3 – 175 ^{o} scattering angle
Initial coverage	4.0 steradian
Full detector complement	8.2 steradian
Flux on sample	~ 1×10^{8} neutrons cm^{-2} s^{-1}

After the diffraction data was collected, PDFgetN software, which is a user-friendly program with a graphical user interface, was used to obtain S(Q) values [393]. It should be mentioned that the beamline scientist, Dr. Joerg Neuefeind, was instrumental in obtaining the data from the diffraction patterns. After obtaining the raw data, the program was utilized to determine the structure factor and subsequently the pair distribution function (PDF) for each specimen condition. The pertinent data that is attained from the database includes the scattering factor, S(Q) (SQ.dat files), and the pair distribution function, g(r) (NOMXXXftf.dat files). Here, Q represents the momentum transfer in reciprocal space [394], while r represents the distance in real space. In the context of the NOMAD data, the PDF is related to the scattering factor via the following relation:

$$g(r) - 1 = A \int_{Q_{min}}^{Q_{max}} [S(Q) - 1] Q \sin(Qr)\, dQ \tag{3-6}$$

where A is an arbitrary constant. After collecting the S(Q) and g(r), it was entered into an Origin file and plotted.

3.3.4 TEM Characterization

To determine whether irradiation induced nanocrystalline formation had occurred in the alloy, transmission electron microscopy (TEM) characterization was performed in the Low Activation Materials Development and Analysis (LAMDA) laboratory at ORNL [377]. TEM foils were fabricated using an FEI Quanta Dual-beam focused ion beam (FIB)/SEM (see figure 3-20). The foils were cut and lifted out of the sample using an omniprobe needle and then deposited onto a molybdenum FIB lift-out grid. After welding the lift-out specimen to the grid, 2 kV Ga^+ ions

were used for the thinning steps where the energy was gradually reduced from 30 keV to 3 keV. Figure 3-21 shows an as-cast BAM-11 BMG welded sample before thinning was commenced. An ion current of 30 pA with a glancing angle of about 4° was used during the final thinning step to minimize ion beam milling damage. Cleaning the specimens was performed in a similar manner as that performed on the ion irradiated specimens (see Section 3.2.7). After polishing, the welded lift-out specimens were then examined and analyzed in a JEOL JEM-2100F TEM/STEM at 200 kV using bright field (BF) imaging and selected area diffraction (SAD). The TEM characterizations of these specimens were performed by Dr. Tengfei Yang and Mr. Yan-Ru Lin.

3.3.5 Nanoindentation Experiments

Nano-indentation hardness measurements were performed at room temperature using a KLA-Tencore G200 Nano-indenter in the continuous stiffness measurement mode with a constant loading rate of 400 μNs^{-1}. The samples used for these experiments were the same ones as listed in Table 3-7. For sample preparation, specimens were cut to dimensions of $3 \times 3 \times 1$ mm^3, cold mounted in epoxy, and then mechanically polished to a mirror finish using colloidal silica. Due to the radioactivity of the irradiated samples (see Table 3-9 for dose measurements), specimen preparation was performed in the hot zone of the LAMDA facility. Figure 3-31 displays a finished sample. In terms of the data, nanoindentation hardness and Young's modulus was calculated using the Oliver and Pharr method [381, 382].

3.3.6.3-Point Bend Test Experiments

Specimens used for this study consisted of rectangular coupons with linear dimensions of $3 \times 5 \times 0.9$ mm^3. Due to the radioactivity of the irradiated samples specimen preparation was

performed in the hot zone of the LAMDA facility. The irradiated samples were cut from the ends of non-deformed tensile bars. Before testing, samples were polished to a mirror finish using colloidal silica. After preparing the as-cast and irradiated samples they underwent room temperature 3-point bending tests using a MTS tensile screw-driven machine (model Insight 2-52; load capacity 2 kN). The system is connected to a computer interface system which utilizes MTS TestSuite™ TW Software to record the stress vs. strain data during the experiment. An image of the instrument is displayed in figure 3-32. The 3-point bend test device used for this study is a specially designed bend assembly for sub-sized specimens [395]. Figures 3-33(a)-(b) presents the bending device (acquired from Dr. Maxim Gussev) and a close up schematic of the three-point bend mechanism. As can be seen, there are three rods contained in the inner potion of the apparatus

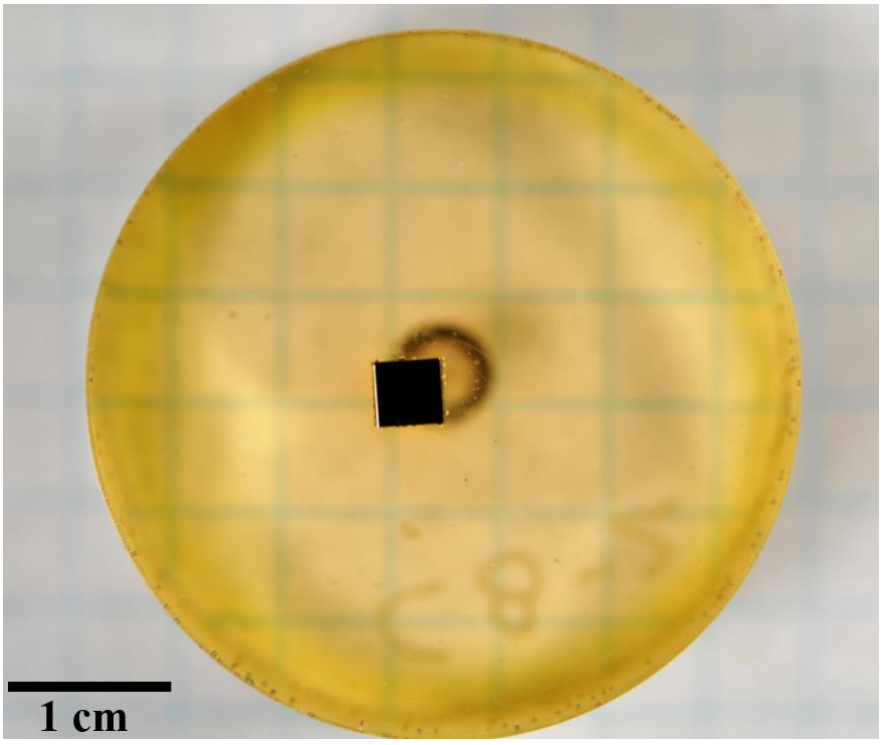

Figure 3-31 Cold mounted post-annealed neutron irradiated (0.1 dpa and then 300 ^{o}C for 2 weeks) BAM-11 BMG specimen (3 × 3 × 1 mm^3) for nanoindentation experiments.

Table 3-9 Surveyed dose rates of the neutron irradiated BAM-11 BMG samples used for the 3-point bend test experiments.

Sample	Contact γ (mrem/hr)	1 ft. γ (mrem/hr)	Contact β (mrad/hr)
BAM-11 BMG 0.1 dpa	280	18	1,092
BAM-11 BMG 0.1 dpa 300 ºC, 2 weeks	425	21	1,235
BAM-11 BMG 0.1 dpa 325 ºC, 72 hours	300	15	1,040

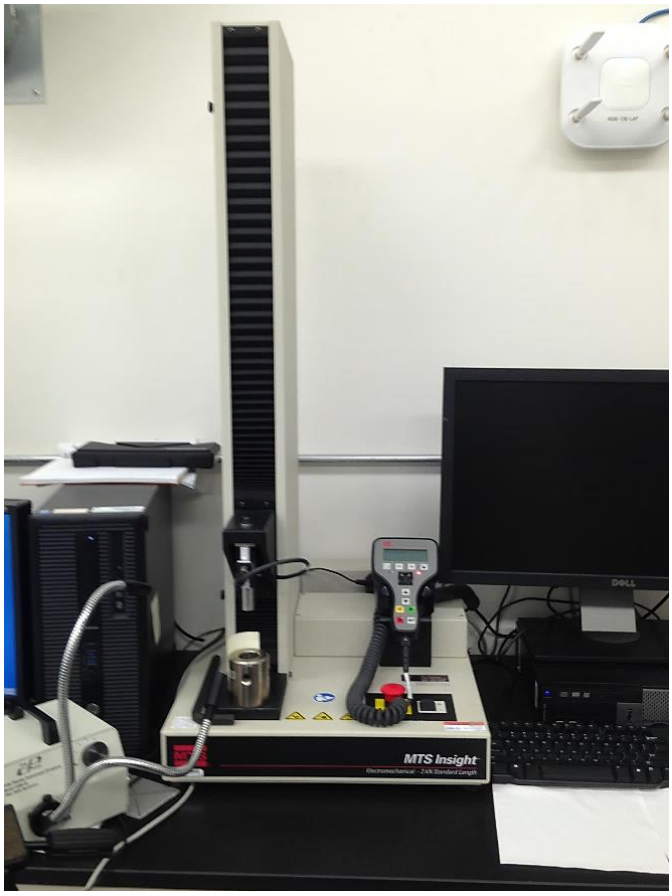

Figure 3-32 MTS tensile screw-driven machine (model Insight 2-52) system used for the 3-point bend test experiments.

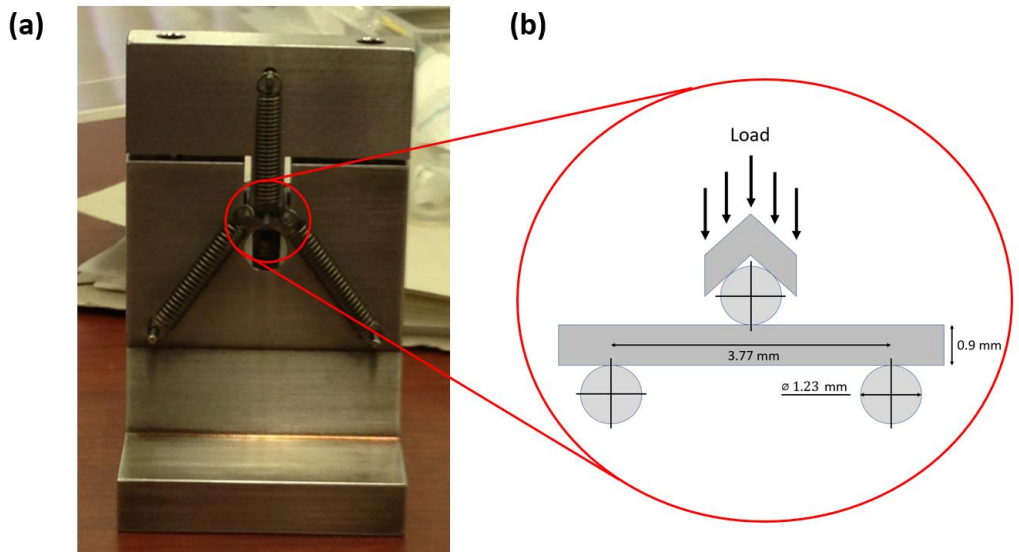

Figure 3-33 (a) 3-point bend test instrument and (b) corresponding scheme of 3-point bend test.

which have a diameter of 1.23 mm each. The bottom two rods have diameters of 1.23 mm with a span distance of 3.77 mm between the rods. For the experiments, an applied strain rate of 0.1 mm/s was applied, and the stress vs. deformation behavior was recorded using computer software.

3.3.7 Immersion Density Measurements

Density measurements were performed on the neutron irradiated and annealed specimens at room temperature using an immersion density instrument, which consists of an ultra-sensitive balance, the Satorius ME215S, a density kit, and a high-precision digital thermometer. Samples that consisted of linear dimensions of $3 \times 2 \times 14$ mm^3 were immersed in a 3M Fluorinert^{TM} Liquid FC-43 which has high density, low surface tension, low thermal expansion, low vapor pressure and low water/air solubility. Each specimen was measured three times and the density was determined using Archimedes principle.

3.4 Thermal Response Experiments

3.4.1 Insitu Synchrotron X-ray Diffraction Compression Tests

BAM-11 BMG specimens were prepared from as-cast rods by an electrical discharge machine. For the compression testing, samples were cut into linear dimensions of $4 \times 2 \times 1.5$ mm^3 and polished to a mirror finish. After fabrication, one of the samples was annealed at 300 ^{o}C for two weeks under vacuum (10^{-6} torr).

High energy XRD studies on the as-cast and the annealed samples were carried out by Hui Wang through synchrotron irradiation at the 1-ID beam line of the Advanced Photon Source (APS), Argonne National Laboratory (ANL). The beam energy at 1-ID was 100 keV ($\lambda = 0.12358$ Å). 2D detectors with 2048 × 2048 pixels and 200 μm × 200 μm pixel size was used to collect data. The detector was placed about 40 cm behind the sample. Calibration was performed using the CeO_2 NIST powder standard. While in the chamber, samples were subjected to compression tests with loads ranging from 0 (control) to 1,500 MPa in 300 MPa increments. High-energy 2D X-ray diffraction data was processed using FIT2D software [396] to correct the data. Figure 3-34 shows a basic setup of the experiment, which features the X-ray beam, the specimen, a beam stopper, and the area target.

Because of the elastic deformation induced anisotropy [256], the pair density function (PDF) analysis of the anisotropic and the isotropic data was applied [257]. The isotropic PDF is related to the structure function in the following manner:

$$g(r) = \frac{1}{2\pi^2 r \rho_0} \int_0^\infty [S(Q) - 1] \sin(Qr)\, Q dQ \tag{3-7}$$

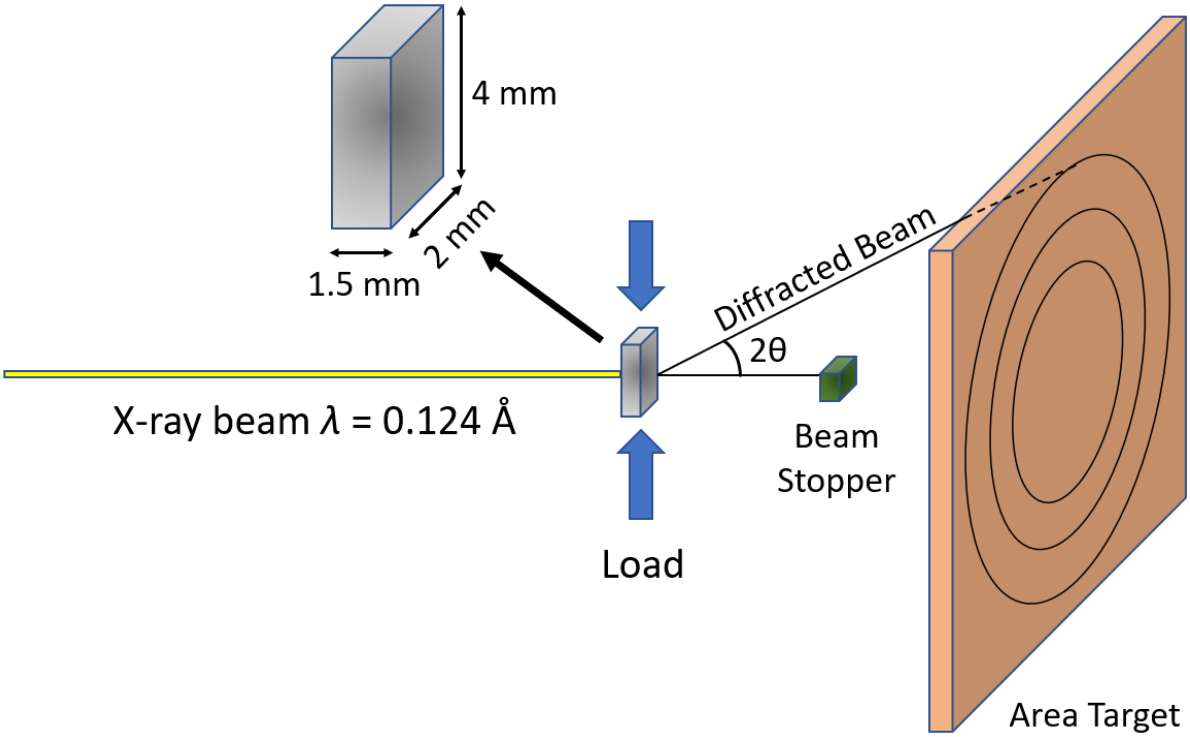

Figure 3-34 General high-energy XRD setup at the beamline 1-ID in the APS located at ANS (Adapted from Ref. [397]).

where S(Q) is the structure function, Q is the diffraction vector (or momentum transfer) that is equal to $4\pi\sin\theta/\lambda$ where θ is the diffraction angle, λ is the wavelength of the probe, and ρ_0 is the atomic number density of the alloy [256]. One can notice the similarities of Eqs. (3-6) (from Section 3.3.3.) and (3-7). To examine the changes to the anisotropic behavior of a BMG under an applied stress, the anisotropic pair density function (PDF) method can be applied to the in situ compression data [258], which is based on spherical harmonics. This method utilizes the spherical harmonics in the following manner:

$$g(\boldsymbol{r}) = \sum_{l,m} g_l^m(r) Y_l^m\left(\frac{\boldsymbol{r}}{r}\right) \tag{3-8}$$

$$S(\boldsymbol{Q}) = \sum_{l,m} S_l^m(Q) Y_l^m\left(\frac{\boldsymbol{Q}}{Q}\right) \tag{3-9}$$

where Y_l^m are the spherical harmonics, g(r) is the radial PDF, and S(Q) is the structure function. The anisotropic radial PDF is related to the structure function via a Bessel transformation:

$$g_l^m(r) = \frac{i^l}{2\pi^2\rho_0}\int_0^\infty S_l^m(Q) J_l(Qr) Q^2 dQ \tag{3-10}$$

here $J_l(Qr)$ is the spherical Bessel function [259]. It should be mentioned that for the isotropic case, i.e., l, m = 0, Eq. (3-10) reduces to Eq. (3-7) [255]. For the purposes of analyzing the elastic deformation, the term for l = 2 will be used [258]. After applying the spherical harmonic expansion and Bessel transformation, the anisotropic PDFs is generated. When analyzing the anisotropic PDF, a reference state of the sample under affine deformation is introduced [255], namely the

affine anisotropic PDF, $\rho^0_{2,aff}(r)$. Here, the affine deformation can be analyzed using the following equation [255, 260]:

$$g^0_{2,aff}(r) = -\varepsilon_{zz,aff}\frac{2(1+\upsilon)}{3\sqrt{5}} r \frac{d}{dr} g^0_0(r) \tag{3-11}$$

where $-\varepsilon_{zz,aff}\frac{2(1+\nu)}{3\sqrt{5}}$ is a fitting parameter, $-\varepsilon_{zz,aff}$ is the affine strain, and υ is Poisson's ratio, which for the purposes of the current experiment, has been experimentally determined as 0.38 [398].

3.4.2 In Situ X-Ray Crystallization Kinetics Experiments

High-temperature X-ray diffraction (HTXRD) measurements were made in vacuum (~10^{-5} torr) using an Anton Paar HTK 1200N environmental oven chamber. Figure 3-35 displays the HTXRD setup, which shows the furnace and vacuum system attached to the Empyrean PANalytical XRD instrument. Samples with dimensions of 2 × 1 × 5 mm^3 were prepared by grinding the specimen surface (2 × 5 mm^2) with silica grit paper ranging from 320 to 1200 grit. Specimens were placed on a silicon zero background plate that was mounted on top of an alumina sample plate. Figure 3-36(a) shows the sample mounted onto the silicon background plate and alumina sample holder. Due to their relatively small size as compared to the stage a silicon zero background plate was used to prevent the overlap of alumina and specimen reflections. In addition, figure 3-36(b) displays the front view of the mount system. After placing the sample holder system into the chamber, it was locked into place.

After securing the samples, the chamber was reduced to a pressure of approximately 8 × 10^{-5} torr using a turbo pump. After reaching the desired pressure, the specimens were heated using

ramp rates of 60 and 180 °C/h. The BAM-11 BMG samples were heated to 760 ºC and 355 ºC while the Cu BMG specimens were heated to 800 ºC and 345 ºC. The higher temperatures correspond to ~0.9 of the melting temperature [368, 399], while the lower temperatures correspond to values below the glass transition [358, 368]. During heating, software provided by PANalytical was used to adjust the height of the sample stage to accommodate for the thermal expansion of the alumina sample plate. However, the software was not able to account for the thermal expansion of the silicon zero background plate since it was not a component of the original stage device. As a result, the apparent peak shift in the diffraction patterns are not due solely to the sample.

Data collection parameters were set such that X-ray counts could be collected in both a rapid and continuous manner during the furnace ramp up that allowed for a detailed analysis of the kinetic phase evolution. The scattering angles used for the in-situ study ranged between 32-46^{o} and 33-45^{o} for the BAM-11 and Cu BMGs, respectively. These range of angles was chosen to balance between resolution and time constraints imposed by the heating rate. The reported temperature during heating is the sample temperature and not the set temperature that was measured by a thermocouple placed directly below the specimen. Instrumental setup and collection parameters were optimized for intensity over resolution and are summarized in Table 3-10.

After the diffraction experiment, the specimen and stage were carefully removed from the chamber to prevent damaging the equipment. Subsequent powder diffraction in conjunction with qualitative and quantitative phase analysis was performed to analyze the crystalline phases in the BMG. Here, qualitative phase identification (ID) was determined using the HighScore Plus software package [400] in conjunction with the Powder Diffraction File-4+ (PDF-4+) database.

Quantitative phase analysis was conducted by Drs. Michael Kohler and John Salasin from the Joint Institute for Advanced Materials. The Rietveld refinement was performed using the

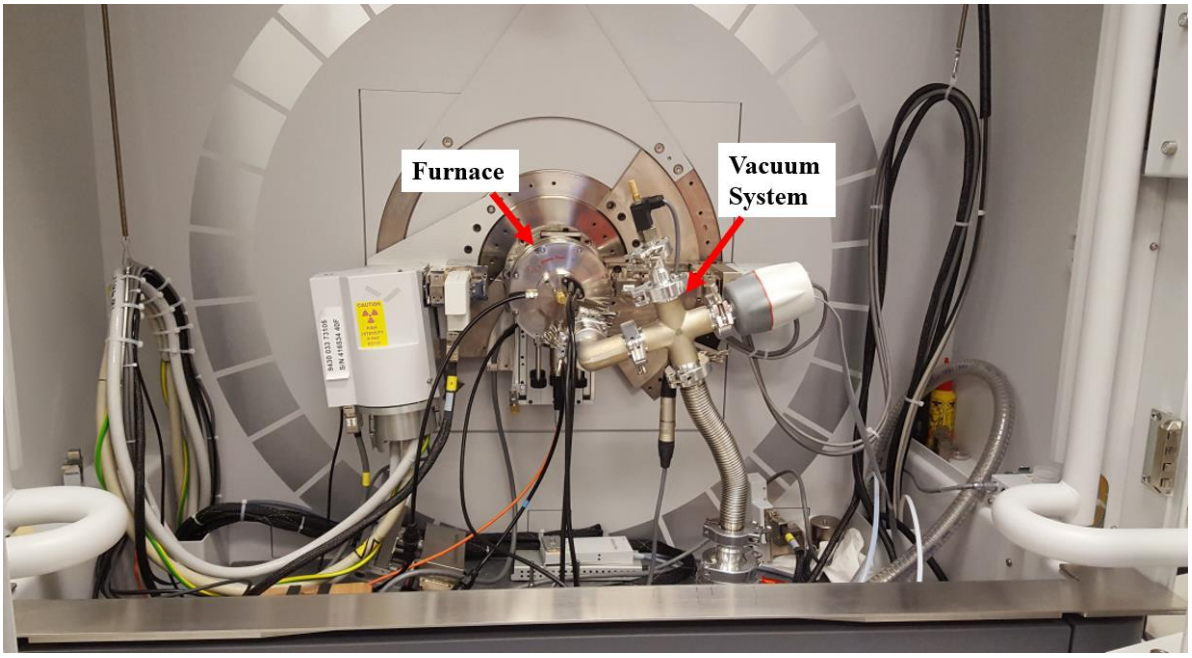

Figure 3-35 Empryean HTXRD setup which includes a furnace and a vacuum system.

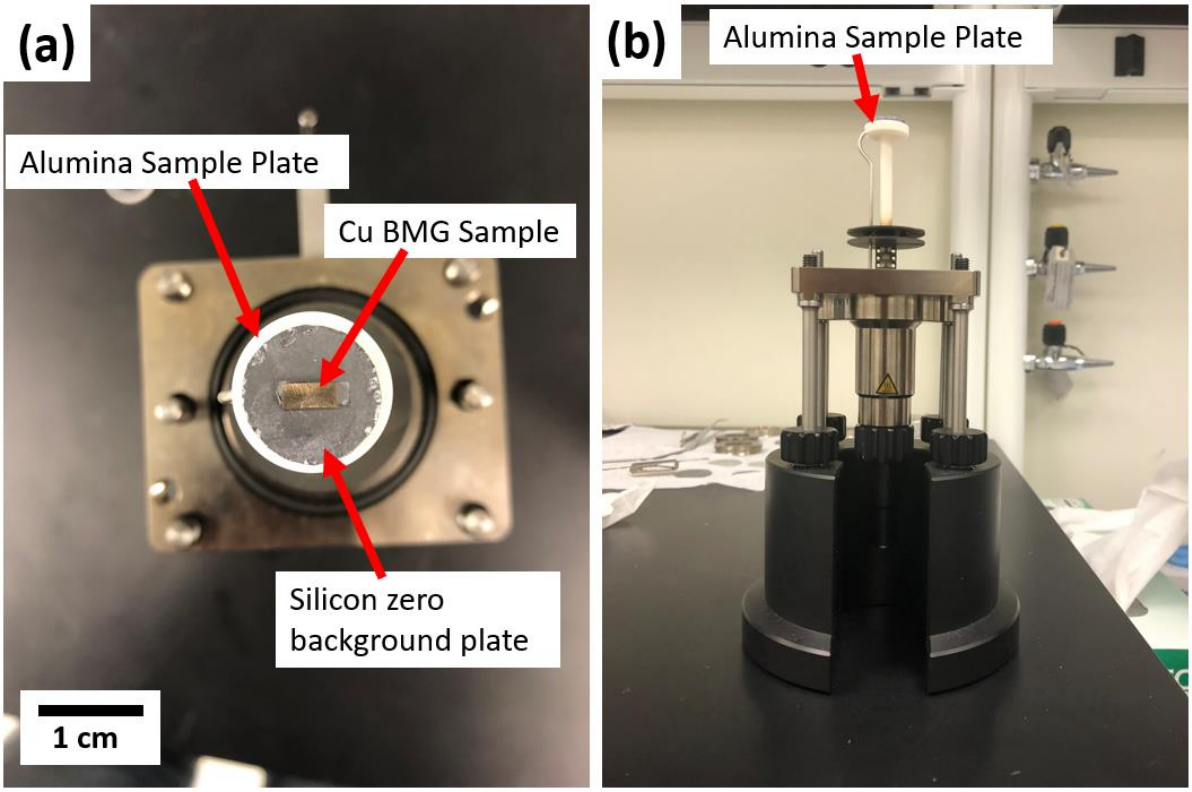

Figure 3-36 (a) Top-down view of the Cu BMG sample mounted on the alumina sample plate and the silicon zero background plate on the sample stage, and (b) the front view of the stage.

GLAS Science Algorithm Software II (GSAS II) software [401]. The software was used to find the lattice parameters, background, phase fractions, and profile parameters relevant to the crystallite size determination.

During the initial phase formation, pseudo-Voight peak fitting [402] was used to determine the change in peak area that corresponds to an increase in the amount of crystalline phase in the matrix. Furthermore, instrumental broadening was characterized using NIST standard SRM 640e (Si) [403]. Importantly, this approach can estimate the crystallite size and size variance of the crystallites. For more details on this specific process, please refer to [239]. To evaluate the rate constant, k, and the JMAK exponent, n, one applies linear regression analysis to the plot of $\mathrm{Ln}\left[\mathrm{Ln}\left(\frac{1}{1-\alpha}\right)\right]$ vs. $\mathrm{Ln}(t - t_0)$.

3.4.2.1 Surface Microstructural Characterizations

To aid in the phase identification process, microstructural characterization was performed to identify precipitation and phase heterogeneity on sample surface and bulk. Characterization of the microstructure was performed at the JIAM microscopy center via scanning electron microscopy (SEM) on a Zeiss EVO MA15 scanning electron microscope. The surface composition was analyzed using electron dispersive spectroscopy (EDS) via a Bruker XFlash 6130 detector. The surface characterization was first performed on the as-diffracted samples. To examine the bulk composition of the specimen using this technique, the surface was first removed via mechanical grinding. Figure 3-37 displays an image of the SEM system, which features the SEM and the computer interface with keyboard.

Table 3-10 HTXRD instrumental and data collection parameters.

Instrument Parameters		
Instrument	PANalytical Empyrean	
Source	Cu $K\alpha_1/K\alpha_2$	
Stage	Anton Parr HTK 1200N	
Detector	PIXcel3D-Medipix3 1x1 detector	
Mode	Scanning Line Detector	
Collimation		
Incident Beam Optics		
Divergence Slit [°]	1/2	
Soller slit [rad]	0.04	
Anti-scatter slit [°]	1	
Mask [mm]	10	
Diffracted Beam Optics		
Anti-scatter slit [°]	1	
Soller Slit [rad]	Large 0.04	
Scan Parameters		
Step Size [°2θ]	0.0131	
Step Time [s]	31.4 (180 ºC/h) 82.4 (60 ºC/h)	
Scan Time [s]	104	
Scan Range [°2θ]	32 – 46 º (BAM-11 BMG) 33 – 45 º (Cu BMG)	

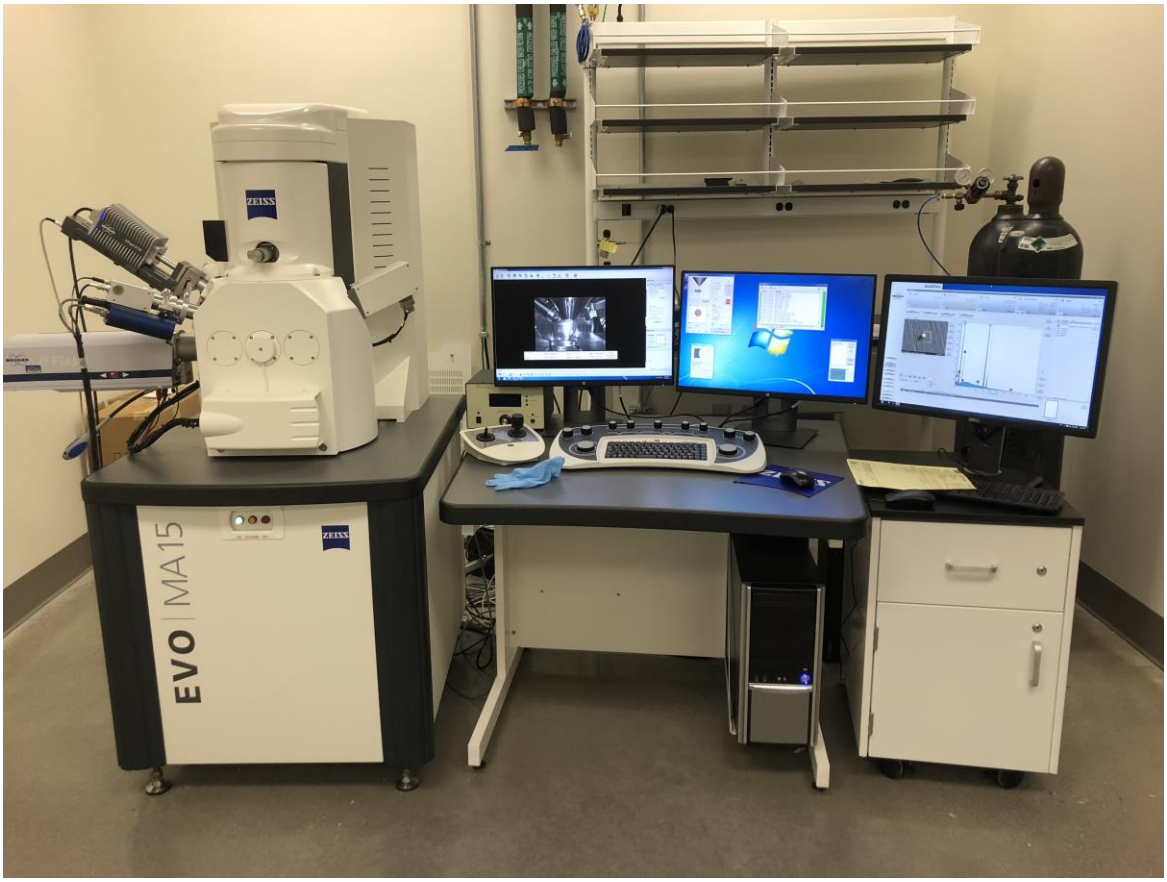

Figure 3-37 Zeiss EVO MA15 FIB/EDS system used for performing surface characterization of post-diffracted BMG specimens.

3.4.2.2 Nanoindentation Experiments

To compare the hardness of the partially crystallized and as-cast material, nano-indentation tests were performed using techniques summarized previously. Here, both as-cast and annealed specimens were indented. To ensure a high-quality surface, the surface was mechanically ground and then polished to a mirror finish using colloidal silica. As for the nanoindentations, ~25 indents were made where hardness was measured as a function of depth from the point of contact of the nanoindenter with the surface to a depth of ~2,500 nm. The hardness and Young's modulus data from the surface to ~100 nm from the specimen surface was omitted due to large data scatter associated with surface roughness. Hardness values were calculated using the Oliver and Pharr method [381, 382].

3.4.3 Compression Testing Experiments

3.4.3.1 Sample Preparation and Experimental Setup

The cast rods for compression tests were prepared with a length of 6 mm and diameter of 3 mm (unconstrained condition). Some samples were encased in a vacuum evacuated quartz tube and then annealed at 300 ^{o}C for two weeks in a Ney® model 3-550 furnace. This temperature was chosen since it well below the glass transition temperature of the BAM-11 BMG (T = 393 ^{o}C) [98]. During the heating, a ramp rate of 5 ^{o}C/min. was used. The furnace is composed of a heavy gauge steel cabinet in which the access door opens vertically to give maximum access to the heating chamber and ensures operator safety. The specifications of the furnace are displayed in Table 3-11 [404]. Prior to heating, the encased specimen is placed in a ceramic heating tray. Figure 3-38(a) shows an encased specimen (for nanoindentation) in the ceramic sample heating

tray, whereas figure 3-38(b) displays the sample and tray inside of the furnace. After annealing, the two compression faces of each sample were carefully polished such that they were parallel to one other to ensure adequate contact with the platens during compression.

The uniaxial compression tests were conducted by Dr. Zhong Wang. Here, the as-cast and annealed BAM-11 BMG specimens compressed at room temperature using a computer-controlled MTS 810 materials testing machine at a constant strain rate. The samples were compressed in the unconstrained condition at strain rates of 2×10^{-5} s^{-1} and 2×10^{-4} s^{-1}. Figure 3-39 displays the testing machine and a sample in compression. The stress vs. time data were recorded using a data-acquisition rate of 100 Hz. To ensure accurate results, the specimen was first placed between the compression platens, ensuring that the specimen center line passes though the center line of the two compression plates. Furthermore, the specimen was visually inspected to ensure there is no slippage between the specimen and the compression plates before initiating the test.

Table 3-11 Specifications of the Ney® model 3-550 furnace (from Ref. [404]).

Specification	Value
Temperature Control	Programmable
Outside Dimensions	16”W × 17”D × 16”H
Chamber Dimensions	9”W × 9”D × 7”H
Height w/Door Open	25”
Maximum Temperature	2,012° F
Firing Time	15 min. to 1000° F

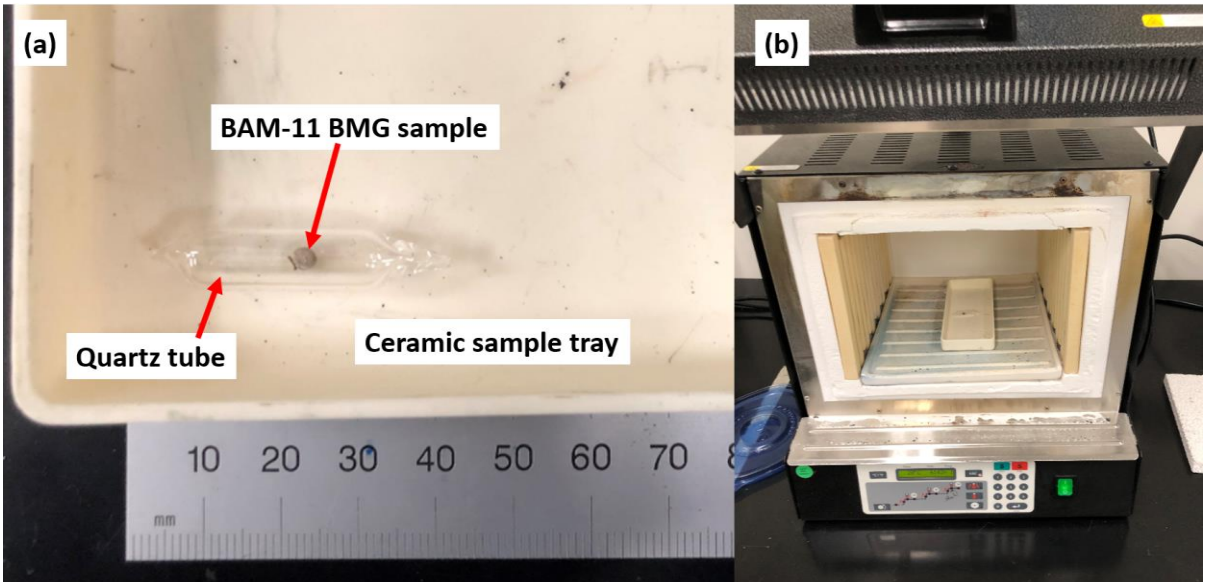

Figure 3-38 (a) BAM-11 BMG specimen encased in an evacuated tube and place in a ceramic plate and (b) sample and tray placed in the Ney® model 3-550 furnace prior to heating.

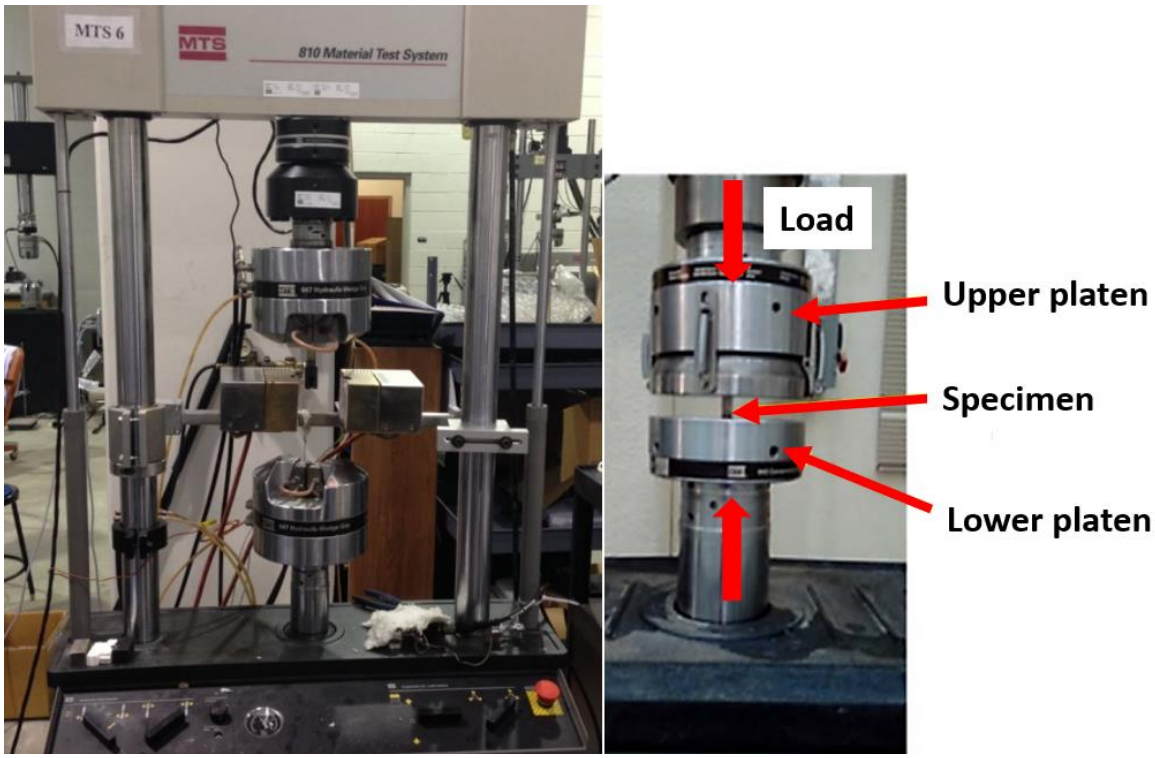

Figure 3-39 Left) The computer-controlled MTS 810 materials testing machine and right) sample in compression (adapted from Ref. [405]).

3.4.3.2 Data Analysis

The stress vs. time data was analyzed using Matlab 2018. The data was examined using the refined composition multiscale entropy method [186], which examines the complexity of a given time series. Here, the stress vs. time curve is first normalized by subtracting away the moving average or polynomial fit of the time-series data [163]. One then generates the coarse-grained time series from the detrended data using the following equation:

$$y_{k,j}^{\tau} = \frac{1}{\tau} \sum_{i=(i-1)\tau+k}^{j\tau+k-1} x_i \quad ; \; 1 \leq j \leq \frac{N}{\tau} \qquad 1 \leq k \leq \tau \tag{3-12}$$

where x_i is a value from the initial data set and τ is the scale factor while k represents an index that determines on which x_i the coarse-graining procedure is initialized. A visual representation of Eq. (3-12) can be seen in figure 3-40. Next the template vectors, $\boldsymbol{y}_{\boldsymbol{k,i}}^{\boldsymbol{\tau,m}}$, of the dimension (or size), m are constructed: [188]:

$$\boldsymbol{y}_{\boldsymbol{k,i}}^{\boldsymbol{\tau,m}} = \left\{ y_{k,i}^{\tau} \;\; y_{k,i+1}^{\tau} \;\ldots.\; y_{k,i+m-1}^{\tau} \right\} \; ; \quad 1 \leq i \leq N-m \, ; \; 1 \leq k \leq \tau \tag{3-13}$$

here $y_{k,i}^{\tau}$ is simply the ith component of the vector and is the quantity defined on the left-hand side of Eq. (3-12). After the template vectors are determined, one calculates the number n of matching sets of distinguishable template vectors using the following relation [190, 197]:

$$d_{ab}^{\tau,m} = \left\| \boldsymbol{y}_{\boldsymbol{a}}^{\boldsymbol{\tau,m}} - \boldsymbol{y}_{\boldsymbol{b}}^{\boldsymbol{\tau,m}} \right\|_{\infty} = \max\left\{ \left| y_{1,a}^{\tau} - y_{1,b}^{\tau} \right| \ldots \left| y_{i+m-1,a}^{\tau} - y_{i+m-1,b}^{\tau} \right| \right\} < r \tag{3-14}$$

where $d_{ab}^{\tau,m}$ is the infinity norm, a and b ($a \neq b$) are the indices of some chosen vector, y, as given in Eq. (3-13), and r is a tolerance value that is typically set as $0.15 \times \sigma$ (σ is the standard deviation of the relevant data) to reduce the standard error in the sample entropy results [186, 192, 193, 406].

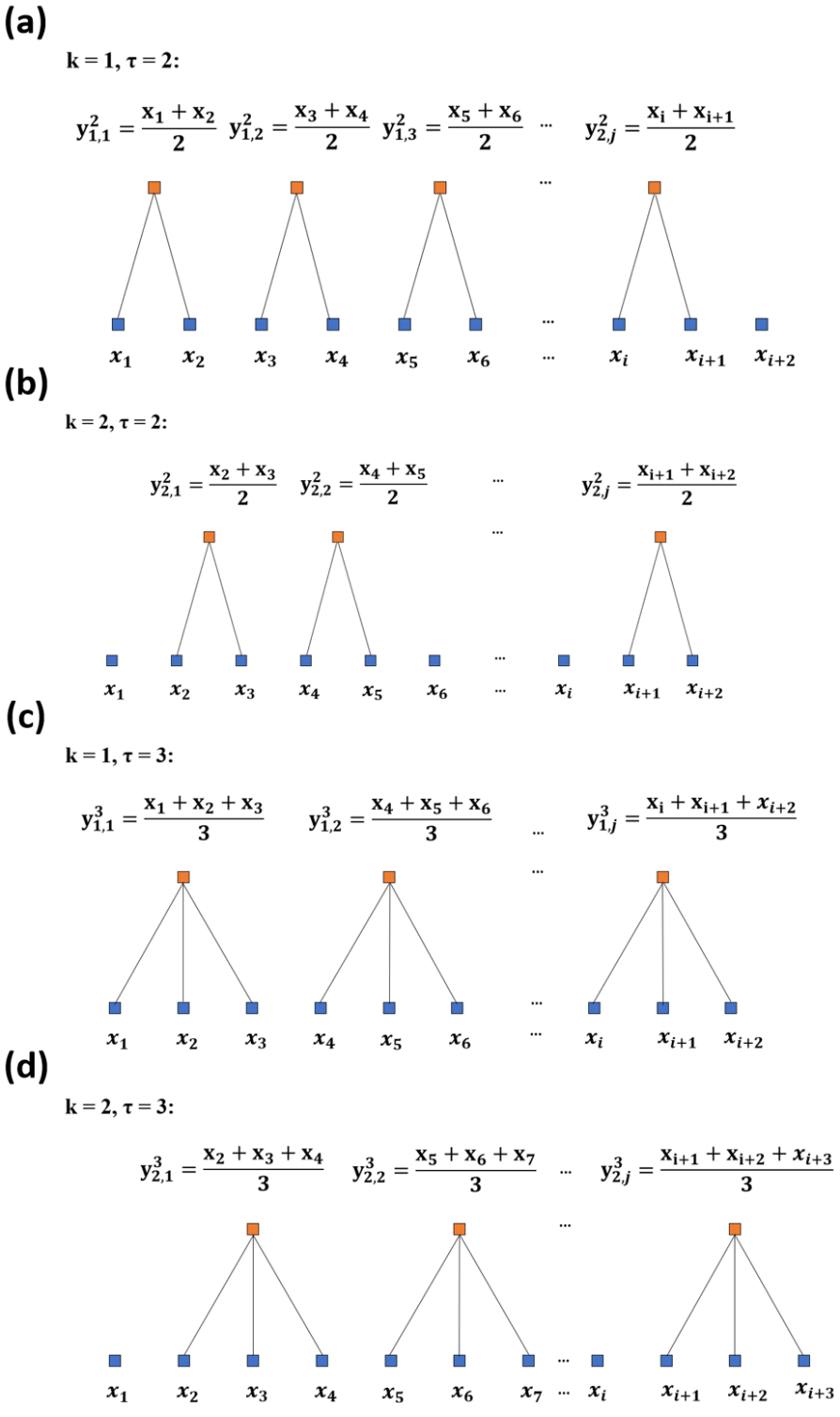

Figure 3-40 Visual representation of the coarse-graining procedure for (a) k = 1, τ = 2, (b) k = 1, τ = 3, (c) k = 2, τ = 2, and (d) k = 2, τ = 3 (from Ref. [186]).

After the number of matching vectors are calculated, this method is performed again for $\boldsymbol{y}_{k,i}^{\tau,m+1}$. Once the total number of matching vectors, n_k^m and n_k^{m+1}, are found, they are summed for k = 1 to τ. Next, the RCMSE value of the data set at a given scale is calculated using the following equation [196]:

$$RCMSE(\boldsymbol{y},\tau,m,r) = Ln\left(\frac{\sum_{k=1}^{\tau} n_{k,\tau}^{m}}{\sum_{k=1}^{\tau} n_{k,\tau}^{m+1}}\right) \tag{3-15}$$

3.5 Helium Diffusion Studies

3.5.1 Sample Preparation

BAM-11 and Cu BMG samples were cut into bars with linear dimensions of 3 mm × 2 mm × 6 mm. Subsequently, one specimen from each alloy was encased in a quartz tube that was evacuated and then heated until the alloy partially crystallized. Here the BAM-11 and Cu BMG samples were heated for 2.5 hours at 520 ^{o}C using a ramp rate of 20 ^{o}C/min [352, 358] at ORNL. After heating, all samples were polished to a mirror finish using colloidal silica. Powder XRD was performed to confirm the amorphous and crystalline structure of the specimens, in which the corresponding diffraction patterns can be seen in figure 3-41. A second set of samples, which were used for further experiments, were cut to linear dimensions of 3 mm × 2 mm × 10 mm, and polished in the same manner as above. These specimens were annealed at the same temperature conditions as listed above under vacuum (pressure of 9 × 10^{-8} torr) at Los Alamos National Laboratory (LANL). XRD later established their crystalline structure.

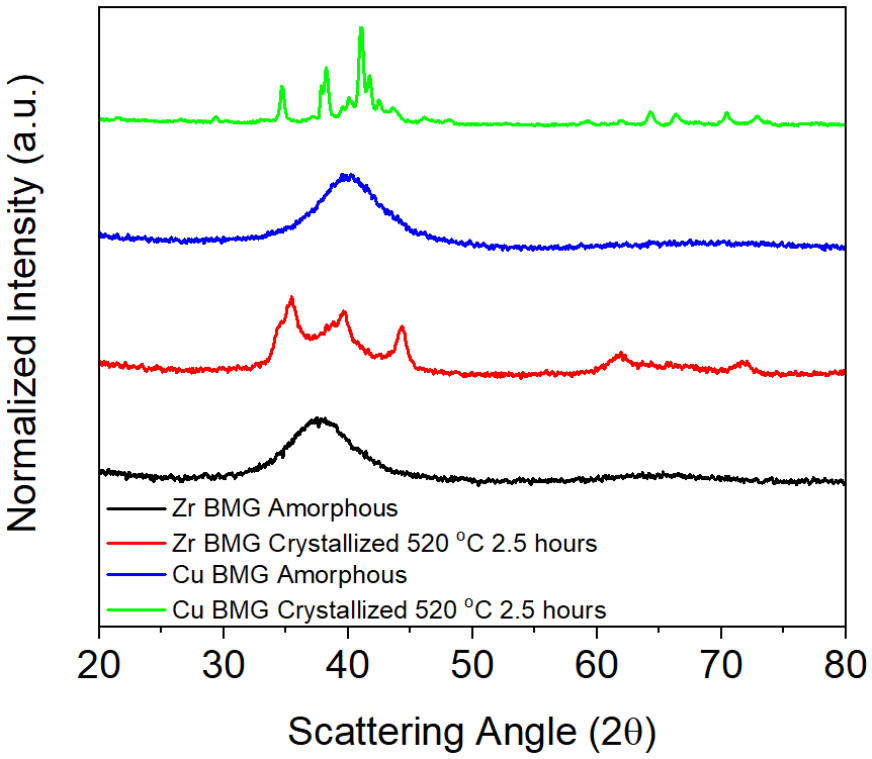

Figure 3-41 XRD patterns of the amorphous and partially crystallized BAM-11 and Cu BMG.

3.5.2 Helium Implantations

Samples were implanted at the Center for Integrated Nanotechnology (CINT) located in LANL. For these experiments, two different sets of implantations were performed. The first set of irradiations involved nuclear reaction analysis, while the second set was conducted for thermal desorption spectroscopy analysis. The implantations involved irradiating specimens at room temperature with 150 keV $^{3}He^{+}$ and $^{4}He^{+}$ ions with a 200 kV Varian ion implanter. Here, ^{3}He was chosen for the deuteron-induced reaction $^{3}He(d,p)^{4}He$ [407] required for the nuclear reaction analysis (NRA) characterization, whereas ^{4}He was chosen for the thermal desorption spectroscopy (TDS) (see Sections 3.5.3. and 3.5.4.). For the first set of implantations, the specimens were irradiated to a fluence 5×10^{15} ions/cm^{2}, while for the second set, specimens were bombarded by

150 keV $^{4}He^{+}$ ions to two different ion fluences, namely 2×10^{15} ions/cm^2 and 5×10^{15} ions/cm^2. The latter helium isotope was chosen because it is relatively inexpensive as compared to ^{3}He. Furthermore, the fluence values for these experiments were chosen to avoid bubble formation in the matrix. Table 3-12 summarizes the experimental parameters of the implantations.

The irradiation induced damage profile and He concentration were calculated using SRIM-2013 Quick Kinchin-Pease Mode [297, 299], using a displacement threshold energy (E_d) of 40 eV for all the elements comprising the BMG matrix. In the BAM-11 BMG the peak damage and peak He concentration were estimated to be roughly 0.12 dpa (500 nm), occurred at 500 nm, and 0.27 at.% (570 nm), respectively. On the other hand, the same values for the Cu BMG were 0.12 dpa (460 nm) and 0.34 at.% (520 nm). The corresponding damage profile and He concentration as a function of depth are displayed in figures 3-42(a)-(b).

Before irradiation, specimens were placed firmly on double sided carbon tape that had already been secured to the surface of the Cu block stage apparatus. Special care was taken when planting the specimens onto the tape as to not scratch the surface. After mounting, the stage and samples were placed into the ion beam chamber where the pressure was reduced to 3×10^{-6} torr.

Table 3-12 Experimental parameters for He implantations.

Parameter	Value
Ion energy (keV)	150
Beam current (μA)	20
Current density (μA/cm^2)	1.75
Analyzer voltage (V)	2.3
M/q ratio	3
Ion Fluence (ions/cm^2)	2×10^{15} and 5×10^{15}
Ion flux (ions/cm^{2}s)	1.1×10^{13}
Chamber temperature (^{o} C)	25
Chamber pressure (torr)	3×10^{-6}

Figure 3-43 shows a basic schematic of the mounted BAM-11 BMG and Cu BMG samples in the chamber during the He irradiation.

After implantation, samples were removed from the chamber and carefully placed back in their respective containers. As mentioned above, two methods were used to investigate the diffusion of helium in the sample, namely nuclear reaction analysis (NRA) [408] and thermal desorption spectroscopy (TDS) [409].

3.5.3 Nuclear Reaction Analysis

To determine the helium distribution in the amorphous and crystallized BMG specimens implanted with ^{3}He, NRA was performed using a 3 MV NEC tandem accelerator at the IBML located in LANL. Before the NRA commenced, some of the implanted samples were annealed in vacuum (~ 10^{-8} torr) at temperatures ranging from 250-600 ^{o}C, using a ramp rate of 20 ^{o}C/min., for times ranging from 30 minutes to 24 hours. The NRA was performed on the as-implanted and annealed specimens to determine whether there was a change in the He profile.

For the NRA, specimens were irradiated with 575-600 keV deuterons in which the deuterons collide with the embedded He. The collision will cause $^{3}He(d, p)^{4}He$ nuclear reactions to take place in which a proton and ^{4}He (α) particle are released with energies of 3.8 MeV and 14.6 MeV, respectively. The released particles will then encounter a 6 μm aluminum foil, where their energy will be sufficiently reduced such that it can be detected by a 2 mm thick Si solid-state surface barrier detector (surface area of 314 mm^{2}) [410]. Figure 3-44 shows a basic schematic of the NRA scattering process.

The SIMNRA simulation code [411, 412] was employed to analyze the outgoing α-particle energy spectrum. The procedure for fitting the data consists of fitting the proton spectrum recorded

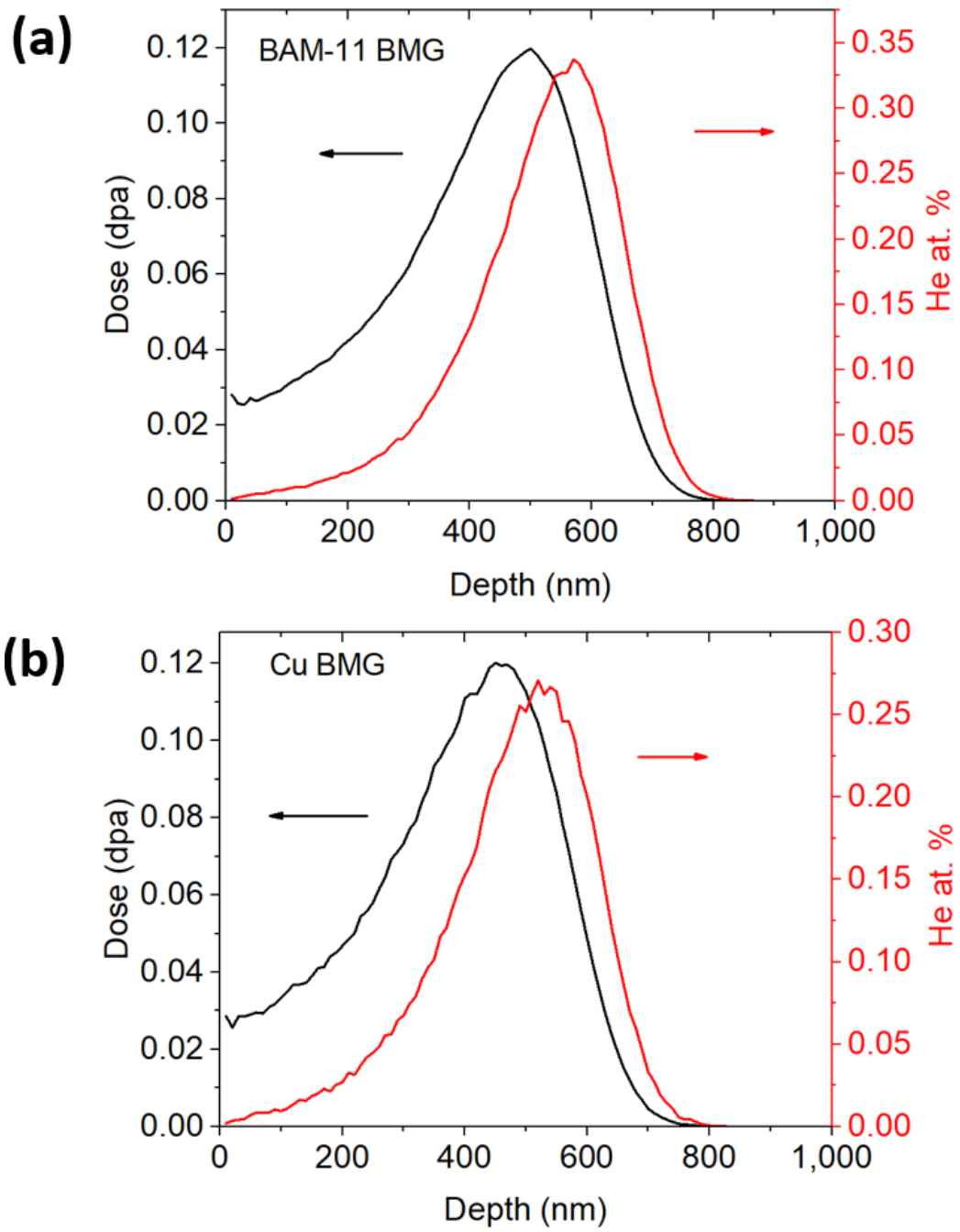

Figure 3-42 Irradiation damage (dpa) profile (fluence of 5×10^{15} cm^{-2}) versus depth and corresponding at. % He versus depth for the (a) BAM-11 BMG and (b) Cu BMG. Both graphs were obtained from SRIM 2013 simulation using quick Kinchin-Pease calculations.

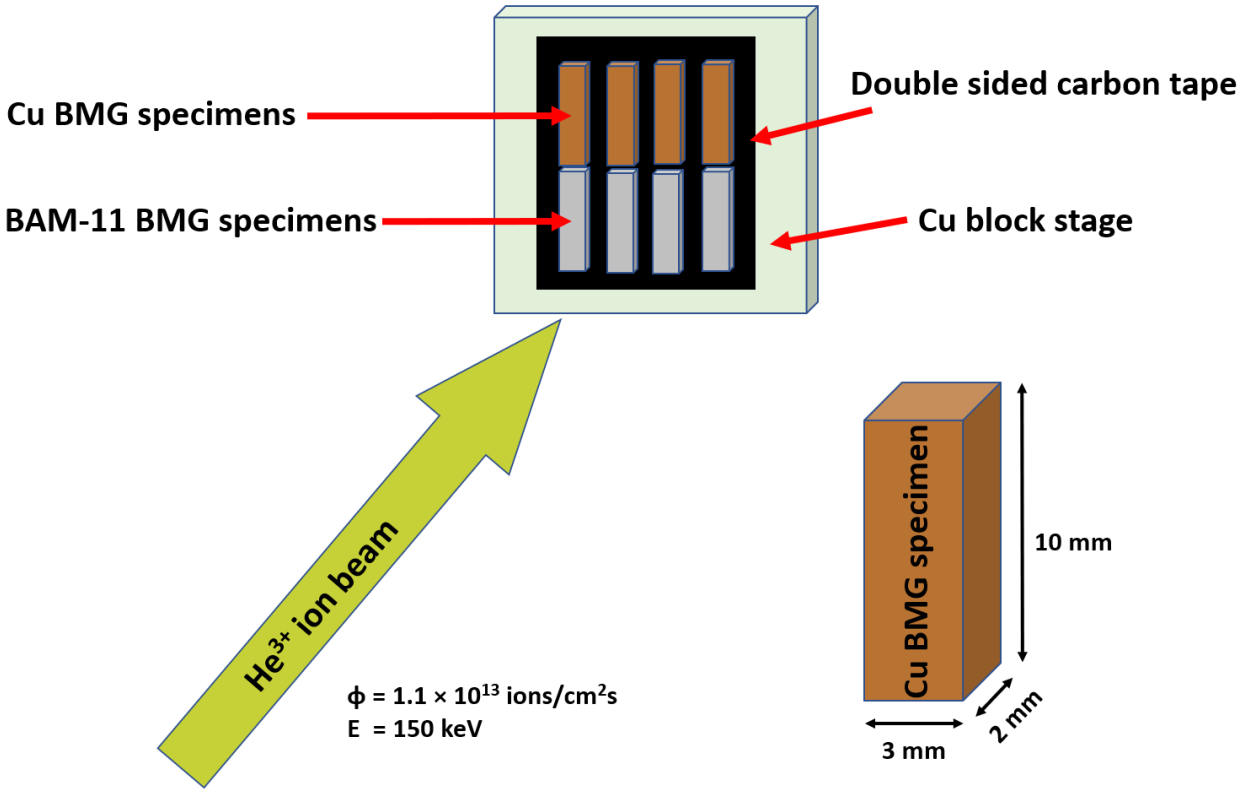

Figure 3-43 Schematic showing the 150 keV $^{3}He^{+}$ ion irradiations of the 3 mm × 2 mm × 10 mm specimens.

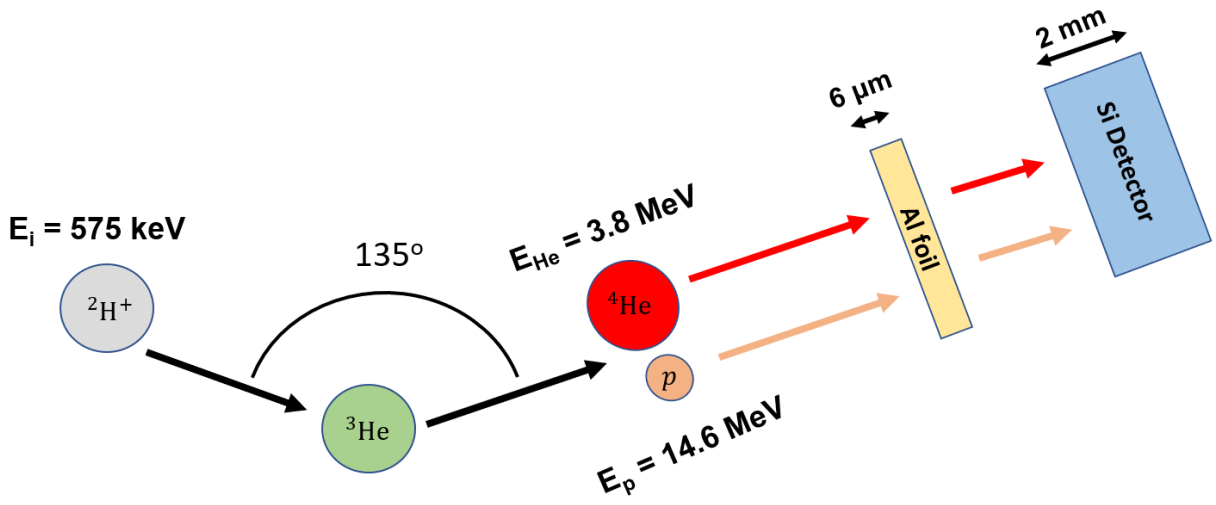

Figure 3-44 Basic schematic of the NRA scattering process (from Ref. [408]).

at the energy corresponding to the maximum NRA yield to minimize the error. For our study, the energy spectrum corresponding to 575 and 600 keV deuteron energies were fitted to obtain the helium depth profile of the as-implanted and annealed samples amorphous and partially crystallized BMGs.

To begin the analysis, the experimental parameters were first input into the software (see figures 3-45(a)-(c) and 3-46). These parameters include the detector energy calibration values, the aluminum foil thickness, detector geometries, detector energy calibration values, nuclear reaction cross sections for each element, and incident beam characteristics. Furthermore, the samples were defined as consisting of multiple layers with varying thicknesses and compositions. The first layer was designated as having no helium and just the elements comprising the BMG. The middle layer was input to contain both the BMG elements and the He. Finally, like the first layer, the last layer (furthest from the surface) was input as containing no He.

To evaluate the helium concentration depth profile ρ(x) one considers the following equations [408]:

$$\rho(x) = \left(\frac{A}{s}\right) \exp\left[-\frac{(x - x_c)^2}{2s^2}\right] \tag{3-16}$$

here A is a normalization constant that is equal to the depth profile integrated area which is proportional to the helium fluence, x_c is the centroid of the distribution (near to mean projected range R_p of the ^{3}He ions), and s is the standard deviation near the longitudinal range straggling (ΔR_p). the variable ρ(x) is the helium concentration depth profile and is approximated via a Gaussian curve [413, 414]:

$$\int_0^\infty \rho(x)dx = A\sqrt{\pi} \tag{3-17}$$

Furthermore, the diffusion coefficient D and effective activation energy ΔE (assuming Arrhenius laws), for the implanted He, can be calculated from the broadening of the Gaussian peak using Eqs. (3-18) and (3-19):

$$D = (s^2 - s_0^2)/2t_a \tag{3-18}$$

$$D \approx D_0 \exp\left(-\frac{\Delta E}{k_B T}\right) \tag{3-19}$$

where D is the diffusion coefficient, s_0 is the standard deviation of the as-implanted profile, t_a is the annealing time, k_B is Boltzmann's constant, and T is the annealing temperature. For more details pertaining to the NRA experiment, please see [415-418].

3.5.4 Thermal Desorption Spectroscopy

As mentioned in the previous section, amorphous and crystallized BAM-11 and Cu BMG specimens (dimensions of 3 mm × 2 mm × 6 mm) were implanted by 150 keV ^{4}He ions to fluences of 2×10^{15} ions/cm^2 and 5×10^{15} ions/cm^2 at CINT in LANL. Following the irradiation, the as-implanted samples were transported to the LAMDA facility in ORNL to undergo thermal desorption spectroscopy (TDS) experiments. The spectroscopy experiments were performed by Dr. Xunxiang Hu. Here, the specimens were heated to 770 ^{o}C (heating rate of 0.4 ^{o}C/s) using a

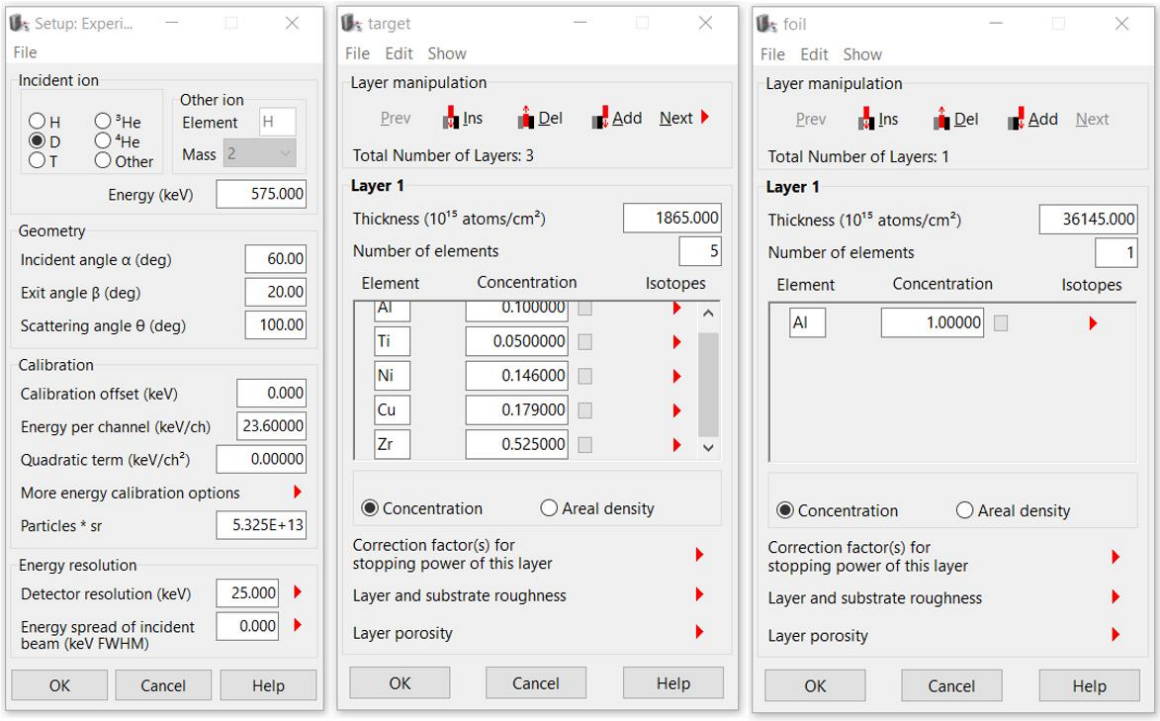

Figure 3-45 SIMNRA software experimental input windows which include the (a) general experimental parameters such as incoming deuteron energy and calibration offsets, (b) specimen target composition and thickness input, and (c) foil composition and thickness input.

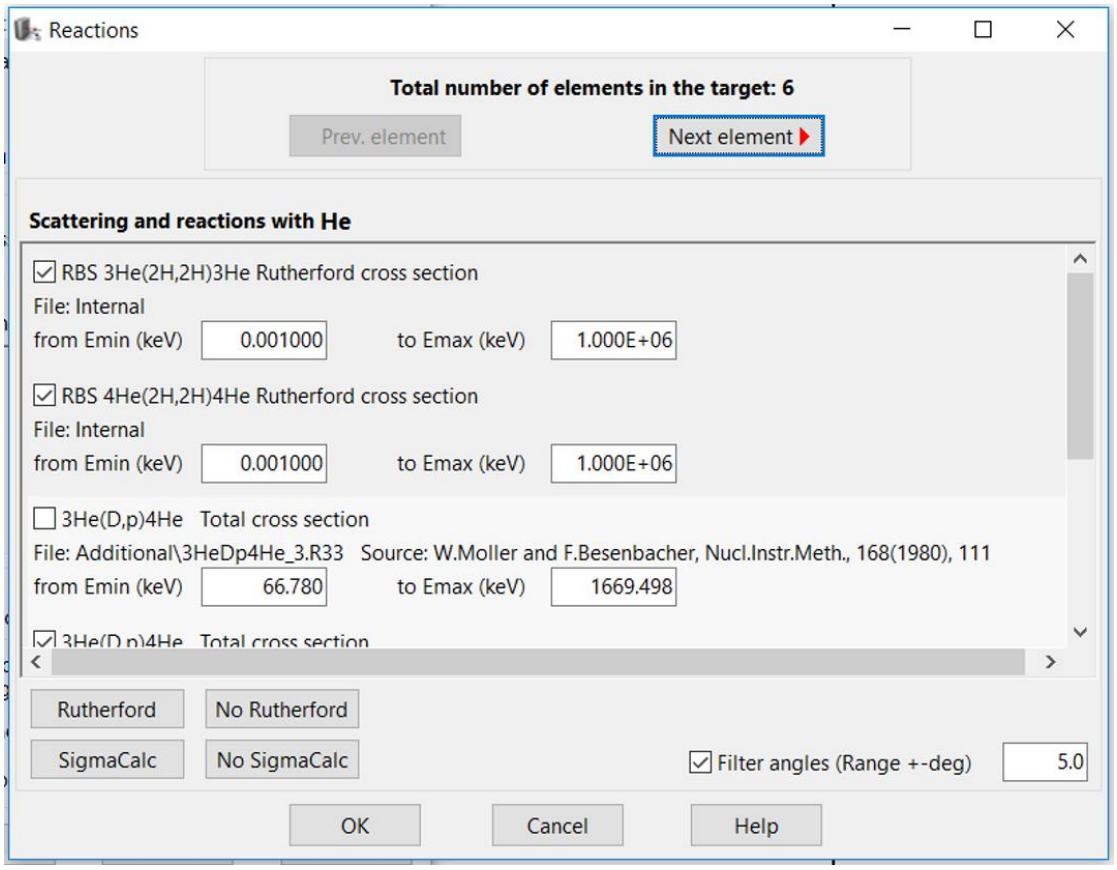

Figure 3-46 The nuclear cross section parameter input screen.

Figure 3-47 TDS equipment located in LAMDA at ORNL.

customized electrical resistivity heater. The maximum temperature used for these experiments was based on the melting temperature (T_m) of the BAM-11 BMG since it is lower than that for the Cu BMG (T_m = 910 ^oC [399]). The chamber pressure was held at approximately ~1 × 10^{-9} torr to reduce the He background to a level of approximately 2 × 10^{10} He/s. A mass spectrometer was used to record the He gas content during the heating of the specimens. Figure 3-47 shows an image of the TDS equipment.

3.5.4.1 Thermal Desorption Analysis

Assuming that the He desorption follows a first order kinetic dissociation model, one can calculate the activation energies that are associated with desorption events by using the following equation [409]:

$$\frac{dN}{dt} = -Nfe^{-E/k_BT} \tag{3-20}$$

where N is the number density of remaining He atoms in the specimen corresponding to a desorption event, f is the Debye frequency (10^{13} s^{-1} [34]), T is the temperature associated with the desorption peak, E is the activation energy associated with the desorption events, and k_B is Boltzmann's constant. Since it was assumed that the desorption follows a first order model, we may assume that the second derivative of the number density with respect to time is zero. Upon taking the derivative of Eq. (3-20) and setting it to zero, yields:

$$\frac{d^2N}{dt^2} = 0 = -\frac{dN}{dt} fe^{-\frac{E}{k_BT}} - \frac{NfE}{k_BT^2} e^{-\frac{E}{k_BT}} \frac{dT}{dt} \tag{3-21}$$

Plugging the identity for dN/dt from Eq. (3-20) into the above equation and simplifying gives:

$$Ln\left(\frac{\beta}{T^2}\right) = Ln\left(\frac{fk_B}{T}\right) - \frac{E}{k_BT} \tag{3-22}$$

here the substitution $\beta = dT/dt$ was used. To solve Eq. (3-21) in terms of E for a given temperature and heating rate, β, one must use non-linear numerical methods. To determine the activation energy associated with a desorption event, one first plots the energies on the same graph as the He desorption spectra data [409]. The energy values that align with the spectrum peaks corresponds to the energy at which He desorption occurs in the specimen.

CHAPTER 4 EXPERIMENTAL RESULTS

4.1 Review of Preliminary Experiments

Preliminary experiments were performed on the BAM-11 BMG to help elucidate the effects of irradiation and annealing on the microstructure and mechanical properties of the alloy. These experiments included irradiating the BAM-11 BMG with 3 MeV Ni^+ ions as well as >0.1 MeV neutrons. In summary, the results of these studies provided useful results on the radiation effects behavior of BMGs using multiple characterization techniques.

Figure 4-1 (a)-(b) displays the BAM-11 BMG as-cast rod and its corresponding bulk XRD pattern indicating that the sample was fully amorphous after fabrication. After fabrication, the rod was cut into sections consisting of linear dimensions of $8 \times 3 \times 1$ mm^3 that were subsequently ground and polished to a mirror finish. Figure 4-2 shows a representative $8 \times 3 \times 1$ mm^3 specimen that was used for the irradiation and annealing experiments.

Preliminary microstructural examination of unirradiated BAM-11 bulk metallic glass was performed on a polished BAM-11 BMG specimen [419]**.** As can be seen infigure 4-3, diffraction patterns showed the amorphous nature of the alloy sample while TEM images revealed the featureless nature of the sample. Additionally, a baseline electron energy loss spectroscopy (EELS) scan performed via TEM gave a composition of Zr-7Al-3.8Ti-6.9Cu-15Ni with oxygen as the only major impurity.

4.1.1 Ion Irradiation Experiments

4.1.1.1 TEM Microstructural Characterization

One study involved the irradiation of BAM-11 BMG by 3 MeV Ni^+ ions to fluences of 4.2

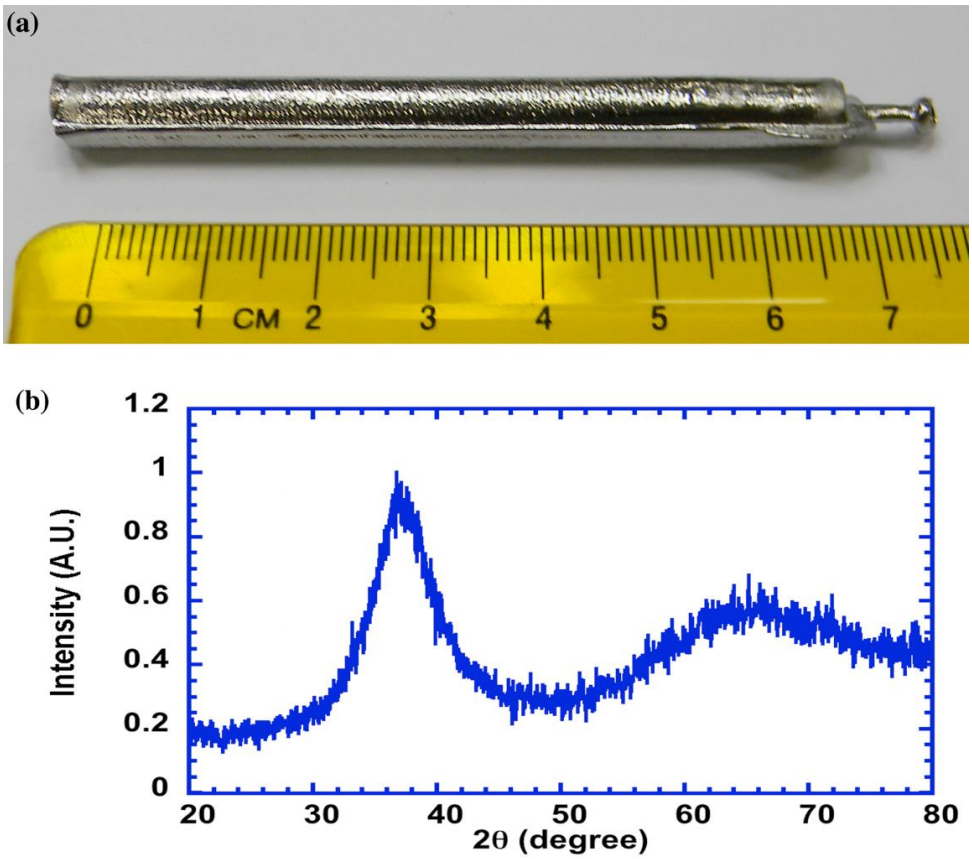

Figure 4-1 (a) Rod of BAM-11 prepared by casting and quenching at Oak Ridge National Laboratory and (b) X-ray diffraction pattern showing the amorphous structure (from Ref. [70]).

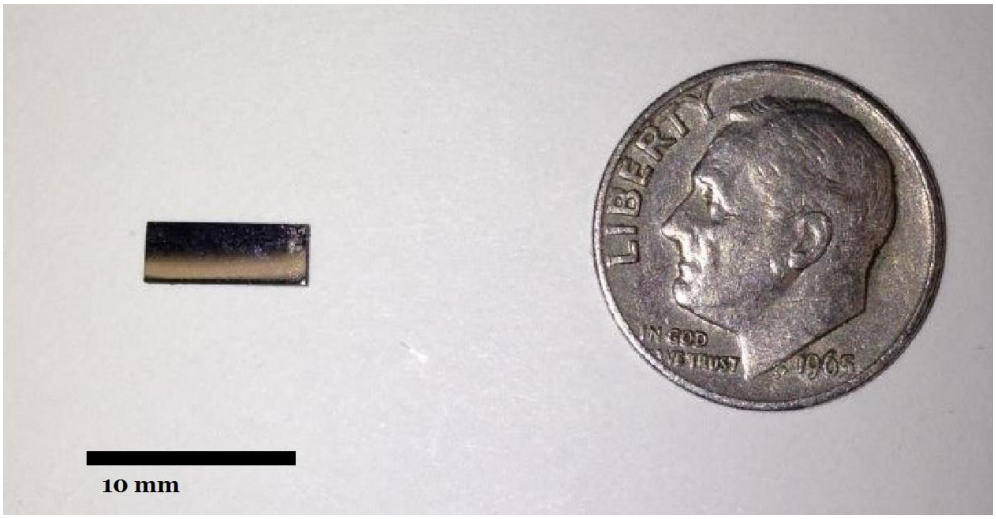

Figure 4-2 3 × 8 × 1 mm coupon of BAM-11 BMG used in preliminary irradiation and annealing experiments.

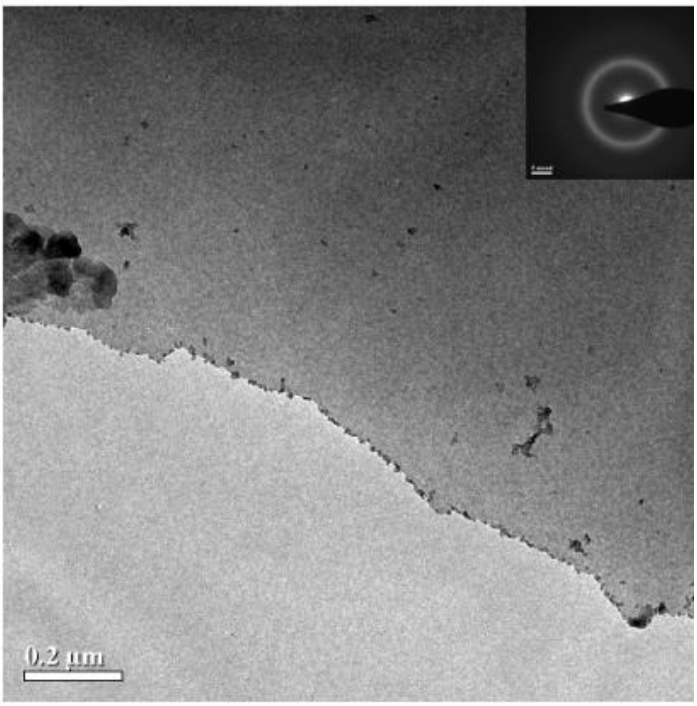

Figure 4-3 TEM micrograph of the unirradiated BAM-11 BMG with diffraction pattern inserted on top right (From Ref. [419]).

$\times 10^{13}$ and 4.2×10^{14} cm^{-2} at both room temperature and 200 ^{o}C. The Ni ions had a projected range of 1.36 μm and these fluences correspond to peak damage levels of 0.1 and 1 dpa, respectively. Figure 4-4 shows TEM micrographs of the irradiated alloy (room temperature and 200 ^{o}C), including the BF images at 9.6 and 135 kx with the respective diffraction pattern (DP) of the sample. The lack of spots in the diffraction patterns revealed that no significant microstructural changes (crystallization) in the samples occurred during irradiation at room temperature and 200 ^{o}C [15]. Also, figure 4-4 features high resolution (HR) images that are shown at 580 kx times magnification. As can be observed in the figure, the specimens appeared feature-free at differing tilt conditions in the TEM, while no point defects or point defect-like structures were noticed at HR.

Another set of experiments involved samples that were irradiated by 3 MeV Ni^{3+} ions, but to peak damage levels of 1 and 10 dpa [420]. These doses respectively corresponded to fluences of 4.2×10^{14} and 4.2×10^{15} cm^{-2}. Furthermore, some as-cast specimens were also annealed at 300 ^{o}C for 48 hours. Figure 4-5 displays the TEM characterization of the as-cast, annealed, and irradiated samples. The TEM, HRTEM and DPs revealed that after irradiation and annealing, the specimens were completely amorphous and feature-free. In addition, tilting on two different axes in the TEM revealed no dislocations or point defect-like structures in the alloy.

4.1.1.2 Nanoindentation Results

For these experiments, nanoindentations were performed on the samples that were irradiated to peak doses of 0.1 and 1 dpa, and at room temperature and 200 ^{o}C. The indentations were utilized a Berkovich tip in which the hardness and Young's modulus were continuously recorded as a function of the indentation depth. The nanoindentations were performed using the CSM method with a constant loading rate [(dP/dt)/P] of 0.05/s with a maximum applied load of 15 mN. Figures 4-6 and 4-7 show the depth dependent hardness and elastic modulus nanoindentation data for the as-cast and ion-irradiated BAM-11 BMG. From the figures, a few things may be noticed. The hardness and modulus values increased in a monotonic fashion with respect to indentation depth. These results will be shown to be at odds with the later experiments where the hardness decreased with respect to the indentation depth. Interestingly, the hardness curves were lower for the irradiated samples, as compared to the as-cast condition. In terms of the modulus, the specimens irradiated at the 200 ^{o}C exhibited modulus values that were higher as compared to the unirradiated sample, for depths beyond 110 nm.

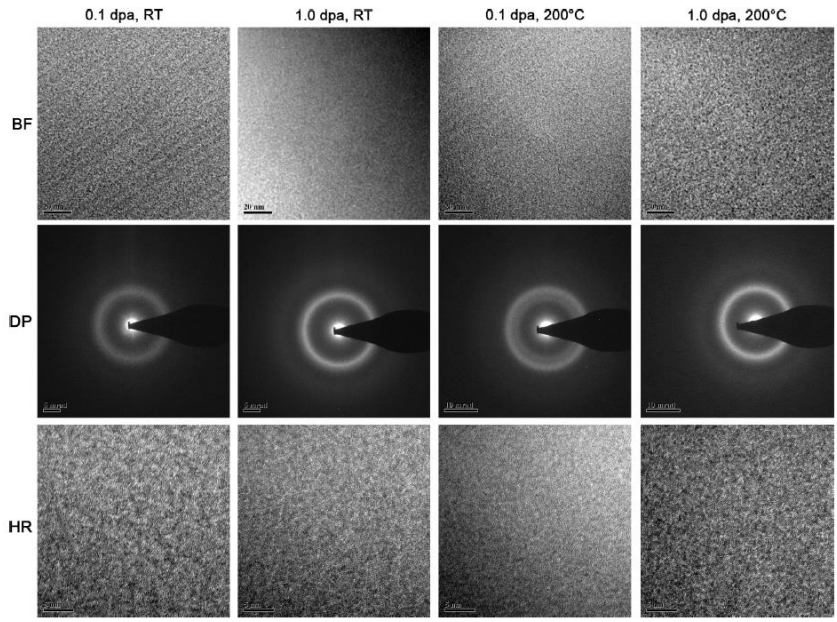

Figure 4-4 TEM image showing bright field images at 135 kx, diffraction patterns, and high-resolution images at 580 kx of ion-irradiated BAM-11 irradiated to 0.1 and 1.0 dpa at room temperature and 200°C (from Ref. [98]).

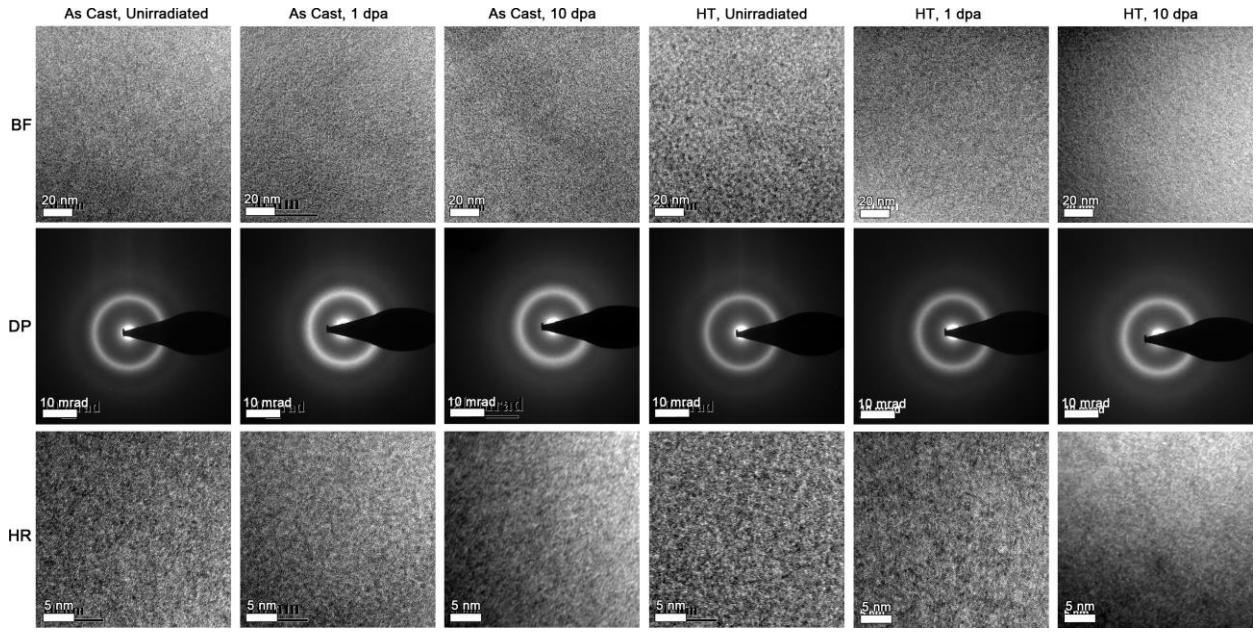

Figure 4-5 TEM BF (135kx), DPs, and HR images (580kx) of as-cast and heat-treated ion-irradiated BAM-11 BMG irradiated to 1 and 10 dpa. No changes in crystallinity or any defect structures were observed (From Ref. [420]).

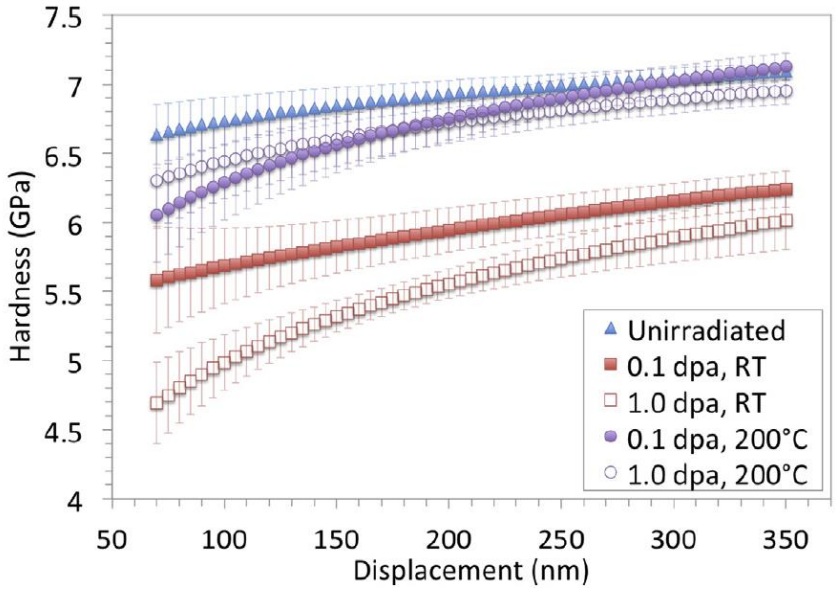

Figure 4-6 Nanoindentation hardness as a function of indenter depth in the unirradiated and ion-irradiated BAM-11 BMG specimens (from Ref. [98]).

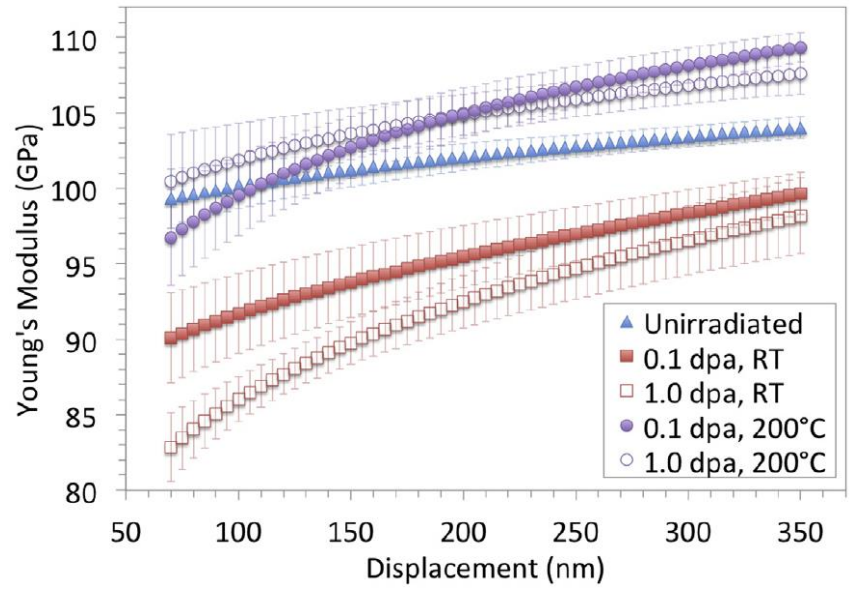

Figure 4-7 Elastic modulus as a function of indenter depth in the unirradiated and ion-irradiated BAM-11 BMG specimens (from Ref [98]).

4.1.2 Neutron Irradiation Experiments

Microstructural and mechanical property tests were performed on the as-cast and neutron irradiated BAM-11 BMG specimens. Here, the samples were exposed to neutron fluences of 1.4×10^{20} n/cm^2 and 1.4×10^{21} n/cm^2, which corresponded to doses of 0.1 and 1.0 dpa. The depth-dependence hardness values of the neutron irradiated BMG specimens are shown in figure 4-8. A pronounced depth dependence was measured for the nanoindentation hardness, particularly for the unirradiated and 0.1 dpa irradiated samples. At 800 nm, there was a decrease in the nano-indentation hardness of about ~6% and ~12% from the unirradiated state for the specimens irradiated to 0.1 dpa and 1 dpa, respectively.

It is notable in figure 4-8 that the nanoindentation hardness exhibits a pronounced depth dependence. Since the nano-indentation hardness is performed at relatively shallow depths compared to the bulk Vickers hardness measurements (< 1 microns vs. ~6.5 microns), the discrepancy between the two hardness tests could be a result of surface effects due to machining or mechanical polishing effects, or a near-surface composition gradient due to chemical inhomogeneity or near-surface radiation induced solute segregation.

The Young's modulus vs. nano-indentation depth can be seen in figure 4-9. As can be seen, the elastic modulus decreases with increasing depth, resembling the trend for nano-indentation hardness. At 800 nm, the data indicates a slight decrease of ~1.4% and ~0.9% after irradiation to 0.1 and 1 dpa, respectively as compared to the unirradiated specimen. The dynamic Young's modulus for the control and sample irradiated to 0.1 dpa can be seen in Table 4-1. There was a decrease of ~5% in the dynamic Young's modulus of the specimens irradiated to 0.1 dpa at 90°C as compared to the control sample.

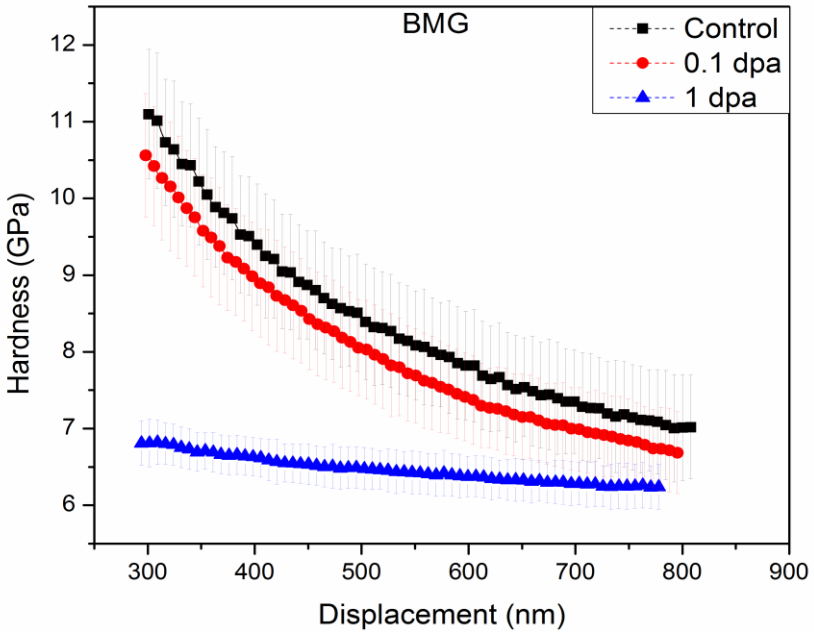

Figure 4-8 Nano-indentation hardness as a function of indenter depth in the neutron irradiated and control BAM-11 BMG specimens.

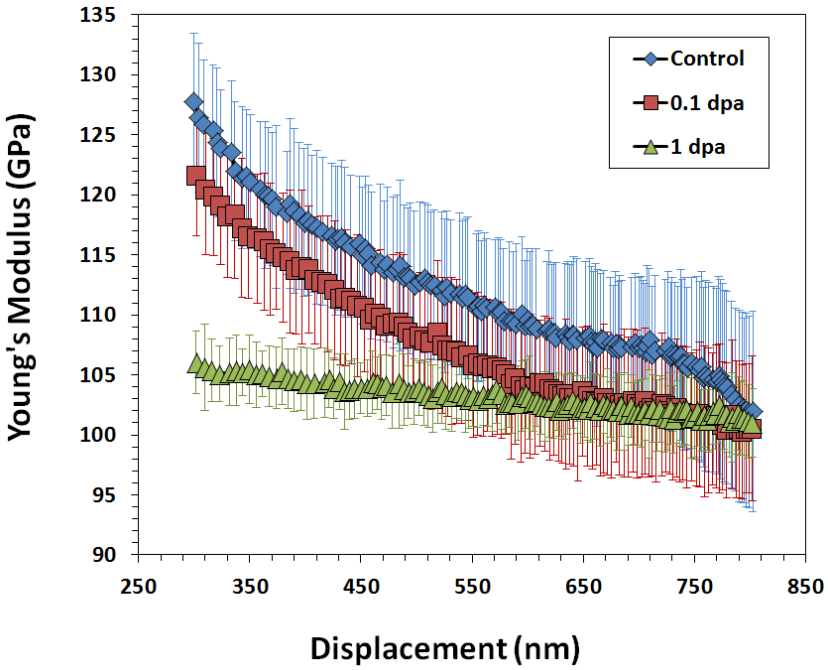

Figure 4-9 Young's modulus vs. nano-indentation depth for neutron irradiated BAM-11 BMG specimens.

Table 4-1 Average dynamic Young's modulus of unirradiated and irradiated BAM-11 BMG specimens.

BAM-11 BMG	Control	0.1 dpa – 70°C
Average Dynamic Young's Modulus (GPa)	79.4	75.7
Std. Dev of Dynamic Young's Modulus (GPa)	0.7	1.8

The measured densities for the control and irradiated specimens are shown in figure 4-10. A decrease in density was found in the irradiated samples as compared to the control specimens. Here the specimens exhibited ~0.4% decrease in density at both irradiation doses. Moreover, the density at 1 dpa was slightly greater than the density at 0.1 dpa. The decrease in density is likely associated with an irradiation induced increase in free volume content.

Previous studies have reported neutron irradiation induced microstructural changes in metallic glasses. For example, a study conducted by Gupta et al. found that thermal neutron irradiation of iron based metallic glass containing 13-20% boron to low doses increased the short range order which was accompanied by a relief in the random internal stresses of the as-received specimens [346]. In contrast to the above studies, the study by Perez-Bergquist et al. found no significant microstructural changes in the BAM-11 BMG after exposure to 3 MeV Ni^{+} ions [419]. In summary, there were relatively slight irradiation induced changes in the bulk hardness, nano-indentation hardness, density and dynamic Young's modulus for the given dose regime. For the first three tests, the exhibited change did not differ significantly between the samples tested at 0.1 and 1 dpa. This result signifies that a saturation of irradiation damage may be occurring in BAM-11 BMG within the examined dose and temperature regime.

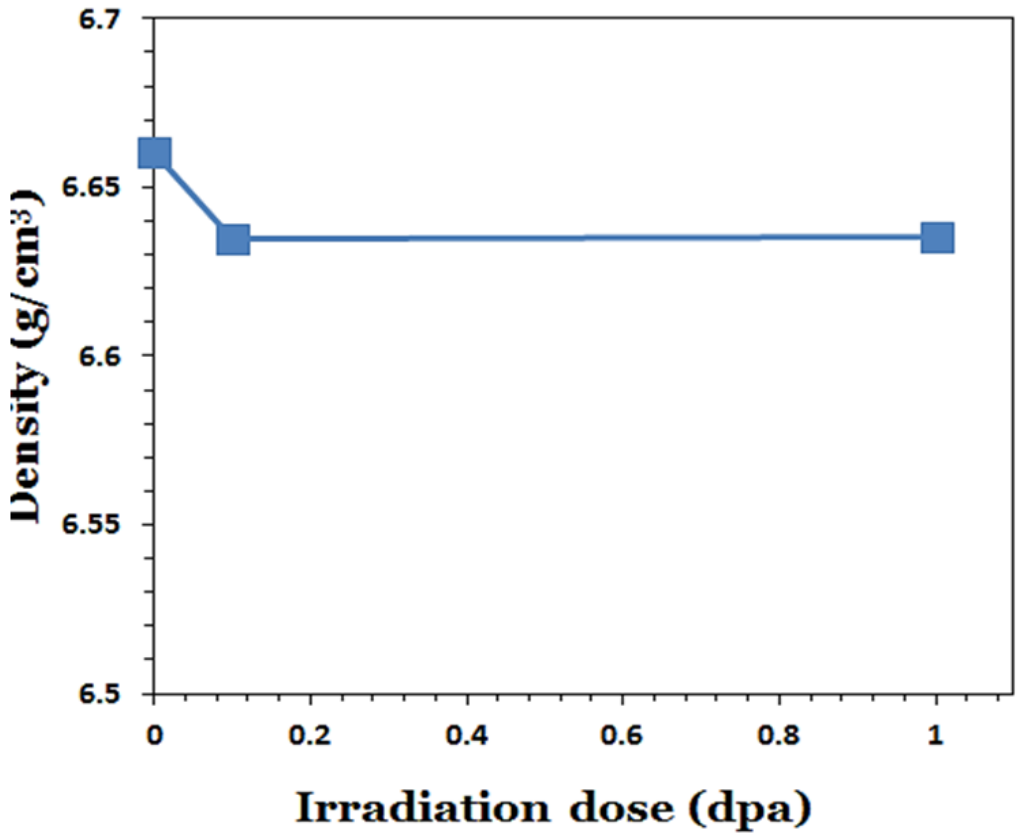

Figure 4-10 Measured density of unirradiated and neutron irradiated (0.1-1 dpa) BAM-11 BMG specimens.

4.2 Current Experimental Results

4.2.1 Ion Irradiation Experiments

To advance our knowledge on the irradiation response of this material system, these investigations will gain insight on how irradiation and temperature modifies the nanoindentation properties of this material. To carry out this investigation, nanoindentation tests and microstructural characterization techniques were performed on specimens irradiated by 9 MeV Ni^{3+} and 5.5 MeV C^{+} ions to midrange doses of 10 dpa and 0.5 at temperatures ranging from 25 - 360 ^{o}C. Nanoindentation tests were performed to measure the depth dependent hardness, while XRD and TEM methods were conducted to examine whether the BMG remained amorphous during irradiation.

4.2.1.1 Microstructural Characterization

4.2.1.1.1 BAM-11 BMG

To obtain a broader ion irradiation region for characterization, ion irradiations for this thesis research utilized 9 MeV Ni ions (vs. 3 MeV Ni ions used for the preliminary studies). In addition, relatively high dose levels were examined (~10 dpa at midrange, ~25 dpa at peak). Figure 4-11 displays the glancing XRD patterns for the as-cast and 9 MeV Ni^{3+} irradiated BAM-11 BMG samples. For the plots, the intensity of the patterns was normalized. The shift in the peak to lower angles suggests that the atomic spacings increased during the irradiation [421]. The patterns for the specimens irradiated at 25 and 290 ^{o}C consisted of a broad hump at diffraction angles ranging from approximately 30 to 46 ^{o}, which indicates that samples remained amorphous during

irradiation. This was opposed to the pattern for the sample irradiated at 360 ^{o}C, where a small discrete peak centered around 45^{o} can be seen in addition to the broad amorphous peak at 30 to 46 degrees. This result indicates that that partial crystallization occurred during irradiation.

To examine whether the crystallization in the sample was induced by thermal or irradiation effects, glancing XRD was also performed on the unirradiated side. In addition, these patterns were compared to one representing a sample that was annealed at 500 ^{o}C for 2.5 hours. This comparison was intended to gain an understanding regarding the XRD patterns for temperatures at ~33 ^{o}C below and ~100 ^{o}C above the glass transition temperature (T_g) of the BAM-11 BMG (393 ^{o}C [352]).

The corresponding patterns are displayed in figure 4-12, and as can be observed, all three patterns are quite similar. The overall similarity in the patterns from the irradiated and unirradiated sides of the specimen indicates that partial crystallization was thermally induced. However, we can note some important differences from this figure. Firstly, the peak at ~45^{o} is more pronounced in the pattern representing the unirradiated side. Secondly, there is an increase in the intensity values for the angles beyond 60^{o}. Thirdly, the peak centered around 38 ^{o}C for the as-cast sample is shifted slightly to the left for the irradiated specimens. Finally, in the patterns for the specimen annealed at 500 ^{o}C, there are more distinct peaks corresponding to scattering angles ranging from 30-50^{o}. This result suggests that specimen heated at 500 ^{o}C experienced more extensive crystallization as compared to the sampled irradiated at 360 ^{o}C for a longer period of time.

In addition to the XRD characterization, TEM was also performed on the sample irradiated at 360 ^{o}C. The TEM BF and SAD images, as featured in figure 4-13, showed no features that would indicate crystallization had occurred. In contrast to the XRD results, the atomic structure

of the lift-out specimen that was examined by TEM (see figure 4-13), showed that it had remained amorphous during irradiation. This result indicates that the crystallization did not occur uniformly throughout the material.

Additional experiments were performed to examine the role of average primary knock-on atom energy on the radiation stability in the BAM-11 and Cu BMGs. Here, the specimens were irradiated by the 9 MeV Ni^{3+} and 5.5 MeV C^{+} to a midrange dose of 0.5 dpa at temperatures ranging from 25 ^{o}C to 360 ^{o}C. Figures 4-14 (a)-(b) display the XRD patterns (with normalized intensity) for the as-cast and irradiated BMG samples. For the samples irradiated by 9 MeV Ni^{3+}, the broad hump centered at scattering angles ranging from 30 to 46^{o} indicates that radiation BAM-11 BMG sample that was irradiated by 5.5 MeV C^{+} at 290 ^{o}C, however, there were several distinct peaks in the pattern, which indicates that partial crystallization occurred in the specimen induced crystallization did not occur in the samples irradiated at any of the temperatures. For the during

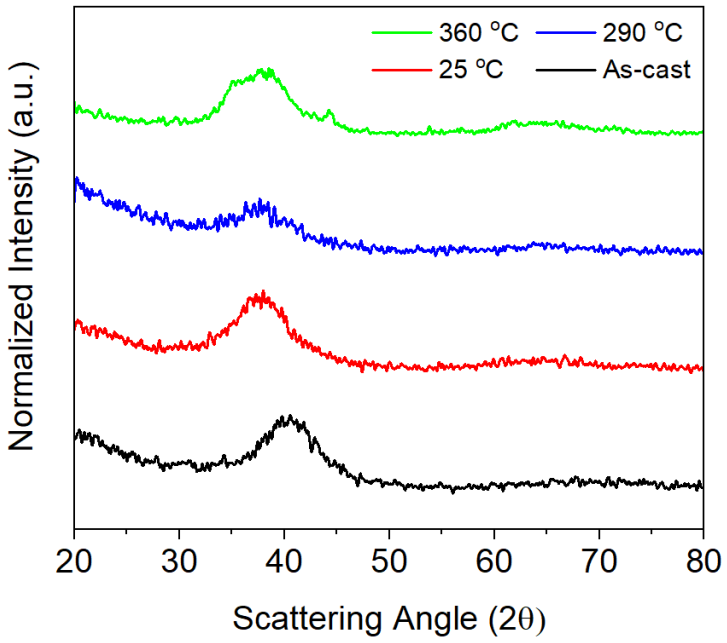

Figure 4-11 Glancing X-ray diffraction patterns for BAM-11 BMG samples in the as-cast and Ni^{3+} irradiated condition (9 MeV, 10 dpa) at different temperatures.

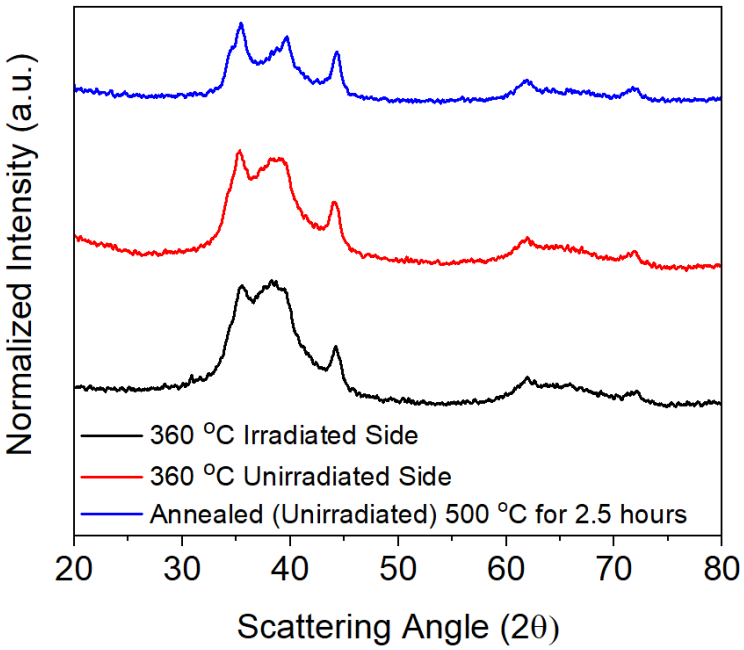

Figure 4-12 Bulk X-ray diffraction patterns for the BAM-11 BMG sample irradiated by Ni^{3+} ions (9 MeV, 10 dpa) at 360 °C (unirradiated and irradiated sides) and the specimen annealed at 500 °C for 2.5 hours.

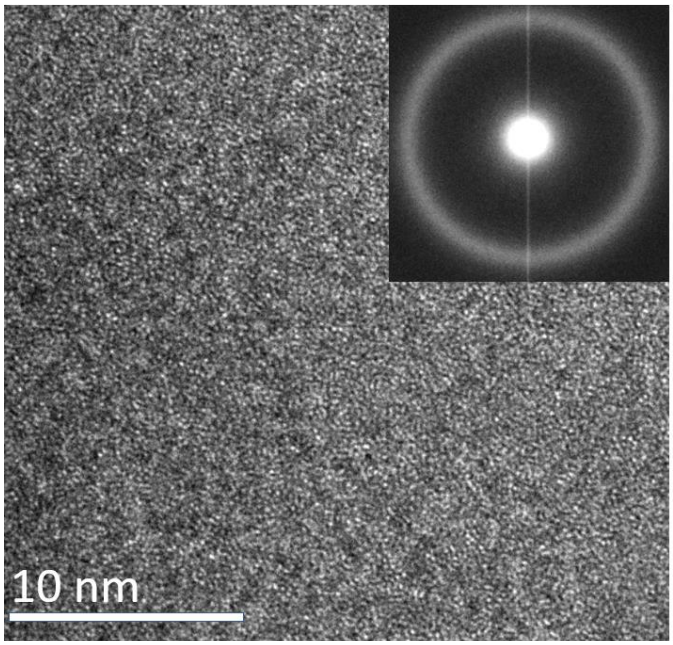

Figure 4-13 TEM Diffraction pattern and inset which contains the corresponding bright field imaging of the irradiated region in the BAM-11 BMG sample irradiated with 9 MeV Ni^{3+} ions to a midrange dose of 10 dpa at 360 °C.

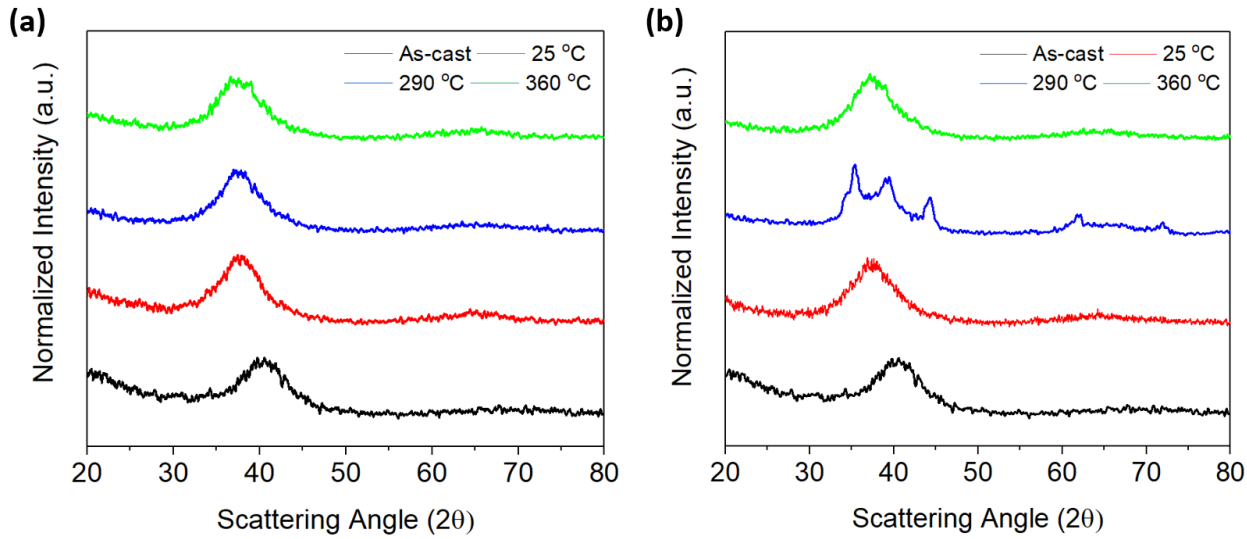

Figure 4-14 Glancing X-ray diffraction patterns for the BAM-11 BMG samples in both the as-cast and (a) 9 MeV Ni^{3+} and (b) 5.5 MeV C^{+} irradiation condition (0.5 dpa) at different temperatures.

irradiation. Interestingly, the specimen irradiated by the same ion but at the higher temperature of 360 ^{o}C did not show any signs of crystallization. This indicates there may have been some issues with thermal contact of some of the samples with the target holder substrate.

4.2.1.1.2 Cu BMG

The XRD patterns of the as-cast and irradiated (9 MeV Ni^{3+}, 25 - 360 ^{o}C) Cu BMG samples are presented in figure 4-15. Here, a broad peak centered at scattering angles ranging from 32 to 46^{o} can be observed in the samples bombarded at 25 and 290 ^{o}C, indicating that the specimens remained amorphous during irradiation. On the other hand, numerous sharp peaks were observed in the XRD patterns for the sample irradiated at 360 ^{o}C, indicating that partial crystallization occurred. Like the BAM-11 BMG sample irradiated at the above temperature, glancing XRD was also performed on the unirradiated side of the specimen. These patterns were then compared with a specimen that was annealed at 520 ^{o}C for 2 hours to induce thermal crystallization.

Figure 4-16 also compares the bulk XRD measurements for the sample irradiated at 360 ^{o}C (irradiated and unirradiated sides) for 7 hours with an unirradiated specimen that was annealed at 520 ^{o}C for 2.5 hours. Again, like the BAM-11 BMG, this comparison was intended to examine the XRD behavior at ~120 ^{o}C below vs. ~40 ^{o}C above the reported T_g of the Cu BMG, which is 480 ^{o}C [358]. As shown in figure 4-16, the pattern for the unirradiated side of the specimen is similar to the one for the irradiated side, implying that the partial crystallization was thermally induced. However, for the pattern of the 520 ^{o}C annealed specimen, the peaks centered at ~37, 39, and 40^{o} exhibited a greater intensity as compared to the same peaks for the sample irradiated at 360 ^{o}C. This result indicates that a greater degree of crystallization occurred in the sample

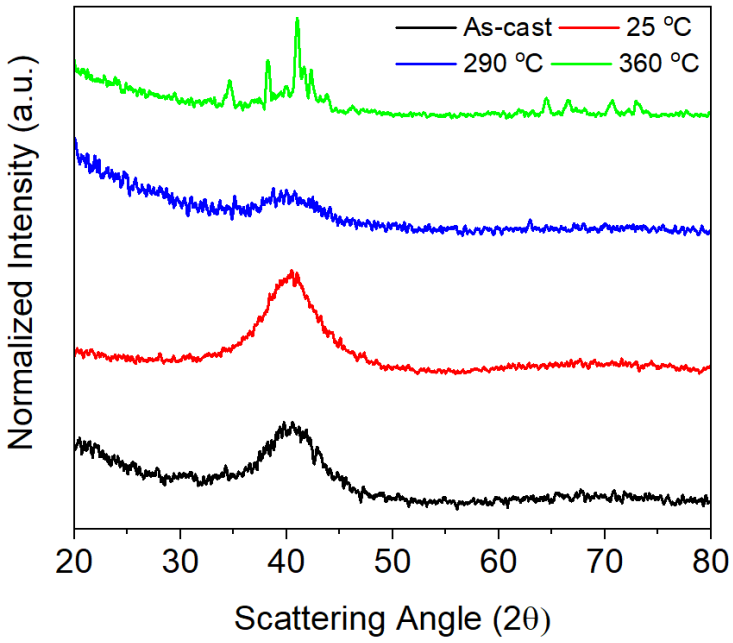

Figure 4-15 Glancing X-ray diffraction patterns for $Cu_{60}Zr_{20}Hf_{10}Ti_{10}$ BMG samples in the as-cast and Ni^{3+} irradiated condition (9 MeV, 10 dpa) at different temperatures.

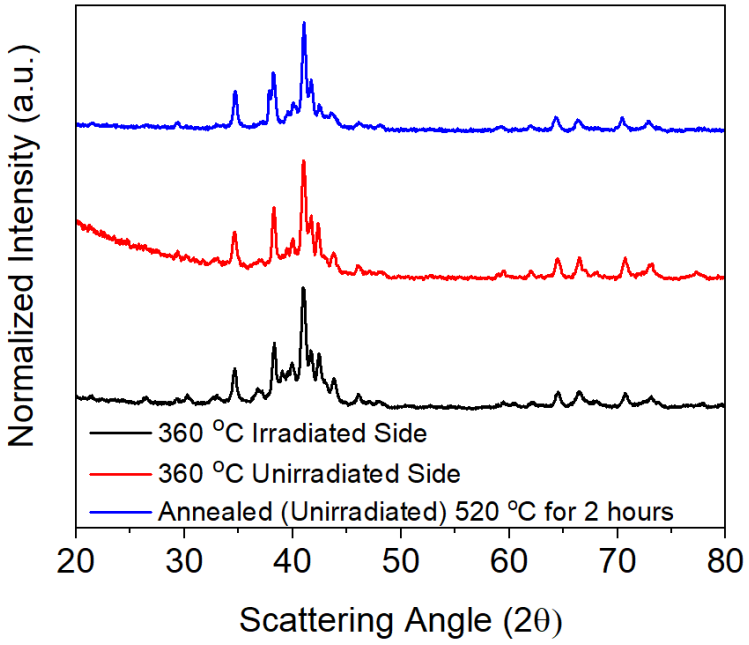

Figure 4-16 Glancing X-ray diffraction patterns of the irradiated and unirradiated sides of the $Cu_{60}Zr_{20}Hf_{10}Ti_{10}$ BMG specimen irradiated by Ni^{3+} at 360 °C (9 MeV, 10 dpa) in addition to a bulk scan of the sample annealed at 520 °C for 2.5 hours.

heated at 520 ^{o}C for 2.5 hours as compared to the 360 ^{o}C (~7 hours) irradiated condition.

Figure 4-17 displays TEM BF image (medium-magnification) of the Cu BMG specimen irradiated by 9 MeV Ni^{3+} ions to a midrange dose of 10 dpa at 360 ^{o}C. The corresponding diffraction pattern is displayed in the upper left corner of the figure. The spots in the SAD and diffracting features in the BF images indicated that crystallization occurred. This result contrasts with the BAM-11 BMG that was irradiated at the same condition, where no such features were observed in the TEM imaging. The crystallites that formed throughout the irradiated region and consisted of various shapes and sizes. Since the XRD patterns exhibited crystalline peaks for both the irradiated and unirradiated near-surface regions of this sample, the crystallization is most likely associated with thermal (overheating) effect rather than a radiation-induced effect.

To analyze the crystal phases in the partially crystallized Cu BMG specimen, qualitative and quantitative phase analysis was performed using Rietveld refinement techniques [239]. The qualitative phase identification (ID) was determined in Highscore using the Powder Diffraction File-4+ (PDF-4+) database, whereas the quantitative phase analysis was performed via Rietveld refinement via the GLAS Science Algorithm Software II (GSAS II) software [401]. Figure 4-18 and Table 4-2 display the results of the analysis. The inset of the figure shows the same data, but for scattering angles between 30 and 50^{o}.

With respect to the results shown in Table 4-2, the crystalline phases were found to be dominated by some form of CuZrTi solid solution phase at 81.7 wt. % with the secondary phase being CuTi at 18.3 wt. %. It was also determined that the CuTi crystallites were of a tetragonal structure corresponding to the P4/mmm space group [422], while the CuTiZr crystallites were composed of a hexagonal structure that corresponded to the $P6_3/mmc$ space group [423].

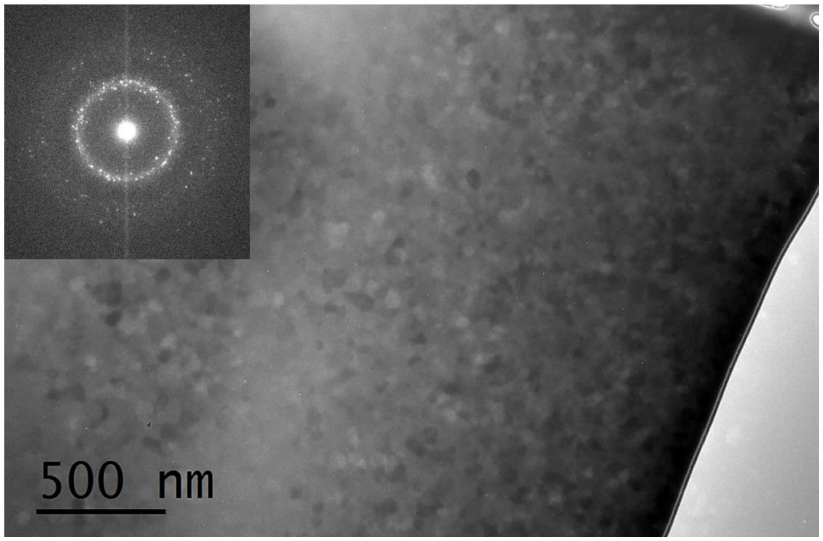

Figure 4-17 TEM bright field imaging and inset which contains the corresponding diffraction pattern of the irradiated region in the $Cu_{60}Zr_{20}Hf_{10}Ti_{10}$ BMG sample irradiated with 9 MeV Ni^{3+} ion beam to a dose of 10 dpa at 360 ºC.

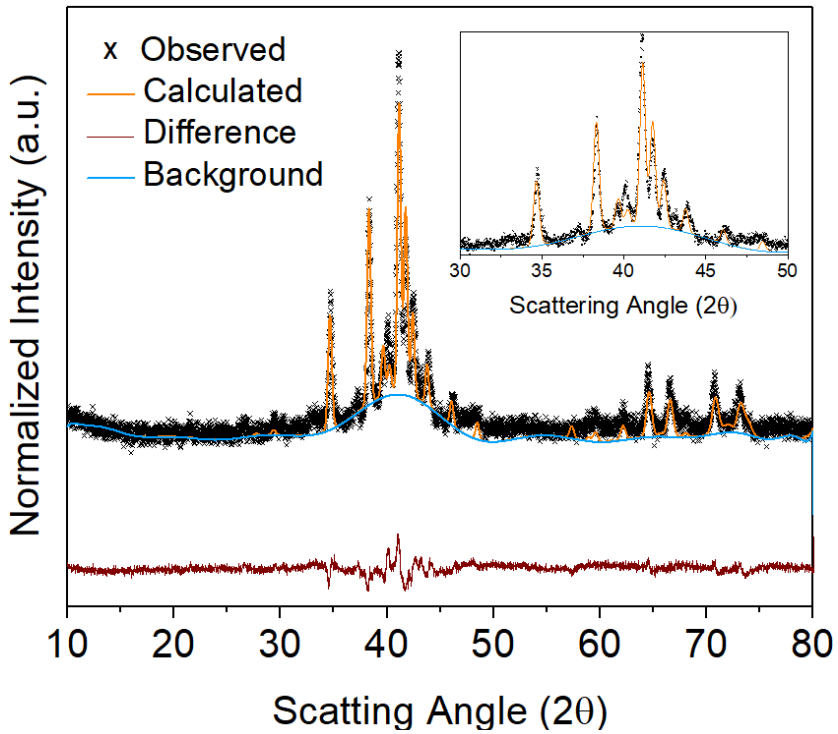

Figure 4-18 Rietveld refinement analysis of X-ray diffraction pattern of partially crystallized $Cu_{60}Zr_{20}Hf_{10}Ti_{10}$ BMG after irradiation by 9 MeV Ni^{3+} to midrange dose of 10 dpa at 360 ºC.

Table 4-2 Rietveld refinement for the goodness of fit (χ^2), software used for the analysis, background fitting function, lattice parameters (a, b, c), the crystal system, the space group, the crystallite volume, and the weight percent for the multi-phase $Cu_{60}Zr_{20}Hf_{10}Ti_{10}$ BMG.

	CuZrTi	**CuTi**
Refinement:		
Goodness of fit, (χ^2)	4.66	
Software	GSAS II [401]	
Variables		
Background	Chebyschev-Background	
Lattice parameters	$a = b, c$	$a = b, c$
Crystal Data:		
Crystal system	Hexagonal	Tetragonal
Space group	$(194)\ P6_3/mmc$	$(123)\ P4/mmm$
$a=b^*$ [Å]	5.167 (2)	3.182 (3)
c^*, [Å]	8.265 (2)	2.853 (3)
Volume, [Å^3]	191.12 (2)	28.904 (9)
Weight Percent	81.7 (7) %	18.3 (5) %

*Estimated standard deviations are 3σ

Interestingly, the results indicated that the Hf in the matrix did not combine with any other elements in the matrix to form compounds. Figures 4-19(a)-(b) displays the glancing XRD patterns (with normalized intensity) for the as-cast and irradiated Cu BMG samples that were irradiated by 9 MeV Ni^{3+} and 5.5 MeV C^{+} to a midrange dose of 0.5 dpa. From both figures it may be observed that for the Cu BMG specimen, no apparent crystallization had occurred during irradiation at any of the irradiation conditions. Again, this lack of evidence for irradiation or thermally induced crystallization is signified by the broad hump for scattering angles ranging from 30 to 46°.

4.2.1.2 Nanoindentation Experiments

4.2.1.2.1 BAM-11 BMG

The nanoindentation indentation data for the BAM-11 BMG specimen irradiated by 9 MeV Ni^{3+} ions to midrange doses of 0.5 and 10 dpa at temperatures ranging from 25 - 360 °C are displayed in figures 4-20(a)-(b). The hardness data below a depth of ~100 nm from the specimen surface was discarded due to large data scatter associated with surface roughness. As discussed in [420, 424], the nanoindenter tip is sensitive to material properties up to 5-10 times beyond its penetration depth. Thus, an indentation depth of approximately 200 nm and 450 nm corresponds to the midrange depth of 1.5 μm and projected ion range of 3 μm, respectively.

The corresponding hardness data for these indentation depths are presented in Table 4-3. Furthermore, evaluation of the depth-dependent hardness, as shown in figure 4-20(a), indicates that an indent depth of 450 nm corresponds to the transition between the ion irradiated and unirradiated

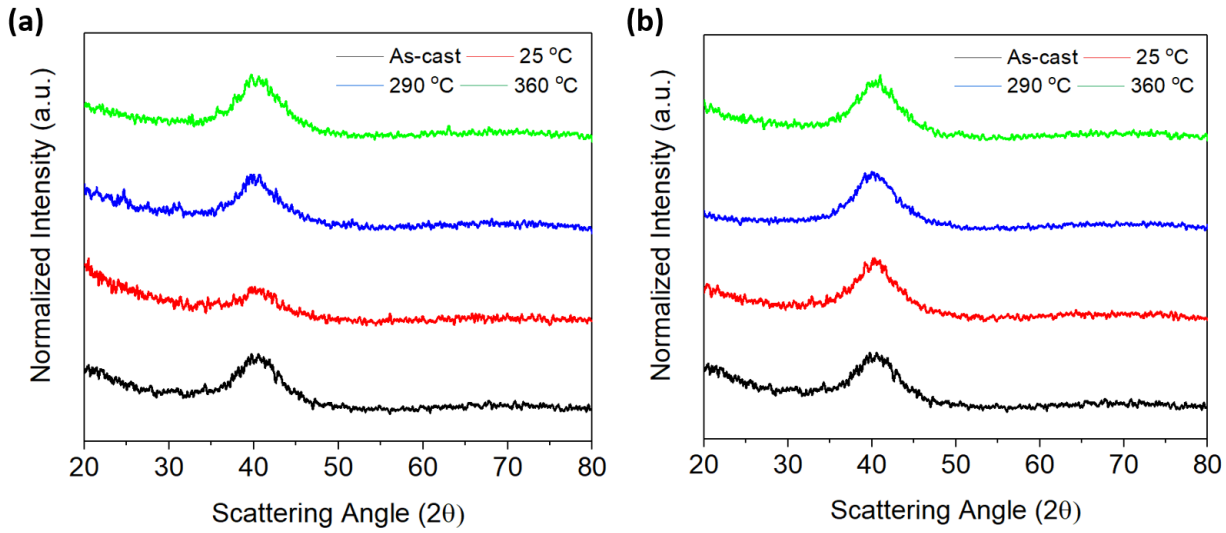

Figure 4-19 Glancing X-ray diffraction patterns for the Cu BMG samples in both the as-cast and (a) 9 MeV Ni^{3+} and (b) 5.5 MeV C^{+} irradiation conditions (0.5 dpa) at different temperatures.

regions. To account for this transition, a vertical line was inserted into figure 4-20(a) to mark the approximate irradiation- and nonirradiation-dominant regimes in the indented regime. Figure 4-20(b) shows a close-up of the irradiated region (100-450 nm indent depths).

In the irradiated region it was found that the hardness for the as-cast condition was within one standard deviation of the room temperature irradiation condition. The above result indicates that a slight, but not statistically significant increase in the hardness of the material occurred during irradiation. It was also observed that with increasing irradiation temperature, the irradiated hardness progressively increased up to the maximum investigated temperature of 360 ^{o}C. As can also be observed in the unirradiated region in figure 4-20(a), the hardness slightly increased between the as-cast condition and the room temperature and 290 ^{o}C irradiation conditions for indent depths beyond 450 nm, where the tip predominantly senses the unirradiated regions. In contrast, the hardness values for the unirradiated region exhibited a large increase for the sample irradiated at 360 ^{o}C, which was associated with the partial crystallization of the specimen. It should also be

(a)

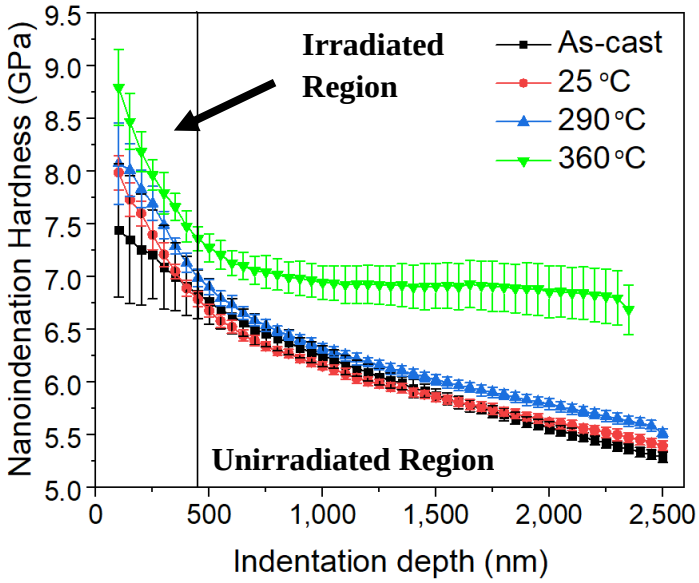

(b)

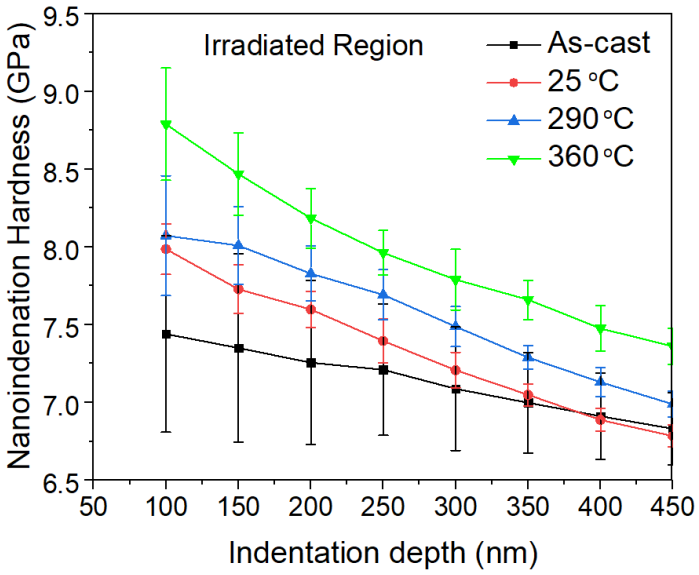

Figure 4-20 Nanoindentation hardness vs. indentation depth for BAM-11 BMG as-cast and irradiated samples (9 MeV Ni^{3+}, 10 dpa) at temperatures ranging from 25 to 360 °C for indent depths ranging from (a) 100-2500 nm (irradiated and unirradiated regions) and (b) the irradiated region (100-450 nm).

Table 4-3 Summary of nanoindentation results on as-cast and irradiated samples (9 MeV Ni^{3+}, dose of 10 dpa) at depths of 200 and 450 nm, corresponding to the midrange and end-of-range regions for the ion irradiated samples.

	Depth (nm)	As-cast	25 °C irr.	290 °C irr.	360 °C irr.
Average Hardness (GPa)	200	7.4 ± 0.6	8.0 ± 0.2	8.1 ± 0.4	8.8 ± 0.4
	450	6.8 ± 0.2	6.8 ± 0.7	7.0 ± 0.1	7.4 ± 0.1

mentioned that the hardness was found to increase with decreasing indent depth, which indicates a significant ISE in the alloy.

Figure 4-21(a) displays the nanoindentation Young's modulus as a function of indenter depth for all the ion irradiation conditions. As can be seen in the graph, the modulus decreased with respect to indentation depth for all conditions. For depths below 200 nm, the modulus for the specimens irradiated to a dose of 10 dpa at 25-360 °C were lower as compared to the as-cast sample. For depths between 250 – 450 nm, the modulus was slightly higher for the irradiated samples, although within error. However, beyond 450 nm, the modulus was significantly higher for the bombarded specimens. Here, the modulus values were within a standard error of each other for the specimens irradiated at room temperature and 290 °C. In addition, the sample irradiated at 360 °C showed a noticeably higher modulus as compared to the other irradiation temperatures although it decreases to values comparable to the other lower temperatures at depths ≥ 2,400 nm. Figures 4-21(b)-(c) show a close-up of both the irradiated (100-450 nm) and unirradiated regions (450-2500 nm).

The ISE hardness analysis based on the Nix-Gao model is plotted in figures 4-22(a)-(c) for the as-cast and the 9 MeV Ni^{3+} ion irradiated BAM-11 BMG specimens. The vertical line in the

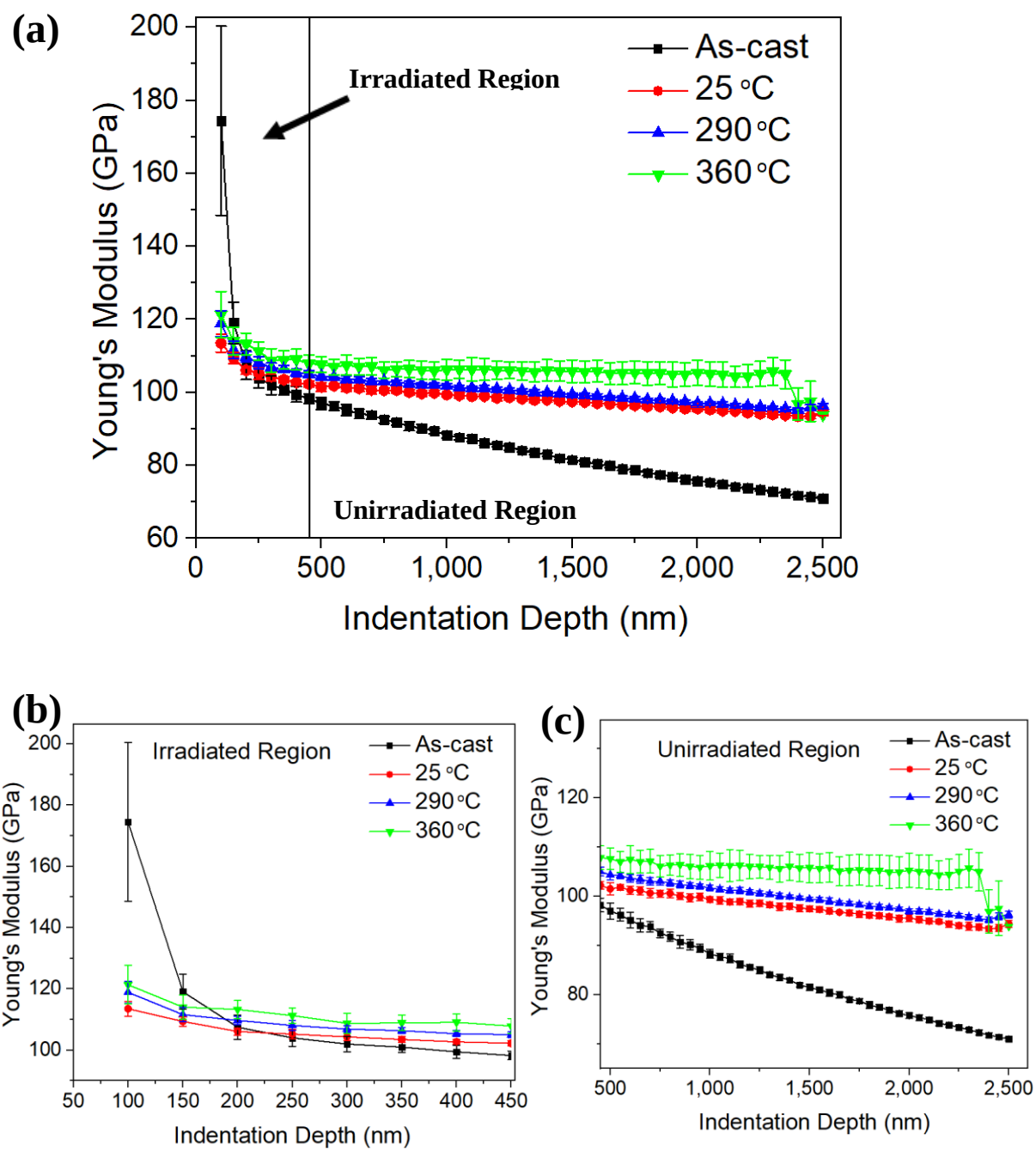

Figure 4-21 Nanoindentation Young's modulus vs. depth for BAM-11 BMG as-cast and irradiated samples (9 MeV Ni^{3+}, 10 dpa) at temperatures ranging from 25 to 360 °C for (a) depths of 100 to 2500 nm, (b) the irradiated region (100-450 nm), and the (c) unirradiated region (450-2500 nm).

plot at 2.2 μm^{-1} [figure 4-22(a)] corresponds to an indenter depth of 450 nm, which is near the expected transition between the hardness dominated by the unirradiated and ion-irradiated regions.

For all indentation depths, the extrapolated hardness values were found to exhibit non-linear behavior with respect to the independent variable, h^{-1}. The ISE hardness analysis from the Lam and Chong model was also plotted for the as-cast material and the specimens irradiated by 9 MeV Ni^{3+} ions [see figures 4-23(a)-(c)]. As was done with the previous figure, a vertical line was inserted into the plot at 1.5 $\mu m^{-0.5}$ [figure 4-23(a)]. This line corresponds to the expected transition between the hardness dominated by the unirradiated and ion-irradiated regions. For every condition, the fitted values based on this latter model did not behave in a linear fashion versus $1/h^{0.5}$ throughout the entire indentation region, although the overall deviation from linear behavior was much less pronounced as compared to figures 4-22(a)-(c). The corresponding fitting parameters are presented in Table 4-4, and as can be observed for the near-surface irradiated region, the fitted bulk hardness value was ~5.8-6.2 GPa for the as-cast and samples irradiated up to 290 ^oC. Also, the reduction was most pronounced for the specimen irradiated at 25 ^oC (-9%), while the sample bombarded at 290 ^oC only softened by about 3%.

Table 4-4 Comparison of the results for the parameters h*, H_0, and the percent change in H_0 [Eq. (3-5)] for the as-cast and the 9 MeV Ni^{3+} irradiated BAM-11 BMG for the irradiated region (100 - 450 nm).

Condition	h^* (nm)	H' (GPa)	Change H_0 (%)
As-cast	3.1	6.4	-
9 MeV Ni^{3+} 25 ^oC	15.2	5.8	-9.4
9 MeV Ni^{3+} 290 ^oC	11.2	6.2	-3.1
9 MeV Ni^{3+} 360 ^oC	19.2	6.2	-3.1

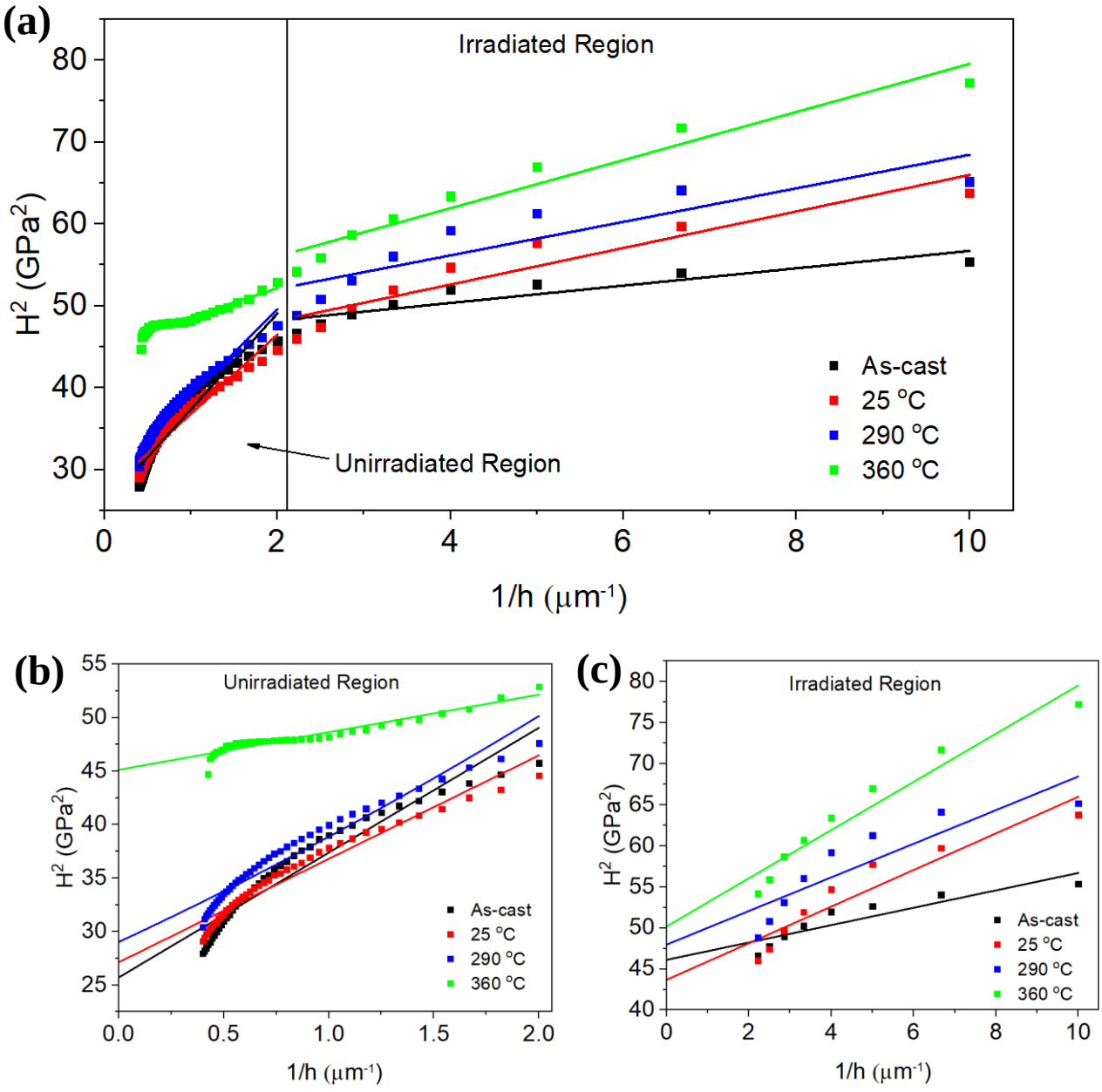

Figure 4-22 H^2 vs. 1/h for BAM-11 BMG in the as-cast and irradiated (9 MeV Ni^{3+}, 10 dpa at different temperatures of 25-360 ^oC) samples for depths of (a) 100-2500 nm, (b) the unirradiated region (450 nm-2500 nm), and (c) the ion irradiated region (150-450 nm).

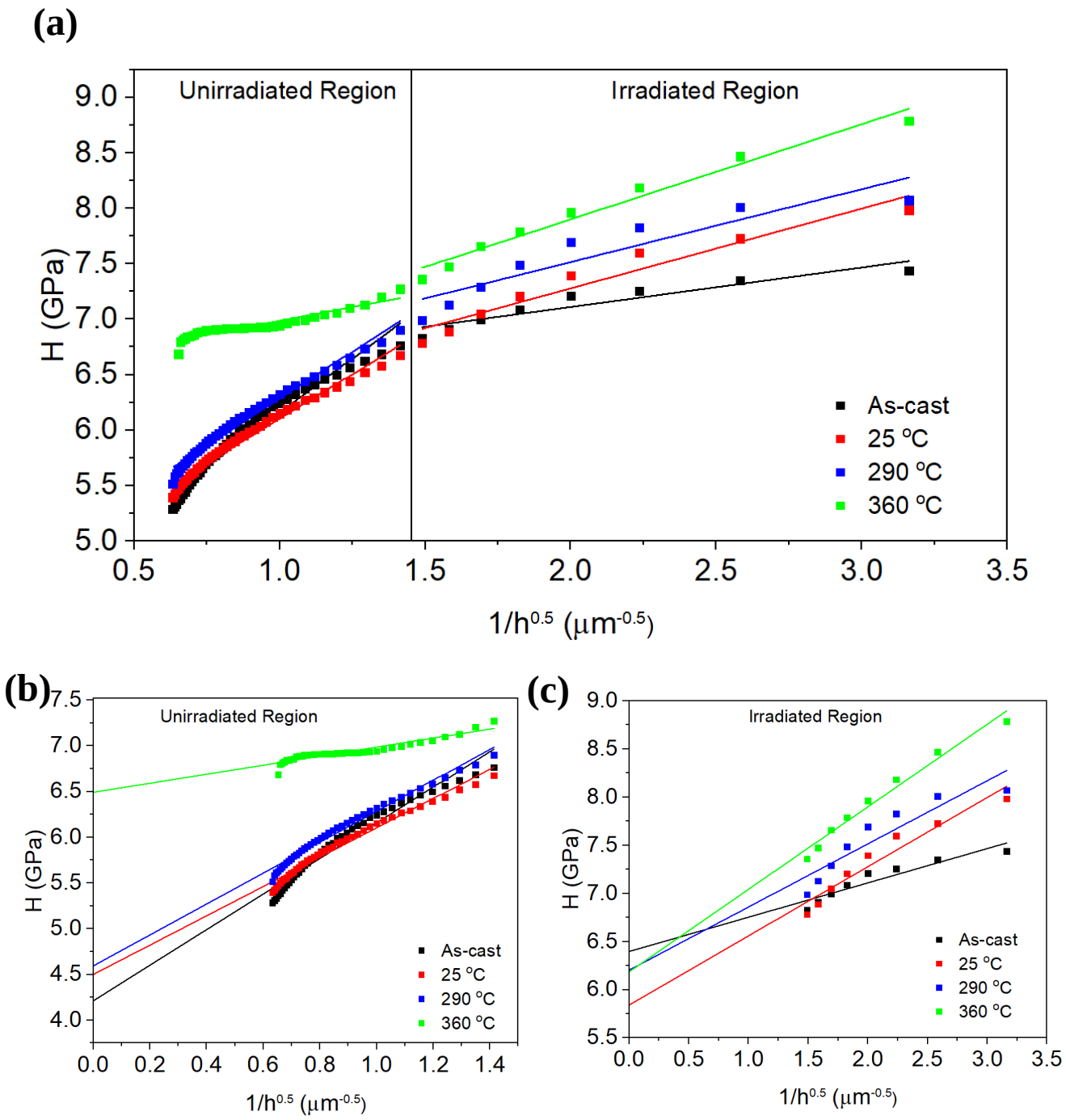

Figure 4-23 H vs. $1/h^{0.5}$ for BAM-11 BMG in the as-cast and irradiated (9 MeV Ni^{3+}, 10 dpa at temperatures of 25-360 °C) samples for depths of (a) 100-2500 nm, (b) the unirradiated region (450 nm-2500 nm), and (c) the ion irradiated region (100-450 nm).

Table 4-5 summarizes the derived hardness parameters, as assessed from the Lam and Chong model, for indentation depths representative of the unirradiated region (500 to ~2500 nm). For the unirradiated region, the extrapolated values of the bulk hardness for the as-cast and irradiated samples up to 290 ^{o}C are ~4.2-4.6 GPa. Comparing the results for the unirradiated and irradiated regions for the specimen irradiated at 360 ^{o}C, H_0 was 6.2 and 6.5 GPa, respectively. Apparently, there is no significant difference in H_0 for either region of the specimen irradiated at the highest temperature, where partial recrystallization occurred throughout the sample during the prolonged exposure. For all conditions, as listed in Table 4-5, the characteristic depth values, i.e. h^*, were one to two orders of magnitude greater than those from the near-surface (ion irradiated) region, as listed in Table 4-4. However, for 360 ^{o}C (partially crystallized), both the irradiated and unirradiated regions have similar h^* values.

The nanoindentation hardness as a function of indenter depth for the as-cast and 9 MeV Ni^{3+} ion irradiated (midrange dose of 0.5 dpa) BAM-11 BMG is presented in figures 4-24(a)-(c). Here, the specimens were irradiated at temperatures ranging from 25 to 360 ^{o}C. Similar to the previous results, the hardness data below a depth of ~100 nm from the specimen surface was discarded due to large data scatter associated with surface roughness. The black line in figure 4-24(a) separates the unirradiated and irradiated regimes in the sample. For depths below 400 nm,

Table 4-5 Comparison of the results for the parameters h*, H_0, and the percent change in H_0 [Eq. (3-5)] for the as-cast and the 9 MeV Ni^{3+} irradiated BAM-11 BMG for the unirradiated region (500 to ~2500 nm).

Condition	h^* (nm)	H_0 (GPa)	Change H_0 (%)
As-cast	210	4.2	-
9 MeV Ni^{3+} 25 ^{o}C	130	4.5	7.1
9 MeV Ni^{3+} 290 ^{o}C	130	4.6	9.5
9 MeV Ni^{3+} 360 ^{o}C	18	6.5	55.8

the alloy exhibited an increase in hardening following ion bombardment to a dose of 0.5 dpa at 25-360 ^{o}C.

As compared to the as-cast condition, there was a slight increase in the hardness although it was within one standard deviation. On the other hand, there was a more pronounced increase in the hardness for the specimens irradiated at 290 and 360 ^{o}C. Moreover, the specimens irradiated at the above temperatures continued to display significantly higher hardness values as compared to the as-cast condition for depths beyond the irradiation region. Unexpectedly, the specimen irradiated at room temperature displayed significantly lower hardness values, beyond three standard deviations as compared to the as-cast state.

Figures 4-25(a)-(c) shows the nanoindentation Young's modulus as a function of indenter depth for the as cast and 9 MeV Ni^{3+} irradiated BAM-11 BMG to a midrange dose of 0.5 dpa (25 to 360 ^{o}C). As with the hardness data, the data below a depth of ~100 nm from the sample surface was discarded due to large data scatter associated with surface roughness. A vertical line was inserted into the figure to separate the irradiated and unirradiated regions in the sample. The modulus decreased with respect to the indentation depth for the as-cast and irradiation conditions.

For indentation depths below 200 nm, the modulus was significantly greater for the irradiated specimens compared to the as-cast condition. Moreover, the modulus for the specimens irradiated at 290 ^{o}C and 360 ^{o}C was slightly greater than the as-cast condition in the entire indentation region. For indent depths greater than 1,000 nm, the measured modulus of the specimen irradiated at room temperature was significantly lower than the as-cast condition, which is similar to the low hardness behavior at deep depths for this irradiation condition [figure 4-24(c)].

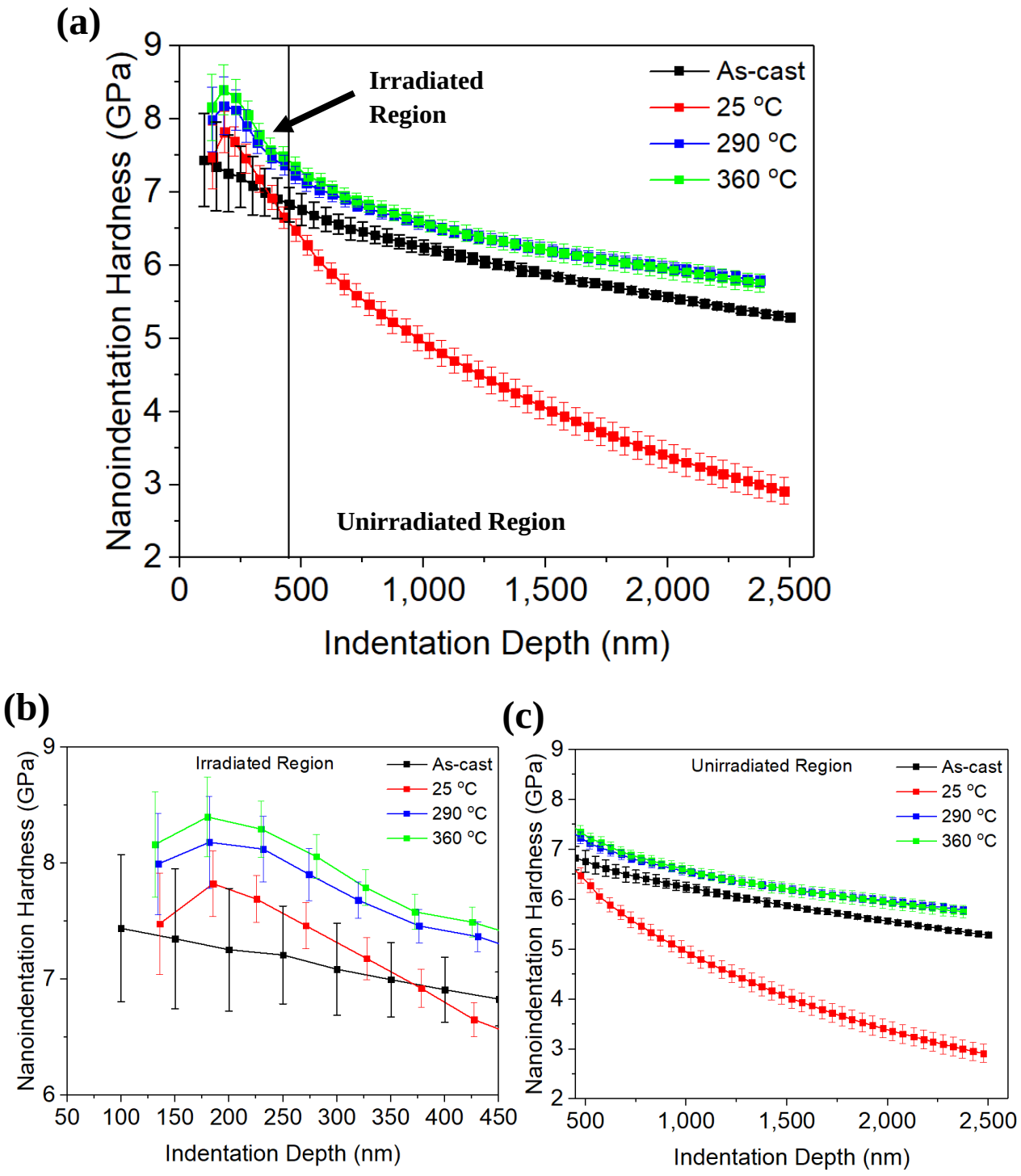

Figure 4-24 Nanoindentation hardness vs. depth for BAM-11 BMG as-cast and irradiated samples (9 MeV Ni^{3+} to 0.5 dpa) at different temperatures for (a) depths from 100 to 2500 nm, (b) the irradiated region (100-450 nm), and the (c) unirradiated region (450-2500 nm).

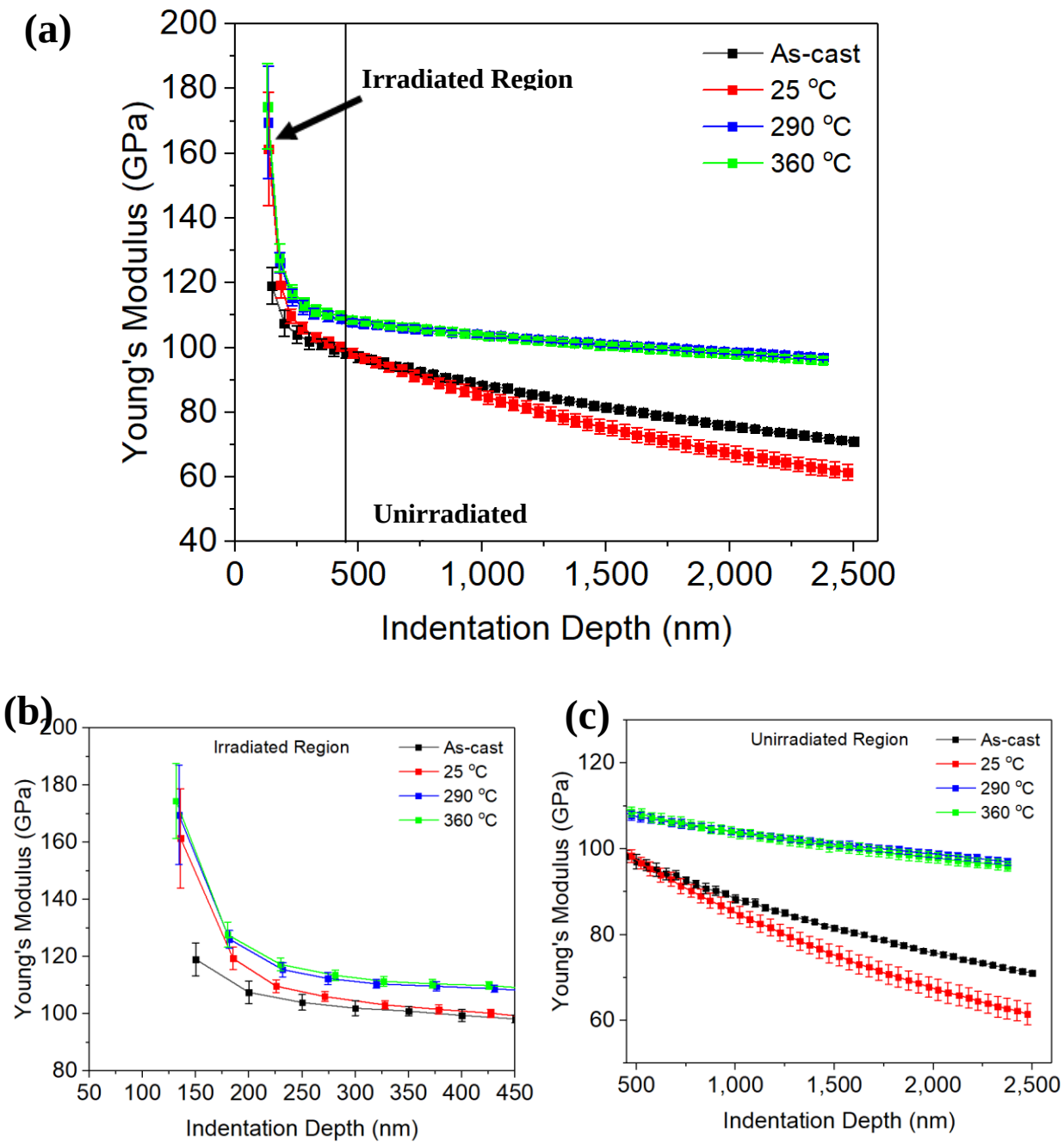

Figure 4-25 Nanoindentation Young's modulus vs. depth for BAM-11 BMG as-cast and irradiated samples (9 MeV Ni^{3+} to 0.5 dpa) at temperatures ranging from 25 to 360 °C for (a) depths of 100-2500 nm, (b) the irradiated region (100-450 nm), and the (c) unirradiated region (450-2500 nm).

Figures 4-26(a)-(c) presents the hardness values for the BAM-11 BMG irradiated by 5.5 MeV C^+ to a midrange dose of 0.5 dpa at temperatures ranging from 25 - 360 ^oC. The sample irradiated at 290 ^oC exhibited significantly higher values as compared to any of the other conditions in both the unirradiated and irradiated regions of the material. The grazing incidence XRD results, as shown in in figure 4-14(b), indicate that the high hardness is associated with partial crystallization of this specimen. On the other hand, the sample irradiated at room temperature exhibited values that were below the hardness values of the as-cast condition for depths between 100 - 2,200 nm. As for the specimen irradiated at 360 ^oC, it displayed similar hardness values as the as-cast condition, although the values were significantly lower for depths beyond ~1,000 nm.

The Young's modulus values for the BAM-11 BMG samples that were irradiated by 5.5 MeV C^+ ions are presented in figures 4-27(a)-(c). In the irradiated region, the measured modulus was similar to the as-cast values. Some anomalous behavior was observed for the BAM-11 BMG specimen irradiated at room temperature, where the modulus values were significantly greater as compared to the as-cast sample for indentation depths greater than ~750 nm. As compared to the as-cast state, the modulus at large depths (corresponding to the unirradiated substrate material) was markedly greater for the specimens irradiated at the higher temperature.

4.2.1.2.2 Cu BMG

The depth dependent nanoindentation hardness for both the as-cast and the 9 MeV Ni^{3+} ion irradiated Cu BMG (midrange dose of 10 dpa) samples is presented in figure 4-28(a). Similar to the BAM-11 BMG, there was a noticeable indentation size effect, indicated by a decrease in the hardness values with respect to the indentation depth. Similar to the previous nanoindentation results for the BAM-11 BMG, the data below 100 nm was omitted, and a line was inserted at 450

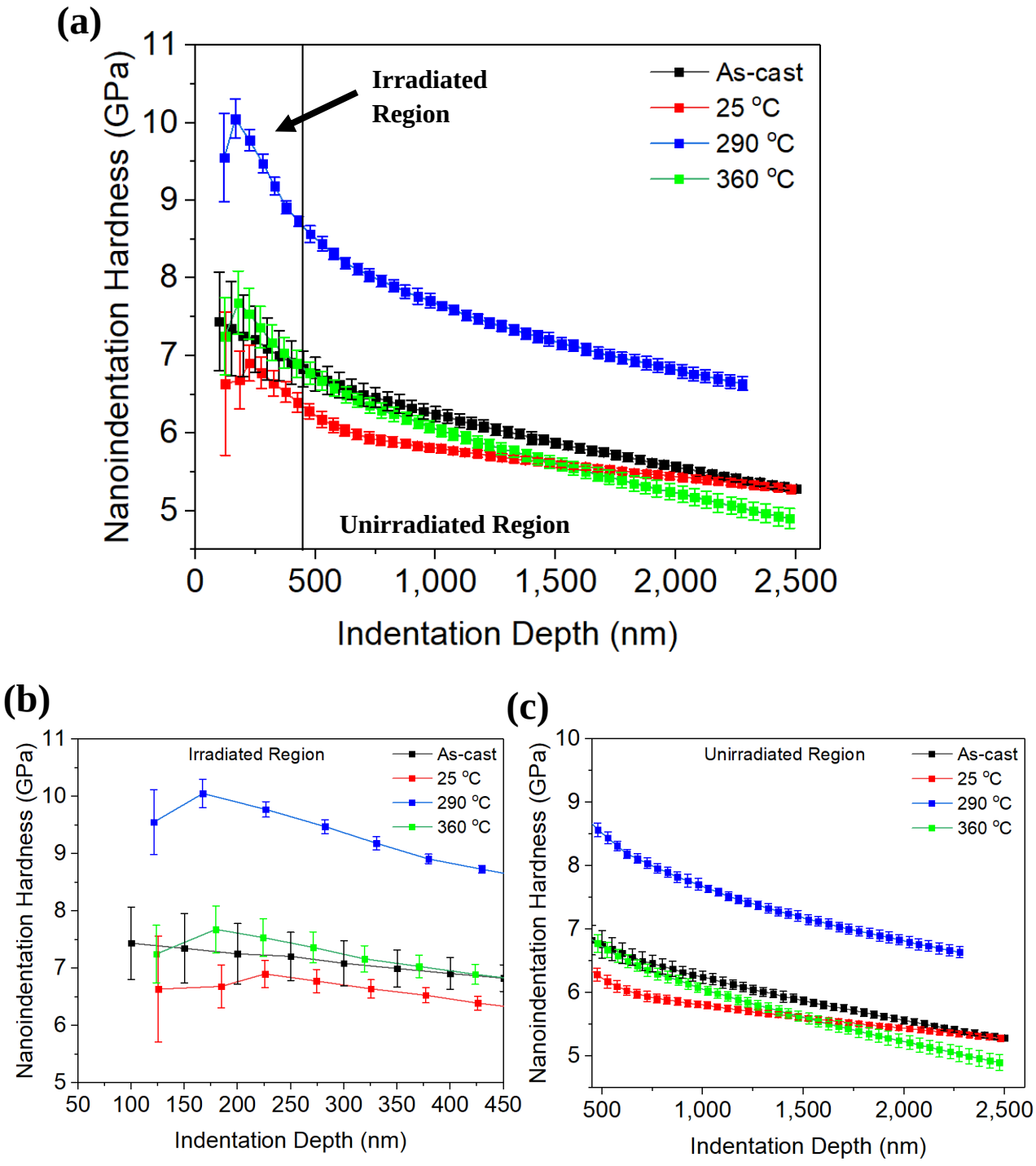

Figure 4-26 Nanoindentation hardness vs. depth for BAM-11 BMG as-cast and irradiated samples (5.5 MeV C^+, 0.5 dpa) at different temperatures (a) depths ranging from 100-2500 nm, (b) the irradiated region (100-450 nm), and the (c) unirradiated region (450-2500 nm).

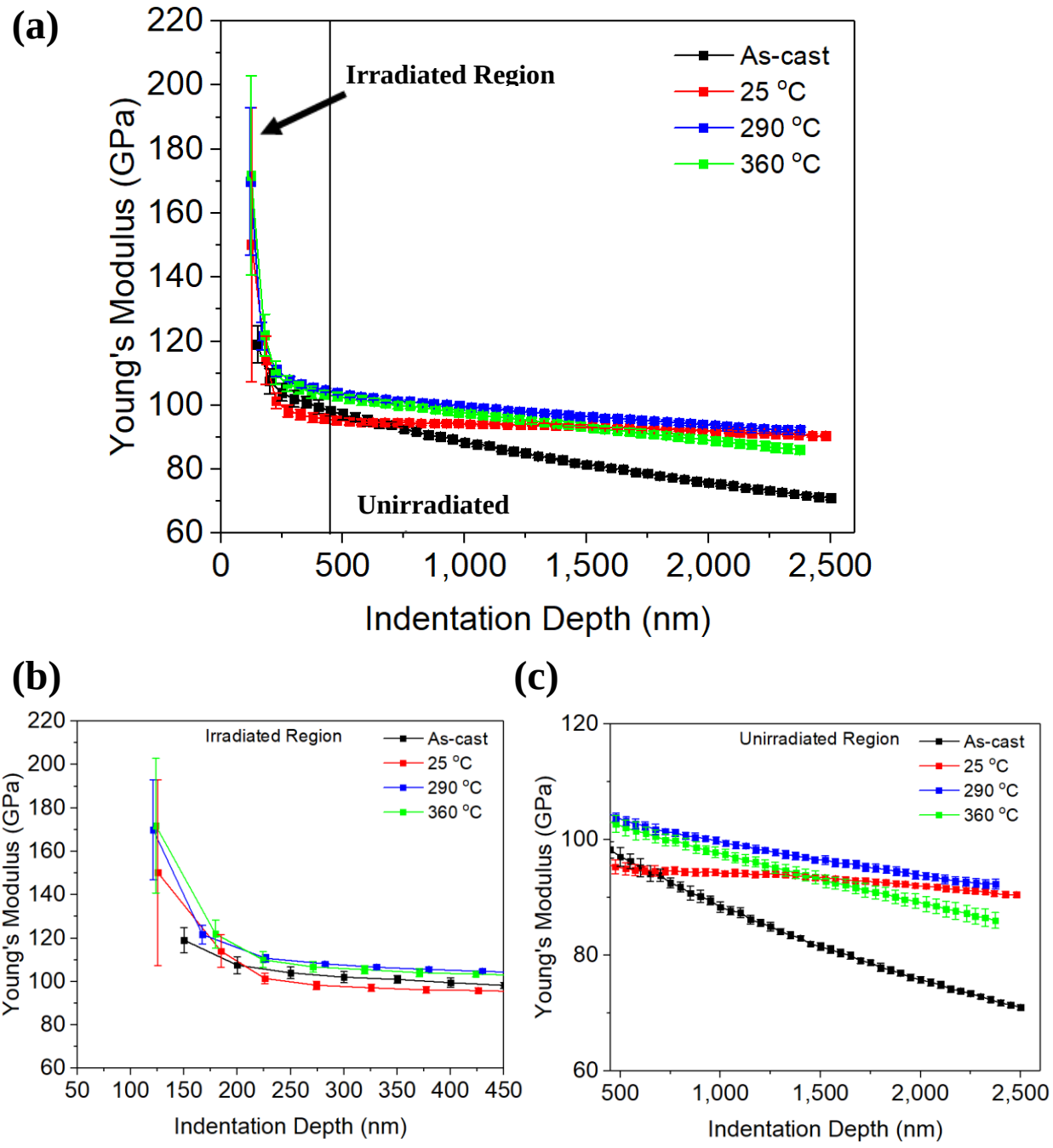

Figure 4-27 Nanoindentation Young's modulus vs. depth for BAM-11 BMG as-cast and irradiated samples (5.5 MeV C^+, 0.5 dpa) at different temperatures for (a) depths of 100 to 2500 nm, (b) the irradiated region (100-450 nm), and the (c) unirradiated region (450-2500 nm).

nm to demarcate between the irradiated and unirradiated regimes. In the Cu BMG, the hardness values which correspond to a midrange dose of 10 dpa and the projected ion range correspond to distances of 1.2 and 2.8 μm beneath the surface. These depth values correspond to depths of 200 and 450 nm since the nanoindenter tip is sensitive to substrate regions that are 5-10 times beyond its penetration depth [98, 424]. The hardness values at these depths are displayed in Table 4-6. Figure 4-28(b) displays the depth dependent hardness data for the irradiated region, which corresponds to depths of 100-450 nm beneath the surface. In the irradiated region, the hardness for the room temperature condition did not noticeably increase as compared to the values for the as-cast condition. The hardness values for the unirradiated region exhibited a large increase for the sample irradiated at 360 ^{o}C due to partial crystallization (in both the irradiated and unirradiated regions).

To compare the effects of annealing and irradiation damage on the nanoindentation properties for the sample that partially crystallized during irradiation at 360 ^{o}C, the nanoindentation hardness was measured in the irradiated and unirradiated regions of the irradiated surface. The unirradiated region of the sample corresponds to the portion of the surface that was shielded by the front plate during irradiation. As can be observed from figure 4-29, which compares the nanoindentation hardness of the two sections, the hardness values were quite similar for all indentation depths.

Table 4-6 Summary of nanoindentation results on as-cast and irradiated $Cu_{60}Zr_{20}Hf_{10}Ti_{10}$ BMG samples (9 MeV Ni^{3+}, midrange dose of 10 dpa) at depths of 200 and 450 nm.

	Depth (nm)	As-cast	25 ^{o}C	290 ^{o}C	360 ^{o}C
Average Hardness (GPa)	200	8.4 ± 0.3	8.4 ± 0.2	8.4 ± 0.3	10.6 ± 0.4
	450	7.6 ± 0.1	7.6 ± 0.1	7.4 ± 0.2	9.5 ± 0.2

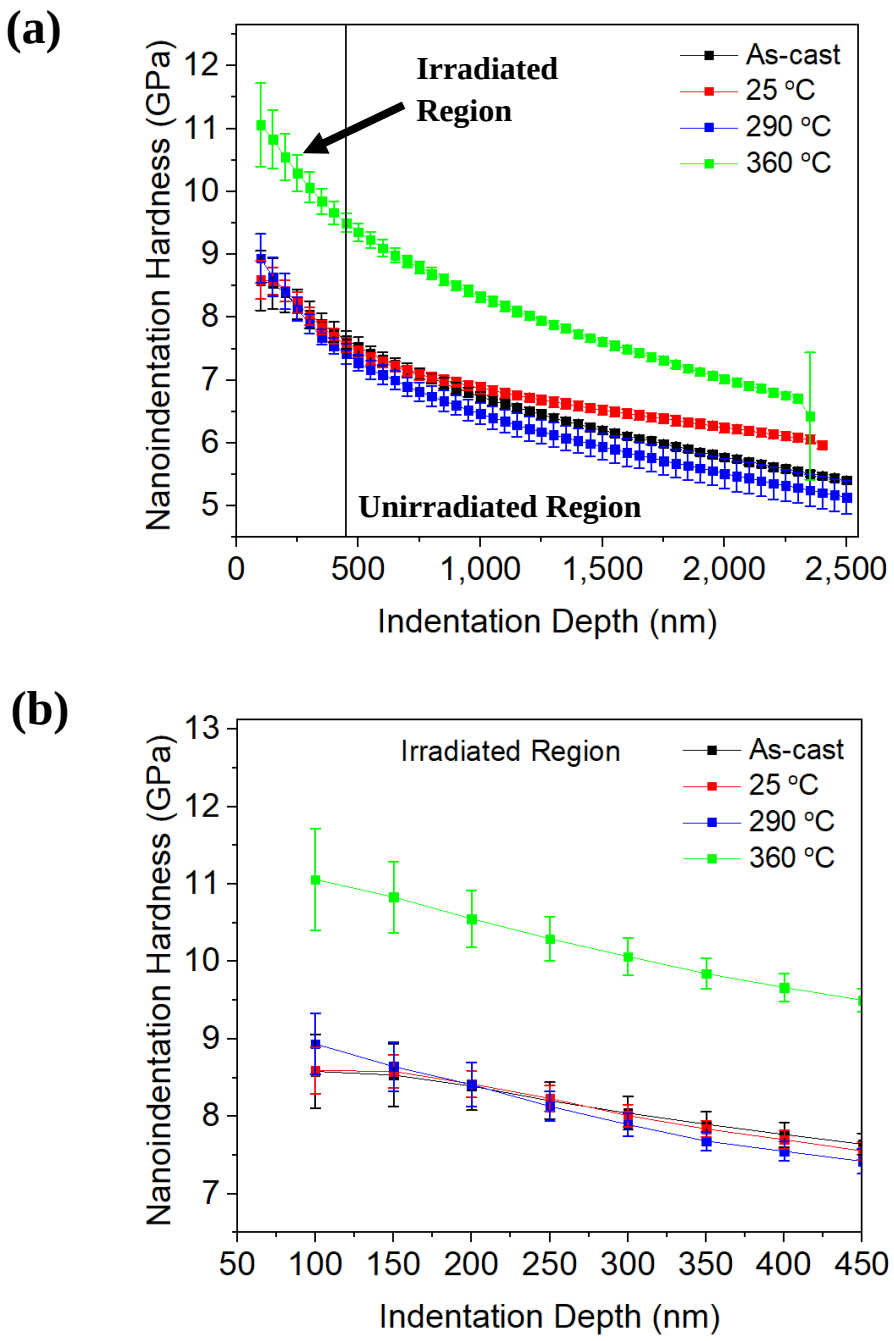

Figure 4-28 Nanoindentation hardness vs. indentation depth for $Cu_{60}Zr_{20}Hf_{10}Ti_{10}$ BMG as-cast and irradiated samples (9 MeV Ni^{3+} to 10 dpa) at different (a) depths ranging from 100-2500 nm and (b) the irradiated region (100-450 nm).

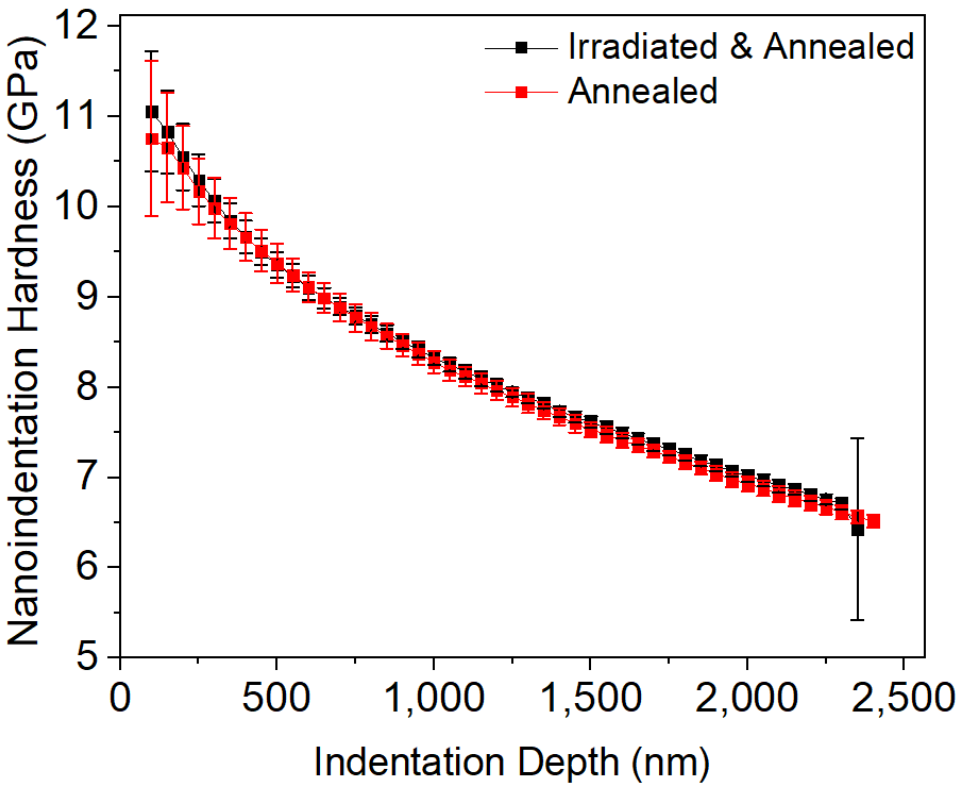

Figure 4-29 A comparison of the nanoindentation hardness in both the irradiated region and the unirradiated substrate (polished front surface shielded from the ion beam) in the $Cu_{60}Zr_{20}Hf_{10}Ti_{10}$ BMG alloy after irradiation by 9 MeV Ni^{3+} to 10 dpa at 360 ^{o}C.

Figures 4-30(a)-(c) display the ISE hardness data for the Lam and Chong model, as applied to the as-cast and irradiated (9 MeV Ni^{3+}) Cu BMG specimens. Similar to figure 4-23(a), a vertical line was inserted at ~1.5 $\mu m^{-0.5}$ in figure 4-30(a) to separate the nonirradiation and irradiation-dominant regimes. As can be observed, the fitted values based on this model for the as-cast and the irradiated specimens did not follow the predicted linear behavior versus $1/h^{0.5}$ throughout the entire indentation region, indicating that the quantitative values derived from this analysis are somewhat unreliable. The corresponding fitting parameters for the irradiated region (100 – 450 nm) are presented in Table 4-7. As can be seen in the table, the fitted H_0 hardness values did not vary significantly for the unirradiated (as-cast) and irradiated samples at 25 and 290 ^oC. For the near-surface irradiated region, the extrapolated bulk hardness was ~7.1 to 7.6 GPa for the as-cast materials and for the samples irradiated up to 290 ^oC. The detailed fitted hardness values imply a slight radiation-induced softening. The fitted reduction in hardness was most pronounced for the specimen irradiated at 290 ^oC (-6.6%), while the sample bombarded at 25 ^oC softened by about 1.3%. However, H_0 was 9.3 GPa for the specimen irradiated at 360 ^oC, which corresponded to an increase in the hardness of 20 % as compared to the as-cast state due to the partial crystallization of the material.

The hardness parameters, as derived from the Lam and Chong model for indentation depths 500 - ~2500 nm (unirradiated region), are presented in Table 4-8. With regards to the extrapolated bulk hardness, H_0, the values ranged from ~4.7 to 5.0 GPa for the as-cast and irradiated samples (25 and 290 ^oC). Comparing the results for the irradiated and unirradiated regions for the specimen irradiated at 360 ^oC, H_0 was 9.3 and 6.0 GPa, respectively. This difference in the hardness was due to non-linearity of the data, which produced different extrapolation values. For all conditions, as listed in Table 4-7, the characteristic depth values, i.e.

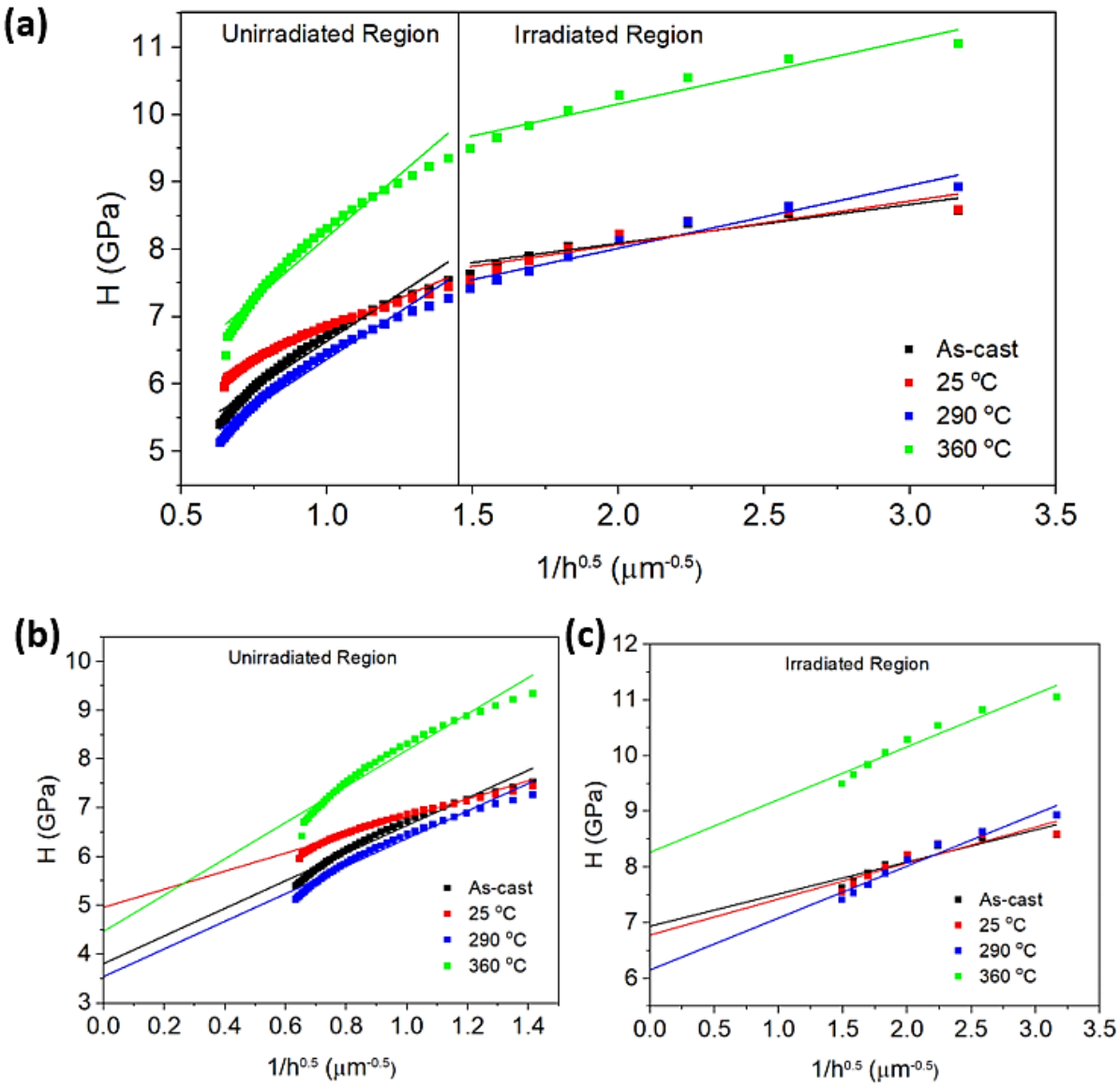

Figure 4-30 H vs. $1/h^{0.5}$ for as-cast vs. irradiated $Cu_{60}Zr_{20}Hf_{10}Ti_{10}$ BMG (9 MeV Ni^{3+}, 10 dpa) at different temperatures for (a) depths ranging from 100-2500 nm, (b) the unirradiated region (450 nm-2500 nm), and (c) the irradiated region (100-450 nm).

Table 4-7 Comparison of the results for the parameters h, H_0, and the percent change in H_0 [Eq. (3-5)] for the as-cast and the 9 MeV Ni^{3+} irradiated $Cu_{60}Zr_{20}Hf_{10}Ti_{10}$ BMG for the irradiated region (100 - 450 nm).

Condition	h^* (nm)	H_0 (GPa)	Change H_0 (%)
As-cast	33.8	7.6	-
9 MeV Ni^{3+} 25 ^oC	38.3	7.5	-1.3
9 MeV Ni^{3+} 290 ^oC	63.2	7.1	-6.6
9 MeV Ni^{3+} 360 ^oC	47.4	9.3	22

h^*, were one order of magnitude greater than those from the near-surface (ion irradiated) region, as listed in Table 4-6.

Figure 4-31(a) presents the nanoindentation hardness as a function of indenter depth for the as cast and 9 MeV Ni^{3+} irradiated (25-360 ^oC) Cu BMG. For depths in the irradiated region, the specimen irradiated at 25 ^oC displayed greater hardening as compared to the specimen irradiated at 290 ^oC. Moreover, the samples irradiated at room temperature and 360 ^oC exhibited significantly greater hardness values as compared to the as-cast state. For depths beyond 450 nm, which correspond to the unirradiated region of the sample, the specimens irradiated at 290 ^oC and 360 ^oC exhibited significantly higher values as compared to the as-cast condition. However, the sample irradiated at room temperature had similar hardness values as compared to the as-cast state, as shown in figure 4-31(c).

Figures 4-32(a)-(c) shows the nanoindentation Young's modulus as a function of indenter depth for the as cast and 9 MeV Ni^{3+} irradiated (0.5 dpa, 25-360 ^oC) Cu BMG. The Young's modulus behavior was similar for the BAM-11 BMG irradiated at the same set of conditions, except that the modulus was significantly higher for the irradiated, as compared to the as-cast

Table 4-8 Comparison of the results for the parameters h*, H_0, and the percent change in H_0 [Eq. (3-5)] for the as-cast and the 9 MeV Ni^{3+} irradiated $Cu_{60}Zr_{20}Hf_{10}Ti_{10}$ BMG for the unirradiated region (500 - ~2500 nm).

Condition	h^* (nm)	H_0 (GPa)	Change H_0 (%)
As-cast	7.2×10^2	5.0	-
9 MeV Ni^{3+} 25 ºC	3.7×10^2	5.8	16.0
9 MeV Ni^{3+} 290 ºC	7.8×10^2	4.7	-6.0
9 MeV Ni^{3+} 360 ºC	8.0×10^2	6.0	20

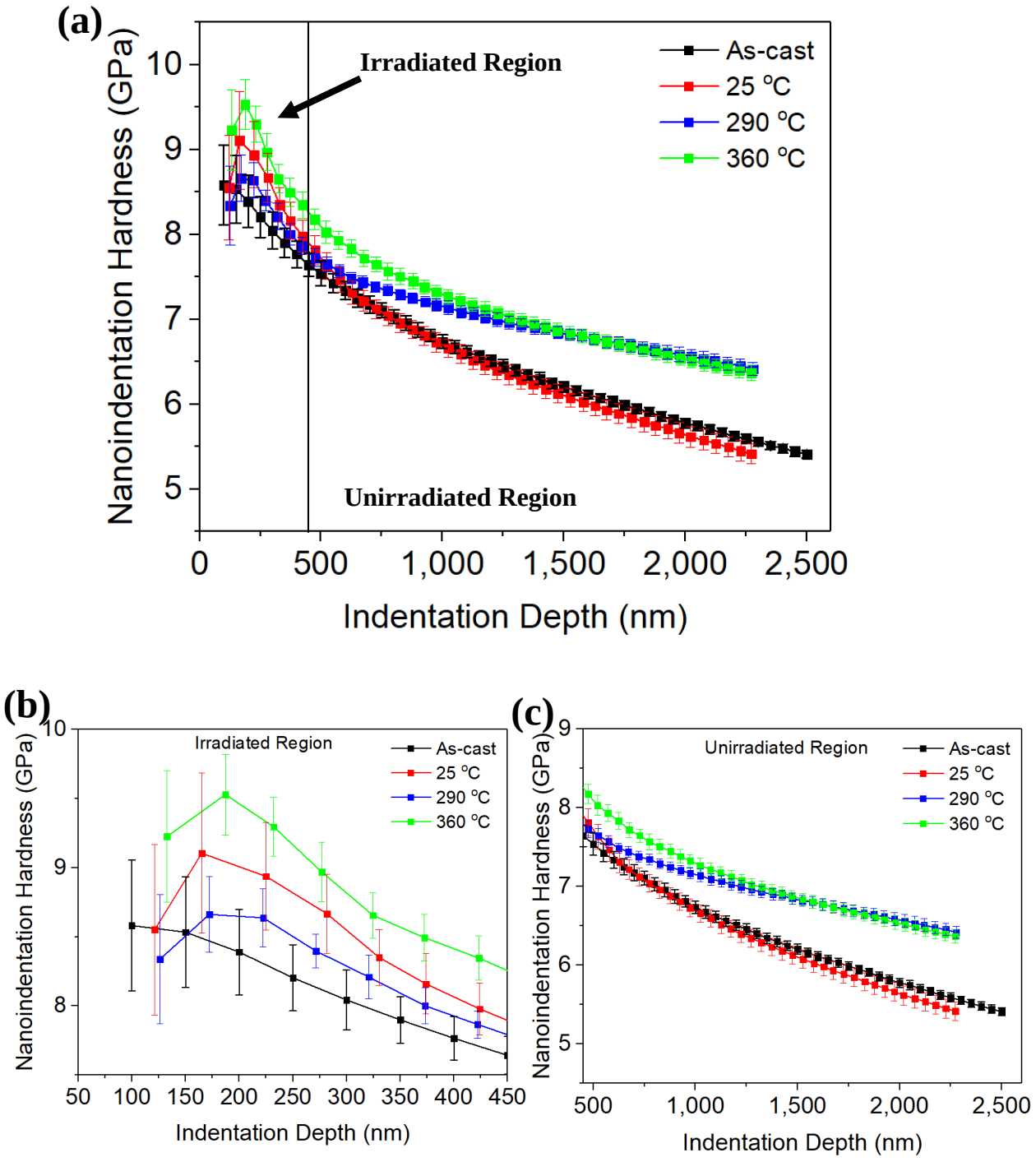

Figure 4-31 Nanoindentation hardness vs. depth for Cu BMG as-cast and irradiated samples (9 MeV Ni^{3+}, 0.5 dpa) at different temperatures for (a) depths ranging from 100-2500 nm, (b) the irradiated region (100-450 nm), and the (c) unirradiated region (450-2500 nm).

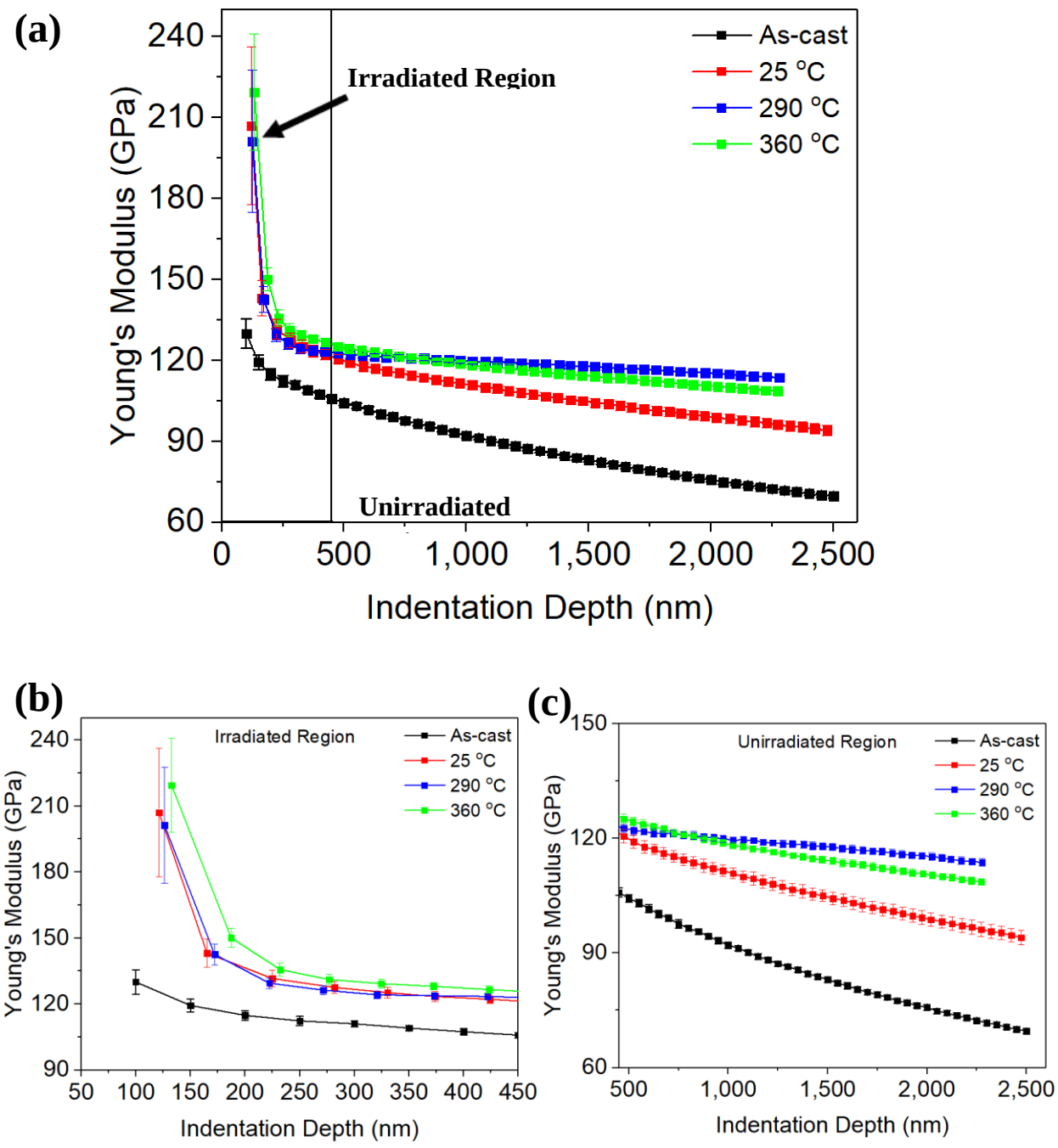

Figure 4-32 Nanoindentation Young's modulus vs. depth for Cu BMG as-cast and irradiated samples (9 MeV Ni^{3+}, 0.5 dpa) at 25-360 °C for (a) depths ranging from 100-2500 nm, (b) the irradiated region (100-450 nm), and the (c) unirradiated region (450-2500 nm).

sample [see figures 4-25(a)-(c)]. The modulus decreased with respect to the indentation depth for all the irradiation conditions. For depths below 200 nm, the modulus was significantly greater for the irradiated specimens, as compared to the as-cast condition. Furthermore, the modulus was significantly greater for the irradiated specimens in the entire indentation region.

Figures 4-33(a)-(c) presents the hardness values for the Cu BMG irradiated by 5.5 MeV C^+ to a midrange dose of 0.5 dpa at temperatures ranging from 25 – 360 ^oC. In the irradiated region, the specimens irradiated at room temperature and 290 ^oC exhibited hardness values that were lower than those for the as-cast state. On the other hand, the hardness values were higher for the sample that had been irradiated at 360 ^oC. In the unirradiated region, the specimen irradiated at 290 ^oC displayed values that were greater than those for the unirradiated sample for depths beyond 1,100 nm.

The Young's modulus values for the Cu BMG specimens that were irradiated by 5.5 MeV C^+, is presented in figure 4-34(a)-(c). As for the BAM-11 BMG [see figures 4-27(a)-(c)], there was some anomalous behavior for the specimen irradiated at room temperature, where the values were significantly greater for indentation depths greater than ~750 nm. Furthermore, the modulus was markedly greater for the samples irradiated at the higher temperature, as compared to the as-cast state.

4.2.2 Neutron Irradiation Experiments

There are no known prior studies on the effects of neutron irradiation on Zr based BMGs. Furthermore, there are no studies which have compared the effects of irradiation damage and heat treatment on the nanoscale mechanical properties of amorphous alloys. The current investigation examines the effects of neutron irradiation and annealing on the nanoindentation hardness and

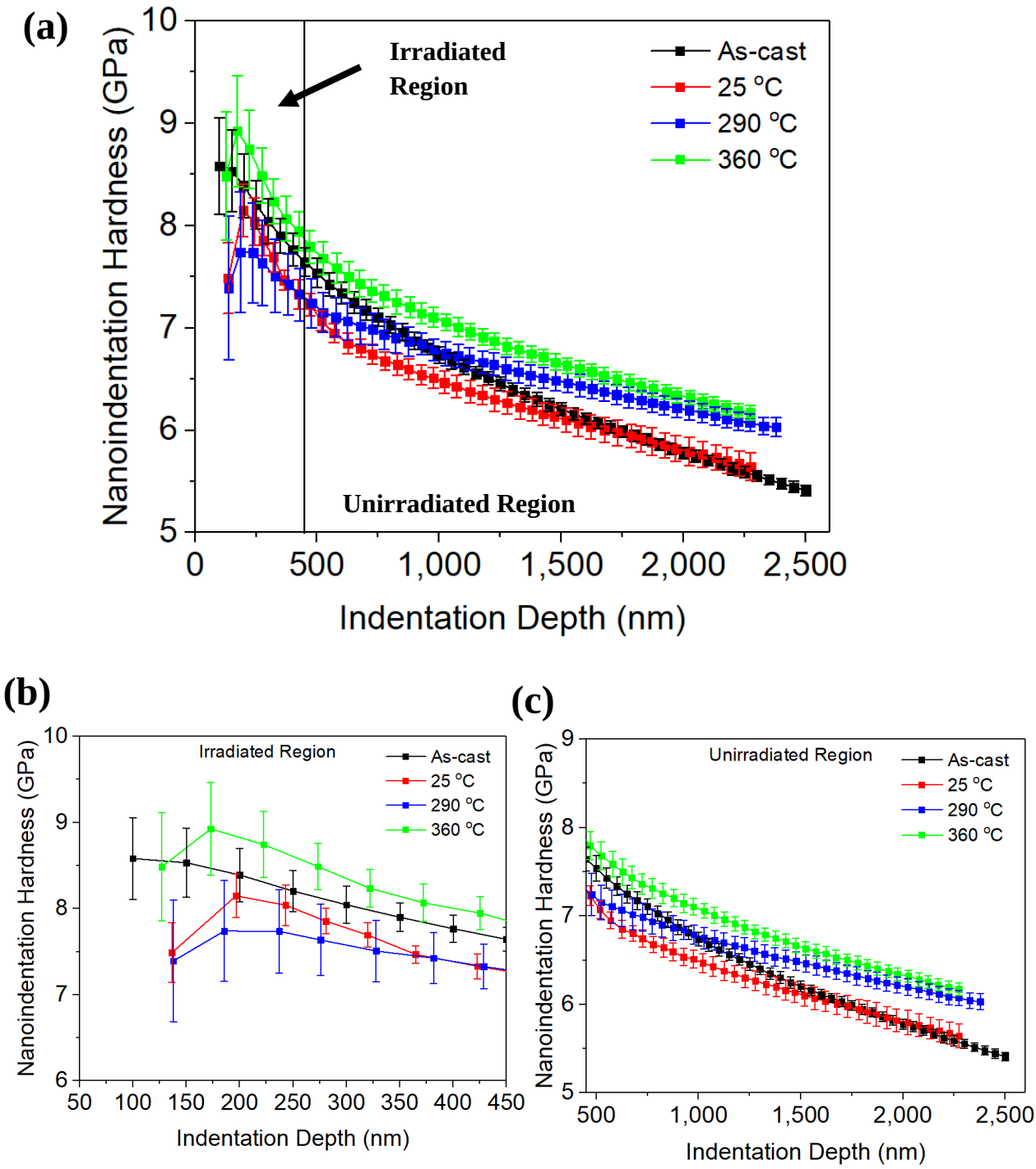

Figure 4-33 Nanoindentation hardness vs. depth for Cu BMG as-cast and irradiated samples (5.5 MeV C^+, 0.5 dpa) at different temperatures for (a) depths ranging from 100-2500 nm, (b) the irradiated region (100-450 nm), and the (c) unirradiated region (450-2500 nm).

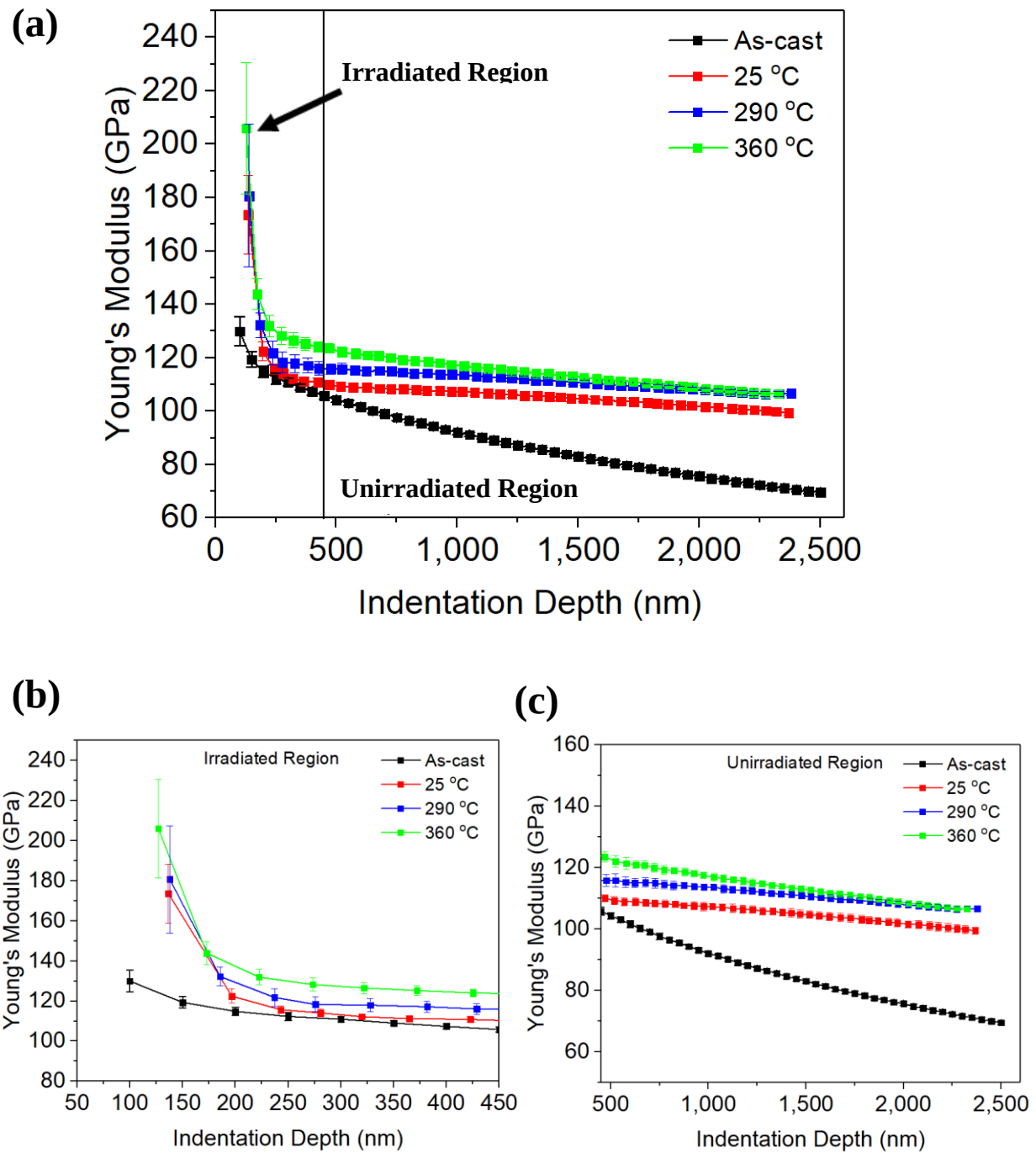

Figure 4-34 Nanoindentation Young's modulus vs. depth for Cu BMG as-cast and irradiated samples (5.5 MeV C^+, 0.5 dpa) at different temperatures for (a) depths of 100-2500 nm, (b) the irradiated region (100-450 nm), and the (c) unirradiated region (450-2500 nm).

short-range ordering of the BAM-11 BMG. Additionally, this work expands upon previous studies that examined the competing effects of irradiation and annealing on the properties of metallic glasses. Importantly, the results, as presented below, is intended to elucidate the effects of annealing and irradiation displacement damage on the behavior of these complex alloy systems.

4.2.2.1 Neutron Diffraction Characterization

Figures 4-35(a)-(b) present the PDF and structure function for the annealed and 0.1 dpa neutron irradiated BAM-11 BMG samples. The inset highlights the upper portion of the first peak for both figures. The fluctuating pattern of the curves signifies that the specimens did not crystallize during annealing or neutron irradiation. Importantly, the changes in the shape of the peaks indicates that irradiation and thermal effects altered the microstructure of the metallic glass. This effect can be seen in the curve representing the non-irradiated sample that was annealed at 300 ^{o}C for two weeks, which had the highest and most narrow peak as compared to the other conditions. This was opposed to the specimen that was irradiated to 0.1 dpa without post-annealing, where the associated curve exhibited an opposite trend. On the other hand, the specimens that were annealed after being neutron irradiated exhibited peak behavior that was intermediate between that of the as-received and the irradiated-only conditions.

4.2.2.2 Transmission Electron Microscopy Characterization

Figure 4-36(a)-(e) displays the TEM BF and diffraction patterns of the as-cast, neutron irradiated (0.1 dpa), and annealed specimens. As can be observed, there were no significant changes in the microstructures of the specimens and the amorphous nature of the specimens. Furthermore, the high-resolution imaging did not reveal the presence of any nanocrystallites. All

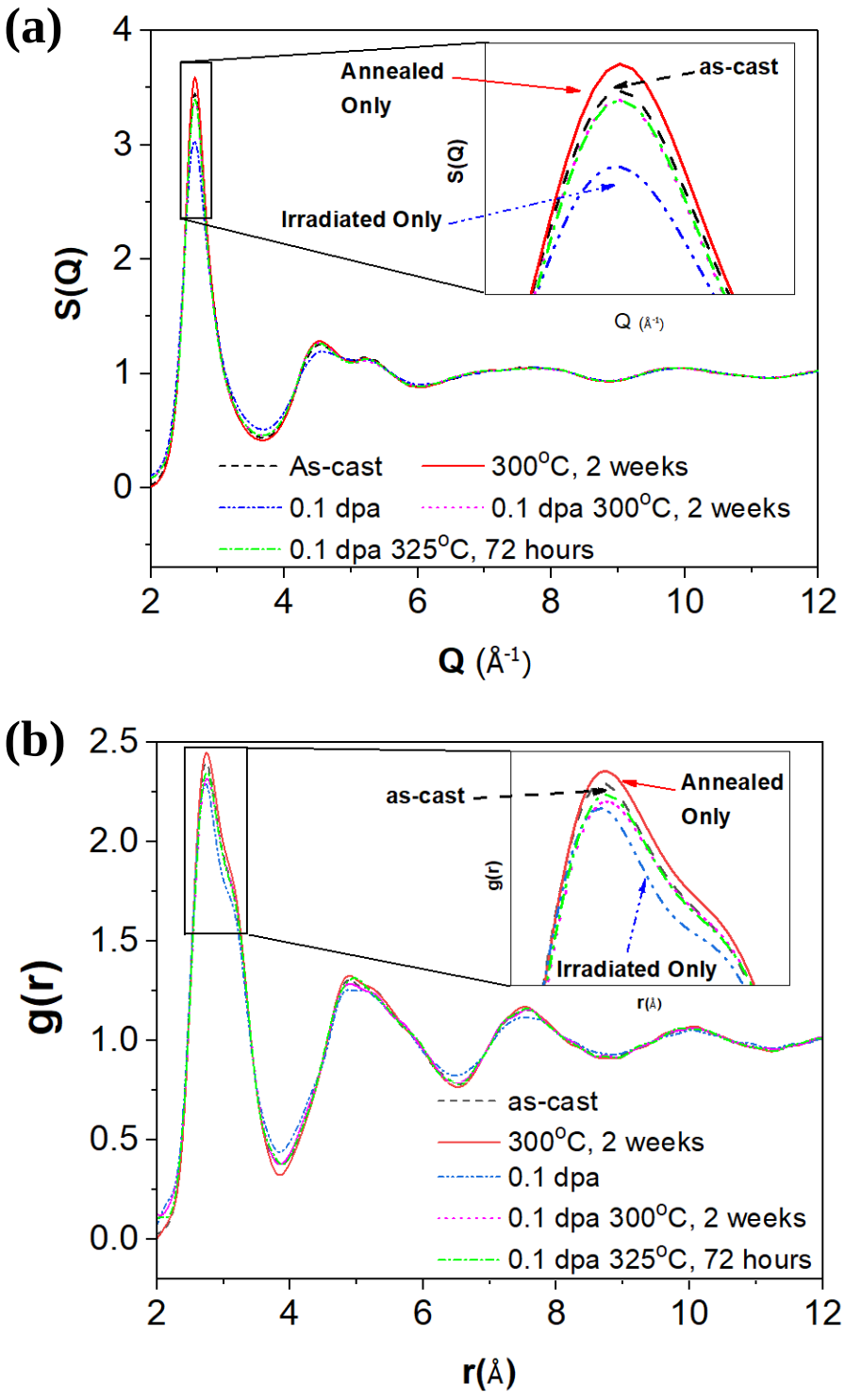

Figure 4-35 The (a) structure function S(Q) and (b) pair distribution function g(r) for the as-cast, neutron irradiated (0.1 dpa), and annealed BAM-11 BMG.

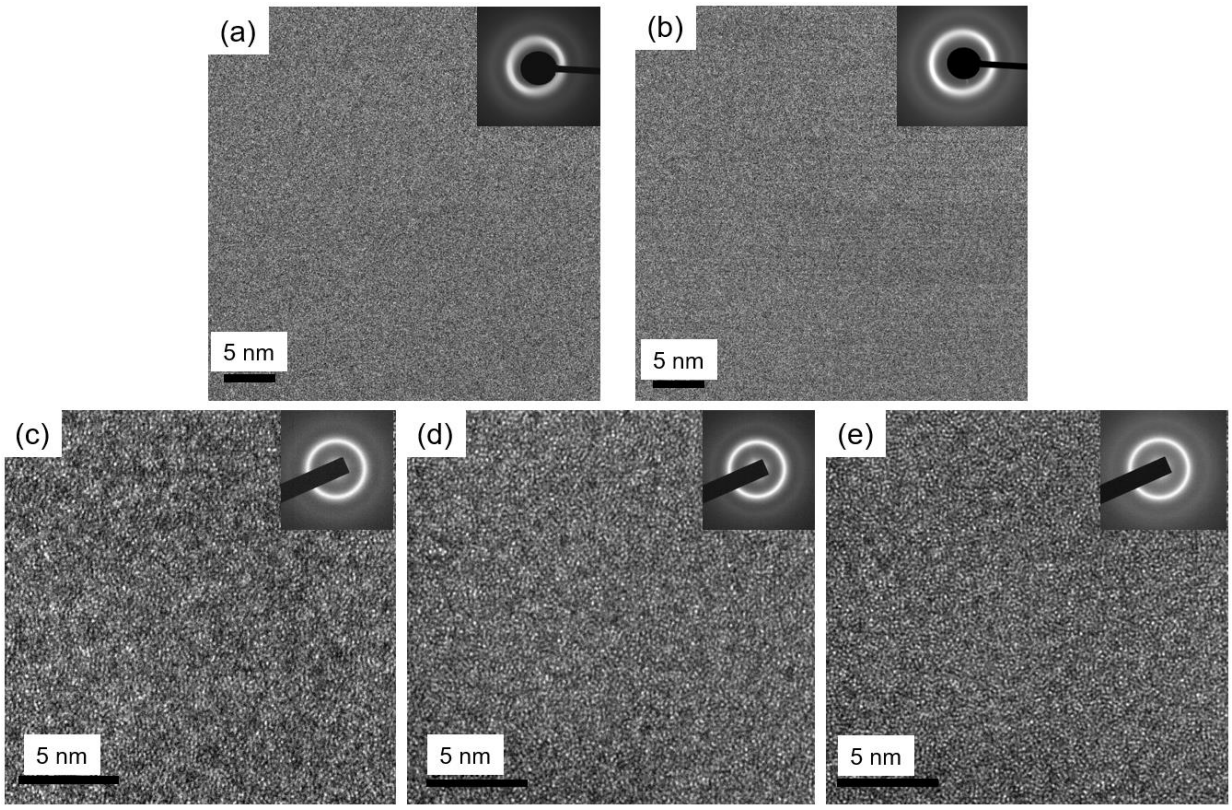

Figure 4-36 TEM SAD and BF images for the (a) as-cast, (b) annealed 300 ^{o}C (2 weeks), (c) neutron irradiated (0.1 dpa), (d) neutron irradiated (0.1 dpa) and post-annealed 325 ^{o}C (72 hours), and (e) neutron irradiated (0.1 dpa) and post-annealed 300 ^{o}C (two weeks).

of the specimens appeared similarly feature-free and did not show any adverse microstructural effects upon radiation or thermal annealing.

4.2.2.3 Density Measurements

Table 4-9 displays the results of the immersion density measurements. As can be observed, the density of the irradiated-only specimen was ~ 2 % below the as-cast density. In contrast, the density was highest for the unirradiated as-cast sample annealed at 300°C for two weeks, with a value ~ 1% higher than that of the as-cast density. Furthermore, thermal annealing of the neutron irradiated specimens restored the density to within ~0.5% of the as-cast density.

Figures 4-37(a)-(c) shows the plot of the immersion density vs. the first three CNs. As can be observed, the macroscopic density was linearly correlated with the coordination numbers. In addition, the degree of correlation decreased as the coordination number increased, where the R^2 values were 0.98, 0.97, and 0.81 for the first, second, and third CNs, respectively. The above result signifies that for smaller r, the density is highly correlated to the number of first and second nearest-neighbor atoms surrounding a central atom.

Table 4-9 Immersion density measurements for the as-cast, neutron irradiated, and annealed BAM-11 BMG.

Sample Condition	Density (g/cm^3)
As-cast	6.67 ± 0.02
Annealed 300 °C 2 weeks	6.73 ± 0.02
0.1 dpa	6.53 ± 0.02
0.1 dpa 300 °C 2 weeks post-anneal	6.64 ± 0.02
0.1 dpa 325 °C 72 hours post-anneal	6.63 ± 0.01

To help elucidate how the amorphous structure of the alloy is affected by neutron irradiation and annealing, the first three coordination numbers (CNs) were estimated from the pair distribution function curves (PDF) [figure 4-35(a)] using Eq. (4-1):

$$C.N._i = 4\pi\rho \int_{r_{i-1}}^{r_i} r^2 g(r) dr \tag{4-1}$$

where $\rho = 5.51 \times 10^{22}$ atoms/cm^3 is the calculated number density of the as-cast BAM-11. Table 4-10 presents, for each experimental condition, the values for the first 3 CNs. The trend exhibited by the CNs is similar to that of the diffraction results. Namely, the neutron irradiation without heat treatment led to a decrease in all three numbers as compared to the as-received condition while annealing without irradiation increased the values. Moreover, the coordination numbers for the samples heat treated after irradiation had larger values as compared to the irradiated only sample. Finally, the CNs for the sample annealed at 300 ^{o}C for two weeks after irradiation were larger than the sample post-annealed at 325 ^{o}C for 72 hours.

Table 4-10 First three coordination numbers for the irradiated and annealed BAM-11 BMG.

Sample Condition	1st C. N.	2nd C. N.	3rd C. N.
As-cast	12.86	49.89	92.26
Annealed 300 ^{o}C 2 weeks	13.07	50.46	94.63
0.1 dpa	12.24	47.97	89.57
0.1 dpa 300 ^{o}C 2 weeks post-anneal	12.67	49.23	91.17
0.1 dpa 325 ^{o}C 72 hours post-anneal	12.64	49.68	91.64

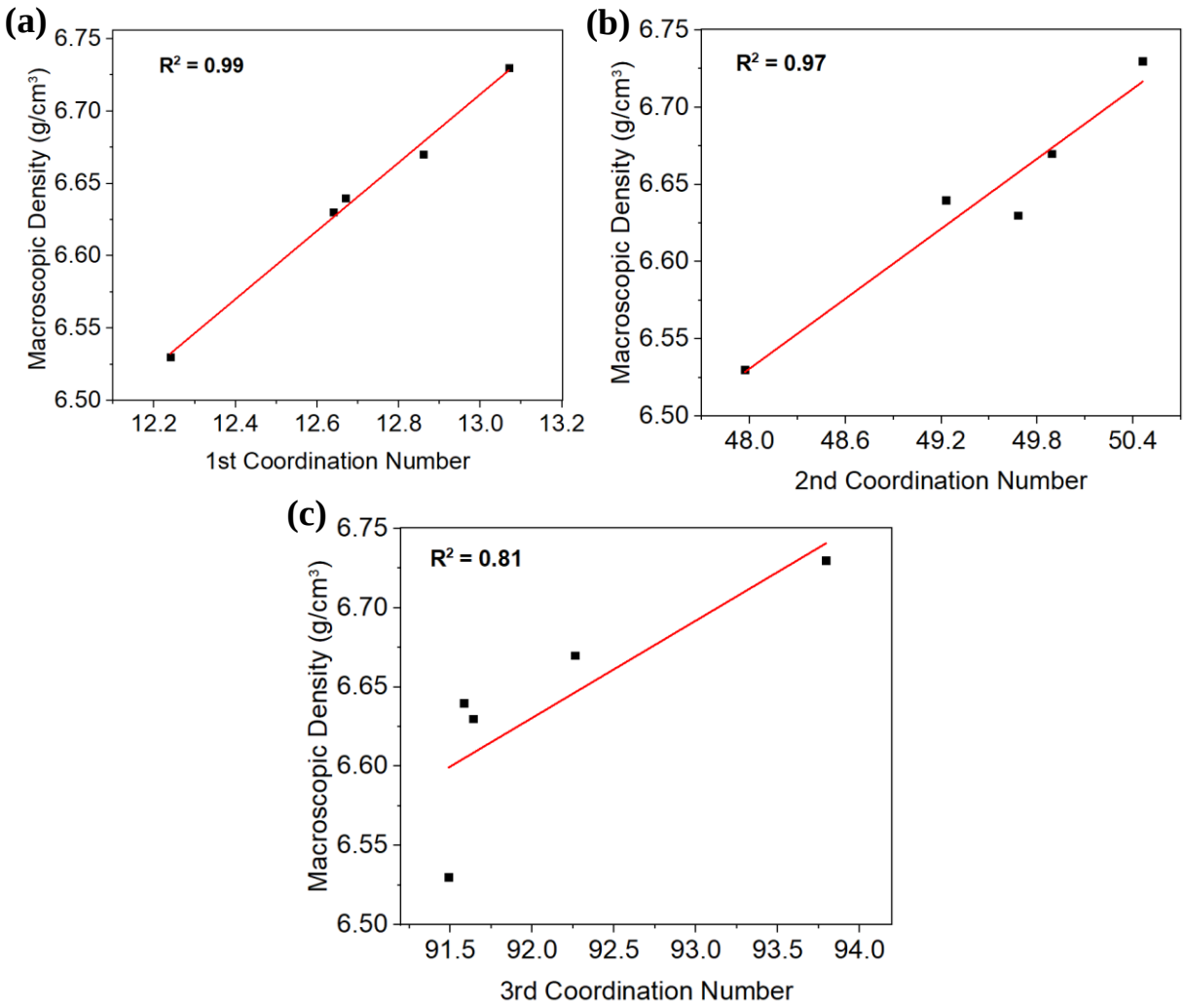

Figure 4-37 The immersion density vs. (a) first coordination number, (b) Second coordination, and the (c) Third coordination number.

4.2.2.4 Mechanical Testing

4.2.2.4.1 Nanoindentation

Figures 4-38 and 4-39 present the nanoindentation hardness and Young's modulus vs. depth results for the five as-cast, neutron irradiated and thermal annealed experimental conditions discussed above (see Table 4-9). The measured hardness and decreases with respect to nanoindentation depth for all conditions (indentation size effect). The Young's modulus also exhibited a similar decreasing trend with respect to the indentation depth. Importantly, neutron irradiation to a dose of 0.1 dpa was found to significantly decrease the hardness and modulus as compared to the as-received state. Similar to the neutron diffraction and immersion density results, annealing to 300 ^{o}C for two weeks had the opposite effect of inducing an increased hardness and modulus, as compared to the as-cast condition. Moreover, heating after irradiation recovered some of the softening induced by irradiation. Interestingly, post-irradiation annealing at 300 ^{o}C for two weeks produced a similar decrease in the hardness as compared to the sample that was annealed at 325 ^{o}C for 72 hours following irradiation.

4.2.2.4.2 3-Point Bend Testing

The flexural stress-displacement (deflection) curves for the 3-point bend testing experiments, are shown in figure 4-40 for the neutron irradiated and annealed BAM-11. Except for the as-cast sample, the specimens fractured before they reached their yielding point. The data for the unirradiated annealed sample (300 ^{o}C, 2 weeks) is not displayed since it fractured after approximately 10 N (0.4 MPa) was applied during the test, and therefore did not show any appreciable deformation during the test. Furthermore, the slope of the curve, which is known as the flexural modulus, was found to be the lowest for the neutron irradiated sample. On the other

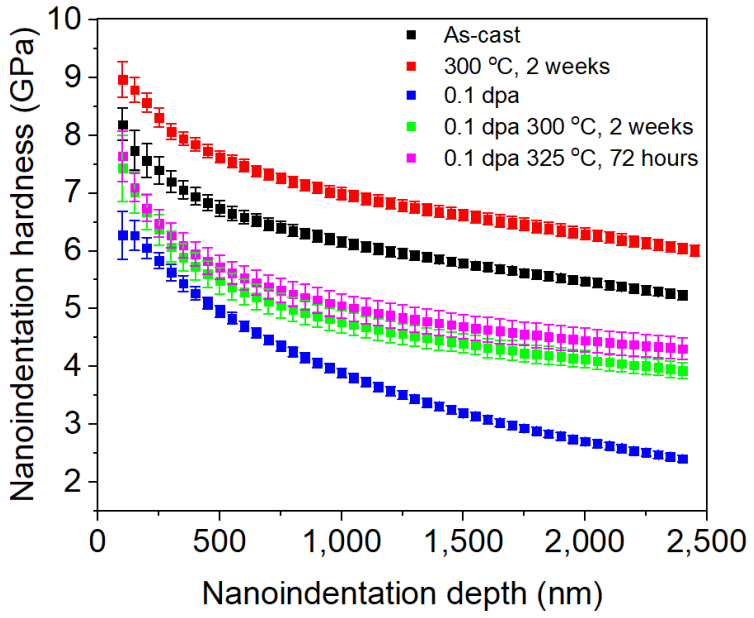

Figure 4-38 The nanoindentation hardness for indentation depth for the neutron irradiated and annealed BAM-11 BMG.

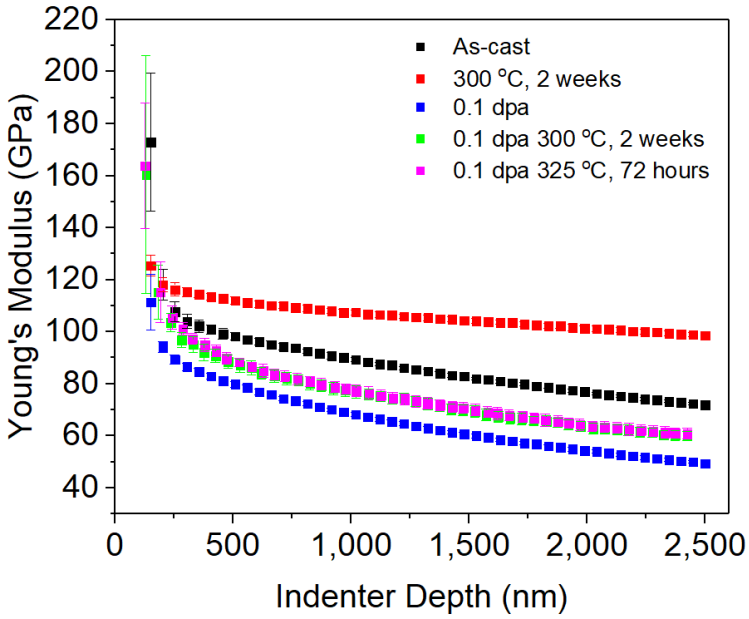

Figure 4-39 The nanoindentation Young's modulus for indentation depth for the neutron irradiated and annealed BAM-11 BMG.

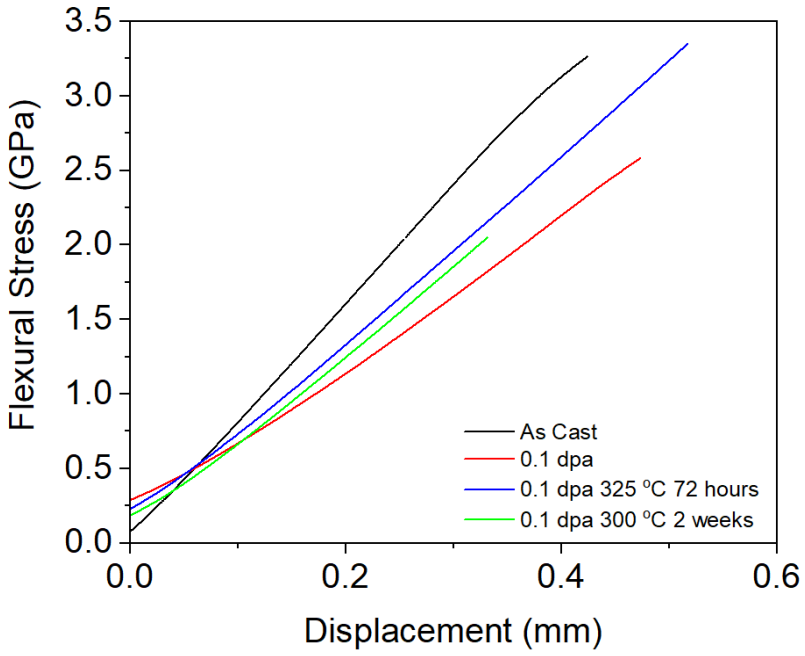

Figure 4-40 Flexural stress–displacement (deflection) curve for the as-cast, neutron irradiated, and annealed BAM-11 BMG.

hand, annealing after irradiation led to gradients that were intermediate between that of the as cast and irradiated specimens. Although these differences can be seen in the graph, they were still comparable.

4.2.3 Nonirradiation Thermal Response Experiments

The goal of these thermal experiments is to investigate the mechanical and microstructural response of BMGs to temperatures ranging from ambient to temperatures approaching the melting point of the alloy. This section will cover experiments involving temperature effects on the nanoindentation and Vickers hardness, in-situ XRD compression tests, serrated flow analysis, and high temperature in situ XRD behavior.

4.2.3.1 Thermal Annealing Nanoindentation Experiments

Figure 4-41 shows the nanoindentation hardness curves for the as-cast and the annealed specimens that were heated at temperatures ranging from 150 to 300 ^{o}C. As can be seen, the annealed samples exhibited significantly higher hardness values, as compared to the as-cast condition, for all indentation depths. Furthermore, the hardness values for the sample heated at 150 ^{o}C for 96 hours and 200 ^{o}C for 72 hours were virtually the same. On the other hand, the hardness values exhibited by the specimens heated at 300 ^{o}C for 48 hours were greater than any of the other conditions. This substantial increase in the hardness suggests that significant short-range atomic rearrangement occurred in the specimen annealed at the highest temperature.

As can be observed in the figure, a pronounced ISE can be observed in the data, which corresponds to rapid decreases in the hardness for small indent depths. Also, this ISE is significantly more pronounced in the thermally annealed samples. The ISE hardness for the Nix-Gao model, with regards to the as-cast and unirradiated specimens that were annealed at temperatures ranging from 150 ^{o}C to 300 ^{o}C, is plotted in figure 4-42. Similar to the ion irradiated and as-cast results for the ion irradiation experiments, the data did not behave in a linear fashion with respect to the independent variable, h^{-1}. In addition, the extrapolated hardness values did not change much for the unirradiated specimens annealed at 150 ^{o}C for 96 hours and 200 ^{o}C for 72 hours, as compared to the as-cast condition. However, annealing at 300 ^{o}C led to an apparent increase in the extrapolated hardness.

A comparison of the extrapolated nanoindentation bulk hardness values that were obtained from applying the Nix-Gao relation with the bulk Vickers hardness data for the as-cast and the annealed specimens for temperatures ranging from 150 to 300 ^{o}C, are displayed in Table 4-10. For the data obtained using Nix-Gao, the hardness was approximately the same as compared to the as-

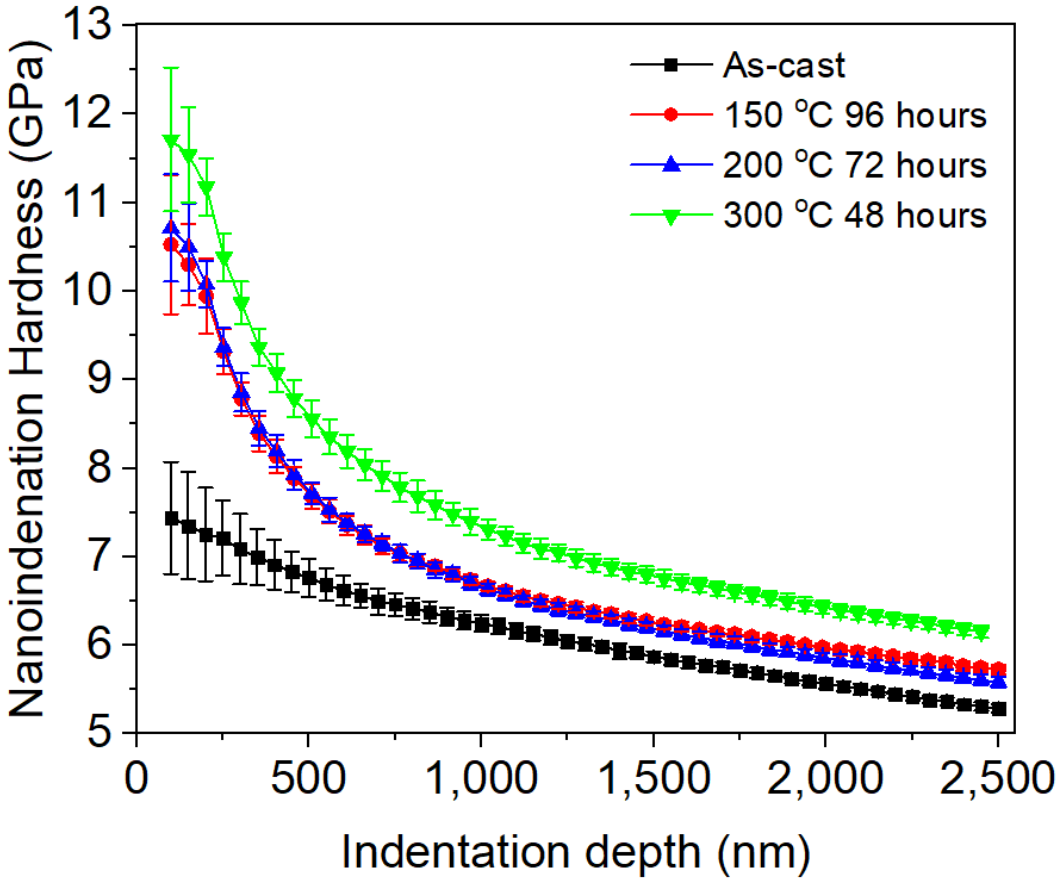

Figure 4-41 Nanoindentation hardness vs. depth for BAM-11 BMG as-cast and annealed samples at different temperatures ranging from 150 °C to 300 °C and respective heating times of 96, 72, and 48 hours for depths ranging from 100-2500 nm.

cast sample for the specimens heated at 150 and 200 ^{o}C. However, the extrapolated hardness was slightly higher for the sample annealed at 300 ^{o}C, as compared to the as-cast state. A similar trend was observed in the data obtained using the Vickers hardness technique. It should also be mentioned that for every condition, the bulk hardness values from the Nix-Gao extrapolation model were 11-17% higher than the values obtained from the Vicker's hardness tests. However, in contrast to the nanoindentation results, where the hardness was higher for all the annealed samples, the Vickers hardness was lower for the samples annealed at 150 ^{o}C and 200 ^{o}C, as compared to the as-cast condition.

The ISE hardness values, as obtained from the Lam and Chong model, are presented in figure 4-43 for the as-cast and annealed specimens (150-300 ^{o}C). Interestingly, the extrapolated hardness values for the as-cast sample was higher, as compared to the annealed samples, when fitting the full set of nanoindentation data for the 100-2,500 nm depths. Therefore, it appears that the extrapolated hardness values obtained by fitting the Lam and Chong model to the day may not be valid since these values are not in agreement with the trend observed in figure 4-42 for the depth dependent hardness.

The extrapolated nanoindentation bulk and Vickers hardness data, as obtained from applying the Lam and Chong model, are listed in Table 4-11 for the as-cast and unirradiated annealed specimens for temperatures ranging from 150 ^{o}C to 300 ^{o}C Similar to Table 4-10, both the extrapolated nanoindentation and Vickers hardness values were comparable for the as-cast, 150, and 200 ^{o}C annealing conditions. Regarding the Vickers data, the hardness was slightly higher for the sample annealed at 300 ^{o}C as compared to the as-cast state. Lastly, the bulk hardness values evaluated using the Lam and Chong extrapolation model were lower by 2-17% as compared to the values evaluated from the Vickers hardness tests, for every condition.

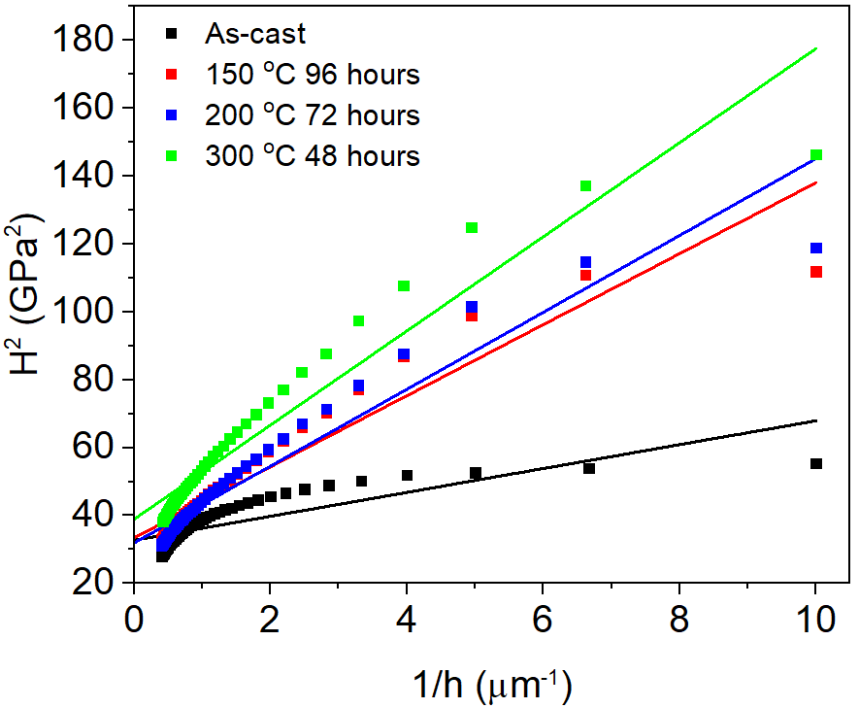

Figure 4-42 H^2 vs. 1/h for BAM-11 BMG, using the Nix-Gao model, in the as-cast vs. annealed samples at temperatures of 150 °C, 200 °C, and 300 °C (respective heating times of 96, 72, and 48 hours). Here the data corresponded to depths ranging from 100 - 2500 nm.

Table 4-11 Comparison of the extrapolated nanoindentation hardness H_0 (Nix-Gao model) and Vickers hardness (1,000 gf) results for the as-cast and annealed samples.

Condition	H_0 (GPa)	Vickers (GPa)	Percent Diff. (%)
As-cast	5.7	5.1 ± 0.01	11.1
150 °C 96 hours	5.8	4.9 ± 0.03	16.8
200 °C 72 hours	5.6	5.0 ± 0.07	11.3
300 °C 48 hours	6.2	5.3 ± 0.05	15.7

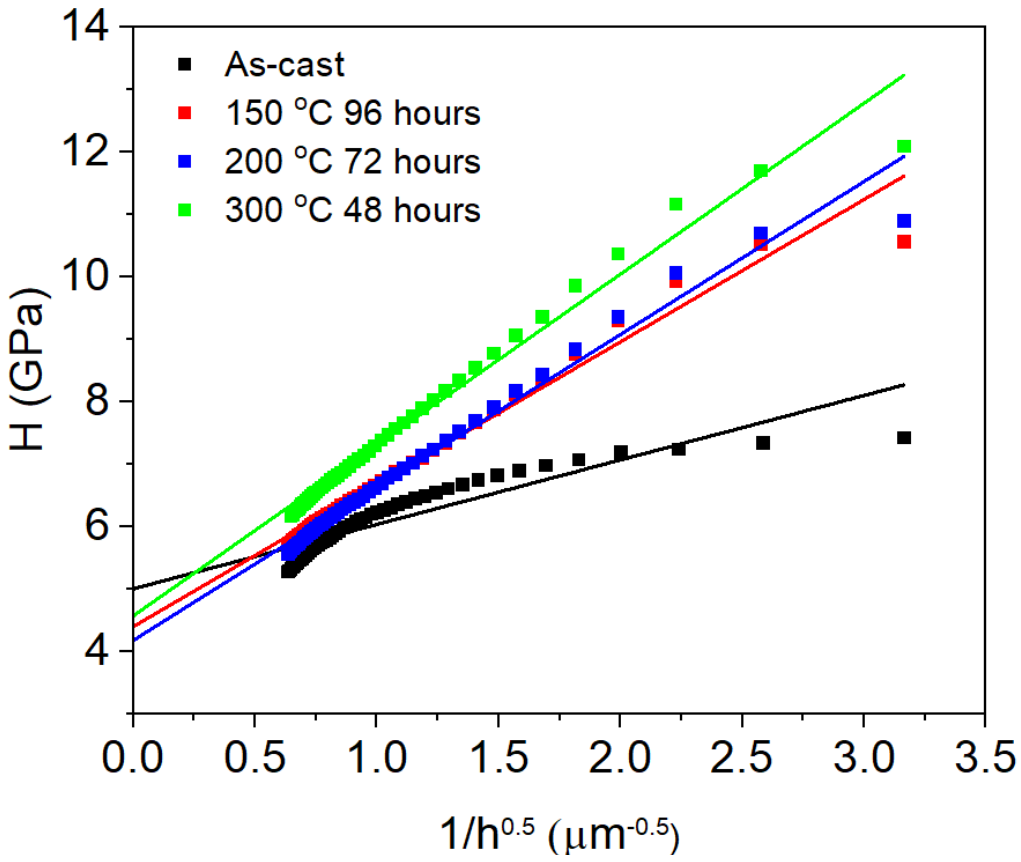

Figure 4-43 H vs. 1/h for BAM-11 BMG, using the Nix-Gao model, in the as-cast vs. annealed samples at temperatures of 150 °C, 200 °C, and 300 °C (respective heating times of 96, 72, and 48 hours). Here the data corresponded to depths ranging from 100-2500 nm.

Table 4-12 Comparison of extrapolated nanoindentation hardness, H_0' (Lam and Chong model) and Vickers hardness (1,000 gf) results for the as-cast and annealed samples.

Condition	H_0' (GPa)	Vickers (GPa)	Percent Diff. (%)
As-cast	5.0	5.1 ± 0.01	2.0
150 °C 96 hours	4.4	4.9 ± 0.03	10.8
200 °C 72 hours	4.2	5.0 ± 0.07	17.4
300 °C 48 hours	4.6	5.3 ± 0.05	14.1

4.2.3.2 In Situ X-Ray Diffraction Crystallization Kinetic Experiments

4.2.3.2.1 BAM-11 BMG

Figure 4-44 displays the HTXRD results for the BAM-11 BMG exposed to a heating rate of 1 ^{o}C/min. that was heated until a maximum temperature of 760 ^{o}C. The graph shows a clear evolution of phase behavior as a function of furnace temperature. An amorphous character is initially observed and retained until ~365 ^{o}C, at which point rapid formation of the tetragonal Zr_2Ni phase, at the expense of the characteristic amorphous hump is observed. Phase stability is observed through ~440 ^{o}C at which point tetragonal Cu-Ti-Zr and ZrO_2 is observed. At 505 ^{o}C, another transition occurs in which the crystalline phases Cubic Ti-Ni-Cu, hexagonal Ni and ZrO_2 were observed. This phase transition occurs in conjunction with a shift and decrease in magnitude of the Zr_2Ni crystal structure characteristic peaks. At approximately 610 ^{o}C, another phase transition occurs in which the phases TiO, Hexagonal Ni, CuO, and ZrO_2 were observed. This phase equilibria remains upon cooling showing a sharp high 2Θ shift in peak position correlated with negative thermal contraction.

Figure 4-45 shows the isothermal masterplot and Avrami fit of the formation of tetragonal Zr_2Ni (ICDD #04-004-3205 [425]). The nine lines in the figure represent the models for the solid-state kinetic transformations, as discussed in [239]. These transformations include different mechanisms such as phase boundary reactions and reactions and 3D diffusion. During the initial stages of the transformation, i.e. $\alpha < 0.5$, the data adheres to line labeled A2 in the graph, which indicates that the rate of the ZrO_2 formation obeys a Johnson-Mehl-Avrami-Kolmogorov Process. Once α becomes greater than 0.5, the data follows the line labeled D4, which suggests that the crystallization process follows a Ginstein-Brounshtin kinetic mechanism. This means that

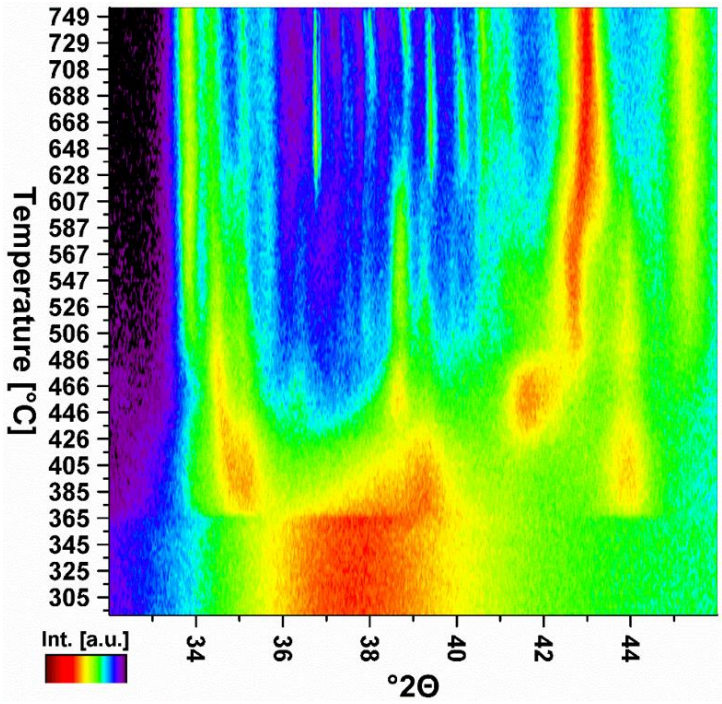

Figure 4-44 Isochronal HTXRD characterization of the BAM-11 BMG under a chamber pressure of ~10^{-5} torr and heating rate of 1 ºC/min. Color is indicative of scan intensity, the independent variable is °2Θ, and the y-axis is the sample temperature.

initially, the crystallites are randomly nucleating and growing isotropically although after there is enough growth, the particles grow via a 3D diffusion growth mechanism.

Figure 4-46 presents the SEM/EDS characterization of the same BAM-11 BMG after the surface layer was removed. Here, the different elements comprising the matrix are represented by their respective color. The heterogenous nature of the elemental suggests that crystalline phase formation occurred during heating. This effect of segregation is especially evident for the Ni and Zr, which indicates that these elements may have formed phases in the matrix.

Figure 4-47 shows the Rietveld summary for the XRD analysis of the bulk BAM-11 BMG sample for scattering angles ranging from 25 to 90 º. As can be seen, there are numerous peaks throughout the diffracted region, in which the taller peaks exist at angles varying from 34 – 42 º,

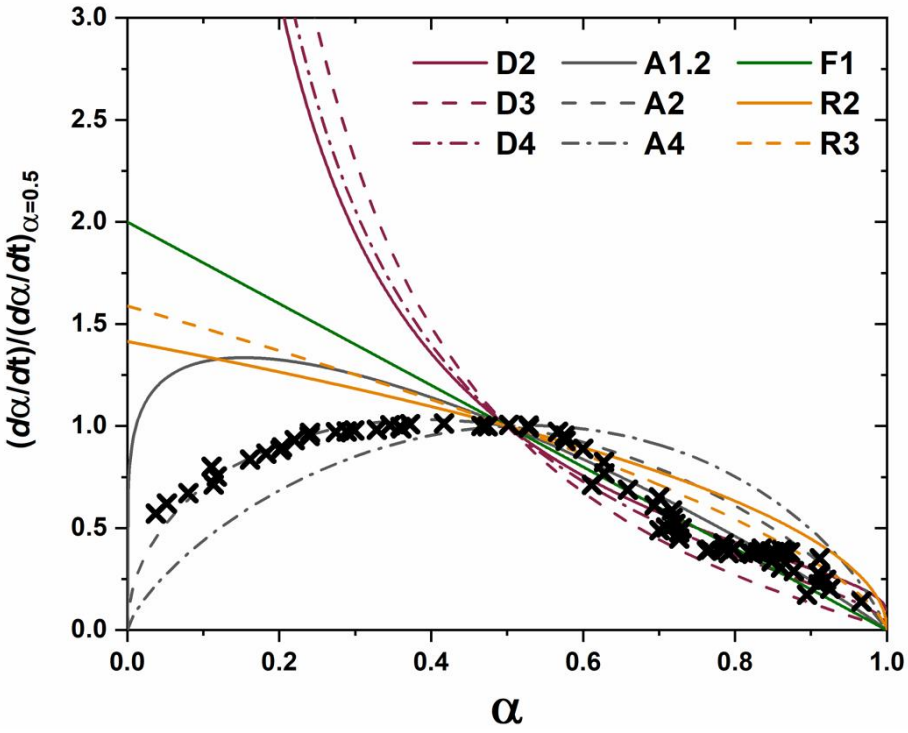

Figure 4-45 Isothermal masterplot and Avrami fit of the formation of tetragonal Zr_2Ni (ICDD #04-004-3205 [425]).

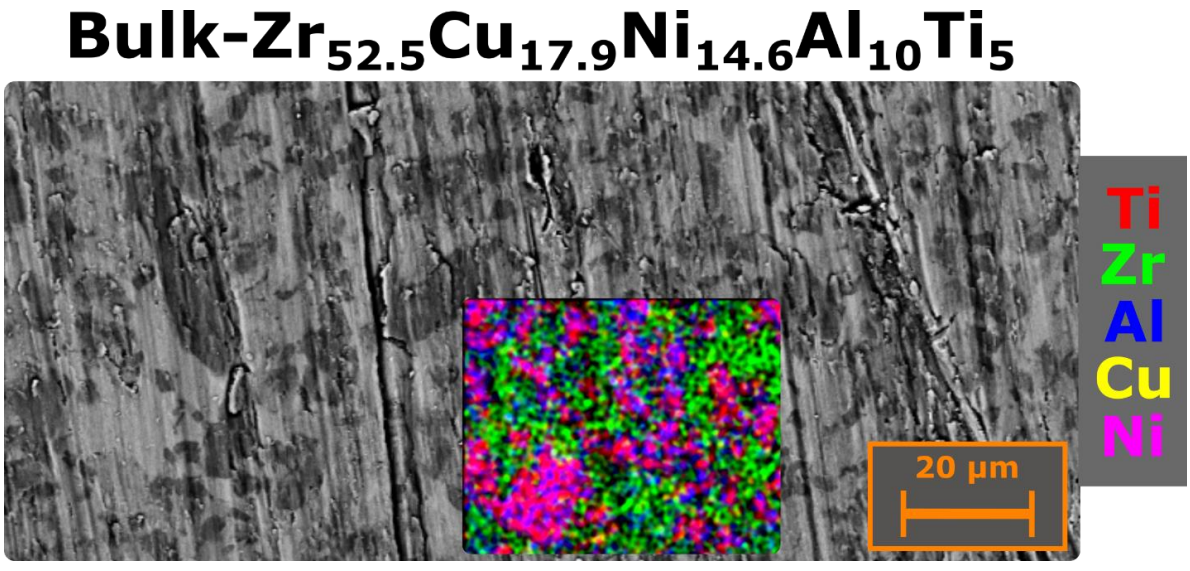

Figure 4-46 Bulk SEM and EDS characterization of the BAM-11 BMG that was heated to a maximum temperature of 760 °C using a ramp rate of 1 °C/min.

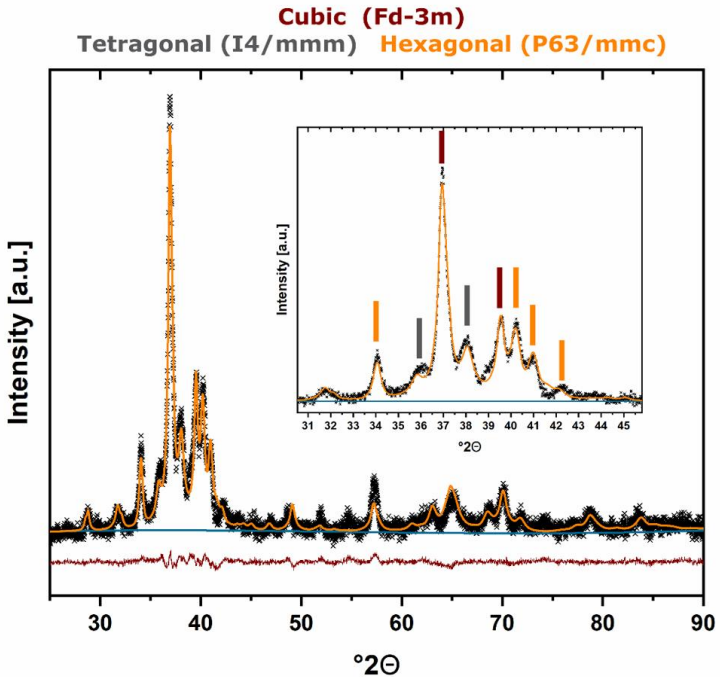

Figure 4-47 Rietveld summary and quantitative phase identification of BAM-11 BMG bulk crystalline phases. Three unique crystalline phases are identified.

which correspond to the amorphous peak in the as-received state. The inset in the graph correspond to the angles where the refinement found three unique crystal structures that had formed in the matrix during annealing. These phases consist of cubic $Fd\bar{3}m$ $CuZr_2$, (ICDD #04-004-2397), Tetragonal $I4/mmm$ $CuZr_2$, and Hexagonal $P63/mmc$ NiTiZr (ICDD #04-005-5411).

The nanoindentation hardness and Young's modulus, as a function of indenter depth for the as-cast and partially crystallized BAM-11 BMG specimens, are displayed in figures 4-48(a)-(b). The crystallized specimen was heated to a maximum temperature of 760 ^{o}C. As can be seen, there was a pronounced indentation size effect exhibited by both specimens where the measured hardness increases rapidly at small indent depths. Furthermore, the ISE is most pronounced in the crystallized specimen due to a more pronounced decrease in the hardness at depths below 700 nm.

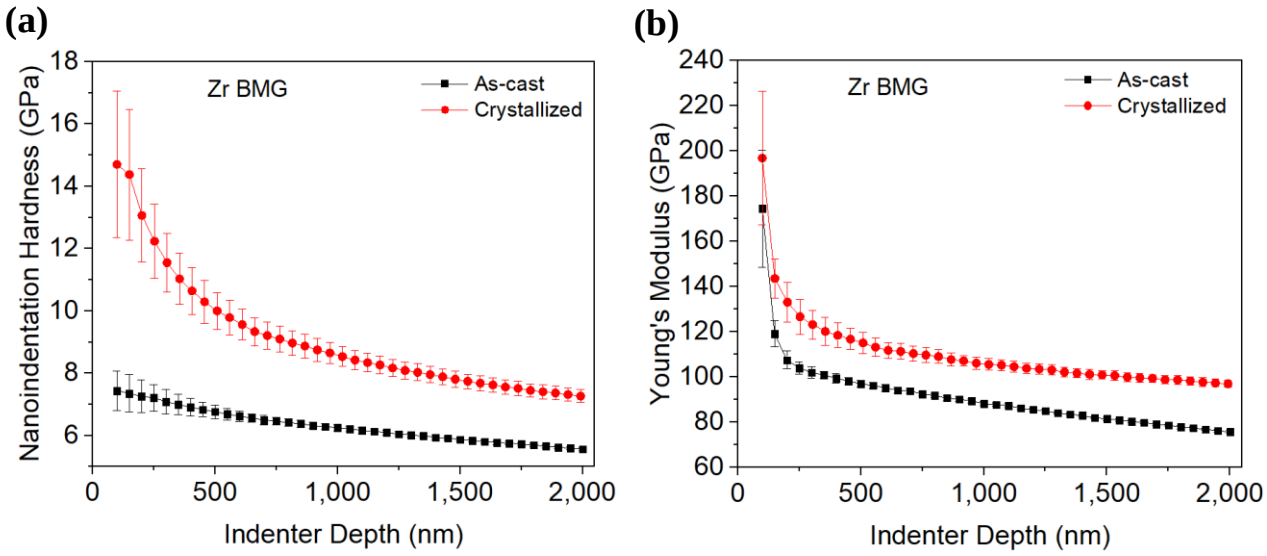

Figure 4-48 The (a) nanoindentation hardness and (b) Young's modulus of the as-cast vs. the crystallized BAM-11 BMG as a function of indenter depth.

Moreover, the hardness was higher at all indent depths for the crystallized sample, as compared to the as-received specimen. In terms of the modulus, it decreased with respect to the indenter depth. Like with the hardness, the partially crystallized specimen exhibited values significantly higher than the as-cast sample at all indentation depths.

4.2.3.2.2 Cu BMG

Figure 4-49 presents the HTXRD evolution for the Cu BMG that was heated to maximum temperature of 800 ^{o}C using a ramp rate of 1^{o}C/min. Similar to the results for the BAM-11 BMG, the nine lines in the figure represent the models for the solid-state kinetic transformations, which include different mechanisms such as phase boundary reactions and reactions and 3D diffusion. There was an evolution of phase behavior as a function of furnace temperature. Initially, an amorphous character is observed and retained until ~360 ^{o}C, at which point there is the rapid

formation of cubic Cu $Fm\bar{3}m$ (ICDD #04-001-3342) and cubic Zr (ICDD # 01-079-9867) $Im\bar{3}m$ phase structures, at the expense of the characteristic amorphous hump. Phase stability is observed through ~500 ^{o}C at which point the appearance of some unknown oxide pha**se** is observed in conjunction with a shift and decrease of the cubic $Fm\bar{3}m$ and $Im\bar{3}m$ characteristic peaks. This phase equilibria remains upon cooling showing a sharp high 2Θ shift in peak position correlated with thermal contraction.

Figure 4-50, which presents the isothermal master plot, indicates that both the nucleation rate and growth rate follow the basic JMAK model. Figures 4-51(a)-(b) and 4-52(a)-(b) presents the kinetic characterization of the formation of cubic $Im\bar{3}m$ and $Fm\bar{3}m$ phases for the isothermal heating of the Cu BMG at 345 ^{o}C. The linear fit of figures 4-51(b) and 4-52(b) demonstrates a clear Avrami type behavior where there is an increasing and decreasing rate of formation. Using this model and fitting the data yields an n value of 2.40 and a rate constant, k, of 6.4×10^{-10} s^{-1} for the $Im\bar{3}m$ phase, while for the for the $Fm\bar{3}m$ phase n was 2.31 and k was 1.4×10^{-9} s^{-1}.

Microstructural characterization, as performed by the SEM and EDS, revealed the precipitation of spherical particles on the surface of the bulk samples, as shown in figure 4-53. Elemental characterization revealed that these precipitates are TiO_2 (space group P21/c ICDD # 04-012-6345 [426]). According to the EDS color map, the grounded surface most likely did not contain any oxide phases but rather Cu and Zr crystalline phases instead.

The nanoindentation hardness and Young's modulus, as a function of indenter depth for the as-cast and partially crystallized Cu BMG specimens, are displayed in figures 4-54 (a)-(b). The crystallized specimen was heated to a maximum temperature of 760 ^{o}C. As can be observed for both the as-cast and partially crystallized conditions, a pronounced indentation size effect is

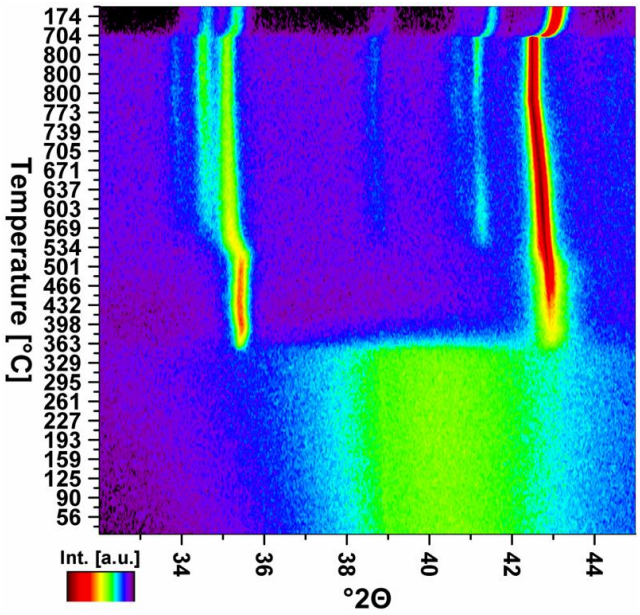

Figure 4-49 Isochronal HTXRD characterization of $Cu_{60}Zr_{20}Hf_{10}Ti_{10}$ BMG under high vacuum. Color is indicative of scan intensity, the independent variable is °2Θ, and the y-axis corresponds to the chamber temperature.

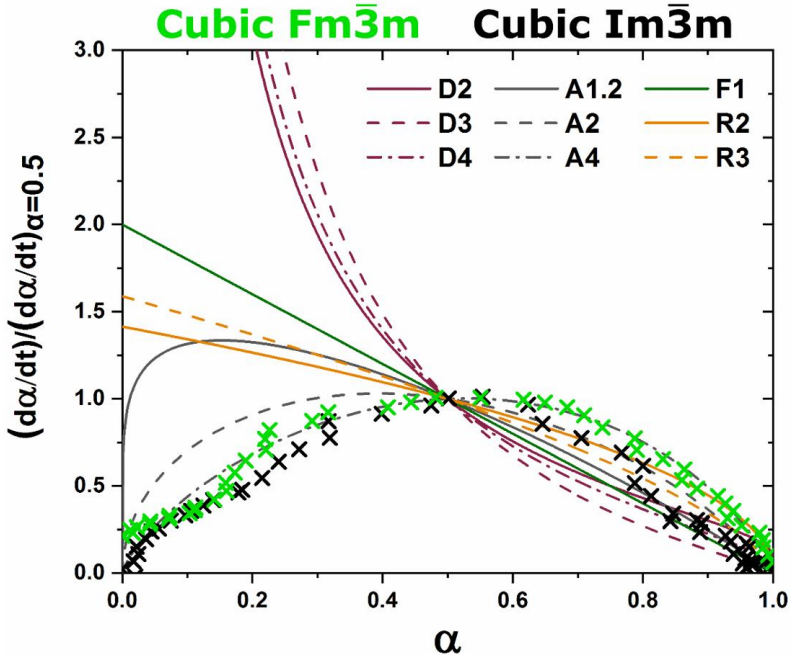

Figure 4-50 Isothermal masterplot (345 °C) and Avrami fit of the formation of cubic Fm$\bar{3}$m and cubic Im$\bar{3}$m for the Cu BMG specimen.

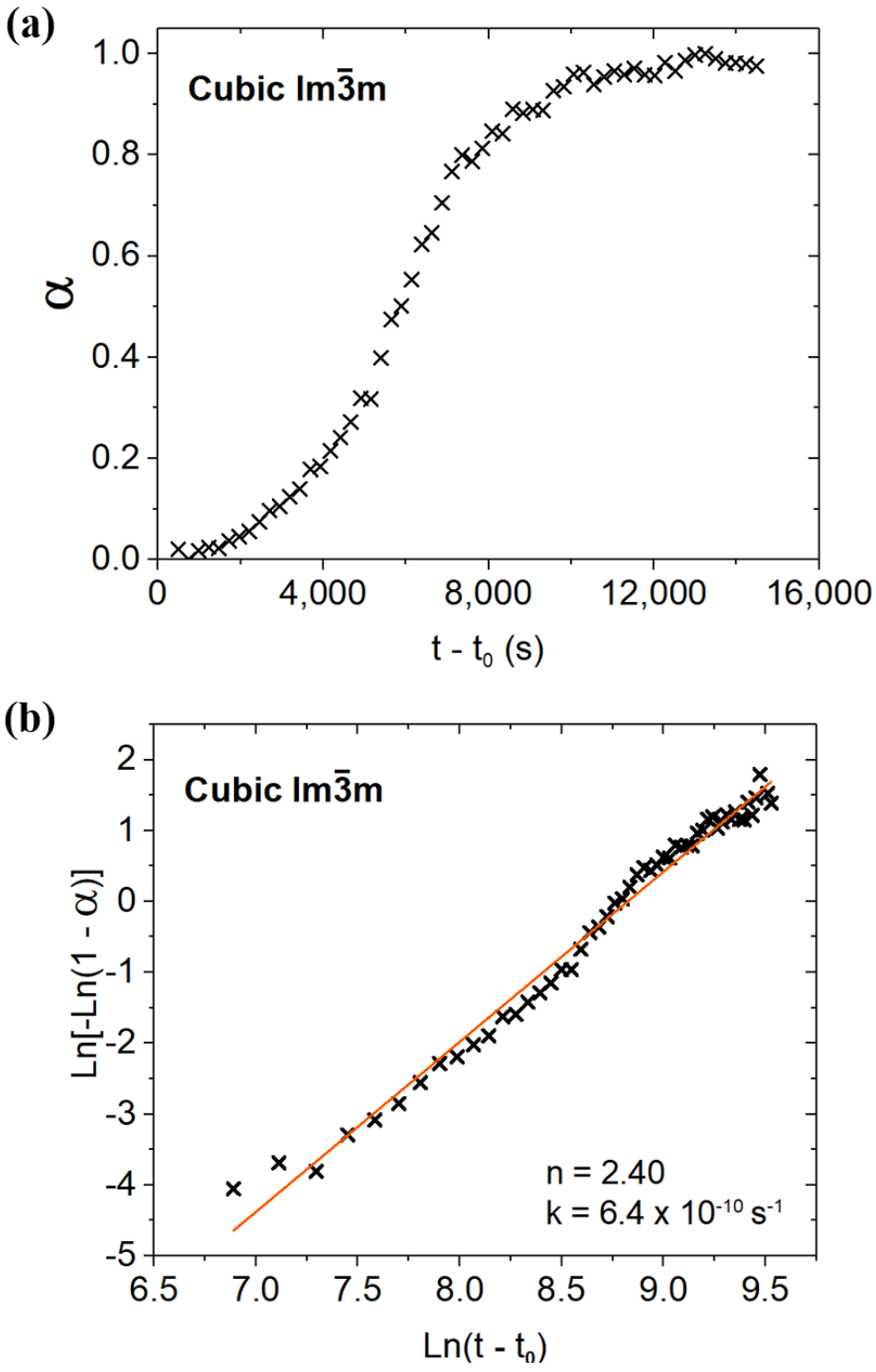

Figure 4-51 The Avrami fit for the isothermal curves (345 ^{o}C) that correspond to the cubic Im$\bar{3}$m phase with coefficients of k = 6.4 × 10^{-10} s^{-1}, n = 2.40.

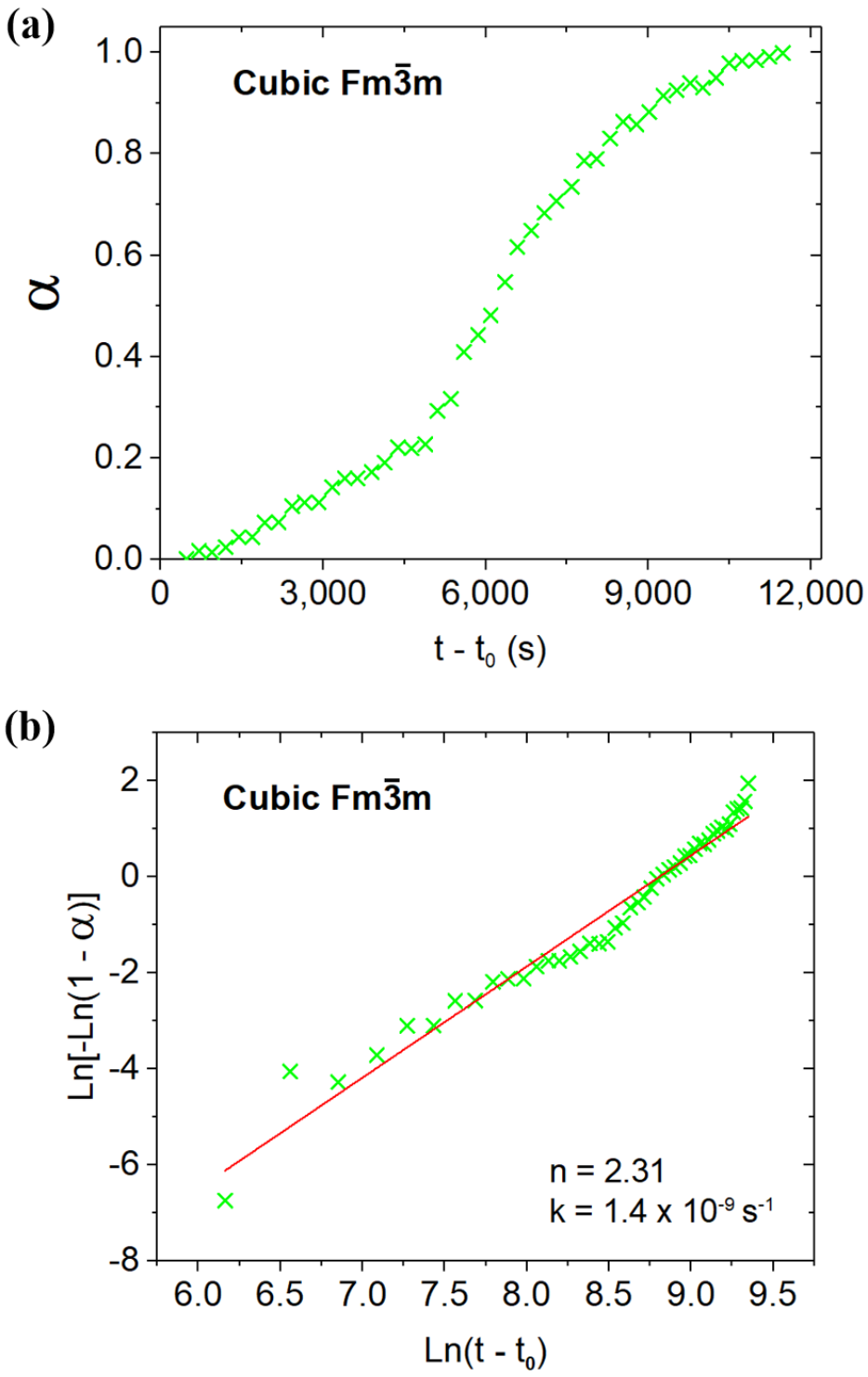

Figure 4-52 The Avrami fit for the isothermal curves (345 ^{o}C) that correspond to the cubic (a) Fm$\bar{3}$m phase of k = 1.4 × 10^{-9} s^{-1}, n = 2.31.

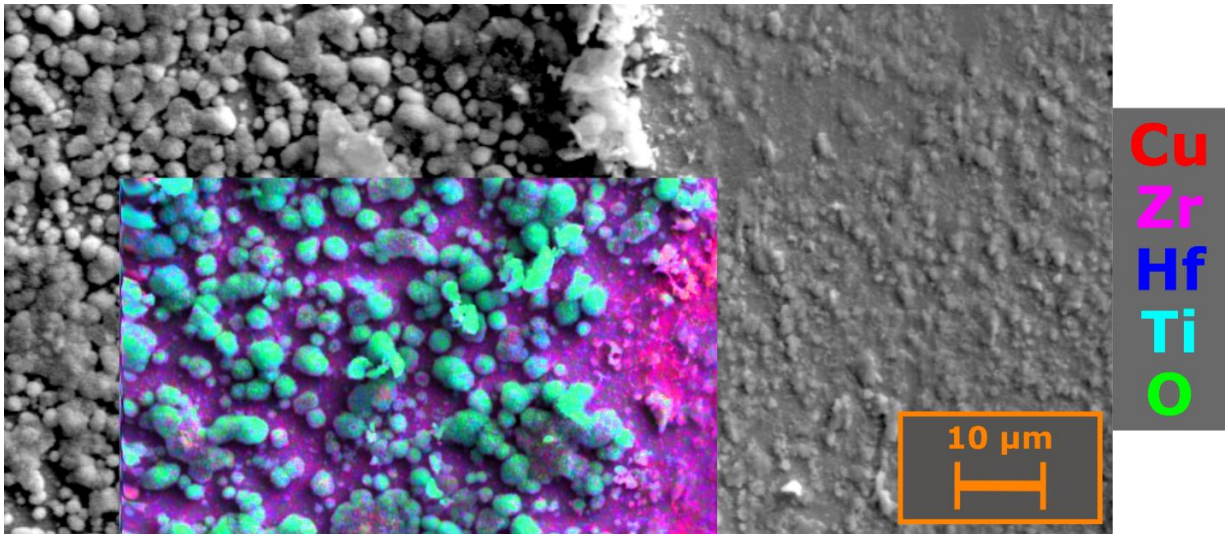

Figure 4-53 SEM and EDS characterization of the surface and the bulk of the Cu BMG.

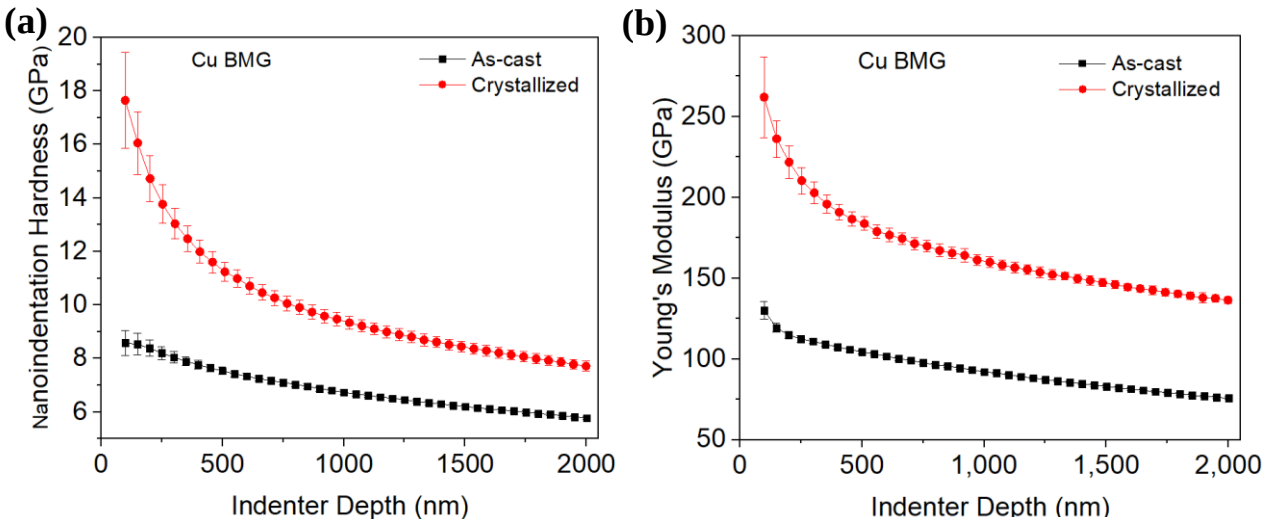

Figure 4-54 The (a) nanoindentation hardness and (b) Young's modulus of the as-cast vs. the crystallized Cu BMG as a function of indenter depth.

observable where the measured hardness and modulus increase rapidly at small indent depths. Furthermore, the ISE is most pronounced in the crystallized specimen due to a more pronounced decrease in the hardness at depths below 700 nm. Moreover, the hardness was higher at all indent depths for the crystallized sample, as compared to the as-received specimen. Similar to the hardness behavior, the partially crystallized specimen exhibited elastic modulus values that were significantly higher than the as-cast sample at all indentation depths. It should also be noted that these values were approximately twice as large as those for the as-cast state.

4.2.3.3 In Situ X-Ray Diffraction Compression Test Experiments

Figures 4-55(a)-(d) compares the high temperature XRD results for the isotropic structure function and PDF of the uncompressed and compressed (1,500 MPa) BAM-11 BMG (as-cast and annealed) specimens. For both the as-cast and the annealed specimens, it was found that the amplitude of the isotropic components of S(Q) and ρ(r) [S_0^0(Q) and ρ_0^0(r)], exhibited very small changes with an increase in the applied stress. Furthermore, the general shape of the curves did not significantly change. As compared to the as-cast sample, the first peak for the specimen annealed at 300 ºC (2 weeks) exhibited a greater amplitude, for both the uncompressed and compressed (1,500 MPa) conditions. Figure 4-56 compares the first peak of the isotropic PDF, $\rho_0^0(r)$, for the as-cast and the annealed specimens (300 ºC 2 weeks). As can be seen in the inset of the figure, the annealed sample exhibits a slightly higher and narrower profile as compared to the as-cast condition.

Figures 4-57(a)-(d) present the elliptical component [256], S_2^0(Q) and ρ_2^0(r) for the applied stresses ranging from 300 MPa to 1,500 MPa. Here, ρ_2^0(r) was calculated using the

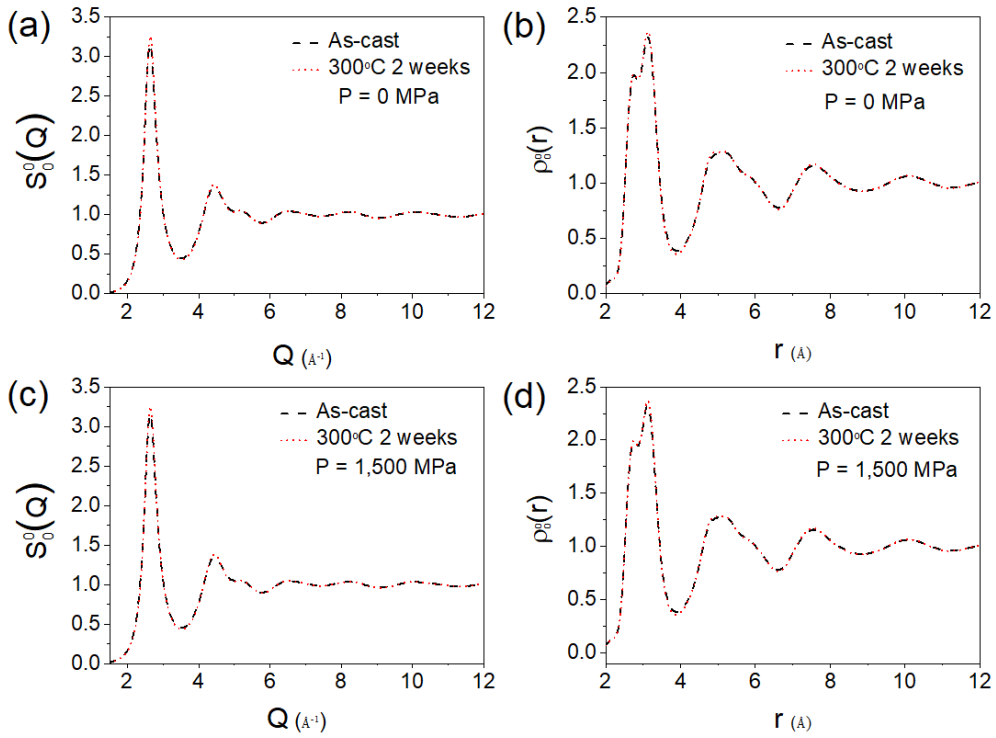

Figure 4-55 Comparison of the isotropic pair distribution function $\rho_0^0(r)$ for the as-cast and the annealed (300°C 2 weeks) BAM-11 BMG samples that were uncompressed (control) and compressed at 1,500 MPa.

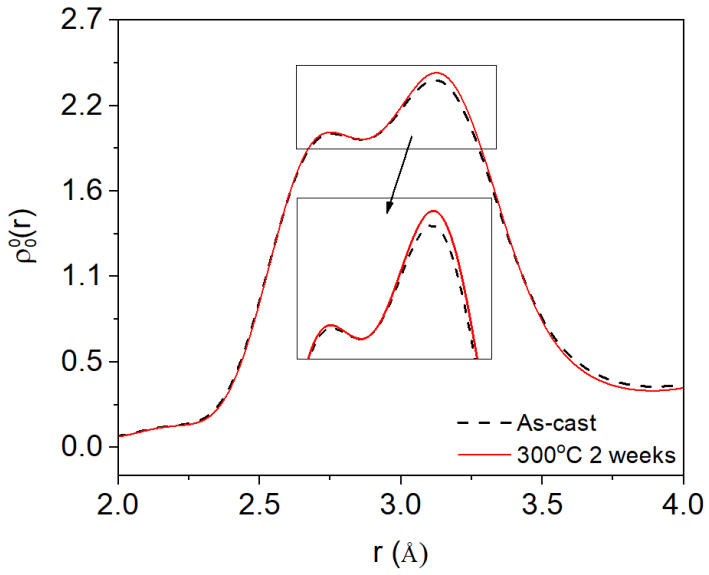

Figure 4-56 Magnification of the first peak in the isotropic pair distribution function $\rho_0^0(r)$ for the as-cast and the annealed (300°C 2 weeks) control (uncompressed) BAM-11 BMG samples.

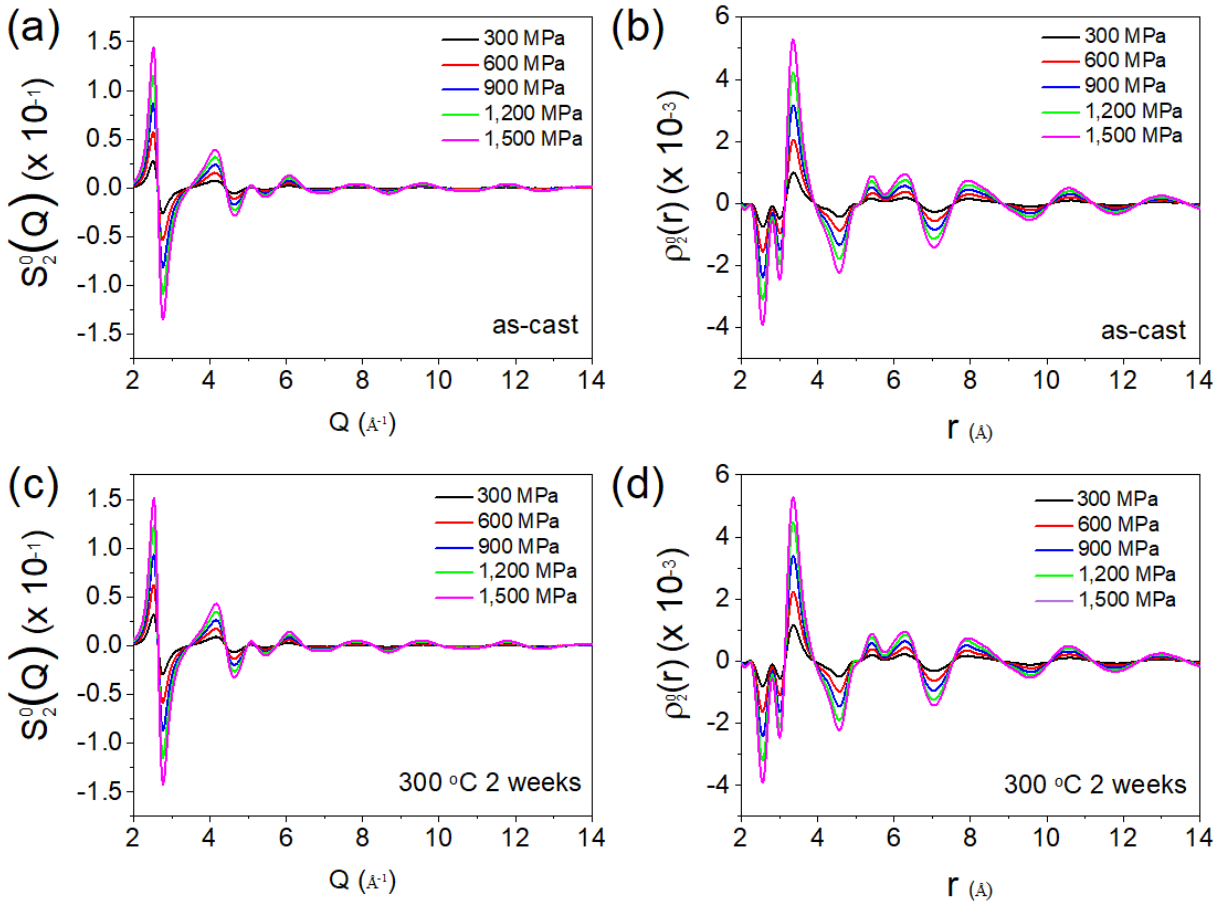

Figure 4-57 Comparison of the anisotropic pair distribution function $\rho_2^0(r)$, and $S_2^0(Q)$ for the as-cast and the annealed (300 °C 2 weeks) samples compressed at stresses ranging from 300 to 1,500 MPa.

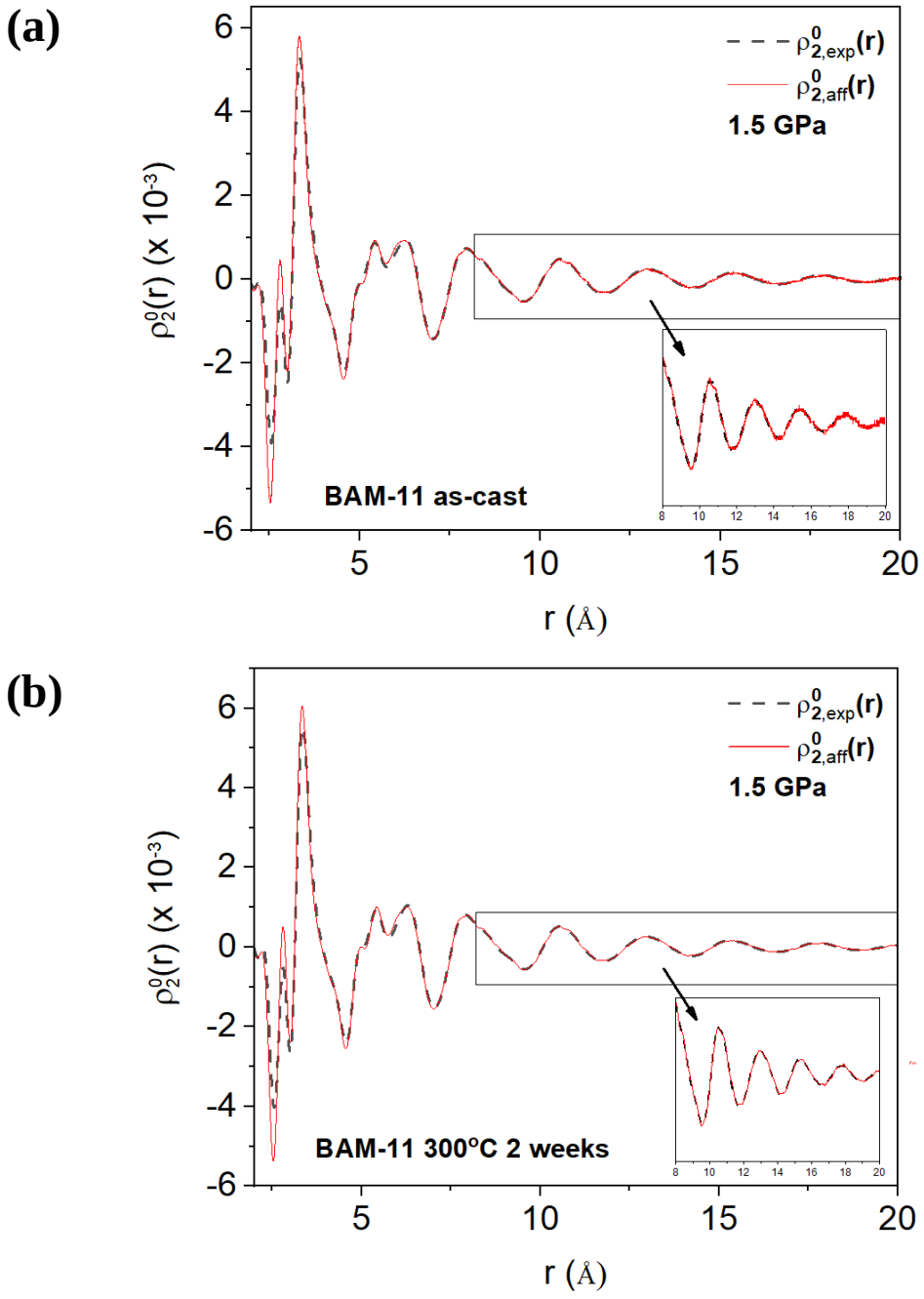

Figure 4-58 The anisotropic PDF, $\rho^0_2(r)$,, of the sample subjected to the stress of 1.5 GPa (black dashed line), compared to the anisotropic PDF of the sample under affine deformation (red solid line) for the (a) as-cast and (b) annealed conditions.

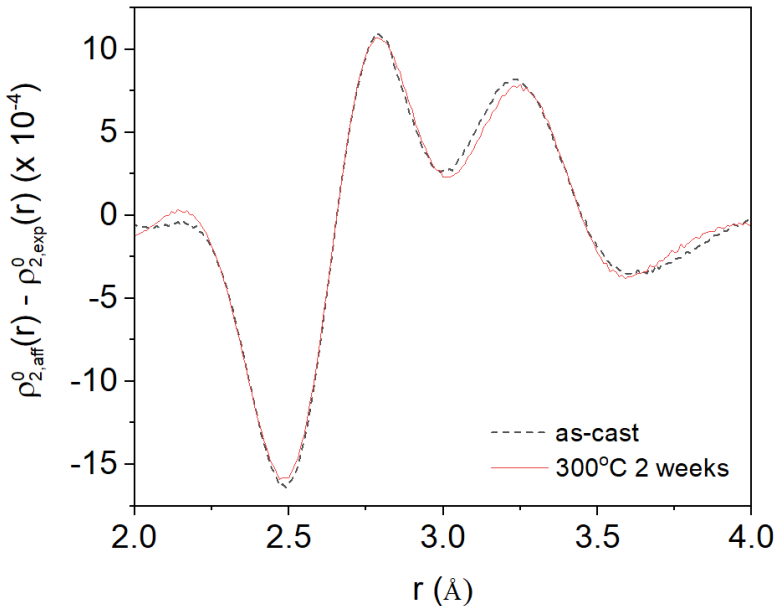

Figure 4-59 The difference $\rho^0_{2,exp} - \rho^0_{2,aff}$ for the as-cast and annealed (300 °C, 2 weeks) BAM-1 BMG.

spherical Bessel transformation from Eq. (3-10). In contrast to the isotropic components, as shown in figures 4-55(a)-(d), the elliptical components show significant changes in which the amplitudes were approximately proportional to the stress. However, similar to the results for the isotropic components [see figures 4-55(a)-(d)], the shape was almost independent of the applied stress. To further analyze the anisotropic PDF, the affine anisotropic PDF, $\rho^0_{2,\mathrm{aff}}(r)$, under affine deformation is introduced [255]. Figures 4-58(a)-(b) present the fitting of the experimental and affine anisotropic PDFs, i.e., $\rho^0_{2,\mathrm{exp}}(r)$ with the $\rho^0_{2,\mathrm{aff}}(r)$, of the as-cast and annealed BAM-11 samples. As shown in the inset, the fitting works well for r > 6.5 Å. On the other hand, there was a noticeable difference for lower r, especially at distances associated with the first nearest neighbor. Figure 4-59 displays the deviation of the experimental anisotropic PDFs from the affine anisotropic

PDF, $\Delta\rho_2^0 = \rho_{2,\text{exp}}^0 - \rho_{2,\text{aff}}^0$ for both conditions. It was found that the as-received condition exhibited larger oscillations in the graph as compared to the annealed specimen in the first shell.

4.2.3.4 Compression Testing

Figure 4-60(a) displays the room temperature stress vs. time curves for the as-cast and annealed (300 ^{o}C, 1 week) BAM-11 BMG compressed at a strain rate of 2×10^{-4} s^{-1}. As can be observed, the annealed sample was compressed for 1,060 s before rupturing (generally high compressive ductility), whereas the as-cast sample fractured after a significantly shorter period of 360 s and much lower plastic compressive deformation. Figures 4-60 (b) and (c) show a close-up of the serration behavior during compression. It is apparent in the figures that the specimen that was annealed exhibited more irregular serrated flow as compared to the as-cast specimen. Figures 4-61(a)-(c) present similar graphs for as-cast and annealed (300 ^{o}C 2 weeks) BAM-11 BMG that was compressed at a strain rate of 2×10^{-5} s^{-1}. From figures 4-61 (b)-(c) it can be observed that the serrated flow for the sample that was annealed at 300 ^{o}C for 2 weeks exhibits a greater number of fluctuations as compared to the as-cast condition.

4.2.3.4.1 Serrated Flow Analysis

Figure 4-62(a) presents the results of the sample entropy (complexity) modeling and analysis for the as-cast BAM-11 BMG compressed in the unconstrained condition at strain rates of 2×10^{-4} and 2×10^{-5} s^{-1}. For both conditions, the sample-entropy curve was found to increase, in general, with increasing scale factor. Beyond a scale factor of 1, the sample entropy for the specimen that was compressed at the higher strain rate exhibited sample entropy values that were greater as compared to the specimen compressed at the lower strain rate.

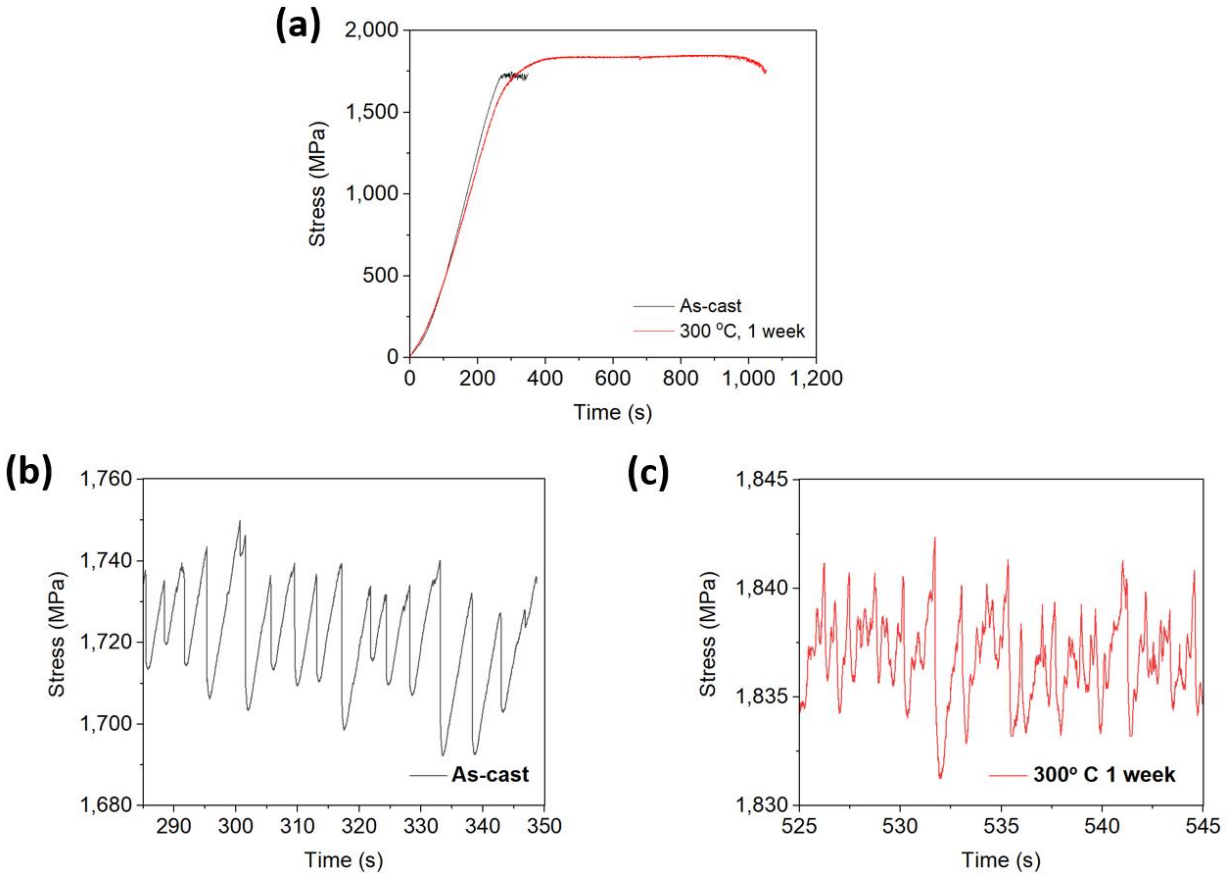

Figure 4-60 Graphs for the (a) stress vs. strain curves for the BAM-11 BMG compressed at a strain rate of 2×10^{-4} s^{-1} and the close-up of the serration behavior for the (b) as-cast specimen and (c) the sample annealed at 300 ^{o}C for 1 week.

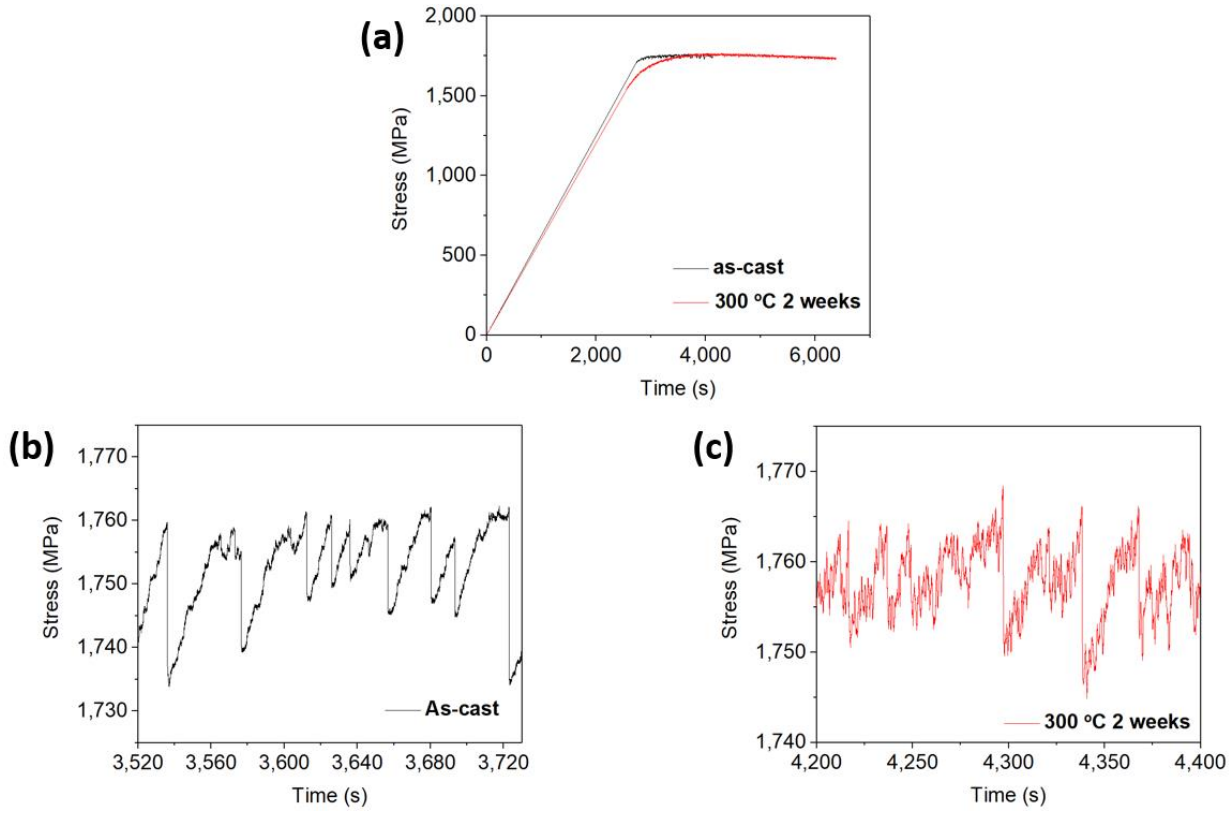

Figure 4-61 Graphs for the (a) stress vs. strain curves for the BAM-11 BMG compressed at a strain rate of 2×10^{-5} s^{-1} and the close-up of the serration behavior for the (b) as-cast specimen and (c) the sample annealed at 300 °C for 2 weeks.

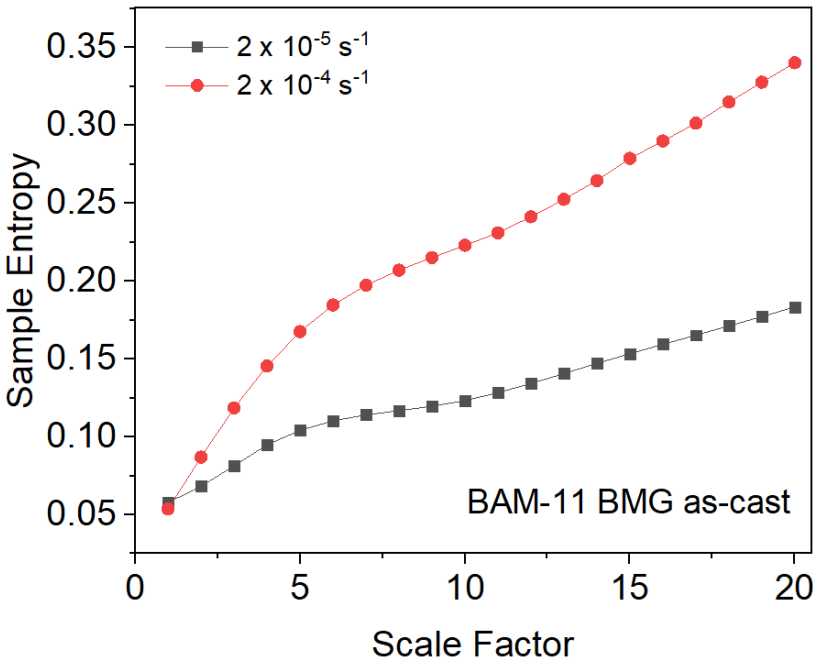

Figure 4-62 The sample entropy vs. the scale factor for the BAM-11 BMG specimen that was compressed in the unconstrained conditions at strain rates of 2×10^{-4} and 2×10^{-5} s^{-1}.

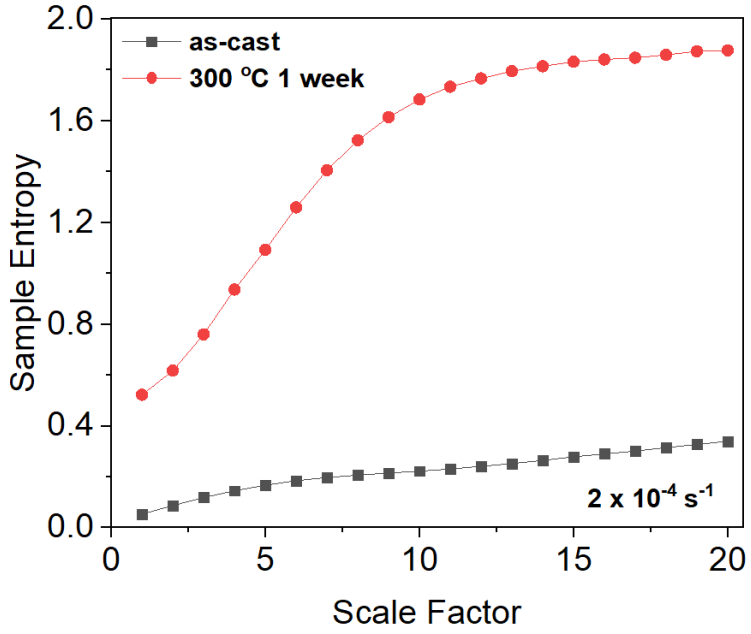

Figure 4-63 The sample entropy vs. the scale factor for the as-cast and annealed (300 ^{o}C, 1 week) BAM-11 BMG specimen that was compressed in the unconstrained conditions at a strain rate of 2×10^{-4} s^{-1}.

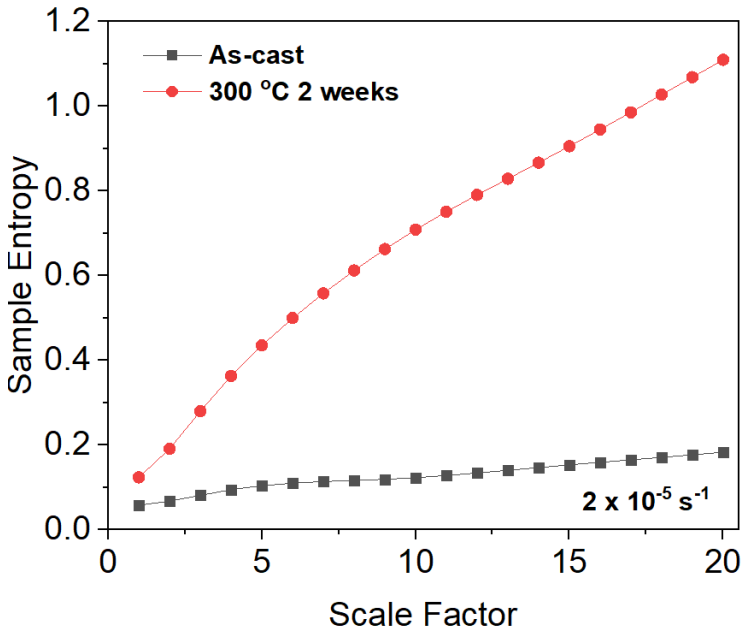

Figure 4-64 The sample entropy vs. the scale factor for the as-cast and annealed (300 °C, 2 weeks) BAM-11 BMG specimen that was compressed in the unconstrained conditions at a strain rate of 2×10^{-5} s^{-1}.

Figure 4-63 presents the sample entropy curves for the as-cast and annealed (300 °C, 1 week) BAM-11 BMG that was compressed in the unconstrained condition at a strain rate of 2×10^{-4} s^{-1}. Similar to the results for figure 4-62, the sample entropy increased with increasing scale factor. For the annealed sample, the sample entropy was significantly higher as compared to the as-cast specimen for all scale factors. Figure 4-64 shows the sample entropy curves for the as-cast and annealed (300 °C, 2 weeks) BAM-11 BMG that was compressed in the unconstrained condition at a strain rate of 2×10^{-5} s^{-1}. As with the previous figure, the sample entropy was larger for the annealed specimen, indicating that the annealed sample exhibited more complex behavior during the serrated flow, as compared to the as-cast condition.

4.2.4 Helium Diffusion Experiments

The goal of these experiments is to gain a greater understanding on how helium diffuses in amorphous, as compared to crystalline, alloys. The current hypothesis is that He diffusion could be significantly higher in noncrystalline materials compared to crystalline materials, which if demonstrated would imply improved resistance to He embrittlement effects, etc. (important for fusion energy applications due to the high amount of transmutation He generation in materials exposed to 14 MeV D-T neutrons). There have been reports that some amorphous materials do indeed exhibit very rapid He diffusion [100]

4.2.4.1 Microstructural Characterization

Figures 4-65(a)-(b) show the TEM BF and corresponding SAD images for two of the BAM-11 BMG specimens that were He irradiated to a fluence of 5×10^{15} cm^{-2}, which amounted to approximately 3×10^{3} atomic parts per million in the implanted region of the alloy. Figure 4-65(a) represents the fully amorphous specimen that was post-annealed at 250 ^{o}C for 15 minutes, while figure 4-65(b) corresponds to the partially crystallized BMG sample that was annealed for the same condition after implantation. It is apparent from figure 4-65(a) that crystallites and bubbles with appreciable size (within the TEM resolution) did not form in the amorphous matrix during the annealing.

4.2.4.2 Nuclear Reaction Analysis

Figures 4-66(a)-(d) compare the results of the nuclear reaction analysis for the as-irradiated and annealed (250 ^{o}C, 15 minutes) amorphous and partially crystallized BAM-11 and Cu BMGs. From the results, two things can be observed in all the figures. Firstly, the peaks did not broaden

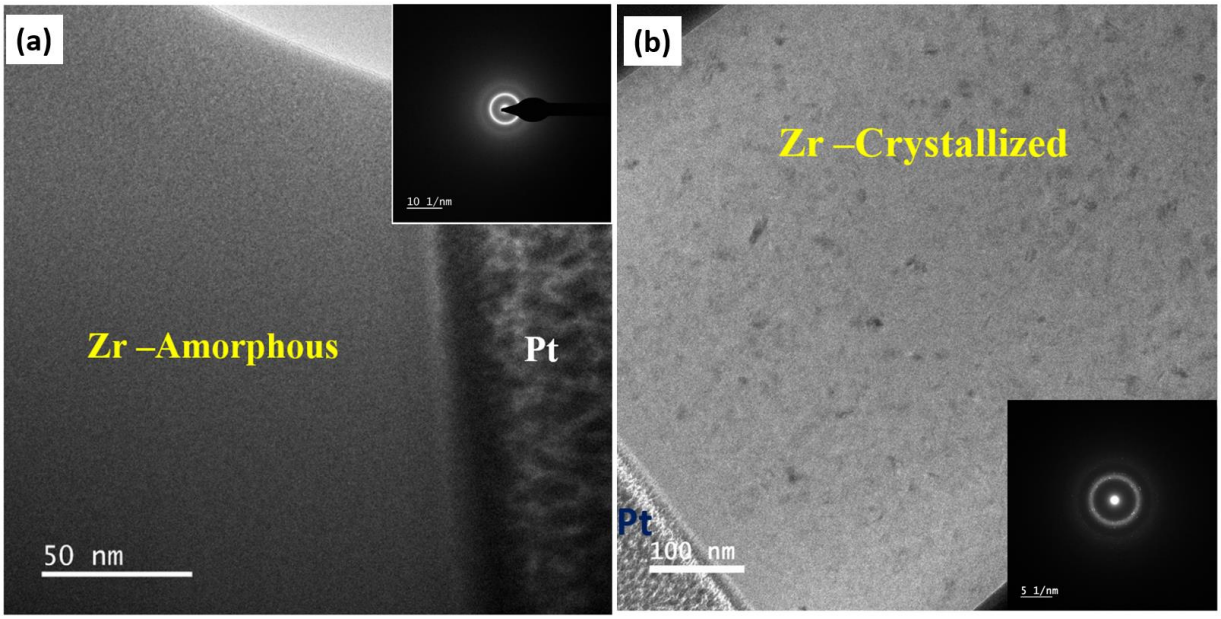

Figure 4-65 TEM BF and corresponding SAD images for the He implanted (5×10^{15} cm^{-2}) (a) amorphous BAM-11 BMG (b) partially crystallized BAM-11 BMG. Both samples were annealed after the He implantation at a temperature of 250 ^{o}C for 15 minutes.

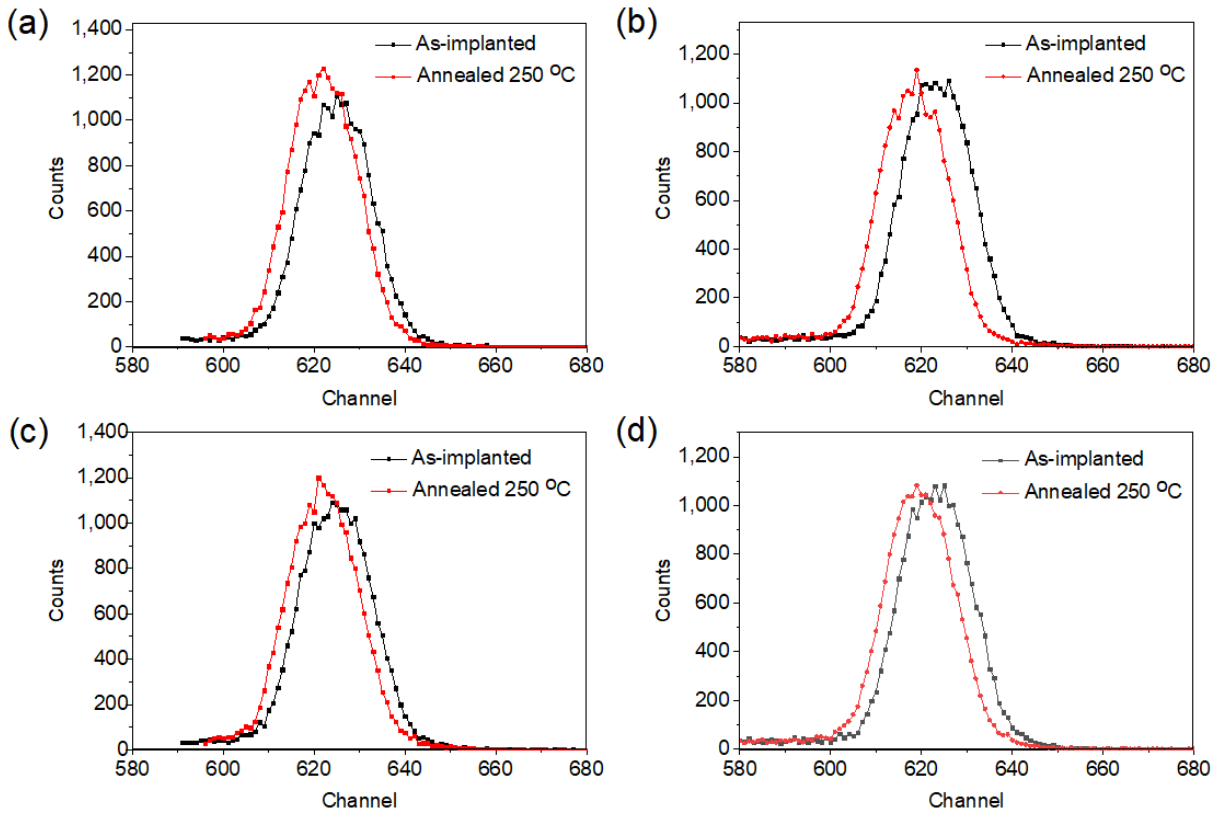

Figure 4-66 Nuclear reaction analysis results for the as-implanted (150 keV He, 5×10^{15} cm^{-2}) and annealed (250 °C, 15 minutes) samples (a) Amorphous BAM-11 BMG, (b) partially crystallized BAM-11 BMG, (c) amorphous Cu BMG, and (d) partially crystallized Cu BMG.

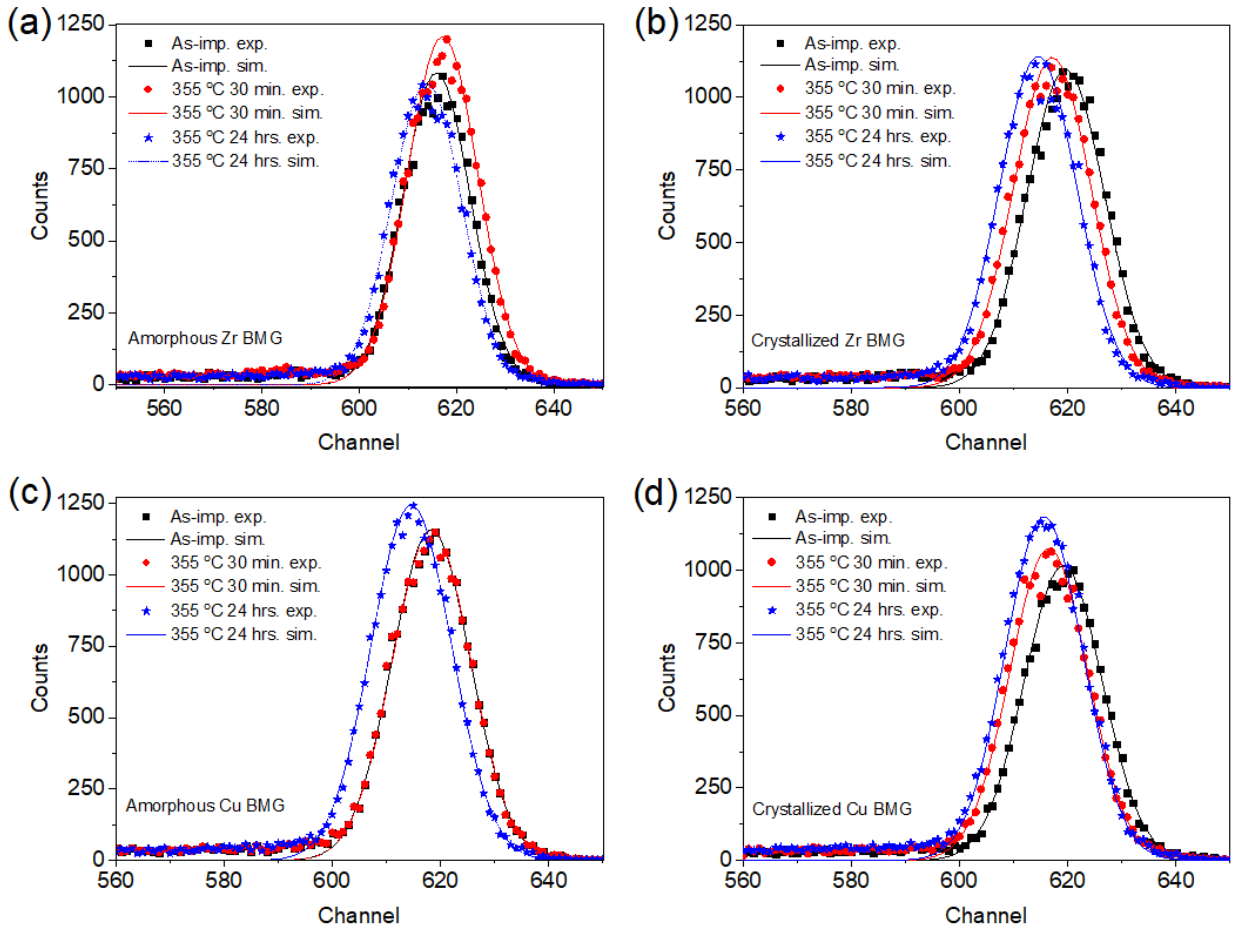

Figure 4-67 NRA results for the (a) amorphous BAM-11 BMG, (b) amorphous Cu BMG, (c) partially crystallized BAM-11 BMG, and (d) partially crystallized Cu BMG after implantation by 150 keV to a fluence of 5×10^{15} cm^{-2}.

to an appreciable extent. Secondly, there was an apparent peak shift to lower channels, and hence closer to the surface.

Figures 4-67(a)-(d) show the latter experiment where the amorphous and partially crystallized BAM-11 and Cu BMGs were irradiated and then post-irradiation annealed at 355 ^{o}C for both 30 minutes and then 24 hours. Similar to figures 4-66(a)-(d), there was no apparent peak broadening. From these results, it can be surmised that the helium did not diffuse in either alloy for the investigated annealing conditions, whether in the amorphous or partially crystalline form.

4.2.4.3 Thermal Desorption Spectroscopy

Figure 4-68 displays the XRD patterns for the originally amorphous and partially crystallized BAM-11 BMG after the TDS was performed. As can be seen, the specimens all displayed multiple peaks throughout the diffracted region, indicating that the samples were partially crystalline after the experiment. Furthermore, the patterns were very similar to one another, indicating that the specimens had similar crystalline structure.

Figures 4-69(a)-(c) compares the results of the He desorption spectra from the amorphous and partially crystallized BAM-11 BMG and Cu BMG specimens that were implanted with 150 keV He ions. The BAM-11 BMG specimens were implanted two fluences, namely 2 and 5×10^{15} cm^{-2}, whereas the Cu BMG was implanted to a fluence of 5×10^{15} cm^{-2}. To produce the spectra, the specimens were thermally annealed with a constant ramping rate of 0.5 ^{o}C/s. Figure 4-69(a) presents the results for the specimens irradiated to a fluence of 2×10^{15} cm^{-2}, while figure 4-69(b) shows a comparison for the samples irradiated to a fluence of 5×10^{15} cm^{-2}. Figure 4-69(c), on the other hand, displays the results for the amorphous and partially crystallized Cu BMG samples.

An energy scale is displayed on the top horizontal axis of the graph, where the values correlate with the temperature scale presented on the bottom axis.

With respect to the figure 4-69(a), the amorphous BAM-11 BMG sample exhibited interesting behavior. For instance, there were a few broad peaks that occurred in a stair-step pattern for temperatures ranging from 330 to 447 ^{o}C. This type of pattern indicates that He is being released from a variety of different trapping sites during heating. Furthermore, the center of these peak steps corresponded to activation energies of 1.77 eV, 1.82 eV and 1.98 eV, respectively. The sharp peak centered around 467 ^{o}C (2.17 eV) is thought to be associated with the desorption of He during a crystallization process that occurs after the initial crystallization of the alloy [368]. Interestingly, no such peak was observed at the crystallization temperature of the alloy (452 ^{o}C

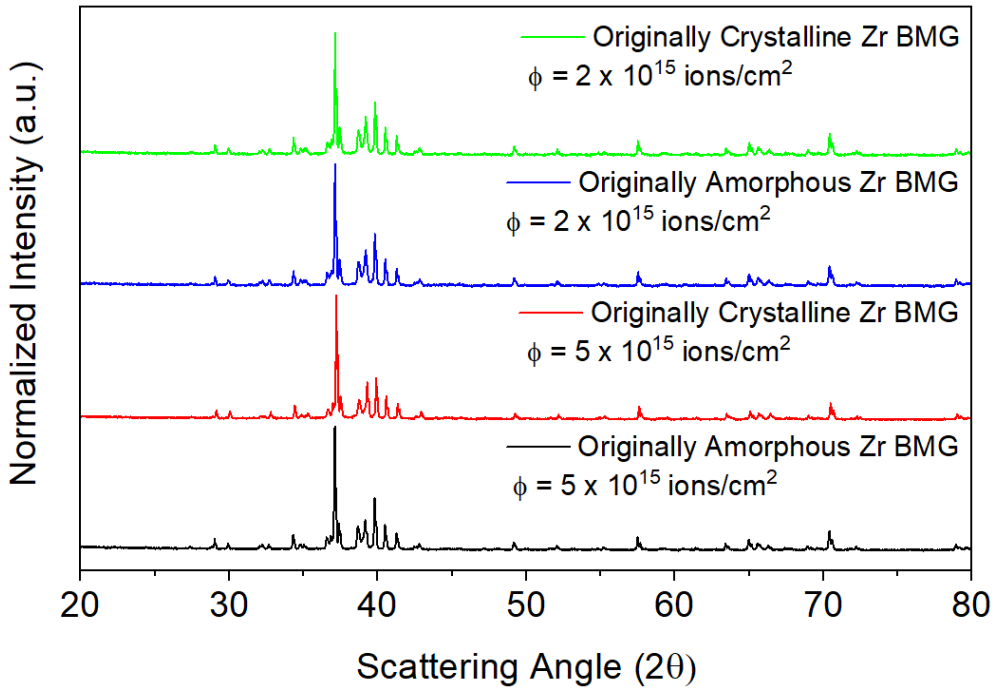

Figure 4-68 XRD patterns for the BAM-11 BMG specimens that in which they were exposed to He fluences of 2×10^{15} cm^{-2} and 5×10^{15} cm^{-2}.

[368]). Another peak centered around 693 ^{o}C (2.85 eV) can be observed in the figure that was followed by a gradual increase in the desorption flux up to the maximum heating temperature of 770 ^{o}C. As for the partially crystallized sample, no significant desorption was observed below a temperature of 670 ^{o}C. However, a final peak can be observed the spectra that is centered 762 ^{o}C, which corresponds to an activation energy of 3.06 eV.

For figure 4-69(b), the partially crystallized alloy released more He as compared to the amorphous sample, for temperatures below 625 ^{o}C. Similar to figure 4-69(a), there were a few broad peaks that occurred in a stair-step pattern for temperatures ranging from 313 to 490 ^{o}C for the partially crystallized specimen. The center of these peak steps corresponded to activation energies of 1.74 eV, 1.82 eV and 2.05 eV, respectively. The amorphous sample exhibited a broad peak centered around 410 ^{o}C, which corresponded to an activation energy of 2.00 eV. Similar to figure 4-69(a), a sharp peak centered around 470 ^{o}C (2.18 eV) can be observed for the amorphous BAM-11 BMG. There was a final peak that was centered for both samples, respectively, at 756 ^{o}C (3.03 eV) and 762 ^{o}C (3.06 eV) for the amorphous and partially crystallized samples.

As for the Cu implanted specimens, as shown in figure 4-69(c), both the amorphous and partially crystallized samples exhibited similar trends below 500 ^{o}C. For instance, a broad peak centered around ~420^{o}C can be observed, which corresponded to an activation energy of 2.03 eV. As for the fully amorphous specimen, there was a sharp peak centered around ~505 ^{o}C, which corresponded to an energy of 2.29 eV. This peak is most likely is attributed to the He released during crystallization the alloy (509 ^{o}C) [358]. For both specimens, there was a final peak that was centered, respectively, at 710 ^{o}C (2.90 eV) and 730 ^{o}C (2.96 eV) for the partially crystallized and amorphous samples.

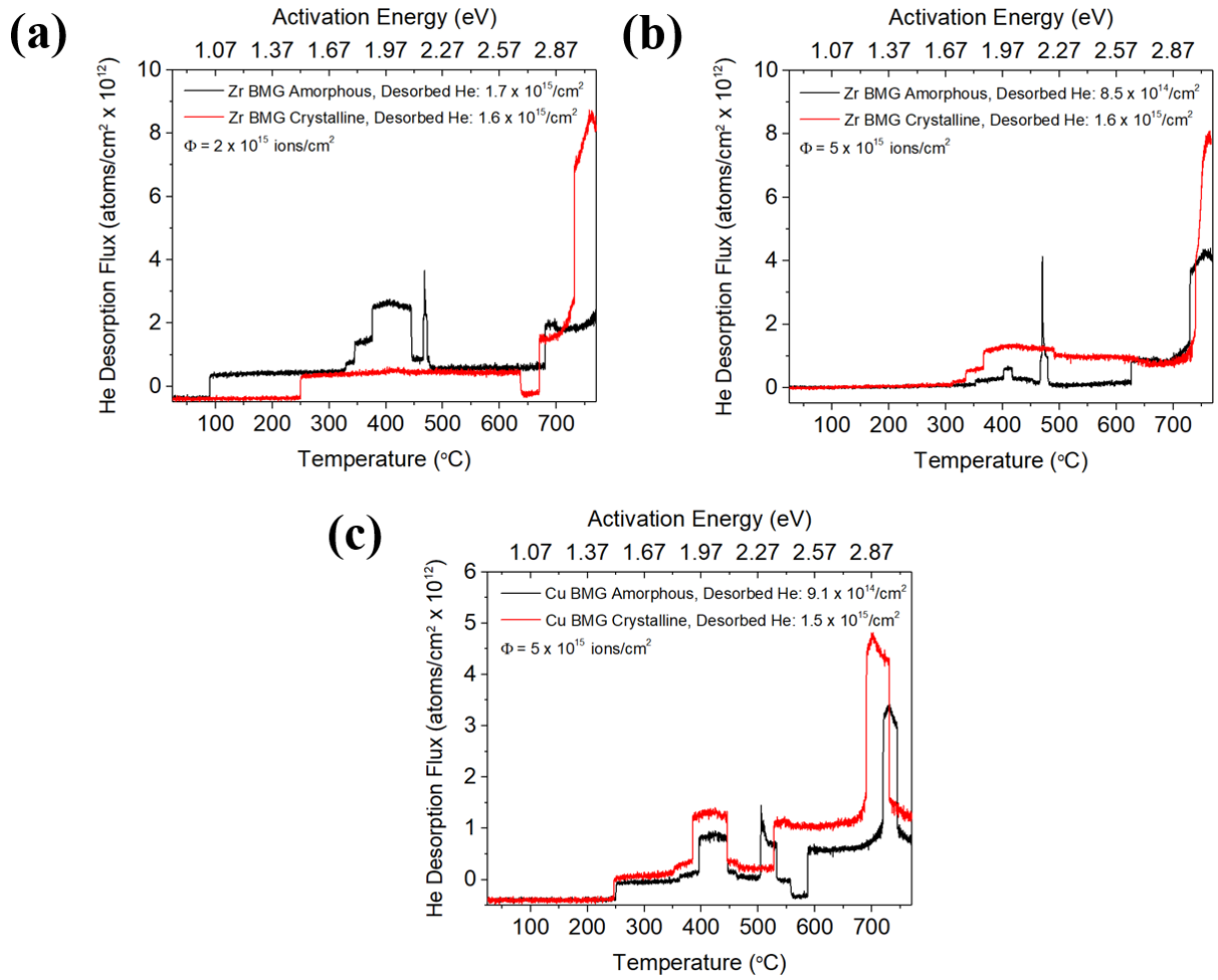

Figure 4-69 Thermal helium desorption spectra of the 150 keV He implantation of the (amorphous and partially crystalline) (a) BAM-11 BMG (2×10^{15} cm^{-2}), (b) BAM-11 BMG (5×10^{15} cm^{-2}), and Cu BMG (5×10^{15} cm^{-2}).

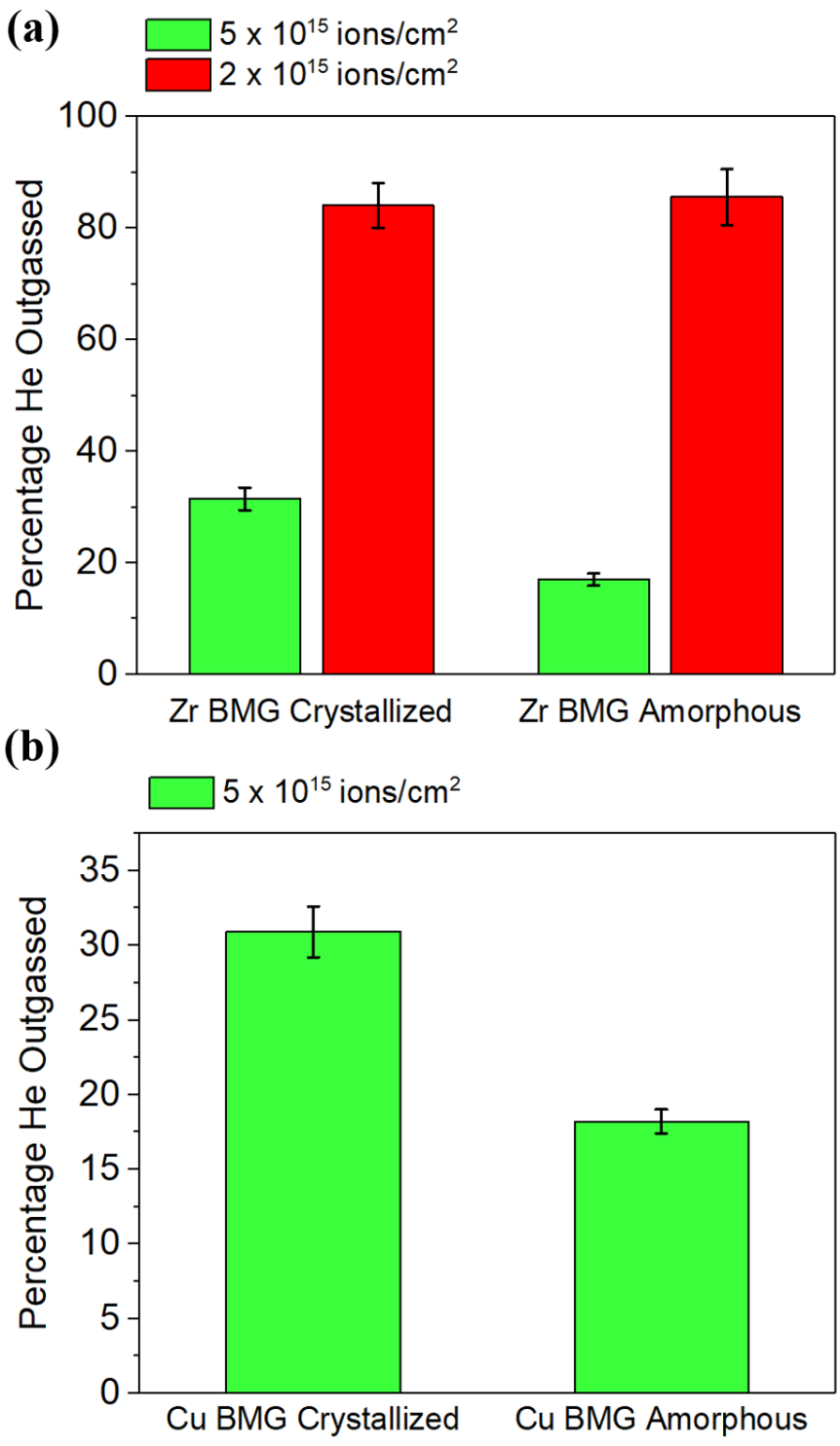

Figure 4-70 Helium outgassing statistics in the (a) BAM-11 BMG samples (implanted He fluences of 2×10^{15} and 5×10^{15} cm^{-2}) and the (b) Cu BMG samples (implanted He fluence of 5×10^{15} cm^{-2}).

Figures 4-70(a)-(b) presents percentage of He that desorbed from the amorphous and partially crystallized Zr and Cu BMG specimens (fluences of 2×10^{15} and 5×10^{15} cm^{-2}). From figures 4-70(a)-(b) it can be observed that at a fluence of 5×10^{15} cm^{-2}, there was significantly more He desorption exhibited by the partially crystallized Zr and Cu BMGs. In contrast, there was no substantial difference in the amount of He released by the BAM-11 BMG that was implanted to a fluence of 2×10^{15} cm^{-2}. For both the amorphous and partially crystallized BAM-11 BMG, more He was released as a proportion to total fluence after implantation to a fluence of 2×10^{15} cm^{-2}. Finally, the data from figures 4-70(a)-(b) indicates that for a fluence of 5×10^{15} cm^{-2}, both the amorphous and partially crystallized BAM-11 and Cu BMGs desorbed approximately the same amount of He. Considering both the NRA (figure 4-66) and TDS (figures. 4-69, 4-70) results, pronounced He diffusion in the two investigated BMGs begins to occur around 360-400C at the lower implantation fluence.

CHAPTER 5 DISCUSSION

5.1 Ion Irradiation Experiments

5.1.1 9 MeV Ni Ion Irradiations

5.1.1.1 BAM-11 BMG

As can be seen in figure 4-11, the glancing XRD patterns indicate that the BAM-11 BMG remained amorphous during the ion irradiation up to 290 ^{o}C. However, the alloy did partially crystallize when irradiated at 360 ^{o}C. To confirm the crystallization mechanism, glancing XRD was performed on the unirradiated side of the sample and then compared to bulk XRD measurements that were performed on a separate sample that was annealed at 500 ^{o}C for 2.5 hours. It should be mentioned that the temperature of 500 ^{o}C was chosen since it is sufficiently above the reported crystallization temperature of the BAM-11 BMG [352, 368].

The similarity of the patterns, as displayed in figure 4-12, indeed confirms that the crystallization mechanism was thermal in nature. In addition, TEM characterization of the bombarded region of the specimen irradiated at 360 ^{o}C shows that not only did the sample partially crystallize during irradiation, but that the crystallization process occurred in a heterogenous fashion. It is also noted that as displayed in figure 4-11, there was an appreciable peak shift to lower values for the irradiated samples. This shift in the peak towards lower angles indicates that there was an increase in the distance between neighboring atoms inside the amorphous matrix [421].

In terms of the nanoindentation behavior of the as-cast and irradiated BAM-11 BMG [see figures 4-20(a)-(b)], the samples exhibited a pronounced indentation size effect on the measured nanoindentation hardness, particularly for indent depths below ~200 nm. For the specimens that were irradiated by 9 MeV Ni^{3+} ions to midrange doses of ~10 dpa at 25-290 ^{o}C, only slight changes

in hardness were observed. This result indicates, therefore, that the nanoscale mechanical properties are not significantly affected by exposure during irradiation to temperatures at or below 290 ^{o}C. In contrast, increased hardening was observed in the ion irradiated region and unirradiated substrate after irradiation at 360 ^{o}C for ~7 hours. As discussed previously, this hardness was attributed to the partial crystallization of the glassy matrix due to thermal annealing effects.

In the majority of cases, the crystallized form of a metallic glass is harder than its amorphous counterpart since nanocrystallites may disturb the passage of shear bands [427]. Such an effect was reported by Luo et al., where it was found that 300 keV Ar^{+} room temperature irradiation to a dose of 37 dpa led to significant increase in the hardness of $Zr_{61.5}Cu_{21.5}Fe_5Al_{12}$ BMG, and was associated with the formation of fcc nanocrystals during irradiation [345]. The current study, however, found that an increase in the hardness of the BAM-11 BMG that was irradiated by 9 MeV Ni^{3+} at 360 ^{o}C (~7 hours) was the result of thermally induced partially crystallization of the amorphous matrix.

In terms of the partial crystallization that occurred during irradiation, there were some sporadic results. For instance, 9 MeV Ni^{3+} irradiation at 360 ^{o}C for 7 hours led to partial crystallization of both the BAM-11 and Cu based BMGs. However, no such crystallization was observed in the specimen that was irradiated by 5.5 MeV C^{+} at 360 ^{o}C for the same amount of time. In addition, the BAM-11 BMG specimen did crystallize during irradiation by 5.5 MeV C^{+} at 290 ^{o}C for the same time period. These spurious results indicate that there were some occasional issues with thermal contact of individual specimens for the sample holder used in these experiments. A careful redesign of the sample holder to provide more reliable sample temperatures is therefore strongly recommended for future studies.

As for the ISE behavior of the as-cast and irradiated BAM-11 BMG specimens, the poor linear fit between the near-surface and deep (> 450 nm indent depth) indents [see figure 4-22(a)], suggests that the Nix-Gao model [212] is not valid to accurately quantify the nanoindentation hardness of the alloy. The discrepancy with this model is somewhat unexpected since it was used successfully in a previous experiment to describe the ISE in this alloy [210].

One possible reason for the deviation may be the result of surface defects formed during mechanical polishing. This effect of surface polishing on the model is inherent in the 1/h dependence in the Nix and Gao model, where this term becomes more significant at shallower depths. Finally, the significantly larger H_0 values for the specimen irradiated at 360 ^{o}C (for the unirradiated region), probably corresponds to the partial crystallization of the specimen. Another reason why the model may not be appropriate for the ISE in the BAM-11 BMG is due to physics considerations, since the model assumes the ISE is associated with geomentrically necessary dislocations whereas the BAM-11 BMG does not produce dislocations during deformation due to its amorphous structure.

In addition to the Nix and Gao model, the equation from the Lam and Chong model [211], as displayed in figure 4-23(a), provided a slightly better fit (albeit still poor) to the nanoindentation data for the as-cast and 9 MeV Ni^{3+} irradiated samples. From the above results it can be surmised that this model is also quantitatively not valid for the ISE of the BAM-11 BMG. As with the Nix-Gao model, the significantly larger H_0 values for the specimen irradiated at 360 ^{o}C are most likely attributed to the partial crystallization of the amorphous matirx.

An extrapolation model recently applied to various metallic glass thin films [217] was also used to analyze the ISE in the as-cast and irradiated BAM-11 BMG, but was ultimately not successful. It was found that this method failed for two reasons, namely the inability of the model

to appropriately fit the data and because the underlying equation produced characteristic length values that were negative. This issue with h^* is especially apparent in the underlying relation $h^* \propto \frac{1}{1-\chi_L}$, where χ_L denotes the fraction of fertile sites [428] contained in the amorphous alloy. Therefore, a negative value of h^* implies that the fertile sites comprise more than 100 % of the matrix, which is an impossibility. In addition to the above, there were more conflicting results with regards to the extrapolated hardness values. For instance, the Lam and Chong model provided H_0 values that were lower for all irradiation temperatures as compared to the as-cast condition, while for the Nix and Gao model, only the room temperature irradiation led to a decrease in H_0.

Previous investigations have also examined the effects of Ni irradiation on the properties of BAM-11 BMG. For instance, Perez-Bergquist et al. examined the response of BAM-11 BMG after irradiation by 3 MeV Ni^+ to varying irradiation dose and thermal conditions [98, 420]. In [98], it was reported that samples irradiated to a midrange dose of 0.1 dpa at 200 ^oC did not exhibit significant changes in hardness. In [420], it was found that the hardness decreased after being annealed at 300 ^oC for 48 hours and subsequently irradiated to a midrange dose of 10 dpa at 25 ^oC. It was found that for both investigations that the material did not crystallize under any irradiation or annealing condition, via TEM characterization. Since the metallic glass can become extremely brittle upon crystallization, this resistance to phase change during irradiation is especially important. Based on the results of the current and previous studies, it can be concluded that the effects of ion irradiation on the microstructure and mechanical properties of BAM-11 BMG appears to be relatively modest for doses up to ~10 dpa at 25-290 ^oC.

5.1.1.2 Cu BMG

The glancing XRD characterization, as displayed in figure 4-15, shows that the $Cu_{60}Zr_{20}Hf_{10}Ti_{10}$ BMG did not crystallize during the ion irradiation up to 290 ºC. However, the Cu BMG sample partially crystallized when irradiated at 360 ºC for 7 hours. This result indicates that the Cu based BMG may not be suitable for irradiation environments where it will be exposed to temperatures greater than ~0.75 T_g for prolonged periods of time.

As reported in [279, 429], it was found that the BAM-11 BMG behaved in a similar fashion to the Cu BMG where it did not crystallize when irradiated by 9 MeV Ni^{3+} ions to a midrange dose of 10 dpa at room temperature and 290 ºC. Perez-Bergquist et al. reported that the same alloy did not crystallize when irradiated by 3 MeV Ni^{+} ions to a midrange dose of 1 dpa at 200 ºC [98]. In terms of microstructure, Yuka et al. observed that 200 MeV Xe irradiation (room temperature) of $Zr_{50}Cu_{40}Al_{10}$ BMG to a dose of 0.25 dpa resulted in a decrease in the free volume content of the material without causing crystallization [430, 431]. This crystallization resistance that is exhibited by the BMGs during irradiation at lower temperatures could be attributed to various factors. These factors include low irradiation enhanced diffusivity and a high required driving force for irradiation-induced crystallization [432].

As can be seen in figure 4-16, glancing XRD that was performed on the unirradiated side of the specimen suggests that the partial crystallization that occurred during irradiation at 360 ºC was most likely caused by thermal annealing, and not irradiation damage. Also shown in the figure is the pattern for the Bulk XRD measurements that were performed on a separate specimen that was annealed at 520 ºC for 2.5 hours. The temperature of 520 ºC was chosen as it is above the reported crystallization temperature (T_x) of the alloy [358]. The apparent similarity between all three patterns gives further evidence that partial crystallization was thermally induced.

In addition to the present work, other investigations have reported on the irradiation induced crystallization of Cu based BMGs. Carter et al. studied the crystallization of $Cu_{50}Zr_{45}Ti_5$ metallic glass during irradiation by 1 MeV Cu ions at room temperature. It was reported that $CuZr_2$ and $Cu_{10}Zr_7$ crystalline phases formed in the amorphous matrix [304]. Wang et al. observed that $Cu_{10}Zr_7$ phases formed when heated to 700 ^oC while exposed to a pressure at 5 GPa during in-situ XRD experiments [358]. In another investigation, Xie et al. examined the nanocrystallization behavior of a $Cu_{50}Zr_{45}Ti_5$ metallic glass melt spun ribbons irradiated at room temperature by 200 keV electrons to fluences of 2.4×10^{21} cm^{-2} - 2.9×10^{22} cm^{-2} [433]. TEM characterization determined that monoclinic CuZr nanocrystallites formed during the irradiation. A subsequent investigation, however, found that room temperature 200 keV electron irradiation to a fluence of 4.4×10^{22} cm^{-2} led to the formation of $Cu_{10}Zr_7$ phases in the same material [434]. Finally, Fu et al. examined the Ar-ion-milling induced nanocrystallization of $Cu_{50}Zr_{45}Ti_5$ metallic glass [435]. TEM characterization revealed the presence of $Cu_{10}Zr_7$ nanocrystals after irradiation by Ar ions with accelerating voltages of 2 to 4 kV at room temperature.

From these investigations it can be surmised that CuZr polymorphs typically form in Cu based BMGs during the crystallization process. However, the outcomes of the present experimental studies involving the Cu BMG appear at odds with their results. More specifically, the results of the Rietveld refinement suggest that the nanocrystallites which formed in the sample that was irradiated at 360 ^oC consisted of tetragonal CuTi and hexagonal CuZrTi phases. This discrepancy may be explained by the following. In the study performed by Wang et al. [358], there were some crystalline peaks that were not identified in the XRD pattern, and could have corresponded to either the CuZrTi or CuTi phases.

Carter et al. hypothesized that crystallites which formed in the $Cu_{50}Zr_{45}Ti_5$ BMG during 1 MeV Cu irradiation (room temperature) was a consequence of the enhanced atomic mobility resulting from the introduction of excessive free volume during quenching [304]. Here, the free volume is spread over a relatively large region, resulting in increased atomic mobility that enhances the short-range order which leads to crystallite nucleation. Importantly, the Cu BMG currently studied did not crystallize during irradiation by a more energetic ion (9 MeV) at temperatures up to 290 ^{o}C. This lack of induced crystallization may be the result of a greater number of elements with differing radii. The greater degree of atomic size mismatch in the $Cu_{60}Zr_{20}Hf_{10}Ti_{10}$ BMG, as opposed to the $Cu_{50}Zr_{45}Ti_5$ BMG, will favor a denser random packing structure. Consequently, atomic rearrangement that can lead to crystallization will be harder to achieve in the $Cu_{60}Zr_{20}Hf_{10}Ti_{10}$ BMG [78, 436, 437].

Interestingly, experiments involving other types of metallic glasses have yielded varying results. For example, a study involving the crystallization of $Co_{86.7}Fe_{3.6}Si_{2.7}Mn_{3.5}B_{3.5}$ metallic glass ribbons reported that that irradiation can induce a different crystallization mechanism in metallic glass, as opposed to thermal annealing [330]. It was observed that although the MG crystallized after irradiation by 30 keV Ar^{+} ions to a peak dose of 840 dpa at 200 ^{o}C, it did not crystallize during thermal annealing until the temperature reached 500 ^{o}C. With respect to the microstructure, XRD revealed that during the thermally induced crystallization, the Co-based solid solution and CoB crystalline phases formed during devitrification. Furthermore, an unknown cubic aperiodical phase was also observed after irradiation, which was thought to be isostructural to the α-Mn aperiodical cubic phase. Thermal annealing after irradiation, at temperatures of 250 ^{o} and 300 ^{o}C (1 hour) recovered the amorphous phase. This recovered amorphous phase was thought

to contain non-crystalline long-range order structures consisting of polytopes with a non-integer order symmetry axis [438].

Before moving on, the odd results regarding the crystallization behavior of the 30 keV Ar ion irradiation Co based MG should be discussed. Perhaps the crystallization of the amorphous ribbon during irradiation at 200 ^{o}C was caused by an increased temperature in the sample induced by beam heating [439]. The high beam fluxes necessary to achieve 840 dpa in a reasonable time period may have also caused beam heating of the sample. Furthermore, the temperature during irradiation may have been higher than reported if the chamber temperature was not being accurately monitored. The lack of details pertaining to how the specimen temperature was monitored during irradiation raises questions as to the accuracy of the reported temperature.

The results of previous irradiation studies on BMGs is summarized in Table 5-1. As can be seen, some of the metallic glasses crystallized during irradiation at various irradiation temperatures, although some remained amorphous. It is apparent that in nearly all of the investigations listed, there was no mention as to how the sample temperature was monitored during the irradiation. This lack of reporting, therefore, raises serious concerns as to the accuracy of the reported irradiation temperatures. This issue with apparent temperature variability was also observed in the individual ion irradiation specimens during the thesis work, which further stresses the need for careful temperature monitoring during irradiation experiments.

Furthermore, several interesting or puzzling results can also be observed in the table. For instance, $Ti_{40}Zr_{10}Cu_{38}Pd_{12}$ BMG was found to crystallize during 200 keV/75 keV Ar ion irradiation at 347 ^{o}C, whereas $Zr_{55}Cu_{28}Al_{10}Ni_{7}$ BMG did not [325]. Moreover, neither of the two BMGs experienced crystallization after room temperature irradiation [325]. Since the T_g, T_x, and ΔT_x of the Zr BMG (429 ^{o}C, 498 ^{o}C, and 69 ^{o}C [440, 441]) is larger than that of the Ti BMG (412

Table 5-1 Summary of ion irradiation studies in amorphous alloys Irr.: Irradiation, Temp.: Temperature, *: Sample crystallized via thermal effects instead of irradiation damage.

Alloy	Specimen Type	Ion	Ion Energy (MeV)	Irr. Dose Rate (dpa/s)	Irr. Dose (dpa)	Irr. Temp. (^{0}C)	Crystallized? (Y/N)	Temp. Measurement	Ref.
$Ti_{40}Zr_{25}Be_{30}Cr_5$	Bulk	C, Cl	25	-	0.1(C) 5.7 (Cl)	25	N	-	[329]
$Ti_{40}Zr_{10}Cu_{38}Pd_{12}$	Bulk	Ar	0.2, 0.075 (consecutive)	0.008	29 (total)	347 25	Y N	- -	[325]
$Fe_{81}B_{13.5}Si_{3.5}C_2$	Ribbon	He	2.8	-	0.05	25	Y	-	[328]
$Fe_{80}Si_{7.43}B_{12.57}$	Ribbon	H	0.25	0.0003	5	25	N	-	[319]
$Fe_{78}B_{13}Si_9$	Ribbon	He	2.8	-	2	25	Y	-	[320]
$Fe_{79}B_{16}Si_5$	Ribbon	He	0.005	0.005	1	25	N	-	[302]
$Fe_{40}Ni_{40}P_{14}B_6$	Ribbon	He	0.04	0.0009	28	400	Y	-	[321]
$Ni_{52.5}Nb_{10}Zr_{15}Ti_{15}Pt_{7.5}$	Ribbon	Ni	1	0.0018	18	25	Y	-	[326]
$Ni_{52.5}Nb_{10}Zr_{15}Ti_{15}Pt_{7.5}$	Ribbon	Xe	18	-	0.00014	25	N	-	[324]
$Co_{61.2}B_{26.2}Si_{7.8}Ta_{4.8}$	Bulk	He	0.5	0.0009	40	25	N	-	[315]
$Co_{86.7}Fe_{3.6}Si_{2.7}Mn_{3.5}B_{3.5}$	Ribbon	Ar	0.03	0.17	840	200	Y	-	[330]
$Zr_{55}Cu_{28}Al_{10}Ni_7$	Bulk	Ar	0.2, 0.075 (consecutive)	0.006	22 (total)	347 25	N N	-	[325]
$Zr_{64}Cu_{17.8}Ni_{10.7}Al_{7.5}$	Bulk	He	0.5	0.00009	40	125	N	-	[315]
$Zr_{52.5}Cu_{17.9}Ni_{14.6}Al_{10}Ti_5$	Bulk	Ni	3	0.005	1	25 200	N	Thermocouple	[98]
$Zr_{52.5}Cu_{17.9}Ni_{14.6}Al_{10}Ti_5$	Bulk	Ni	9	0.0004	10	25 290 360	N N Y*	Thermocouple	[279, 429]
$Zr_{50}Cu_{40}Al_{10}$	Bulk	Xe	200	-	0.25	25	N	-	[430]
$Zr_{55}Cu_{30}Al_{10}Ni_5$	Ribbon	Cu	1	0.0001	16	< 50	Y	-	[310]
$Zr_{55}Cu_{30}Al_{10}Ni_5$	Bulk	Co	0.04	0.34	160	< 140	Y	-	[444, 445]
$Zr_{50}Cu_{35}Al_7Pd_5Nb_3$	Ribbon	Kr	1	-		420	Y	-	[323]
$(Cu_{47}Zr_{45}Al_8)_{98.5}Y_{1.5}$	Bulk	Ar	3	-	7.5	25	N	-	[446]
$Cu_{50}Zr_{45}Ti_5$	Ribbon	Cu	1	0.001	16	25	Y	-	[304]
$(Cu_{47}Zr_{45}Al_8)_{98.5}Y_{1.5}$	Bulk	He	0.5	0.0012	40	25	N	-	[314, 315]
$Cu_{60}Zr_{20}Hf_{10}Ti_{10}$	Bulk	Ni	9	0.0004	10	25 290 360	N N Y*	Thermocouple	This work

^{o}C, 447 ^{o}C, and 35 ^{o}C [442]), it is expected that that the former Zr BMG has greater glass formability and thermal stability that would make it more resistant to irradiation [443]. Finally, the $Ni_{52.5}Nb_{10}Zr_{15}Ti_{15}Pt_{7.5}$ metallic glass was found to crystallize when it was irradiated by 1 MeV Ni to a dose of 18 dpa, but did not crystallize during irradiation by 18 MeV Xe to a dose of 1.4×10^{-4}. This result suggests that irradiation dose may be a larger contributing factor to the crystallization of metallic glass during irradiation.

Despite the raised concerns, the results of these studies have important implications pertaining to the irradiation response of amorphous alloys. Firstly, in some metallic glasses total irradiation dose appears to be more of an influence as to whether a metallic glass will crystallize as compared to ion mass or energy. Secondly, it appears that the chemical complexity of the metallic glass may perhaps play an important role in determining the radiation resistance of the material. In this context, the enhanced irradiation resistance may be influenced by the mass disparity in addition to the "confusion principle" in which the stability (and T_g) of the glass increases as the number of elements in the metallic glass increases [125, 447]. It should also be mentioned that oxygen impurities may promote crystallization of the material during irradiation [355]. These impurities can assist in the heterogeneous nucleation of intermetallic phases, effectively decreasing the temperature or heating time at which crystallization can occur. Finally. considering only the few ion irradiation studies that utilized thermocouples to monitor the irradiation temperature ([98, 279, 429] and the current study) along with the studies from [324, 325], it appears that recrystallization has been reported only for irradiation temperatures approaching T_g for the given BMG.

On the other hand, beam heating may have been a contributing factor to the crystallization of the specimen during irradiation. It has been reported that in commercial ion implanters, ion

beam heating can result in temperature increases approaching hundreds of degrees [439]. Therefore, if not properly monitored, the sample temperature during irradiation could reach values that would result in the thermal-induced crystallization of the sample.

In terms of the nanoindentation behavior, only slight hardening was observed in the Cu BMG after irradiation by 9 MeV Ni^{3+} to midrange doses of ~10 dpa at 25 ^{o} and 290 ^{o}C (see figures 4-20(a)-(b)]. In contrast, the sample irradiated at 360 ^{o}C for 7 hours exhibited a significant increase in hardness, which is indicative of partial crystallization of the matrix during irradiation. Moreover, the nanoindentation hardness and XRD evaluation, as respectively shown in figures 4-20 and 4-15, indicate similar crystallization and depth-dependent hardness changes for the unirradiated and irradiated regions. Thus, these changes appear to be the result of thermal annealing effects instead of irradiation damage.

In terms of other Cu based BMGs, crystallization induced hardening has also been observed in He irradiated $Cu_{50}Zr_{45}Ti_5$ metallic glass [305]. The crystallization was found to occur in the specimens after room temperature 140 keV He irradiation to a dose of 4 dpa, which amounts to approximately 11 at.% He. Subsequent TEM characterization revealed the presence of either He bubbles and/or voids in the matrix. It was also found, via microindentation tests, that the irradiated sample exhibited greater hardness as compared to the as-cast condition. Furthermore, the enhanced hardness reached a maximum at the interrogated depth of 600 nm below the surface, which coincided with the presence of implanted He or the maximal nuclear stopping power at that depth.

The poor linear fit, as can be observed in figure 4-23(a) for all the sample conditions, suggests that the ISE model as derived by Lam and Chong [211] is not sufficient for analyzing the ISE in the Cu BMG. Perhaps the inadequate fit may arise from either surface artifacts created

during sample preparation or an inherent limitation of the model. Moreover, the nonlinear behavior is particularly noticeable in the irradiated region of the specimens, where the deviation becomes more significant at larger depths. Importantly, this behavior in the deeper region is unexpected for the as-cast specimen, since a variation in hardness vs. depth should not be observed there.

Importantly there was also a discrepancy in the linear fitting of the Lam and Chong model that was not accounted for by Lam et al. [209]. This discrepancy is related to the apparent deviation away from linearity for indentation depths beyond ~1.6 μm, which suggests that the model may not be applicable to BMGs. It should be mentioned that the Nix-Gao extrapolation method was also applied to the data. However, like with the BAM-11 BMG, this model gave a poorer fit as compared to the previous method. As discussed before, it is not surprising that the Nix Gao model does not provide an adequate fit to the data, since it is based on proximity to geometrically necessary dislocations to induce plastic deformation whereas such defects do not exist in Cu BMG. Based on the results of the BAM-11 and Cu BMGs, therefore, it can be surmised that a new model may be needed to examine the ISE in BMGs.

5.1.2 Lower Dose (0.5 dpa) Ion Irradiation Experiments

In general, there was no evidence for pronounced irradiation spectrum effects from a comparison of the nanoindentation mechanical properties behavior of the two investigated BMGs following irradiation with 9 MeV Ni ions (relatively high average primary knock-on energy of ~20 keV) versus 5.5 MeV C ions (relatively low average primary knock-on energy of ~5 keV). For both the BAM-11 and Cu BMGs, ion irradiation near room temperature produced similar hardening behavior as the as-cast material [figures 4-24(a), 4-26(a), 4-31(a), and 4-33(a)]. Either

slight hardening (Ni ion irradiation) or slight softening (C ion irradiation) was observed for the irradiated samples. At irradiation temperatures of 290 and 360 ^{o}C (excluding the anomalous result for C ion irradiated BAM-11 at 290 ^{o}C where thermal crystallization occurred), Ni ion irradiation generally produced slightly more hardening in the irradiated region compared to the C ion irradiations for both BMG materials. A more marked effect appeared to occur for the neutron irradiated sample compared to the ion irradiated samples, where pronounced softening was observed after neutron irradiation near room temperature (figure 4-38).

This significant increase in the hardness without apparent crystallization during the high temperature irradiation may be the result of thermally induced structural relaxation occurring in the amorphous matrix [448]. The idea that structural relaxation during irradiation leads to an increase in the hardness in metallic glass was theorized by Jiang et al. [449]. Here they postulated that a decrease in free volume, which accompanies structural relaxation, results in a higher resistance to localized plastic deformation (i.e., an increase in hardness). Another reason for the lack of crystal phase detection may be that the crystallite phases that formed during irradiation consist of sizes that are below the resolution of the XRD.

5.2 Neutron Irradiation Experiments

As displayed in figure 4-35(a), the sample irradiated to 0.1 dpa exhibited a slightly lower and broader pair distribution function peak as compared to the as-cast condition, suggesting that neutron displacement damage led to slight rejuvenation in the alloy. This rejuvenation of the alloy is typically associated with an increase in the atomic disorder of the BMG [450]. In contrast, annealing the BAM-11 BMG at 300 ^{o}C for 2 weeks resulted in a taller and narrower peak, which is evidence for structural relaxation that is associated with an increase in the short-range order. It

was also found that annealing the glass after neutron bombardment led to a peak that had a width and height that was intermediate between the ones for the as-cast and irradiated only condition. This result suggests that annealing the sample reverses the effects of disordering brought about by the neutron irradiation. Moreover, annealing at 325 ^{o}C for 72 hours appears to have a slightly greater reversing effect as compared to heating at 300 ^{o}C for 2 weeks, as illustrated by a relatively higher peak.

Also, the macroscopic density appears to be correlated with the neutron diffraction results, as evident from Tables 4-9, 4-10 and figures 4-37(a)-(c). Pairing these results suggests that with an increase in the disordering during neutron irradiation there is a corresponding decrease in the density. Furthermore, annealing of the sample leads to structural ordering that corresponds to an increase in the density. In terms of the figures 4-37(a)-(c), the correlation between the density and the coordination number is more pronounced for the first nearest neighbor shell. Thus, it may be said that neutron irradiation leads to an increase in the interatomic spacings in the material.

Egami et al. showed that an increase in the interatomic spacings in a metallic glass enhance the number of liquid-like sites in the glassy matrix [451, 452]. Furthermore, these sites are associated with free volume/anti-free volume defects in the amorphous matrix [238, 453]. Thus, it appears that rejuvenation in the alloy, as induced by neutron irradiation, leads to the creation of free volume/anti-free volume defects (see figure 5-1). This change in the structure can also be elucidated from the neutron scattering PDF. Here, a broadening in the curve is associated with an increase in the number of short and long inter-atomic distances [448]. Therefore, atomic mixing caused by neutron collisions leads to an increase in the number of regions with shorter and longer interatomic distances. These regions with the shorter atomic bonds will be associated with the anti-free volume sites while the regions with the longer bonds are associated with the free-volume

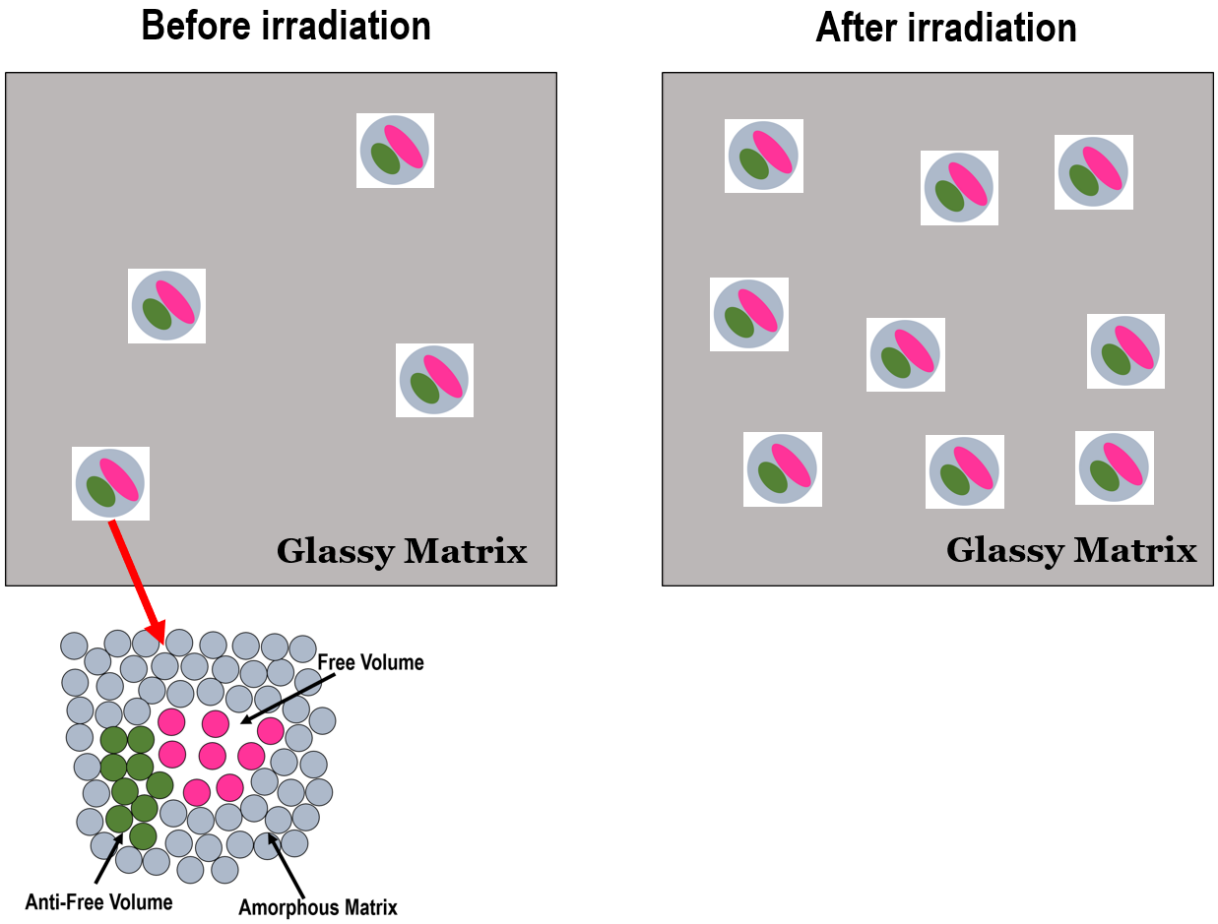

Figure 5-1 A schematic of the BAM-11 BMG before and after neutron irradiation. The figure on the bottom left of the figure represents the free volume and anti-free volume defects in the glassy matrix.

regions with atoms. Furthermore, annealing will have the opposite effect on the interatomic distances, thereby annihilating these liquid-like sites.

In terms of the nanoindentation and three-point bend test results, as shown in 4-38 and 4-40, the data apparently follows a similar trend as that of the immersion density and neutron diffraction measurements. Firstly, the irradiation leads to softening in the metallic glass, while annealing results in hardening. Based on the neutron PDF [see figure 4-35(a)], this softening is accompanied by an increase in the atomic disordering (rejuvenation) and creation of free volume/anti-free volume defects. The rejuvenation of the alloy also appears to be related to the decrease in the flexural modulus, while relaxation corresponds to its increase. Furthermore, it may be suggested that this decrease in the hardness may be linked to the creation of soft-zone defects, as discussed in [454].

On the other hand, the increase in hardness is most likely due to the thermally induced structural relaxation, and therefore destruction of defects, occurring in the alloy [455]. The above result supports the idea that particle collisions led to the production of soft-zone defects while annealing at 300 ^{o}C for 2 weeks caused their annihilation. From here it can be thought that the degree of hardness in the alloy is related to the amount of soft zone defects contained in the matrix. However, it should be mentioned that in the same study, Vickers hardness tests revealed that the irradiation led to a modest increase of ~7% and ~10% in the hardness at neutron doses of 0.1, 1 dpa respectively. It should also be mentioned that the link between free volume and hardness was also discussed in [449], where they theorized that a decrease in free volume, which accompanies structural relaxation, results in a higher resistance to plastic deformation.

These results are similar to those reported by Pan et al., where they observed that rejuvenation in a metallic glass via mechanical deformation led to a decrease in the microhardness

in $Zr_{64.13}Cu_{15.75}Ni_{10.12}Al_{10}$ BMG [450]. Furthermore, they suggested that rejuvenation in a metallic glass also reduces the initial yield stress. Since the results suggest that the free volume content is inversely related to the density, it appears that inducing regions of lower density into the specimen corresponds to a decreased resistance to deformation.

Perez-Bergquist *et al.* found that 3 MeV Ni^{+} (10 dpa) irradiation of the BAM-11 BMG at room temperature resulted in a small decrease in the nanoindentation hardness [420]. In another investigation, they reported that the hardness slightly decreased after irradiation to a peak dose of 1 dpa at both room temperature and 200 ^{o}C [419]. Furthermore, irradiation at the higher temperature (200 ^{o}C) was found to decrease the hardness by a smaller margin as compared to irradiation at room temperature. The decrease in hardness during irradiation at 200 ^{o}C indicates that softening via irradiation has a greater effect on the hardness behavior as compared to hardening induced by annealing. Therefore, it can be surmised that there exists a competition between knock-on collisions and thermal effects on the mechanical properties, which are linked to changes in the free volume content.

This creation of free volume defects by charged particle collisions was also theorized in a study involving the MeV electron irradiation of Ni based metallic glass ribbons [432]. Because of the disappearance of these liquid-like sites, the ability of the material to resist plastic deformation is increased, which corresponds to an increase in the nanoindentation hardness of the alloy. On the other hand, collision cascades lead to more soft-zone defects, resulting in a softening of the BMG. It should be mentioned that other studies have found similar irradiation induced softening in nickel irradiated Vitreloy 1 BMG [343]. An additional study found that irradiation of a Ti based BMG by 25 MeV Cl^{4+} ions also led to softening of the material, which they surmised was linked to the corresponding free volume creation [329]. Their hypothesis that creation of free-volume

defects or nano-voids via collision cascades further corroborates the findings from this investigation.

Based on the nanoindentation results of the ion and neutron irradiated specimens, it is hypothesized that there exists a threshold temperature at which the irradiation and thermal effects balance out, creating no net change in the nanoindentation hardness. However, despite no change in the mechanical response of the alloy, there may still be changes in the short-range ordering due to atomic collisions and diffusion. It should also be stated that beyond the threshold temperature, destruction of defects overrides the creation of them, resulting in a hardening of the alloy.

The increase in the modulus during annealing may be due to the thermal annihilation of soft-zone defects during structural relaxation. Since these defects consist of free volume, and hence are lower in density, their destruction would lead to a decrease of the local interatomic distance throughout the matrix. Since the modulus is inversely proportional to the distance between neighboring atoms, a decrease in the quantity of these defects, therefore, would lead to an increase in the modulus. Conversely, irradiation would lead to a decrease in the modulus via the reduction in density caused by the creation of these structures via energetic atomic mixing caused by particle bombardment. Bian et al. found that Xe irradiation led to the increase in the free volume fraction of a Zr based BMG [456].

5.3 Thermal Response Experiments

5.3.1 In situ X-Ray Diffraction Crystallization Kinetic Experiments

As mentioned earlier , the process of crystallization in the BMGs is very complex. This complexity can be seen in the color intensity maps as displayed in figures 4-44 and 4-49. From the figures it is evident that the BAM-11 BMG underwent a more complex crystallization process as compared to the Cu BMG. Furthermore, the greater quantity of diffraction peaks in the BAM-11 BMG diffraction patterns made the analysis of the crystal structure in the Zr based alloy matrix comparatively much more difficult as compared to the Cu BMG. It should also be mentioned that, similar to the irradiation studies, the crystallization of the specimens was accompanied by a significant increase in the nanoindenation hardness and Young's modulus due to the introduction of nanocrystallites into the matrix.

In terms of the Rietveld analysis, there were some interesting results. In general, the crystalline phases typically followed the JMAK kinetic process in both BMGs, which means that the crystallites nucleated randomly throughout the matrix and then grew in a uniform fashion. However, for BAM-11 BMG, the Zr_2Ni phase exhibited a two-state nuclei-growth, where the first 50% of the transformation ($0 < \alpha < 0.5$) corresponded to a JMAK process, which was followed by the Ginstein-Brounshtin diffusion mechanism. A schematic of these kinetic models is shown in figures 5-2(a)-(b) [239]. Therefore, in terms of the BAM-11 BMG, once the material reaches 365 ^{o}C, Zr_2Ni nuclei begin to form in random positions throughout the matrix. Over time, these nuclei will grow in a uniform fashion. Once the volume fraction of the phase reaches 50 %, however, the nuclei will begin to grow through a three-dimensional diffusional process.

There were also some unexpected results. For instance, oxide phases were observed in both alloys once they reached sufficiently high temperatures. More specifically, the oxides appeared in the BAM-11 BMG at 440 ^{o}C, while it was 500 ^{o}C for the Cu BMG. The reasons for the formation of the oxide phases in the matrix were thought to be caused by oxygen contained in

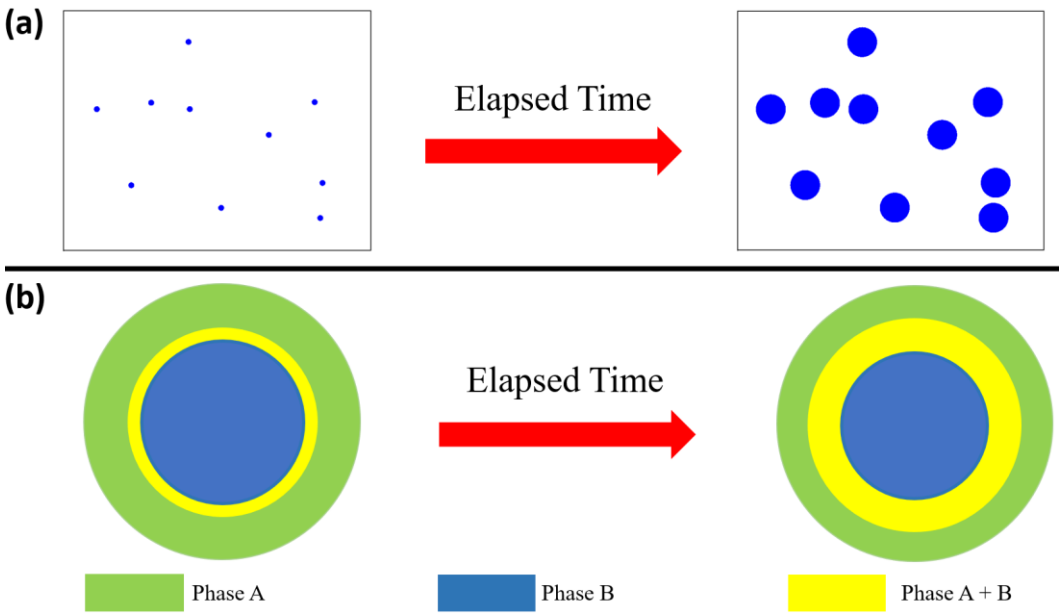

Figure 5-2 Schematic of the (a) JMAK and (b) diffusion controlled crystallization processes (from Ref. [239]).

the insulating elements of the heating chamber or by oxygen impurities in the original BMG ingot. Additionally, the BMGs began to crystallize well below the glass transition temperature. The reason that the glasses crystallized at temperatures well below T_g may be the result of oxygen impurities in the ingot after fabrication [355].

5.3.2 In Situ X-Ray Diffraction Compression Test Experiments

As discussed earlier, it has been theorized that soft-zone defects, which can be thought of as liquid-like atoms and their neighbors [428, 457], consist of structural heterogeneities [458] that can accommodate shear deformation under an applied load. Thus, these defects can be thought of as loosely packed regions that are less resistive during an applied stress. Furthermore, annealing leads to the annihilation of these structures. For instance, Li et al. [207, 454] found that annealing reduces the concentration of these defects in the matrix, which in turn leads to embrittlement of

the alloy. This suggestion is supported by the results of the high energy X-ray diffraction, where the difference in the anisotropic PDFs were larger for the as-cast sample, as compared to the annealed sample (figure 4-59).

As can be seen in figure 4-56, the taller but narrower first peak in the pair distribution function corresponding to the annealed sample indicates that annealing led to a slight structural relaxation, and hence atomic ordering in the BMG. The good fitting for relatively large r, as displayed in figures 4-58(a)-(b), implies that the strain at longer distances is similar to ε_{affine}. On the other hand, the local strain is smaller than the ε_{affine} for the first nearest neighbor shell, which results in the local strain relaxation. Therefore, this local strain relaxation is most likely caused by the local topological rearrangement (LTR) of the BMG sample under an applied stress [256]. It can therefore be surmised that the BAM-11 BMG will become more ductile as the activated LTRs increase. Therefore, as compared to the as-cast sample, the annealed sample will be embrittled.

As can be observed in figure 4-59, there was a larger difference in $\Delta\rho_2^0$ during compression for the as-cast specimen as compared to the sample annealed at 300 ^{o}C for two weeks. The above result suggests that annealing reduces the ductility of BAM-11. If this change in ductility follows a similar trend as that of the free volume content, then it can be thought that neutron irradiation will lead to an increase in the ductility of the alloy. Therefore, it can be thought for neutron irradiation that the softening that occurs in the BAM-11 BMG may correspond to an increase in the ductility of the alloy. Furthermore, the hardening experienced by the BAM-11 BMG after long-term annealing at 300 ^{o}C (see figure 4-38) may perhaps correspond to a decreased ductility as observed by the in-situ compression results (see figure 4-58).

5.3.3 Compression Testing

As shown in figures 4-50 and 4-51, the sample-entropy curves for the samples that were annealed at 300 ^{o}C for 1 and 2 weeks were noticeably different. The higher sample entropy for the samples that were annealed indicates that there is a higher degree of "meaningful structural richness" [192] in the serrated flow. Comparison with the compressive deformation behavior in figures 4-60 (b)-(c) and 4-61 (b)-(c) indicates that this richness in the dynamics may correspond to stress fluctuations that are more irregular.

To better convey the concept of dynamical richness and irregularity, the sample entropy was plotted and compared for three different types of colored noise, namely brown, white, and pink noise [190]. These particular noises were chosen since they yield significantly different sample entropy profiles. The results can be seen in figure 5-3, which contains plots for the three types of colored noises where the corresponding sample entropy data. The entropy was plotted for scale factors of 1-30. In addition, the noise plots contain both the original waveform and its associated coarse-grained average set, where the data was averaged over every 30 points.

As mentioned previously, the sample entropy curves are noticeably different from each other. For instance, the curve which corresponds to the white noise monotonically decreases for all scale factors. This decrease in the sample entropy with increasing scale factor reflects the idea that white noise only has information on the shortest time scale [192]. On the other hand, the sample entropy for the brown noise increases monotonically. While for the pink noise, the curve stays relatively constant over the given domain. It should also be stated that for scale factors greater than 3, the sample entropy values for the pink noise are greater than those for the white and brown noise. This result means that the pink noise contains more complex behavior across a wider range of spatio-temporal scales [193], as compared to the other types of aforementioned signals.

The idea that the pink noise is the most complex noise in nature has been discussed previously in the literature [190, 192, 459].

The above concepts become clearer once the sample entropy data is compared to the coarse-grained data sets. For the white noise signal, coarse-graining the data set causes the amplitude to decrease in magnitude and become more regular. The opposite was true for the brown noise, where coarse-graining led to more irregular fluctuations. In the present context, irregularity means that given an arbitrary data point from the set, it will be harder to predict what value a subsequent point in the time series will be. Pink noise, on the other hand, displayed no significant change in the dynamical behavior after coarse-graining. The above statement combined with the fact that the sample entropy values for pink noise is greater than brown and white noise (scale factor > 3) implies that pink noise exhibits the most complex behavior, in general.

Using the above ideas, we will now attempt to explain the sample entropy values that correspond to the time dependent serration behavior of the BAM-11 BMG. For this analysis, we will assume that the information of the system, over time, is intimately related to the defect interactions during the serrated flow. As discussed in [206, 458], metallic glasses are regarded as a topologically-disordered material that contains soft-zone defects. These defects are similar to liquid-like sites, which are lower in density and contain higher free volumes, or n-type defects [457], as compared to the matrix. These lower-density regions are coupled with more condensed regions that are known as the anti-free volume, or p-type defects [238, 457]. Furthermore, during compression, the free volume content (and soft zone defects) in an amorphous alloy increases with an increase in the strain rate [460]. To compensate for an increase in the quantity of soft zones, there will also be an increase in the p-type (anti-free volume) defects [461] in the matrix.

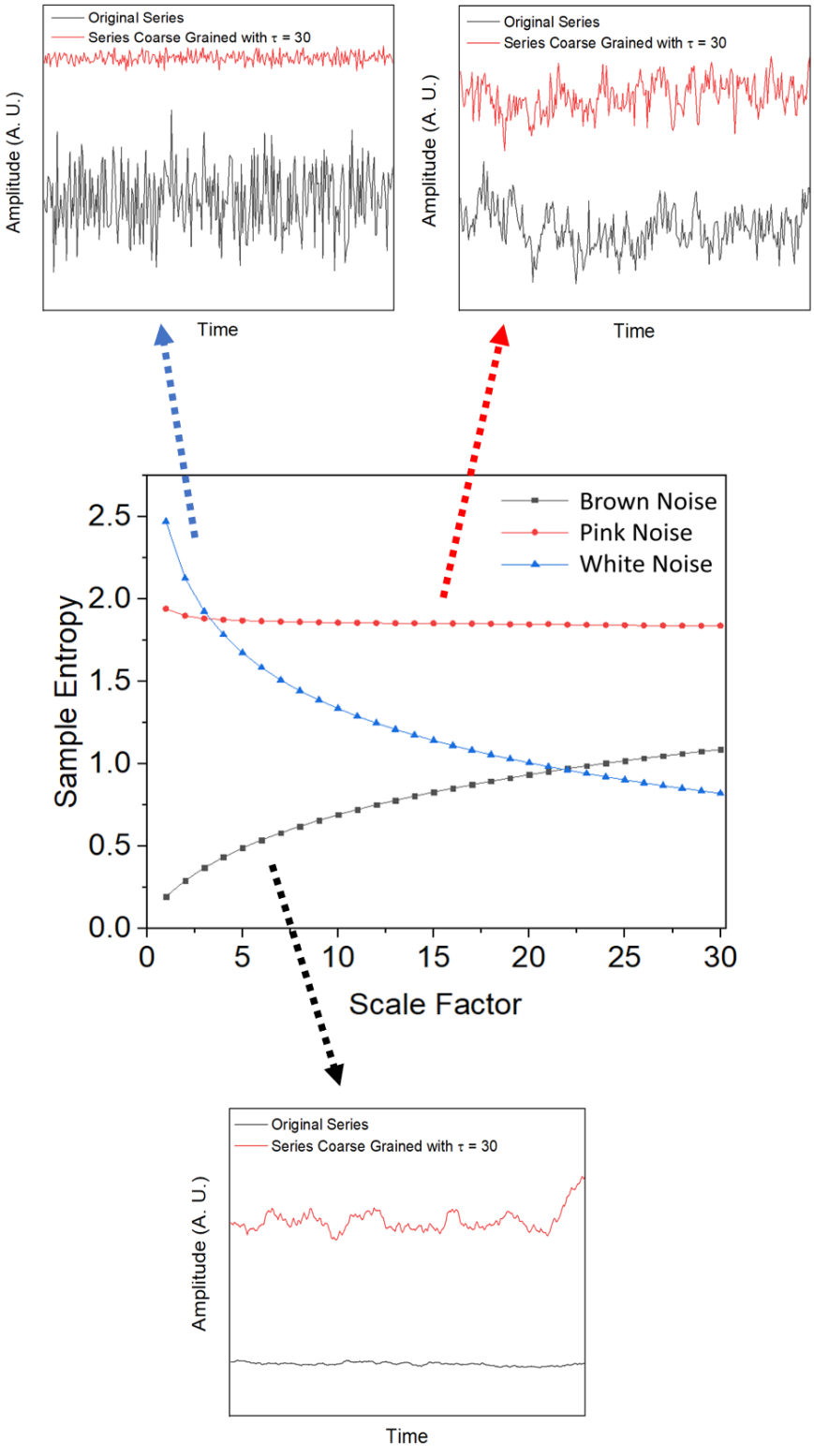

Figure 5-3 Comparison of the sample entropy for brown, pink, and white noise signals.

The complexity in the serrated flow was also noticeably higher for the sample compressed at the higher strain rate (2×10^{-4} s^{-1}) as displayed in figure 4-62. It is known that an increase in the strain rate leads to an increase in the free volume during compression [460]. Furthermore, an increase in the local concentration of free volumes will eventually lead to the creation of voids that can spontaneously coalesce into microcracks [462]. Thus, with an increasing deformation rate, there should be a rise in the variety of interactions between adjacent microcracks in the matrix. This increase in the variety of interactions should consequently lead to serrated flow that exhibits more complex behavior.

Therefore, an increase in the dynamical complexity of the serration behavior with an increasing strain rate may be linked to an enhanced frequency of defect creation at the higher strain rate [460]. Thus, a higher strain rate will lead to a greater number of both p-type and n-type defects that can interact with propagating microcracks during the serrated flow. This enhancement in the variety of interactions is reflected by the results of the RCMSE modeling and analysis where it increases for the higher compression rates. In this context, the higher sample entropy of the serrated flow at the higher strain rate, namely 2×10^{-4} s^{-1}, may correspond to weak spots that are more spatially linked, in general. Also, the complexity may gauge the ability of weak spots to "communicate" with one another during an avalanche. Therefore, if we relate the defect interactions to the information content of the dynamical system, the serrated flow will contain underlying dynamics that are of a more complex nature as the density of defects increases in the alloy.

As for the higher sample entropy in the specimens that were annealed, it may be explained by the following. After the specimens are annealed, the soft zone defects are reduced in numbers. As the sample is compressed, there is less of a barrier for propagating microcracks, which allow

them to interact at a higher rate. Furthermore, the increase in the interaction rate results in an overlap of perennial plastic events which leads to a hierarchy of length scales, and hence more complex serrated flow at large time scales.

5.3.4 Indentation Experiments

The nanoindentation hardness vs. indentation depth data for the as-cast and annealed samples, as displayed in figure 4-41, indicates annealing to temperatures ranging from 150 - 300 ^{o}C for 2 to 4 days led to a significant increase in the hardness of the material. A slight increase in hardness due to the annealing of BAM-11 BMG has been reported in a previous study where the nanoindentation hardness (350 nm) increased by ~4 % after being heated at 310 ^{o}C for 30 minutes [449]. Similar to figure 4-20(a), all thermally annealed BAM-11 BMG specimens exhibited a more pronounced indentation size effect on the measured nanoindentation hardness as compared to the as cast sample.

Although XRD was not performed on the unirradiated annealed samples, it was assumed that the specimens remained amorphous since a previous study found that the material did not crystallize during exposure to 300 ^{o}C for 48 hours [420]. This assumption is further confirmed by work performed by Li et al., where XRD patterns revealed that the BAM-11 BMG did not crystallize when heated at 300 ^{o}C for a week [206]. From these results, in addition to those from the specimens irradiated by 9 MeV Ni^{3+} to a midrange dose of 10 dpa, it can be said that both the BAM-11 and Cu based BMGs are limited to temperatures of 300 ^{o}C or lower due to thermally induced partial crystallization that occurs during long-term (7 hours) exposure at 360 ^{o}C.

In terms of the ISE behavior for the as-cast and thermally annealed specimens, the poor linear fit between shallow (<450 nm indent depth) and deep indents (4-42, 4-43), indicates that the

model proposed by Nix and Gao [212], and Lam and Chong [209], are not quantitatively valid for the indentation hardness of the BAM-11 BMGs. Furthermore, there were discrepancies when comparing the extrapolated hardness and the Vickers hardness results. For the same model, the extrapolated hardness values were higher than the Vickers hardness, while the opposite was true for model prescribed by Lam and Chong. Moreover, as compared to the as-cast state, the Vickers hardness was found to be less for the samples annealed at 150 ^{o}C and 200 ^{o}C (5.1 GPa vs. 4.9 GPa and 5.0 GPa), which appears contradictory to the results for the depth dependent hardness. Since the standard deviation ranged from 0.01 to 0.07 for the above specimens, these changes appear to be statistically significant. The above discrepancy may be the result of different deformation responses between the macroindentation and the ISE from nanoindentation. The above discrepancies, when combined with the insufficiency of all three models to properly fit the data, suggests that a new model is needed to properly analyze the ISE in this BMG system.

5.4 Helium Diffusion Experiments

This section of the PhD work included three main objectives. The first objective was to investigate the role of microstructure, such as grain boundaries, on the behavior of He. This behavior includes diffusion, bubble formation (or lack thereof), and release. The second objective was to gain a better understanding on the role of helium concentration on the diffusion of helium. The third and final objective was to examine the role of composition on the diffusion of He in the BMG.

The lack of He peak broadening in the NRA results [see figures 4-66(a)-(d) and 4-67(a)-(d)] suggests that there was no He diffusion in any of the samples heated at the investigated temperature conditions. This lack of observable broadening in the profiles may be explained by

the following. As the implanted specimen is being heated, He atoms diffuse only a small distance before encountering another He atom, forming atomic clusters. Consequently, the clusters become immobilized. Since these newly formed clusters probably only consist of a few atoms each, they would not be detected by the TEM.

In contrast, the TDS results, as presented in figures 4-69(a)-(c), clearly showed that the helium diffused through the samples. The sharp peak at ~470 ^{o}C (BAM-11 BMG) and ~505 ^{o}C (Cu BMG) in the figures for the amorphous BMGs indicates that the He release was associated with a phase change in the material. For the Cu BMG, this phase change is most likely due to the crystallization of the alloy since it is around the reported T_x (509 ^{o}C [358]) of the alloy. However, for the BAM-11 BMG, the peak occurred above its crystallization temperature of 452 ^{o}C at approximately its second exothermic peak (467 ^{o}C) [368]. Therefore, the He release in the BAM-11 BMG is more likely associated with the growth of a new crystalline phase in the already partially crystallized matrix.

Furthermore, there were observable differences in the peaks for the amorphous and crystalline BAM-11 BMG samples. This effect of structure on the peak is expected since the peak is usually associated with He release from various trapping sites that reach a given activation energy during the heating sequence [463]. It should also be mentioned that sharp peaks, as opposed to broad and overlapping peaks, are thought to correspond to distribution of gas pressure found in bubbles that is in concert with specific mechanical and microstructural properties [464]. In addition to the above, there were also some peculiar, yet interesting features in the spectra. For instance, the stepwise peaks suggest that the trapping sites in the material consist of groups, yet similar dissociation energy. In addition, the wide peaks in the figures are associated with multiple types of trapping sites in the material. Finally, the crystalline BAM-11 BMG that was irradiated

to a fluence of 2×10^{15} cm^2 exhibited no outgassing of helium until the temperature reaches values exceeding 700 ^oC.

Figures 4-70(a)-(b), indicate that at an implantation fluence of 2×10^{15} cm^{-2}, He outgassed faster in the in the partially crystallized BAM-11 and Cu BMGs. On the other hand, this means that the He mobility was reduced in the fully amorphous BMGs. This result appears to corroborate a previous study that observed relatively slower gas diffusion in a metallic glass. Schirmacher et al. investigated the diffusion of hydrogen in $Ni_{24}Zr_{76}$ metallic glass ribbons [465]. Samples were implanted with hydrogen to a concentration of 8 at. %. Quasi-elastic neutron scatting revealed that the hydrogen displayed subdiffusive motion in the observed frequency range of 2×10^9 $s^{-1} \leq \omega \leq 4 \times 10^{10}$ s^{-1}. The authors concluded that the anomalous behavior exhibited by the protons corresponded to activated jump diffusion processes with a broad distribution of activation energies.

The reason for the slower diffusion in the fully amorphous BMGs may be explained by the following. As the He diffuses through the amorphous matrix, anti-free volume sites provide a barrier for He motion due to their relatively small atomic spacing. Since in this scenario there is less space for the He to move around, there is probably higher chance that He atoms will encounter one another as they migrate. Furthermore, the greater atomic spacing in the free volume regions of the metallic glass may provide a stable region for He atoms to coalesce into bubbles where they could remain trapped.

Other studies have also examined He diffusion in disordered materials. For instance, Su et al. studied the He migration in amorphous SiOC [100]. Here, 50 keV He^+ implantations were performed to a fluence of 1.58×10^{21} m^{-2}, which corresponded to a peak dose and He concentration of 10 atom % and 6 dpa, respectively. Proton backscattering characterization revealed that the He outgassed at a rapid rate. The rapid outgassing of the He in the SiOC was thought to result from

small He interstitial formation and migration energies as well as a negligible He dimer interaction energies. Altemose examined the He permeation rate in 20 different oxide glasses [466]. The results indicated that alkali ions inhibited the gas permeation as much as the heavier lead ions. From here he concluded that density played a role in the permeation of the He as it relates to the closeness of the packing of the network as opposed to the weight percent.

CHAPTER 6 CONCLUSIONS AND SUGGESTIONS FOR FUTURE WORK

6.1 Conclusions

The main conclusions that have resulted from this thesis study are listed below. In addition, suggested topics that should be pursued in the future are provided at the end of this chapter.

6.1.1 Ion Irradiation Studies

Results of the 9 MeV Ni^{3+} ion irradiations to a midrange dose of ~10 dpa ion irradiation and thermal annealing experiments revealed several interesting conclusions. In terms of the BAM-11 BMG, the maximum operating temperature for the alloy (T_g = 393 ^oC) appears to be limited to 300 ^oC or lower. This limitation arises from the thermally induced partial crystallization that occurs during exposure to the above temperature for periods of time that exceed ~7 hours. As indicated by the XRD characterization, irradiation does not appear to lead to any obvious radiation-enhanced partial crystallization of the irradiated samples. Increased hardening was observed in the samples irradiated by 9 MeV Ni^{3+} ions to a midrange dose of ~10 dpa at 360 ^oC (~7 hours), and is attributed to the thermally induced partial crystallization of the sample. Subsequent TEM characterization provided evidence that the sample only partially crystallized during irradiation at the highest temperature. In terms of the lower temperature irradiations (25-290 ^oC), only slight changes in hardness were observed following (25 dpa at peak damage region).

A pronounced indentation size effect was exhibited by all of the BAM-11 BMG samples for the measured nanoindentation hardness and elastic modulus. This behavior was particularly evident for indentation depths below ~200 nm. Three different extrapolation models were used to analyze this phenomenon in the BAM-11 BMG. Unfortunately, none of these models provided a linear fit to the data. For instance, the Nix-Gao model, which pertains to dislocation mechanics in

crystalline solids, is not expected to work for BMGs since these materials arew noncrystalline and do not contain dislocations. A model that has been applied to noncrystalline materials (Lam and Chong) was also examined. Although the model produced a slightly better fit to the nanoindentation data as compared to Nix and Gao model, it was still unsuccessful for obtaining the predicted linear fit. A third model, which has been applied to thin film metallic glasses, was also unsuccessful since like the other models, it did not provide a linear fit to the data. Furthermore, it provided nonsensical values for the characteristic length, h^* and the fraction of fertile sites in the matrix. Based on the observed poor fitting of the nanoindentation results with existing indentation size effect models, a new model may be needed to study the ISE in the BAM-11 BMGs.

A similar investigation which examined the irradiation response of $Cu_{60}Zr_{20}Hf_{10}Ti_{10}$ BMG after exposure to the same irradiation conditions as above, led to several important results. As with the BAM-11 BMG, the maximum operating temperature for the Cu BMG was determined to be ~300 ^oC since partial crystallization occurred during prolonged (~7 hours) exposure to an environmental temperature of 360 ^oC. Furthermore, there does not appear to be any pronounced radiation-enhanced crystallization of the irradiated samples at 25-290 ^oC, as indicated by the XRD patterns. The subsequent TEM characterization revealed that the crystallites in the sample irradiated at 360 ^oC consisted of various morphologies. Rietveld refinement also showed that the crystallized portion of the specimen that was irradiated at the above temperature was comprised of tetragonal Cu-Ti (P4/mmc) and hexagonal Cu-Zr-Ti ($P6_3$/mmc) and phases.

The nanoindentation hardness also behaved in a similar fashion to the BAM-11 BMG. For instance, after irradiation by 9 MeV Ni^{3+} ions to a midrange dose of ~10 dpa (peak dose of 25 dpa) at temperatures of 25 ^{o} and 290 ^oC only slight changes were observed in the hardness. On the other

hand, irradiation at 360 ^{o}C for ~7 hours led to a significant increase in the hardness at all indentation depths. Similar to the BAM-11 BMG, this hardening was associated to the partial crystallization that occurred due to thermal annealing effects. This significant hardening at all depths indicates that the partial crystallization was not caused by irradiation, but by thermal effects.

With respect to the irradiated region of the surface, all of the specimens displayed a pronounced indentation size effect, similar to the BAM-11 BMG. Unirradiated as-cast specimens also exhibited a pronounced indentation size effect. The nanoindentation experiments revealed that as compared to the as-cast state, there was no apparent change in the depth dependent hardness during irradiation at room temperature to 290 ^{o}C. The Lam and Chong extrapolation method, that has been previously used to examine the ISE in metallic glass, was employed on Cu BMG. However, the analysis revealed that the model provided a poor quantitative fit to the nanoindentation hardness data. This failure suggests that, like with the BAM-11 BMG, a new model is needed to properly analyze the ISE phenomenon in amorphous alloy systems.

In addition, other experiments examined the effects of 9 MeV Ni^{3+} and 5.5 MeV C^{+} ion irradiation (midrange dose of 0.5 dpa) on the microstructural and mechanical behavior of BAM-11 and Cu based BMGs. For this study, nanoindentation and microstructural characterization were performed on BAM-11 and Cu based BMGs to examine the radiation response of the alloy. Specimens were irradiated by 9 MeV Ni^{3+} and 5.5 MeV C^{+} ions to a midrange dose of 0.5 dpa at temperatures ranging from ambient to 360 ^{o}C. To further examine the effects of collision cascades on the nanoindentation behavior, samples were irradiated by neutrons (E > 0.1 MeV) to a dose of 0.1 dpa at ~90 ^{o}C. In general, the lack of observed cavity formation in addition to a small change in density and hardness indicate that the BMG exhibited good radiation resistance.

There was no evidence for pronounced irradiation spectrum effects on the nanoindentation mechanical properties behavior of the two investigated BMGs following irradiation with 9 MeV Ni ions (relatively high average primary knock-on energy of ~20 keV) versus 5.5 MeV C ions (relatively low average primary knock-on energy of ~5 keV).There was some indication of slightly increased hardening for the Ni ion irradiation conditions compared to the C ion irradiation conditions at 25, 290 and 360 ^{o}C.

6.1.2 Neutron Irradiation Studies

In addition to the ion irradiation, BAM-11 BMG specimens were irradiated by neutrons (E > 0.1 MeV) to a dose of 0.1 dpa (fluence of 1.4×10^{20} cm^{-2}) at ~70 ^{o}C. Neutron irradiation and thermal annealing were observed to act as competing processes with regards to their effect on the mechanical and microstructural properties of the BAM-11 BMG. For instance, annealing after irradiation largely reversed the atomic disordering effects caused by the irradiation. Nanoindentation hardness measurements found that irradiation led to softening in the alloy while annealing caused an increase in hardness. Similarly, the sample density was reduced by ~2% after neutron irradiation but was increased by ~1% after annealing at 300 ^{o}C. Neutron diffraction results indicated that primary knock-on events caused rejuvenation (disordering) while annealing resulted in structural relaxation. However, flexural bend bar testing indicated very low tensile elongation for all test conditions (neutron irradiated and thermal annealed). In general, an increase in the disorder of the matrix is linked to a softening of the alloy and perhaps also linked to a higher concentration of soft-zone defects in the matrix. Furthermore, results indicate that hardening caused by heat treatment corresponds to structural relaxation, densification, and a loss of ductility

in the alloy. Finally, the decrease in the ductility appears linked to the annihilation of soft-zone defects, and thus the free volume of BAM-11 BMG.

6.1.3 Thermal Response Studies

For the thermal response studies, there were three main objectives. The first objective was to examine how annealing affected the complexity of the serrated flow in the BAM-11 BMG. The second objective was to investigate how the crystal structures evolve in the matrix of the BAM-11 BMG and the Cu based BMG. Finally, the third objective was to elucidate how temperature effects the ductility of the BAM-11 BMG via in situ synchrotron XRD compression testing.

With respect to the first goal, it was found that both annealing and increased strain rate resulted in a noticeable increase in the complexity of the serrated flow exhibited by the BAM-11 BMG during compression. As for the first factor, it was believed that an increase in the strain rate leads to the creation of free volume content and its associated defects during compression. These newly formed defects will then interact in a more varied way during deformation, leading to the higher sample entropy values. As for the effects of annealing, the destruction of the soft zone defects increases the interaction rate between propagating cracks in the matrix. Consequently, this increase in the activity during the serrated flow leads to interactions spanning a hierarchy of spatiotemporal scales, resulting in more complex serration behavior.

Additionally, the synchrotron XRD compression tests linked the temperature induced structural relaxation of the alloy to a loss of ductility and increase in nanoindentation hardness, which agrees with the literature. Furthermore, results indicate that nanoindentation hardening caused by heat treatment corresponds a loss of ductility in the BAM-11 BMG. Finally, the

decrease in the ductility appears linked to the annihilation of soft-zone defects, and thus the free volume of BAM-11 BMG.

6.1.4 Helium Diffusion Studies

This dissertation also focused on the study of helium behavior in BMGs which are potential candidates in nuclear fusion systems. These alloys are promising candidates since they have high strength, hardness, shape formability, and lack grain boundaries that can trap helium. Furthermore, it is thought that the free volume in these material systems might provide a pathway for efficient He release.

According to the NRA results, it was found that the He did not diffuse in any of the specimens that were annealed at temperatures ranging from 250 to 600 ^{o}C. Furthermore, TEM analysis revealed that bubbles did not form in the matrix. Therefore, it was thought that perhaps He atoms coalesced to form atomic clusters with sizes that were below the resolution of the TEM. On the other hand, the lack of peak broadening may have been related to the insensitivity of the solid-state detector apparatus. However, for the TDS experiments, He was found to exhibit interesting off-gassing behavior in a couple of the specimens. This interesting behavior was thought to be associated with sets of distinct sites where gas was released. At the current moment, however, the origin of these trapping sites is not well understood.

6.2 Suggestions for Future Work

The following is suggested for future work:

1. More work needs to be done to examine the indentation size effects in BMGs. To achieve this goal, a couple of approaches could be done. A good step would be to perform nanoindentations using a constant deformation rate vs. constant loading rate, with each analyzed using Nix-Gao and the Lam-Chong models.
2. Perform further investigations on the He diffusion in BMGs. As for the nuclear reaction analysis, should conduct higher flux implantations on amorphous and partially crystallized BMGs to examine the effects of grain boundaries on bubble formation in the matrix. Finally, could perform complementary experiments such as laser induced breakdown spectroscopy to gain a more fundamental understanding of the diffusion behavior in the BMGs.
3. Further irradiation studies on the neutron irradiated and annealed samples to elucidate the interplay between relaxation and rejuvenation effects in the BMGs. For instance, differential scanning calorimeter experiments could be performed on the specimens to elucidate the effects of neutron induced disordering and thermal reordering on the fictive temperature of the BMG. Since the fictive temperature is related to the ductility of the BMG, a possible link could be established between the irradiation induced structural modifications and the ductility of the material.
4. Perform compression testing on the neutron irradiated samples to examine the effects of irradiation on the complexity of the serrated flow in the alloy. This experiment would be important since such a study has never been performed. Furthermore, the results of the experiment would help elucidate the relationship between the creation of soft-zone defects and the way in which the microstructure behaves during stress-drop events.

5. Conduct in situ stress relaxation and creep testing on the BAM-11 and Cu BMGs. Here, X-ray diffraction would be performed at temperatures ranging from room temperature to 90 % of the melting temperature under vacuum. These experiments would have the goal of examining the link between the collective defect behavior and the microstructure, especially during the crystallization of the samples.
6. Perform dual beam He irradiation studies on the BMGs to better simulate reactor conditions. Here, the specimens would be simultaneously irradiated by a midsized ion such as Ni, and He under a range of temperatures ranging from ambient to 90% of the melting temperature. Characterization techniques such as nanoindentation, TEM and XRD would be employed to examine the effects of dual irradiation on the microstructural and mechanical properties of the alloys.

REFERENCES

[1] S. J. Zinkle, L. L. Snead, Designing Radiation Resistance in Materials for Fusion Energy, in: D.R. Clarke (Ed.), Annual Review of Materials Research, Vol 44, Annual Reviews, Palo Alto, 2014, pp. 241-267.
[2] F. F. Chen, Introduction to Plasma Physics and Controlled Fusion: Volume 1: Plasma Physics, Springer US, Boston, MA, 1984.
[3] A. Einstein, Is the inertia of a body dependent on its energy content?, Annalen Der Physik 18(13) (1905) 639-641.
[4] A. Einstein, On the electrodynamics of moving bodies, Annalen Der Physik 17(10) (1905) 891-921.
[5] F. Hasenohrl, The theory of radiation in moving bodies, Annalen Der Physik 15(12) (1904) 344-370.
[6] F. Hasenohrl, The theory of radiation in moved bodies. Correction, Annalen Der Physik 16(3) (1905) 589-U13.
[7] R. Rhodes, The Making of the Atomic Bomb, Simon & Schuster2012.
[8] C. Seife, Sun in a Bottle: The Strange History of Fusion and the Science of Wishful Thinking, Viking2008.
[9] J.K. Shultis, R.E. Faw, Fundamentals of Nuclear Science and Engineering, Taylor & Francis2002.
[10] American Chemical Society, Chemistry in the Community (ChemCom), W. H. Freeman2011.
[11] D. Naujoks, Plasma-Material Interaction in Controlled Fusion, Springer Berlin Heidelberg2006.
[12] S. J. Zinkle, J. T. Busby, Structural materials for fission & fusion energy, Materials Today 12(11) (2009) 12-19.
[13] L.C. Woods, Theory of Tokamak Transport: New Aspects for Nuclear Fusion Reactor Design, Wiley2006.
[14] M. Ariola, A. Pironti, Magnetic Control of Tokamak Plasmas, Springer International Publishing2016.
[15] Y. Song, W. Wu, S. Du, Tokamak Engineering Mechanics, Springer Berlin Heidelberg2013.
[16] V. Stefan, Nonlinear and Relativistic Effects in Plasmas, American Inst. of Physics1991.
[17] N.R. Council, D.E.P. Sciences, B.P. Astronomy, P.S. Committee, C.R.U.S.I.S.P.P. Process, A Review of the DOE Plan for U.S. Fusion Community Participation in the ITER Program, National Academies Press2009.
[18] S. J. Zinkle, CHALLENGES IN DEVELOPING MATERIALS FOR FUSION TECHNOLOGY-PAST, PRESENT AND FUTURE, Fusion Sci. Technol. 64(2) (2013) 65-75.
[19] V. Firouzdor, L. Wilson, K. Sridharan, B. Semerau, B. Hauch, J. Brechtl, J. I. Cole, T. R. Allen, Development of Diffusion Barrier Coatings for Mitigation of Fuel-Cladding Chemical Interactions, in: A.R. Boccaccini, O. VanDerBiest, R. Clasen, J.H. Dickerson (Eds.), Electrophoretic Deposition: Fundamentals and Applications Iv, Trans Tech Publications Ltd, Durnten-Zurich, 2012, pp. 3-+.
[20] V. Firouzdor, J. Brechtl, L. Wilson, B. Semerau, K. Sridharan, T. R. Allen, Development of Yttrium Stabilized Zirconia (YSZ) diffusion barrier coatings for mitigation of Fuel–Cladding Chemical Interactions, Journal of Nuclear Materials 438(1) (2013) 268-277.
[21] V. Firouzdor, J. Brechtl, L. Wilson, B. Semerau, K. Sridharan, T. R. Allen, Development of titanium diffusion barrier coatings for mitigation of fuel-cladding chemical interactions, Surf. Coat. Technol. 219 (2013) 59-68.

[22] V. Firouzdor, J. Brechtl, B. Hauch, K. Sridharan, T. R. Allen, Electrophoretic deposition of diffusion barrier titanium oxide coatings for nuclear reactor cladding applications, Appl. Surf. Sci. 282 (2013) 798-808.
[23] D.R. Olander, United States. Energy Research, Development Administration. Division of Reactor Development, Demonstration, Fundamental Aspects of Nuclear Reactor Fuel Elements, Technical Information Center, Office of Public Affairs, Energy Research and Development Administration1976.
[24] M. Wang, M. Song, C. R. Lear, G. S. Was, Irradiation assisted stress corrosion cracking of commercial and advanced alloys for light water reactor core internals, Journal of Nuclear Materials 515 (2019) 52-70.
[25] C. J. Czajkowski, INVESTIGATION OF CORROSION AND STRESS-CORROSION CRACKING IN BOLTING MATERIALS ON LIGHT WATER-REACTORS, International Journal of Pressure Vessels and Piping 26(2) (1986) 87-96.
[26] S. J. Zinkle, G. S. Was, Materials challenges in nuclear energy, Acta Materialia 61(3) (2013) 735-758.
[27] S. J. Zinkle, N. M. Ghoniem, Operating temperature windows for fusion reactor structural materials, Fusion Engineering and Design 51-52 (2000) 55-71.
[28] S. J. Zinkle, M. Victoria, K. Abe, Scientific and engineering advances from fusion materials R&D, Journal of Nuclear Materials 307 (2002) 31-42.
[29] N. Baluc, K. Abe, J. L. Boutard, V. M. Chernov, E. Diegele, S. Jitsukawa, A. Kimura, R. L. Klueh, A. Kohyama, R. J. Kurtz, R. Lasser, H. Matsui, A. Moslang, T. Muroga, G. R. Odette, M. Q. Tran, B. Van der Schaaf, Y. Wu, I. Yu, S. J. Zinkle, Status of R&D activities on materials for fusion power reactors, Nucl. Fusion 47(10) (2007) S696-S717.
[30] B. D. Wirth, K. Nordlund, D. G. Whyte, D. Xu, Fusion materials modeling: Challenges and opportunities, MRS Bull. 36(3) (2011) 216-222.
[31] J. Roth, E. Tsitrone, A. Loarte, T. Loarer, G. Counsell, R. Neu, V. Philipps, S. Brezinsek, M. Lehnen, P. Coad, C. Grisolia, K. Schmid, K. Krieger, A. Kallenbach, B. Lipschultz, R. Doerner, R. Causey, V. Alimov, W. Shu, O. Ogorodnikova, A. Kirschner, G. Federici, A. Kukushkin, Efda Pwi Task Force, Iter Pwi Team, Energy Fusion, D. I. V. Itpa Sol, Recent analysis of key plasma wall interactions issues for ITER, Journal of Nuclear Materials 390-91 (2009) 1-9.
[32] R. A. Pitts, S. Carpentier, F. Escourbiac, T. Hirai, V. Komarov, A. S. Kukushkin, S. Lisgo, A. Loarte, M. Merola, R. Mitteau, A. R. Raffray, M. Shimada, P. C. Stangeby, Physics basis and design of the ITER plasma-facing components, Journal of Nuclear Materials 415(1) (2011) S957-S964.
[33] J. Linke, HIGH HEAT FLUX PERFORMANCE OF PLASMA FACING MATERIALS AND COMPONENTS UNDER SERVICE CONDITIONS IN FUTURE FUSION REACTORS, Fusion Sci. Technol. 61(2T) (2012) 246-255.
[34] G. S. Was, Fundamentals of Radiation Materials Science, 1 ed., Springer Science & Business Media, New York, 2007.
[35] S. A. Fabritsiev, A. S. Pokrovsky, S. J. Zinkle, Effect of neutron dose and spectra, He/dpa ratio and Ni and Zn accumulation on irradiation damage of pure copper and PH and DS copper alloys, Fusion Engineering and Design 38(4) (1998) 459-473.
[36] S. N. Fabritsiev, A. S. Pokrovsky, Plasma Devices Oper. 5 (1997) 13-141.
[37] S. Yamamoto, T. Shikama, V. Belyakov, E. Farnum, E. Hodgson, T. Nishitani, D. Orlinski, S. Zinkle, S. Kasai, P. Stott, K. Young, V. Zaveriaev, A. Costley, L. deKock, C. Walker,

G. Janeschitz, Impact of irradiation effects on design solutions for ITER diagnostics, Journal of Nuclear Materials 283 (2000) 60-69.
[38] G. Vayakis, E. R. Hodgson, V. Voitsenya, C. I. Walker, Generic diagnostic issues for a burning plasma experiment, Fusion Sci. Technol. 53(2) (2008) 699-750.
[39] S. J. Zinkle, E. R. Hodgson, RADIATION-INDUCED CHANGES IN THE PHYSICAL-PROPERTIES OF CERAMIC MATERIALS, Journal of Nuclear Materials 191 (1992) 58-66.
[40] F. A. Garner, B. M. Oliver, L. R. Greenwood, D. J. Edwards, S. M. Bruemmer, M. L. Grossbeck, Generation and retention of helium and hydrogen in austentic steels irradiated in a variety of LWR and test reactor spectral environments, Oak Ridge, 2006, pp. 127-147.
[41] J. E. Pawel, E. E. Bloom, L. K. Mansur, A. F. Rowcliffe, S. J. Zinkle, R. E. Stoller, P. J. Maziasz, Toward a mechanistic understanding of radiation effects in materials, Radiat. Eff. Defects Solids 144(1-4) (1998) 287-309.
[42] H. Ullmaier, THE INFLUENCE OF HELIUM ON THE BULK PROPERTIES OF FUSION-REACTOR STRUCTURAL-MATERIALS, Nucl. Fusion 24(8) (1984) 1039-1083.
[43] D. N. Braski, H. Schroeder, H. Ullmaier, EFFECT OF TENSILE-STRESS ON THE GROWTH OF HELIUM BUBBLES IN AN AUSTENITIC STAINLESS-STEEL, Journal of Nuclear Materials 83(2) (1979) 265-277.
[44] D. A. Woodford, J. P. Smith, J. Moteff, EFFECT OF HELIUM GAS BUBBLES ON CREEP DUCTILITY OF AN AUSTENITIC ALLOY, Journal of Nuclear Materials 29(1) (1969) 103-&.
[45] W. R. Kanne, M. R. Louthan, D. T. Rankin, M. H. Tosten, Weld repair of irradiated materials, Mater. Charact. 43(2-3) (1999) 203-214.
[46] Y. Dai, G. R. Odette, T. Yamamoto, The Effects of Helium in Irradiated Structural Alloys, Elsevier Science Bv, Amsterdam, 2012.
[47] H. Trinkaus, B. N. Singh, Helium accumulation in metals during irradiation - where do we stand?, Journal of Nuclear Materials 323(2-3) (2003) 229-242.
[48] E. E. Bloom, R. W. Conn, J. W. Davis, R. E. Gold, R. Little, K. R. Schultz, D. L. Smith, F. W. Wiffen, Low activation materials for fusion applications, Jounal of Nuclear Materials 122(1-3) (1984) 17-26.
[49] K. Ehrlich, E. E. Bloom, T. Kondo, International strategy for fusion materials development, Journal of Nuclear Materials 283 (2000) 79-88.
[50] S. J. Zinkle, Fusion materials science: Overview of challenges and recent progress, Physics of Plasmas 12(5) (2005).
[51] E. E. Bloom, S. J. Zinkle, F. W. Wiffen, Materials to deliver the promise of fusion power - progress and challenges, Journal of Nuclear Materials 329 (2004) 12-19.
[52] C. L. Smith, The need for fusion, Fusion Engineering and Design 74(1-4) (2005) 3-8.
[53] S. Kavithaa, R. Subramanian, P. C. Angelo, Yttria dispersed 9Cr martensitic steel synthesized by mechanical alloying - hot isostatic pressing, Trans. Indian Inst. Met. 63(1) (2010) 67-74.
[54] M. B. Toloczko, F. A. Garner, V. N. Voyevodin, V. V. Bryk, O. V. Borodin, V. V. Mel'nychenko, A. S. Kalchenko, Ion-induced swelling of ODS ferritic alloy MA957 tubing to 500 dpa, Journal of Nuclear Materials 453(1-3) (2014) 323-333.
[55] R. Schaeublin, T. Leguey, P. Spatig, N. Baluc, M. Victoria, Microstructure and mechanical properties of two ODS ferritic/martensitic steels, Journal of Nuclear Materials 307 (2002) 778-782.

[56] J. Hissam, R. Romanosky, S. Dryepondt, Qualification of new, commericial ODS Alloys for use in advanced fuel processes. https://www.netl.doe.gov/research/factsheet-print?k=FWP-FEAA109, 2011).
[57] K. Oka, S. Ohnuki, S. Yamashita, N. Akasaka, S. Ohtsuka, H. Tanigawa, Structure of nano-size oxides in ODS steels and its stability under electron irradiation, Materials Transactions 48(10) (2007) 2563-2566.
[58] M. K. Miller, K. F. Russell, D. T. Hoelzer, Characterization of precipitates in MA/ODS ferritic alloys, Journal of Nuclear Materials 351(1-3) (2006) 261-268.
[59] Chanho Lee, Gian Song, Michael C. Gao, Rui Feng, Peiyong Chen, Jamieson Brechtl, Yan Chen, Ke An, Wei Guo, Jonathan D. Poplawsky, Song Li, A. T. Samaei, Wei Chen, Alice Hu, Hahn Choo, Peter K. Liaw, Lattice distortion in a strong and ductile refractory high-entropy alloy, Acta Materialia 160 (2018) 158-172.
[60] T. Egami, W. Guo, P. D. Rack, T. Nagase, Irradiation resistance of multicomponent alloys, Metallurgical and Materials Transactions A 45A (2014) 180-183.
[61] T. Egami, M. Ojha, O. Khorgolkhuu, D. M. Nicholson, G. M. Stocks, Local Electronic Effects and Irradiation Resistance in High-Entropy Alloys, Jom 67(10) (2015) 2345-2349.
[62] S. Q. Xia, X. Yang, T. F. Yang, S. Liu, Y. Zhang, Irradiation resistance in $Al_xCoCrFeNi$ high entropy alloys, JOM 67(10) (2015) 2340-2344.
[63] S. Xia, M. C. Gao, T. Yang, P. K. Liaw, Y. Zhang, Phase stability and microstructures of high entropy alloys ion irradiated to high doses, Journal of Nuclear Materials 480 (2016) 100-108.
[64] N. A. P. Kiran Kumar, C. Li, K. J. Leonard, H. Bei, S. J. Zinkle, Microstructural stability and mechanical behavior of FeNiMnCr high entropy alloy under ion irradiation, Acta Materialia 113 (2016) 230-244.
[65] Tengfei Yang, Songqin Xia, Shi Liu, Chenxu Wang, Shaoshuai Liu, Yuan Fang, Yong Zhang, Jianming Xue, Sha Yan, Yugang Wang, Precipitation behavior of $Al_xCoCrFeNi$ high entropy alloys under ion irradiation, Scientific Reports 6 (2016) 32146.
[66] M.-R. He, S. Wang, K. Jin, H. Bei, K. Yasuda, S. Matsumura, K. Higashida, I. M. Robertson, Enhanced damage resistance and novel defect structure of CrFeCoNi under in situ electron irradiation, Scripta Materialia 125 (2016) 5-9.
[67] T. Yang, S. Xia, W. Guo, R. Hu, J. D. Poplawsky, G. Sha, Y.Fang, Z. Yan, C. Wang, C. Li, Y. Zhang, S. J. Zinkle, Y.Wang, Effects of temperature on the irradiation responses of $Al_{0.1}CoCrFeNi$ high entropy alloy, Scripta Materialia 144 (2018) 31-35.
[68] Yanwen Zhang, G. Malcolm Stocks, Ke Jin, Chenyang Lu, Hongbin Bei, Brian C. Sales, Lumin Wang, Laurent K. Béland, Roger E. Stoller, German D. Samolyuk, Magdalena Caro, Alfredo Caro, William J. Weber, Influence of chemical disorder on energy dissipation and defect evolution in concentrated solid solution alloys, Nature Communications 6 (2015) 8736.
[69] Congyi Li, Junqi Yin, Khorgolkhuu Odbadrakh, Brian C. Sales, Steven J. Zinkle, G. Malcolm Stocks, Brian D. Wirth, First principle study of magnetism and vacancy energetics in a near equimolar NiFeMnCr high entropy alloy, Journal of Applied Physics 125(15) (2019) 155103.
[70] Oak Ridge National Laboratory Proposal:Structural Materials of Potentially Unique Irradiation Resistance, Oak Ridge National Laboratory, 2011.
[71] N. Mattern, Structure formation in liquid and amorphous metallic alloys, Journal of Non-Crystalline Solids 353(18-21) (2007) 1723-1731.

[72] M. Miller, P. K. Liaw, Bulk Metallic Glasses: An Overview, Springer, New York, 2008.
[73] Z. P. Lu, C. T. Liu, A new glass-forming ability criterion for bulk metallic glasses, Acta Materialia 50(13) (2002) 3501-3512.
[74] Z. Mahbooba, L. Thorsson, M. Unosson, P. Skoglund, H. West, T. Horn, C. Rock, E. Vogli, O. Harrysson, Additive manufacturing of an iron-based bulk metallic glass larger than the critical casting thickness, Applied Materials Today 11 (2018) 264-269.
[75] L. Deng, S. Wang, P. Wang, U. Kühn, S. Pauly, Selective laser melting of a Ti-based bulk metallic glass, Materials Letters 212 (2018) 346-349.
[76] Y. Shen, Y. Li, C. Chen, H. L. Tsai, 3D printing of large, complex metallic glass structures, Materials and Design 117 (2017) 213-222.
[77] W. H. Wang, C. Dong, C. H. Shek, Bulk metallic glasses, Materials Science and Engineering Reports 44(2-3) (2004) 45-89.
[78] A. Inoue, Stabilization of metallic supercooled liquid and bulk amorphous alloys, Acta Materialia 48(1) (2000) 279-306.
[79] A. Inoue, B. Shen, N. Nishiyama, Bulk Metallic Glasses, Springer, New York, 2008.
[80] S. V. Madge, A. Caron, R. Gralla, G. Wilde, S. K. Mishra, Novel W-based metallic glass with high hardness and wear resistance, Intermetallics 47 (2014) 6-10.
[81] M. N. M. Patnaik, R. Narasimhan, U. Ramamurty, Spherical indentation response of metallic glass, Acta Materialia 52(11) (2004) 3335-3345.
[82] Fu-Fa Wu, K. C. Chan, Song-Shan Jiang, Shun-Hua Chen, Gang Wang, Bulk metallic glass composite with good tensile ductility, high strength and large elastic strain limit, Scientific Reports 4 (2014) 5302.
[83] X. Gu, G. J. Shiflet, F. Q. Guo, S. J. Poon, Mg-Ca-Zn bulk metallic glasses with high strength and significant ductility, Journal of Materials Research 20(8) (2005) 1935-1938.
[84] S. J. Pang, T. Zhang, K. Asami, A. Inoue, Bulk glassy Fe-Cr-Mo-C-B alloys with high corrosion resistance, Corros. Sci. 44(8) (2002) 1847-1856.
[85] L. Huang, D. C. Qiao, B. A. Green, P. K. Liaw, J. F. Wang, S. J. Pang, T. Zhang, Bio-corrosion study on zirconium-based bulk-metallic glasses, Intermetallics 17(4) (2009) 195-199.
[86] W. H. Peter, R. A. Buchanan, C. T. Liu, P. K. Liaw, M. L. Morrison, Jr. C. A. Carmichael, J. L. Wright, Localized Corrosion behavior of a zirconium-based bulk metallic glass relative to its crystalline state, Intermetallics 10(11-12) (2002) 1157-1162.
[87] G. Y. Wang, P. K. Liaw, M. L. Morrison, Progress in studying the fatigue behavior of Zr-based bulk-metallic glasses and their composites, Intermetallics 17(8) (2009) 579-590.
[88] G. Y. Wang, M. D. Demetriou, J. P. Schramm, P. K. Liaw, W. L. Johnson, Compression-compression fatigue of $Pd_{43}Ni_{10}CU_{27}P_{20}$ metallic glass foam, Journal of Applied Physics 108(2) (2010).
[89] G. Y. Wang, P. K. Liaw, Y. Yokoyama, A. Peker, W. H. Peter, B. Yang, M. Freels, Z. Y. Zhang, V. Keppens, R. Hermann, R. A. Buchanan, C. T. Liu, C. R. Brooks, Studying fatigue behavior and Poisson's ratio of bulk-metallic glasses, Intermetallics 15(5-6) (2007) 663-667.
[90] G. Y. Wang, P. K. Liaw, Y. Yokoyama, A. Inoue, C. T. Liu, Fatigue behavior of Zr based bulk-metallic glasses, Materials Science & Engineering A 494(1-2) (2008) 314-323.
[91] W. Zhang, A. Inoue, Formation and mechanical properties of Ni-based Ni–Nb–Ti–Hf bulk glassy alloys, Scripta Materialia 48(5) (2003) 641-645.
[92] A. Inoue, T. Zhang, W. Zhang, A. Takeuchi, Bulk Nd-Fe-Al amorphous alloys with hard magnetic properties, Materials Transactions, JIM 37(2) (1996) 99-108.

[93] A. Inoue, H. Koshiba, T. Itoi, A. Makino, Ferromagnetic Co-Fe-Zr-B amorphous alloys with glass transition and good high-frequency permeability, Applied Physics Letters 73(6) (1998) 744-746.
[94] S. V. Madge, Toughness of Bulk Metallic Glasses, Metals 5(3) (2015) 1279-1305.
[95] C. A. Schuh, T. C. Hufnagel, U. Ramamurty, Overview No.144 - Mechanical behavior of amorphous alloys, Acta Materialia 55(12) (2007) 4067-4109.
[96] Mehdi Jafary-Zadeh, Gideon Praveen Kumar, Paulo Sergio Branicio, Mohsen Seifi, John J. Lewandowski, Fangsen Cui, A Critical Review on Metallic Glasses as Structural Materials for Cardiovascular Stent Applications, Journal of functional biomaterials 9(1) (2018) 19.
[97] Y. Petrusenko, A. Bakai, V. Borysenko, A. Astakhov, D. Barankov, Investigation of bulk metallic glass structure by means of electron irradiation, Intermetallics 17(4) (2009) 246-248.
[98] A. G. Perez-Bergquist, H. Bei, K. J. Leonard, Y. Zhang, S. J. Zinkle, Effects of ion irradiation on $Zr_{52.5}Cu_{17.9}Ni_{14.6}Al_{10}Ti_5$ (BAM-11) bulk metallic glass, Intermetallics 53 (2014) 62-66.
[99] W. J. Weber, R. C. Ewing, C. A. Angell, G. W. Arnold, A. N.Cormack, J. M. Delaye, D. L. Griscom, L. W. Hobbs, A. Navrotsky, D. L. Price, A. M. Stoneham, M. C. Weinberg, Radiation effects in glasses used for immobilization of high-level waste and plutonium disposition, J. Mater. Res. 12(8) (1997) 1946-1978.
[100] Q. Su, H. P. Ding, L. Price, L. Shao, J. A. Hinks, G. Greaves, S. E. Donnelly, M. J. Demkowicz, M. Nastasi, Rapid and damage-free outgassing of implanted helium from amorphous silicon oxycarbide, Scientific Reports 8 (2018) 9.
[101] T. Nagase, Y. Umakoshi, Thermal stability and electron irradiation effect on Zr-based amorphous alloys, Journal of Applied Physics 93(2) (2003) 912-918.
[102] C. Janot, Quasicrystals: A Primer, Clarendon Press, Oxford, 1994.
[103] M. Zhang, Y. J. Wang, L. H. Dai, Bridging shear transformation zone to the atomic structure of amorphous solids, Journal of Non-Crystalline Solids 410 (2015) 100-105.
[104] J. D. Bernal, Geometry of the Structure of Monatomic Liquids, Nature 185 (1960) 68.
[105] J. D. Bernal, A Geometrical Approach to the Structure Of Liquids, Nature 183 (1959) 141.
[106] J. D. Bernal, The Bakerian Lecture, 1962, Proc. R. Soc. London Ser. A. 280 (1964) 445-469.
[107] M. W. Chen, Mechanical behavior of metallic glasses: Microscopic understanding of strength and ductility, Annu. Rev. Mater. Res. 38(1) (2008) 445-469.
[108] D. B. Miracle, A structural model for metallic glasses, Nat. Mater. 3 (2004) 697-702.
[109] A. Inoue, A. Takeuchi, Recent progress in bulk glassy alloys, Materials Transactions 43(8) (2002) 1892-1906.
[110] J. Eckert, N. Mattern, M. Zinkevitch, M. Seidel, Crystallization behavior and phase formation in Zr-Al-Cu-Ni metallic glass containing oxygen, Materials Transactions, JIM 39(6) (1998) 623-632.
[111] W. H. Wang, E. Wu, R. J. Wang, S. J. Kennedy, A. J. Studer, Phase transformation in a $Zr_{41}Ti_{14}Cu12.5Ni_{10}Be_{22.5}$ bulk amorphous alloy upon crystallization, Physical Review B 66(10) (2002).
[112] O. Haruyama, T. Miyazawa, J. Saida, A. Inoue, Change in electrical resistivity due to icosahedral phase precipitation in $Zr_{70}Pd_{20}Ni_{10}$ and $Zr_{65}Al_{7.5}Cu_{7.5}Ni_{10}Ag_{10}$ glasses, Applied Physics Letters 79(6) (2001) 758-760.
[113] W. H. Wang, C. Dong, C. H. Shek, Bulk metallic glasses, Mater. Sci. Eng. R-Rep. 44(2-3) (2004) 45-89.

[114] H. W. Sheng, W. K. Luo, F. M. Alamgir, J. M. Bai, E. Ma, Atomic packing and short-to-medium-range order in metallic glasses, Nature 439 (2006) 419.
[115] F. C. Frank, Supercooling of liquids, PROC. OF THE ROYAL SOCIETY OF LONDON SERIES A 215(1120) (1952) 43-46.
[116] K. F. Kelton, Crystallization of liquids and glasses to quasicrystals, Journal of Non-Crystalline Solids 334 (2004) 253-258.
[117] K. F. Kelton, G. W. Lee, A. K. Gangopadhyay, R. W. Hyers, T. J. Rathz, J. R. Rogers, M. B. Robinson, D. S. Robinson, First x-ray scattering studies on electrostatically levitated metallic liquids: Demonstrated influence of local icosahedral order on the nucleation barrier, Physical review Letters 90(19) (2003).
[118] N. C. Wu, M. Yan, L. Zuo, J. Q. Wang, Correlation between medium-range order structure and glass-forming ability for Al-based metallic glasses, Journal of Applied Physics 115(4) (2014) 7.
[119] C. Y. Liu, F. Wang, F. F. Rao, Y. S. Hou, S. Y. Wang, Q. Sun, Y. Jia, Glass-forming ability of Al-Co alloy under rapid annealing, Journal of Applied Physics 113(15) (2013) 5.
[120] J. Sietsma, B. J. Thijsse, AN INVESTIGATION OF UNIVERSAL MEDIUM RANGE ORDER IN METALLIC GLASSES, Journal of Non-Crystalline Solids 135(2-3) (1991) 146-154.
[121] T. C. Hufnagel, S. Brennan, Short- and medium-range order in (Zr70Cu20Ni10)(90-x)TaxAl10 bulk amorphous alloys, Physical Review B 67(1) (2003) 8.
[122] J. Sietsma, B. J. Thijsse, COLLECTIVE AND SPECIFIC TYPES OF SHORT AND MEDIUM RANGE ORDER IN METALLIC GLASSES, Journal of Non-Crystalline Solids 101(2-3) (1988) 135-150.
[123] D. B. Miracle, The efficient cluster packing model - An atomic structural model for metallic glasses, Acta Materialia 54(16) (2006) 4317-4336.
[124] D. B. Miracle, A. L. Greer, K. F. Kelton, Icosahedral and dense random cluster packing in metallic glass structures, Journal of Non-Crystalline Solids 354(34) (2008) 4049-4055.
[125] A. Lindsay Greer, Confusion by design, Nature 366(6453) (1993) 303-304.
[126] F. Spaepen, A microscopic mechanism for steady state inhomogeneous flow in metallic glasses, Acta Metallurgica 25 (1977) 407-415.
[127] M. H. Cohen, D. Turnbull, MOLECULAR TRANSPORT IN LIQUIDS AND GLASSES, J. Chem. Phys. 31(5) (1959) 1164-1169.
[128] E. A. Kramer, W. L. Johnson, C. Cline, The effects of neutron irradiation on a superconducting metallic glass, Appl. Phys. Lett. 35(10) (1979) 815-818.
[129] R. Gerling, F. P. Schimansky, R. Wagner, Restoration of the ductility of thermally embrittled amorphous-alloys under neutron-irradiation, Acta Metallurgica 35(5) (1987) 1001-1006.
[130] D. A. Lucca, A. Zare, M. J. Klopfstein, L. Shao, C. Q. Xie, Investigation of the mechanical behavior of ion irradiated Ni-free Ti-based metallic glass by nanoindentation, CIRP Ann-Manuf. Technol. 63(1) (2014) 533-536.
[131] R. Gerling, F. P. Schimansky, R. Wagner, RADIATION-INDUCED CHANGES OF THE DUCTILITY OF AMORPHOUS FE40NI40B20, Scripta Metallurgica 17(2) (1983) 203-208.
[132] A. S. Argon, PLASTIC-DEFORMATION IN METALLIC GLASSES, Acta Metallurgica 27(1) (1979) 47-58.

[133] A. J. Foreman, M. A. Jaswon, J. K. Wood, FACTORS CONTROLLING DISLOCATION WIDTHS, Proceedings of the Physical Society of London Section A 64(374) (1951) 156-163.
[134] J. S. Langer, Shear-transformation-zone theory of deformation in metallic glasses, Scripta Materialia 54(3) (2006) 375-379.
[135] S. X. Song, T. G. Nieh, Direct measurements of shear band propagation in metallic glasses - An overview, Intermetallics 19(12) (2011) 1968-1977.
[136] James Antonaglia, Xie Xie, Gregory Schwarz, Matthew Wraith, Junwei Qiao, Yong Zhang, Peter K. Liaw, Jonathan T. Uhl, Karin A. Dahmen, Tuned critical avalanche scaling in bulk metallic glasses, Scientific Reports 4 (2014) 4382.
[137] H. Chen, Y. He, G. J. Shiflet, S. J. Poon, DEFORMATION-INDUCED NANOCRYSTAL FORMATION IN SHEAR BANDS OF AMORPHOUS-ALLOYS, Nature 367(6463) (1994) 541-543.
[138] W. H. Jiang, F. E. Pinkerton, M. Atzmon, Deformation-induced nanocrystallization in an Al-based amorphous alloy at a subambient temperature, Scripta Materialia 48(8) (2003) 1195-1200.
[139] J. Li, X. Gu, T. C. Hufnagel, Using fluctuation microscopy to characterize structural order in metallic glasses, Microscopy and Microanalysis 9(6) (2003) 509-515.
[140] J. Li, F. Spaepen, T. C. Hufnagel, Nanometre-scale defects in shear bands in a metallic glass, Philos. Mag. A-Phys. Condens. Matter Struct. Defect Mech. Prop. 82(13) (2002) 2623-2630.
[141] Y. Hirotsu, T. G. Nieh, A. Hirata, T. Ohkubo, N. Tanaka, Local atomic ordering and nanoscale phase separation in a Pd-Ni-P bulk metallic glass, Physical Review B 73(1) (2006) 4.
[142] P. E. Donovan, W. M. Stobbs, THE STRUCTURE OF SHEAR BANDS IN METALLIC GLASSES, Acta Metallurgica 29(8) (1981) 1419-1436.
[143] P. Rodriguez, Serrated plastic flow, Bull. Mater. Sci. 6(4) (1984) 653-663.
[144] E. Pekarskaya, C. P. Kim, W. L. Johnson, In situ transmission electron microscopy studies of shear bands in a bulk metallic glass based composite, Journal of Materials Research 16(9) (2001) 2513-2518.
[145] B. Yang, C. T. Liu, T. G. Nieh, M. L. Morrison, P. K. Liaw, R. A. Buchanan, Localized heating and fracture criterion for bulk metallic glasses, Journal of Materials Research 21(4) (2006) 915-922.
[146] S. X. Song, T. G. Nieh, Flow serration and shear-band viscosity during inhomogeneous deformation of a Zr-based bulk metallic glass, Intermetallics 17(9) (2009) 762-767.
[147] Q. Wang, S. Gravier, J. J. Blandin, J. M. Pelletier, J. Lu, Deformation and crystallization of a Zr41.2Ti13.8Cu12.5Ni10Be22.5 bulk metallic glass in the supercooled liquid region, Mater. Sci. Eng. A-Struct. Mater. Prop. Microstruct. Process. 435 (2006) 405-411.
[148] Z. Q. Liu, W. H. Wang, M. Q. Jiang, Z. F. Zhang, Intrinsic factor controlling the deformation and ductile-to-brittle transition of metallic glasses, Philosophical Magazine Letters 94(10) (2014) 658-668.
[149] A. Inoue, Bulk amorphous and nanocrystalline alloys with high functional properties, Mater. Sci. Eng. A-Struct. Mater. Prop. Microstruct. Process. 304 (2001) 1-10.
[150] C. J. Gilbert, R. O. Ritchie, W. L. Johnson, Fracture toughness and fatigue-crack propagation in a Zr-Ti-Ni-Cu-Be bulk metallic glass, Applied Physics Letters 71(4) (1997) 476-478.

[151] C. J. Gilbert, V. Schroeder, R. O. Ritchie, Mechanisms for fracture and fatigue-crack propagation in a bulk metallic glass, Metall. Mater. Trans. A-Phys. Metall. Mater. Sci. 30(7) (1999) 1739-1753.
[152] P. Lowhaphandu, J. J. Lewandowski, Fracture toughness and notched toughness of bulk amorphous alloy: Zr-Ti-Ni-Cu-Be, Scripta Materialia 38(12) (1998) 1811-1817.
[153] J. H. Schneibel, J. A. Horton, P. R. Munroe, Fracture toughness, fracture morphology, and crack-tip plastic zone of a Zr-based bulk amorphous alloy, Metall. Mater. Trans. A-Phys. Metall. Mater. Sci. 32(11) (2001) 2819-2825.
[154] W. L. Johnson, K. Samwer, A universal criterion for plastic yielding of metallic glasses with a (T/Tg) 2/3 temperature dependence, Phys Rev Lett 95(19) (2005) 195501.
[155] Y. Zhang, T. T. Zuo, Z. Tang, M. C. Gao, K. A. Dahmen, P. K. Liaw, Z. P. Lua, Microstructures and properties of high-entropy alloys, Progress in Materials Science 61 (2014) 1-93.
[156] S. Niu, H. Kou, Y. Zhang, J. Wang, J. Li, The characteristics of serration in $Al_{0.5}CoCrFeNi$ high entropy alloy, Materials Science and Engineering: A 702 (2017) 96-103.
[157] J. Antonaglia, W. J. Wright, X. Gu, R. R. Byer, T. C. Hufnagel, M. LeBlanc, J. T. Uhl, K. A. Dahmen, Bulk metallic glasses deform via slip avalanches, Physical Review Letters 112(155501) (2014) 1-5.
[158] J. J. Li, Z. Wang, J. W. Qiao, Power-law scaling between mean stress drops and strain rates in bulk metallic glasses, Materials and Design 99 (2016) 427-432.
[159] F. H. D. Torre, D. Klaumünzer, R. Maaß, J.F. Löffler, Stick–slip behavior of serrated flow during inhomogeneous deformation of bulk metallic glasses, Acta Materialia 58 (2010) 3742-3750.
[160] R. Maaß, D. Klaumünzer, J.F. Löffler, Propagation dynamics of individual shear bands during inhomogeneous flow in a Zr-based bulk metallic glass, Acta Materialia 59 (2011) 3205-3213.
[161] B. Shi, S. Y. Luan, P. P. Jin, Crossover from free propagation to cooperative motions of shear bands and its effedt on serrated flow in metallic glass, Journal of Non-Crystalline Solids 482 (2018) 126-131.
[162] W. H. Jiang, G. J. Fan, F. X. Liu, G. Y. Wang, H. Choo, P. K. Liaw, Spatiotemporally inhomogeneous plastic flow of a bulk-metallic glass, International Journal of Plasticity 24(1) (2008) 1-16.
[163] A. Sarkar, S. A. Maloy, K. L. Murty, Investigation of Portevin-LeChatelier effect in HT-9 steel, Materials Science and Engineering A 631 (2015) 120-125.
[164] Y. Zhang, J. P. Liu, S. Y. Chen, X. Xie, P. K. Liaw, K. A. Dahmen, J. W. Qiao, Y. L. Wang, Serration and noise behaviors in materials, Progress in Materials Science 90 (2017) 358-460.
[165] D. M. Field, D. C. Van Aken, Dynamic strain aging phenomena and tensile response of medium-Mn TRIP steel, Metallurgical and Materials Transactions A 49A(4) (2018) 1152-1166.
[166] P. Lan, J. Q. Zhang, Serrated flow and dynamic strain aging in Fe-Mn-C TWIP steel, Metallurgical and Materials Transactions A 49A(1) (2018) 147-161.
[167] P. D. Zavattieri, V. Savic, L. G. Hector, J. R. Fekete, W. Tong, Y. Xuan, Spatio-temporal characteristics of the Portevin-Le Chatelier effect in austenitic steel with twinning induced plasticity, International Journal of Plasticity 25(12) (2009) 2298-2330.

[168] M. Madivala, A. Schwedt, S. L. Wong, F. Roters, U. Prahl, W. Bleck, Temperature dependent strain hardening and fracture behavior of TWIP steel, International Journal of Plasticity 104 (2018) 80-103.
[169] J. Brechtl, B. Chen, X. Xie, Y. Ren, J. D. Venable, P. K. Liaw, S. J. Zinkle, Entropy modeling on serrated flows in carburized steels, Materials Science and Engineering: A 753 (2019) 135-145.
[170] S. Chen, X. Xie, B. L. Chen, J. W. Qiao, Y. Zhang, Y. Ren, K. A. Dahmen, P. K. Liaw, Effects of temperature on serrated flows of $Al_{0.5}$CoCrCuFeNi high-entropy alloy, JOM 67(10) (2015) 2314-2320.
[171] Robert Carroll, Chi Lee, Che-Wei Tsai, Jien-Wei Yeh, James Antonaglia, Braden A. W. Brinkman, Michael LeBlanc, Xie Xie, Shuying Chen, Peter K. Liaw, Karin A. Dahmen, Experiments and model for serration statistics in low-entropy, medium-entropy, and high-entropy alloys, Scientific Reports 5 (2015) 16997.
[172] S. Y. Chen, X. Yang, K. A. Dahmen, P. K. Liaw, Y. Zhang, Microstructures and crackling noise of AlxNbTiMoV high entropy alloys, Entropy 16 (2014) 870-884.
[173] S. Chen, L. Yu, J. Ren, X. Xie, X. Li, Y. Xu, G. Zhao, P. Li, F. Yang, Y. Ren, P. K. Liaw, Self-similar random process and chaotic behavior in serrated flow of high entropy alloys, Scientific Reports 6 (2016) 29798.
[174] S. Chen, X. Xie, W. Li, R. Feng, B. Chen, J. Qiao, Y. Ren, Y. Zhang, K. A. Dahmen, P. K. Liaw, Temperature effects on the serrated behavior of an $Al_{0.5}$CoCrCuFeNi high-entropy alloy, Materials Chemistry and Physics 210 (2018) 20-28.
[175] M. Komarasamy, N. Kumar, R. S. Mishra, P. K. Liaw, Anomalies in the deformation mechanism and kinetics of coarse-grained high entropy alloy, Materials Science & Engineering A 654 (2016) 256-263.
[176] S. Chen, W. Li, X. Xie, J. Brechtl, B. Chen, P. Li, G. Zhao, F. Yang, J. Qiao, K. A. Dahmen, P. K. Liaw, Nanoscale serration and creep characteristics of $Al_{0.5}$CoCrCuFeNi high-entropy alloys, Journal of Alloys and Compounds 752 (2018) 464-475.
[177] J. Brechtl, S. Y. Chen, X. Xie, Y. Ren, J. W. Qiao, P. K. Liaw, S. J. Zinkle, Towards a greater understanding of serrated flows in an Al-containing high-entropy-based alloy, International Journal of Plasticity 115 (2019) 71-92.
[178] A. Sarkar, P. Barat, P. Mukherjee, Multiscale entropy analysis of the Portevin-Le Chatelier effect in an Al-2.5%Mg alloy, Fractals 18(3) (2010) 319-325.
[179] A. Chatterjee, A. Sarkar, P. Barat, P. Mukherjee, N. Gayathri, Character of the deformation bands in the (A + B) regime of the Portevin-Le Chatelier effect in Al-2.5%Mg alloy, Materials Science and Engineering A 508 (2009) 156-160.
[180] M. A. Valdes-Tabernero, R. Sancho-Cadenas, I. Sabirov, M. Y. Murashkin, I. A. Ovid'ko, F. Galvez, Effect of SPD processing on mechanical behavior and dynamic strain aging of an Al-Mg alloy in various deformation modes and wide strain rate range, Materials Science & Engineering A 696 (2017) 348-359.
[181] N. Chibane, H. Ait-Amokhtar, C. Fressengeas, On the strain rate dependence of the critical strain for plastic instabilities in Al-Mg alloys, Scripta Materialia 130 (2017) 252-255.
[182] D. Yuzbekova, A. Mogucheva, D. Zhemchuzhnikova, T. Lebedkina, M. Lebyodkin, R. Kaibyshev, Effect of microstructure on continuous propagation of the Portevin-Le Chatelier deformation bands, International Journal of Plasticity 96 (2017) 210-226.
[183] M. Jobba, R. K. Mishra, M. Niewczas, Flow stress and work-hardening behaviour of Al-Mg binary alloys, International Journal of Plasticity 65 (2015) 43-60.

[184] A. Yilmaz, The Portevin-Le Chatelier effect: a review of experimental findings, Sci. Technol. Adv. Mater. 12 (2011).
[185] A. Humeau-Heurtier, The multiscale entropy algorithm and Its variants: a review, Entropy 17 (2015) 3110-3123.
[186] S.-D. Wu, C.-W. Wu, S.-G. Lin, K.-Y. Lee, C.-K. Peng, Analysis of complex time series using refined composite multiscale entropy Physics Letters A 378 (2014) 1369-1374.
[187] M. Costa, C.-K. Peng, A. L. Goldberger, J. M. Hausdorff, Multiscale entropy analysis of human gait dynamics, Physica A 330 (2003) 53-60.
[188] S.-D. Wu, C.-W. Wu, S.-G. Lin, C.-C. Wang, K.-Y. Lee, Time series analysis using composite multiscale entropy, Entropy 15 (2013) 1069-1084.
[189] A. C. Iliopoulos, N. S. Nikolaidis, E. C. Aifantis, Analysis of serrations and shear bands fractality in UFGs, Journal of the Mechanical Behavior of Materials 24(1-2) (2015) 1-9.
[190] J. Brechtl, X. Xie, P. K. Liaw, S. J. Zinkle, Complexity modeling and analysis of chaos and other fluctuating phenomena, Chaos, Solitons & Fractals 116 (2018) 166-175.
[191] M. D. Costa, A. L. Goldberger, Generalized multiscale entropy analysis: Application to quantifying the complex volatility of human heartbeat time series, Entropy 17 (2015) 1197-1203.
[192] M. Costa, A. L. Goldberger, C. K. Peng, Multiscale entropy analysis of biological signals, Physical Review E 71(2) (2005) 021906.
[193] M. Costa, A. L. Goldberger, C. K. Peng, Multiscale entropy analysis of complex physiologic time series, Physical Review Letters 89(6) (2002) 068102.
[194] E. A. F. Ihlen, A. Weiss, A. Bourke, J. L. Helbostad, J. M. Hausdorff, The complexity of daily life walking in older adult community-dwelling fallers and non-fallers, J. Biomech. 49(9) (2016) 1420-1428.
[195] M. C. Chang, C. K. Peng, H. E. Stanley, Emergence of dynamical complexity related to human heart rate variability, Physical Review E 90(6) (2014) 5.
[196] S. Reulecke, S. Charleston-Villalobos, A. Voss, R. Gonzalez-Camarena, J. A. Gonzalez-Hermosillo, M. J. Gaitan-Gonzalez, G. Hernandez-Pacheco, R. Schroeder, T. Aljama-Corrales, Temporal analysis of cardiovascular and respiratory complexity by multiscale entropy based on symbolic dynamics, IEEE J. Biomed. Health Inform. 22(4) (2018) 1046-1058.
[197] J. Brechtl, X. Xie, K. A. Dahmen, P. K. Liaw, Complexity Analysis of Chaos and Other Fluctuating Phenomena, ArXiv e-prints, 2017.
[198] J. Brechtl, X. Xie, P. K. Liaw, Investigation of chaos and memory effects in the Bonhoeffer-van der Pol oscillator with a non-ideal capacitor, Commun. Nonlinear Sci. Numer. Simul. 73 (2019) 195-216.
[199] J. Brechtl, X. Xie, K. A. Dahmen, P. K. Liaw, S. J. Zinkle, On the Study of Chaos and Memory Effects in the Bonhoeffer-van der Pol Oscillator with a Non-Ideal Capacitor, (2018).
[200] S. H. Strogatz, Nonlinear Dynamics and Chaos with Applications to Physics, Biology, Chemistry, and Engineering, Perseus Books Publishing, LLC, Cambridge, 1994.
[201] A.C. Fischer-Cripps, Nanoindentation, Springer New York2013.
[202] A.C. Fischer-Cripps, Introduction to Contact Mechanics, Springer US2007.
[203] W. C. Oliver, G. M. Pharr, AN IMPROVED TECHNIQUE FOR DETERMINING HARDNESS AND ELASTIC-MODULUS USING LOAD AND DISPLACEMENT

SENSING INDENTATION EXPERIMENTS, Journal of Materials Research 7(6) (1992) 1564-1583.
[204] W. C. Oliver, G. M. Pharr, Nanoindentation in materials research: Past, present, and future, MRS Bull. 35(11) (2010) 897-907.
[205] W. C. Oliver, G. M. Pharr, Measurement of hardness and elastic modulus by instrumented indentation: Advances in understanding and refinements to methodology, Journal of Materials Research 19(1) (2004) 3-20.
[206] Weidong Li, H. Bei, Y. Tong, W. Dmowski, Y. F. Gao, Structural heterogeneity induced plasticity in bulk metallic glasses: From well-relaxed fragile glass to metal-like behavior, Applied Physics Letters 103(17) (2013) 171910.
[207] W. Li, Y. Gao, H. Bei, On the correlation between microscopic structural heterogeneity and embrittlement behavior in metallic glasses, Sci Rep 5 (2015) 14786.
[208] Y. V. Milman, A. A. Golubenko, S. N. Dub, Indentation size effect in nanohardness, Acta Materialia 59(20) (2011) 7480-7487.
[209] D. C. C. Lam, A. C. M. Chong, Model and experiments on strain gradient hardening in metallic glass, Mater. Sci. Eng. A-Struct. Mater. Prop. Microstruct. Process. 318(1-2) (2001) 313-319.
[210] J. I. Jang, B. G. Yoo, Y. J. Kim, J. H. Oh, I. C. Choi, H. B. Bei, Indentation size effect in bulk metallic glass, Scripta Materialia 64(8) (2011) 753-756.
[211] D. C. C. Lam, A. C. M. Chong, Indentation model and strain gradient plasticity law for glassy polymers, Journal of Materials Research 14(9) (1999) 3784-3788.
[212] W. D. Nix, H. Gao, Indentation size effects in crystalline materials: a law for strain gradient plasticity, J. Mech. Phys. Solics 46(3) (1998) 411-425.
[213] Y. Huang, F. Zhang, K. C. Hwang, W. D. Nix, G. M. Pharr, G. Feng, A model of size effects in nano-indentation, J. Mech. Phys. Solids 54(8) (2006) 1668-1686.
[214] T. Y. Zhang, W. H. Xu, Surface effects on nanoindentation, Journal of Materials Research 17(7) (2002) 1715-1720.
[215] T. Y. Zhang, W. H. Xu, M. H. Zhao, The role of plastic deformation of rough surfaces in the size-dependent hardness, Acta Materialia 52(1) (2004) 57-68.
[216] A. S. Argon, THEORY FOR LOW-TEMPERATURE PLASTIC-DEFORMATION OF GLASSY POLYMERS, Philos. Mag. 28(4) (1973) 839-865.
[217] C. Wang, Q. P. Cao, T. Feng, X. D. Wang, D. X. Zhang, S. X. Qu, J. Z. Jiang, Indentation size effects of mechanical behavior and shear transformation zone in thin film metallic glasses, Thin Solid Films 646 (2018) 36-43.
[218] B. Dibner, The new rays of Professor Röntgen, Burndy Library1963.
[219] J. J. Thomson, The Röntgen Rays, Nature 53 (1896) 391.
[220] W. H. Bragg, The reflection of X-rays by crystals, Nature 91 (1913) 477-477.
[221] W. H. Bragg, The reflection of X-rays by crystals, Physikalische Zeitschrift 14 (1913) 472-473.
[222] W. H. Bragg, W. L. Bragg, The reflection of X-rays by crystals, Proceedings of the Royal Society of London Series a-Containing Papers of a Mathematical and Physical Character 88(605) (1913) 428-438.
[223] W.D. Callister, D.G. Rethwisch, Fundamentals of Materials Science and Engineering: An Integrated Approach, 5th Edition, Wiley2016.

[224] Chris M. Fancher, Zhen Han, Igor Levin, Katharine Page, Brian J. Reich, Ralph C. Smith, Alyson G. Wilson, Jacob L. Jones, Use of Bayesian Inference in Crystallographic Structure Refinement via Full Diffraction Profile Analysis, Scientific Reports 6 (2016) 31625.
[225] D. Okai, T. Fukami, M. Asada, I. Noda, T. Yamasaki, Y. Yokoyama, A. Inoue, Comparison of crystallization process of amorphous Zr2Ni alloy and metallic Zr2Cu glass, Materials Transactions 48(7) (2007) 1689-1693.
[226] P. Ramasamy, M. Stoica, A. H. Taghvaei, K. G. Prashanth, R. Kumar, J. Eckert, Kinetic analysis of the non-isothermal crystallization process, magnetic and mechanical properties of FeCoBSiNb and FeCoBSiNbCu bulk metallic glasses, Journal of Applied Physics 119(7) (2016) 9.
[227] M. J. Duarte, A. Kostka, A. Crespo, J. A. Jimenez, A. C. Dippel, F. U. Renner, G. Dehm, Kinetics and crystallization path of a Fe-based metallic glass alloy, Acta Materialia 127 (2017) 341-350.
[228] M. J. Duarte, J. Klemm, S. O. Klemm, K. J. J. Mayrhofer, M. Stratmann, S. Borodin, A. H. Romero, M. Madinehei, D. Crespo, J. Serrano, S. S. A. Gerstl, P. P. Choi, D. Raabe, F. U. Renner, Element-Resolved Corrosion Analysis of Stainless-Type Glass-Forming Steels, Science 341(6144) (2013) 372-376.
[229] M. J. Duarte, A. Kostka, J. A. Jimenez, P. Choi, J. Klemm, D. Crespo, D. Raabe, F. U. Renner, Crystallization, phase evolution and corrosion of Fe-based metallic glasses: An atomic-scale structural and chemical characterization study, Acta Materialia 71 (2014) 20-30.
[230] T. Paul, A. Loganathan, A. Agarwal, S. P. Harimkar, Kinetics of isochronal crystallization in a Fe-based amorphous alloy, Journal of Alloys and Compounds 753 (2018) 679-687.
[231] P. Gong, S. B. Wang, F. W. Li, X. Y. Wang, Kinetics of Glass Transition and Crystallization of a Zr40Hf10Ti4Y1Al10Cu25Ni7Co2Fe1 Bulk Metallic Glass with High Mixing Entropy, Metall. Mater. Trans. A-Phys. Metall. Mater. Sci. 49A(7) (2018) 2918-2928.
[232] T. Xu, Z. Y. Jian, F. E. Chang, L. C. Zhuo, T. Zhang, Non-isothermal crystallization kinetics of Fe75Cr5P9B4C7 metallic glass with a combination of desired merits, Vacuum 152 (2018) 8-14.
[233] X. L. Han, F. L. Ding, Y. S. Qin, D. Y. Wu, H. Xing, Y. Shi, K. K. Song, C. D. Cao, Compositional dependence of crystallization kinetics in Zr-Ni-Al metallic glasses, Vacuum 151 (2018) 30-38.
[234] Z. Q. Xu, Y. F. Xu, A. Zhan, J. Y. Wang, Z. M. Wang, Oxidation of amorphous alloys, Journal of Materials Science & Technology 34(11) (2018) 1977-2005.
[235] W. Kai, W. S. Chen, Y. H. Wu, P. C. Lin, C. P. Chuang, P. K. Liaw, Air-oxidation of a Cu50Zr50 binary amorphous ribbon at 350-425 degrees C, Journal of Alloys and Compounds 536 (2012) S103-S108.
[236] Z. Song, D. L. Tan, F. He, X. H. Bao, Surface segregation behaviors of amorphous Ni65Nb35 alloy under oxidation in O-2 at various temperatures, Appl. Surf. Sci. 137(1-4) (1999) 142-149.
[237] C. Y. Tam, C. H. Shek, Oxidation behavior of Cu60Zr30Ti10 bulk metallic glass, Journal of Materials Research 20(6) (2005) 1396-1403.
[238] T. Egami, K. Maeda, D. Srolovitz, V. Vitek, Local structure of amorphous metals, Journal De Physique Colloques 41(C8) (1980) C8-272-C8-275.
[239] John Robert Salasin, Claudia Rawn, In-Situ Kinetic Investigation of Calcium Aluminate Formation, 2018.

[240] C. Manfredotti, M. Truccato, G. Rinaudo, D. Allasia, P. Volpe, P. Benzi, A. Agostino, Annealing temperature dependence of the 2223 phase volume fraction in the Bi-Sr-Ca-Cu-O system, Physica C 353(3-4) (2001) 184-194.
[241] B.D. Cullity, Elements of X Ray Diffraction - Scholar's Choice Edition, Scholar's Choice2015.
[242] E.J. Mittemeijer, U. Welzel, Modern Diffraction Methods, Wiley2013.
[243] F. J. Gotor, J. M. Criado, J. Malek, N. Koga, Kinetic analysis of solid-state reactions: The universality of master plots for analyzing isothermal and nonisothermal experiments, J. Phys. Chem. A 104 (2000) 10777-10782.
[244] J. H. Sharp, G. W. Brindley, B. N. N. Achar, Numerical data for some commonly used solid state reaction equations, J. Am. Ceram. Soc. 49(7) (1966) 379-&.
[245] Pedro E. Sánchez-Jiménez, Luis A. Pérez-Maqueda, Antonio Perejón, José M. Criado, Generalized Kinetic Master Plots for the Thermal Degradation of Polymers Following a Random Scission Mechanism, The Journal of Physical Chemistry A 114(30) (2010) 7868-7876.
[246] Melvin Avrami, Kinetics of Phase Change. I General Theory, The Journal of Chemical Physics 7(12) (1939) 1103-1112.
[247] Melvin Avrami, Kinetics of Phase Change. II Transformation-Time Relations for Random Distribution of Nuclei, The Journal of Chemical Physics 8(2) (1940) 212-224.
[248] Melvin Avrami, Granulation, Phase Change, and Microstructure Kinetics of Phase Change. III, The Journal of Chemical Physics 9(2) (1941) 177-184.
[249] A. Kolmogorov, Zur Statistik der Kristallisationsvorgänge in Metallen, Izv. Akad. Nauk SSSR Ser. Mat. 1(3) (1937) 355-359.
[250] William A. Johnson, Robert F. Mehl, Reaction Kinetics in Processes of Nucleation and Growth (Reprinted from Transactions of the American Institute of Mining & Metallurgical Engineers, vol 135, pg 416, 1939), 2010.
[251] M.E. Brown, D. Dollimore, A.K. Galwey, Reactions in the Solid State, Elsevier Science1980.
[252] A. Khawam, D. R. Flanagan, Solid-state kinetic models: Basics and mathematical fundamentals, J. Phys. Chem. B 110(35) (2006) 17315-17328.
[253] W.E. Garner, Chemistry of the Solid State, Butterworths Scientific Publications1955.
[254] Camelia V. Stan, Christine M. Beavers, Martin Kunz, Nobumichi Tamura, X-Ray Diffraction under Extreme Conditions at the Advanced Light Source, Quantum Beam Science 2(1) (2018) 4.
[255] T. Egami, Y. Tong, W. Dmowski, Deformation in metallic glasses studied by synchrotron x-ray diffraction, Metals 6(22) (2016).
[256] W. Dmowski, T. Iwashita, C.-P. Chuang, J. Almer, T. Egami, Elastic Heterogeneity in Metallic Glasses, Phys. Rev. Lett. 105(20) (2010).
[257] T. Egami, T. Iwashita, W. Dmowski, Mechanical properties of metallic glasses, Metals 3 (2013) 77-113.
[258] Y. Suzuki, J. Haimovich, T. Egami, Bond-orientational anisotropy in metallic glasses observed by X-ray diffraction, Phys. Rev. B 35 (1987) 2162-2168.
[259] T. Egami, S. J. L. Billinge, Underneath the Bragg Peaks: Structural Analysis of Complex Materials, 2nd ed., Elsevier, Amsterdam, The Netherlands, 2012.
[260] W. Dmowski, T. Iwashita, C.-P. Chuang, J. Almer, T. Egami, Elastic heterogeneity in metallic glasses, Phys. Rev. Lett. 105 (2010) 205502.

[261] D.B. Williams, C.B. Carter, Transmission Electron Microscopy: A Textbook for Materials Science, Springer US2013.
[262] David B. Williams, C. Barry Carter, Transmission Electron Microscopy: A Textbook for Materials Science, 2 ed., Boston, MA: Springer US, Boston, MA, 2009.
[263] David B. Williams, Transmission Electron Microscopy : A Textbook for Materials Science, Boston, MA : Springer US : Imprint: Springer1996.
[264] X. D. Liu, K. Lu, B. Z. Ding, Z. Q. Hu, OBSERVATION OF THE CRYSTALLIZATION OF AMORPHOUS FE-CU-SI-B ALLOY BY IN-SITU TRANSMISSION ELECTRON-MICROSCOPY, Mater. Sci. Eng. A-Struct. Mater. Prop. Microstruct. Process. 179 (1994) 386-389.
[265] G. Dehm, J.M. Howe, J. Zweck, In-situ Electron Microscopy: Applications in Physics, Chemistry and Materials Science, Wiley2012.
[266] T. Koziel, A. Zielinska-Lipiec, Z. Kedzierski, T. Czeppe, Transmission electron microscopy study of crystallization in Fe-Si-B-Cr-C amorphous alloy, Journal of Microscopy 224 (2006) 27-29.
[267] J. S. C. Jang, I. H. Wang, L. J. Chang, G. J. Chen, T. H. Hung, J. C. Huang, Crystallization kinetics and thermal stability of the Zr60Al7.5Cu17.5Ni10Si4B1 amorphous alloy studied by isothermal differential scanning calorimetry and transmission electron microscopy, Mater. Sci. Eng. A-Struct. Mater. Prop. Microstruct. Process. 449 (2007) 511-516.
[268] J. Saida, M. Matsushita, C. Li, A. Inoue, Comparative study of grain growth behavior from a supercooled liquid region of Zr65Cu27.5Al7.5 and Zr65Cu35 metallic glasses, Journal of Materials Science 35(14) (2000) 3539-3546.
[269] J. Saida, C. Li, M. Matsushita, A. Inoue, Grain growth kinetics in a supercooled liquid region of Zr65Cu27.5Al7.5 and Zr65Cu35 metallic glasses, Journal of Materials Science 35(16) (2000) 4143-4149.
[270] U. Koster, J. Meinhardt, S. Roos, H. Liebertz, Formation of quasicrystals in bulk glass forming Zr-Cu-Ni-Al alloys, Applied Physics Letters 69(2) (1996) 179-181.
[271] A. Hirata, T. Morino, Y. Hirotsu, K. Itoh, T. Fukunaga, Local atomic structure analysis of Zr-Ni and Zr-Cu metallic glasses using electron diffraction, Materials Transactions 48(6) (2007) 1299-1303.
[272] W. McBride, D. J. H. Cockayne, The structure of nanovolumes of amorphous materials, Journal of Non-Crystalline Solids 318(3) (2003) 233-238.
[273] H. F. Li, R. V. Ramanujan, In situ hot stage transmission electron microscopy observations of nanocrystal formation in a Co65Si15B14Fe4Ni2 amorphous magnetic alloy, Thin Solid Films 514(1-2) (2006) 316-322.
[274] P. Duhaj, P. Svec, TRANSMISSION ELECTRON-MICROSCOPY STUDY OF CRYSTALLIZATION IN AMORPHOUS FE40NI40B20 ALLOY, Physica Status Solidi a-Applied Research 80(1) (1983) 231-236.
[275] J. Li, Z. L. Wang, T. C. Hufnagel, Characterization of nanometer-scale defects in metallic glasses by quantitative high-resolution transmission electron microscopy, Physical Review B 65(14) (2002) 6.
[276] A. Hirata, Y. Hirotsu, T. G. Nieh, T. Ohkubo, N. Tanaka, Direct imaging of local atomic ordering in a Pd-Ni-P bulk metallic glass using C-s-corrected transmission electron microscopy, Ultramicroscopy 107(2-3) (2007) 116-123.

[277] H. Rosner, M. Peterlechner, C. Kubel, V. Schmidt, G. Wilde, Density changes in shear bands of a metallic glass determined by correlative analytical transmission electron microscopy, Ultramicroscopy 142 (2014) 1-9.
[278] V. K. Sethi, R. Gibala, A. H. Heuer, TRANSMISSION ELECTRON-MICROSCOPY OF SHEAR BANDS IN AMORPHOUS METALLIC ALLOYS, Scripta Metallurgica 12(2) (1978) 207-209.
[279] J. Brechtl, S. Agarwal, M. L. Crespillo, T. Yang, H. Bei, S. J. Zinkle, Evolution of the microstructural and mechanical properties of BAM-11 bulk metallic glass during ion irradiation and annealing, Journal of Nuclear Materials (submitted Dec. 1, 2018).
[280] C. A. English, M. L. Jenkins, CHARACTERIZATION OF DISPLACEMENT CASCADE DAMAGE PRODUCED IN CU3AU BY FAST-PARTICLE IRRADIATION, Journal of Nuclear Materials 96(3) (1981) 341-357.
[281] S.J. Zinkle, Effects of thermal annealing and ion irradiation on the properties and microstructures of copper alloys. [AMZIRC(Cu-Zr) and AMAX-MZC(Cu-Cr-Zr-Mg)], Univ. of Wisconsin,Madison, WI; Wisconsin Univ., Madison (USA), 1985, p. Medium: X; Size: Pages: 273.
[282] M. J. Norgett, M. T. Robinson, I. M. Torrens, PROPOSED METHOD OF CALCULATING DISPLACEMENT DOSE-RATES, Nuclear Engineering and Design 33(1) (1975) 50-54.
[283] R. S. Averback, ION-IRRADIATION STUDIES OF CASCADE DAMAGE IN METALS, Journal of Nuclear Materials 108(1-2) (1982) 33-45.
[284] R. S. Averback, R. Benedek, K. L. Merkle, EFFICIENCY OF DEFECT PRODUCTION IN CASCADES, Journal of Nuclear Materials 69-7(1-2) (1978) 786-789.
[285] M.T. Robinson, Radiation Induced Voids in Metals, in: J.W. Corbett, L.C. Ianniello (Eds.) Oak Ridge National Laboratory, Oak Ridge, TN, 1977, p. 392.
[286] R. S. Averback, M. Ghaly, Fundamental aspects of defect production in solids, Nuclear Instruments & Methods in Physics Research Section B-Beam Interactions with Materials and Atoms 127 (1997) 1-11.
[287] S. J. Zinkle, B. N. Singh, ANALYSIS OF DISPLACEMENT DAMAGE AND DEFECT PRODUCTION UNDER CASCADE DAMAGE CONDITIONS, Journal of Nuclear Materials 199(3) (1993) 173-191.
[288] R. S. Averback, ATOMIC DISPLACEMENT PROCESSES IN IRRADIATED METALS, Journal of Nuclear Materials 216 (1994) 49-62.
[289] S. J. Kim, M. A. Nicolet, R. S. Averback, D. Peak, LOW-TEMPERATURE ION-BEAM MIXING IN METALS, Physical Review B 37(1) (1988) 38-49.
[290] G. H. Vineyard, THERMAL SPIKES AND ACTIVATED PROCESSES, Radiat. Eff. Defects Solids 29(4) (1976) 245-248.
[291] J. Lindhard, V. Nielsen, M. Scharff, APPROXIMATION METHOD IN CLASSICAL SCATTERING BY SCREENED COULOMB FIELDS, Matematisk-Fysiske Meddelelser Udgivet Af Det Kongelige Danske Videnskabernes Selskab 36(10) (1968) 3-&.
[292] Michael Nastasi, James W. Mayer, Ion Implantation and Synthesis of Materials, Berlin, Heidelberg: Springer Berlin Heidelberg, Berlin, Heidelberg, 2006.
[293] J. F. Ziegler, J. P. Biersack, U. Littmark, The stopping and range of ions in solids, Pergamon Press, New York, 1985.
[294] J. F. Ziegler, SRIM-2003, Nuclear Instruments & Methods in Physics Research Section B-Beam Interactions with Materials and Atoms 219 (2004) 1027-1036.

[295] J. F. Ziegler, J. M. Manoyan, THE STOPPING OF IONS IN COMPOUNDS, Nuclear Instruments & Methods in Physics Research Section B-Beam Interactions with Materials and Atoms 35(3-4) (1988) 215-228.
[296] J. F. Ziegler, Stopping of energetic light ions in elemental matter, Journal of Applied Physics 85(3) (1999) 1249-1272.
[297] J. F. Ziegler, M. D. Ziegler, J. P. Biersack, SRIM - The stopping and range of ions in matter (2010), Nuclear Instruments & Methods in Physics Research B 268 (2010) 1818-1823.
[298] C. M. Parish, R. M. White, J. M. LeBeau, M. K. Miller, Response of nanostructured ferritic alloys to high-dose heavy ion irradiation, Journal of Nuclear Materials 445(1-3) (2014) 251-260.
[299] R.E. Stoller, M.B. Toloczko, G.S. Was, A.G. Certain, S. Dwaraknath, F.A. Garner, On the use of SRIM for computing radiation damage exposure, Nuclear Instruments & Methods in Physics Research Section B-Beam Interactions with Materials and Atoms 310 (2013) 75-80.
[300] ASTM E521—16, Standard Practice for Neutron Radiation Damage Simulation by Charged-Particle Irradiation, West Conshohocken www.astm.org (2016).
[301] G. L. Kulcinski, JL Brimhall, HE Kissinger, Production of voids in pure metals by high-energy heavy-ion bombardment, in: J. Corbett, L. Ianiello (Eds.) Proceedings of Radiation-Induced Voids in Metals, CONF-710601, USAEC Technical Information Center, Oak Ridge, TN, 1972, p. 453.
[302] Q. Xu, K. Sato, T. Yoshiie, Nucleation of He bubbles in amorphous FeBSi alloy irradiated with He ions, Philosophical Magazine Letters 92(10) (2012) 527-533.
[303] G. E. Abrosimova, Evolution of the structure of amorphous alloys, Physics-Uspekhi 54(12) (2011) 1227-1242.
[304] J. Carter, E. G. Fu, M. Martin, G. Q. Xie, X. Zhang, Y. Q. Wang, D. Wijesundera, X. M. Wang, W. K. Chu, L. Shao, Effects of Cu ion irradiation in Cu50Zr45Ti5 metallic glass, Scripta Materialia 61(3) (2009) 265-268.
[305] J. Carter, E. G. Fu, G. Bassiri, B. M. Dvorak, N. D. Theodore, G. Q. Xie, D. A. Lucca, M. Martin, M. Hollander, X. H. Zhang, L. Shao, Effects of ion irradiation in metallic glasses, Nuclear Instruments & Methods in Physics Research Section B-Beam Interactions with Materials and Atoms 267(8-9) (2009) 1518-1521.
[306] J. Carter, E. G. Fu, S. McDeavitt, X. H. Zhang, G. Q. Xie, L. Shao, Characterization of high strength alloy formed by ion irradiation of metallic glasses, in: Y.W. Chang, N.J. Kim, C.S. Lee (Eds.), Pricm 6: Sixth Pacific Rim International Conference on Advanced Materials and Processing, Pts 1-3, Trans Tech Publications Ltd, Durnten-Zurich, 2007, pp. 1737-+.
[307] M. Iqbal, A. Qayyum, J. I. Akhter, Surface modification of Zr-based bulk amorphous alloys by using ion irradiation, Journal of Alloys and Compounds 509(6) (2011) 2780-2783.
[308] S. Nagata, S. Higashi, B. Tsuchiya, K. Toh, T. Shikama, K. Takahiro, K. Ozaki, K. Kawatusra, S. Yamamoto, A. Inouye, Ion irradiation effects on amorphization and thermal crystallization in Zr-Al-Ni-Cu alloys, Nuclear Instruments & Methods in Physics Research Section B-Beam Interactions with Materials and Atoms 257 (2007) 420-423.
[309] S. Nagata, M. Sasase, K. Takahiro, B. Tsuchiya, A. Inouye, S. Yamamoto, T. Shikama, Ion induced structural modification and nano-crystalline formation of Zr-Al-Ni-Cu metallic glasses, Nuclear Instruments & Methods in Physics Research Section B-Beam Interactions with Materials and Atoms 267(8-9) (2009) 1514-1517.

[310] J. Carter, E. G. Fu, M. Martin, G. Xie, X. Zhang, Y. Q. Wang, D. Wijesundera, X. M. Wang, W.-K. Chu, S. M. McDeavitt, L. Shao, Ion irradiation induced nanocrystal formation in amorphous Zr55Cu30Al10Ni5 alloy, Nuclear Instruments and Methods in Physics Research Section B: Beam Interactions with Materials and Atoms 267(17) (2009) 2827-2831.
[311] M. Iqbal, J. I. Akhter, Z. Q. Hu, H. F. Zhang, A. Qayyum, W. S. Sun, Mechanical properties and ion irradiation of bulk amorphous Zr55Cu30Al10Ni5 alloy, J. Non-Cryst. Solids 353(24-25) (2007) 2452-2458.
[312] S. Nagata, S. Higashi, B. Tsuchiya, K. Toh, T. Shikama, K. Takahiro, K. Ozaki, K. Kawatusra, S. Yamamoto, A. Inouye, Ion irradiation effects on amorphization and thermal crystallization in Zr-Al-Ni-Cu alloys, Nuclear Instruments and Methods in Physics Research Section B: Beam Interactions with Materials and Atoms 257(1-2) (2007) 420-423.
[313] G. Q. Xie, L. Shao, D. V. Louzguine-Luzgin, A. Inoue, He ion irradiation induced nanocrystallization in Cu50Zr45Ti5 glassy alloy, Surf. Coat. Technol. 206(5) (2011) 829-833.
[314] X. X. Mei, B. Wang, C. Dong, F. Q. Gong, Y. N. Wang, Z. G. Wang, Anti-irradiation performance against helium bombardment. in bulk metallic glass (Cu47Zr45Al8)(98.5)Y-1.5, Nuclear Instruments & Methods in Physics Research Section B-Beam Interactions with Materials and Atoms 307 (2013) 11-15.
[315] B. Wang, X. X. Mei, W. J. Hou, Y. N. Wang, Z. G. Wang, C. Dong, Behavior of high resistance to He2+ induced irradiation damage in metallic glass, Nuclear Instruments & Methods in Physics Research Section B-Beam Interactions with Materials and Atoms 312 (2013) 84-89.
[316] Y. J. Huang, H. B. Fan, X. Y. Zhou, P. Xue, Z. L. Ning, D. Daisenberger, J. F. Sun, J. Shen, Structure and mechanical property modification of a Ti-based metallic glass by ion irradiation, Scripta Materialia 103 (2015) 41-44.
[317] H. C. Chen, G. Q. Cao, R. D. Liu, G. Wang, L. Yan, X. T. Zhou, Ion irradiation induced element-enriched and depleted nanostructures in Zr-Al-Cu-Ni metallic glass, Journal of Applied Physics 118(3) (2015) 4.
[318] H. C. Chen, L. Yan, R. D. Liu, M. B. Tang, G. Wang, H. F. Huang, Y. Hai, X. T. Zhou, Anisotropic nanocrystallization of a Zr-based metallic glass induced by Xe ion irradiation, Intermetallics 52 (2014) 15-19.
[319] H. R. Zhang, X. X. Mei, Y. M. Wang, Z. G. Wang, Y. Wang, Resistance to H+ induced irradiation damage in metallic glass Fe80Si7.43B12.57, Journal of Nuclear Materials 456 (2015) 344-350.
[320] M. Sorescu, D. Barb, Interaction of alpha particle beams with metallic glasses, Acta Materialia 46(15) (1998) 5523-5531.
[321] N. Hayashi, T. Takahashi, IRRADIATION EFFECTS IN THE AMORPHOUS ALLOY FE40NI40P14B6, Japanese Journal of Applied Physics 20(9) (1981) L627-L630.
[322] W. J. Hou, X. X. Mei, Z. G. Wang, Y. N. A. Wang, Resistance to He2+ irradiation damage in metallic glass Fe80Si7.43B12.57, Nuclear Instruments & Methods in Physics Research B 342 (2015) 221-227.
[323] L. Shao, E. G. Fu, L. Price, D. Chen, T. Y. Chen, Y. Q. Wang, G. Q. Xie, D. A. Lucca, Sink property of metallic glass free surfaces, Scientific Reports 5 (2015) 6.

[324] M. T. Myers, S. Charnvanichborikarn, C. C. Wei, Z. P. Luo, G. Q. Xie, S. O. Kucheyev, D. A. Lucca, L. Shao, Phase transition, segregation and nanopore formation in high-energy heavy-ion-irradiated metallic glass, Scripta Materialia 67(11) (2012) 887-890.
[325] E. Menendez, A. Hynowska, J. Fornell, S. Surinach, J. Montserrat, K. Temst, A. Vantomme, M. D. Baro, E. Garcia-Lecina, E. Pellicer, J. Sort, Influence of the irradiation temperature on the surface structure and physical/chemical properties of Ar ion-irradiated bulk metallic glasses, Journal of Alloys and Compounds 610 (2014) 118-125.
[326] Michael Myers, E. G. Fu, Michelle Myers, Haiyan Wang, Guoqiang Xie, X. Wang, W. K. Chu, Lin Shao, An experimental and modeling study on the role of damage cascade formation in nanocrystalization of ion-irradiated Ni52.5Nb10Zr15Ti15Pt7.5 metallic glass, Scripta Materialia 63(11) (2010) 1045-1048.
[327] Naoto Onodera, Akito Ishii, Yuka Fukumoto, Akihiro Iwase, Yoshihiko Yokoyama, Fuminobu Hori, Local structure and hardness change of Zr50Cu40Al10 bulk glassy alloy after heavy ion irradiation, Nuclear Instruments and Methods in Physics Research Section B: Beam Interactions with Materials and Atoms 282 (2012) 1-3.
[328] M. Sorescu, Comparative characterization of the irradiation effects induced in metallic glasses by pulsed laser and alpha particle beams, Journal of Alloys and Compounds 284(1) (1999) 232-236.
[329] Z. Hu, Z. Q. Zhao, Y. P. Hu, J. S. Xing, T. Lu, B. C. Wei, Effect of Ion Irradiation on Mechanical Behaviors of Ti40Zr25Be30Cr5 Bulk Metallic Glass, Mater. Res.-Ibero-am. J. Mater. 15(5) (2012) 713-717.
[330] V. S. Kraposhin, V. S. Khmelevskaya, M. Y. Yazvitsky, I. A. Antoshina, Crystallization of Co-based amorphous alloys under the impact of the ion irradiation and recovery of the amorphous phase, Journal of Non-Crystalline Solids 353(32-40) (2007) 3057-3061.
[331] M. Miglierini, A. Lančok, M. Pavlovič, CEMS studies of structural modifications of metallic glasses by ion bombardment, The Physics of Metals and Metallography 109(5) (2010) 469-474.
[332] Marcel Miglierini, Adriana Lančok, Márius Pavlovič, Ion bombardment of Fe-based amorphous metallic alloys, Springer Berlin Heidelberg, Berlin, Heidelberg, 2009, pp. 45-52.
[333] R. S. Averback, H. Hahn, Fu-Rong Ding, Ion beam mixing and radiation-enhanced diffusion in metallic glasses, Journal of the Less Common Metals 140 (1988) 267-275.
[334] H. Hahn, R. S. Averback, Dependence of tracer diffusion on atomic size in amorphous Ni-Zr, Physical Review B 37(11) (1988) 6533-6535.
[335] A. K. Tyagi, M. P. Macht, V. Naundorf, Enhanced diffusion of nickel in ion-irradiated FeNiB metallic glass, Journal of Nuclear Materials 179-181 (1991) 1026-1029.
[336] A. K. Tyagi, M. P. Macht, V. Naundorf, Diffusion coefficients of 63Ni in Fe40Ni40B20 metallic glass, Acta Metallurgica et Materialia 39(4) (1991) 609-617.
[337] J. Horvath, H. Mehrer, TRACER DIFFUSION OF FE-59 IN AMORPHOUS FE40NI40B20, Crystal Lattice Defects and Amorphous Materials 13(1) (1986) 1-14.
[338] P. Jung, Creep and electrical resistivity of metallic glass $Ni_{78}B_{14}Si_8$ under proton irradiation, Journal of Applied Physics 86 (1999) 4876-4880.
[339] Francisco Eiichi Fujita, Tsuyoshi Masumoto, Masataka Kitaguchi, Mikio Ura, On the Structure of Fe-P-C Amorphous Alloys, Japanese Journal of Applied Physics 16(10) (1977) 1731-1738.

[340] J. L. Walter, F. Bacon, F. E. Luborsky, An Auger analysis of the embrittlement of the amorphous alloy Ni40Fe40P14B6, Materials Science and Engineering 24(2) (1976) 239-245.
[341] B. Wang, X. X. Mei, H. R. Zhang, W. J. Hou, Y. N. Wang, Z. G. Wang, C. Dong, Resistance to He2+ induced irradiation damage in metallic glass Zr64Cu17.8Ni10.7Al7.5, Journal of Nuclear Materials 444(1-3) (2014) 342-348.
[342] R. Raghavan, K. Boopathy, R. Ghisleni, M. A. Pouchon, U. Ramamurty, J. Michler, Ion irradiation enhances the mechanical performance of metallic glasses, Scripta Materialia 62 (2010) 462-465.
[343] R. Raghavan, B. Kombaiah, M. Döbeli, R. Erni, U. Ramamurty, J. Michler, Nanoindentation response of an ion irradiated Zr-based bulk metallic glass, Materials Science & Engineering A 532 (2012) 407-413.
[344] P. Murali, U. Ramamurty, Embrittlement of a bulk metallic glass due to sub-Tg annealing, Acta Materialia 53(5) (2005) 1467-1478.
[345] W. D. Luo, B. Yang, G. L. Chen, Effect of Ar+ ion irradiation on the microstructure and properties of Zr-Cu-Fe-Al bulk metallic glass, Scripta Materialia 64(7) (2011) 625-628.
[346] A. Gupta, S. Habibi, G. Principi, Neutron irradiation effects in metallic glasses, Materials Science and Engineering A134 (1991) 992-995.
[347] R. Gerling, R. Wagner, Properties of in-core reactor-irradiated amorphous Fe40Ni40B20, Journal of Nuclear Materials 107 (1982) 311-317.
[348] R. Gerling, R. Wagner, Density of neutron irradiated and annealed amorphous $Fe_{40}Ni_{40}B_{20}$, Scripta Metallurgica 16 (1982) 963-967.
[349] W. L. Johnson, A. R. Williams, Structure and properties of transition-metal-metalloid glasses based on refractory metals, Physical Review B 20(4) (1979) 1640-1655.
[350] I. Skorvanek, R. Gerling, T. Graf, M. Fricke, J. Hesse, Neutron irradiation effects on the structural, magnetic and mechanical properties of amorphous and nanocrystalline Fe73.5Cu1Nb3Si13.5B9, IEEE Transactions on magnetics 30(2) (1994) 548-551.
[351] A. Gupta, S. Habibi, G. Principi, Study of short range order in Fe-Ni-Si-B amorphous alloys, Materials Science and Engineering A304-A306 (2001) 1058-1061.
[352] C. T. Liu, L. Heatherly, D. S. Easton, C. A. Carmichael, J. H. Schneibel, C. H. Chen, J. L. Wright, M. H. Yoo, J. A. Horton, A. Inoue, Test environments and mechanical properties of Zr-base bulk amorphous alloys, Metall. Mater. Trans. A-Phys. Metall. Mater. Sci. 29(7) (1998) 1811-1820.
[353] M. L. Morrison, R. A. Buchanan, P. K. Liaw, B. A. Green, G. Y. Wang, C. Liu, J. A. Horton, Four-point-bending-fatigue behavior of the Zr-based Vitreloy 105 bulk metallic glass, Mater. Sci. Eng. A-Struct. Mater. Prop. Microstruct. Process. 467(1-2) (2007) 190-197.
[354] J. Xu, U. Ramamurty, E. Ma, The fracture toughness of bulk metallic glasses, Jom 62(4) (2010) 10-18.
[355] X. H. Lin, W. L. Johnson, W. K. Rhim, Effect of oxygen impurity on crystallization of an undercooled bulk glass forming Zr-Ti-Cu-Ni-Al alloy, Materials Transactions Jim 38(5) (1997) 473-477.
[356] S. E. Naleway, R. B. Greene, B. Gludovatz, N. K. N. Dave, R. O. Ritchie, J. J. Kruzic, A Highly Fatigue-Resistant Zr-Based Bulk Metallic Glass, Metall. Mater. Trans. A-Phys. Metall. Mater. Sci. 44A(13) (2013) 5688-5693.
[357] J. J. Lewandowski, W. H. Wang, A. L. Greer, Intrinsic plasticity or brittleness of metallic glasses, Philosophical Magazine Letters 85(2) (2005) 77-87.

[358] Z. X. Wang, D. Q. Zhao, M. X. Pan, W. H. Wang, T. Okada, W. Utsumi, Formation and crystallization of CuZrHfTi bulk metallic glass under ambient and high pressures, J. Phys.-Condes. Matter 15(35) (2003) 5923-5932.
[359] A. Inoue, W. Zhang, T. Zhang, K. Kurosaka, Formation and mechanical properties of Cu-Hf-Ti bulk glassy alloys, Journal of Materials Research 16(10) (2001) 2836-2844.
[360] Y. Zhang, M. L. Crespillo, H. Xue, K. Jin, C. H. Chen, C. L. Fontana, J. T. Graham, W. J. Weber, New ion beam materials laboratory for materials modification and irradiation effects research, Nuclear Instruments & Methods in Physics Research Section B-Beam Interactions with Materials and Atoms 338 (2014) 19-30.
[361] 3 MV Tandem accelerator system. https://tandem.nipne.ro/~agata/grup/technical_specifications_3MV_Tandem.PDF, (accessed 12-2015.).
[362] R. Middleton, A survey of negative ions from a cesium sputter source, Nuclear Instruments and Methods 144(3) (1977) 373-399.
[363] C. Tuniz, W. Kutschera, D. Fink, G.F. Herzog, J.R. Bird, Accelerator Mass Spectrometry: Ultrasensitive Analysis for Global Science, Taylor & Francis1998.
[364] B. Schmidt, K. Wetzig, Ion Beams in Materials Processing and Analysis, Springer Vienna2012.
[365] D. W. Clark, Ion Irradiation Characterization Studies of MAX Phase Ceramics. , Nuclear Engineering, University of Tennessee, Knoxville, TN, 2015.
[366] Author, FeCrAl alloy, Journal Volume(Issue) (2003) US6569221B2.
[367] J. C. Haley, S. A. Briggs, P. D. Edmondson, K. Sridharan, S. G. Roberts, S. Lozano-Perez, K. G. Field, Dislocation loop evolution during in-situ ion FeCrAl alloys, Acta Materialia 136 (2017) 390-401.
[368] X. Gu, L. Q. Xing, T. C. Hufnagel, Glass-forming ability and crystallization of bulk metallic glass (Hf_xZr_{1-x})(52.5)Cu-17.9Ni14.6Al10Ti5, Journal of Non-Crystalline Solids 311(1) (2002) 77-82.
[369] P. J. Doyle, K. M. Benensky, S. J. Zinkle, Modeling the impact of radiation-enhanced diffusion on implanted ion profiles, Journal of Nuclear Materials 509 (2018) 168-180.
[370] W. G. Wolfer, Vacancy cluster evolution in metals under irradiation AU - Wehner, M. F, Philosophical Magazine A 52(2) (1985) 189-205.
[371] S. J. Zinkle, L. L. Snead, Opportunities and limitations for ion beams in radiation effects studies: Bridging critical gaps between charged particle and neutron irradiations, Scripta Materialia 143 (2018) 154-160.
[372] J. B. Whitley, P. Wilkes, G. L. Kulcinski, H. V. Smith Jr., DEPTH DEPENDENT DAMAGE PROFILE IN NICKEL IRRADIATED WITH NICKEL OR COPPER IONS, Journal of Nuclear Materials 79(1) (1979) 159-169.
[373] M. L. Crespillo, J. T. Graham, Y. Zhang, W. J. Weber, Temperature measurements during high flux ion beam irradiations, Review of Scientific Instruments 87(2) (2016) 7.
[374] M. L. Crespillo, J. T. Graham, Y. Zhang, W. J. Weber, Insitu luminescence monitoring of ion-induced damage evolution in SiO_2 and Al_2O_3, J. Lumin 127 (2016) 208-218.
[375] M. Koehler, C. Taylor, M. Patel, PANalytical Empyrean: Powder XRD procedure manual The University of Tennessee, Knoxville, TN, 2017.
[376] M. F. Toney, T. C. Huang, S. Brennan, Z. Rek, X-ray depth profiling of iron oxide thin films, J. Mater. Res. 3(2) (1988) 351-356.

[377] C. M. Parish, N. A. P. Kiran Kumar, L. L. Snead, P. D. Edmondson, K. G. Field, C. Silva, A. M. Williams, K. Linton, K. J. Leonard, Lamda: Irradiated-materials microscopy at Oak Ridge National Laboratory, Microsc. Microanal. 21 (2015) 1003-1004.
[378] P. Jia, Z. D. Zhu, E. Ma, J. Xu, Notch toughness of Cu-based bulk metallic glasses, Scripta Materialia 61(2) (2009) 137-140.
[379] D. W. Clark, S. J. Zinkle, M. K. Patel, C. M. Parish, High temperature ion irradiation effects in MAX phase ceramics, Acta Materialia 105 (2016) 130-146.
[380] S. Attaway, Matlab: A Practical Introduction to Programming and Problem Solving, Elsevier Science2011.
[381] W.C. Oliver, G.M. Pharr, An improved technique for determining hardness and elastic modulus using load and displacement sensing indentation experiments, J. Mater. Res. 7(6) (1992) 1564-1583.
[382] W.C. Oliver, G.M. Pharr, Measurement of hardness and elastic modulus by instrumented indentation: Advances in understanding and refinements to methodology, J. Mater. Res. 19(1) (2004) 3-20.
[383] N. Xoubi, R. T. Primm, G. I. Maldonado, Loading beryllium targets to extend the high flux isotope reactor's cycle length, Annals of Nuclear Energy 33(8) (2006) 664-672.
[384] David Chandler, G Ivan Maldonado, Trent Primm, Reactivity Accountability Attributed to Reflector Poisons in the High Flux Isotope Reactor, ; Oak Ridge National Lab. (ORNL), Oak Ridge, TN (United States); High Flux Isotope Reactor, 2009, p. Medium: ED.
[385] Germina Ilas, David Chandler, Brian J Ade, Eva E Sunny, Benjamin R Betzler, Daniel Pinkston, Modeling and Simulations for the High Flux Isotope Reactor Cycle 400, ; Oak Ridge National Lab. (ORNL), Oak Ridge, TN (United States). High Flux Isotope Reactor (HFIR), 2015, p. Medium: ED; Size: 136 p.
[386] F. T. Binford, E. N. Cramer, THE HIGH FLUX ISOTOPE REACTOR. VOLUME 1. A FUNCTIONAL DESCRIPTION, ; Oak Ridge National Lab., Tenn., 1964, p. Medium: ED; Size: Pages: 378.
[387] Not Available, Operating manual for the High Flux Isotope Reactor. Volume I. Description of the facility, ; Oak Ridge National Lab., TN (USA), 1982, p. Medium: ED; Size: Pages: 484.
[388] J.C. Griess, H.C. Savage, J.L. English, EFFECT OF HEAT FLUX ON THE CORROSION OF ALUMINUM BY WATER. PART IV. TESTS RELATIVE TO THE ADVANCED TEST REACTOR AND CORRELATION WITH PREVIOUS RESULTS, ; Oak Ridge National Lab., Tenn., 1964, p. Medium: ED; Size: Pages: 37.
[389] S. Calder, K. An, R. Boehler, C. R. Dela Cruz, M. D. Frontzek, M. Guthrie, B. Haberl, A. Huq, S. A. J. Kimber, J. Liu, J. J. Molaison, J. Neuefeind, K. Page, A. M. dos Santos, K. M. Taddei, C. Tulk, M. G. Tucker, A suite-level review of the neutron powder diffraction instruments at Oak Ridge National Laboratory, Review of Scientific Instruments 89(9) (2018) 092701.
[390] D.L. Price, F. Fernandez-Alonso, Neutron Scattering – Fundamentals: Chapter 1. An Introduction to Neutron Scattering, Elsevier Science2013.
[391] Jörg Neuefeind, Mikhail Feygenson, John Carruth, Ron Hoffmann, Kenneth K. Chipley, The Nanoscale Ordered MAterials Diffractometer NOMAD at the Spallation Neutron Source SNS, Nuclear Instruments and Methods in Physics Research Section B: Beam Interactions with Materials and Atoms 287 (2012) 68-75.

[392] O.R.N.L., Nanoscale-Ordered Materials Diffractometer NOMAD | BL-1B | SNS. https://neutrons.ornl.gov/nomad, (accessed 8-1-2018.).
[393] P. F. Peterson, M. Gutmann, Th. Proffen, S. J. L. Billinge, PDFgetN: a user-friendly program to extract the total scattering structure factor and the pair distribution function from neutron powder diffraction data, J. Appl. Crystallogr. 33(4) (2000) 1192-1192.
[394] A. K. Soper, Computer simulation as a tool for the interpretation of total scattering data from glasses and liquids, Molecular Simulation 38(14-15) (2012) 1171-1185.
[395] M. N. Gussev, K. G. Field, J. T. Busby, Deformation localization and dislocation channel dynamics in neutron-irradiated austenitic stainless steels, Journal of Nuclear Materials 460 (2015) 139-152.
[396] A. P. Hammersley, S. O. Svensson, A. Thompson, H. Graafsma, A. Kvick, J. P. Moy, Calibration and correction of distortions in 2D detector systems, Rev. Sci. Instr. 66 (1995) 2729-2733.
[397] Peter Hedström, Deformation and martensitic phase transformation in stainless steels, Luleå University of Technology, Luleå, Sweden, 2007.
[398] Z. Zhang, V. Keppens, P. K. Liaw, Y. Tokoyama, A. Inoue, Elastic properties of Zr-based bulk metallic glasses studied by resonant ultrasound spectroscopy, J. Mater. Res. 22(2) (2007) 364-367.
[399] Z. X. Wang, D. Q. Zhao, M. X. Pan, P. Wen, W. H. Wang, T. Okada, W. Utsumi, Crystallization mechanism of Cu-based supercooled liquid under ambient and high pressure, Physical Review B 69(9) (2004) 4.
[400] Thomas Degen, Mustapha Sadki, Egbert Bron, Uwe König, Gwilherm Nénert, The HighScore suite, Powder Diffraction 29(S2) (2014) S13-S18.
[401] B. H. Toby, R. B. Von Dreele, GSAS-II: the genesis of a modern open-source all purpose crystallography software package, J. Appl. Crystallogr. 46 (2013) 544-549.
[402] V. Pecharsky, P. Zavalij, Fundamentals of Powder Diffraction and Structural Characterization of Materials, Second Edition, Springer US2008.
[403] National Institute of Standards and Technology, SRM 640e - Line Position and Line Shape Standard for Powder Diffraction (Silicon Powder). https://www-s.nist.gov/srmors/view_detail.cfm?srm=640E).
[404] Gesswein, Ney Vulcan® Furnaces. https://www.gesswein.com/p-1622-ney-vulcan-furnaces.aspx?gclid=EAIaIQobChMIobf5maPI4AIVSUsNCh1XBwVDEAQYAiABEgIhUfD_BwE, (accessed 12-3-2018.).
[405] Zahid Hussain, Fahad A. Al-Mufadi, Sivasankaran Subbarayan, Osama M. Irfan, Microstructure and mechanical properties investigation on nanostructured Nickel 200 alloy using multi-axial forging, Materials Science and Engineering: A 712 (2018) 772-779.
[406] S. M. Pincus, Approximate entropy as a measure of system complexity, Proc. Natl. Acad. Sci. 88 (1991) 2297-2301.
[407] S. M. Myers, Nuclear-reaction analysis of helium-3 and tritium in tritium-exposed austenitic steels, United States, 1987, p. 11.
[408] Shradha Agarwal, Helium mobility in advanced nuclear ceramics, Universite Paris-Sud, France, 2014.
[409] Xunxiang Hu, Kevin G. Field, Stephen Taller, Yutai Katoh, Brian D. Wirth, Impact of neutron irradiation on thermal helium desorption from iron, Journal of Nuclear Materials 489 (2017) 109-117.

[410] S. Miro, J. M. Costantini, J. Haussy, L. Beck, S. Vaubaillon, S. Pellegrino, C. Meis, J. J. Grob, Y. Zhang, W. J. Weber, Nuclear reaction analysis of helium migration in silicon carbide, Journal of Nuclear Materials 415(1) (2011) 5-12.
[411] M. Mayer, SIMNRA User's Guide, Max-Planck-Institut für Plasmaphysik, Garching, Germany, 1997.
[412] M. Mayer, SIMNRA User's Guide, Max-Planck-Institut für Plasmaphysik, Garching, Germany, 2017.
[413] J. M. Costantini, P. Trocellier, J. Haussy, J. J. Grob, Nuclear reaction analysis of helium diffusion in britholite, Nuclear Instruments & Methods in Physics Research Section B-Beam Interactions with Materials and Atoms 195(3-4) (2002) 400-407.
[414] J. M. Costantini, J. J. Grob, J. Haussy, P. Trocellier, P. Trouslard, Nuclear reaction analysis of helium migration in zirconia, Journal of Nuclear Materials 321(2-3) (2003) 281-287.
[415] S. Agarwal, P. Trocellier, D. Brimbal, S. Vaubaillon, An experimental study of helium diffusion and helium induced microstructural evolution in ion implanted polycrystalline titanium nitride, Acta Materialia 121 (2016) 1-14.
[416] S. Agarwal, P. Trocellier, S. Vaubaillon, S. Miro, Diffusion and retention of helium in titanium carbide, Journal of Nuclear Materials 448(1) (2014) 144-152.
[417] S. Agarwal, P. Trocellier, Y. Serruys, S. Vaubaillon, S. Miro, Helium mobility in advanced nuclear ceramics, Nuclear Instruments and Methods in Physics Research Section B: Beam Interactions with Materials and Atoms 327 (2014) 117-120.
[418] M. Nastasi, J.W. Mayer, Y. Wang, Ion Beam Analysis: Fundamentals and Applications, Taylor & Francis2014.
[419] A. G. Perez-Bergquist, H. Bei, Y. Zhang, S. J. Zinkle, Effects of ion irradiation on BAM-11 bulk metallic glass, Fusion Materials Semiannual Progress Report for Period Ending June 30, 2013, DOE/ER- 0313/54, U.S. Department of Energy, 154., 2013.
[420] A. G. Perez-Bergquist, J. Brechtl, H. Bei, Y. Zhang, S. J. Zinkle, Effects of ion irradiation on bam-11 bulk metallic glass, Fusion Materials Semiannual Progress Report for Period Ending June 30, 2014, DOE/ER- 0313/56, U.S. Department of Energy, 184., 2014.
[421] M. Apreutesei, P. Steyer, L. Joly-Pottuz, A. Billard, J. Qiao, S. Cardinal, F. Sanchette, J. M. Pelletier, C. Esnouf, Microstructural, thermal and mechanical behavior of co-sputtered binary Zr–Cu thin film metallic glasses, Thin Solid Films 561 (2014) 53-59.
[422] R. J. Furlan, G. Bambakidis, J. S. Cantrell, R. C. Bowman, A. J. Maeland, THERMAL STABILITIES OF THE CRYSTALLINE AND AMORPHOUS TIYCUHX SYSTEMS, Journal of the Less-Common Metals 116(2) (1986) 375-388.
[423] X. L. Yan, X. Q. Chen, A. Grytsiv, P. Rogl, R. Podloucky, V. Pomjakushin, H. Schmidt, G. Giester, Crystal structure, phase stability and elastic properties of the Laves phase ZrTiCu2, Intermetallics 16(5) (2008) 651-657.
[424] L. E. Samuels, T. O. Mulhearn, AN EXPERIMENTAL INVESTIGATION OF THE DEFORMED ZONE ASSOCIATED WITH INDENTATION HARDNESS IMPRESSIONS, J. Mech. Phys. Solids 5(2) (1957) 125-134.
[425] M.E. Kirkpatrick, W.L. Larsen, PHASE RELATIONSHIPS IN THE NICKEL-ZIRCONIUM AND NICKEL-HAFNIUM ALLOY SYSTEMS, Trans. Am. Soc. Metals (1961) Medium: X; Size: Pages: 580-90.
[426] V. Swamy, L. S. Dubrovinsky, N. A. Dubrovinskaia, F. Langenhorst, A. S. Simionovici, M. Drakopoulos, V. Dmitriev, H. P. Weber, Size effects on the structure and phase transition behavior of baddeleyite TiO2, Solid State Communications 134(8) (2005) 541-546.

[427] Tim Burgess, M. Ferry, Nanoindentation of metallic glasses, Materials Today 12(1) (2009) 24-32.
[428] Binbin Wang, Liangshun Luo, Enyu Guo, Yanqing Su, Mingyue Wang, Robert O. Ritchie, Fuyu Dong, Liang Wang, Jingjie Guo, Hengzhi Fu, Nanometer-scale gradient atomic packing structure surrounding soft spots in metallic glasses, npj Computational Materials 4(1) (2018) 41.
[429] J. Brechtl, M. L. Crespillo, T. Yang, H. Wang, J. Salasin, I. Gussev, L. Mora, Y. Zhang, H. Bei, J. Neuefeind, W. Dmowski, T. Egami, M. Lang, S. J. Zinkle, Effects of irradiation and annealing on the microstructure and mechanical properties of bulk metallic glass alloys Fusion Materials Semiannual Progress Report for Period Ending June 30, 2017, DOE/ER-0313/62, U.S. Department of Energy., 2017.
[430] Fukumoto Yuka, Ishii Akito, Iwase Akihiro, Yokoyama Yoshihiko, Hori Fuminobu, Behavior of free volume in ZrCuAl bulk metallic glass after irradiation, Journal of Physics: Conference Series 225(1) (2010) 012010.
[431] F. Hori, N. Onodera, Y. Fukumoto, A. Ishii, A. Iwase, A. Kawasuso, A. Yabuuchi, M. Maekawa, Y. Yokoyama, A study of defects in electron- and ion-irradiated ZrCuAl bulk glassy alloy using positron annihilation techniques, in: S.J. Buckman, J.P. Sullivan, C. Makochekanwa, R. White (Eds.), 12th International Workshop on Slow Positron Beam Techniques, Iop Publishing Ltd, Bristol, 2011.
[432] T. Nagase, T. Sanda, A. Nino, W. Qin, H. Yasuda, H. Mori, Y. Umakoshi, J. A. Szpunar, MeV electron irradiation induced crystallization in metallic glasses: Atomic structure, crystallization mechanism and stability of an amorphous phase under the irradiation, Journal of Non-Crystalline Solids 358(3) (2012) 502-518.
[433] G. Q. Xie, Q. S. Zhang, D. V. Louzguine-Luzgin, W. Zhang, A. Inoue, Nanocrystallization of Cu50Zr45Ti5 metallic glass induced by electron irradiation, Materials Transactions 47(8) (2006) 1930-1933.
[434] E. G. Fu, J. Carter, M. Martin, G. Xie, X. Zhang, Y. Q. Wang, R. Littleton, L. Shao, Electron irradiation-induced structural transformation in metallic glasses, Scripta Materialia 61(1) (2009) 40-43.
[435] E. G. Fu, J. Carter, M. Martin, G. Q. Xie, X. Zhang, Y. Q. Wang, R. Littleton, S. McDeavitt, L. Shao, Ar-ion-milling-induced structural changes of Cu50Zr45Ti5 metallic glass, Nuclear Instruments & Methods in Physics Research Section B-Beam Interactions with Materials and Atoms 268(6) (2010) 545-549.
[436] Na Chen, Laura Martin, Dmitri V. Luzguine-Luzgin, Akihisa Inoue, Role of Alloying Additions in Glass Formation and Properties of Bulk Metallic Glasses, Materials (Basel, Switzerland) 3(12) (2010) 5320-5339.
[437] Takeshi Nagase, Yukichi Umakoshi, Electron Irradiation Induced Crystallization of the Amorphous Phase in Zr-Cu Based Metallic Glasses with Various Thermal Stability, MATERIALS TRANSACTIONS 45(1) (2004) 13-23.
[438] I. V. Lyasotskyi, N. B. Dyakonova, D. L. Dyakonov, V. S. Kraposhin, Quasiperiodic and Frank-Kasper phases formation during primary crystallization of Fe-base amorphous alloys, in: P.S. Popel (Ed.), 13th International Conference on Liquid and Amorphous Metals, Iop Publishing Ltd, Bristol, 2008.
[439] G. Dearnaley, Ion Implantation, North-Holland Publishing Company1973.
[440] N. Van Steenberge, S. Hobor, S. Surinach, A. Zhilyaev, F. Houdellier, F. Mompiou, M. D. Baro, A. Revesz, J. Sort, Effects of severe plastic deformation on the structure and thermo-

mechanical properties of Zr55Cu30Al10Ni5 bulk metallic glass, Journal of Alloys and Compounds 500(1) (2010) 61-67.
[441] N. Ismail, M. Uhlemann, A. Gebert, J. Eckert, Hydrogenation and its effect on the crystallisation behaviour of Zr55Cu30Al10Ni5 metallic glass, Journal of Alloys and Compounds 298(1-2) (2000) 146-152.
[442] J. Fornell, N. Van Steenberge, A. Varea, E. Rossinyol, E. Pellicer, S. Surinach, M. D. Baro, J. Sort, Enhanced mechanical properties and in vitro corrosion behavior of amorphous and devitrified Ti40Zr10Cu38Pd12 metallic glass, Journal of the Mechanical Behavior of Biomedical Materials 4(8) (2011) 1709-1717.
[443] Wenbo Dong, Haifeng Zhang, Wensheng Sun, Bingzhe Ding, Zhuangqi Hu, Formation, Thermal Stability and Mechanical Properties of Zr-Nb-Cu-Ni-Al Bulk Metallic Glasses, MATERIALS TRANSACTIONS 47(5) (2006) 1294-1298.
[444] Y. Z. Yang, P. J. Tao, G. Q. Li, Z. X. Mu, Q. Ru, Z. W. Xie, X. C. Chen, Effects of ion implantation on surface structures and properties for bulk metallic glass, Intermetallics 17(9) (2009) 722-726.
[445] P. J. Tao, Y. Z. Yang, X. J. Bai, Z. X. Mu, G. Q. Li, Z. W. Xie, X. C. Chen, Study on implantation of Co ions in ZrCuNiAl bulk metallic glass, Surf. Coat. Technol. 203(12) (2009) 1656-1659.
[446] X. N. Zhang, X. X. Mei, X. Ma, Y. M. Wang, J. B. Qiang, Y. N. Wang, Ar12+ Induced Irradiation Damage in Bulk Metallic Glass (Cu47Zr45Al8)(98.5)Y-1.5, Chin. Phys. Lett. 32(2) (2015) 5.
[447] K. Zhao, X. X. Xia, H. Y. Bai, D. Q. Zhao, W. H. Wang, Room temperature homogeneous flow in a bulk metallic glass with low glass transition temperature, Applied Physics Letters 98(14) (2011) 141913.
[448] W. Dmowski, C. Fan, M. L. Morrison, P. K. Liaw, T. Egami, Structural changes in bulk metallic glass after annealing below the glass-transition temperature, Mater. Sci. Eng. A-Struct. Mater. Prop. Microstruct. Process. 471(1-2) (2007) 125-129.
[449] W. H. Jiang, F. X. Liu, H. Choo, P. K. Liaw, Effect of structural relaxation on mechanical behavior of a Zr-based bulk-metallic glass, Materials Transactions 48(7) (2007) 1781-1784.
[450] J. Pan, Y. X. Wang, Q. Guo, D. Zhang, A. L. Greer, Y. Li, Extreme rejuvenation and softening in a bulk metallic glass, Nature Communications 9(1) (2018) 560.
[451] T. Egami, S. J. Poon, Z. Zhang, V. Keppens, Glass transition in metallic glasses: A microscopic model of topological fluctuations in the bonding network, Physical Review B 76(2) (2007) 6.
[452] D. Srolovitz, K. Maeda, V. Vitek, T. Egami, Structural defects in amorphous solids Statistical analysis of a computer model, Philosophical Magazine A 44(4) (1981) 847-866.
[453] W. H. Wang, Y. Yang, T. G. Nieh, C. T. Liu, On the source of plastic flow in metallic glasses: Concepts and models, Intermetallics 67 (2015) 81-86.
[454] W. Li, H. Bei, Y. Tong, W. Dmowsk, Y. F. Gao, Structural heterogeneity induced plasticity in bulk metallic glasses: From well-relaxed fragile glass to metal-like behavior, Appl. Phys. Lett. 103 (2013).
[455] J. Ketkaew, M. Fan, M. D. Shattuck, C. S. O'Hern, J. Schroers, Structural relaxation kinetics defines embrittlement in metallic glases, Scripta Materialia 149 (2018) 21-25.
[456] X. L. Bian, G. Wang, H. C. Chen, L. Yan, J. G. Wang, Q. Wang, P. F. Hu, J. L. Ren, K. C. Chan, N. Zheng, A. Teresiak, Y. L. Gao, Q. J. Zhai, J. Eckert, J. Beadsworth, K. A.

Dahmen, P. K. Liaw, Manipulation of free volumes in a metallic glass through Xe-ion irradiation, Acta Materialia 106 (2016) 66-77.
[457] T. Egami, Mechanical failure and glass transition in metallic glasses, Journal of Alloys and Compounds 509 (2011) S82-S86.
[458] W. Li., Y. Gao, H. Bei, On the correlation between microscopic structural heterogeneity and embrittlement behavior in metallic glasses, Scientific Reports 5 (2015).
[459] J. M. Halley, P. Inchausti, The increasing importance of 1/f-noises as models of ecological variability, Fluctuation and Noise Letters 4(2) (2004) R1-R26.
[460] B. Yuan, J.-J. Li, J.-W. Qiao, Statistical analysis on strain-rate effects during serrations in a Zr-based bulk metallic glass, Journal of Iron and Steel Research, International 24 (2017) 455-461.
[461] T. Egami, V. Vitek, Local structural fluctuations and defects in metallic glasses, Journal of Non-Crystalline Solids 61-2(JAN) (1984) 499-510.
[462] W. Zheng, Y. J. Huang, G. Y. Wang, P. K. Liaw, J. Shen, Influence of Strain Rate on Compressive Deformation Behavior of a Zr-Cu-Ni-Al Bulk Metallic Glass at Room Temperature, Metall. Mater. Trans. A-Phys. Metall. Mater. Sci. 42A(6) (2011) 1491-1498.
[463] O. El-Atwani, C. N. Taylor, J. Frishkoff, W. Harlow, E. Esquivel, S. A. Maloy, M. L. Taheri, Thermal desorption spectroscopy of high fluence irradiated ultrafine and nanocrystalline tungsten: helium trapping and desorption correlated with morphology, Nucl. Fusion 58(1) (2018) 14.
[464] C. N. Taylor, M. Shimada, B. J. Merrill, Deuterium retention and blistering in tungsten foils, Nuclear Materials and Energy 12 (2017) 689-693.
[465] W. Schirmacher, M. Prem, J. B. Suck, A. Heidemann, Anomalous diffusion of hydrogen in amorphous metals, Europhys. Lett. 13(6) (1990) 523-529.
[466] V. O. Altemose, Helium Diffusion through Glass, Journal of Applied Physics 32(7) (1961) 1309-1316.

VITA

Jamieson Brechtl is currently a PhD student in the Bredesen Center for Interdisciplinary Research and Graduate Education at the University of Tennessee. Here he is studying the effects of irradiation and annealing on the microstructure and mechanical properties of bulk metallic glasses while under the supervision of Dr. Steven Zinkle. So far, his work during his PhD research has resulted in four first author publications and three Department of Energy Semi-annual progress reports. Additionally, he has two papers which are currently under review. He is also currently working on 6 first author publications which are in the process of being completed for submission. Prior to becoming a PhD student, Jamieson was pursuing his Master's at the University of Wisconsin-Madison where he studied the electrophoretic deposition of metallic and ceramic coatings for application in sodium cooled fast reactors. While there, his work contributed to 4 publications and a best student poster award at the Nuclear Fuels and Structural Materials conference in 2012.